

REPORT DOCUMENTATION PAGE

1a. REPORT SECURITY CLASSIFICATION Unclassified			1b. RES	
2a. SECURITY CLASSIFICATION AUTHORITY			3. DISTI App AFRL-SR-BL-TR-00- Dist 0695	
2b. DECLASSIFICATION / DOWNGRADING SCHEDULE			4. PERFORMING ORGANIZATION REPORT NUMBER(S) RU-TR-MAE-204-F	
4. PERFORMING ORGANIZATION REPORT NUMBER(S) RU-TR-MAE-204-F			5. MONITORING ORGANIZATION REPORT NUMBER(S)	
6a. NAME OF PERFORMING ORGANIZATION Dept. Mech and Aero Eng Rutgers University		6b. OFFICE SYMBOL (If applicable)		7a. NAME OF MONITORING ORGANIZATION Air Force Office of Scientific Research
6c. ADDRESS (City, State, and ZIP Code) 98 Brett Road Piscataway, NJ 08854-8058		7b. ADDRESS (City, State, and ZIP Code) 801 N. Randolph Street Arlington, VA 22203-1977		
8a. NAME OF FUNDING / SPONSORING ORGANIZATION Air Force Office of Sci Res		8b. OFFICE SYMBOL (If applicable)		9. PROCUREMENT INSTRUMENT IDENTIFICATION NUMBER F49620-99-1-0159
8c. ADDRESS (City, State, and ZIP Code) 801 N. Randolph Street Arlington, VA 22203-1977		10. SOURCE OF FUNDING NUMBERS		
		PROGRAM ELEMENT NO. 2307AS	PROJECT NO.	TASK NO. WORK UNIT ACCESSION NO.
11. TITLE (Include Security Classification) unclassified Second Air Force Office of Scientific Research Conference on DNS and LES				
12. PERSONAL AUTHOR(S)				
13a. TYPE OF REPORT Final		13b. TIME COVERED FROM 99/03/01 TO 99/09/30		14. DATE OF REPORT (Year, Month, Day) 99/08/12
15. PAGE COUNT 512				
16. SUPPLEMENTARY NOTATION				
17. COSATI CODES			18. SUBJECT TERMS (Continue on reverse if necessary and identify by block number)	
FIELD	GROUP	SUB-GROUP	Direct Numerical Simulation, Large Eddy Simulation, Turbulence	
19. ABSTRACT (Continue on reverse if necessary and identify by block number)				
<p>The report contains the papers presented at the Second AFOSR International Conference on DNS and LES, held at Rutgers University on June 7-9, 1999.</p>				
20. DISTRIBUTION / AVAILABILITY OF ABSTRACT <input type="checkbox"/> UNCLASSIFIED/UNLIMITED <input type="checkbox"/> SAME AS RPT. <input type="checkbox"/> DTIC USERS			21. ABSTRACT SECURITY CLASSIFICATION	
22a. NAME OF RESPONSIBLE INDIVIDUAL			22b. TELEPHONE (Include Area Code)	22c. OFFICE SYMBOL

20010109 046

Recent Advances in DNS and LES

Proceedings of the
Second AFOSR International Conference
on DNS and LES

Held at

Rutgers - The State University of New Jersey
New Brunswick, New Jersey
June 7-9, 1999

Edited by

Doyle Knight
Department of Mechanical and
Aerospace Engineering
Rutgers University
98 Brett Road
Piscataway, NJ 08854

Leonidas Sakell
US Air Force Office of
Scientific Research
AFOSR/NM
801 N. Randolph Street
Arlington, VA 22203

DISTRIBUTION STATEMENT A
Approved for Public Release
Distribution Unlimited

PREFACE

The Second AFOSR International Conference on Direct Numerical Simulation (DNS) and Large Eddy Simulation (LES) was held at Rutgers University on June 7-9, 1999. The conference was sponsored by the Air Force Office of Scientific Research (AFOSR) and Rutgers - The State University of New Jersey. The conference continued the tradition established at the First AFOSR International Conference on DNS and LES organized by Prof. Chaoqun Liu of Louisiana Tech University at Ruston, Louisiana, in August 1997. Six invited papers and thirty-nine contributed papers were presented during the two and one-half day conference. The program covered a broad range of topics in DNS and LES, and provided a state-of-the art assessment of this exciting field to the seventy-four attendees.

I would like to thank Dr. Len Sakell (AFOSR) for his continued support of the conference. I wish to thank the members of the Scientific Organizing Committee which selected the invited speakers and reviewed the contributed papers. I also wish to express my sincere appreciation to the Local Organizing Committee who assisted in the multiplicity of tasks associated with the conduct of the conference. Finally, I would like to thank Rutgers University for its hospitality and support of the conference.

Doyle Knight
Conference Chairperson

TABLE OF CONTENTS

Invited Papers

Large Eddy Simulations of Incompressible and Compressible Shear Flows	
P. Comte	1
Direct Numerical Simulation of Turbulent Compressible and Incompressible Wall-Bounded Shear Flows	
R. Friedrich, R. Lechner, J. Sesterhenn and T. Hüttl	13
Direct Navier-Stokes Simulation of Sounds Generated by Shock-Vortex/Vortex-Vortex Interaction	
O. Inoue	27
Optimal LES: How Good Can an LES Be?	
R. Moser, J. Langford and S. Völker	37
DNS to Help Understanding of Non-Premixed Turbulent Flames	
L. Vervisch	49

Contributed Papers

Modelling of the Length Scale and Variance of Subgrid Quantities in a Turbulent Channel Flow	
K. Alvelius and A. Johansson	61
DNS of Compressible Reacting Mixing Layers With Parallel Compact Scheme	
X. Cai and F. Ladeinde	73
Large Eddy Simulation of Stationary Premixed Flames using a Subgrid Flamelet Approach	
V. Chakravarthy and S. Menon	85
On the Use of LES with a Dynamic Subgrid Scale Model for Optimal Control of Wall Bounded Turbulence	
S. Collis and Y. Chang	99
Robustness of Flow Phenomena in a Spatially Developing Turbulent Mixing Layer	
I. deBruin, B. Guerts, C. Driesen and J. Kuerten	111
The Subgrid-Scale Estimation Model	
J. Domaradzki and K.-C. Loh	121

Direct Numerical Simulation of Transitions Toward Turbulence in Complex Channel Flows	
B. Duncan and K. Ghia	133
Implementation of an SGS model in a B-Spline Spectral Method and LES of a Turbulent Axial Vortex	
B. Eshpuniyani and G. Blaisdell	143
Large Eddy Simulation of Scalar Transport in a Turbulent Jet Flow	
S. Garrick, F. Jaber and P. Givi	155
DNS and Modeling of Spray Turbulent Mixing	
R. Hauguel, J. Réveillon and L. Vervisch	167
Assessment of the Generalized Scale-Similarity Model in Homogeneous Turbulence Subjected to Rotation	
K. Horiuti	179
Direct Numerical Simulation of Turbulent Flame Kernels	
K. Jenkins and R. Cant	191
Direct Numerical Simulation of Boundary Layer Receptivity for Subsonic Flow Around Airfoil	
L. Jiang, H. Shan and C. Liu	203
High-Order Non-Reflecting Boundary Conditions in Curvilinear Coordinates	
L. Jiang, H. Shan, C. Liu and M. Visbal	219
Modulation and Subgrid Scale Modeling of Gas-Particle Turbulent Flow	
T. Kajishima, S. Takiguchi and Y. Miyake	235
Large Eddy Simulation using Unstructured Spectral/HP Elements	
G.-S. Karamanos, S. Sherwin and J. Morrison	245
Numerical Modeling of Fuel/Air Mixing in a Dry Low-Emission Premixer	
W.-W. Kim and S. Menon	257
Dynamic Inverse Modeling in LES of the Temporal Mixing Layer	
J. Kuerten, B. Guerts and R. van Buuren	269
Comparison of the ENO and Compact Schemes for DNS/LES of Turbulence	
F. Ladeinde, X. Cai, M. Visbal and D. Gaitonde	279
DNS for Flow Past a 3D Flexible Wing	
I. Lomtev, R. Kirby and G. Karniadakis	291
DNS of a Mach 4 Reacting Turbulent Boundary Layer	
M. P. Martin and G. Candler	305

Accounting for Scale-Dependence in the Dynamic Smagorinsky Model	
C. Meneveau, F. Porté-Agel and M. Parlange	317
Direct Numerical Simulation of High Subsonic Jets	
F. Owis and P. Balakumar	329
Generation of a One-Parameter Family of Residuals for the Filtered Equations of Fluid Motion	
G. Pantelis	341
Multiblock Large Eddy Simulations of Turbulent Boundary Layers	
A. Pascarelli, U. Piomelli and G. Candler	349
Eulerian Time-Domain Filtering for Spatial LES	
C. Pruett	361
DNS of a Turbulent Boundary Layer Under a Strong Adverse Pressure Gradient	
M. Skote and D. Henningson	373
A High-Order Accurate Compact Difference Algorithm for the Incompressible Navier-Stokes Equations	
R. Steijl and H. Hoeijmakers	385
Large Eddy Simulation of Turbulent Flow Around a Circular Cylinder with Non-Eddy Viscosity SGS Model	
M. Su and Q. Kang	397
Direct Numerical Simulation of the Micro-Fluid Dynamics of Acoustic Liners	
C. Tam and K. Kurbatskii	407
Direct Numerical Simulation of Expanding Compressible Flows	
T. Treurniet and F. Nieuwstadt	419
Large Eddy Simulation of Rectangular Jets in Crossflow: Effect of Hole Aspect Ratio	
M. Tyagi and S. Acharya	431
Compressible Large Eddy Simulation Using Unstructured Grid: Supersonic Boundary Layer	
G. Urbin and D. Knight	443
The Stretched-Vortex SGS Model in Physical Space	
T. Voelkl, D. Pullin and R. Henderson	459
Application and Comparison of Two SGS models in Large Eddy Simulation of Free Turbulent Jet Flow	
H. Yan and M. Su	465

Direct Numerical Simulation of Görtler Instability in Hypersonic Boundary Layers	
C. Whang and X. Zhong	473
Study on Transportation of Passive Scalar in Shearless Mixing Layer by Large Eddy Simulation	
Z. Zhang, Y. Chen, G. Cui, C. Xu, L. Shao and J. Bertoglio	485
DNS of Boundary Layer Receptivity to Freestream Sound for Hypersonic Flow Over Blunt Elliptical Cones	
X. Zhong	493
 <i>Personnel</i>	
Scientific Organizing Committee	505
Local Organizing Committee	506
Conference Participants	507

LARGE-EDDY SIMULATIONS OF COMPRESSIBLE SHEAR FLOWS

P. COMTE

LEGI/IMG, BP 53, F38041 Grenoble cedex 9, FRANCE

e-mail: Pierre.Comte@hmg.inpg.fr

IMF, 2 rue Boussingault, F67000 Strasbourg, FRANCE

(as from September 1999)

Abstract. LES of compressible boundary layers performed with a variable-density extension of the *filtered* and *selective structure-function* models presented in Lesieur & Métais, 1996, *Ann. Rev. Fluid Mech.*, **28**, 45-82). Quasi-incompressible transitional boundary layers show the establishment of a streak system of spanwise spacing $\sim 100w.u.$ well upstream of the peak of skin friction, which bolsters up the explanations in terms of algebraic instabilities (e.g. Landahl, 1980, *J. Fluid Mech.*, **98**, 243-251). A supersonic compression-ramp flow is found to develop Dean-Görtler vortices with intense and quasi-steady spanwise fluctuations of wall heat-flux.

1. Introduction

Large-Eddy Simulations can be seen as an approximative way of reaching larger Reynolds numbers than in DNS with the aid of simple SubGrid Scale turbulence models, namely, eddy-viscosity and eddy-diffusivity models. A straightforward variable-density extension of these models for compressible flows is advocated, in section 2, in the framework of the Navier-Stokes equations in their conservation form, in cartesian or curvilinear co-ordinates. On the other hand, it has been known since Kraichnan (1976) that two-point stochastic closures in the spectral space show a wavenumber dependence due to the absence of separation of scales in developed turbulent energy spectra, a feature which is ignored by most SGS models in the physical space. It can be shown that this "cusp" behaviour, as coined by Kraichnan, can be approximated by combining a regular eddy-viscosity model with a hyperviscosity model. This yields a class of *structure-function* and *generalized hyperviscosity*

models formulated either in the spectral and the physical space, fully described in Lesieur & Métais (1996) and briefly recalled in section 3. Section 4 shows results of a spatially-growing transitional boundary layer at Mach 0.3 performed with the *filtered structure-function* model. Finally, a supersonic isothermal ramp-flow LES performed with the *selective structure-function* model is presented in section 5.

2. Compressible Filtering Procedure

As in the incompressible regime, and whatever the numerical method used, the discretization of the Navier-Stokes equations introduces a cut-off scale Δx which is, in Large-Eddy Simulation, larger than the Kolmogorov scale. This can be accounted for by an implicit low-pass filter of width Δx , characterized by its convolution kernel $G_{\Delta x}(\mathbf{x})$ and denoted $\overline{\cdot}$. This operator $\overline{\cdot}$ commutes with the space and time derivatives in the case of uniform cubic meshes of side Δx . For an ideal gas, the filtered Navier-Stokes equations read, in their conservation form,

$$\frac{\partial \overline{U}}{\partial t} + \frac{\partial \overline{F}_1}{\partial x_1} + \frac{\partial \overline{F}_2}{\partial x_2} + \frac{\partial \overline{F}_3}{\partial x_3} = 0 \quad , \quad (1)$$

with the resolved total energy per unit volume

$$\overline{\rho e} = \overline{\rho C_v T} + \frac{1}{2} \overline{\rho(u_1^2 + u_2^2 + u_3^2)} \quad (2)$$

and the filtered equation of state

$$\overline{p} = \overline{\rho R T} \quad (3)$$

At this level, it is convenient to introduce the density-weighted (or Favre, 1965) filter $\widetilde{\cdot}$ defined, for a given variable ϕ , by $\widetilde{\phi} = \overline{\rho \phi} / \overline{\rho}$. We then have

$$\overline{U} = T(\overline{\rho}, \overline{\rho u_1}, \overline{\rho u_2}, \overline{\rho u_3}, \overline{\rho e}) \quad , \quad (4)$$

and the resolved total energy

$$\overline{\rho e} = \overline{\rho e} = \overline{\rho} C_v \widetilde{T} + \frac{1}{2} \overline{\rho(u_1^2 + u_2^2 + u_3^2)} \quad . \quad (5)$$

The resolved fluxes \overline{F}_i read

$$\overline{F}_i = \begin{pmatrix} \overline{\rho u_i} \\ \overline{\rho u_i u_1} + \overline{p} \delta_{i1} - \overline{\mu S_{i1}} \\ \overline{\rho u_i u_2} + \overline{p} \delta_{i2} - \overline{\mu S_{i2}} \\ \overline{\rho u_i u_3} + \overline{p} \delta_{i3} - \overline{\mu S_{i3}} \\ (\overline{\rho e} + \overline{p}) u_i & - \overline{\mu S_{ij} u_j} - k \frac{\partial T}{\partial x_i} \end{pmatrix} \quad , \quad (6)$$

with the filtered equation of state

$$\bar{p} = \bar{\rho} R \tilde{T} \quad . \quad (7)$$

2.1. THE SIMPLEST POSSIBLE CLOSURE

The usual subgrid-stress tensor $\bar{\bar{\tau}}$ of components

$$\tau_{ij} = -\overline{\rho u_i u_j} + \bar{\rho} \tilde{u}_i \tilde{u}_j \quad (8)$$

is introduced and split into its isotropic and deviatoric parts, the latter being noted $\bar{\bar{\tau}}$:

$$\tau_{ij} = \underbrace{\tau_{ij} - \frac{1}{3} \tau_{ll} \delta_{ij}}_{\tau_{ij}} + \frac{1}{3} \tau_{ll} \delta_{ij} \quad . \quad (9)$$

Equations (6) and (5) then read

$$\bar{F}_i = \begin{pmatrix} \bar{\rho} \tilde{u}_i \\ \bar{\rho} \tilde{u}_i \tilde{u}_1 + (\bar{p} - \frac{1}{3} \tau_{ll}) \delta_{i1} - \tau_{i1} - \frac{\mu S_{i1}}{\bar{\rho}} \\ \bar{\rho} \tilde{u}_i \tilde{u}_2 + (\bar{p} - \frac{1}{3} \tau_{ll}) \delta_{i2} - \tau_{i2} - \frac{\mu S_{i2}}{\bar{\rho}} \\ \bar{\rho} \tilde{u}_i \tilde{u}_3 + (\bar{p} - \frac{1}{3} \tau_{ll}) \delta_{i3} - \tau_{i3} - \frac{\mu S_{i3}}{\bar{\rho}} \\ (\bar{\rho} e + \bar{p}) \tilde{u}_i - \mu S_{ij} u_j - k \frac{\partial T}{\partial x_i} \end{pmatrix} \quad . \quad (10)$$

and

$$\bar{\rho} \tilde{e} = \bar{\rho} C_v \tilde{T} + \frac{1}{2} \bar{\rho} (\tilde{u}_1^2 + \tilde{u}_2^2 + \tilde{u}_3^2) - \frac{1}{2} \tau_{ll} \quad (11)$$

There are two options for the treatment of the uncomputable term τ_{ll} :

- simply neglect it, arguing as in Erlebacher *et al.* (1992) that it can be re-written as $\tau_{ll} = \gamma M_{sgs}^2 \bar{p}$, in which the *subgrid Mach number* M_{sgs} can be expected to be small when M_∞ is small.
- model it, as proposed by Yoshizawa (1986) in a way which is consistent with the model chosen for $\bar{\bar{\tau}}$ (see *e.g.* Moin *et al.*, 1991). Note that this was the initial choice of Erlebacher *et al.* (1987).

We will here choose the first option, as in Normand & Lesieur (1992), bringing another argument: the incompressible LES formalism often involves the *macro-pressure*

$$\varpi = \bar{p} - \frac{1}{3} \tau_{ll} \quad . \quad (12)$$

It thus seems a good idea to re-write equation (11) as

$$\bar{\rho} \tilde{e} = \bar{\rho} C_v \left(\tilde{T} - \frac{1}{2 C_v \bar{\rho}} \tau_{ll} \right) + \frac{1}{2} \bar{\rho} (\tilde{u}_1^2 + \tilde{u}_2^2 + \tilde{u}_3^2) \quad (13)$$

and introduce a *macro-temperature*

$$\vartheta = \tilde{T} - \frac{1}{2C_v \bar{\rho}} \mathcal{T}_{ll} \quad , \quad (14)$$

computable out of \bar{U} thanks to equation (13). The filtered equation of state (7) then reads

$$\begin{aligned} \varpi &= \bar{\rho} R \vartheta + \left(\frac{R}{2C_v} - \frac{1}{3} \right) \mathcal{T}_{ll} \\ &= \bar{\rho} R \vartheta + \frac{3\gamma - 5}{6} \mathcal{T}_{ll} \quad . \end{aligned} \quad (15)$$

Thus, if $\gamma = 5/3$ (monoatomic gases like argon or helium), \mathcal{T}_{ll} does not contribute to equation (15) and ϖ is computable for all Mach numbers. For the other gases, the approximation

$$\varpi \simeq \bar{\rho} R \vartheta \quad (16)$$

is justified when $[(3\gamma - 5)/6] \gamma M_{\text{sgs}}^2 \ll 1$, which is significantly less stringent than $\gamma M_{\text{sgs}}^2 \ll 1$. For diatomic gases and air ($\gamma = 7/5$), the gain in M_{sgs} exceeds a factor of 2.

Considering from now on ϖ computable, it is sensible to involve it in the definition of a subgrid heat-flux vector, noted \mathbf{Q} , of components

$$Q_i = -(\bar{\rho} e + p) u_i + (\bar{\rho} \tilde{e} + \varpi) \tilde{u}_i \quad . \quad (17)$$

Provided acceptable models are proposed for $\bar{\tilde{T}}$ and \mathbf{Q} , the *resolved fluxes* already look more tractable:

$$\bar{F}_i = \begin{pmatrix} \bar{\rho} \tilde{u}_i \\ \bar{\rho} \tilde{u}_i \tilde{u}_1 + \varpi \delta_{i1} - \tau_{i1} - \overline{\mu S_{i1}} \\ \bar{\rho} \tilde{u}_i \tilde{u}_2 + \varpi \delta_{i2} - \tau_{i2} - \overline{\mu S_{i2}} \\ \bar{\rho} \tilde{u}_i \tilde{u}_3 + \varpi \delta_{i3} - \tau_{i3} - \overline{\mu S_{i3}} \\ (\bar{\rho} \tilde{e} + \varpi) \tilde{u}_i & - Q_i - \overline{\mu S_{ij} u_j} - k \frac{\partial T}{\partial x_i} \end{pmatrix} \quad . \quad (18)$$

The remaining non-computable terms are viscous terms, which can be considered of less importance when the Reynolds number is sufficiently large. We therefore simply replace (18) by

$$\bar{F}_i \simeq \begin{pmatrix} \bar{\rho} \tilde{u}_i \\ \bar{\rho} \tilde{u}_i \tilde{u}_1 + \varpi \delta_{i1} - \tau_{i1} - \mu \tilde{S}_{i1} \\ \bar{\rho} \tilde{u}_i \tilde{u}_2 + \varpi \delta_{i2} - \tau_{i2} - \mu \tilde{S}_{i2} \\ \bar{\rho} \tilde{u}_i \tilde{u}_3 + \varpi \delta_{i3} - \tau_{i3} - \mu \tilde{S}_{i3} \\ (\bar{\rho} \tilde{e} + \varpi) \tilde{u}_i & - Q_i - \mu \tilde{S}_{ij} \tilde{u}_j - k \frac{\partial \vartheta}{\partial x_i} \end{pmatrix} \quad , \quad (19)$$

in which μ and k are linked to ϑ through the Sutherland relation and the constant Prandtl number assumption $Pr = C_p \mu(\vartheta)/k(\vartheta) = 0.7$ for air.

The system is finally closed with the aid of variable-density eddy-viscosity and diffusivity models, in the form

$$\tau_{ij} \simeq \bar{\rho} \nu_t \widetilde{S}_{ij} \quad (20)$$

$$Q_i \simeq \bar{\rho} \frac{\nu_t}{Pr_t} \frac{\partial \vartheta}{\partial x_i} \quad (21)$$

in which $\nu_t(\tilde{\mathbf{u}})$ and Pr_t are given by the incompressible models presented in Lesieur (1997) (see also Lesieur & Métais, 1996, for a review). The following LES make use of the *filtered* and *selective structure-function* models, whose definitions are briefly recalled in section 3.

2.2. EXTENSION TO CURVILINEAR CO-ORDINATES

When the domain is no longer cubic or parallelepipedic, it is still convenient to use body-fitted co-ordinates, that is, co-ordinates (ξ_1, ξ_2, ξ_3) such that each boundary of the domain corresponds either to constant ξ_1 , ξ_2 or ξ_3 . An appropriate grid generator can provide a set of vectors $\boldsymbol{\xi}$ which are the co-ordinates of the cell vertices or centres. Assume that the domain (hereafter referred to as “physical domain”) can be remapped onto a cubic domain (called “computational”) meshed with a uniform grid of spacing Δ as in the above sections. Let \mathbf{x} be the co-ordinates of the cell vertices or centres of these cubic meshes. There exists a mapping function \mathbf{h} such that $\boldsymbol{\xi} = \mathbf{h}(\mathbf{x})$ and $\mathbf{x} = \mathbf{h}^{-1}(\boldsymbol{\xi})$. It is characterized by its Jacobian J which satisfies $d\xi_1 d\xi_2 d\xi_3 = J dx_1 dx_2 dx_3$.

To each nodal variable $\phi(\mathbf{x})$ of the “computational” (i.e. cubic) domain corresponds a nodal variable $\psi(\boldsymbol{\xi})$ of “physical” domain, such that $\psi(\boldsymbol{\xi}) = \phi(\mathbf{x})$. Afterwards, the filter $\overline{}$ is applied onto ϕ . It can then be proved that this new operator $\overline{}$, defined in the “physical” domain, commutes with the partial derivatives with respect to ξ_i up to second order (see e.g. Ghosal and Moin, 1995, who coined the expression *Second-Order Commuting Filter*). Straightforward application of the chain rule to (1) yields, after some manipulations (Viviand, 1974)

$$\frac{\partial \hat{U}}{\partial t} + \frac{\partial \hat{F}_1}{\partial \xi_1} + \frac{\partial \hat{F}_2}{\partial \xi_2} + \frac{\partial \hat{F}_3}{\partial \xi_3} = 0 \quad (22)$$

with

$$\hat{U} = \overline{U}/J \quad ; \quad \hat{F}_i = \frac{1}{J} \left[\left(\frac{\partial \xi_i}{\partial x_1} \right) \overline{F}_1 + \left(\frac{\partial \xi_i}{\partial x_2} \right) \overline{F}_2 + \left(\frac{\partial \xi_i}{\partial x_3} \right) \overline{F}_3 \right] \quad (23)$$

The chain rule has to be used again to express all the derivatives which arise in the fluxes \hat{F}_i as functions of the curvilinear co-ordinates ξ_i only. Note also that vector \hat{U} is still a function of the cartesian co-ordinates x_i and time t .

In practice, we solve the system (22) by means of a (2,4) extension of the fully-explicit McCormack scheme devised by Gottlieb and Turkel (1976). The reader is referred to Comte & Lesieur (1998) for a presentation of the multi-block implementation and its *non-reflective* boundary conditions used here).

3. Structure-Function and Generalized Hyperviscosity Models

The shortcomings of the eddy-viscosity and eddy-diffusivity assumptions in the physical space have clearly been identified, in particular in incompressible plane channel flows. However, all cures proposed so far involve a considerable increase in complexity and computational cost which is detrimental to rapid progress of LES in the industrial community. On the other hand, all the implications of these assumptions have not been fully exploited yet, in particular the near-cut-off wavenumber dependence (*cusp*) of the spectral eddy-viscosity in incompressible isotropic turbulence, which was discovered by Kraichnan (1976) and retrieved in DNS by Domaradzki *et al.* (1987)

Making use of isotropic EDQNM expansions assuming spectra $E(k) \propto k^{-m}$ for all wavenumbers k larger than the cut-off wavenumber $k_c = \pi/\Delta x$, Métais and Lesieur (1992) proposed spectral models of the form

$$\nu_t(k, t) = \begin{cases} 0.31 \frac{5-m}{m+1} \sqrt{3-m} C_K^{-3/2} \nu_t^*(k/k_c) \sqrt{\frac{E(k_c, t)}{k_c}} & \text{for } m < 3, \\ 0 & \text{for } m \geq 3, \end{cases} \quad (24)$$

$$\kappa_t(k, t) = \nu_t(k, t)/Pr_t \quad \text{with } Pr_t = 0.18(5-m), \quad (25)$$

in which C_K denotes Kolmogorov's constant and $\nu_t^*(k/k_c)$ a normalized function that can be approximated by $\left[\nu_{t_0}^* + \nu_{t_n}^* \left(\frac{k}{k_c} \right)^{2n} \right]$ with $2n \sim 3.7$, $\nu_{t_0}^* = 0.441 C_K^{-3/2}$ and $\left(\nu_{t_0}^* + \frac{1}{3n/2+1} \nu_{t_n}^* \right) = \frac{2}{3} C_K^{-3/2}$ for $m = 5/3$.

In the case of plane turbulent channel flows (with and without rotation) up to $h^+ \sim 400$, Lamballais *et al.* (1998) obtained correct statistics with this model and a dynamic determination of $m(y, t)$ obtained by computing, every timestep, energy spectra in planes parallel to the wall and evaluating their slopes between k_c and $k_c/2$ by means of least-square fits. This model has also given excellent results in the case of temporal mixing layers (Silvestrini *et al.*, 1998).

When spectral methods cannot be used, we strive to determine eddy-viscosities out of a measure of the kinetic energy at the smallest resolved

scale. One of these local spectra is $F_{2\Delta x}(\mathbf{x}, t)$, the second-order structure function of the resolved velocity field, evaluated by averaging over the closest neighbours of point \mathbf{x} , either in all 3 directions of space (6-neighbour formulation) or on planes normal to the wall or mean shear (4-neighbour formulation). In the case of infinite Kolmogorov spectra, energy-conservation arguments (Leslie & Quarini, 1979) yield the *Structure-Function* model (Métais and Lesieur, 1992), defined by

$$\nu_t^{SF}(\tilde{\mathbf{x}}, t) = 0.105 C_K^{-3/2} \Delta \sqrt{F_{2\Delta x}(\mathbf{x}, t)} \quad , \quad (26)$$

consistent with the spectral model (25) without cusp.

This SF model appears to be slightly less dissipative than the Smagorinsky model with the constant 0.18 given by the same assumptions (infinite Kolmogorov cascade, see e.g. Comte *et al.*, 1994). As it involves velocity increments instead of derivatives, it also has the advantage of being defined independently of the numerical scheme used. It is nevertheless not much better for transition than the Smagorinsky model: low-wavenumber velocity fluctuations corresponding to unstable modes yield ν_t 's large enough to affect the growth rate of weak instabilities like Tollmien-Schlichting waves. So far, we have found two ways of remedying this:

- apply a high-pass filter onto the resolved velocity field before computing its structure function. With a triply-iterated second-order finite-difference Laplacian filter denoted $\check{\cdot}$, one finds $\check{E}(k)/E(k) \approx 40^3 (k/k_c)^9$ for all k , almost independently of the velocity field and resolution. With the same arguments as for the structure-function model, this yields the *Filtered Structure-Function model*, proposed by Ducros *et al.* (1996) in the form

$$\nu_t^{FSF}(\mathbf{x}, t) = 0.0014 C_K^{-3/2} \Delta \sqrt{\check{F}_{2\Delta}(\mathbf{x}, t)} \quad . \quad (27)$$

This model enabled them to perform the LES of a spatially-growing transitional boundary layer over an adiabatic flat plate up to the fully-turbulent regime.

- switch the original structure-function model off when the flow is not three-dimensional enough in the small scales. In practice, an average vorticity vector $\overline{\omega}(\mathbf{x}, t)$ is computed over \mathbf{x} and its (4 or 6) closest neighbours. The Structure-Function model (26) is applied only if the magnitude of the angle $\alpha = (\omega(\mathbf{x}, t), \overline{\omega}(\mathbf{x}, t))$ exceeds a certain threshold α_0 . Simulations of incompressible isotropic turbulence at resolutions ranging between 32^3 and 64^3 gave pdf's of $|\alpha|$ peaking around 20° . Having found the choice of α_0 not critical between 10 and 45° , we finally retained $\alpha_0 = 20^\circ$. The model's constant was finally multiplied by 1.56, a least-square fit between our test-simulations yielding the average dissipation over the domain closest to the values given by the SF-model. Dispersion was found small enough to justify

this in first approximation, but work is in progress in order to reduce the arbitrariness in this model. In any case, the most surprising conclusion about the filtered and selective structure-function models (hereafter FSF and SSF, respectively) is that they can be interchanged without much difference in the results (Comte *et al.*, 1994). This comes from the fact that they both considerably shrink the support of ν_t (with respect to that of the original SF model), and that both supports are almost the same (Figure 1, middle and right plots). In any case, they do not react to Λ -vortices, whereas the SF model does (left plot in Figure 1).



Figure 1. From left to right: isosurfaces $\nu_t = 2/3 \nu$ given by the SF, FSF and SSF models, respectively, in the transitional portion of the spatially-growing boundary layer presented in Ducros *et al.* (1996). The same velocity field was used for the three plots (a priori test). *Courtesy F. Ducros.*

4. Quasi-incompressible transitional boundary layer

Still with the FSF model, this is the follow-up of Ducros *et al.* (1996) at lower Mach number ($M_\infty = 0.3$), with upstream perturbations that are solutions of (weakly) non-linear Parabolized Stability Equations (Herbert & Bertolotti, 1991, Airiau, 1994), either in the harmonic case (K mode, after Klebanoff *et al.*, 1962) or the sub-harmonic case (H mode, after Herbert, 1982). In both cases, the upstream Reynolds number is $Re_{\delta_1} = 1000$ and two grids have been used, with resolutions $(\Delta x_1^+, \Delta x_2^+, \Delta x_3^+) = (20, 2, 12)$ and $(20, 1, 8)$ in the streamwise, wall-normal and spanwise directions, respectively, at the beginning of the fully-turbulent region.

Figure 2 shows the emergence of the streak system downstream of the transitional Λ -vortices, which are aligned in the K case and staggered in the H case. In both cases, the Λ vortices travel at the group velocity $c = 0.5 U_\infty$. Arch vortices, well materialized by isosurfaces $Q = (\Omega_{ij}\Omega_{ij} - S_{ij}S_{ij})/2 > 0$, are shed at their tips and travel downstream at $c = 0.8 U_\infty$, which creates high-speed streaks on both sides. In the K case, the Λ vortices also are flanked by elongated high-speed regions and the resulting transitional high-speed streaks are more intense than in the H case. This might be the reason why transition occurs sooner in the K case: with the same amplitude of the upstream perturbations, the peak skin friction is reached at $x_1 = 490 \delta_i$ in

the K case and at $x_1 = 550 \delta_i$ in the H case (left plot in Figure 3, in which the solid and dashed lines correspond to the fine and coarse grids, respectively). In both cases, the spanwise velocity correlations show a preferential spanwise spacing of about 100 wall units, significantly upstream of the peak skin friction (right plot in Figure 3, in the K-case only).

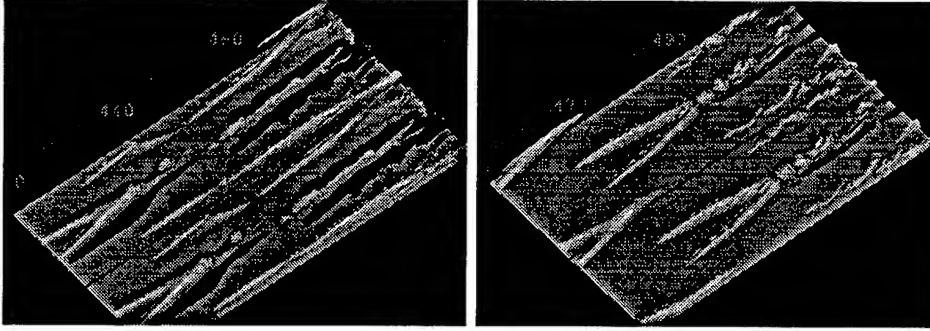


Figure 2. Zoom upstream of the peak skin-friction coefficient, showing the isosurfaces $u'_1 = \pm 0.2 U_\infty$ (positive in dark, negative in pale) and $Q = 0.1 U_\infty/\delta_i$ (medium grey). Courtesy E. Briand.

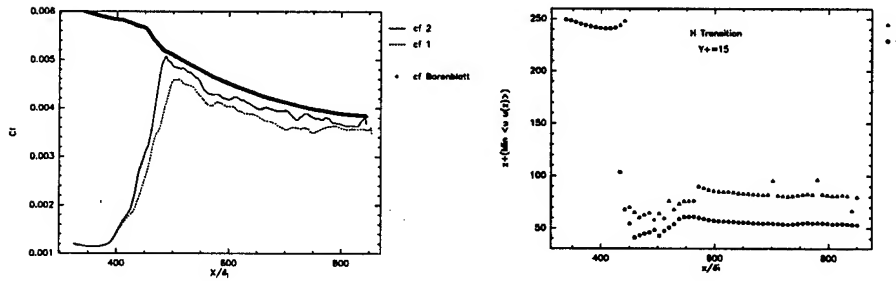


Figure 3. K-type transition: downstream evolution of the mean skin friction coefficient for both grids (left, with the theoretical prediction of Barenblatt, 1993) and the spanwise correlations at $x_2^+ = 15$ (right). Courtesy E. Briand.

5. Supersonic compression-ramp flow

Let us now illustrate the potentialities of the formalism presented in section 2 in the case of the detached boundary layer over a curved isothermal compression ramp at Mach 2.6, which corresponds to the wind-side region of a 1/90 model of the late European space shuttle HERMES with its body flap extended at $\alpha_0 = 20^\circ$. The inflow conditions come from a RANS calculation performed by Dassault-Aviation on the full model at Mach 10 and

angle of attack 30° . They were found to be transitional, that is, with laminar profiles and a low level of fluctuations that we represented by white noise of amplitude $2 \cdot 10^{-3} U_\infty$ superimposed onto the 3 components of the velocity at each time step. The external conditions of the LES correspond to post-bow-shock conditions, namely, $M = 2.6$ and $T_\infty = 460K$. The wall temperature is $T_w = 290K$, which yields an adiabatic recovery temperature $T_{ad} = T_\infty \left(1 + \sqrt{Pr} \frac{\gamma-1}{2} M_\infty^2\right) = 1050K$ and a cooling ratio $T_w/T_{ad} = 0.28$ close to the true-flight ratio expected from radiative balance.

The left plot in Figure 4 corresponds to a 2D calculation at an upstream Reynolds number $Re_{\delta_1} = 280$ on a 220×140 point grid. It shows the Λ -shock which focalizes near the domain's outlet, with unsteadiness due to the large vortices in the recirculation zone around the hinge. The remaining wiggles disappear in LES with the SSF model and only 25 points in the spanwise direction, as can be seen in the right plot of the figure. The isobaric surface plotted also shows a streamwise tube which corresponds to the strongest of the two couples of counter-rotating Dean-Görtler vortices shown in Figure 5. The strong correlation between skin-friction and heat flux is evident, with an average analogy factor $\langle St \rangle / 2 \langle C_f \rangle$ of about 0.5, which is lower than the commonly accepted value $s = 1.24$ for high-Reynolds number flat-plate boundary layers. The same trend ($s = 0.8$) was also observed on a strongly heated wedge ($T_w/T_{ad} = 2.9$) at Mach 0.5, see Comte *et al.* (1994).

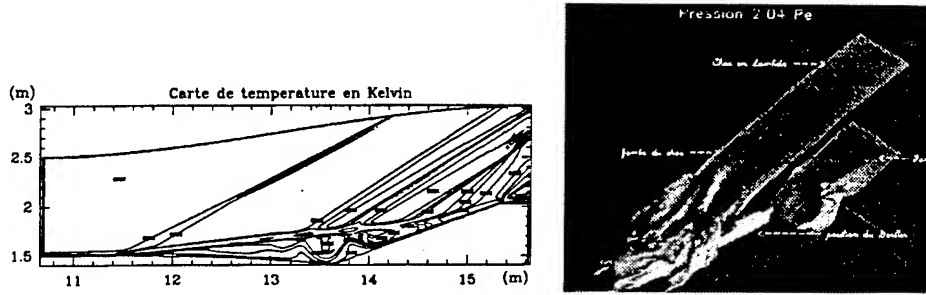


Figure 4. Ramp flow. Instantaneous temperature map obtained from a preliminary 2D simulation (left), and isobaric surface in LES (right) showing the shock, one branch of the trailing-edge expansion fan and one of the couples of Görtler vortices. *Courtesy E. David.*

6. Conclusion

The *filtered* and *selective structure-function* models were applied to weakly- and highly-compressible transitional and fully-turbulent shear flows through a simple variable-density extension of the incompressible LES formalism involving a *macro-temperature*. In the case of quasi-incompressible boundary

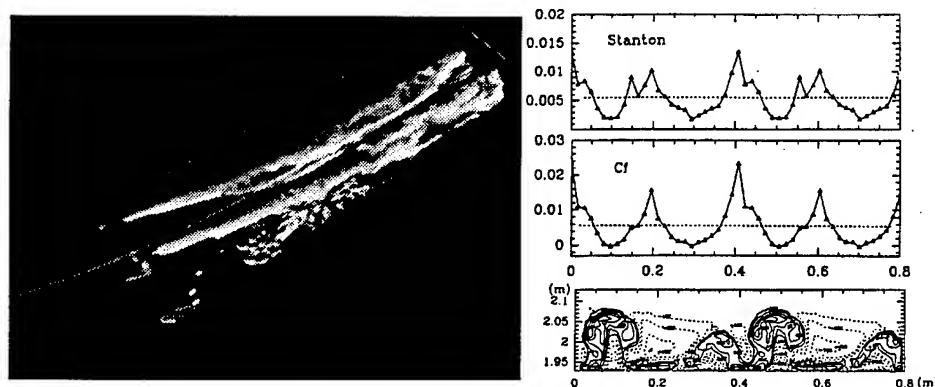


Figure 5. Ramp flow. Zoom on the hinge and body-flap region showing an isosurface of the vorticity magnitude shaded by temperature (left plot). Colour animations clearly show hot fluid in the outer part of the boundary layer being downwashed to the wall, which brings about wall-heat-flux fluctuations. The right plot is a cross section of the corresponding temperature field, with spanwise duplication, together with spanwise profiles of the skin-friction coefficient and Stanton number. *Courtesy E. David.*

layers, new information (to the best of our knowledge) about the formation of the streak system was found: a preferential spanwise scale of about 100 local wall units was found in the transitional region, as soon as the Λ -vortices became identifiable, that is, even before they shed arch vortices at their tips. This strongly suggests that this spacing is due to a streamwise-independent instability, as proposed by Landahl (1980). On the other hand, the same modelling and numerical techniques were applied at lower resolution to a supersonic compression ramp flow, showing couples of quasi-steady Dean-Görtler vortices downstream of the (unsteady) shock. These vortices were found to induce severe thermal loads at the ramp's wall that RANS calculations proved unable to reproduce. A high level of correlation was found between skin friction and wall heat flux, but with an analogy factor $s = St/2C_f$ significantly lower than the values found in textbooks in the case of high-Reynolds number flat plate boundary layers. The clarification of this point is in progress, in the case of plane channel flows over isothermal walls, with comparisons against the DNS data of Coleman *et al.* (1995).

7. Acknowledgements

M. Lesieur, O. Métais, E. David and E. Briand are warmly thanked for their contribution to the work presented here. A large part of the computational resources was allocated free by IDRIS, the French supercomputing centre of the CNRS.

References

- AIRIAU, C. (1994) "Stabilité linéaire et faiblement non linéaire d'une couche limite laminaire incompressible par un système d'équations parabolisé (PSE)", PhD Thesis, Toulouse University.
- BARENBLATT, G. (1993), *J. Fluid Mech.*, **248**, 513-529.
- COLEMAN, G.N., KIM, J., MOSER, R.D. (1995), *J. Fluid Mech.*, **305**, pp. 159-183.
- COMTE, P., DUCROS, F., SILVESTRINI, J.H., DAVID, E., LAMBALLAIS, E., MÉTAIS, O. & LESIEUR, M. (1994), 74th AGARD Fluid Dynamics Panel Meeting, Crete.
- COMTE, P. & LESIEUR, M. (1998) Large-eddy simulations of compressible turbulent flows. *Advances in turbulence modelling*, VKI Lecture Series 1998-05.
- DOMARADZKI, J.A., METCALFE, R.W., ROGALLO, R.S. & RILEY, J.J. (1987) Analysis of subgrid-scale eddy viscosity with the use of the results from direct numerical simulations. *Phys. Rev. Lett.*, **58**, 547-50.
- DUCROS, F., COMTE, P. AND LESIEUR, M. (1996) "Large-eddy simulation of transition to turbulence in a boundary-layer developing spatially over a flat plate", *J. Fluid Mech.*, **326**, 1-36.
- ERLEBACHER G., HUSSAINI M.Y., SPEZIALE C.G., ZANG T.A. (1987) ICASE Report, 87-20; and also (1992) "Toward the large-eddy simulation of compressible flows", *J. Fluid Mech.*, **238**, 155.
- FAVRE, A. (1965) *J. de Mécanique*, **4**, 361.
- GHOSAL S. & MOIN, P. (1995) *J. Comp. Phys.*, **118**, 24.
- GOTTLIEB D. & TURKEL E. (1976) *Math. Comp.*, **30**, 703.
- HERBERT, T. (1988) Secondary instability of boundary layers. *Ann. Rev. Fluid Mech.*, **20**, 487-526.
- HERBERT, T. & BERTOLOTI, F.P. 1991 Analysis of the linear stability of compressible boundary layer using PSE, *Theoret. and Comp. Fluids Dynamics*, **3**, 117-124.
- KLEBANOFF, P.S., TIDSTROM, K.D. & SARGENT, L.M. (1962) *J. Fluid Mech.*, **12**, 1-34.
- KRAICHNAN, R.H. (1976) "Eddy viscosity in two and three dimensions", *J. Atmos. Sci.*, **33**, 1521-1536.
- LAMBALLAIS, E., MÉTAIS, O. & LESIEUR, M. (1998) "Spectral-dynamic model for large-eddy simulations of turbulent rotating channel flow", *Theor. Comp. Fluid Dyn.*, **12**, 149-177.
- LANDAHL, M.T. (1980) "A note on an algebraic instability of inviscid parallel shear flows", *J. Fluid Mech.*, **98**, pp. 243-251.
- LESIEUR, M. (1997) "Spectral dynamic models for LES of turbulence", in *Advances in DNS/LES - Proceedings of the First AFOSR International Conference on DNS/LES*, C. Liu, Z. Liu and L. Sakell, eds.
- LESIEUR, M. & MÉTAIS, O. (1996) 'New trends in large-eddy simulations of turbulence', *Ann. Rev. Fluid Mech.*, **28**, 45-82.
- LESLIE, D.C. & QUARINI, G.L. (1979) "The application of turbulence theory to the formulation of subgrid modelling procedures". *J. Fluid Mech.*, **91**, 65-91.
- MÉTAIS, O. & LESIEUR, M. (1992) "Spectral large-eddy simulations of isotropic and stably-stratified turbulence", *J. Fluid Mech.*, **239**, 157-194.
- MOIN, P., SQUIRES, K., CABOT, W. & LEE, S. (1991) "A dynamic subgrid-scale model for compressible turbulence and scalar transport", *Phys. Fluids A*, **3**, (11), pp. 2746-2757.
- NORMAND, X. & LESIEUR, M. (1992) "Direct and large-eddy simulation of transition in the compressible boundary layer", *Theor. Comp. Fluid Dyn.*, **3**, pp. 231-352.
- SILVESTRINI, J. H., LAMBALLAIS, E. & LESIEUR, M. (1998) "Spectral-dynamic model for LES of free and wall shear flows", *International Journal of Heat and Fluid Flow*, **19**, 492-504.
- VIVIAND, H. (1974) *Rech. Aeros.*, **1**, 65.
- YOSHIZAWA, Y. (1986) *Phys. Fluids*, **29**, 2152.

DIRECT NUMERICAL SIMULATION OF TURBULENT COMPRESSIBLE AND INCOMPRESSIBLE WALL-BOUNDED SHEAR FLOWS

R. FRIEDRICH, R. LECHNER, J. SESTERHENN, T.J. HÜTTL
Lehrstuhl für Fluidmechanik
TU München
D-85748 Garching
Germany

1. Introduction

Active research in turbulent compressible flow dates back to the fifties and was mainly driven by the aim to make flight at supersonic speeds possible. Considerable progress in measuring such flows and in predicting them numerically was achieved since then. Yet, a lot more has to be understood about the physics of compressible turbulence, especially what effects of compressibility due to turbulent fluctuations (intrinsic compressibility effects) is concerned. During the last decade direct numerical simulation (DNS) has made valuable contributions in this direction.

Progress started with the fundamental work of Blaisdell et al. (1991, 1993) and Sarkar et al. (1991), Sarkar (1992) on homogeneous shear turbulence. Blaisdell et al. showed this flow to be independent of initial conditions and thus suitable for model testing, to exhibit a reduced growth rate of turbulent kinetic energy (TKE) compared to incompressible flow and a completely different structure of the solenoidal and dilatational parts of both the Reynolds stress and the dissipation rate tensors. Sarkar (1992) derived a statistical model for the pressure dilatation and used DNS to demonstrate that only the correlation between an incompressible part of the pressure fluctuation and the dilatation fluctuation is statistically relevant. Sarkar (1995) finally clarified that the stabilizing long-time effect of compressibility results from the reduction in the Reynolds shear stress and not from explicit compressibility terms like pressure-dilatation and scalar compressible dissipation rate. While these latter terms contribute to the TKE budget and have to be taken into account in statistical predictions,

see Speziale et al. (1995), they play a negligible role in wall-bounded flows. Investigation of compressibility effects in channel flow was the aim of Coleman et al.'s (1995) work. Their DNS of supersonic channel flow and the data analysis with respect to modelling issues by Huang et al. (1995) show that rms pressure, density and temperature fluctuations are small compared to their local mean values. Although the turbulent Mach number reaches values of 0.25 (at $M = 3$), pressure-dilatation and compressible dissipation rate of TKE are negligibly small compared to the solenoidal rate of dissipation. It also turned out that any turbulence model strongly overpredicts these quantities. At present, it is not at all clear which mechanism keeps the level of intrinsic compressibility so low in wall-bounded flows and what makes it increase with the global Mach number while it decreases with the gradient Mach number in homogeneous shear turbulence. Questions of this kind motivated us to start investigating compressible wall-bounded turbulence.

Our motivation to study incompressible turbulence in coiled pipes stems from the fact that curvature and torsion can have a strong effect on the turbulence structure providing a challenge for statistical modelling. Flow in coiled pipes is of great practical importance. In many industrial applications, pipe curvature and torsion are only required for geometrical reasons, in others they are e.g. used to generate swirl. In any case, the engineer is interested in the change in mixing properties of the flow and in the increase in flow resistance or volume rate reduction for a given pressure gradient. While laminar flow in coiled pipes has been investigated both theoretically and numerically in the past, little work has been done to achieve a better understanding of how curvature and torsion affect fully developed turbulence. Lai et al. (1991) use a Reynolds stress model and the parabolized Reynolds equations to investigate the secondary flow in a curved pipe. Since stronger secondary motions are of elliptic nature, their results are restricted to large radii of curvature. Boersma and Nieuwstadt (1995, 1997) have performed large-eddy simulations with the Smagorinsky model and direct simulations of turbulent flow in curved pipes. The Reynolds number of the DNS was 230, based on the surface averaged friction velocity and the pipe radius R . The radius of curvature was $10R$. It turned out that different initial conditions lead to different statistical data. This surprising result can only be explained by the fact that the flow partly 'relaminarizes'.

2. A pressure-velocity-entropy formulation of the compressible Navier-Stokes equations

Loosely spoken, vorticity, pressure and entropy are the 'modes' of compressible turbulence. Trying to compute these 'modes' as directly as pos-

sible, one conveniently starts from a (p, u_i, s) -, i.e. a pressure-, velocity-, entropy-formulation of the Navier-Stokes equations.

For cartesian coordinates, a special form of these equations for thermally and calorically perfect gas is (cf. Sesterhenn (1999)):

$$\begin{aligned} \frac{\partial p}{\partial t} = & -\frac{\rho c}{2} ((X^+ + X^-) + (Y^+ + Y^-) + (Z^+ + Z^-)) \\ & + \frac{p}{C_v} \left(\frac{\partial s}{\partial t} + X^s + Y^s + Z^s \right) \end{aligned} \quad (1)$$

$$\frac{\partial u}{\partial t} = -\left(\frac{1}{2}(X^+ - X^-) + Y^u + Z^u \right) + \frac{1}{\rho} \frac{\partial \tau_{1j}}{\partial x_j} \quad (2)$$

$$\frac{\partial v}{\partial t} = -\left(X^v + \frac{1}{2}(Y^+ - Y^-) + Z^v \right) + \frac{1}{\rho} \frac{\partial \tau_{2j}}{\partial x_j} \quad (3)$$

$$\frac{\partial w}{\partial t} = -\left(X^w + Y^w + \frac{1}{2}(Z^+ - Z^-) \right) + \frac{1}{\rho} \frac{\partial \tau_{3j}}{\partial x_j} \quad (4)$$

$$\frac{\partial s}{\partial t} = -(X^s + Y^s + Z^s) + \frac{R}{p} \left(-\frac{\partial q_i}{\partial x_i} + \Phi \right) \quad (5)$$

with the following abbreviations:

$$X^+ := (u + c) \left(\frac{1}{\rho c} \frac{\partial p}{\partial x} + \frac{\partial u}{\partial x} \right); \quad X^- := (u - c) \left(\frac{1}{\rho c} \frac{\partial p}{\partial x} - \frac{\partial u}{\partial x} \right); \quad (6)$$

$$X^v := u \frac{\partial v}{\partial x}; \quad X^w := u \frac{\partial w}{\partial x}; \quad X^s := u \frac{\partial s}{\partial x}; \quad (7)$$

$$Y^+ := (v + c) \left(\frac{1}{\rho c} \frac{\partial p}{\partial y} + \frac{\partial v}{\partial y} \right); \quad Y^- := (v - c) \left(\frac{1}{\rho c} \frac{\partial p}{\partial y} - \frac{\partial v}{\partial y} \right); \quad (8)$$

$$Y^u := v \frac{\partial u}{\partial y}; \quad Y^w := v \frac{\partial w}{\partial y}; \quad Y^s := v \frac{\partial s}{\partial y}; \quad (9)$$

$$Z^+ := (w + c) \left(\frac{1}{\rho c} \frac{\partial p}{\partial z} + \frac{\partial w}{\partial z} \right); \quad Z^- := (w - c) \left(\frac{1}{\rho c} \frac{\partial p}{\partial z} - \frac{\partial w}{\partial z} \right); \quad (10)$$

$$Z^u := w \frac{\partial u}{\partial z}; \quad Z^v := w \frac{\partial v}{\partial z}; \quad Z^s := w \frac{\partial s}{\partial z}; \quad (11)$$

The pressure transport equation (1) has been obtained from the continuity equation by replacing the material density derivative by material derivatives of pressure and entropy. The first bracket on the r.h.s of (1) expresses the interaction of (acoustic) waves travelling in the three cartesian coordinate directions $(x, y, z) \leftrightarrow (x_1, x_2, x_3)$. The momentum transport in x_i -direction depends on wave interactions in this direction and on convective transport in the remaining two directions besides molecular transport.

τ_{ij} , q_i and Φ are the viscous stress tensor, the conductive heat flux vector and the rate of energy dissipation. ρ , c , R , c_v are the density, the speed of sound, the specific gas constant and the specific heat at constant volume. The shear viscosity and heat conductivity vary as the 0.7th power of the temperature. The Prandtl number $Pr = c_p \mu / \lambda$ is assumed equal to 0.72 for air. One advantage of this form of the Navier-Stokes equations lies in the fact that wall boundary conditions can be formulated consistently. In contrast to Poinso and Lele (1992) no 'local associated one-dimensional inviscid approximations' are needed and all terms can be retained. In parallel computations, domain decomposition and data exchange are straightforward tasks.

Boundary conditions for a solid, isothermal wall:

Assume the x -coordinate to coincide with the stationary wall and the z -coordinate to be perpendicular to it. Then, the kinematic and thermal boundary conditions

$$u = v = w = 0 \quad , \quad T = \text{const} \quad \text{at } z = 0 \quad (12)$$

can be written as:

$$\frac{\partial u}{\partial t} = \frac{\partial v}{\partial t} = \frac{\partial w}{\partial t} = \frac{\partial T}{\partial t} = 0 \quad , \quad \text{at } z = 0 \quad . \quad (13)$$

Equations (1 - 5) are used along with these conditions to derive boundary conditions which allow for accurate wave reflection at the wall. Figure 1 illustrates the situation.

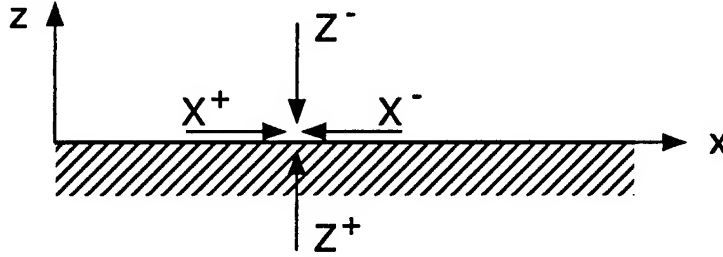


Figure 1. Illustration of boundary treatment at a solid wall.

The momentum balance in z -direction, (4), allows to compute the unknown 'wave' Z^+ at the wall:

$$Z^+ = Z^- + \frac{2}{\rho} \frac{\partial \tau_{3j}}{\partial x_j}, \quad \text{at } z = 0. \quad (14)$$

From (1) we get:

$$\frac{\partial p}{\partial t} = -\frac{\rho c}{2} (Z^+ + Z^-) + \frac{p}{c_v} \frac{\partial s}{\partial t}, \quad \text{at } z = 0. \quad (15)$$

Using Gibbs' fundamental relation, the temperature boundary condition (13) leads to an expression relating pressure and entropy:

$$\frac{\partial s}{\partial t} = -\frac{R}{p} \frac{\partial p}{\partial t}, \quad \text{at } z = 0. \quad (16)$$

Combining (15) and (16) finally provides the entropy and pressure wall boundary conditions:

$$\frac{\partial s}{\partial t} = \frac{R}{2c} (Z^+ + Z^-), \quad \text{at } z = 0. \quad (17)$$

$$\frac{\partial p}{\partial t} = -\frac{p}{2c} (Z^+ + Z^-), \quad \text{at } z = 0. \quad (18)$$

Space/time discretization

The equations and boundary conditions above have been discretized in space by a pseudo-spectral method using Fourier series in the homogeneous x - and y -directions and Chebyshev polynomials in the wall normal direction. The time advancement scheme is a third order explicit Runge-Kutta scheme in a low storage formulation (Williamson (1980)).

3. Results for supersonic channel flow

We use Coleman et al.'s (1995) DNS of fully developed turbulent isothermal-wall channel flow as a test case for code validation, before we proceed to the investigation of intrinsic compressibility effects in other wall-bounded flows in the near future. The Mach number based on bulk velocity u_m and sound speed at wall temperature, c_w , is $M = 1.5$. The Reynolds number based on bulk mass flux, $\rho_m u_m$, channel half width h and viscosity at wall temperature, μ_w , is $Re = 3000$. The Prandtl number is 0.7, the ratio of specific heats $\gamma = 1.4$ and the viscosity varies with temperature as $\mu \sim T^{0.7}$. The mean centerline-to-wall temperature ratio achieves the value 1.38 in the computation. Supersonic flow needs wall cooling. The driving

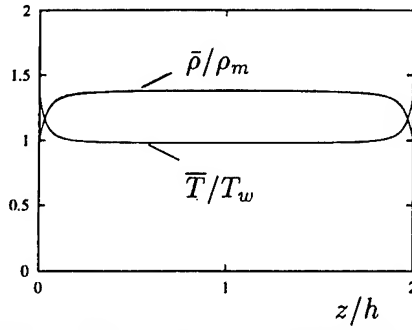


Figure 2. Mean density and temperature.

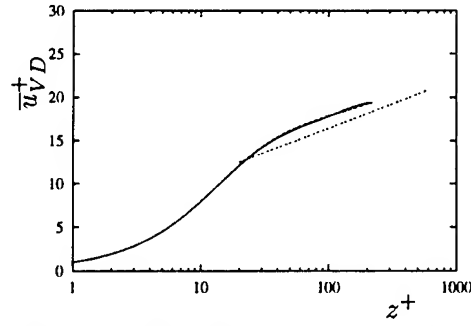
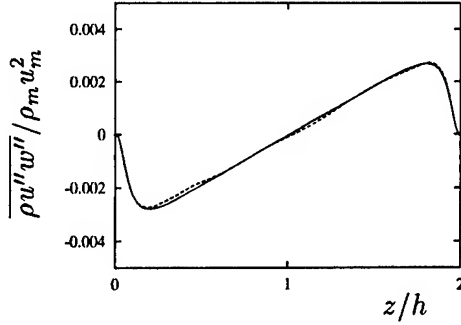
Figure 3. Van Driest transformed mean velocity. ---, $2.44 \ln z^+ + 5.2$.

Figure 4. Reynolds shear stress.

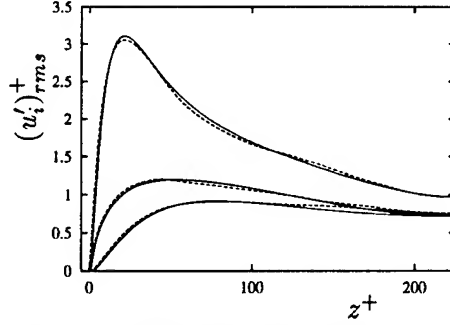


Figure 5. RMS velocity fluctuations in wall units.

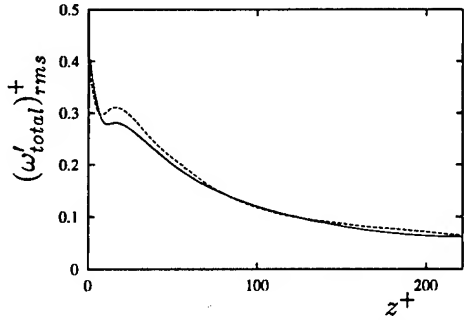


Figure 6. Total RMS vorticity fluctuations.

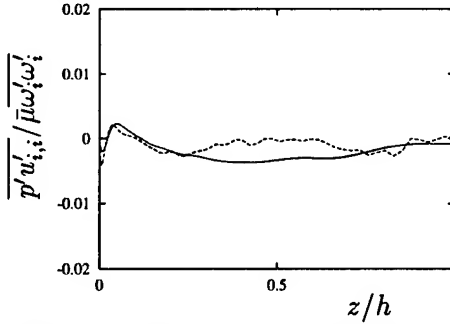


Figure 7. Ratio of pressure-dilatation correlation to solenoidal dissipation rate.

force of the flow, the mean axial pressure gradient, is replaced by a body force which is assumed homogeneous in planes parallel to the wall. Thus, the computed flow turns out to be homogeneous in axial direction, but has an effective axial pressure gradient which varies in wall-normal direction. As Huang et al. (1995) point out, this artificial effect has no real impact on conclusions drawn with respect to intrinsic compressibility in supersonic channel flow.

The computational domain, measured in units of h , is 4π long and $4\pi/3$ wide. The number of collocation points in streamwise, spanwise and wall normal directions (x, y, z) is $128 \times 64 \times 129$. Thus the grid is only marginally coarser in (x, y) -directions, but finer in wall normal direction than that of Coleman et al. The first collocation point has the distance $z^+ \approx 0.07$ from the wall and the first ten points are within $z^+ \approx 6.64$. The simulation has been started from an instantaneous fully developed flow field provided by G. Coleman (1998) and ran over two problem times h/u_τ ($u_\tau = (\tau_w/\rho_w)^{1/2}$). The preliminary results presented below were obtained from averaging in planes parallel to the walls and over nearly two problem times.

Figures 2-5 show profiles of the mean density, temperature, the Van Driest transformed mean velocity, the Reynolds shear stress and the rms-velocity fluctuations. Solid/dashed lines correspond to Coleman et al.'s/present results. Ignoring the lack of statistical sampling, our results show close agreement with those of Coleman et al. Greater differences are observed in the rms fluctuations of the total vorticity $(\omega'_{total})_{rms} = (\omega'_i \omega'_i)^{1/2}$ in Figure 6 and in the ratio of compressible to solenoidal dissipation rate (not shown). We believe that these differences can be removed by a higher resolution in streamwise and spanwise directions. The ratio of pressure dilatation correlation to solenoidal dissipation rate, Figure 7, attains very small values and thus demonstrates the fact that intrinsic compressibility effects are negligibly small in supersonic channel flow.

4. DNS of incompressible turbulent flow in coiled pipes

The geometry of a helical pipe can be viewed as a pipe of radius R coiled around a cylinder of constant radius $(r_a - R)$, see Figure 8. With the pitch p_s , defined by the increase in elevation per revolution of coils $2\pi p_s$, we obtain the curvature $\kappa = r_a / (r_a^2 + p_s^2)$ and the torsion $\tau = p_s / (r_a^2 + p_s^2)$ of the helical pipe axis. As suggested by Germano (1982, 1989), an orthogonal helical coordinate system can be established with respect to the master cartesian coordinate system, see Figure 9. The Navier-Stokes equations in helical coordinates have been derived in Hüttl and Friedrich (1998a) using the helical coordinates s for the axial, r the radial and θ the circumferential directions. A finite volume method on staggered grids is used to discretize these equations leading to central differences of second order accuracy for the mass and momentum fluxes across the cell faces. A semi-implicit time-integration scheme treats all those convection and diffusion terms implicitly and with 2nd order accuracy which contain derivatives in the θ -direction. The remaining convection terms are integrated in time with a second order accurate leapfrog-step. An averaging step at each 50th time step avoids possible $2\Delta t$ -oscillations. Diffusive terms with derivatives in s - and r -directions

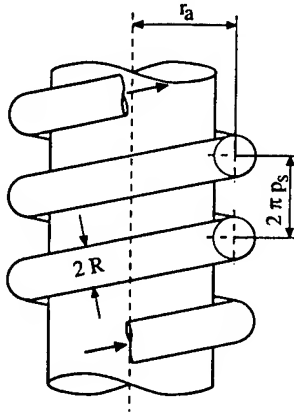
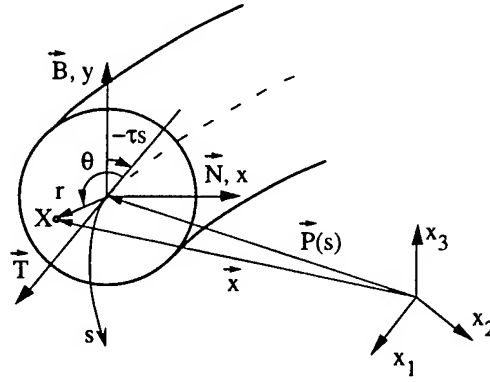


Figure 8. Helically coiled pipe.

Figure 9. Helical (s, r, θ) -coordinates.

are treated with a first-order Euler backward step. The size of the time step is selected according to a linear stability argument. The use of a projection step leads to a 3D Poisson problem for the pressure correction, which is solved by a Conjugate Gradient method for unsymmetric matrices, with Jacobi-preconditioning.

At the walls impermeability and no-slip boundary conditions are realized. Velocity components needed on the pipe axis are obtained by interpolation across the axis. In the circumferential direction all variables are periodic by definition. In the main flow direction periodic boundary conditions are used, too. For helically coiled pipes this means that the rotation of the coordinate system along the s -axis must be taken into account and the perfect matching of the cells at corresponding in- and out-flow boundaries, achieved by choosing a suitable combination of axial length and number of grid points in the θ -direction, avoids data interpolation (see Hüttl et al. (1997)). The Navier-Stokes code for helical coordinates has been validated in different ways. Laminar flows through coiled pipes were computed and compared with published experimental and numerical data (Hüttl (1999)). Computations of turbulent flow in the straight pipe have finally been validated against results of Eggels et al. (1994), proving the reliability of the present method.

DNS results of fully developed flow in a curved pipe (case DT, $\kappa R = 0.1$, $\tau R = 0$) and a helically coiled pipe (case DXXH, $\kappa R = 0.1$, $\tau R = 0.165$) are presented and compared with DNS results of flow in straight pipes (case DSP at $Re_\tau = 230$). Further results are discussed by Hüttl and Friedrich (1998a, 1998b, 1999a, 1999b, 1999c). The Reynolds number Re_τ based on the surface averaged friction velocity u_τ and pipe radius R has been taken as 230 for all cases of coiled pipes. The averaged friction velocity is related to the mean pressure gradient on the axis by $\rho u_\tau^2 = -R/2$.

$\partial \langle p \rangle / \partial s$. The Reynolds number $Re_b = 2u_b R / \nu$, based on bulk velocity u_b and pipe diameter $2R$, results from the simulation and varies between 5576 and 6926. For all simulations the same computational domain ($15.2R$ long) and the same number of grid points ($n_s = 256, n_\theta = 180, n_r = 70$) have been taken. In the wall-normal direction, close to the wall a clustering of grid points is provided. The first grid point is at $y^+ = 0.5$ and the first ten points lie within $y^+ \approx 11.6$. The statistical results discussed below are based on 200 statistically independent time samples and on averaging in main flow direction. Computations were run on 1 CPU of the Fujitsu VPP700. The computational cost per flow was close to 3000 CPU hours for cases DT and DXXH.

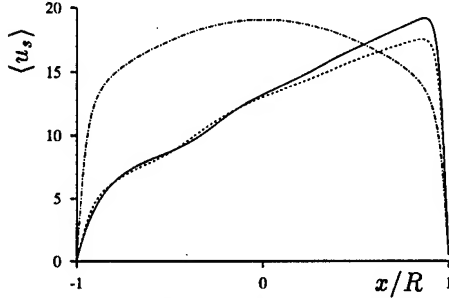


Figure 10. Mean axial velocity: — · — · DSP, — DT, - - - DXXH.

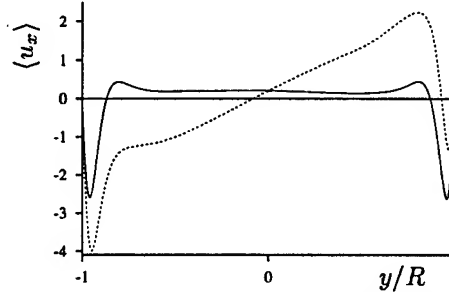


Figure 11. Mean horizontal velocity. Symbols as in Fig. 10.

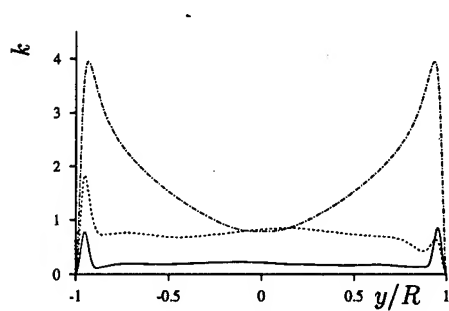


Figure 12. Turbulent kinetic energy. Symbols as in Fig. 10.

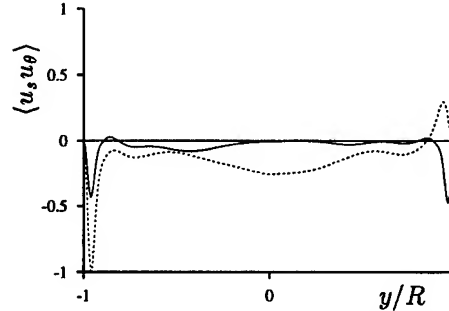


Figure 13. Reynolds shear stress $\langle u_s u_\theta \rangle$. Symbols as in Fig. 10.

5. Effects of curvature and torsion

Pipe curvature and torsion can have remarkable effects on the turbulent flow. With increasing curvature, the maximum of the mean axial velocity component moves from the axis to the outer wall as a consequence of centrifugal effects, Figure 10. A mean secondary motion is induced consisting

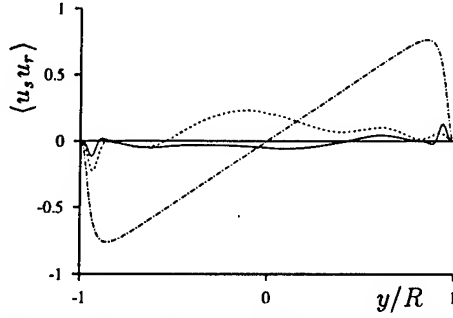


Figure 14. Reynolds shear stress $\langle u_s u_r \rangle$. Symbols as in Fig. 10.

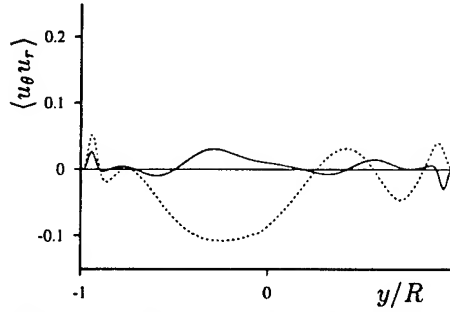


Figure 15. Reynolds shear stress $\langle u_\theta u_r \rangle$. Symbols as in Fig. 10.

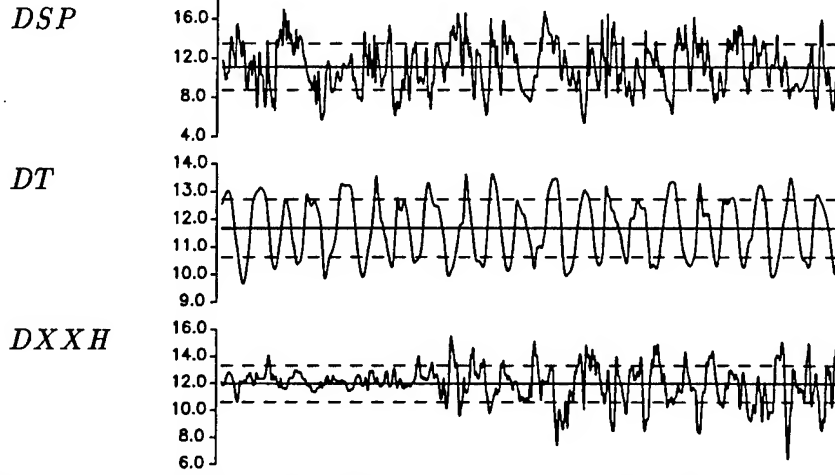


Figure 16. Time series of axial velocity component at position $(R-r)^+ = 14$, $\theta = 0$ (near upper wall). Ten dimensionless times $t_p = R/u_r$ are shown for each case.

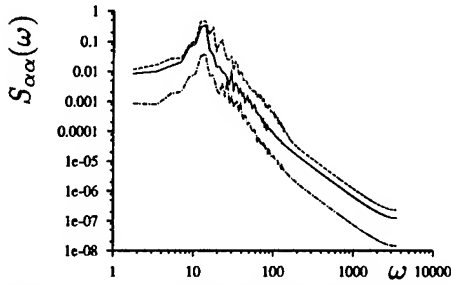


Figure 17. Frequency spectra $S_{\alpha\alpha}$ of the three velocity fluctuations of case DT at $(R-r)^+ = 14$, $\theta = 0$: — $S_{u_s u_s}$, - - - $S_{u_\theta u_\theta}$, ···· $S_{u_r u_r}$.

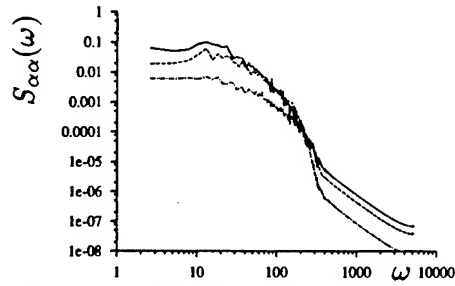
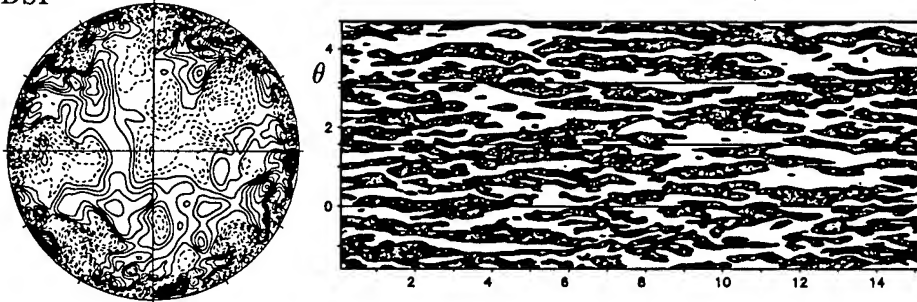
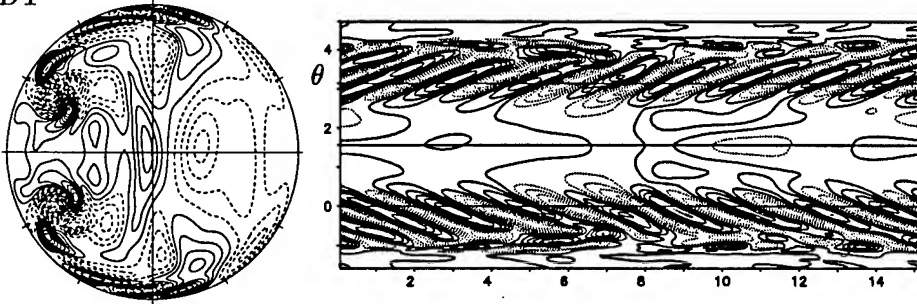


Figure 18. Frequency spectra $S_{\alpha\alpha}$ of the three velocity fluctuations of case DXXH at $(R-r)^+ = 14$, $\theta = 0$: — $S_{u_s u_s}$, - - - $S_{u_\theta u_\theta}$, ···· $S_{u_r u_r}$.

DSP



DT



DXXH

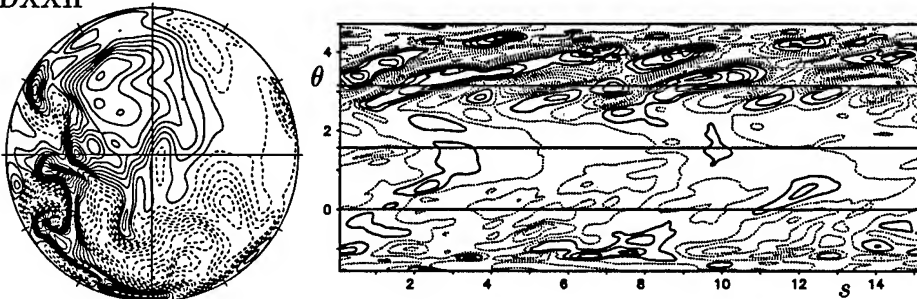


Figure 19. Contour lines of axial velocity fluctuations u''_s in pipe cross sections (left) and (s, θ) -surfaces at a distance of $(R - r)^+ = 14$ from the wall (right) for simulations DSP, DT and DXXH: — values > 0 , values < 0 .

in two counter-rotating Dean-cells which are symmetric with respect to the horizontal x -axis. The effect of torsion on the $\langle u_s \rangle$ -component is weak. It is much stronger on the mean circumferential velocity. In fact, this component indicates clockwise swirling motion in case DXXH, in most of the pipe cross section except for a thin layer close to the upper wall. This is shown in Figure 11, in terms of profiles of the mean horizontal velocity $\langle u_x \rangle$ along a vertical y -axis crossing the pipe centre. Close to the lower wall ($y/R \approx -0.95$) the circumferential velocity (or $\langle u_x \rangle$) reaches ampli-

tudes up to 20% of the maximum axial velocity. Curvature and torsion also affect the turbulence fluctuations in different ways, Figure 12 contains turbulent kinetic energy profiles along the y -axis. It turns out that a radius of curvature as small as $10R$ strongly inhibits the turbulence activity whereas the addition of torsion enhances it nearly everywhere. While fully developed turbulent flow through straight pipes is characterized by four non-zero components of the Reynolds stress tensor, there are six non-zero components in coiled pipes. Their amplitudes sometimes reach values of the order of u_τ^2 locally. Figures 13-15 show profiles of the three shear stresses along the y -axis. Near the pipe axis these profiles reveal some lack of statistical sampling. Close to the wall, however, they are quite stable. Note that profiles of case DT should be symmetric with respect to the pipe axis ($y/R = 0$), those of case DXXH, of course, not. Again, torsion enhances the turbulence activity and causes remarkable structural changes in these components. Further insight into the complexity of flow in coiled pipes is provided by time series of the instantaneous axial velocity and of contour lines of the axial velocity fluctuation. Figure 16 compares time series of u_s taken at a distance of 14 wall units from the upper wall during 10 problem times R/u_τ , the total simulation time ranging from $(60 \div 90)R/u_\tau$. In case DT the frequency spectrum of the three velocity fluctuations becomes very narrow-banded and shows a peak at a frequency of $13u_\tau/R$, cf. Figure 17. Case DXXH reveals an intermittent character in the sense that time intervals of different length with weak fluctuations are followed by periods with strong fluctuations. Consequently, the frequency spectrum is much broader than in case DT, see Figure 18.

For simulations DSP, DT and DXXH Figure 19 shows contour lines of the axial velocity fluctuations u_s'' in a cross section and in (s, θ) -surfaces at a distance of $(R - r)^+ = 14$ from the wall. For straight pipe flow (DSP) the streaky structures can clearly be seen. Completely different structures appear in case DT, where curvature is high. An almost regular pattern of flow structures is observed near the upper ($\theta = 0$) and lower wall ($\theta = \pi$). In these structures high speed fluid is transported to the wall and low speed fluid away from the wall. They are also the reason for the oscillations, shown in the autocorrelation functions. The fact that no such pattern occurs near the inner and outer wall confirms that the turbulence activity is low at these positions. The cross section shows an almost symmetric pattern of the contour lines and the influence of the secondary flow on the structures is evident. In case DXXH only the lower wall produces remarkable structures of alternating positive and negative axial velocity fluctuations. The pattern is, however, not as regular as that in case DT.

6. Summary and Conclusions

A special pressure-velocity-entropy formulation of the compressible Navier-Stokes equations which allows to specify boundary conditions in a natural and consistent way is used for DNS of supersonic turbulent channel flow with a Fourier-Chebyshev pseudo-spectral space discretization and a third-order accurate low-storage Runge-Kutta time-advance scheme. Mach and Reynolds numbers of the bulk flow are 1.5 and 3000, in agreement with Coleman et al.'s (1995) DNS. The present results are in close agreement with those of Coleman et al., indicating the suitability of the special form of the Navier-Stokes equations for DNS of compressible turbulence.

Incompressible turbulent flow in coiled pipes is investigated with second order central schemes and a semi-implicit time discretization of second order accuracy. The Reynolds number based on the surface averaged friction velocity and the pipe radius is 230 in all cases. As the radius of curvature of the pipe decreases, the secondary flow gets stronger and the near-wall coherent structures disappear from the outer and inner regions while they turn into very regular structures on the upper and lower sides. At the same time the turbulence activity is greatly reduced. The addition of torsion (while curvature is kept constant) increases the turbulence level again and causes further structural changes in the Reynolds stress components. For strong curvature and torsion the flow reveals an intermittent character.

References

1. Blaisdell, G.A., Mansour, N.N., Reynolds, W.C.: 'Numerical simulations of compressible homogeneous turbulence'. Report No. TF-50, Dept. of Mechanical Engineering, Stanford University, Stanford, California, 1991.
2. Blaisdell, G.A., Mansour, N.N., Reynolds, W.C.: 'Compressibility effects on the growth and structure of homogeneous turbulent shear flow.' *J. Fluid Mech.* 256, pp. 443-485, 1993.
3. Boersma, B. J.: 'Electromagnetic effects in cylindrical pipe flow', Ph. D. Thesis, Delft University Press, 1997.
4. Boersma, B. J., Nieuwstadt, F. T. M.: 'Large Eddy simulation of turbulent flow in a curved pipe', In: Tenth symposium on turbulent shear flows, The Pennsylvania State University, 1, Poster Session 1, P1-19 - P1-24, 1995.
5. Boersma, B. J., Nieuwstadt, F. T. M.: 'Non-Unique Solutions in Turbulent Curved Pipe Flow', In: J.-P. Chollet et al. (eds.), *Direct and Large-Eddy Simulation II*, Kluwer Academic Publishers, pp. 257-266, 1997.
6. Coleman, G.: Private communication, 1998.
7. Coleman, G.N., Kim, J., Moser, R.D.: 'A numerical study of turbulent supersonic isothermal - wall channel flow.' *J. Fluid Mech.* 305, pp. 159-183, 1995.
8. Eggels, J.G.M., Unger, F., Weiss, M.H., Westerweel, J., Adrian, R.J., Friedrich, R., Nieuwstadt, F.T.M.: 'Fully developed turbulent pipe flow: a comparison between direct numerical simulation and experiment', *J. Fluid Mech.* 268, 175-209, 1994.
9. Germano, M.: 'On the effect of torsion on a helical pipe flow', *J. Fluid Mech.*, 125, pp. 1-8, 1982.
10. Germano, M.: 'The Dean equations extended to a helical pipe flow', *J. Fluid Mech.*,

- 203, pp. 289-305, 1989.
11. Huang, P.G., Coleman, G.N., Bradshaw, P.: 'Compressible turbulent channel flows - DNS results and modelling'. J. Fluid Mech. 305, pp. 185-218, 1995.
12. Hüttl, T.J.: 'Direkte Numerische Simulation turbulenter Strömungen in gekrümmten und tordierten Rohren', Ph. D. Thesis, Technische Universität München, Fortschr.-Ber. VDI Reihe 7, VDI-Verlag, Düsseldorf, 1999.
13. Hüttl, T.J., Friedrich, R.: 'Direct Numerical Simulation of Turbulent Flows in Curved and Helically Coiled Pipes', Proc. of the Third Asian Comp. Fluid Dynamics Conf. (ACFD3), Dec. 7-11 '98, Bangalore India, vol. 2, pp. 183-188, 1998a.
14. Hüttl, T.J., Friedrich, R.: 'Fully developed turbulent flow in conduits with circular cross section' In: Proc. DGLR-STAB'98 Symp., Nov. 1998, Berlin, 1998b.
15. Hüttl, T.J., Friedrich, R.: 'High Performance Computing of Turbulent Flow in Complex Pipe Geometries', -In: High Performance Computing in Science and Engineering '98, Transactions of the High Performance Computing Center Stuttgart (HLRS) 1998, E. Krause, W. Jäger (Eds.), Springer Verlag, pp. 236-251, 1999a.
16. Hüttl, T.J., Friedrich, R.: 'Influence of curvature and torsion on turbulent flows in helically coiled pipes', Engineering Turbulence Modelling and Experiments 4, W. Rodi, D. Laurence (Eds.), Elsevier Science Ltd, pp. 247-256, 1999b.
17. Hüttl, T.J., Friedrich, R.: 'Turbulent flow in coiled pipes', Proc. Isaac Newton Symp. & Third ERCOFTAC Workshop on 'Direct and Large-Eddy Simulation', May 12-14, 1999, Univ. of Cambridge, Isaac Newton Institute For Math. Sciences, vol. 3, Paper 3.6, Cambridge (UK), 1999c.
18. Hüttl, T.J., Wagner, C., Friedrich, R.: 'Navier Stokes Solutions of Laminar Flows Based on Orthogonal Helical Coordinates', *Numerical methods in laminar and turbulent flow*, C. Taylor, J. Cross (eds.), Pineridge Press, Swansea UK, vol. 10, pp. 191-202, 1997.
19. Lai, Y.G., So, R.M.C., Zhang, H.S.: 'Turbulence-Driven Secondary Flows in a Curved Pipe', Theoret. Comput. Fluid Dynamics, 3:163-180, 1991.
20. Poinso, T.J., Lele, S.K.: 'Boundary conditions for direct simulations of compressible viscous flows', J. Comp. Phys. 101, 104-129, 1992.
21. Sarkar, S.: 'The pressure-dilatation correlation in compressible flows.' Phys. Fluids A4, pp. 2674-2682, 1992.
22. Sarkar, S.: 'The stabilizing effect of compressibility in turbulent shear flow.' J. Fluid Mech. 282, pp. 163-186, 1995.
23. Sarkar, S., Erlebacher, G., Hussaini, M. Y.: 'Direct simulation of compressible turbulence in a shear flow.' Theor. Comput. Fluid Dyn. 2, pp. 291-305, 1991.
24. Sesterhenn, J.: 'A characteristic-type formulation of the Navier-Stokes equations for discretization with high order upwind schemes.' Submitted to Computers & Fluids, 1999.
25. Speziale, C.G., Abid, R., Mansour, N.N.: 'Evaluation of Reynolds stress turbulence closures in compressible homogeneous shear flow'. ZAMP, Special Issue, ed. by J. Casey & M.J. Crochet, S717-S736, 1995.
26. Williamson, J.H.: 'Low-Storage Runge-Kutta schemes', J. Comp. Phys. 35, 48-56, 1980.

DIRECT NAVIER-STOKES SIMULATION OF SOUNDS GENERATED BY SHOCK-VORTEX / VORTEX-VORTEX INTERACTIONS

OSAMU INOUE

Institute of Fluid Science, Tohoku University

2-1-1 Katahira, Aoba-ku, Sendai 980-8577, Japan

Abstract. Flow fields generated by the interactions between a shock wave and vortices and between two vortex rings are simulated numerically, and the generation and propagation mechanisms of sounds are studied. The unsteady, compressible Navier-Stokes equations are solved by a finite difference method over the entire acoustic field from near to far fields. The sixth-order-accurate compact Padé scheme is used for spatial derivatives, together with the fourth-order-accurate Runge-Kutta scheme for time integration. The results show that the basic nature of the sounds depends strongly on the generation of reflected shock waves and expansion waves for shock-vortex interaction problems, and on the vortex motions induced by mutual interaction for vortex-vortex interaction problems. The results also show that the pressure peaks of the sounds decay in inverse proportion to the distance from the sound source for three-dimensional flows and to the square root of the distance for two-dimensional flows, in agreement with theory.

1. Introduction

Direct numerical simulations of sounds have become feasible in the recent years (Tam 1995; Lele 1997; Wells and Renaut 1997; Moin and Mahesh 1998; Inoue and Hattori 1998, 1999). In these simulations, the Navier-Stokes/Euler equations are solved by using highly accurate schemes both for space and time in order to precisely capture the sound pressure in the far field, which is much smaller than the pressure in the near-field fluid flow. In this paper, we simulate the entire acoustic fields produced by shock-vortex/vortex-vortex interactions, by solving the compressible Navier-Stokes equations. The purpose of this paper is to increase our un-

derstanding of the generation and propagation mechanisms of the sounds in these flow fields. We consider the following interactions:

- [1] shock-vortex interactions:
 - (1.1) two-dimensional shock-single vortex interaction,
 - (1.2) axisymmetric shock-vortex ring interaction,
- [2] axisymmetric vortex-vortex interactions:
 - (2.1) head-on collision of two vortex rings,
 - (2.2) leapfrogging and merging of two vortex rings.

In all cases, the compressible Navier–Stokes equations are solved by a finite difference method. For spatial derivatives, a sixth-order-accurate compact Padé scheme (third-order-accurate at the boundaries) proposed by Lele (1992) is adopted. The fourth-order Runge–Kutta scheme is used for time-integration. A non-uniform mesh system is applied. At the boundaries, either non-reflecting conditions (Poinsot and Lele 1992) or periodic conditions are used.

2. Shock-Vortex Interactions

2.1. 2D SHOCK WAVE–SINGLE VORTEX INTERACTIONS

The flow model and the numerical method used in this computation are essentially the same as in Inoue and Hattori (1999). The Mach number of a shock wave (M_s) is prescribed to be either 1.05 or 1.2. Through the interaction with a vortex, the shock wave shows a Mach reflection when $M_s = 1.2$ and a regular reflection when $M_s = 1.05$. The Mach number of the vortex (M_v), defined by $M_v = u_{\theta\max}/a_\infty$, is prescribed to be 0.25 or 0.5. Here $u_{\theta\max}$ is the maximum tangential velocity and a_∞ is the sound speed. The Reynolds number is based on the vortex core radius R and the sound velocity and is prescribed to be 800. For more details on the numerical method, readers are referred to Inoue and Hattori (1999).

As a typical example, a flow field for the case of $M_s=1.05$, $M_v=0.25$ and $Re = 800$, at a time sufficiently after the beginning of the interaction, is presented in terms of the sound pressure in Fig. 1. The sound pressure Δp is defined as $\Delta p = (p - p_s)/p_s$ where p_s is the pressure behind the shock wave. As shown by Inoue and Hattori (1999), through the shock-vortex interaction, the precursor appears first, and then the two reflected shock waves are generated. The sound pressure field in Fig. 1 shows that the sounds are generated three times (the precursor, the second and the third sounds), and each sound has a quadrupolar nature.

The radial distributions of the sound pressure, measured at $\theta = 45^\circ$, are plotted in Fig. 2 for the same case as in Fig. 1. The numerics 1 to 3 in Fig. 2 denote the precursor, the second sound and the third sound, respectively.

We can see from Fig. 2 that the three sounds propagate radially from the vortex center with time, and that the peak values of the sound pressure decay with the radial distance r from the vortex center. After the third sound, any appreciable pressure waves are not observed; the sounds are generated three times, as expected by Inoue and Hattori (1999). This result suggests that the generation and the nature of the sounds are closely related to the generation of the reflected shock waves.

The sound pressure peaks of the three sounds are plotted against the radial distance r in Fig. 3 for the same case as in Figs. 1 and 2. It is known that the decay of the sound pressure in two-dimensional flows is inversely proportional to $r^{1/2}$ in the far field (Landau and Lifshitz 1984). The results in Fig. 3 show that all three sounds decay in proportion to the $r^{-1/2}$ in the far field, in agreement with the theory.

2.2. AXISYMMETRIC SHOCK-VORTEX RING INTERACTIONS

In this case, a vortex ring moves, by its self-induced velocity, either in the same direction to the shock wave (passing type) or in the opposite direction to it (collision type). The flow situation is quite similar to that for the case of 2D vortex pair considered in Inoue and Hattori (1999).

As an example of the collision type interaction, a flow field for the case of $M_s=1.2$, $M_v=0.1$ and $Re = 800$, at a time sufficiently after the beginning of the interaction, is presented in terms of a computational shadowgraph in Fig. 4 and in terms of the sound pressure in Fig. 5. In Fig. 5, the solid lines denote the compression region ($\Delta p > 0$), and the dashed lines denote the rarefaction region ($\Delta p < 0$). The Reynolds number is based on the vortex ring radius and the sound speed. Through the interaction, the precursor appears first. Then, two sets of reflected shock waves are generated; each set has two reflected shock waves with different strengths. The stronger reflected shock wave of one set catches up with the weaker reflected shock wave of another set and eventually two reflected shock waves merge into a single structure; in Figs. 4 and 5, the precursor and two merged reflected shock waves are observed. In Fig. 4 we can also see two slip lines emanated from the triple points. The qualitative features shown in Figs. 4 and 5 are quite similar to those of the mild collision interaction of the 2D vortex pair (Inoue and Hattori 1999), and through the interaction acoustic waves are observed three times, basically. The pressure peaks of the sounds decay in inverse proportion to the distance r from the vortex ring center.

It should be mentioned that the flow features and the generation mechanisms of the sounds are strongly dependent on the vortex Mach number M_v ; for a large M_v , shock wave focusing occurs and additional shock waves and expansion waves appear, leading to the generation of additional sounds.

3. Axisymmetric Vortex-Vortex Interactions

In this section, we examine the basic nature of the sounds generated by the interactions of two vortex rings with an equal strength. The vortex rings are set initially to move along the x -axis. The radial coordinate is expressed by y . The vortex rings are assumed to have a Gaussian distribution of the vorticity initially. The Mach number M of the vortex rings is prescribed to be $M = 0.075$ to 0.3 . The Reynolds number is based on the ring radius and the initial translational velocity and is prescribed to be $Re = 500$ to 2000 . The ratio r_c of the core radius to the ring radius is prescribed to be $r_c = 0.1$ to 0.3 .

3.1. HEAD-ON COLLISION OF TWO VORTEX RINGS

The two vortex rings are assumed to have the opposite sense of rotation and move along the x -axis in the opposite direction to each other. With increased time, the two vortex rings approach along the x -axis and then stretch along the direction perpendicular to the x -axis; the vortex cores move outward from the x -axis, and the radii of the vortex rings grow with time.

Instantaneous sound pressure fields at times after the beginning of the stretching are presented in Fig. 6 for the case of $M = 0.15$, $r_c = 0.15$ and $Re = 500$. The sound pressure Δp is defined as $\Delta p = p - p_\infty$. Figure 6 shows that sounds are generated twice (the first and the second sounds). Each sound has a quadrupolar nature but opposite alternating signs of circumferential pressure variation to each other.

Radial distributions of the sound pressure, Δp , for the same flow as in Fig. 6 are plotted against the distance r from the origin in Fig. 7 for $\theta = 0^\circ$ (along the x -axis). As seen from Fig. 7, both the first and the second sounds propagate radially with time. The propagation velocity of the sounds is equal to the sound speed. If we assume that the sounds are radiated from the origin ($r = 0$), the estimated time of sound radiation is approximately equal to the starting time of stretching.

It is also seen from Fig. 7 that the peak values of Δp of both the first and the second sounds decay with r . The peak values of the sound pressure of the first sound measured along the $\theta = 0^\circ$ and 90° lines are plotted in Fig. 8 for the two vortex core sizes: $r_c = 0.15$ and $r_c = 0.3$. In the figure, the solid line denotes the inverse proportion to r . We can see from Fig. 8 that in the far-field the sound pressure decays in inverse proportion to the distance r , in agreement with the theoretical prediction (Landau & Lifshitz 1987)

3.2. LEAPFROGGING AND MERGING OF TWO VORTEX RINGS

The two vortex rings are assumed to have the same sense of rotation and move along the x -axis towards the positive x -direction. With increased time, mutual interaction between them leads to the so-called leapfrogging.

Instantaneous vorticity and sound pressure fields for the case of $M = 0.15$, $r_c = 0.15$ and $Re = 800$ are presented in Figs. 9(a) and 9(b), respectively. In this case, the rear vortex ring undergoes the first slip-through and emerge ahead of the front ring (Fig. 9a). Then, the front ring try to undergo the second slip-through, but before completing the slip-through the two rings merge into a single ring. The merging has already completed by $t = 80$, and in Fig. 9(b) the resulting single ring exists around $x = 13.5$. We can see from Fig. 9(b) that the slip-through process and the merging process respectively produce sounds. Due to the Doppler effect, stronger sounds with higher frequencies are generated in the front side ($x > 0$) of the vortex ring than in the rear side.

4. Concluding Remarks

Entire acoustic fields from near to far fields produced by the interactions of shock-vortex and of two vortex rings were simulated by solving the unsteady, compressible Navier-Stokes equations. The generation mechanisms of the sounds through the interactions and the basic nature of the sounds generated were examined.

For the case of shock-vortex interaction, the sound generation and the basic nature of the generated sounds are closely related to the generation of the reflected shock waves. For the case of vortex-vortex interaction, the vortex motions induced by mutual interaction strongly affect the generation mechanisms of the sounds. The sound pressure has been confirmed to decay in the far field in proportion to the distance r^{-1} for 3D flows and to $r^{-1/2}$ for 2D flows, in agreement with theory.

The present results show that the direct Navier-Stokes simulation is a very powerful tool to analyze the generation mechanisms of sounds at least for such simple flows as those treated in this work. With an improved performance of supercomputers, the application of DNS to more complicated flows may be promising.

The author expresses his sincere gratitude to Asako Inoue for her continuous encouragement. Thanks are also given to Dr. Y. Hattori, Kyushu Institute of Technology, and to Mr. S. Onuma, Institute of Fluid Science (IFS), Tohoku University, for their useful discussion and technical assistance. Computations were performed with the CRAY C916 at IFS.

References

- Inoue, O. and Hattori, Y. (1998) Direct simulation of acoustic sound generated by two vortex rings. *AIAA Paper 98-2329, 4th AIAA/CEAS Aeroacoustics Conference, A Collection of Technical Papers, Part 2*, 758-764
- Inoue, O. and Hattori, Y. (1999) Sound generation by shock-vortex interactions. *J. Fluid Mech.*, **380**, 81-116.
- Landau, L. D. and Lifshitz, E. M. (1984) *Fluid Mechanics* (Pergamon, 2nd edn, Vol. 6.)
- Lele, S. K. (1992) Compact finite difference schemes with spectral-like resolution. *J. Comp. Phys.* **103**, 16-42.
- Lele, S. K. (1997) Computational aeroacoustics: a review. *AIAA Paper 97-0018*
- Moin, P. and Mahesh, K. (1998) Direct numerical simulation: a tool in turbulence research. *Ann. Rev. Fluid Mech.* **30**, 539-578.
- Poinsot, T. and Lele, S. K. (1992) Boundary conditions for direct simulation of compressible viscous flows. *J. Comp. Phys.* **101**, 104-129.
- Tam, C. K. W. (1995) Computational aeroacoustics: issues and methods. *AIAA J.* **33**, 1788-1796.
- Wells, V. L. and Renaut, R. A. (1997) Computing aerodynamically generated noise. *Ann. Rev. Fluid Mech.* **29**, 161-199.

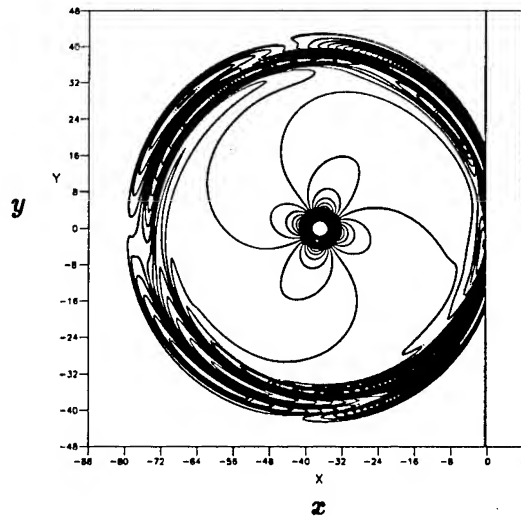


Figure 1. Isobars of the sound pressure. 2D shock-vortex interaction. $M_s = 1.05$, $M_v = 0.25$. $t = 40.0$.

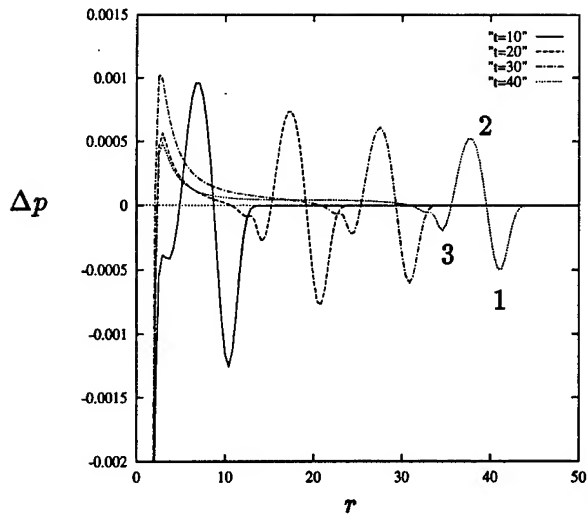


Figure 2. Radial distributions of the sound pressure. $\theta = 45^\circ$. $M_s = 1.05$, $M_v = 0.25$.
 —: $t = 10.0$, - - - - -: $t = 20.0$, - · - · -: $t = 30.0$, · · · · ·: $t = 40.0$.

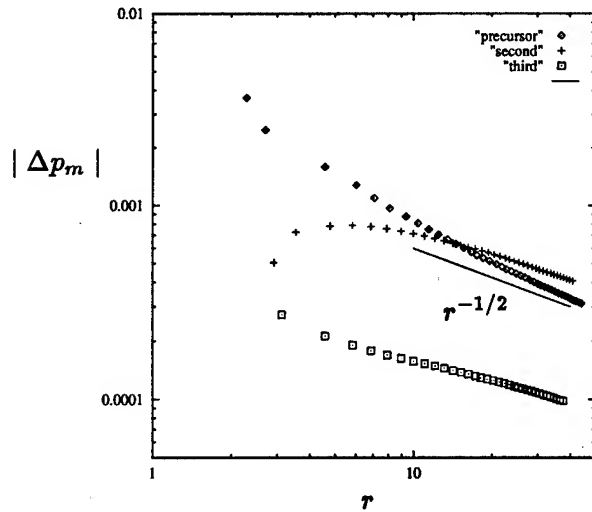


Figure 3. Decay of the sound pressure. $\theta = -45^\circ$. \diamond : precursor, + : second sound, \square : third sound, — : $\Delta p_m \propto r^{-1/2}$.

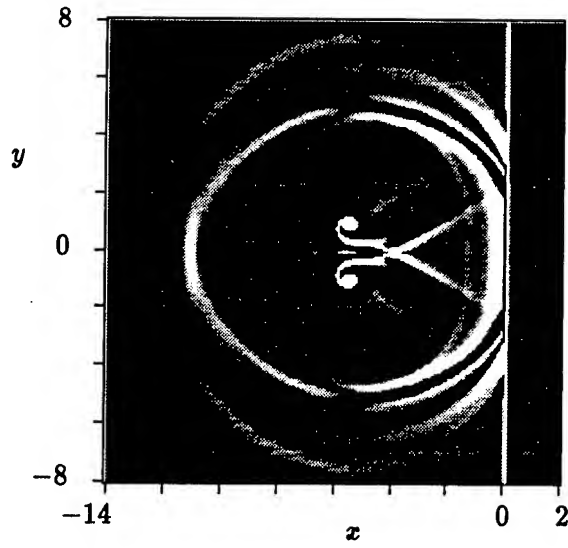


Figure 4. Computational shadowgraph. Shock-vortex ring interaction. $M_s = 1.2$, $M_v = 0.1$. $t = 15.0$.

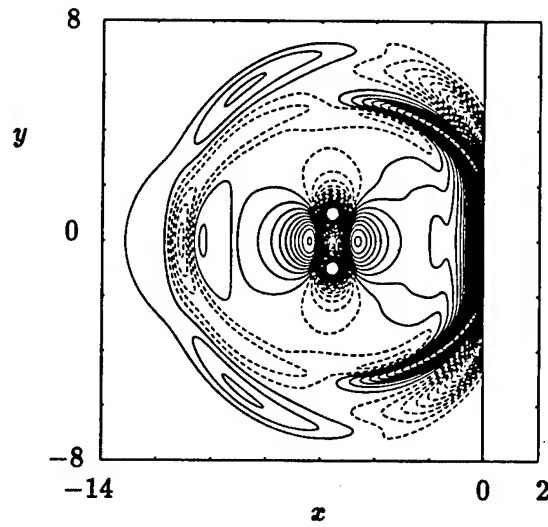


Figure 5. Isobars of the sound pressure. Shock-vortex ring interaction. $M_s = 1.2$, $M_v = 0.1$. $t = 15.0$.

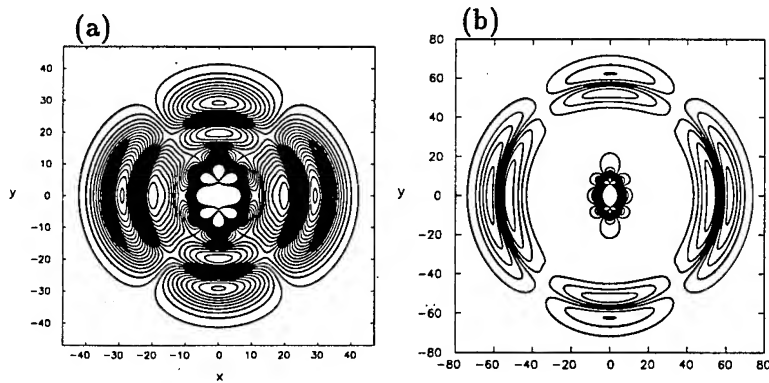


Figure 6. Isobars of the sound pressure. Head-on collision of two vortex rings. $M = 0.15$, $\tau_c = 0.15$, $Re = 500$. (a) $t = 88$, (b) $t = 120$.

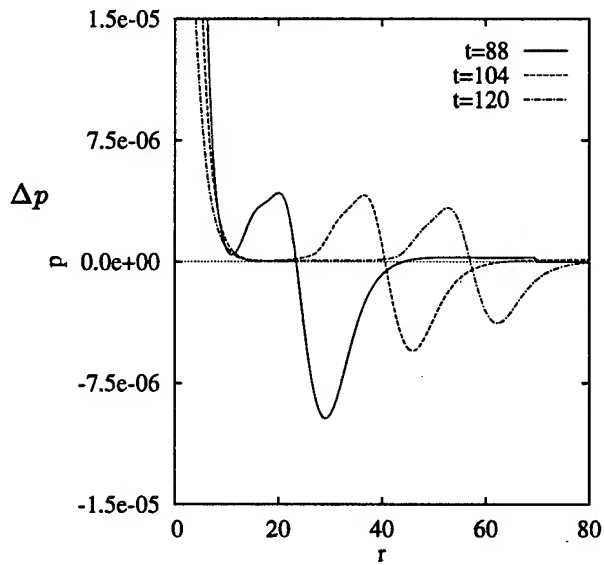


Figure 7. Radial distributions of the sound pressure. $M = 0.15$, $\tau_c = 0.15$, $Re = 500$. $\theta = 0^\circ$. — $t = 88$, --- $t = 104$, - · - · - $t = 120$,

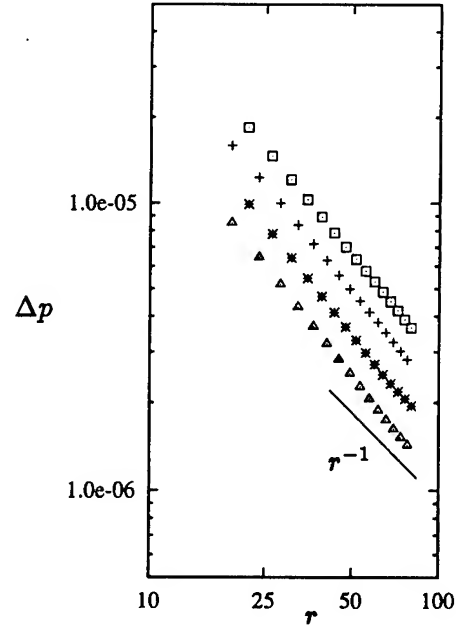


Figure 8. Decay of the peaks of the sound pressure. $M = 0.15$, $Re = 500$. First sound.
 \square : $r_c = 0.3, \theta = 0^\circ$. $*$: $r_c = 0.3, \theta = 90^\circ$. $+$: $r_c = 0.15, \theta = 0^\circ$. Δ : $r_c = 0.15, \theta = 90^\circ$.
 — $\propto r^{-1}$,

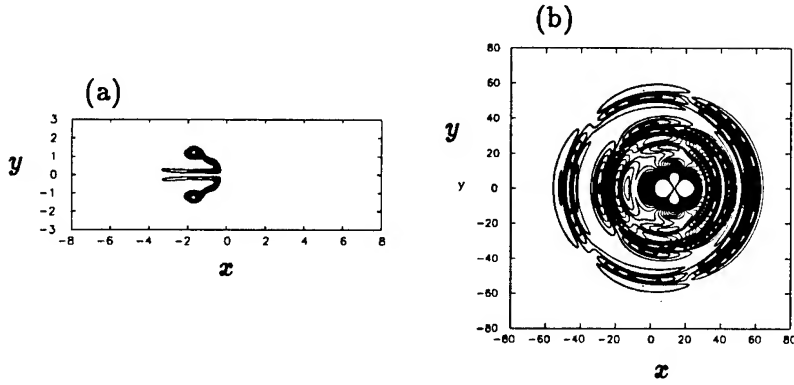


Figure 9. Leapfrogging and merging of two vortex rings. $M = 0.15$, $r_c = 0.15$, $Re = 800$.
 (a) Vorticity contours, $t = 32$. (b) Isobars of the sound pressure. $t = 80$.

OPTIMAL LES: HOW GOOD CAN AN LES BE?

R. D. MOSER, J. A. LANGFORD AND S. VÖLKER

*Dept. of Theoretical and Applied Mechanics
Univeristy of Illinois at Urbana-Champaign
Urbana, IL 61801*

Abstract.

In this paper, we approach Large Eddy Simulation (LES) by asking: How good is it possible for an LES to be? Taking a probabilistic approach, it is shown that by formally minimizing the rms error in the time derivative of the large scales, one can guarantee that the LES will reproduce the large scale statistics exactly. The LES model that minimizes the rms error in the time derivative is written as a conditional average, and we consider this to be the ideal LES model. Unfortunately, we do not know, nor can we practically compute this conditional average. The problem of LES modeling can therefore be considered to be a problem of finding a good approximation to the conditional average. Using direct numerical simulation data from a forced isotropic turbulence and a turbulent channel, estimates of the conditional average have been obtained, and the results are very instructive. Using the results, the nature of good LES models, the effects of filter definition, and the impact of inhomogeneity are explored. Also discussed is a program for developing practical LES models based on these ideas.

1. Introduction

Large-eddy simulation of turbulence (LES) is a promising technique for predicting the effects of turbulence in flows of technological interest (Rogallo and Moin, 1984; Lesieur and Métais, 1996). Because of its great promise, much recent research has been aimed at developing robust and accurate LES models. The dynamic Smagorinsky model (Germano et al., 1991; Lilly, 1992), new variants of the scale similarity model (Liu et al., 1994), the structure function model (Métais and Lesieur, 1992) and the stretched vortex model (Misra and Pullin, 1997) have all been developed over the

last 10 years. These models have allowed LES to be applied in a variety of flows, and have greatly improved the veracity of LES simulations.

All of these LES models are derived based on restrictive assumptions about the nature of the sub-grid turbulence. For example, both the dynamic model and the scale similarity model are predicated on the assumption that the filter width is well into an inertial range. Further, the Smagorinsky model underlies the most common implementation of the dynamic model, and it is derived assuming homogeneity and isotropy. However, these assumptions are violated in flow situations of common interest such as near walls. Development of wall models that will not require the refinement of the near wall grid with increasing Reynolds number is considered by many to be the most pressing challenge in LES research.

Current LES models also suffer from a range of less commonly recognized difficulties. These include: an inadequately formulated dependence of the model on the characteristics of the filter; unaccounted for numerical errors; and poor treatment of “commutation” errors that arise when filters are inhomogeneous; further details are available in (Langford and Moser, 1999).

All of these difficulties could be addressed if there were a well-defined procedure by which LES models could be constructed in general. In this paper we describe such a procedure that is based on the requirement that the LES model be “as good as possible.” This leads to the question posed in the title: “How good can an LES be?” which is answered in §2. The application of these ideas to isotropic turbulence and turbulent channel flow is discussed in §3 and §4 respectively. A strategy for translating this procedure into LES models for practical applications is presented in §5, and concluding remarks are given in §6.

2. Ideal and Optimal LES

For any LES field w , there is a unique evolution dw/dt that produces exact single-time spatial statistics and that minimizes the error of the short-time large-scale dynamics (Langford and Moser, 1999). These two properties are all that one can ask for in an LES, so this evolution will be called an *ideal LES*. The ideal evolution is given by the conditional average

$$\frac{dw}{dt} = \left\langle \frac{d\bar{u}}{dt} \middle| \bar{u} = w \right\rangle, \quad (1)$$

where u is an unfiltered turbulent field from the real system, and over-bar indicates the filter. The result on accuracy of single-time statistics comes from consideration of the pdf evolutions of the real and LES systems (Pope, 1997; Langford and Moser, 1999). In fact, all single point statistics of an

LES will match the statistics of a real turbulence *if and only if* the LES evolves according to (1). The accuracy of short-time large-scale dynamics comes from the observation that the conditional average minimizes error measured on $\partial \bar{u}/\partial t$ (Papoulis, 1965) and that $\partial \bar{u}/\partial t$ is the leading order term in a prediction of the filtered field at a future time (Adrian, 1990). Note that the conditional average in the ideal evolution equation is conditioned on the *entire* large-scale field, so that as a matter of practice the ideal evolution can never be found. However, one can approximate the conditional average using standard stochastic estimation techniques (Adrian, 1977; Adrian and Moin, 1988; Adrian et al., 1989; Langford and Moser, 1999). These approximations will be referred to as *optimal estimates*, and are used to investigate properties of the ideal model, as well as to construct computable LES models.

An integral part of any LES is the filter that is used to define the large scale turbulence to be simulated. To be useful for LES, the filter must be a non-invertible operator; that is, it must discard information. If one were to use an invertible filter, the ideal evolution (1) would be the exact evolution, and the LES would be a DNS, with the same resolution requirements as a DNS. Since a useful LES filter is non-invertible, there are many real turbulence fields that produce the same filtered (LES) field. The conditional average in (1) is then an average over all the turbulence fields that map to a single LES field. However, some commonly used filters for LES (e.g. Gaussian and top-hat filters) are formally invertible. When such filters are used, it is the numerical discretization, such as sampling on a grid, that introduces the non-invertibility. In these cases, the discretization that causes the loss of information can be considered to be part of the filter, so the analysis here applies.

The incompressible LES equations are usually written as the Navier-Stokes operator acting on the filtered field plus a model term:

$$\frac{\partial w_i}{\partial t} + \frac{\partial w_i w_j}{\partial x_j} = -\frac{1}{\rho} \frac{\partial \bar{p}}{\partial x_i} + \nu \frac{\partial^2 w_i}{\partial x_j \partial x_j} + m_i, \quad (2)$$

where the model term m_i is an approximation to an exact sub-grid force term M_i that depends on the unresolved scales. The exact term M_i includes the usual sub-grid stress term $\frac{\partial}{\partial x_j} (\bar{u}_i \bar{u}_j - \bar{u}_i \bar{u}_j)$, as well as terms that arise when inhomogeneous filters do not commute with differentiation, and from the imposition of the divergence-free condition. To recover the ideal LES evolution equations (1), one should use the ideal sub-grid model $m_i(w) = \langle M_i(u) | \bar{u} = w \rangle$. The use of such a model guarantees that the statistical and dynamical properties of ideal LES are obtained.

The ideal model is constructed as an average of the sub-grid forcing terms over all possible turbulent fields that match in the large scales. The

ideal model is thus the deterministic part of the sub-grid force—the part of the sub-grid force that is common to all turbulent states with a given large-scale field. The component of instantaneous sub-grid force that does not contribute to the ideal model is associated with the stochastic nature of the sub-grid field. This stochastic nature can be quantified by measuring the root-mean-square difference between the exact term M_i and the best estimate m_i . This difference is equal to the error between $\partial \bar{u}_i / \partial t$ and the ideal LES evolution $\partial w_i / \partial t$, so it is also a measure of error committed in approximating the large-scale dynamics. The ideal model minimizes this error, but in general it is nonzero. So, for a given problem and filter, there is a minimum level of dynamical error that must be tolerated in a large-eddy simulation.

One is obviously interested in knowing what the ideal model looks like, and what the lower bound on error is. Unfortunately the ideal model and the minimum error cannot be directly measured because the information in the conditional average is tremendous. We have thus been using stochastic estimation techniques to approximate the conditional average and estimate the minimum error. The stochastic estimates are constructed as

$$m_i(x) = \int L_{ij}(x, \xi) w_j(\xi) d\xi + \int Q_{ijk}(x, \xi) w_j(\xi) w_k(\xi) d\xi + \dots \quad (3)$$

and the estimate of error is $e_i = M_i - m_i$. To solve for the kernels L_{ij} and Q_{ijk} , the mean-square error $\langle |e|^2 \rangle$ is minimized and two-point correlations from the real system are needed. Note that in minimizing $\langle |M - m|^2 \rangle$, one also minimizes $\langle |(\langle M(u) | \bar{u} = w \rangle - m)|^2 \rangle$, so that the optimal estimates can be regarded as approximations of the ideal model, and $\langle |e|^2 \rangle$ can be regarded as an estimate of the smallest possible error in the dynamics of the large-eddy simulation.

3. Isotropic Turbulence

Optimal LES models were computed for a case of forced isotropic turbulence that has been simulated using DNS ($256 \times 256 \times 256$, $k_{\max} = 128$, $R_\lambda = 167$). The filters tested were sharp Fourier cutoff filters with $k_c = 16$, $k_c = 32$, and $k_c = 64$. The filter with cutoff at $k_c = 16$ appeared to be in a short inertial range, while the higher wavenumber cutoffs were well into the dissipative range. The true sub-grid force to be modeled in this case was $M_i = \mathcal{P} \left(\frac{\partial}{\partial x_j} (\bar{u}_i \bar{u}_j - \bar{u}_i \bar{u}_j) \right)$, where \mathcal{P} is the solenoidal projection that arises from the imposition of continuity. The spectrum of M_i is compared to that of $\partial \bar{u}_i / \partial t$ in figure 1(a). It can be seen that at the lowest wavenumbers the mean-square magnitude of M_i is much smaller than that of $\partial \bar{u}_i / \partial t$, but that near the cutoff the mean-square magnitude is approximately 50% of

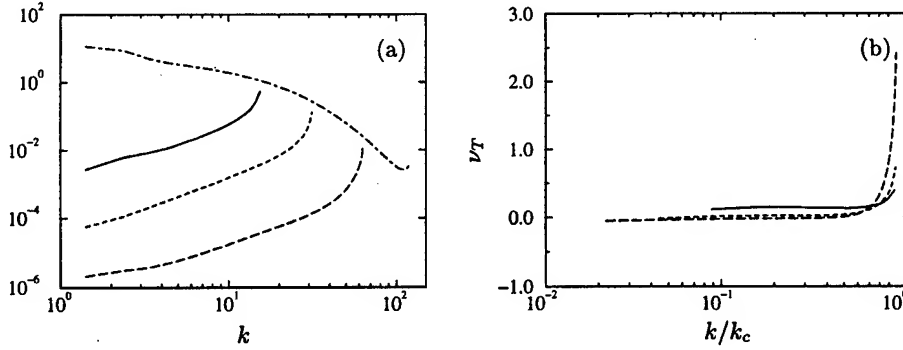


Figure 1. The (a) spectrum of the sub-grid terms $\mathcal{P}(\frac{\partial}{\partial x_j}(\bar{u}_i \bar{u}_j - \bar{u}_i \bar{u}_j))$ and (b) the optimal eddy-viscosities ν_T normalized by $[E(k_c)/k_c]^{\frac{1}{2}}$ for sharp Fourier cutoff filters at cutoffs $k_c = 16$ (—), $k_c = 32$ (---), and $k_c = 64$ (- - -). Also shown in (a) is the spectrum of $\partial \bar{u}_i / \partial t$ (· · · · ·).

that of $\partial u_i / \partial t$. It is clear that the importance of the sub-grid model is most significant near the cutoff.

For isotropic turbulence the stochastic estimates of (3) simplify considerably. The linear term can be written in wave-space in terms of an optimal eddy-viscosity $\hat{m}_i(k) = -k^2 \nu_T(k) \hat{u}_i(k)$, where the optimal eddy viscosity is

$$\nu_T = -\frac{1}{k^2} \frac{\langle \hat{M}_i(k) \hat{u}_i(-k) \rangle}{\langle \hat{u}_i(k) \hat{u}_i(-k) \rangle}. \quad (4)$$

The optimal eddy viscosity ν_T is shown for the three cutoff filters in figure 1(b). They all turn up sharply near the cutoff as predicted by (Kraichnan, 1976) and observed by (Domaradzki et al., 1987; Lesieur and Rogallo, 1989). Also note that the eddy viscosities are nearly zero, and in fact go negative far from the cutoff for the two highest wavenumber cutoffs. These cases are consistent with the results of (Domaradzki et al., 1987), who also obtained slightly negative plateau values when the cutoffs were in a dissipative range. It has been suggested by (Lesieur, 1998) that when the cutoff is located where the spectrum has a significantly steeper slope than the $k^{-5/3}$ of the Kolmogorov inertial range, then the plateau level of the eddy viscosity should go to zero. The $k_c = 16$ case has behavior that is more representative of a high Reynolds number LES with the cutoff in the inertial range. Results of E.D.Q.N.M. suggest that for cutoff in the inertial range, the eddy viscosity has a plateau value of 0.267 (Chollet and Lesieur, 1981), which is the basis of the structure function model (Métais and Lesieur, 1992). A plateau value of 0.09 was observed by (Lesieur and Rogallo, 1989), and in our case of $k_c = 16$ the plateau value is approximately 0.13, which is consistent with the other results.

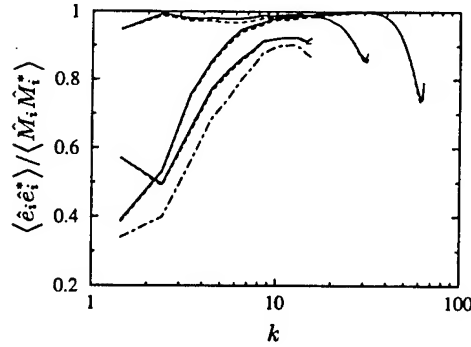


Figure 2. Spectra of the estimation errors for the linear (—), quadratic (---), and 46-term (- · - · -) estimates of the sub-grid term at three different sharp cutoff widths, normalized by the spectrum of the real sub-grid term.

Figure 2 shows the spectrum of the estimation error $e_i = M_i - m_i$, normalized by the spectrum of M_i . With this normalization one can see exactly what fraction of the sub-grid forcing term M_i is unrepresented by the estimate. Errors are shown for linear and quadratic models, where the quadratic models include both terms of (3). In the case of filter cutoff $k_c = 16$, a 46-term model has also been included. The 46-term model contains enough terms to subsume the Smagorinsky and scale-similarity models, and includes the cubic terms suggested by the RNG analysis of (Zhou and Vahala, 1993). For a listing of the 46 terms, see (Langford and Moser, 1999). Of the 46 terms, the linear term was the most significant. Further, there was no other term that appeared to offer a significant contribution; rather the improvement of the 46-term model over the linear model came as a cumulative effect. Recall that the errors shown in figure 2 are only approximations to the limiting error of the ideal model. Nevertheless, this result suggests that it is likely that the sub-grid force is mostly stochastic, and that the fundamental errors associated with modeling the sub-grid term may be large.

It can be shown that the linear (optimal eddy-viscosity) model has the *a priori* property that all two-point velocity statistics are correct (Langford and Moser, 1999). But, it cannot be proven that this property will be retained in actual simulations (this is in contrast to results for the ideal model which do apply to actual simulation). To determine how well a linear model actually performs, a large-eddy simulation was run with an optimal linear model. The three-dimensional energy spectrum $E(k)$ and the third order structure function are shown for the LES and DNS in figure 3. It is clear that the linear LES recovers the energy spectrum well. In figure 3(b), note

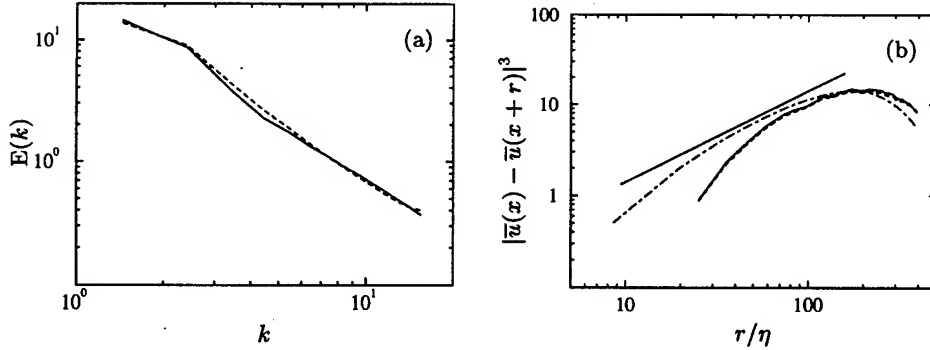


Figure 3. The (a) 3-D energy spectrum and (b) third-order structure function for filtered DNS (—), optimal linear LES (---) and in (b) the unfiltered DNS (····). In (b) the straight line indicates a slope of 1, which is the inertial range result.

that the filtered DNS and unfiltered DNS structure functions are different because the sharp Fourier cutoff filter has nonlocal effects in physical space. It is also remarkable that the linear LES recovers the correct third-order structure function; this property is not even expected *a priori*.

4. Wall-Bounded Turbulence

The isotropic turbulence results discussed in §3 are not directly applicable to an inhomogeneous flow. A variety of complications arise when the turbulence is inhomogeneous and anisotropic. Among these are: the need for an inhomogeneous filter, and the resulting “commutation error;” the inability to use the simplifications of Fourier analysis; and a possible lack of small-scale homogeneity or isotropy, which impacts the very nature of the sub-grid term. These issues all occur in wall-bounded turbulence, and LES modeling of near-wall turbulence is the major problem that needs to be addressed in LES modeling. For these reasons, we chose the turbulent channel flow in which to apply the ideas presented in §2.

4.1. INHOMOGENEOUS FILTERING

When an inhomogeneous filter is used, the model term m_i in (2) includes corrections for the fact that filtering and differentiation do not commute. The magnitude of this commutation term is of some importance, since current modeling approaches do not account for it, and it could significantly increase the magnitude of the sub-grid term to be modeled. We chose to study a Chebychev cut-off filter, which is natural in the context of the DNS data of (Moser et al., 1999) used in the study. The truncation is performed in such a way as to preserve continuity and the boundary conditions.

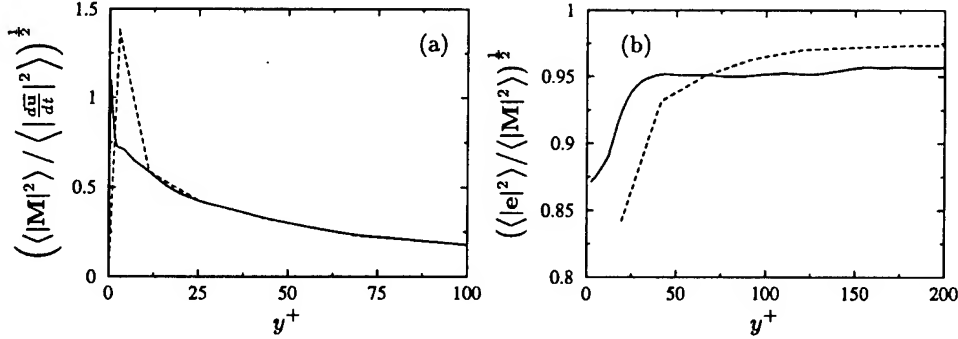


Figure 4. Results of analysis of the turbulent channel near the wall (y coordinate is in wall-units, where the center of the channel is at $y^+ = 590$). (a) The magnitude of the sub-grid term normalized by the magnitude of the filtered time-derivative and (b) the magnitude of the relative error in estimating the sub-grid term, with no wall-normal filter (—) and Chebychev filter (---). The event data are described in §4.2.

The filter was applied to the $Re_\tau = 590$ channel flow DNS data of (Moser et al., 1999). The data was filtered in the horizontal spatial directions (x and z) using a Fourier cut-off filter, with cut-off wavenumbers of 16 and 32 in x and z respectively, which reduces the “grid size” in both directions to 32 from the value of 384 in the DNS data. In one case, no wall-normal filtering was applied. In the other case, the Chebychev filter was applied, truncating the system from 257 modes in the DNS to 33 modes for the LES. With this filter, the rms magnitude of the real sub-grid term M_i was computed, and is plotted normalized by the true $\partial \bar{u} / \partial t$ in figure 4(a). Whether or not the wall-normal filter is used, the relative size of the model term is the same, except for the narrow peak one “grid point” from the wall. This peak may be a consequence of the method by which the boundary conditions are enforced. The fact that the relative magnitudes are nearly identical with or without wall-normal filtering suggests that the commutation error is not particularly important.

Away from the wall the model term is only 20% of $\partial \bar{u} / \partial t$, but it increases to about 75% near the wall (not including the peak at the wall). Thus, unlike in isotropic turbulence, near the wall, the Navier-Stokes terms in (2) do not represent most of the large-scale dynamics. This is unfortunate since we then do not have the benefit of modeling a relatively small term. This is of concern given the large relative errors in the estimates.

4.2. CHANNEL ESTIMATION ERRORS

Estimates were performed using a wide variety of event data. The terms included many of those used in the 46-term model in §3. However, in the

channel flow, we are not able to obtain as good a statistical sample of the estimation quantities as we were in isotropic turbulence. The reason is that there are only two homogeneous directions to average over, and we cannot take advantage of isotropy to do shell averaging. The consequence is that we cannot support nearly as many estimation events before we run into statistical sample problems.

It was found that the model term at any y location could be best estimated using the velocity and its derivatives, and the divergence of the quadratic products of the velocity evaluated at the estimation point. Estimates based on events at different points (in y) near the estimation point were also evaluated and found to not be significantly better than this local estimate. Note that the estimates were done in Fourier space in x and z (as for the isotropic case), so the estimate is essentially global in those directions.

The estimation error, normalized by the magnitude of the sub-grid term, is shown as a function of y in figure 4(b). The relative errors are between 90% and 95% through most of the channel, consistent with the large errors found for isotropic turbulence, the errors are significantly lower very near the wall. This suggests that there is more being estimated than just the isotropic dissipation we were able to model for isotropic turbulence. Though the relative errors are smaller near the wall, this is not enough to compensate for the larger magnitude of the sub-grid term in this region. Thus, in balance, the percentage error in $\partial\bar{u}/\partial t$ will be larger near the wall. This is troublesome since it implies that the short-time large-scale dynamics will be poorly represented near the wall. Though, if our estimates are good approximations of the ideal model (1), this will not impact the accuracy of the statistics. The nature of the estimates is currently being analyzed to obtain computable models for near-wall turbulence, which can be implemented and evaluated in an actual LES.

5. Developing Practical LES Models

There are clearly several obstacles to the direct application of the above modeling techniques to practical LES simulations. These obstacles and our strategy for overcoming them are described briefly below.

The Fourier and other cut-off filters used here are not broadly applicable. Instead, it is more common to use a finite volume filter. The definition of a finite-volume filter (often called a top-hat filter) is rather straight forward. One defines an array of discrete volumes covering the domain and defines a filtered quantity \bar{u}_j to be the average of the quantity over each

volume, thus:

$$\bar{u}_j = \int_{V_j} u \, dv, \quad (5)$$

where V_j is the j th volume. Note that unlike the Fourier cut-off filter, the result of applying the filter operator in this case is a set of discrete volume averages, rather than a continuous function. As a consequence, without making further approximations, we cannot define the spatial derivative of the filtered function. Thus defining the Navier-Stokes terms as in the analysis discussed in §2 is problematic. Even defining the divergence of the filtered velocity is a problem.

However, the ideal LES evolution (1) is still valid in this case. In fact, we need not even include the Navier-Stokes terms. Instead, using stochastic estimation, the time derivative of the filtered velocity (volume averages) can be estimated directly based on knowledge of the the current filtered velocity. If the estimate is based on sufficiently general quadratic event data, it will subsume all sensible finite volume approximations of the Navier-Stokes equations, making the inclusion of explicit Navier-Stokes terms unnecessary. Indeed, it may be possible to interpret such an estimate as a finite volume flux approximation.

The main ingredient of the estimation models discussed here is extensive two-point cross-correlation data. This poses two problems: 1) how to obtain sufficient data and 2) how to deal with flows for which no data is available. The three-dimensional multi-point cross-correlation data needed for the estimation models is currently only available from direct numerical simulation (DNS). However, DNS is restricted to low Reynolds numbers, while the problems of most interest for LES are at very large Reynolds number. To extrapolate the low-Reynolds number correlations obtained from DNS to higher Reynolds numbers, two-dimensional field measurements, such as those available via PIV, are needed. A strategy for using such two-dimensional data in this context is discussed in (Moser and Adrian, 1998).

Of course, an LES model would not be very useful if it can only be used in flows for which extensive DNS and experimental data are available. Thus, it is of great importance to be able to apply available data to other flows. The attractive feature of LES for turbulence prediction has always been that only the small-scales need be modeled, and the small scales are not nearly as sensitive to the details of the flow as the turbulence as a whole. There is thus good reason to expect that DNS and experimental data from a relatively small number of model flows will be sufficient to produce sub-grid models for a large class of flows. It is anticipated that data from isotropic turbulence, wall-bounded flows, separated flows and flows with embedded small-scale laminar features (e.g. cylinder in cross-flow) will be needed. Isotropic turbulence and channel flow were chosen for

the studies discussed in §3 and §4 to fulfill these requirements, and studies on cylinder in cross flow, and forward facing and backward facing steps are planned for the same reason.

6. How Good Can an LES Be?

So how good can an LES be? If one is interested in single-time statistics, in principle it can be perfect, since there is an ideal sub-grid model (the conditional average, (1)) that guarantees accurate single-time statistics. Following is a brief list of what we have learned about this ideal model:

1. The ideal model minimizes error in the sub-grid term, but this error appears not to be small. If true, this would explain the common observation that a sub-grid model may perform very poorly in *a priori* tests, while performing well when implemented in an LES.
2. In isotropic turbulence, the sub-grid terms are small, so the large error discussed above is not of great concern. But, this is not true near the wall in the channel flow.
3. The ideal model cannot be directly computed, but in isotropic turbulence with a Fourier cut-off filter, even a simple linear estimate of the ideal yields a remarkably good LES. Indeed, in this case, the only non-stochastic effect of the sub-grid turbulence that we could identify was the dissipative energy transfer represented by the linear estimate.
4. In the channel flow, there is apparently more than just dissipation that can be modeled near the wall.

The existence of the ideal sub-grid model, and its important properties, completely changes the sub-grid modeling endeavor. There is now a clearly defined goal for sub-grid models (i.e. the ideal model). In addition, there is a systematic technique (stochastic estimation) for constructing models that approach the goal. Thus, in principle, LES models can be very good indeed, and it is "just" a matter of time and effort to make them so.

The research reported here was jointly supported by the National Science Foundation and the Air Force Office of Scientific Research under NSF grant CTS-9616219, by NASA under grant NGT 2-52229 and by DOE under University of California grant B341494.

References

- Adrian, R. J. (1977). On the role of conditional averages in turbulence theory. In J. Zakin and G. Patterson, Eds. *Turbulence in Liquids*. Princeton, NJ: Science Press.
- Adrian, R. J. (1990). Stochastic estimation of sub-grid scale motions. *Appl. Mech. Rev.*, 43(214).

- Adrian, R. J., Jones, B. G., Chung, M. K., Hassan, Y., Nithianandan, C. K., and Tung, A. (1989). Approximation of turbulent conditional averages by stochastic estimation. *Phys. Fluids*, 1(6):992-998.
- Adrian, R. J. and Moin, P. (1988). Stochastic estimation of organized turbulent structure: homogeneous shear flow. *J. Fluid Mech.*, 190:531-559.
- Chollet, J. and Lesieur, M. (1981). Parameterization of small scales of three-dimensional isotropic turbulence using spectral closures. *J. Atmos. Sci.*, 38:2747-2757.
- Domaradzki, J., Metcalfe, R., Rogallo, R., and Riley, J. (1987). Analysis of subgrid-scale eddy viscosity with use of results from direct numerical simulations. *Phys. Rev. Lett.*, 68(6):547-550.
- Germano, M., Piomelli, U., Moin, P., and Cabot, W. H. (1991). A dynamic subgrid-scale eddy viscosity model. *Phys. Fluids*, 3:1760-1765.
- Kraichnan, R. (1976). Eddy viscosity in two and three dimensions. *J. Atmos. Sci.*, 33:1521-1536.
- Langford, J. and Moser, R. (1999). Optimal large-eddy simulation formulations for isotropic turbulence. submitted to *The Journal of Fluid Mechanics*.
- Lesieur, M. (1998). Spectral eddy-viscosity based LES of incompressible and compressible shear flows. AIAA-98-2894.
- Lesieur, M. and Métais, O. (1996). New trends in large-eddy simulations of turbulence. *Annu. Rev. of Fluid Mech.*, 28:45-82.
- Lesieur, M. and Rogallo, R. (1989). Large-eddy simulation of passive scalar diffusion in isotropic turbulence. *Phys. Fluids*, 1(4):718-722.
- Lilly, D. K. (1992). A proposed modification of the Germano subgrid-scale closure method. *Phys. Fluids*, 4(3):633-635.
- Liu, S., Meneveau, C., and Katz, J. (1994). On the properties of similarity subgrid-scale models as deduced from measurements in a turbulent jet. *J. Fluid Mech.*, 275:83-119.
- Métais, O. and Lesieur, M. (1992). Spectral large-eddy simulation of isotropic and stably stratified turbulence. *J. Fluid Mech.*, 239:157.
- Misra, A. and Pullin, D. I. (1997). A vortex-based subgrid model for large-eddy simulation. *Phys. Fluids*, 9:2443-2454.
- Moser, R. D. and Adrian, R. J. (1998). Turbulence data for les development and validation. In *Proceedings of FEDSM'98*, FEDSM98-5092.
- Moser, R. D., Kim, J., and Mansour, N. N. (1999). Direct numerical simulation of turbulent channel flow up to $re_\tau = 590$. *pof*, 11:943-945.
- Papoulis, A. (1965). *Probability, Random Variables, and Stochastic Processes*. McGraw-Hill, New York.
- Pope, S. B. (1997). private communication.
- Rogallo, R. S. and Moin, P. (1984). Numerical simulation of turbulent flows. *Annu. Rev. of Fluid Mech.*, 16:99-137.
- Zhou, Y. and Vahala, G. (1993). Reformulation of recursive-renormalization-group-based subgrid modeling of turbulence. *Phys. Rev. E*, 47:2503-2519.

DNS TO HELP UNDERSTANDING OF NON-PREMIXED TURBULENT FLAMES

LUC VERVISCH

Institut National des Sciences Appliquées de Rouen

LMFN / UMR CNRS / CORIA 6614

Avenue de l'Université - BP 8

FR-76801 Saint Etienne du Rouvray Cedex, France

e-mail: vervisch@coria.fr

1. Introduction

Numerical simulation of flames is a rapidly growing field bringing important improvements to our understanding of combustion. Even though Computational Fluid Dynamics (CFD) is widely applied to flames, it is not yet intensively used as an optimization tool for practical combustion systems. Some trends are interestingly predicted by CFD, but detailed simulations of a real combustion chamber are far from being routine. This is due to the complexity of combustion problems, involving strong coupling between chemistry, transport phenomena and fluid dynamics (Bray, 1996).

There are many practical issues that cannot be addressed carefully using available numerical combustion codes. For example, the description and control of unsteady combustion are crucial in the development of high-efficiency gas turbines, and existing CFD techniques are mostly based on Reynolds Averaged Navier Stokes (RANS) models (Jones, 1994). These models have difficulties to deal with strong unsteady flows, combustion instabilities, flame blow-off or flashback. Large Eddy Simulation (LES) can help to progress in this direction, since unsteady large scale mixing (between fresh and burnt gases in premixed flames or between fuel and oxidizer in non-premixed burners) is directly simulated, instead of being averaged with small scales effects. Nevertheless, as in RANS, the complex coupling between micro-mixing and chemical reactions occurring at unresolved scales needs models. These models rely on assumptions for both chemistry and transport, assumptions which have to be carefully formulated according to the fundamental properties of turbulent flames.

Direct Numerical Simulation (DNS) appears as an interesting research instrument to develop these sub-models, via the creation of synthetic laminar or turbulent flames. In DNS, all the scales (length and time) are calculated without resorting to closure models. These simulations were originally devoted to the study of non-reactive flows (Moin and Mahesh, 1998), but during the last 10 years, DNS techniques have found important applications in combustion (Jou and Riley, 1989; Givi, 1989; Poinso et al., 1996; Vervisch and Poinso, 1998).

Almost all practical systems operate with fuel and oxidizer not perfectly premixed before entering the combustion chamber. Moreover, even in premixed systems, partial premixing is sometimes desirable to control pollution (stratified charge engines). In consequence, understanding of non-premixed turbulent flames is a central issue of combustion. In what follows, we present a short review of DNS applied to these flames.

2. DNS of non-premixed turbulent flames

2.1. BACKGROUND

In diffusion or non-premixed turbulent flames, large scale motions lead to a partial mixing of the reactants, while turbulent micro-mixing mechanisms are necessary to bring fuel and oxidizer into contact in the reaction zones where heat is released. The properties of non-premixed turbulent burners thereby depend a lot on the aerodynamic and turbulent mixing.

According to results of analysis of laminar diffusive-reactive layers (Liñán, 1974), in the vicinity of the stoichiometric surface, it is expected to observe quasi-steady combustion when the heat transferred by diffusion and convection is balanced by the heat released in the reaction zone. While finite rate chemistry effects, or even local quenching, can be found when heat transfer is so large than the chemistry cannot keep up with it.

The extent of mixing between fuel and oxidizer is measured using the mixture fraction $Z = (\phi(Y_F/Y_{F,o}) - (Y_O/Y_{O,o}) + 1)/(\phi + 1)$, where ϕ is the fuel/air mass stoichiometric ratio, Y_F and Y_O are the fuel and oxidizer mass fraction respectively. The subscript o denotes quantities measured in pure streams. Defined in this manner, Z is a passive scalar verifying $Z = 0$ in pure air and $Z = 1$ in the fuel stream (Bilger, 1989). The control parameters of laminar diffusion flames are: a diffusive time τ_χ , measured from the scalar dissipation rate $\chi = D |\nabla Z|^2 = (\tau_\chi)^{-1}$, and, a chemical time τ_c . Both are retained to build a Damköhler number $Da = (\tau_c \chi)^{-1}$. In turbulent burners, the response of relevant quantities (temperature, species mass fraction) plotted versus Z allows to distinguish various situations, corresponding to strong or weak flow/chemistry interaction (Masri et al., 1988).

2.2. REGIMES IN NON-PREMIXED TURBULENT FLAMES

Before discussing the limitations of DNS calculations, one needs to identify the key control parameters of non-premixed turbulent combustion, used to discriminate between combustion regimes. The literature on this subject shows that this is not an easy task (Bilger, 1988; Bray and Peters, 1994; Lee and Pope, 1995; Cook and Riley, 1996). The main difficulty arises from the fact that these flames are mixing controlled, and do not have a fixed and unique reference length. Moreover, in opposition to premixed flames, diffusion flames do not propagate by themselves, and there is no obvious specific speed involved in the problem.

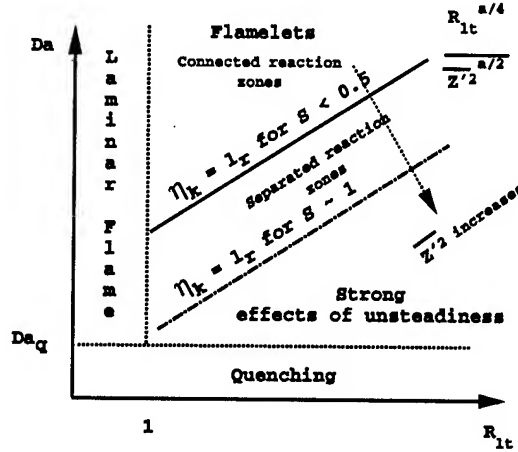


Figure 1. Approximation of combustion regimes for non-premixed turbulent flames. Da is a Damköhler number, Da_q its value at quenching, Re_{lt} is a Reynolds number based on the integral length scale, l_r is the thickness of the reaction zone, η_k is the Kolmogorov length scale, Z is the mixture fraction and S denotes the unmixedness.

An attempt to build a generic classification is achieved by introducing the level of non-homogeneities in the mixing between the reactants measured by \tilde{Z}''^2 , a Reynolds number $Re_{lt} = (k^{1/2}l_t/\nu)$, and a global Damköhler number $Da = (Da^*/\tilde{Z}''^2)$, with $Da^* = (\tau_t/\tau_c)$. Where k is the kinetic energy of the turbulence, l_t an integral length scale, ν the kinematic viscosity, τ_c a characteristic chemical time and τ_t an eddy break up turbulent mixing time. The use of a number Da inversely proportional to \tilde{Z}''^2 accounts directly for the fact that a high level of fluctuations of mixture fraction can promote finite rate chemistry, or even the extinction of the reaction zone. This Da naturally appears from a direct analogy with the laminar flames where $Da = (\tau_c\chi)^{-1}$. Here it was extended to turbulent flows using a linear relaxation model for the mean scalar dissipation rate, e.g. $\tilde{\chi} = (\tilde{Z}''^2/\tau_t)$ (Dopazo, 1994).

The condition where the turbulence micro-scale is of the order of the reaction zone thickness delineates situations where a strong coupling between unsteady micro-mixing and reaction occurs. Introducing scaling laws for laminar diffusive-reactive layers (Williams, 1971), this limit can be approximated as: $Da_c = (Re_{lt}^{1/2} / \widetilde{Z}''^2)^{a/2}$, where $a = \nu_F + \nu_O + 1$ is defined from the order of the chemical reaction.

With the unmixedness $\tilde{S} = \widetilde{Z}''^2 / (\widetilde{Z}(1 - \widetilde{Z}))$ varying between zero and unity, various regimes may be distinguished. For $Da > (Re_{lt}^{1/2} / \widetilde{Z}''^2)^{a/2} \gg Da_q$, quasi-steady laminar diffusion-reaction layers (flamelets) are expected, with connected reaction zones for $\tilde{S} < 1$ and separated reaction zones for $\tilde{S} \rightarrow 1$. When $Da_q < Da < (Re_{lt}^{1/2} / \widetilde{Z}''^2)^{a/2}$, unsteady effects become dominant. For $\tilde{S} < 0.5$, the mean reaction zone is thickened by the turbulence, and if $\tilde{S} \rightarrow 1$ local extinctions can appear and further develop if $\tilde{S} \rightarrow 1$. These various regimes are summarized in fig. 1. This classification may be seen as intermediate between the one using the parameters Da and Re_{lt} (Libby and Williams, 1994) and those which have retained Da and \widetilde{Z}''^2 (Bray and Peters, 1994). To refine the description, additional lengths may be introduced using thicknesses of profiles in mixture fraction space (Bilger, 1988).

From this classification of non-premixed turbulent flames (fig. 1), it is concluded that three quantities should be given to properly calibrate a DNS problem: a Reynolds number, the level of fluctuation of mixture fraction and a Damköhler number.

2.3. LIMITATIONS OF DNS CALCULATIONS

In DNS, the reaction zone and the Kolmogorov micro-scale need to be captured by the grid. In the case of species with a Schmidt number of the order of unity, we note by N the number of grid points in a direction of the problem, and n_r the number of points necessary to resolve the reaction zone. The number n_{l_i} of integral length scales embedded within the computational domain is chosen to quantify the role played by large scales.

The representative mesh size is given by $\Delta x = n_{l_i} l_i / N$, and resolving dissipative eddies requires $\Delta x \approx \eta_k$, whereas the reaction zone is captured when $\Delta x < l_r / n_r$. Using the relations introduced above to determine combustion regimes, two criteria emerge:

$$Re_{lt} < \left(\frac{N}{n_{l_i}} \right)^{4/3}; \quad (\widetilde{Z}''^2 Re_{lt})^{1/2} Da^{1/(a+1)} < \left(\frac{N}{n_{l_i} n_r} \right)$$

They are discussed in fig. 2. Notice that the Reynolds number is not the only limiting factor, even for a simple single-step reaction, increasing the

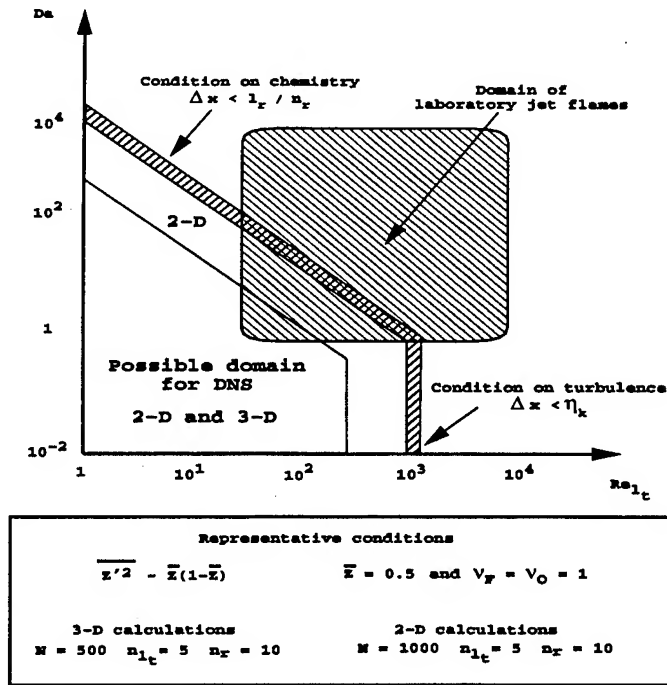


Figure 2. Limitations of DNS calculations in a $Da - Re_t$ diagram. N is the number of grid points in one direction, n_{l_t} the number of integral length scales l_t within the computational domain, and n_r the number of points required to resolve the thickness of the reaction zone l_r . Δx denotes the mesh size and η_k the Kolmogorov length. The jet flame domain corresponds to typical laboratory experiments. (Vervisch and Poinso 1998.)

Damköhler number implies a decrease of the turbulence intensity, or, of the integral length scale. However, actual supercomputers allow to approach conditions making DNS a unique instrument for the study of turbulent combustion.

2.4. DNS FOR MODELING

The necessity to deal with the non-linear character of chemistry has promoted the emergence of tools suited for the description of turbulent flames with CFD (probability density function, flame surface, conditional moments). These tools have to provide routes for estimating rates of production, or consumption, of chemical species. Either time (RANS) or space (LES) filtered values are needed. The methods are based on various analysis:

- In the geometrical analysis of flames, one focusses on the behavior of

iso-value surfaces (iso- Z). Then DNS can be probed to collect information on turbulent mixing (Kollmann and Chen, 1994) and to develop models based on the concept of flame surface (Van-Kalmthout and Veynante, 1998).

- In the flame normal analysis, one studies quantities along the normal to the flame surface ($Z = Z_{st}$). When compared to one-dimensional profiles of stagnation point flame, DNS data are useful to evaluate and improve flamelets models (Peters, 1986). Unsteadiness (Mell et al., 1994; Cuenot and Poinso, 1994; Mahalingam et al., 1995) or effects of strong finite rate chemistry and local quenching can be investigated (Delhaye et al., 1994; Chang et al., 1991).
- The edge-flame analysis, further discussed thereafter (§2.5), is useful to collect information on the behavior of the edges of reaction zones, in order to understand stabilization or quenching (Ruetsch et al., 1995; Domingo and Vervisch, 1996; Echekki and Chen, 1998; Favier and Vervisch, 1998).
- A generic statistical view of the flow is obtained when using a one-point analysis. Probability density function of any quantity can be extracted from DNS (Overholt and Pope, 1996; Lee and Pope, 1995) along with conditional moments (Mell et al., 1993; Swaminathan and Bilger, 1999).

All these modeling approaches are linked via the scalar dissipation rate $\tilde{\chi}$, which is a quantity of fundamental interest in any turbulent flames. DNS has shown that for reproducing the mean burning rate, not only the mean value of χ is important, but also the Lagrangian time history of micro-mixing ($\chi(t, \underline{x})$). In other words, the conditional value of χ at the stoichiometric surface and the time during which this value is applied to the flame can be more relevant than the mean by itself (Mastorakos et al., 1996; Domingo and Vervisch, 1996; Im et al., 1999). This last observation leads us to think of LES, where the feeding of the reaction zones by large scale motions is fully resolved, as a good candidate for improving the computations of non-premixed turbulent flames (Pierce and Moin, 1999). Along these lines, DNS was utilized to calibrate many sub-grid combustion models (McMurtry et al., 1993; Cook and Riley, 1994; Réveillon and Vervisch, 1996; Réveillon and Vervisch, 1998b; Cook and Bushe, 1999).

2.5. EDGE-FLAME AND TRIPLE-FLAME

Peculiar structures bordering the reaction zones were observed in DNS of non-premixed combustion, they are connected to the appearance of a partially premixed combustion regime. Depending on the value of the scalar dissipation rate χ at the edge of the reaction zone, it was found that the

flame adjoining the extinguished region of the stoichiometric surface can take on two general forms: (a) For moderate values of χ , one observes a partially premixed front with a stoichiometric kernel evolving into a rich flame in the direction of the fuel stream, while a lean flame develops on the air side (fig. 3 (a)). This structure is a triple-flame and it is the subject of multiple studies (Hartley and Dold, 1991; Ghosal and Vervisch, 1998); (b) high values of χ are followed by large heat transfer at the edge of the reaction zone, and when the thickness of the diffusive layer is small enough, the partially premixed front cannot be observed (3 (b)).

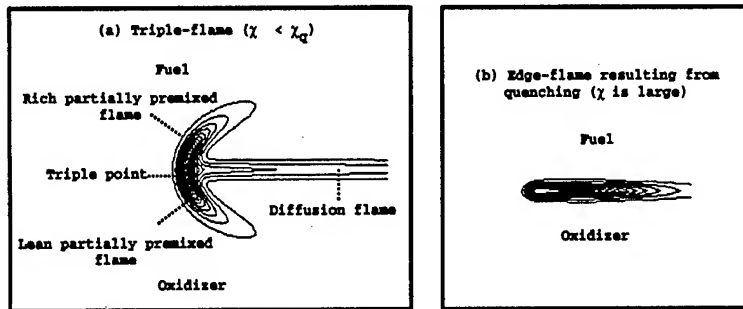


Figure 3. Two generic types of diffusion flame extremities: (a) For moderate values of the scalar dissipation rate χ , a triple flame may develop and propagates along the stoichiometric line; (b) After quenching of a diffusion flame, heat fluxes are larger than heat release at the edge of the reaction zone and an extinction front can develop. χ_q denotes the quenching value of the scalar dissipation rate.

DNS of flame/vortex interaction was retained to seek out conditions where an edge-flame submitted to unsteady fuel/air mixing would propagate combustion along a stoichiometric line, or promote the development of a quenching front (Favier and Vervisch, 1998). This point is relevant for developing sub-grid LES models able to handle flame stabilization mechanisms. For instance in a lifted turbulent flame, the stoichiometric surface is highly stretched (Muñiz and Mungal, 1997) and the quenching of the trailing diffusion flames attached to the flame base will continuously generates new reaction zone edges, which are new candidates for contributing to ignition and stabilization.

From DNS it was found that a triple-flame like structure can take benefit from vorticity and unsteady mixing to progress in an environment where a diffusion flame would be quenched, with an absolute velocity greater than its corresponding laminar burning velocity. Depending on positions in a diagram constructed from propagation and micro-mixing properties (fig. 4), the edge-flame exhibits two different behaviors: (1) It progresses within the flow along the stoichiometric-line, then combustion is sustained

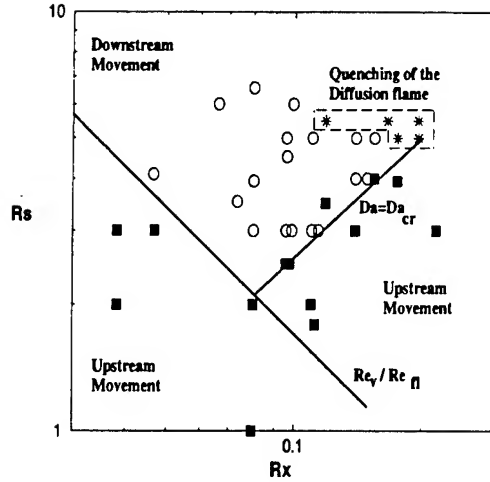


Figure 4. Diagram delineating various edge-flame behaviors in flame/vortex interaction. R_x is the ratio between the scalar dissipation rate of the edge-flame and the scalar dissipation rate imposed by the pair of vortices. R_s is the ratio between the characteristic vortex speed and the displacement speed of the edge-flame. Re_v is the Reynolds number of the vortex, Re_f is the Reynolds number of the flame. $R_s R_x = (Re_v / Re_f)$ and $Da = (R_x / R_s)$ is a Damköhler number. Square: the edge-flame moves upstream contributing to the stabilization. Star: upstream movement with quenching of the trailing diffusion flame. Circle: the edge-flame moves downstream (blowout) (Favier and Vervisch 1998).

within a stabilization zone; (2) The edge of the reaction zone is pushed away downstream and blowout occurs.

When submitting the extremity of a planar diffusion flame to three-dimensional freely decaying turbulence (Vervisch and Trouvé, 1998), all these pictures are observed depending on the turbulence and flame properties (fig. 5). The modeling of these complex behaviors and of their global impact on flame stabilization is still a great challenge for RANS or LES of combustion chambers.

3. Conclusion

Results from Direct Numerical Simulation have been widely utilized to understand and to model non-premixed turbulent combustion. Great challenges still exist in the modeling of these flames, like for instance accounting for spray and pollutants emission. Recent works have been done along these lines using DNS (Réveillon and Vervisch, 1998a; Haworth et al., 1998), confirming that DNS is a precious research tool in continuous development.

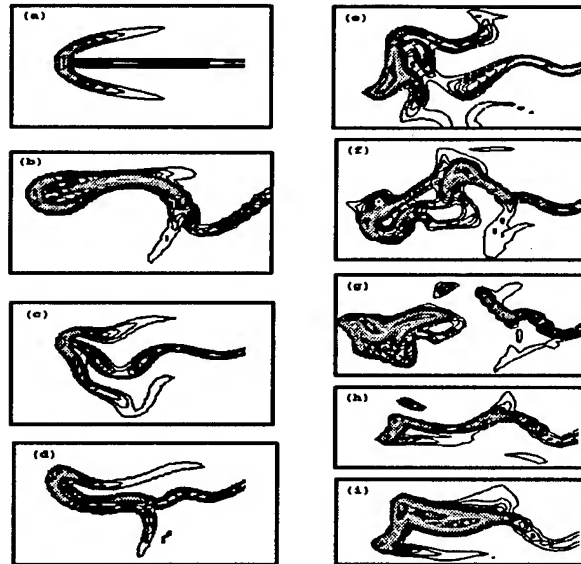


Figure 5. Iso-line of reaction rate in the vicinity of a stabilization zone of a non-premixed turbulent flame. Various snapshots taken in different planes of a 3-D calculations are presented. (a): Laminar triple-flame. (b)-(d): DNS where the characteristics of the turbulence lead to a flame featuring a structure close to a triple-flame. (e)-(i): For higher turbulence intensity, local extinctions are found and the topology of the reaction zone is more complex (Vervisch and Trouvé, 1998).

Acknowledgments

The author has benefited from fruitful interactions with K.N.C. Bray, P. Domingo, V. Favier, T. Poinsot, J. Réveillon, A. Trouvé and D. Veynante. The support from the European Community, SNECMA, Air-Liquide, Hispano-Suiza, IDRIS-CNRS and the Center for Turbulence Research (CTR) at Stanford University and NASA Ames is gratefully acknowledged.

References

- Bilger, R. W. (1988). The structure of turbulent non premixed flames. In *Proceedings of the Twenty-Second Symposium (International) on Combustion*. The Combustion Institute, Pittsburgh.
- Bilger, R. W. (1989). Turbulent diffusion flames. *Ann. Rev. Fluid Mech.*, 21:101-35.
- Bray, K. and Peters, N. (1994). Laminar flamelets in turbulent flames. In Libby, P. and Williams, F., editors, *Turbulent Reacting Flows*, pages 63-113. Academic Press London.
- Bray, K. N. C. (1996). The challenge of turbulent combustion. In *Proceedings of the Twenty-Sixth Symposium (International) on Combustion, Naples*. The Combustion Institute, Pittsburgh.
- Chang, C., Dahm, W., and Trygvason, G. (1991). Lagrangian model simulations of

- molecular mixing, including finite rate chemical reactions, in a temporally developing shear layer. *Phys. Fluid*, 3(5):1300-1311.
- Cook, A. and Riley, J. J. (1996). Direct numerical simulation of a turbulent reactive plume on a parallel computer. *J. Comp. Phys.*, 129(2):263-283.
- Cook, A. W. and Riley, J. J. (1994). A subgrid model for equilibrium chemistry in turbulent flows. *Phys. Fluids*, 8(6):2868-2870.
- Cook, W. and Bushe, W. K. (1999). A subgrid-scale model for the scalar dissipation rate in nonpremixed combustion. *Phys. Fluids*, 11(3):746-748.
- Cuenot, B. and Poinso, T. (1994). Effects of curvature and unsteadiness in diffusion flames, implications for turbulent diffusion combustion. In *Proceedings of the Twenty-Fifth Symposium (International) on Combustion, Irvine*. The Combustion Institute, Pittsburgh.
- Delhay, B., Veynante, D., and Candel, S. (1994). Simulation and modeling of reactive shear layers. *Theoret. Comput. Fluid Dynamics*, 6:67-87.
- Domingo, P. and Vervisch, L. (1996). Triple flames and partially premixed combustion in autoignition of nonpremixed mixtures. In *Proceedings of the Twenty-Sixth Symposium (International) on Combustion, Naples*, pages 233-240. The Combustion Institute, Pittsburgh.
- Dopazo, C. (1994). Recent developments in pdf methods. In Libby, P. and Williams, F., editors, *Turbulent Reacting Flows*, pages 375-474. Academic Press London.
- Echekki, T. and Chen, J. H. (1998). Structure and propagation of methanol-air triple flames. *Combust. Flame*, 114(1/2):231-245.
- Favier, V. and Vervisch, L. (1998). Effects of unsteadiness in edge-flames and liftoff in non-premixed turbulent combustion. In *Twenty-Seventh Symposium (International) on Combustion, The Combustion Institute*, pages 1239-1245.
- Ghosal, S. and Vervisch, L. (1998). Asymptotic theory of triple flame including effects of heat release. *Submitted*.
- Givi, P. (1989). Model free simulations of turbulent reactive flows. *Prog. Energy Combust. Sci.*, 15:1-107.
- Hartley, L. J. and Dold, J. W. (1991). Flame propagation in a nonuniform mixture: analysis of a propagating triple-flame. *Combust. Sci. and Tech.*, 80:23-46.
- Haworth, D., Cuenot, B., Poinso, T., and Blint, R. (1998). Numerical simulation of turbulent propane-air combustion with non-homogeneous reactants: initial results. In *Studying turbulence using numerical databases - VII*, pages 5-24. Center for Turbulence Research, Stanford U.
- Im, H. G., Chen, J. H., and Chen, J.-Y. (1999). Chemical response of methane/air diffusion flame to unsteady strain rate. *Combust. Flame*, 118(1/2):204-212.
- Jones, W. P. (1994). Turbulence modelling and numerical solution methods for variable density and combustions flows. In Libby, P. and Williams, F., editors, *Turbulent Reacting Flows*, pages 309-368. Academic Press London.
- Jou, W. H. and Riley, J. J. (1989). Progress in direct numerical simulation of turbulent reacting flows. *AIAA Journal*, 27:1543-1557.
- Kollmann, W. and Chen, J. H. (1994). Dynamics of the flame surface area in turbulent non-premixed combustion. In *Twenty-Fifth Symposium (International) on Combustion. The Combustion Institute*.
- Lee, Y. Y. and Pope, S. B. (1995). Nonpremixed turbulent reacting flow near extinction. *Combust. Flame*, 101:501-528.
- Liñán, A. (1974). The asymptotic structure of counterflow diffusion flames for large activation energies. *Acta Astronautica*, 1007(1).
- Libby, P. A. and Williams, F. A. (1994). Turbulent combustion: Fundamental aspects and a review. In Libby, P. and Williams, F., editors, *Turbulent Reacting Flows*, pages 2-61. Academic Press London.
- Mahalingam, S., Chen, J., and Vervisch, L. (1995). Finite-rate chemistry and transient effects in direct numerical simulations of turbulent nonpremixed flames. *Combust. Flame*, 102(3):285-297.

- Masri, A., Bilger, R., and Dibble, R. (1988). Turbulent non-premixed flames of methane near extinction. *Combust. Flame*, 73:261-258.
- Mastorakos, E., Baritaud, T., and Poinso, T. (1996). Numerical simulations of autoignition in turbulent mixing flows. In Baritaud, T., Poinso, T., and Baum, M., editors, *Direct Numerical Simulation for Turbulent Reacting Flows*, pages 242-276. Editions Technip.
- McMurtry, P. A., Menon, S., and Kerstein, A. E. (1993). Linear eddy modeling of turbulent combustion. *Energy & Fuels*, 7:817-826.
- Mell, W. E., Nilsen, V., Kosaly, G., and Riley, J. J. (1994). Investigation of closure models for nonpremixed turbulent reacting flows. *Phys. Fluids*, 6(3):1331-1356.
- Mell, W. E., Nilsen, V. N., Kosály, G., and Riley, J. J. (1993). Direct numerical simulation investigation of the conditional moment closure model for nonpremixed turbulent reacting flows. *Combust. Sci. and Technology*, 91:179-186.
- Moin, P. and Mahesh, K. (1998). Direct numerical simulation: A tool in turbulence research. *Annu. Rev. Fluid Mech.*, 30:539-578.
- Muñiz, L. and Mungal, M. G. (1997). Instantaneous flame-stabilization velocities in lifted-jet diffusion flames. *Combust. Flame*, 111(1/2):16-31.
- Overholt, M. R. and Pope, S. B. (1996). Direct numerical simulation of a passive scalar with imposed mean gradient in isotropic turbulence. *Phys. Fluids*, 8(11):3128-3148.
- Peters, N. (1986). Laminar flamelet concepts in turbulent combustion. In *Proceedings of the 21st Symposium (international) on Combustion*, Irvine, pages 1231-1250. The Combustion Institute Pittsburgh.
- Pierce, C. and Moin, P. (1999). A dynamic model for subgrid-scale variance and dissipation rate. *Phys. Fluids*, 10(12):3041-3044.
- Poinso, T., Candel, S., and Trounev, A. (1996). Direct numerical simulation of premixed turbulent combustion. *Prog. Energy Combust. Sci.*, 12:531-576.
- Réveillon, J. and Vervisch, L. (1996). Response of the dynamic les model to heat release induced effects. *Phys. Fluids*, 8(8).
- Réveillon, J. and Vervisch, L. (1998a). Accounting for spray vaporization in turbulent combustion modeling. In *Studying turbulence using numerical databases - VII*, pages 25-38. Center for Turbulence Research, Stanford U.
- Réveillon, J. and Vervisch, L. (1998b). Subgrid mixing modeling: a dynamic approach. *AIAA Journal*, 36(3):336-341.
- Ruetsch, G., Vervisch, L., and Liñán, A. (1995). Effects of heat release on triple flame. *Phys. Fluids*, 6(7):1447-1454.
- Swaminathan, N. and Bilger, R. W. (1999). Assessment of combustion submodels for turbulent nonpremixed hydrocarbon flames. *Combust. Flame*, 116(4):519-545.
- Van-Kalmthout, E. and Veynante, D. (1998). Direct numerical simulation analysis of flame surface density models for nonpremixed turbulent combustion. *Phys. Fluids*, 10(9):2347-2368.
- Vervisch, L. and Poinso, T. (1998). Direct numerical simulation of non-premixed turbulent flame. *Annu. Rev. Fluid Mech.*, 30:655-692.
- Vervisch, L. and Trounev, A. (1998). Les modeling for lifted turbulent jet flames. In *Studying turbulence using numerical databases - VII*, pages 83-100. Center for Turbulence Research, Stanford U.
- Williams, F. A. (1971). Theory of combustion in laminar flows. *Annu. Rev. Fluid Mech.*, 3:171-88.

MODELLING OF THE LENGTH SCALE AND VARIANCE OF SUBGRID SCALE QUANTITIES IN A TURBULENT CHANNEL FLOW

KRISTER ALVELIUS AND ARNE JOHANSSON

Department of Mechanics, KTH, S-100 44 Stockholm, Sweden

Abstract.

Direct numerical simulations (DNS) of turbulent plane channel flow at the wall friction Reynolds numbers $Re_\tau = 180$ and $Re_\tau = 360$ have been performed, both with and without system rotation. From these simulations subgrid scale (SGS) quantities are evaluated and compared with SGS model predictions in *a priori* tests. Although the mean behaviour of the SGS dissipation is captured relatively well by the Smagorinsky model, the variation of the modelled SGS dissipation is too slow and too small in space. These drawbacks are reduced by the introduction of a stochastic SGS model parameter, which increases the variance and reduces the length scale of the model. The performance of the stochastic model is also investigated in a large eddy simulation (LES) at $Re_\tau = 360$, and the results are compared with the predictions of the DNS.

1. Introduction

In turbulent flows there is a large range of scales. The size of the smallest scales is determined by the dissipation rate of turbulence kinetic energy, whereas the size of the largest scales is typically determined by the geometry. In order to reduce the computational effort, while still retaining a major part of the turbulence dynamics, the smallest scales are modelled in LES. The effect of the small scales on the resolved scales enters through the SGS stress tensor

$$\tau_{ij} = \overline{u_i u_j} - \bar{u}_i \bar{u}_j. \quad (1)$$

Standard models for τ_{ij} are expressed in terms of the resolved velocity field (e.g. the Smagorinsky model[12], the mixed model[2], the spectral model[5] and the velocity estimation model[6]). This naturally gives a length scale of the model which is characteristic for the filtered field.

The performance of a model can be measured by doing *a priori* tests, where subgrid-scale quantities are computed from a DNS velocity field. This allows for evaluation of the model prediction of any quantity you chose. The most important quantity to capture in the modeling of τ_{ij} is the SGS dissipation

$$\epsilon_{sgs} = -\tau_{pq}\bar{s}_{pq}. \quad (2)$$

Hence, by SGS dissipation we mean the dissipation of resolved turbulence kinetic energy by the subgrid-scales. The primary aim is to get a correct mean behaviour $\langle \epsilon_{sgs} \rangle$ with the model. Since the SGS stress tensor fluctuate in time and space it is also desirable to capture that behaviour. The strongest requirement is that the model should have a large correlation with the actual stresses. However, *a priori* tests have shown that this correlation usually is rather low. It should be pointed out that there is an infinite number of different velocity fields u_i that yields the same filtered field \bar{u}_i , and it is impossible to determine τ_{ij} uniquely through \bar{u}_i . The somewhat stochastic nature of the SGS stresses was discussed by Schumann[11], who stressed the importance to incorporate backscatter and to have a random behaviour of the model. Here we require that the statistical properties of the spatial and temporal fluctuations, i.e the variance, the length scales and the time scale, should be captured correctly by the model.

Although *a priori* tests give a good indication of the performance of a model, it is also necessary to perform actual simulations with the model in order to know how it performs in a real situation, where the interaction with the resolved flow dynamics is present.

2. Stochastic differential equations

Most stochastic processes can be generated through a standard stochastic differential equation (SDE) on the form

$$dX(t) = \mu(t)dt + \sigma(t)dW(t), \quad (3)$$

where W is a wiener process, and μ and σ are two stochastic processes adapted to the sigma algebra generated by $\{W_s\}_{s \leq t}$. Consider statistically stationary processes with the expectation value $E[\dot{X}(t)] = 0$. Such a process is obtained with e.g. the choice $\mu(t) = -aX(t)$ and $\sigma(t) = b$, where a and b are constants. This gives the simple SDE

$$dX(t) = -aX(t)dt + bdW(t). \quad (4)$$

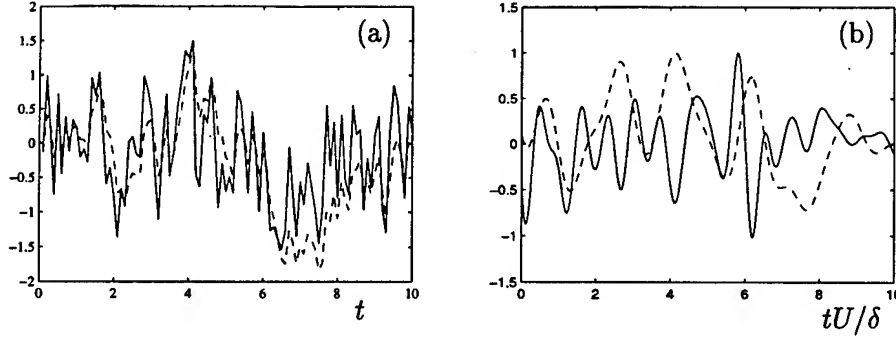


Figure 1. (a) Two realizations of the stochastic process $X(t)$ with the variance $V_X = 1/3$. Solid line: $a = 6$, dashed line: $a = 1.5$. (b) The time realizations of $(\tau_{11} - \langle \tau_{11} \rangle) / \max(\tau_{11} - \langle \tau_{11} \rangle)$ (solid line) and $(\bar{u}_1 \bar{u}_1 - \langle \bar{u}_1 \bar{u}_1 \rangle) / \max(\bar{u}_1 \bar{u}_1 - \langle \bar{u}_1 \bar{u}_1 \rangle)$ (dashed line) in the center of the plane channel flow at $Re_\tau = 180$.

It follows that the expectation value for the asymptotic state of the resulting stochastic process $X(t)$ is zero, and that the variance $\text{Var}[X(t)]$ approaches $b^2/2a \equiv V_X$, independent of the initial value.

If the integral $\int_{t_n}^{t_{n+1}} X(s) ds$ is approximated with $X(t_n) \Delta t_n \equiv X_n \Delta t_n$ we get the discretized SDE

$$X_{n+1} = X_n(1 - a\Delta t_n) + b\Delta W_n, \quad (5)$$

where ΔW_n has the normal distribution $N(0, \sqrt{\Delta t_n})$. If the process ΔW_n is approximated with a uniformly distributed variable Y , then the requirement on the variance gives the density function to $\mu_Y(y) = I_{[-k_w, k_w]}(y)/2k_w$, where I is the indicator function and $k_w = \sqrt{3\Delta t_n}$.

For a given desired variance the term b can be determined from $b^2 = 2aV_X$. The time scale τ_X of the process is determined by the decay rate of the correlation $E[X(t)X(t-\tau)]/V_X = \exp(-a\tau)$. It follows that $\tau_X = 1/a$ increases with decreasing values of a . In figure 1a two time realizations of solutions to the discrete SDE (5), with two different choices of a , illustrates this fact.

3. Stochastic modeling

The area of stochastic modeling in LES have been treated by several authors (e.g. Chasnov[4], Leith[7], Mason & Thomson[9] and Schumann[11]). The main concern of the previous work has been to obtain correct backscatter with the model. The main aim of the present work is to see how we can reduce the length scale and increase the variance of the SGS stress model by the inclusion of a stochastic term.

When the large scale energy input is modelled through a random volume force it is advantageous to have the time scale of the forcing much smaller than any turbulence time scale (Alvelius[1]). This makes the force neutral in the sense that it does not correlate with any of the turbulence scales, and the energy (net) input is determined by the force-force correlation. This approach was adopted by e.g. Leith[7] in stochastic modeling of the SGS stresses. However, as is seen in figure 1b the SGS stresses, which behaviour we try to mimic, have a time scale comparable to the resolved stresses, and the main effect from the stochastic model should enter through correlations with the resolved turbulent field. The need of finite temporal correlation was pointed out by Bertoglio[3] and Schumann[11].

Mason & Thomson[9] used a stochastic model formulated as the curl of a random vector potential. Schumann[11] modelled the fluctuating fluxes through fluctuating velocities, generated randomly, with zero ensemble mean. In this way he guaranteed that the fluxes will be realizable. In present investigation we use the Smagorinsky model[12] together with a stochastic model parameter to describe the SGS stress tensor

$$\tau_{ij} = \frac{1}{3}\tau_{kk}\delta_{ij} - 2\nu_T\bar{s}_{ij}, \quad (6)$$

$$\nu_T = (C_s^2 + C_f^2 X(\mathbf{x}, t))\Delta^2(2\bar{s}_{pq}\bar{s}_{pq})^{1/2}, \quad (7)$$

where $\bar{s}_{ij} = (\bar{u}_{i,j} + \bar{u}_{j,i})/2$, Δ is the filter width, C_s is the standard Smagorinsky constant, X is a stochastic process and C_f is an amplitude constant. The stochastic process X is determined through the SDE (5), independently at each \mathbf{x} . When $X < -C_s^2/C_f^2$ the eddy viscosity is locally negative and we have backscatter (negative ϵ_{sgs}). Negative viscosity generally gives numerical problems and has to be treated carefully in LES. In particular a large value of C_f compared to C_s increases the occurrences of negative dissipation and a large time scale of X increases the duration of a locally negative dissipation, both giving larger stability problems. The SDE (5) should be solved in an Lagrangian frame of reference, moving with each fluid particle. The error of neglecting the convective effects increases when the time scale of X is increased, and particularly becomes large in the center of the channel where the mean velocity magnitude is large.

Two approaches to determine the term $C_s^2\Delta^2$ are used, the method of damping the constants in the vicinity of walls (Tafti and Vanka[13]) and the method of determining the constant locally from the flow in the dynamic approach (Lilly[8]), with $\Delta = (\Delta x \Delta y \Delta z)^{1/3}$. Here the dynamic Smagorinsky constant is considered to only be a function of the wall normal distance.

4. The numerical simulations

Both *a priori* tests using DNS data, and real LES are performed in order to investigate the behaviour of the SGS model and its effect on the SGS quantities. A standard pseudo spectral method, with Fourier representation in the stream wise (x) and span wise (z) directions and Chebyshev representation in the wall normal (y) direction, together with a mixed four stage Runge-Kutta and a second order Crank-Nicolsson time integration method, is used for the simulations.

The degree of turbulence in the channel is measured by the wall friction Reynolds number $Re_\tau = u_\tau \delta / \nu$, where $u_\tau = (\nu dU/dy|_{wall})^{1/2}$ is the wall friction velocity, and δ is half the channel width. The DNS, for the *a priori* tests, are carried out with two different wall friction Reynolds numbers, $Re_\tau = 180$ and $Re_\tau = 360$. The lower Reynolds number simulation is performed with a $4\pi\delta \times 2\delta \times 2\pi\delta$ computational domain in the x , y and z directions, whereas the domain size in the higher Reynolds number simulation is $4\pi\delta \times 2\delta \times 4\pi\delta/3$. The DNS are represented on a $192 \times 129 \times 160$ and a $384 \times 257 \times 240$ mesh for the lower and higher Reynolds number respectively. In the *a priori* test a sharp spectral cut-off filter is used in the x and z direction. In the y direction there is no explicit filtering. The filtered field is represented on a 48×40 and a 64×48 mesh in the x and z directions for the lower and higher Reynolds number respectively. This gives the filter widths in wall units $\Delta x^+ = 47.1$ and $\Delta z^+ = 28.3$ for the $Re_\tau = 180$ field and $\Delta x^+ = 70.7$ and $\Delta z^+ = 35.3$ for the $Re_\tau = 360$ field. Simulations with system rotation in the z direction is also carried out with $Re_\tau = 180$ and the rotation number $Ro = 2\delta\Omega/U_m = 0.8$, where Ω is the system angular velocity and U_m is the mean bulk velocity.

The LES is carried out with $Re_\tau = 360$ and the same domain and resolution as the filtered DNS representation, except for the y direction which is represented on 97 grid points. This corresponds to the averaged grid spacing $\bar{\Delta y}^+ = 7.4$.

5. Results

In the *a priori* tests the time scale of the stochastic term is unimportant, and X is therefore generated independently at each \mathbf{x} as a stochastic variable with the variance $1/3$. In the LES, however, the time scale of the model is very important of its effect on the flow, and the SDE (5) with $V_X = 1/3$ and $a = 37$ is used to generate X .

In addition to the mean behaviour also the variance and length scale of ϵ_{sgs} are investigated. The variance of the SGS dissipation is

$$\text{Var}[\epsilon_{sgs}] = \langle \epsilon'_{sgs} \epsilon'_{sgs} \rangle^{1/2}, \quad (8)$$

where a prime denotes the fluctuating part. The stream wise integral length scale

$$L_x[\epsilon_{sgs}], \quad (9)$$

is defined from the two-point correlation of the SGS dissipation in the stream wise direction.

5.1. A PRIORI TESTS

In the non-rotating cases the method of damping C_s close to the walls is used. The value of C_s is chosen so that a correct magnitude of the mean dissipation is obtained (figures 2a,4a). This yields the values $C_s = 0.12$ at $Re_\tau = 180$ and $C_s = 0.035$ at $Re_\tau = 360$. The dynamic approach is used in the rotating channel flow, where the method of damping severely over predicts the dissipation on the stable side (figure3a). For the non-rotating case the dynamic approach predicts values in the core of the channel which is $C_s \approx 0.16$ at $Re_\tau = 180$ and $C_s \approx 0.15$ at $Re_\tau = 360$. Meneveau[10] concluded from *a priori* tests of homogeneous turbulence that the dynamic model yields the coefficient at the test-filter level instead of the original filter level. In the present simulation there is only a small difference in the predictions if that approach is used. Hence, the dissipation becomes severely over predicted with the dynamic approach at the highest Reynolds number. However, close to the walls ($y^+ < 50$) the dynamical approach yields a good prediction of the SGS dissipation for both Reynolds numbers.

In the $Re_\tau = 180$ case the stochastic amplitude C_f was set to either 0 (the standard Smagorinsky model) or $4C_s$. The addition of the stochastic term does, as expected, not change the mean behaviour of ϵ_{sgs} (figure2a). From figures 2b,c it is seen that the standard Smagorinsky model under predicts the variance of ϵ_{sgs} and gives a too large length scale $L_x[\epsilon_{sgs}]$ compared to the predicted DNS results. It is also seen that variance is increased and the length scale decreased, when the stochastic term is included, giving results close to the DNS predictions. The amplitude of the mean value and the variance does, however, depend directly on the value of C_s , while the length scale does only depend on the ratio C_f/C_s . The stochastic model does also predict backscatter (figure2d) which is of the same order as the backscatter given by the DNS. However, the values close to the walls are slightly lower.

In the rotating case (figure3) the general trends are the same as in the non-rotating case, except for the need of the dynamic determination of C_s^2 . The length scale $L_x[\epsilon_{sgs}]$ is too low close to the stable wall for the stochastic model. However, since the mean SGS dissipation as well as the backscatter is zero at that position, the miss prediction of the length scale has no effect on the flow.

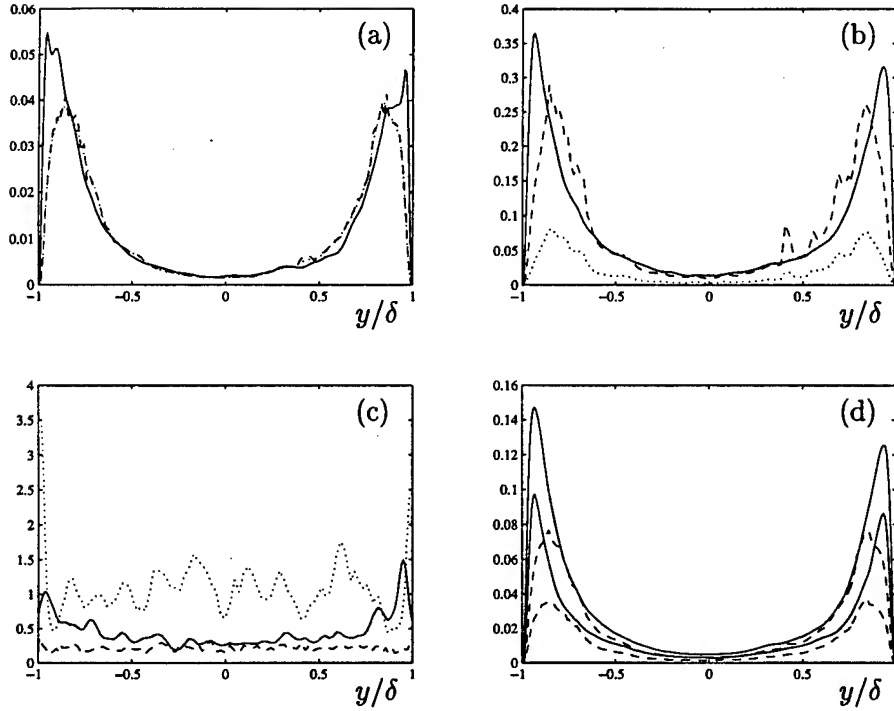


Figure 2. *A priori* test at $Re_\tau = 180$. Quantities evaluated from the real SGS stress tensor (solid lines) and the modelled SGS stress tensor with $C_f = 0$ (dotted lines) and $C_f = 4C_s$ (dashed lines). (a) The mean dissipation $\langle \epsilon_{sgs} \rangle$. (b) The variance $\text{Var}[\epsilon_{sgs}]$. (c) The length scale $L_x[\epsilon_{sgs}]/\Delta x$. (d) The forward scatter and back scatter of resolved energy

In the $Re_\tau = 360$ case the variance increases and the length scale decreases compared to the $Re_\tau = 180$ case. The stochastic amplitude was set to $C_f = 0$ and $C_f = 2C_s$. The value $C_s = 2C_s$ is sufficient to reduce the length scale of the modelled ϵ_{sgs} to the same magnitude as the real, but is too low to increase the variance and the backscatter sufficiently. As was mentioned before the variance of the modelled dissipation depends strongly on C_s , and the choice $C_s = 0.1$ yields a variance and backscatter from the stochastic model which is in close agreement with the suggested DNS prediction.

From all the DNS cases it is seen that the predictions of $L_x[\epsilon_{sgs}]$ is significantly smaller than Δx , while the non-stochastic model yields a length scale which is approximately equal to Δx in most parts of the flow. With the stochastic model it is possible to reduce the length scale, which also increases the variance and yield backscatter.

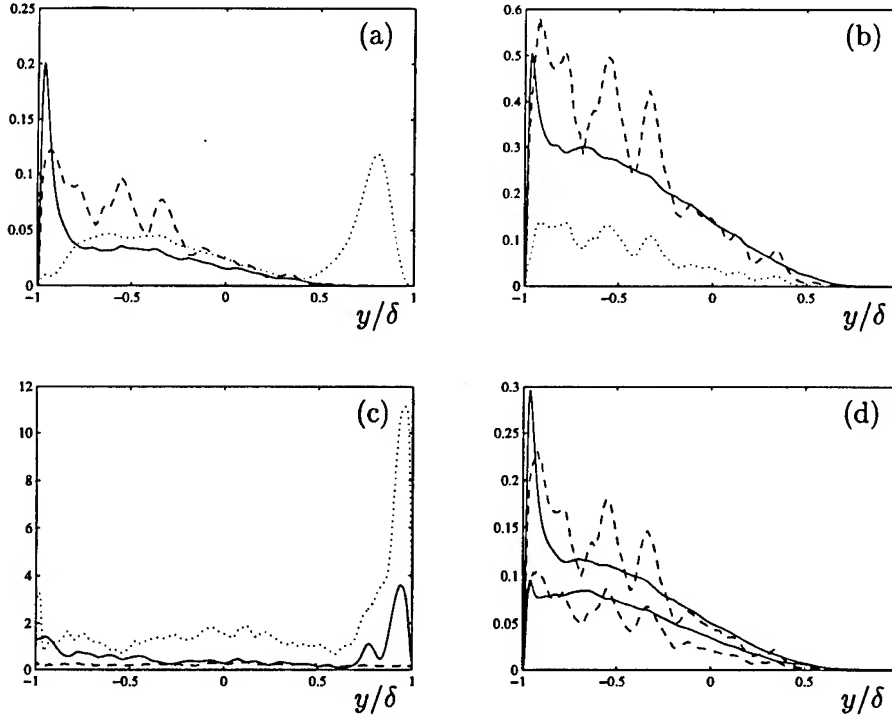


Figure 3. *A priori* test at $Re_\tau = 180$ and $Ro = 0.8$. Quantities evaluated from the real SGS stress tensor (solid lines) and the modelled SGS stress tensor with $C_f = 0$ (dotted lines) and $C_f = 4C_s$ (dashed lines). (a) The mean dissipation $\langle \epsilon_{sgs} \rangle$. Here only the $C_f = 0$ case is shown with the dynamic determination of C_s^2 (dashed line) and the method of damping C_s^2 (dotted line). (b) The variance $\text{Var}[\epsilon_{sgs}]$. (c) The length scale $L_x[\epsilon_{sgs}]/\Delta x$. (d) The forward scatter and back scatter of resolved energy

5.2. LARGE EDDY SIMULATIONS

Since the stochastic model allows for negative eddy viscosity the negative values of X has to be controlled. This is done by not allowing the local SGS dissipation to fall below a certain threshold. This threshold is determined, at the first iteration for each y , by the maximum value of ϵ_{sgs} calculated with $C_f = 0$. Typically this maximum SGS dissipation becomes 20–30 times larger than the mean SGS dissipation. Whenever the local value of ϵ_{sgs} falls below the negative value of the threshold the stochastic amplitude C_f^2 is set locally to C_s^2/X at that discrete time, giving a zero SGS dissipation, which prevents the simulation to explode. The occurrence of these limiting events will depend on the parameters in the SDE determining X and the amplitude C_f . This limiting procedure will slightly change the expectation

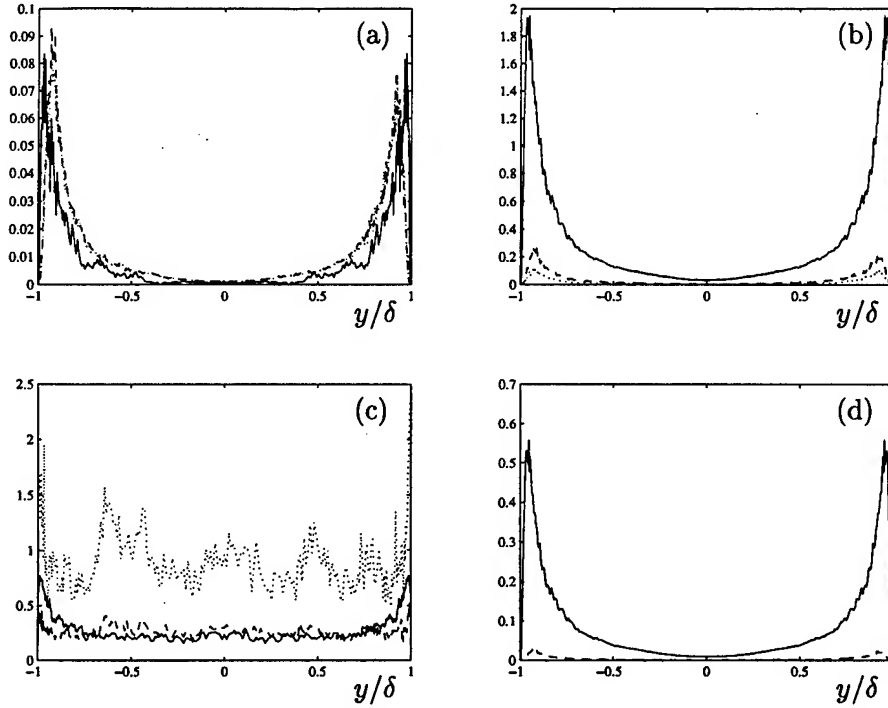


Figure 4. *A priori* test at $Re_\tau = 360$. Quantities evaluated from the real SGS stress tensor (solid lines) and the modelled SGS stress tensor with $C_f = 0$ (dotted lines) and $C_f = 2C_s$ (dashed lines). (a) The mean dissipation $\langle \epsilon_{sgs} \rangle$. (b) The variance $\text{Var}[\epsilon_{sgs}]$. (c) The length scale $L_x[\epsilon_{sgs}]/\Delta x$. (d) The back scatter of resolved energy.

value of the stochastic term $C_f^2 X$ to be non-zero.

LES, both with and without the stochastic term, have been carried out, with the parameter values $C_s = 0.1$, $C_f = 0$ for the standard Smagorinsky model, and $C_s = 0.08$ and $C_f = 4C_s$ for the stochastic model. This gives that ϵ_{sgs} is limited in approximately 0.5% of the grid points.

The mean SGS dissipation from the stochastic model is similar to that from the standard Smagorinsky model (figure 5a). They are also both close to the predicted dissipation from the DNS. The stochastic model shows backscatter in good agreement with the DNS results, and the variance and length scale is significantly improved compared to the standard Smagorinsky model. There is still a need to increase the ratio C_f/C_s in the LES to get an even closer agreement of the length scale and variance with the DNS predictions. This would, however, make the backscatter too large.

Figure 6a shows that the mean velocity profile from the LES becomes too large in the core region of the flow compared to the DNS predictions.

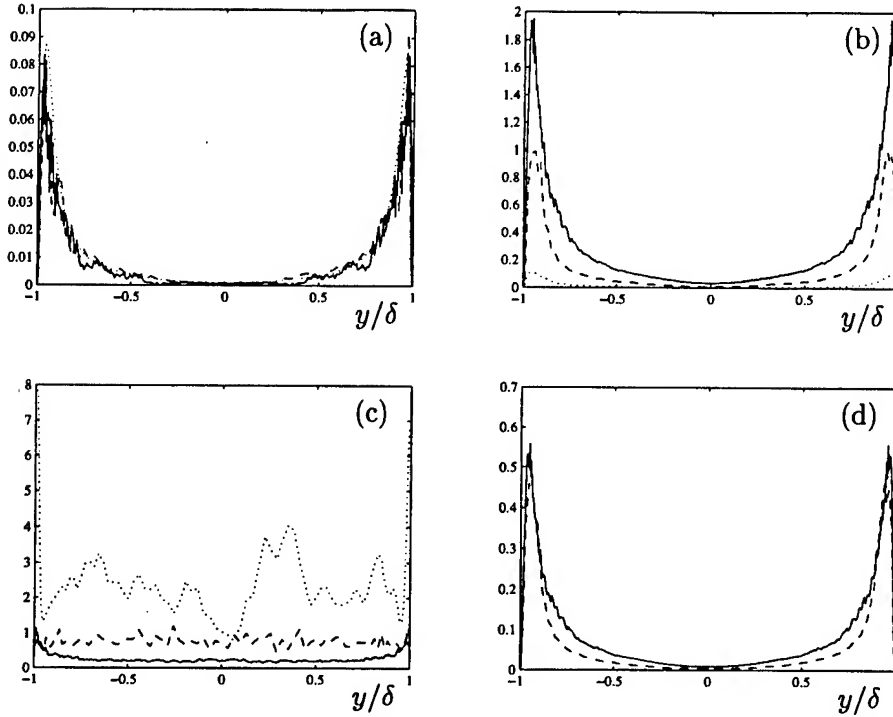


Figure 5. LES at $Re_\tau = 360$, with the stochastic model (dashed lines) and the standard Smagorinsky model (dotted lines), compared with DNS results (solid lines). (a) The mean dissipation $\langle \epsilon_{sgs} \rangle$. (b) The variance $\text{Var}[\epsilon_{sgs}]$. (c) The length scale $L_x[\epsilon_{sgs}]/\Delta x$. (d) The backscatter of resolved energy.

The stochastic model does not manage to change the profile. The velocity fluctuations are relatively well predicted by the LES in the core region (figures 6b,c,d). Close to the walls the stream wise fluctuations are over predicted by the LES, while the wall normal and span wise fluctuations are under predicted. The stochastic model manages to increase the wall normal and stream wise fluctuations close to the walls, giving a better agreement with the DNS results.

6. Conclusions

Both the *a priori* test and the LES show that the standard Smagorinsky model yields too low variance and too large length scale of the modelled SGS dissipation. This was improved by the inclusion of a simple stochastic model which also gave backscatter of SGS energy. The results might be improved if the SDE (5) is solved in a Lagrangian frame of reference. More

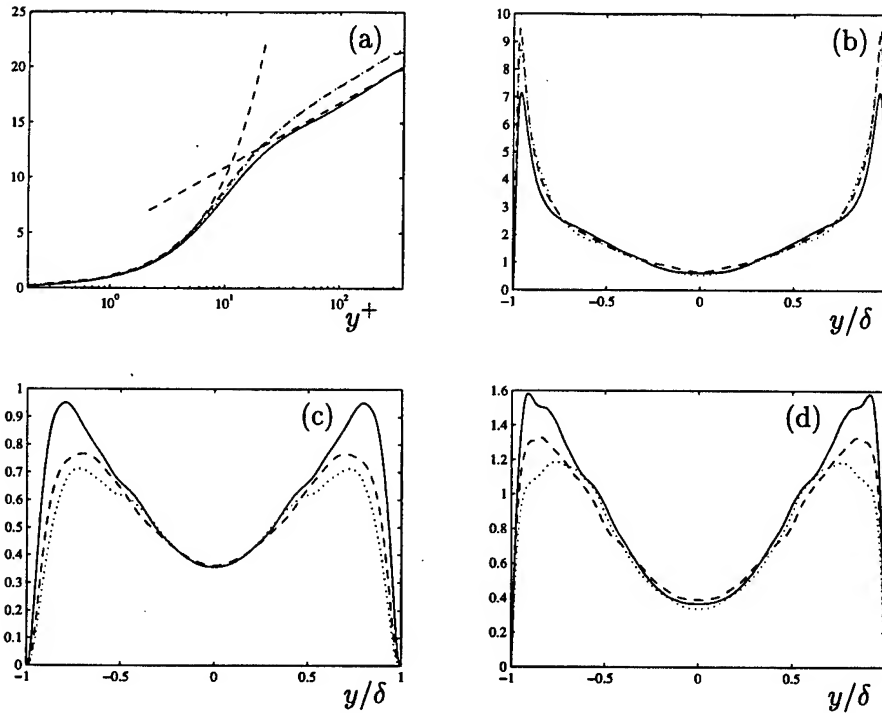


Figure 6. LES at $Re_\tau = 360$, with the stochastic model (dashed lines) and the standard Smagorinsky model (dotted lines), compared with DNS predictions (solid lines). (a) The mean velocity profile U^+ . The curves $\log y^+ / 0.39 + 5$ and y^+ are also included. (b) $\langle uu \rangle^+$. (c) $\langle vv \rangle^+$. (d) $\langle ww \rangle^+$.

'realistic' stochastic models, which are not written in terms of a eddy viscosity, should be used in order to avoid the stability problem with negative dissipation. Also another form of the model might help to reduce the length scale of ϵ_{sgs} without increasing the variance and backscatter. This requires means for determining the characteristics of the stochastic stresses in the flow. Although the *a priori* test suggested that the value $C_s = 0.1$ would severely over predict the SGS dissipation, LES with that constant gave a SGS dissipation in good agreement with the DNS predictions. This shows that one have to be careful when interpreting *a priori* tests.

Acknowledgments

Computer time was provided by the Center for Parallel Computers (PDC) at the Royal Institute of Technology (KTH), the The National Supercomputer Center in Sweden (NSC) at Linköping University.

References

1. K. Alvelius. Random forcing of three-dimensional homogeneous turbulence. *Physics of Fluids A*, 1999. Accepted for publication.
2. J. Bardina, J. H. Ferziger, and W. C. Reynolds. Improved subgrid scale models for large eddy simulation. In *AIAA 13th Fluid & Plasma Conference*, July 14–16 1980.
3. J. P. Bertoglio. A stochastic-grid model for sheared turbulence. In *Macroscopic modelling of turbulent flows*, editors, U. Frisch, J. B. Keller, G. Papanicolaou, and O. Pironneau, pages 100–119. Springer, 1985.
4. J. R. Chasnov. Simulation of the Kolmogorov inertial subrange using an improved subgrid model. *Physics of Fluids A*, 3(1):188–200, 1991.
5. J. P. Chollet. Two-point closure used for a sub-grid scale model in large eddy simulations. In F. Durst and B. Launder, editors, *Turbulent Shear Flow IV*, pages 62–72. Springer-Verlag, Heidelberg, 1984.
6. J. A. Domaradzki and E. M. Saiki. A subgrid-scale model based on the estimation of unresolved scales of turbulence. *Physics of Fluids*, 9(7):2148–2164, 1997.
7. C. E. Leith. Stochastic backscatter in a subgrid-scale model: Plane shear mixing layer. *Physics of Fluids A*, 2(3):297–299, 1990.
8. D. K. Lilly. The representation of small-scale turbulence in numerical simulation experiments. In *Proceedings of the IBM Scientific Computing Symposium on Environmental Science*, IBM Form No. 320-1951, page 195, 1967.
9. P. J. Mason and D. J. Thomson. Stochastic backscatter in large-eddy simulations of boundary layers. *Journal of Fluid Mechanics*, 242:51–78, 1992.
10. C. Meneveau. The dynamic Smagorinsky model and scale-dependent coefficients in the viscous range of turbulence. *Physics of Fluids*, 9(12):3932–3934, 1997.
11. U. Schumann. Stochastic backscatter of turbulence energies and scalar variance by random subgrid-scale fluxes. *Proceedings of the Royal Society of London, Series A*, 451:293–318, 1995.
12. J. Smagorinsky. General circulation experiments with the primitive equations. *Monthly Weather Review*, page 99, 1963.
13. D. K. Tafti and S. P. Vanka. A numerical study of the effects of spanwise rotation on turbulent channel flow. *Physics of Fluids A*, 3(4):642–656, 1991.

DNS OF COMPRESSIBLE REACTING MIXING LAYERS WITH PARALLEL COMPACT SCHEME

XIAODAN CAI AND FOLUSO LADEINDE
Aerospace Research Corporation, L.I.
P.O. Box 1527
Stony Brook, NY 11790-0609

Abstract.

The complexity associated with the DNS calculation of chemically-reacting high-speed mixing layers is briefly reviewed in this paper, with a focus on recent understanding of the three-mode mixing mechanism. The extension of the foregoing is of interest but requires the implementation of high-order finite difference formulas on supercomputers in order to take advantage of the massive parallelization. The high-order differencing and filtering formulas are complicated to parallelize. This paper therefore presents the progress that has been made toward the development of an efficient and scalable parallel procedure for investigating nonlinear three-mode mixing mechanisms.

1. Introduction

Research has been undertaken to achieve an improved understanding of the physical phenomena present in the idealized designs of high-speed propulsion systems. Reacting mixing layers have been used to model the real engine system in order to provide a solvable problem that retains the basic mixing and reacting processes (Curran, 1991). Two main issues exist for the model flow: the turbulent structure and chemical kinetics. The turbulence behavior has been found to be dominated by large-scale, two-dimensional structures in the incompressible non-reacting mixing layers (Brown and Roshko, 1974). These large-scale structures are centrally located in the layer and play a critical role in the mixing process through the entrainment of reactants from both streams, and hence it is referred as the "central" mode by Day *et al.* (1998). However, with an increase in the convective Mach number

and the addition of heat from chemical reaction, the large-scale structures change their nature and shape. In addition to the reduced growth rate and the development of three-dimensional central mode structures, the compressible reacting mixing layer can generate two “outer” modes which are associated with the fast and slow free streams, respectively.

The mixing processes induced by the outer modes are found to be quite different from those of the central mode. Each outer mode mixes only fresh reactant from its stream with product from the center of the layer. It has been shown that this mixing mechanism reduces the global reaction rate of a one-step, fast-limit chemical scheme (Planché and Reynolds, 1992). It is conceivable that this mixing mechanism can also affect the distribution of the chemical species, including the radical concentrations which form a critical part of realistic chemical reaction systems. The goal of the present project is to investigate two high-speed reacting mixing layer models with one- and two-step reactions respectively, and examine the effects of the new mixing mechanism on the reaction rate.

It is important to note that with increasing maximum flight speed, the fuel of choice for the engine typically changes from the conventional kerosene fuels at low speeds, to cryogenic fuels such as methane (CH_4) for flows with Mach numbers around 7~8 or liquid hydrogen (H_2) for flows with Mach numbers larger than 10 (Curran, 1991). The H_2 /Air reactions in high speed flows have been investigated numerically and experimentally (for example, Miller *et al.*, 1994). However, high-speed CH_4 /Air reactions have not received enough attention. The CH_4 /Air reactions are free of strong differential diffusivity effects which have been described as the source of many abnormal phenomena in H_2 /Air reacting flows (Chakraborty *et al.*, 1997). The chemical kinetic mechanism we adopted is representative of the reaction between a methane/nitrogen mixture and air.

Direct numerical simulation (DNS) is used to solve the Navier-Stokes equations coupled with the transport equations for the chemical species. The DNS approach is based on a sixth-order modified Padé compact scheme in space, and a fourth order explicit Runge-Kutta scheme in time (Visbal and Gaitonde, 1998). Several steps have been taken and assumptions made to accommodate the computations. First, the mixing layers are set to be temporally developing, instead of spatially developing, which allows the use of periodic boundary conditions streamwise, thereby reducing the computational domain size. Second, reduced chemical mechanisms are used to represent the full chemical kinetics. Previous studies of laminar flame calculations have already shown that a two-step reaction model could capture the flame structure of the CH_4 /Air reaction (Card *et al.*, 1996). Thus, we employ this level of approximation, as well as a single step reaction model in the present study. Third, parallel computer systems are used to take

advantage of the massive parallelization in these systems. Finally, in addition to the use of the high-order compact scheme, the investigated flows are restricted to regimes with affordable Reynolds numbers, Mach numbers and Damkholder numbers. The present paper represents our progress on this topic.

2. Chemistry Mechanism

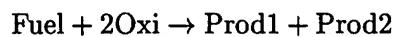
Chemical kinetics plays an important role in the development of laminar flame structures. Because of the limited size of the activation energy of any realistic combustion system, the details of a specific kinetic mechanism significantly affect the production rates of some intermediate species and can be crucial for practical applications in which there is interest in pollutant production rates and near ignition/extinction flame structures. However, previous studies found that a true, detailed chemical-kinetic mechanism is very difficult to tackle even for one-dimensional laminar flame analysis. Therefore, simplification of the chemical kinetics is almost mandatory for more realistic calculations.

There exist several systematic approaches to simplify chemical kinetic mechanisms, and generally include two steps: development of the starting and reducing mechanisms (Peters, 1985). The starting mechanism represents a subset of the detailed mechanism, obtained by elimination of elementary reactions to diminish the number of total species in the system by as much as 90%. The reduced mechanism is then achieved by systematic applications of steady-state approximations to various intermediate species. In the past decade, these reduced mechanisms have been successfully applied in both analytical and numerical studies for CH_4/Air flames (Card, *et al.*, 1996). It turns out that a two-step approximation, which consists of a fuel-consumption step and an oxygen-consumption step, can be made for turbulence modeling and the physics in turbulent diffusive flame, which is the case in the current studies.

The two-step mechanism of the CH_4/Air reaction can be described as:



where Fuel is CH_4 , Oxi is O_2 , Int is $\frac{2}{1+\alpha}(\text{H}_2 + \alpha\text{CO})$, Prod1 is $\frac{2\alpha}{1+\alpha}\text{H}_2\text{O} + \frac{1-\alpha}{1+\alpha}\text{CO}_2$ and Prod2 is $(\frac{2}{1+\alpha}\text{H}_2\text{O} + \frac{2\alpha}{1+\alpha}\text{CO}_2)$. The coefficient α is determined from the water-gas equilibrium. For comparison, we also give the one-step fast-limit chemical mechanism which is described by



3. Initial Conditions

To facilitate the instability of the mixing layers and reduce the computations, the initialization of the calculations is often done by the superposition of the mean flow quantities and perturbations from the linear stability analysis. To make use of the results from Day *et al.* (1998), the mean flow variables are self-similar solutions with fast-limit chemical reaction, and the eigenfunctions and eigenvalues are obtained from the most unstable modes in the corresponding mean flows. Since the characteristics of the eigenmodes depend strongly on the flow properties such as the compressibility, the heat release and the density ratio *etc.*, and determine the final forms of the mixing mechanism mentioned above, a test case with $M_c = 0.5$, $S = 1.0$ and $\Theta = 0$ is selected for initial calculations, where M_c denotes the convective Mach number, which represents the flow compressibility; S denotes the slow-stream/fast-stream density ratio; and Θ denotes the heat release, which is defined as $\Theta = \frac{T_f^*}{T_{ref}^*} - 1$, T_f^* is the adiabatic flame temperature. The test case corresponds to the flow with vortex structures dominated by the two-dimensional “central” mode,

Compared to the cases studied by Day *et al.*, the current stability problem has the same characteristic equations except that the characteristic disturbance frequency ($\omega = (\omega_r, \omega_i)$) is complex and the characteristic wave number (α) is real. Therefore, the same shooting method is used in our work to determine the most unstable mode for the test case, which has the eigenvalues:

$$\omega^{(n)} = (0.02858, 0.1363), \quad \alpha^{(n)} = (0.7577, 0.0) .$$

Note that the most unstable mode for hyperbolic-tangent mean velocity profile, has eigenvalues as $\omega^{(n)} = (0.0, 0.1364)$, $\alpha^{(n)} = (0.730, 0.0)$. It is also pointed out that some group transformations are manipulated in our temporal stability analysis. For example, if the coordinate is moving with a velocity \bar{u}_c , we have:

$$\omega^{(n)} = \omega^{(0)} - \bar{u}_c \cdot \alpha^{(0)}, \quad \alpha^{(n)} = \alpha^{(0)} ;$$

and, if the velocity scale is changed by a factor of F , we have:

$$\omega^{(n)} = F \cdot \omega^{(0)}, \quad \alpha^{(n)} = \alpha^{(0)} .$$

With the above generated eigenvalues and the corresponding eigenfunctions into the initial fields, the test case is run on serial computers by FDL3DI, a code developed in Wright-Patterson Laboratory. Figure 1 reproduces the vortex roll-ups from the simulations of the two-dimensional

temporally mixing layer in the test case. The development in the rest of this paper pertains to the three-dimensional model.

4. Numerical Procedure

Our calculations are based on FDL3DI, which is a research code that uses high-order compact differencing schemes combined with high-order filtering formulas in curvilinear coordinate formulation. Its high-order features have shown great savings in both the memory and the time required to simulate highly curvilinear, realistic aerospace systems (Gaitonde and Shang, 1997; Visbal and Gaitonde, 1998; Gaitonde and Visbal, 1999). The extension of FDL3DI to handle the DNS of turbulent combustion systems must include the solution of the transport equations for the reacting species and the use of modern parallel computers because of the large number of equations and the stringent resolution requirements of reacting flows.

Parallelization of compact difference schemes in FDL3DI is not a trivial task, particularly since this will be based on the current distributed-memory computer platforms (IBM SP2, for example). The obvious challenges come from the absence of any automatic tool that can transform sequential code to parallel code, and the users have to design their own data-mapping and message-passing procedures case-by-case. FDL3DI is a product of many years of work and has relatively complex program structures and data managements. Any parallelization effort must preserve the reliability and accuracy of the code.

Another challenge to the parallelization of FDL3DI pertains to the treatment of a series of tridiagonal systems generated by the compact difference schemes in the code. On sequential computers, solving a tridiagonal system can be done quite efficiently with the Thomas algorithm. However, the recurrence processes used in the Thomas algorithm are serial in nature, and any straightforward parallelization induces a significant idle time in waiting for the updated data from the previous calculations.

To meet these challenges, the following issues which pertain to the parallelization of FDL3DI have been addressed in our study.

4.1. DOMAIN DECOMPOSITION

FDL3DI contains the capability for multi-block calculations. In this method, the computational domain is divided into subdomains, and each subdomain advances the solution independently with individual interior and boundary scheme in the same manner as in single-domain calculations. Data are exchanged across the interface between adjacent domains at the end of each stage in Runge-Kutta integrations. This sequential concept is consistent with what is done in parallel computing except that the message pass-

ing in the overlapped domain is done using MPI subroutines in parallel computing instead of writing over memory locations, as done in sequential multi-block calculations. The procedure above produces a straightforward parallel algorithm, named OOP (one-sided boundary scheme for compact differencing and one-sided boundary scheme for filtering at the interface). However, the above procedures solve the local tridiagonal systems independently in each domain with one-sided lower-order scheme for the interface and may cause serious distortion of flow structures. Gaitonde and Visbal (1999) have addressed this problem and found that the use of a high-order one-sided filtering scheme can significantly improve the accuracy. Efficient, high-fidelity parallel tridiagonal solvers are desirable for DNS. For comparison, we implemented two other parallel procedures, one is to use the parallel tridiagonal solver for compact differencing and filtering (PPP). The other uses the parallel tridiagonal solver for compact differencing and one-sided boundary scheme for filtering (POP).

4.2. DATA MAPPING

Data mapping determines data transformation from the global index to the local index. Unlike the shared-memory computers, the distributed-memory computers have a limitation of memory size and usually cannot afford extra space for the data required in the local computations. It is thus necessary to decompose the global data array into separate local data array, and generate mapping information for message-passing among the processors. In our implementations, the data mappings are generated so that the code structure is retained in the SPMD (Single Program-Multiple Data stream) fashion. For example, a local data array for the procedure with one block per processor has a form like

$$\begin{aligned} &(\text{IBLKST}(i) - r : \text{IBLKEN}(i) + r, \quad \text{JBLKST}(i) - r : \text{JBLKEN}(i) + r, \\ &\quad \text{KBLKST}(i) - r : \text{KBLKEN}(i) + r) \end{aligned}$$

where $\text{*BLKST}(i)$, $\text{*BLKEN}(i)$ respectively, are the start and end global index for the i th block in the x , y , and z directions; r are the depth of the overlapped domain and can be varied for OOP but fixed at 2 for PPP and POP.

4.3. PARALLEL TRIDIAGONAL SOLVERS

There exist several candidate parallel tridiagonal solvers: the transposed, the pipelined and the distributed. To estimate the role of a specific parallel tridiagonal solver in the overall performance, it is worthwhile to look at the CPU time profile taken by the sequential tridiagonal solver in FDL3DI (Table I). For a viscous, single block calculations with filter, system profiling

shows that the tridiagonal solver, TDGCOMP, is the most time-consuming kernel and takes approximately 27.1% of the overall CPU time. If a kernel which takes time fraction F_i in sequential calculations can be parallelized with efficiency η_i , it can be seen that the overall parallel efficiency can be estimated as

$$\eta = \frac{1}{\sum_i F_i / \eta_i}. \quad (\text{III})$$

Table I. Profiling data for dominant subroutines in FDL3DI.

Viscous Calculations		Inviscid Calculations	
Name	%Time	Name	%Time
.tdgcomp	27.1	.tdgcomp	19.9
.deriv	16.0	.deriv	10.5
.vcmpxrhs	12.5	.runge	8.3
.sweepi	9.7	.ztcomp	8.1
.vcmpyrhs	8.3	.finsbdy	8.1
.insbdy	6.6	.etcomp	5.7
.runge	2.3	.xicomp	5.7
.ztcomp	2.3	.convrt	5.3

In FDL3DI, the computational kernels, other than the solution of the tridiagonal system, are procedures for the Runge-Kutta integration or DO-LOOP preparations for the tridiagonal solutions, and parallel procedures with $\eta_i \geq 99\%$ can be obtained without any significant difficulties. It therefore results in a conclusion that a parallel tridiagonal solver with $\eta_i \geq 70\%$ can be good enough to achieve an overall performance of more than 90%. This estimation provides an important guide in the development of an appropriate parallel procedure for our implementations.

The performance of various parallel algorithms for non-periodic tridiagonal systems is described in Table II. To produce Table II, we choose Sun's reduced PDD (Parallel Diagonal Dominated) approach as the representative for the distributed algorithm (Sun and Moitra, 1996). Sun's approach is the most efficient parallel solver for diagonal dominated tridiagonal system in this category. The pipelined algorithm is also presented without the optimization suggested by Povitsky (1998). In Table II, α , β and γ are, respectively, the time for starting a communication operation, for sending a double precision data, and for one floating point operation; P denotes the number of processors, N , N_1 are respectively, the order and the columns of right hand sides for the tridiagonal systems, and k is the number of groups in the pipelined algorithm; j is the reduced number in Sun's algorithm, which is determined by the accuracy requirement and range from 10 to $\frac{N_1}{P}$. From the table, it can be seen that Sun's algorithm has much less communication cost, and a little more computation operations than the other two

algorithms, which are the gains of this algorithm in the current computer architectures which can perform the floating point operations much faster than it performs communication. For example, a typical performance on IBM SP2 system leads to $\frac{\gamma}{\beta} \sim \frac{1}{30}$ and $\frac{\alpha}{\beta} \sim 200$. Therefore, Sun's algorithm is preferred in our implementations.

Table II. Performance comparison for different parallel tridiagonal solvers (Non-Periodic).

System	Algorithm	Computation	Communication	Idle
Multiple right sides	Thomas	$n_1(5n-3)\gamma$	0	0
	Transposed	$\frac{n_1}{P}(5n-3)\gamma$	$\alpha + \frac{n \times n_1}{P}\beta$	0
	Pipelined	$T_1 = n_1 \left(5\frac{n}{P} - 3\right)\gamma$	$T_2 = 2k\alpha + 2n_1\beta$	$\frac{(P-1)(T_1+kT_2)}{k}$
	Distributed	$n_1 \left(5\frac{n}{P} + 3j + 1\right)\gamma$	$2\alpha + 2n_1\beta$	0
Single system	Thomas	$(8n-7)\gamma$	0	0
	Distributed	$(11\frac{n}{P} + 6j - 4)\gamma$	$2\alpha + 12\beta$	0

Figure 2 shows the speed-up, $\frac{T_S}{T_P}$, of Sun's reduced PDD algorithm achieved in our implementations, where T_S is the CPU time from sequential calculations and T_P is the CPU time from the parallel calculations. For a single tridiagonal system with the size of 960, the parallel performance is very low because of the dominant communication latency as well as the larger computational operations from the PDD algorithm. At the same time, it can be seen that the parallel efficiency, $\eta = \frac{T_S}{P \times T_P}$, reduces from 41.4% at $P = 2$ to 11.3% at $P = 8$. If the tridiagonal system has multiple right sides, the performance improves significantly, for example, the parallel efficiency for 240×960 , where 240 is the size in the difference direction and 960 are the multiple right size, reaches 80% at $P = 2$. These observations are consistent with the predictions in Table II.

4.4. PARALLEL FDL3DI

Three parallel procedures, OOP, POP and PPP have been implemented in FDL3DI. Their performance has been assessed on IBM SP2 at Cornell Theory Center. To explore the issues involved, consider the unsteady inviscid flow due to a convecting vortex in an otherwise uniform flow at a freestream Mach number $M_\infty = 0.1$. The initial flow field and vortex strength are set as in Gaitonde and Visbal (1999). The domain considered extends $-6 < X < 18$, $-6 < Y < 6$. The z-direction is a dummy for which 7 grid points are used. To test for the accuracy of the calculations, we use a uniform mesh of $60 \times 30 \times 7$, and two processors for the three parallel procedures. The domain decomposition is located at $X=6$. Figure

3 displays the vorticity contours obtained with non-periodic boundary conditions from the three parallel calculations as well as a reference sequential calculation. The reference calculation uses the C4 compact scheme coupled with an interior filter of tenth-order accuracy and a LOC (lower-order-centered) boundary filter scheme, $F10^{0.4} - 0, 2, 4, 6, 8$. The results show that the OOP and POP procedures reproduce the single-domain results, while the vortex experiences a significant decay for the PPP procedure. The PPP procedure, however, was implemented with a low-order filter scheme. A large overlap region, which is required for high-order filter formulas, will be too expensive.

Figure 4(a) shows the speed-up for the three parallel procedures without filtering. The results are obtained with 5 time steps for a system with grid size of $240 \times 120 \times 14$. (The grid size of $60 \times 30 \times 7$ is too small for meaningful parallel computing.) For OOP, the performance is excellent until $P = 8$ when the z-direction goes through decomposition. The deviation from the idealized speed-up (Figure 2) results from the fact that OOP requires extra calculations for the overlap region. The same situation occurs for PPP. Although the performance of PPP is worse than that of OOP, it can be seen that the situation improves as the grid size becomes large with PPP showing improved performance. This practical observation is consistent with the analysis shown in Table II. The same can be said of POP since POP is exactly PPP with the filter turned off in the calculations. Figure 4(b) shows a similar performance as the filtering scheme is turned on.

Finally, the behavior of speedup at 8 processors in figures 4(a) and 4(b) deserves explanation. For $P < 8$, the domain is split in only the x- and y-directions. Splitting in z-direction for $P \geq 8$ reduces the speedup because of the few number of nodal points in z, a sizable portion of which are in the overlap.

5. Conclusion

In this paper we have discussed some related issues in the DNS of compressible, turbulent, reacting mixing layers. It is pointed out that the use of reduced chemical-kinetic mechanisms, the right choice of initial conditions are not only essential for the correct physics, but also for affordable calculations on the current computer architectures. Several parallel strategies for the general-purpose code, FDL3DI, have also been proposed and tested. It is found that the technique with one-sided boundary treatment in multi-block calculations can be extended to handle parallel computing. The parallel tridiagonal solvers are preferable when the problem size is large relative to the number of processors.

Finally, the present paper is intended to remind the reader of the com-

plexity in the analysis of turbulent reacting flows. The difficulties pertain to finite-rate chemical kinetics, turbulence, and computational mathematics. The progress made in this direction are summarized.

Acknowledgments

The first author wants to remark that the interest in the investigation of the mixing effects on finite-rate flame structures originated from several discussions with Dr. M. Day, Stanford University, while the first author was in residence at the Center for Turbulence Research at Stanford University. Funding for the work is provided by the Aerospace Research Corporation, Long Island. The collaboration with Drs. Miguel Visbal and Datta Gaitonde of the Air Force Research Lab, WPAFB is acknowledged. The Aerospace Research Corporation, Long Island is a Division of Thaeocomp Technical Corporation and a Corporate Partner of Cornell University.

References

- Brown, G. and Roshko, A. (1974). On density effects and large structure in turbulent mixing layers, *J. Fluid Mech.* **64**, 775.
- Cai, X.D., Ladeinde, F. and O'Brien, E.E. (1997). Parallel DNS on the SP2 with MPI, *the First AFOSR International Conference on DNS/LES* held at Louisiana Tech University, Ruston, Louisiana, USA.
- Card, J.M., Ryden, R. and Williams, F.A. (1996). Influences of flame-vortex interactions on formation of oxides of nitrogen in curved methane-air diffusion flamelets, *Comb. and Flame* **105**(3), 373.
- Chakraborty, D., Upadhyaya, H.V., Paul, P.J. and Mukunda, H.S., (1997) A thermochemical exploration of a two-dimensional reacting supersonic mixing layer, *Phys. Fluids* **9**, No.11, 3513.
- Curran, E.T. (1991). "Introduction" in *High-speed fly propulsion systems* edited by S.N.B. Murthy and E.T. Curran.
- Day, M.J., Reynolds, W.C. and Mansour, N.N. (1998). The structure of the compressible reacting mixing layer: Insights from linear stability analysis, *Phys. Fluids* **10**, No.4, 993.
- Gaitonde, D. and Shang, J.S. (1997). Optimized compact-difference-based finite-volume schemes for linear wave phenomena. *J. Comp. Phys.* **138**:617-643.
- Gaitonde, D. and Visbal, M.R. (1999). Further development of a Navier-Stokes solution procedure on high-order formulas. *AIAA Paper* 99-0557.
- Lele, S.K. (1992). Compact finite difference schemes with spectral-like resolution, *J. Comp. Phys.* **103**, 16.
- Miller, R.S., Madnia, C.K. and Givi, P. (1994). Structure of a Turbulent reacting mixing layer, *Comb. Sci. and Tech.* **99** (3), 1.
- Planche, O.H. and Reynolds, W.C. (1992). A numerical investigation of the compressible mixing reacting mixing layer, Report No. TF-56, Department of Mechanical Engineering, Stanford University.
- Povitsky, A. (1998) Parallel directionally split solver based on reformulation of pipelined Thomas algorithm. ICASE Report No.98-45.
- Sun, X.-H. and Moitra, S. (1996). A fast parallel tridiagonal algorithm for a class CFD applications. *NASA TP* 3585.
- Visbal, M.R. and Gaitonde, D. (1998). High-order accurate methods for unsteady vortical flows on curvilinear meshes. *AIAA Paper* 98-0131.

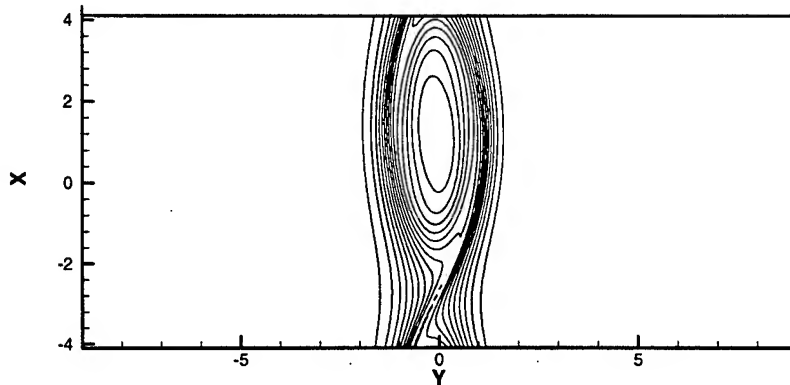


Fig.1 Vorticity contour from the DNS of two-dimensional non-reacting flows dominated by "central" mode with FDL3DI.

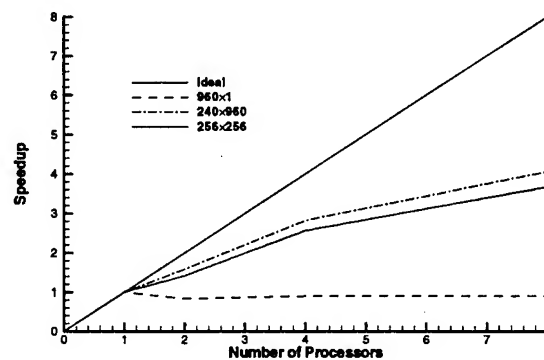


Fig. 2 Speedup of the reduced PDD parallel tridiagonal solver for systems with different size.

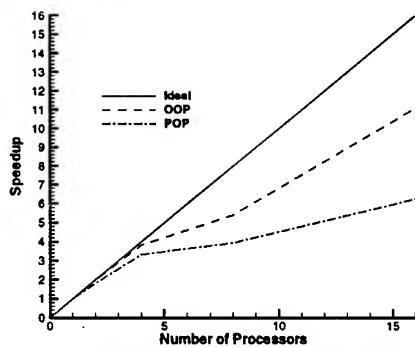


Fig. 4(a) Speedup of different procedures for parallel FDL3DI with filter turned off.

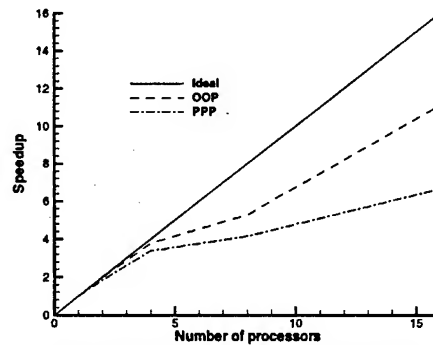


Fig. 4(b) Speedup of different procedures for parallel FDL3DI with filter turned on.

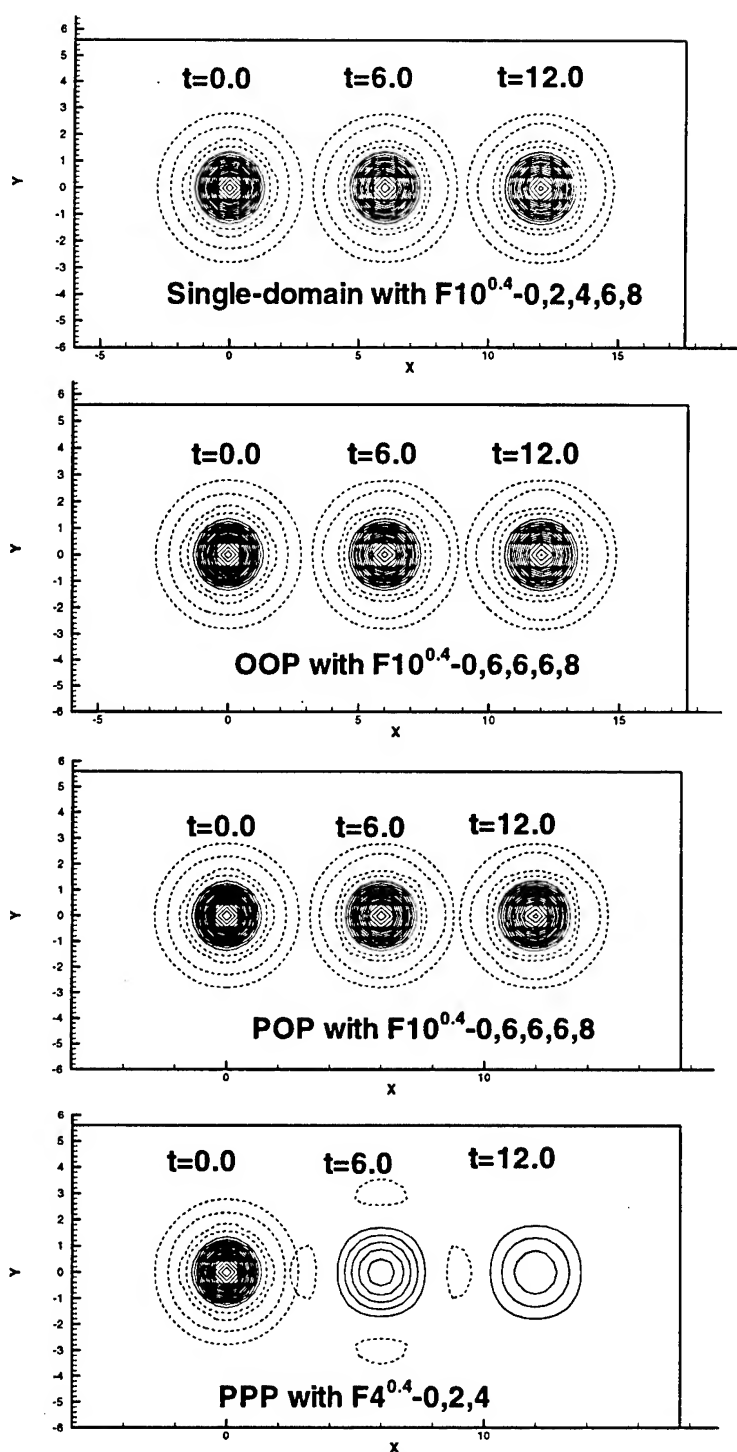


Fig. 5 Vorticity contours generated from various parallel procedures.

LARGE EDDY SIMULATION OF STATIONARY PREMIXED FLAMES USING A SUBGRID FLAMELET APPROACH

V. K. CHAKRAVARTHY AND S. MENON

*School of Aerospace Engineering
Georgia Institute of Technology
Atlanta, GA 30332
U.S.A*

Abstract

A subgrid combustion model is used to simulate premixed planar flames stabilized by stagnating flows and a confined swirl stabilized flame in an engineering combustor. Flamelet type combustion is assumed for both types of flames and experimental conditions are used for the simulations. The geometric characteristics of the flame surfaces and their effects on fluid dynamics are well predicted for the former type of flames. For the combustor simulation, the qualitative effects of heat release on the flow field are captured. The turbulence predictions in the combustor is highly sensitive to the characteristics of inflow turbulence. The turbulence modeling capability needs to be improved in order to better test the model in this case.

1. Introduction

The flamelet regime of turbulent combustion is characterized by a laminar flame thickness (δ_f) much smaller than the smallest energetic eddy size (Kolmogorov length scale η). Hence, the internal flame structure (flame normal profiles of specie, temperature, etc.) is unchanged by the fluid dynamics and the flame can be approximated as an infinitely thin surface convected by the local fluid velocity and propagating normal to itself at the laminar flame speed, S_L . The task of modeling the flamelets is then reduced to the geometric tracking of the flame surface.

The flame surface is wrinkled by eddies ranging from η to L (the integral length scale), leading to an increase in the flame surface area. Since the local propagation rate equals S_L everywhere on the flame surface, the flame area is a direct measure of the reactant consumption rate. A direct numerical simulation (DNS), which can fully account for eddies of all sizes in high Reynolds number flows and their effect on the flame is impractical at present. In the present study, a large eddy simulation (LES) approach with a stochastic subgrid combustion model is used to simulate (statistical stationary) premixed flames in the flamelet regime.

In LES, eddies resolvable on the grid are simulated and the effect of the unresolved small scales is approximated using a subgrid model. However, the distinguishing aspects

of flamelet combustion, i.e., local laminar propagation and small scale wrinkling are highly localized small scale phenomena and cannot be accounted in an overly simplified model. Here, a subgrid version of the linear eddy mixing (LEM) model (Kerstein, 1989; Menon et al., 1993; Smith and Menon, 1996) is used to model the effects of unresolved turbulence on the flame structure. This approach has been used in the past to model three dimensional (3D) flame kernels (Chakravarty and Menon, 1997) and flames in two-dimensional stagnating turbulence (Smith and Menon, 1998). The present study focuses on flames stabilized by the axial strain rate in stagnating flows and swirl flows.

The stagnation flames are perfect candidates for studying turbulence-flame interactions. The flame brush is fairly planar and the turbulence is nearly homogeneous in the spanwise direction. Thus, the flame speed can be obtained without any ambiguity. Also, the turbulence intensity (u') that the flame encounters can be controlled using the inflow conditions. This is important because the effects of turbulence on the flame (turbulent flame speed, turbulent flame brush width, flame surface density) are quantified as functions of characteristics (intensity, length scale, etc.) of incident turbulence, which, in some configurations (e.g., premixed flames in bluff body wakes and dump combustors) may be difficult to measure (or control) at the flame locations. Although stagnation premixed flames have been studied extensively using experiments (Cho et al., 1986; Cho et al., 1988; Cheng and Shepherd, 1989), there appears to be no study of this flame using unsteady simulations. The simulations reported here are the first 3D LES of turbulent stagnation flames under experimental conditions.

In stagnation point flames, u'/S_L is usually of order unity. This is seldom the case in engineering combustors where swirl is employed to stabilize the flame (Cheng, 1995; Kim and Menon, 1998; Kim et al., 1999). A lean, premixed, swirl stabilized turbulent flame in a full-scale combustor is chosen to test the current modeling approach. In this combustor (General Electric LM 6000) δ_f/η is approximately 4 and u'/S_L is about 55. While the stagnation flames are definitely in the flamelet regime, the LM6000 flame falls into the extended flamelet regime (Poinot et al., 1991). Nevertheless, for the purpose of the present study, it is assumed that the flamelet assumption of undisturbed locally laminar flame propagation (at speed S_L) still applies to this flame.

2. Modeling approach

The closure of subgrid stresses in the LES equations is carried out using an eddy viscosity assumption. The eddy viscosity is modeled in terms of the LES filter width and the subgrid kinetic energy (Schumann, 1975). The subgrid kinetic energy is obtained by solving a model evolution equation (Kim and Menon, 1998; Kim et al., 1999). In most LES approaches, the turbulent dissipation is assumed to balance subgrid kinetic energy production at all times. The model equation for subgrid kinetic energy used here introduces a first-order non-equilibrium for the subgrid relaxation since the production of subgrid kinetic energy no longer equals dissipation. The subgrid kinetic energy in the present approach further determines the extent of influence that subgrid scales have on the flame dynamics.

The chemical and thermodynamic state of the fluid is represented by a state variable G . It varies between 0 (product) and 1 (reactant). Hence, it can be assumed to be complementary to the reaction progress variable, i.e. $C = 1 - G$. The evolution of G field involves both subgrid and supergrid processes. The underlying idea of this separation of processes is to model each physical phenomenon at its own characteristic length and time scales. Subgrid processes include stirring (flame wrinkling due to subgrid scales) and laminar

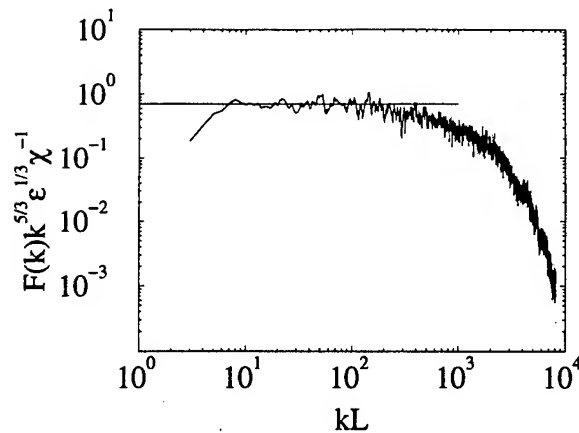


Figure 1. LEM prediction of inertial-convective range in passive scalar spectrum. Plateau indicates the value of β , the Obukhov-Corrsin constant

propagation. Advection of the scalar field, which leads to mean motion of the scalar and wrinkling at large scales (resolved on LES grid), is the only supergrid process.

The subgrid processes occurring within each LES cell are modeled by the LEM approach (Menon and Calhoun, 1996; Smith and Menon, 1998). Henceforth, this approach is identified as LEM-LES. The flame propagation and subgrid wrinkling are modeled by solving the stochastic Lagrangian-Eulerian equation: $\partial G/\partial t = -S_L|\nabla G| + F_s$ on a one-dimensional domain within each LES cell. A finite volume scheme is used to solve this equation and the one-dimensional finite volume cells are called LEM cells. The total volume of the LEM cells on each subgrid domain equals the corresponding LES cell volume. There is no mean convection term in this equation since the subgrid field is isotropic and does not move the flame in any one particular direction. The equation is hyperbolic and admits discontinuous solutions. Thus, G is given a binary representation on the subgrid domains with each 0-1 (1-0) interface representing an infinitely thin flame propagating into the reactants with a laminar propagation velocity S_L .

The subgrid stirring is modeled by a set of Lagrangian scalar field rearrangement mappings (on the subgrid one-dimensional domains), symbolically represented by the term F_s in the subgrid G equation. Each mapping represents the stirring of the scalar field (flame wrinkling) by a single turbulent eddy (Menon et al., 1993). The stirring events are stochastic and the frequency is reflective of the energy content in the subgrid scales. The sizes of eddies participating in the subgrid stirring range from the Kolmogorov eddy size to the LES filter width and the eddy size distribution is derived using inertial range turbulent scaling laws. The characteristics of stirring are derived in the present case by assuming a Kolmogorov constant (that characterizes inertial range energy spectrum) of 1.5.

To evaluate the ability of LEM to capture scalar mixing, turbulent diffusion of a passive (diffusive) scalar ($Re_L \sim 20000$) is modeled using these stirring rules in LEM and the predicted inertial-convective spectrum is shown in figure 1. The spectrum is normalized using the Obukhov-Corrsin scaling (Obukhov, 1949; Corrsin, 1951) so that the plateau in normalized spectrum corresponds to the Obukhov-Corrsin constant. In this figure, χ and ϵ denote the scalar and turbulent dissipation, respectively.

As seen in figure 1, LEM predicts a value of 0.7 for the Obukhov-Corrsin constant (β) which is very close to values obtained from experiments (Sreenivasan, 1996; Mydlarski and Warhaft, 1998). Note that β_1 quoted from experiments correspond to one-dimensional spectral scaling which is $3\beta/5$. Since the Obukhov-Corrsin is approximately the quantitative measure of the effect of inertial range turbulence on scalar mixing (specifically in the inertial range), the accurate prediction of this constant confirms the ability of LEM to predict scalar mixing by the inertial range turbulence. The one-dimensional G equation (as shown above) when used with the same form of LEM (subgrid stirring) was shown (Smith and Menon, 1996) to predict the turbulent flame speed of freely propagating flames in isotropic turbulence (which is assumed in LEM). Further details about LEM, being available in cited literature, are avoided here for brevity.

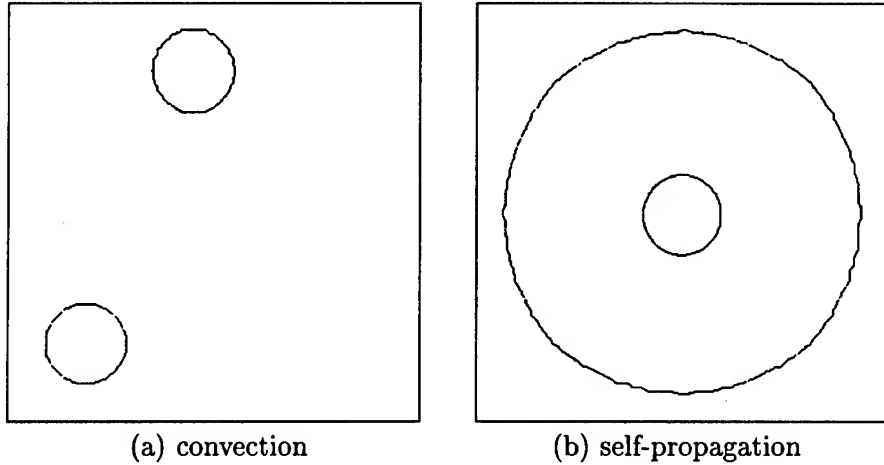


Figure 2. Scalar interface tracking using the LEM-LES advection scheme

The large scale advection of the scalar field (due to the LES filtered velocity) is conducted using a Lagrangian volume transport method (Smith and Menon, 1998). In this method, the subgrid LEM cells are transported between the subgrid domains to account for volume transport between LES cells. The method is Lagrangian and is similar (not identical) to the volume of fluid method used for volume tracking. When using a finite difference or finite volume scheme, an initially thin scalar front gets dispersed and artificially thickened by the numerics. Using the present advection scheme, the scalar interfaces (self-propagative or otherwise) can be advected with no artificial thickening and with minimal distortion. This (front capturing) ability of the present advection scheme is illustrated in figure 2. The advection of a thin scalar interface by uniform velocity and the outward burning of a circular laminar flame are simulated on a Cartesian grid. The initial and final states of the fronts (shown in figure 2), indicate that the fronts are well captured with minimal artificial distortion or dispersion. This feature is essential to capture the flamelet type burning since the flame thickness is always smaller than all the fluid dynamic scales.

When the flame profile is captured over several grid points (as in a conventional LES with a flame speed model (Kim and Menon, 1998)), the internal flame structure can be modified by the fluid dynamics, thereby changing its local propagation speed and violating the flamelet assumption. To illustrate the need for the LEM-LES approach in the flamelet

regime, the present results are compared to prediction obtained by conventional LES using a flame speed model (Yakhot, 1988).

3. Flow configurations

The stagnation flame configuration consists of a premixed flame held by a turbulent jet flow impinging on an adiabatic wall. The turbulent jet is surrounded by a laminar co-flow at the same speed to prevent the formation of any shear generated structures at the edges. The flame interacts with nearly isotropic turbulence generated by the honeycomb grid at the inflow of the jet. At the inflow, isotropic turbulence with a von Karman type spectrum (at a required intensity, u' and length scale, L) is added to the mean flow velocity, U_o . The configuration and the flow conditions are chosen to match the experimental conditions in past studies (Cho et al., 1986; Cho et al., 1988; Cheng and Shepherd, 1989). The temperature rises by a factor of 7 due to chemical heat release which is typical of near stoichiometric hydrocarbon premixed flames. Simulations are conducted for u'/S_L values of 0.75, 1.5, 4.0 and 8.0 with a fixed integral length scale (L) of 5mm. The flame with u'/S_L of 0.75 is the closest to the experiments and hence, the conventional LES is also conducted for this case.

In case of stagnation flames, a $69 \times 89 \times 89$ grid is used for LEM-LES, whereas a finer $89 \times 129 \times 129$ grid is used for the conventional LES. In general, the grid requirement for the two cases are different. In LEM-LES, the LES is used primarily to provide fluid dynamic information to the subgrid domains (where the flame propagation and small-scale stirring processes are well resolved). For the conventional LES, a very finer grid is required in order to accurately resolve (track) the flame on the three-dimensional grid. Since the computational cost of three-dimensional simulations increases rapidly with increasing grid resolution, a $89 \times 129 \times 129$ grid is used for conventional LES based on cost restrictions.

The swirl combustor simulated here is a close approximation to the GE LM6000 and consists of a $15.24\text{cm} \times 8.28\text{cm} \times 7.01\text{cm}$ rectangular chamber into which a highly swirling flow enters through a circular pipe of 3.35 cm diameter. The inflow turbulent kinetic energy is approximately 14% of mean kinetic energy. The flame speed corresponds to a premixed mixture of methane-air at an equivalence ratio of 0.5, 75 psi pressure and 600 K. The flame temperature is around 3 times the initial temperature. A $101 \times 89 \times 61$ Cartesian grid is used to simulate this flow field. In the experiments (used for comparison here), cooling air is pumped into the combustion chamber along its side walls at a location around 5.0 cm downstream of the inflow. A more detailed description of the combustor is given elsewhere (Kim and Menon, 1998; Kim et al., 1999). However, this cooling effect is not included in the simulations. Given the fact that the flame is located well upstream of the cooling air, it is assumed that this omission does not affect the predictions severely.

4. Results and discussion

The results obtained using the LES-LEM method is compared with predictions obtained using conventional flame speed model and experimental data. We first discuss the stagnation point flame and then the swirl-stabilized flame.

4.1. STAGNATION POINT FLAMES

The fluid dynamics are substantially altered due to the density variations across the wrinkled flame surface in all the simulations. While the flame fluctuates with a low amplitude about its mean location in case of low u'/S_L flames, the fluctuations are more pronounced at high u'/S_L leading to a highly convoluted flame structure. This transition from wrinkled flamelet regime ($u'/S_L \sim 1$) to the corrugated flamelet regime ($u'/S_L = 8$) is well illustrated in figure 3. In these figures, the flame surface shown is obtained by averaging the subgrid G fields and thus, represents a LES-resolved flame structure. This type of 'filtering' loses information on the finer 3D scales of wrinkling as discussed later.

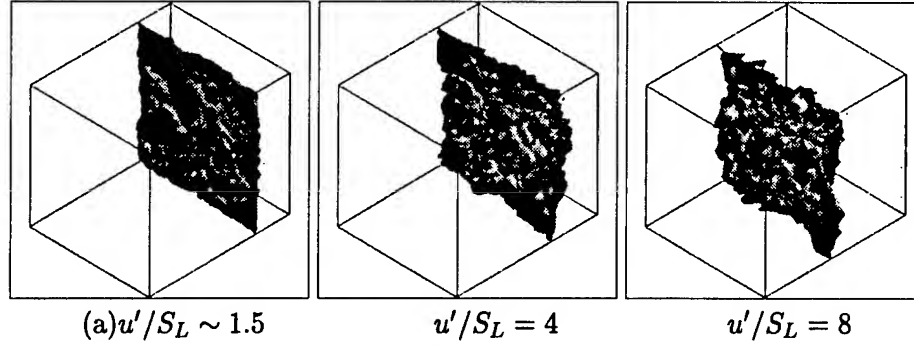


Figure 3. Effect of turbulent intensity on flame wrinkling

TABLE 1. σ_θ predictions for premixed flames

Case	u'/S_L	σ_θ
LEM-LES	0.75 - 1.5	0.47 - 0.55
LEM-LES	4.0 - 8.0	0.706 - 0.74
stagnation flames (Shepherd and Ashurst, 1992)	0.6 - 0.8	0.696 - 0.721
oblique planar flame (Driscoll et al., 1994)	1.7 - 2.7	0.707
freely propagating (DNS) (Trounev and Poinso, 1994)	3.3 - 4.5	0.7

At higher u'/S_L , the instantaneous flame normal tends to move away from the normal to the mean flame surface. This behavior can be quantified by the mean direction cosine (σ_θ) of the flame normal relative to the flame brush plane as in the Bray-Moss-Libby (BML) theory (Bray et al., 1984). In BML theory, it is computed using the exact flame shape whereas, the flame surface resolved on the LES grid is used here. The small scale wrinkles, which are more three-dimensional are not captured on the LES grid. As a result, the LES resolved flame normal is likely to be closer to the normal to the mean flame brush than the normal to the actual (exact) flame surface. Hence, an under prediction of σ_θ is expected when using the resolved field in the LEM-LES. Table 1 compares the present data

with past results. For the stagnation flames simulated here, σ_θ is found to increase with u'/S_L , which indicates an increased tendency for three-dimensional wrinkling (corrugated flamelets) at higher intensities.

The flow across the flame surface experiences tremendous acceleration in the normal direction due to a significant (factor of 7) drop in density. When a surface, across which there is a significant velocity gradient, oscillates, it produces a very high level of intermittency in the velocity field. Since the flame normal is more aligned towards the axial direction at lower turbulent intensity, the velocity changes are more prominent for the axial component of the velocity. The *rms* values of the axial and radial velocities predicted by LEM-LES and the flame speed model are shown along with the experimental data in figure 4.

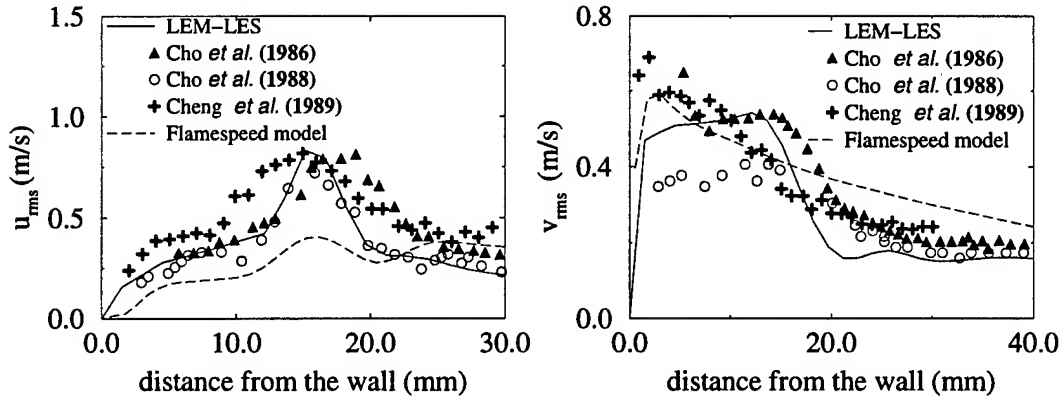


Figure 4. Prediction of turbulent intensities on the centerline

Since the intermittency is higher for the axial component, u_{rms} attains a peak value within the flame brush. In the post flame zone, the density of the products is uniform and there are no density fluctuations. Thus, u_{rms} quickly drops almost to a value upstream of the flame brush. However, the radial velocity fluctuations increase steadily through the flame brush and persist in the post flame zone. As seen in the experiments, the flame brush has essentially created anisotropy in the (flame-generated) turbulence by increasing v_{rms} .

Both the flow intermittency and the turbulence generation mechanism are dependent on the density gradients across the local flame normal. Since the flame is captured as a thin front in LEM-LES, it captures the sharp density gradients better than the conventional LES (which captures the flame profile over several grid points thus producing a thickened flame width). To capture sharp density gradients, a conventional LES would need a much finer (and computationally more expensive) grid than the one used here. It is worth noting that any iso-surface of the three-dimensional G field can be considered a flame (level set method) if the flame is passive. If there are density changes associated with the flame, the flame speed is a function of the density, i.e. flame speed as seen from the products side is different from the flame speed (usually quoted) with reference to the reactants side. If level set assumption is used, the flame speed is discontinuous across the infinitely thin iso-surface and the motion of three-dimensional G field can not be modeled using a finite difference equation.

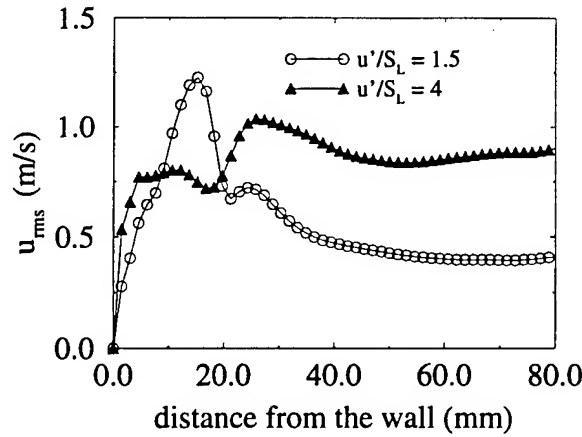


Figure 5. Effect of u'/S_L on axial intermittency of the flow

With increasing u'/S_L , the axial flow intermittency reduces due a more random orientation of the flame and the peak in u_{rms} is less pronounced. This is illustrated in figure 5. However, it is apparent from this figure that a small peak in u_{rms} is produced upstream of the flame brush. This feature is also observed in the experiments (Cho et al., 1988; Cheng and Shepherd, 1989). Interestingly, although most features of planar premixed flames were well captured by the Reynolds averaged second moment closure method (Lindstedt and Vaos, 1999), it failed to predict this peak. This points to the unsteady flame-turbulence interactions as one likely reason for this feature.

The topological (structural) features of the flame surface cannot be extracted from the time averaged data. Flame-turbulence interactions are also inherently unsteady and have to be characterized statistically using instantaneous data. This is done by constructing the probability density functions (PDFs) of local properties over the flame surface. Only the geometric features of the flame surfaces are presented here since other features such as the flame alignment with local vortical structures and strain rates are discussed elsewhere (Chakravarty and Menon, 1999).

The principle curvatures (and radii) of the flame surface (Shepherd and Ashurst, 1992) are computed at several locations and PDFs are constructed. Comparison of mean curvature PDFs (non-dimensionalized using the integral length scale) predictions in figure 6 show that the curvature PDF is more symmetric in case of LEM-LES. Also, the likelihood of higher negative curvatures is seen in the LEM-LES approach. At low turbulence levels, premixed flames develop cusps (as observed in experiments) with very high curvatures pointing towards the product side. Hence, there is likelihood of encountering higher negative curvatures on the flame surface. The flame propagation model in LEM-LES is capable of handling these cusps since the (subgrid) averaged G field is not necessarily continuous on the LES grid. The conventional LES on the other hand, requires the scalar field to be continuous and smooth for stable integration and therefore, is incapable of fully resolving regions of high curvature in the scalar field.

In addition to the curvatures, the shape factors H (ratio of curvatures) (Shepherd and Ashurst, 1992) are also computed. It is well known that the turbulent eddies are most likely cylindrical ($H = 0$) and by wrapping the flame sheet around them, cause the local flame surface to be predominantly cylindrical. This is predicted by both the LEM-LES

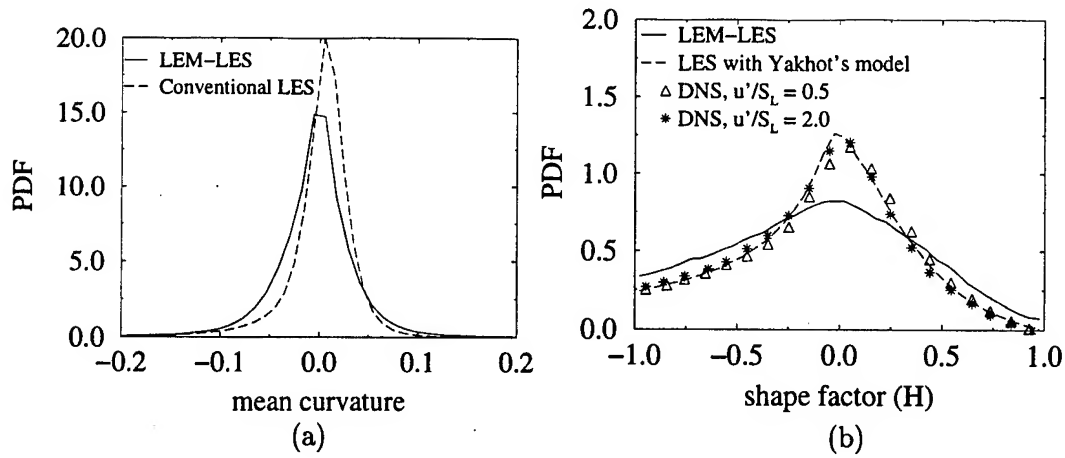


Figure 6. Geometric characteristics of the flame surface

and the flame speed simulations as shown in figure 6.

It is seen that the probability of finding locally spherical ($H = 1$) and saddle ($H = -1$) regions is higher in case of LEM-LES. This can be attributed to the stochastic nature of burning in LEM-LES. In conventional LES, the G field and its propagation rate are relatively continuous. As a result, the flame sheet wraps around fairly smoothly cylindrical eddies. Thus, the predicted shape factor PDF agrees well with the corresponding predictions from a DNS (Shepherd and Ashurst, 1992). It is also interesting to note that heat release seems to have minimal effect of the shape factor PDF since the DNS data was obtained for passive (non-exothermic) flames. It is to be realized that the heat release effects on fluid and the flame dynamics are felt through density gradients. Due to artificial thickening of the flame and the subsequent reduction of density gradients in conventional LES, it is likely that the heat release effects (density gradients) on flame surface dynamics are insignificant. As a result, the conventional LES result agrees well with the DNS data for no heat release case.

In LEM-LES, the stochastic nature of subgrid processes leads to perturbations on the cylindrical flame surface which would result in non-zero shape factors. This reasoning is consistent with observations (Shepherd and Ashurst, 1992) that spherical and saddle shapes are formed by the bending of a cylindrical surface in directions opposite to each other.

The burning rate per unit volume is proportional to the flame surface density which is the flame area per unit volume. The variation of the normalized flame surface density with the mean progress variable ($\langle C \rangle$) is shown in figure 7 along with the theoretical BML expression: $k \langle C \rangle (1 - \langle C \rangle)$ (Bray et al., 1984), where k is a constant. It is seen that the current data is skewed to the right of the theoretical symmetric curve. The peak occurs closer to $\langle C \rangle$ of 0.6 instead of 0.5. This skewness is often seen in experimental studies (Cheng and Shepherd, 1991; Shepherd, 1996; Mounaim-Rousselle and Gokalp, 1994) and an explanation for the shift (Cheng and Shepherd, 1991) is related to bimodal flamelet combustion. It is interesting that even at relatively high u'/S_L , the LEM-LES approach retains the flamelet type characteristics.

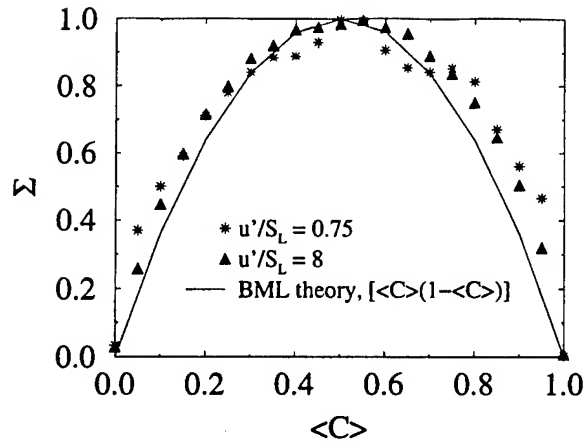


Figure 7. Flame surface density variation with the mean progress variable

4.2. COMBUSTOR FLOW

A flame shape typical of corrugated flamelet regime is found in the combustor. Occasionally, pockets of premixed reactants break away from the primary reactants zone and burn up completely in the midst of products. This is expected given that u'/S_L is extremely high (around 55) in this case.

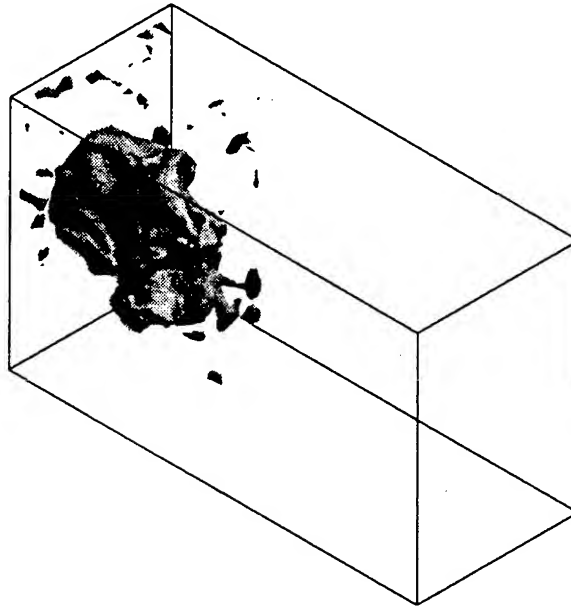


Figure 8. Geometry of the resolved flame surface

The iso-level surface corresponding to resolved G field (obtained using subgrid averages) of 0.1 is shown in figure 8. This surface approximately indicates what the flame might look like in the combustor. The surface shown here is relatively more wrinkled than

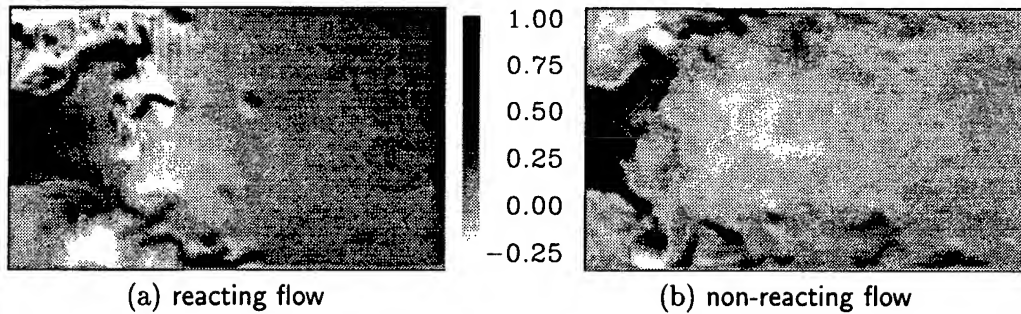


Figure 9. Effect of chemical heat release on the axial velocity field

the surface obtained using the conventional LES predictions (shown in (Kim and Menon, 1998)). As seen in case of stagnation flames, this is once again due to the difference in the flame tracking between LEM-LES and the conventional simulations.

The maximum swirl velocity at the inflow is higher than the maximum axial velocity. Due to the high swirl, there is tremendous radial acceleration and as a consequence, the axial velocity drops rapidly downstream of the inflow. Eventually, the axial flow reverses direction on the centerline thus creating a pocket of recirculating flow. This recirculating flow is expected to hold the flame in position by preventing it from moving downstream. As in the experiments, the recirculation zone is pushed farther away from the inflow when the flow is reacting (when compared to the non-reacting flow). This is illustrated graphically using the axial velocity fields in figure 9.

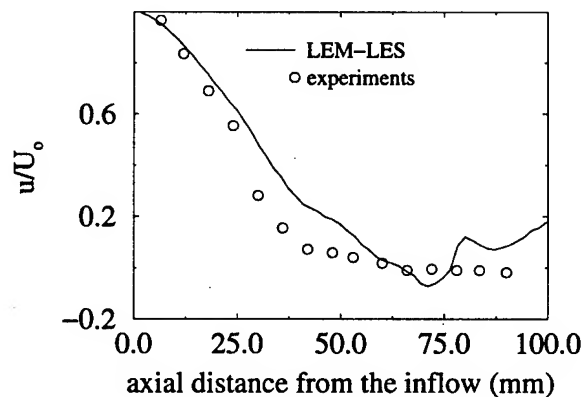


Figure 10. Prediction of axial velocity on the centerline

The mean axial velocity predicted by LEM-LES is compared to the experiments in figure 10. It is seen that the velocity drop in the simulation is under predicted leading to higher axial velocities in the LES when compared to experiments. As a result, the flame is expected to be farther from the inflow in the simulations than in the experiments. Figure 11

shows the u_{rms} predictions from the reacting and the non-reacting simulations. It is seen that the evolution of turbulence is not captured accurately by the simulations. These predictions are also found to be very sensitive to the inflow turbulence characteristics such as the turbulent length scale. Unlike in the stagnation flame simulations, the turbulent length scale is unknown at the inflow in this case. Also, the wide variations in the velocity values close to the inflow (evident from the experimental velocity PDFs not shown here) indicate that the unsteadiness in this inflow may consist of large scale structures in addition to turbulence. Since the simulations use mean flow with added isotropic turbulence as inflow conditions, the kinetic energy growth downstream is not predicted accurately.

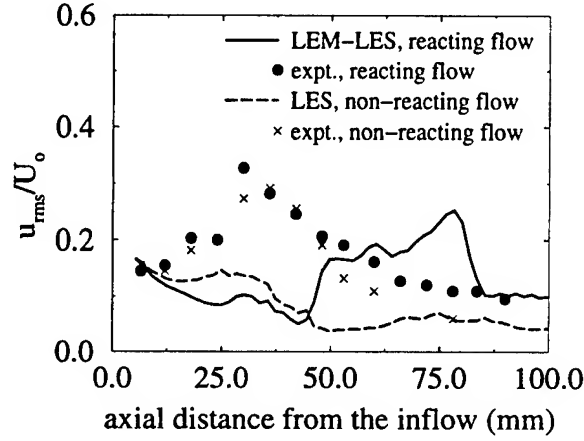


Figure 11. Prediction of velocity fluctuations on the centerline

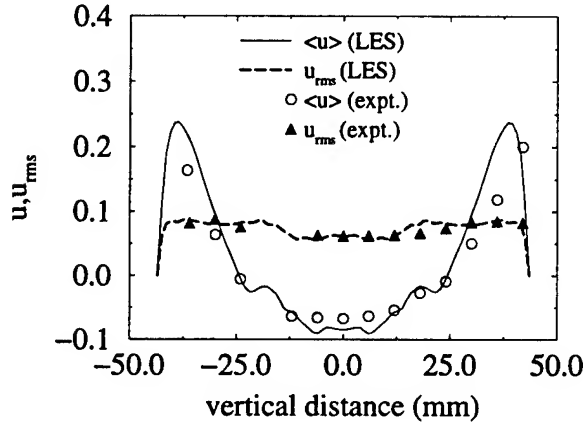


Figure 12. Vertical profiles on axial velocity moments at $x = 78\text{mm}$

Downstream of the centerline recirculation zone, the velocity and turbulence recover reasonably well in the non-reacting flow simulations. The vertical profiles of mean and rms of the axial velocity at a location 78mm from the inflow are shown in figure 12. In case of reacting flow, the vertical profile of axial velocity (similar to figure 12 but not shown here) obtained using experiments indicates a value of 8 m/s of the axial velocity. However, it's

value as seen from figure 10 seems to be negative in experiments and 7 m/s in LEM-LES. This points to some error in the experimental measurements.

The error in turbulence predictions in the near field has made it difficult to validate the subgrid combustion modeling approach in this flow. Better inflow conditions and perhaps a finer LES grid are required to better capture the turbulence evolution. LES with finer grids are currently being undertaken and the subgrid approach can be better tested when the turbulence predictions are accurate.

5. Conclusions

The subgrid flamelet method used here captures, quite accurately, the geometric and propagation characteristics of flame surfaces and their effects on the fluid dynamics. The current method can also account for the effects of exothermic nature of the flame on flame-turbulence interactions (Chakravarthy and Menon, 1997; Chakravarthy and Menon, 1999) accurately and predicts counter-gradient diffusion (Chakravarthy and Menon, 1999) at greater than unity Bray numbers as seen in DNS (Veynante et al., 1997). The contrast between the predictions by LEM-LES and a conventional LES establishes the necessity to model each of the physical processes at their characteristic length and time scales. The validation of the modeling approach for real combustor still remains inconclusive. However, it establishes the feasibility of coupling subgrid modeling strategies with large eddy simulations of realistic reacting flows using parallel computers.

Acknowledgments

This work was supported in part by the Army Research Office. Computational support was provided under a DoD HPC Grand Challenge Project at SMDC, AL and NAVOCEANO, MS HPC centers. The first author is currently at the Oak Ridge National Laboratory, Oak Ridge, TN and is grateful for their support during the preparation of this manuscript.

References

- Bray, K., Libby, P., and Moss, J. (1984). Flamelet crossing frequencies and mean reaction rates in premixed turbulent combustion. *Combustion Science and Technology*, 41:143-172.
- Chakravarthy, V. and Menon, S. (1997). Characteristics of a subgrid model for turbulent premixed combustion. *AIAA-97-3331*.
- Chakravarthy, V. K. and Menon, S. (1999). Modeling of turbulent premixed flames in the flamelet regime. In *First International Symposium on TURBULENCE and SHEAR FLOW PHENOMENA*. to appear.
- Cheng, R. (1995). Velocity and scalar characteristics of premixed turbulent flames stabilized by weak swirl. *Combustion and Flame*, 101:1-14.
- Cheng, R. and Shepherd, I. (1989). A comparison of the velocity and scalar spectra in premixed turbulent flames. *Combustion and Flame*, 78:205-221.
- Cheng, R. and Shepherd, I. (1991). The influence of burner geometry on premixed turbulent flame propagation. *Combustion and Flame*, 85:7-26.
- Cho, P., Law, C., Cheng, R., and Shepherd, I. (1988). Velocity and scalar fields of a turbulent premixed flame in a stagnation flow. In *Twenty-second Symposium (International) on Combustion*, pages 739-745.
- Cho, P., Law, C., Hertzberg, J., and Cheng, R. (1986). Structure and propagation of turbulent premixed flame stabilized in a stagnation flow. In *Twenty-first Symposium (International) on Combustion*, pages 1493-1499.
- Corrsin, S. (1951). On the spectrum of isotropic temperature fluctuations in isotropic turbulence. *Journal of Applied Physics*, 22:469-473.
- Driscoll, J., Sotkous, D., Roberts, W., Post, M., and Goss, L. (1994). Strain exerted by a vortex on a flame - determined from velocity field images. *Combustion Science and Technology*, 96:213-229.
- Kerstein, A. R. (1989). Linear-eddy model of turbulent transport ii. *Combustion and Flame*, 75:397-413.

- Kim, W.-W. and Menon, S. (1998). Large eddy simulation of reacting flow in a dump combustor. *AIAA-98-2432*.
- Kim, W.-W., Menon, S., and Mongia, H. C. (1999). Large eddy simulation of a gas turbine combustor flow. *Combustion Science and Technology*. To appear.
- Lindstedt, R. P. and Vaos, E. M. (1999). Modeling of premixed turbulent flames with second moment methods. *Combustion and Flame*, 116:461-485.
- Menon, S. and Calhoun, W. H. (1996). Subgrid mixing and molecular transport modeling in a reacting shear layer. In *Twenty-sixth Symposium (International) on Combustion*, pages 59-66.
- Menon, S., McMurtry, P., and Kerstein, A. (1993). A linear eddy mixing model for LES of turbulent combustion. In Galerpin, B. and Orszag, S., editors, *LES of Complex Engineering and Geophysical flows*, pages 287-314. Cambridge Univ. Press.
- Mounaim-Rousselle, C. and Gokalp, I. (1994). Strain effects on the structure of counterflowing turbulent premixed flames. In *Twenty-fifth Symposium (International) on Combustion*, pages 1199-1205.
- Mydlarski, L. and Warhaft, Z. (1998). Passive scalar statistics in high-peclet number grid turbulence. *Journal of Fluid Mechanics*, 358:135-175.
- Obukhov, A. (1949). Structure of temperature field in turbulent flows. *Izv. Akad. Nauk. SSSR, Geogr. Geofiz.*, 13:58-69.
- Poinsot, T., Veynante, D., and Candel, S. M. (1991). Quenching processes and premixed turbulent combustion diagrams. *Journal of Fluid Mechanics*, 228:561-605.
- Schumann, U. (1975). Subgrid scale model for finite difference simulations of turbulent flows in plane channels and annuli. *Journal of Computational Physics*, 18:376-404.
- Shepherd, I. and Ashurst, W. T. (1992). Flame front geometry in premixed turbulent flames. In *Twenty-fourth Symposium (International) on Combustion*, pages 485-491.
- Shepherd, I. G. (1996). Flame surface density and burning rate in premixed turbulent flames. In *Twenty-sixth Symposium (International) on Combustion*, pages 373-379.
- Smith, T. and Menon, S. (1996). One-dimensional simulations of freely propagating turbulent premixed flames. *Combustion Science and Technology*, 128:99-130.
- Smith, T. and Menon, S. (1998). Subgrid combustion modeling for premixed turbulent reacting flows. *AIAA-98-0242*.
- Sreenivasan, K. (1996). The passive scalar spectrum and the obukhov-corrsin constant. *The Physics of Fluids*, 8(1):189-196.
- Trounev, A. and Poinsot, T. (1994). The evolution equation for the flame surface density in turbulent premixed combustion. *Journal of Fluid Mechanics*, 278:1-31.
- Veynante, D., Trounev, A., Bray, K., and Mantel, T. (1997). Gradient and counter gradient scalar transport in turbulent premixed flames. *Journal of Fluid Mechanics*, 332:263-293.
- Yakhot, V. (1988). Propagation velocity of premixed turbulent flames. *Combustion Science and Technology*, 60:191-214.

ON THE USE OF LES WITH A DYNAMIC SUBGRID-SCALE MODEL FOR OPTIMAL CONTROL OF WALL BOUNDED TURBULENCE

S. SCOTT COLLIS AND YONG CHANG

*Department of Mechanical Engineering and Materials Science
Rice University, Houston, TX 77005-1892*

Abstract. This paper presents techniques for optimal control of turbulent flows based on the dynamic subgrid-scale LES model. This control scheme has been implemented using a finite time-window approach where the flow sensitivity is computed from the adjoint LES equations. LES results for optimal control of terminal turbulent kinetic energy are compared to Direct Numerical Simulation (DNS) under similar conditions. These comparisons indicate that optimal control based on LES can relaminarize low Reynolds number turbulent channel flow similar to results obtained using DNS but with significantly lower computational expense. Results are also presented for a novel hybrid LES/DNS scheme in which the optimization iterations are performed using LES while the flow is advanced in time using DNS. These hybrid simulations retain the computational efficiency of LES and the accuracy of DNS. Results from hybrid simulations clearly demonstrate that the controls computed based on LES optimization are also viable in the context of DNS. In all cases, the agreement between LES, DNS, and hybrid LES/DNS indicates that reliable turbulence control strategies can be efficiently developed based on LES.

1. Introduction

Flow control offers the potential for modifying turbulent flows to achieve a variety of objectives including skin-friction drag reduction, noise suppression, and heat transfer modification. Previously, both passive and active turbulence control schemes have been studied and [13] provides a recent review. In this article, we focus on optimal control which provides a framework to systematically derive the most efficient means of control to achieve

a desired effect. The control distribution that results from optimal control theory can be used to guide the development of heuristic control approaches as well as identify the merits of various actuator/sensor combinations.

However, optimal control theory requires a high-fidelity means of predicting the flow field response which makes the method computationally intensive. In the context of turbulence control, optimal control theory has been applied to reduce the drag in a low Reynolds number, turbulent channel flow using Direct Numerical Simulation (DNS) to predict the flow response [3, 11, 14] and recent results indicate that, for certain objective functionals, relaminarization is possible [4, 19]. Unfortunately, the computational expensive of DNS makes the method intractable for the high Reynolds number, complex-flows typical of engineering applications. The current work addresses this limitation by modeling the flow field using Large Eddy Simulation (LES) with a dynamic subgrid-scale model. LES greatly reduces the computational expense, compared to DNS, allowing solutions at higher Reynolds numbers and for more complicated flow systems. The goal of the current work is to determine whether realistic optimal-control strategies can be developed based on LES. For this purpose, we have applied our LES formulation to turbulent channel flow and comparisons are made to DNS results.

2. Large Eddy Simulation

We begin by considering incompressible, fully-developed turbulent flow in a planar channel where the fluid motion is predicted using LES. In the following discussion the coordinate system for the channel flow is x_1 in the streamwise direction, x_2 in the wall-normal direction, and x_3 in the spanwise direction. The flow in the streamwise and spanwise directions is assumed to be periodic.

Large Eddy Simulation is performed by removing the small scale turbulent structures through a low-pass filtering operation. Doing so leads to the filtered, nondimensional, incompressible Navier–Stokes equations

$$\bar{u}_{i,t} + (\bar{u}_i \bar{u}_j)_{,j} - \frac{1}{Re} \bar{u}_{i,jj} + \bar{p}_{,i} + \bar{f}_i + \tau_{ij,j} = 0 \quad (1a)$$

$$\bar{u}_{i,i} = 0 \quad (1b)$$

where a bar denotes the grid filter operator, τ_{ij} is the subgrid-scale (SGS) stress defined as $\tau_{ij} = \bar{u_i u_j} - \bar{u}_i \bar{u}_j$, and $\bar{f}_i = \delta_{i1} P_x$ is the body force required to enforce the mean pressure gradient for turbulent channel flow. To close the equations, the anisotropic component of the SGS stress term is approximated using the Smagorinsky model [18]

$$\tau_{ij} - \frac{1}{3} \delta_{ij} \tau_{kk} = -2C \bar{\Delta}^2 |\bar{S}| \bar{S}_{ij} \quad (2)$$

where $\bar{\Delta}$ is the grid-filter width, \bar{S}_{ij} is the strain rate tensor defined as $\bar{S}_{ij} = \frac{1}{2}(\bar{u}_{i,j} + \bar{u}_{j,i})$, and $|\bar{S}| = (2\bar{S}_{ij}\bar{S}_{ij})^{1/2}$. The dimensionless model coefficient C can be obtained using the dynamic procedure [7, 12], which has been successfully used to study a variety of complex inhomogeneous flows [1, 2, 6–8, 15, 16].

Using the dynamic model, the parameter C in the model (2) can be written as

$$C = \frac{\langle L_{ij}M_{ij} \rangle}{\langle M_{kl}M_{kl} \rangle} \quad (3)$$

where $L_{ij} = \widehat{\bar{u}_i\bar{u}_j} - \widehat{\bar{u}_i}\widehat{\bar{u}_j}$ and $M_{ij} = -2\widehat{\bar{\Delta}}^2|\widehat{\bar{S}}|\widehat{\bar{S}}_{ij} + 2\bar{\Delta}^2|\bar{S}|\bar{S}_{ij}$. The $\langle \rangle$ denotes the average over planes parallel to the walls and a hat denotes the test-filtering operator with the width as $\widehat{\bar{\Delta}}$, which satisfies $\widehat{\bar{\Delta}} > \bar{\Delta}$. We use $\widehat{\bar{\Delta}} = 2\bar{\Delta}$.

The LES equations for turbulent channel flow are solved using a hybrid Fourier-spectral and finite difference method [1, 14] which has been modified to run efficiently on workstation class computers and shared memory parallel computers. Fourier transforms are used to compute spatial derivatives in the homogeneous directions and a conservative second-order finite difference scheme is used to compute spatial derivatives in the wall-normal direction. The computational grid is staggered in the wall-normal direction. The flow is advanced in time using an implicit Crank-Nicholson method for wall-normal derivative terms; an explicit, third-order Runge-Kutta method for terms involving derivatives in homogeneous directions; and a fractional step algorithm is used for the pressure.

For most of the computations reported here, the computational domain is $(4\pi\delta, 2\delta, 4\pi\delta/3)$ in the x_1 , x_2 , and x_3 directions respectively, where δ is the channel half-height. We choose δ as the reference length scale, and $u_\tau = (\tau_w/\rho)^{1/2}$ as reference velocity scale, where τ_w is the average stress on the walls. The reference (convective) time scale is then δ/u_τ and $Re_\tau = u_\tau\delta/\nu$. In presenting results, we also report viscous time units which are defined as $t^+ = tu_\tau^2/\nu$.

Quantitative comparisons of the $Re_\tau = 180$ statistics are shown in Figures 1 and 2. In Figure 1, the current LES statistics are compared with the results of a filtered DNS [7, 10]. Our LES results match the DNS results very well with only $(48 \times 65 \times 48)$ grid points compared with $(192 \times 129 \times 160)$ grid points in the DNS calculations – a factor of 32 reduction. In Figure 1(a), our mean-flow profile, in wall units ($u^+ = u/u_\tau$, $y^+ = yu_\tau/\nu$), is in excellent agreement with the DNS, the law of the wall, and the log layer. Similarly the *rms* velocities from our LES (also shown in Figure 1) are in good agreement with the filtered DNS. Figure 2(a) shows the spanwise velocity correlations which demonstrate that the turbulence is uncorrelated

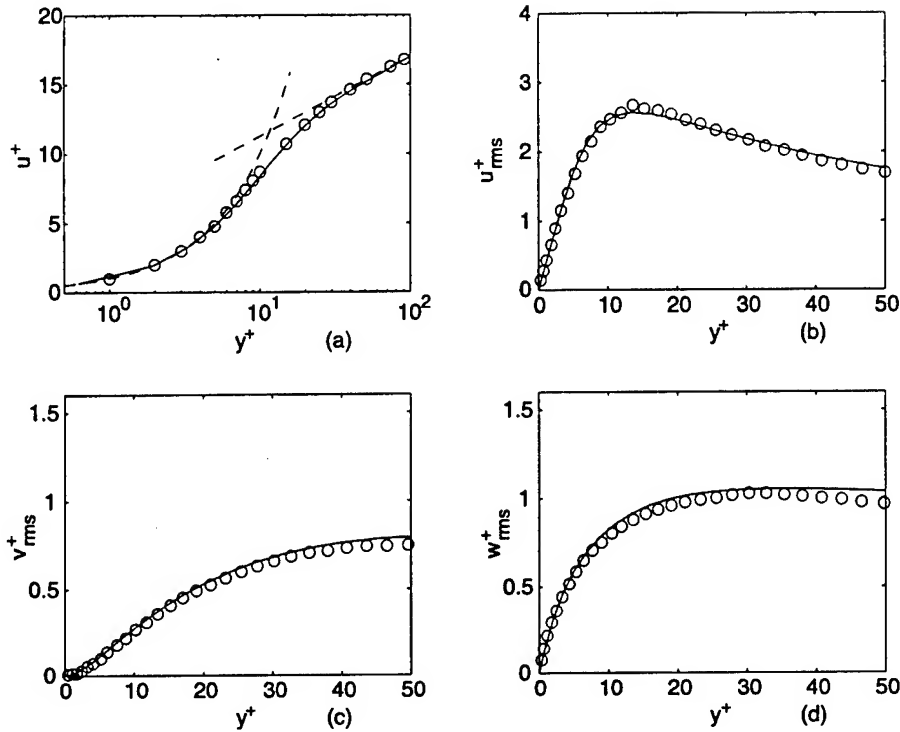


Figure 1. Mean and Root-Mean-Square velocity profiles at $Re_\tau = 180$ with $48 \times 65 \times 64$ grid points, the channel domain is $(4\pi, 2, 4\pi/3)$. (a) Mean velocity profile. — : present LES result; ---- : law of the wall, $u^+ = y^+$ and $u^+ = 2.5 \ln y^+ + 5.5$. (b) (c) (d) Turbulence intensities $\langle u_i'^2 \rangle^{1/2}$. — : present result; o : filtered DNS [7, 10]

over the width of the computational domain. The spanwise energy spectra in Figure 2(b) shows that the grid and test filter cutoffs are both in the inertial range in the present LES. The total stress is linear in Figure 2(d) which indicates that second order statistics are well converged. The *rms* velocity profiles in global coordinates are shown in Figure 2(c) compared with unfiltered DNS and good agreement is achieved with the LES slightly lower than the DNS as expected. In summary, our no-control LES results are in excellent quantitative agreement with available DNS data (similar agreement is obtained at $Re_\tau = 100$) and the LES results are obtained at a fraction of the computational expense required for DNS.

3. Optimal Control Formulation

We consider optimal control of fully developed turbulent flow in a planar channel that is subject to wall-normal transpiration $\bar{u}_i = \bar{\Phi} n_i$ on the walls with the initial condition $\bar{u}_i = \bar{g}_i$ at $t = 0$, where \bar{g}_i is an instantaneous

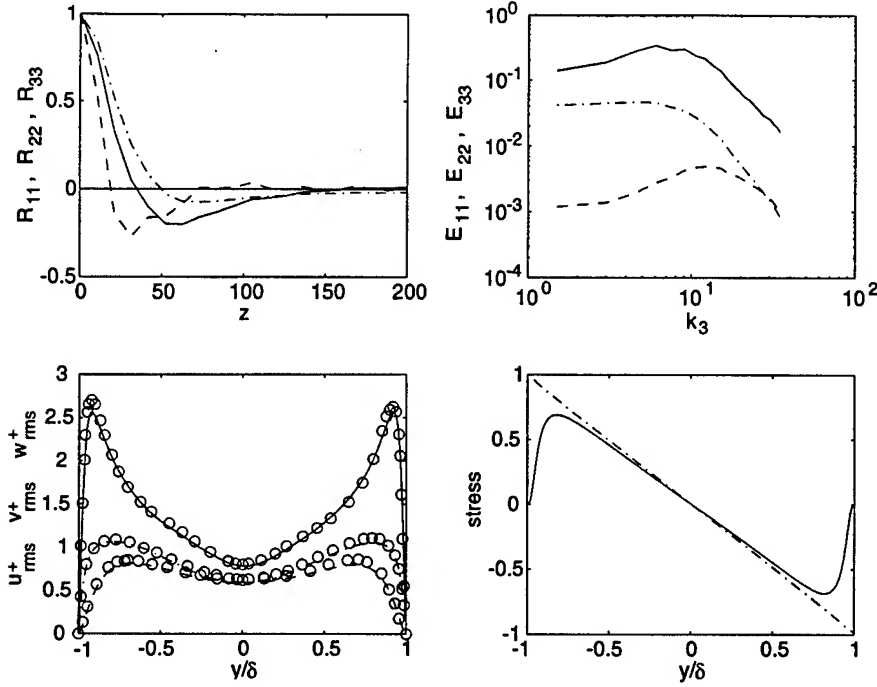


Figure 2. (a) Spanwise two-point correlations at $y^+ = 12$. — : R_{11} ; ---- : R_{22} ; -.- : R_{33} . (b) Spanwise one-dimensional energy spectra at $y^+ = 12$. — : E_{11} ; ---- : E_{22} ; -.- : E_{33} . (c) Profiles of rms velocity fluctuations. — : u_{rms} ; ---- : v_{rms} ; -.- : w_{rms} . \circ : DNS [10]. (d) Profiles of Reynolds stress and total stress: — : Reynolds stress, $-\overline{u'v'}$; ---- : total shear stress, $-\overline{u'v'} + (1/Re)\partial\bar{u}/\partial y$.

velocity field from an uncontrolled LES calculation.

One possible formulation of optimal control is to determine the control $\bar{\Phi}$, such that the drag is minimized while also minimizing the magnitude of the control. However, prior numerical experiments using DNS show that this is not the most effective way to reduce the drag [3]. Since the turbulence is responsible for increasing the momentum transport from the center of the channel to the near-wall region, and thus increasing the drag, it is reasonable for the cost functional to target the turbulence directly rather than the drag. This appears to be advantageous since the kinetic energy responds faster to changes in the flow than does the drag. In other words, turbulent kinetic energy is the *cause* and drag is the *effect*. In addition, temporary increases in the turbulent kinetic energy are allowable, so long as the value at the end of the optimization interval is reduced [4]. This leads to a cost functional that minimizes the turbulent kinetic energy only

at the end of each optimization period,

$$\mathcal{J}(\bar{\Phi}) = \int_{\Gamma_w} \int_{t_0}^{t_0+T} \frac{l}{2} \bar{\Phi}^2 dt d\Gamma + \int_{\Omega} \left[\frac{\bar{u}_i \bar{u}_i}{2} \right]_{t=t_0+T} d\Omega \quad (4)$$

The first term regularizes the control and is integrated over the wall boundaries, Γ_w , and over a fixed time interval $[t_0, t_0 + T]$. The second term minimizes the TKE at the end of each time window. Note that for LES, the cost functional only acts on the resolved scales of motion, the implications of which will be discussed below. In optimal control, the objective is to find the control, $\bar{\Phi}$, (in our case the wall transpiration velocity) which minimizes (4). This is achieved using the methods of calculus of variations which leads to the gradient of the cost functional with respect to the control

$$\frac{D\mathcal{J}(\bar{\Phi})}{D\bar{\Phi}} = l\bar{\Phi} - p^* + E_{22}^* \quad (5)$$

where p^* and E_{22}^* are obtained from solutions of the following adjoint LES equations

$$\begin{aligned} & -u_{i,t}^* - 2\bar{u}_j S_{ij}^* - \frac{1}{Re} u_{i,jj}^* + p_{,i}^* - \\ & \left(2C\bar{\Delta}^2 |\bar{S}| S_{ij}^* + 4C\bar{\Delta}^2 \frac{\bar{S}_{kl} \bar{S}_{ij}}{|\bar{S}|} S_{kl}^* \right)_{,j} - E_{ij,j}^* - F_i^* = 0 \end{aligned} \quad (6a)$$

$$u_{i,i}^* = 0 \quad (6b)$$

subject to the boundary condition $u_i^* = 0$ on the walls, with periodicity in the streamwise and spanwise directions, and the end condition $u_i^*(t_0 + T) = \bar{u}_i(t_0 + T)$. In the adjoint equations $S_{ij}^* = (u_{i,j}^* + u_{j,i}^*)/2$ is the adjoint strain rate and the two tensors E_{ij}^* and F_i^* are complicated functions of the resolved scales given by

$$\begin{aligned} E_{ij}^* = & -2\widehat{\bar{\Delta}^2 (|\bar{S}| D_{ij}^*)} - 4\widehat{\bar{\Delta}^2 \left(\frac{\bar{S}_{kl} \bar{S}_{ij}}{|\bar{S}|} D_{kl}^* \right)} + \\ & 2\bar{\Delta}^2 |\bar{S}| \widehat{D_{ij}^*} + 4\bar{\Delta}^2 \frac{\bar{S}_{kl} \bar{S}_{ij}}{|\bar{S}|} \widehat{D_{kl}^*}, \end{aligned} \quad (7a)$$

$$F_i^* = 2 \left(\widehat{B_{ij}^* \bar{u}_j} - \widehat{B_{ij}^*} \bar{u}_j \right) \quad (7b)$$

where

$$B_{ij}^* = \frac{\langle 2\bar{\Delta}^2 |\bar{S}| \bar{S}_{mn} S_{mn}^* \rangle}{\langle M_{kl} M_{kl} \rangle} M_{ij}, \quad (8a)$$

$$D_{ij}^* = \frac{\langle 2\bar{\Delta}^2 |\bar{S}| \bar{S}_{mn} S_{mn}^* \rangle}{\langle M_{kl} M_{kl} \rangle} (L_{ij} - 2CM_{ij}), \quad (8b)$$

This research represent the first derivation and solution of the adjoint LES equations (6) for the dynamic subgrid-scale model as initially reported in [5].

Before discussing the numerical method used to solve the adjoint equations, it is instructive to observe that the first line of the LES adjoint momentum equations (6a) is exactly the adjoint NS operator acting on the grid filtered state. The second line in (6a) is entirely due to the variation of the SGS model with respect to the control. Focusing on the second line in more detail, the terms in parentheses arise due to the variation of the resolved strain-rate with respect to the control. Likewise, the term $E_{ij,j}^*$ represents a stress and F_i^* a body force where both terms are due to the variation of the dynamically predicted model coefficient C with respect to the control.

In the current approach, called the *LES adjoint*, we have performed the optimization after introducing the LES model into the state equation. Similar to the differences that arise when one switches the order between discretization and optimization, the relative ordering of modeling, optimization, and discretization influences both the tractability of the procedure as well as the final results. For the large-scale continuous problems under consideration here it is likely necessary to perform discretization as the final step in the solution process. However, it is feasible to consider switching the order of the modeling and optimization steps. If, instead of the current approach, we had first optimized then modeled, the adjoint equations would be exactly the adjoint NS operator acting on the grid filtered scales plus an adjoint SGS stress that must be modeled in order to close the equation. One would be free to select *any* reasonable model for these term. An advantage of this approach is that the adjoint SGS model could be selected to be computationally simpler than that given in (6 - 8).

For example, a reasonable model for the adjoint SGS stress term might be the terms in parentheses in equation (6a) which would be a Smagorinsky type model for the adjoint where the coefficient C is assumed to be fixed by the dynamic procedure applied to the state. We call this approach the *modeled adjoint*. Another way of interpreting this approach is that C is assumed to be given and fixed for the purpose of computing the adjoint using (6a) which would allow both E_{ij}^* and F_i^* to be set to zero in (6a). In this context, we call this an *approximate LES adjoint*. In either case, the

computational expense in solving the adjoint equations is reduced and in the next section we present results using this approach along with interpretations based on both the *modeled adjoint* and *approximate LES adjoint* points of view.

The optimization time window T is an important parameter. The larger the window, the more the cost functional represents the optimal control objective. But larger T increases the difficulty of the computation and may even cause the computation to diverge because the adjoint equations are sensitive to errors. By choosing a suitable time window T , we minimize the cost functional on a time window $[t_0, t_0 + T]$, then repeat this on the next time window $[t_0 + T, t_0 + 2T]$, and so on in the same manner as [4]. In the future we plan to combine the current LES approach with more efficient iterative methods for solving large-scale optimal control problems [9].

The numerical method for solving the adjoint equations (6) is analogous to that of the LES flow solver. Since the last two terms in the adjoint equation are quite complicated, these terms are treated explicitly even though they include derivatives in the wall-normal direction. However, these terms arise due to the variation of the dynamic model parameter C with respect to the control which is found to be small, so that this treatment does not cause severe time-step limitations. Due to the term $\bar{S}_{kl}S_{kl}^*$ in the adjoint momentum equations, the LES adjoint equations become a coupled block-tridiagonal linear system after discretization in the wall-normal direction. This is in contrast to the three independent tridiagonal systems obtained for the adjoint NS equations. Because of this, the adjoint LES equations are more expensive to solve than the adjoint NS equations.

Once the adjoint equations are solved, the gradient of the cost functional to the control can be obtained by equation (5). The control is updated for each time window using an iterative method based on the Polak-Ribiere conjugate gradient algorithm [17],

$$\bar{\Phi}^{k+1} = \bar{\Phi}^k + \alpha^k \mathbf{h}^k \quad (9)$$

where the update direction $\mathbf{h}^k = -\mathbf{g}^k + \beta^k \mathbf{h}^{k-1}$, \mathbf{g}^k is the gradient obtained from (5), $\beta^k = (\mathbf{g}^k - \mathbf{g}^{k-1}) \cdot \mathbf{g}^k / (\mathbf{g}^{k-1} \cdot \mathbf{g}^{k-1})$. The best value of α^k is calculated by using several test α^k to minimize \mathcal{J}^{k+1} using line minimization.

4. Results: Terminal TKE control

Figure 3 shows the evolution of drag and turbulent kinetic energy (TKE) at $Re_\tau = 100$ using the terminal TKE optimal control described in §3. These LES results are for a mesh resolution of $(32 \times 49 \times 32)$ and computation domain size of $(4\pi, 2, \frac{4}{3}\pi)$. This domain size is the same as the DNS simulations reported in [4] which use a resolution of $(42 \times 65 \times 42)$. Similar to

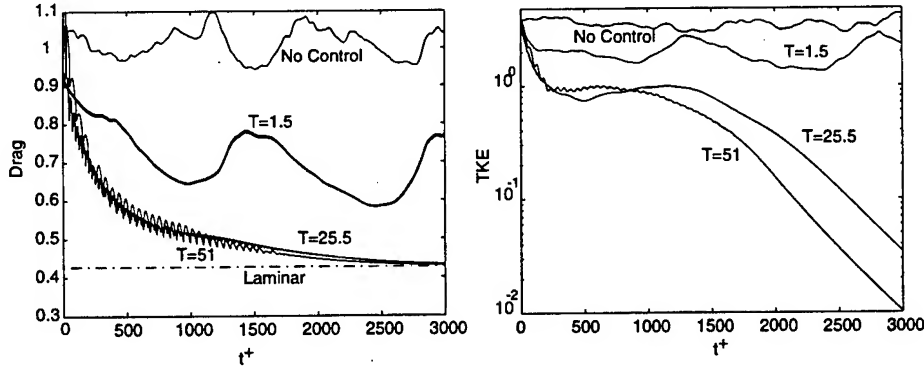


Figure 3. Drag and TKE histories for LES based terminal TKE control for different optimization windows T : $(32 \times 49 \times 32)$, $Re_\tau = 100$.

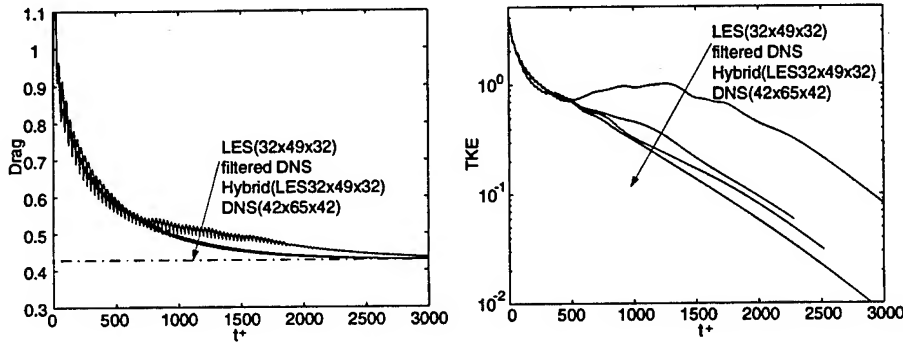


Figure 4. Drag and TKE comparison for LES, DNS, filtered DNS and Hybrid DNS/LES at $T = 30$, $Re_\tau = 100$.

the DNS results, LES based optimal control achieves relaminarization for $T \geq 25$, and the LES results are in excellent agreement with the DNS at all values of T . Similar results, not shown here, have been obtained with coarser LES meshes ($16 \times 33 \times 24$) which are five times smaller than the mesh used in the DNS study and larger savings are expected for higher Reynolds numbers.

In order to explore the viability of the controls predicted by LES, we have implemented a novel hybrid LES/DNS algorithm in which the optimization is performed based on LES and, once the optimal control is found, the flow is advanced in time to the next time window using DNS. The details of this algorithm will be discussed in a future article. Figure 4 compares the results from LES, DNS, and hybrid LES/DNS for $T = 30$. In interpreting these results it is important to distinguish between the different forms of the objective functions used in each simulation.

Although the general form of the objective function is the same for all cases (terminal observation of TKE), in LES and LES/DNS both the velocity field and controls are on the grid filtered mesh as indicated in (4), whereas, for DNS, the full control Φ and velocities u_i are used in the objective functional. As seen in figure 4, all methods converge to the laminar state for this value of T , although the LES takes more time to relaminarize. The quickest convergence to the laminar state is obtained using DNS, which is not surprising since the DNS possesses the full stage of the turbulence. Interestingly, the hybrid LES/DNS, where the resolution used during the optimization is the same as the full LES run, relaminarizes at nearly the same rate as the full DNS. It appears that accurate state prediction is more critical than having the exact DNS optimal control. To explain this further, results from a filtered DNS run are also included in the figure where the velocity field is filtered to the LES resolution in x and z . The filtering delays the relaminarization, making the filtered DNS nearly identical to the hybrid LES/DNS. This again is strong evidence that the accuracy of the state is more important than the accuracy of the control. In fact, for the first 500 viscous time units, the drag and TKE evolution for all methods, including full LES, are nearly identical. This suggests that the optimization initially targets the large scale structures in the turbulence and it is only after the large scales are significantly reduced that differences due to the filtered scales and modeling errors become noticeable. Importantly, the LES with dynamic subgrid-scale model not only converges to the laminar state consistent with DNS, but the controls computed based on LES optimization are also valid for DNS. This indicates that LES can be reliably used as a reduced order model for optimal control of turbulence. In particular, we have also performed a hybrid LES/DNS where the LES resolution is very coarse ($16 \times 65 \times 16$) and the flow still relaminarized with a convergence similar to the LES run shown in figure 4. This run was four times faster than the full DNS run.

As a final result, figure 5 shows the effect of fixing C as described in §3. We see that by introducing this approximation in the adjoint, convergence to the laminar state is not obtained and the drag saturates at approximately 40% reduction. This is indicative of errors in the gradient predictions which stem from making approximations in the LES adjoint. Likewise, this suggests that modeled adjoints will likely not be able to fully converge to the optimal solution. We emphasize, however, that depending on the application and the objective functional, the errors incurred by approximating or modeling the adjoint may not be important. The current example case is particularly demanding of the optimization algorithm since we are requiring the flow to completely relaminarize.

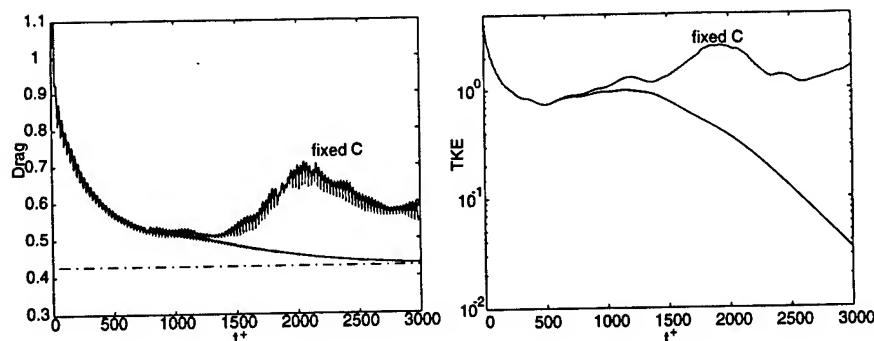


Figure 5. Drag and TKE comparison for LES with and without fixed C : $T = 30$, $Re_\tau = 100$.

5. Conclusions

Our research demonstrates that LES based optimal control can relaminarize fully developed turbulent channel flow with results that are in complete agreement with DNS. To verify that the controls predicted by LES are reliable, a novel hybrid LES/DNS scheme is used where optimization is performed using LES and the flow is advanced in time using DNS. Results from hybrid runs, even those that use a very coarse LES optimization, still give results that are in excellent agreement with full DNS, with a factor of four savings in computational cost, and these savings are expected to increase for higher Reynolds number flows. The current results demonstrate the viability of LES as a tool for studying turbulence control that engenders considerable savings over DNS. Based on these findings, we are currently extending our turbulence control research to higher Reynolds numbers and complex, multi-physics flows.

6. Acknowledgment

The authors are grateful for helpful discussions with Prof. Thomas Bewley of UCSD and Prof. Matthias Heinkenschloss of Rice University. This research has been supported by the Texas Advanced Technology Program under Grant No. 003604-017 with computer time supplied by the NASA-IT program.

References

1. Knut Akselvoll and Parviz Moin. *Large Eddy Simulation of Turbulent Confined Coannular Jets and Turbulent Flow Over A Backward Facing Step*. PhD thesis, Stanford University, 1995.

2. Elias Balaras, Carlo Benocci, and Ugo Piomelli. Finite-difference computations of high Reynolds number flows using the dynamic subgrid-scale model. *Theoretical and Computational Fluid Dynamics*, 7:207–216, 1995.
3. Thomas Bewley and Parviz Moin. Optimal control of turbulent channel flows. In *Active Control of Vibration and Noise*, ASME-DE, volume 75, 1994.
4. Thomas R. Bewley, Parviz Moin, and Roger Teman. DNS-based predictive control of turbulence: an optimal target for feedback algorithms. *Under preparation for submission to J. Fluid Mech.*, 1999.
5. S. Scott Collis and Yong Chang. Computer simulation of active control in complex turbulent flows. *Modeling and Simulation Based Engineering*, 1:851–856, 1998. www.ruf.rice.edu/~collis/papers/.
6. T. Ciesla, H. Braun, G. Biswas, and N.K. Mitra. Large eddy simulation in a channel with exit boundary conditions. Technical report, ICASE, 1996.
7. Massimo Germano, Ugo Piomelli, Parviz Moin, and William H. Cabot. A dynamic subgrid-scale eddy viscosity model. *Phys. Fluids A*, 3(7):1760–1765, 1991.
8. Sandip Ghosal, Thomas S. Lund, Parviz Moin, and Knut Akselvoll. A dynamic localization model for large-eddy simulation of turbulent flows. *J. Fluid Mech.*, 286:229–255, 1995.
9. Matthias Heinkenschloss. From suboptimal to optimal control. NSF Workshop on Control of Flows, 1999. www-ames.ucsd.edu/research/krstic/workshop.html.
10. J. Kim, P. Moin, and R. Moser. Turbulence statistics in fully developed channel flow at low Reynolds number. *J. Fluid Mech.*, 177:133–166, 1987.
11. Changhoon Lee, John Kim, and Haechon Choi. Suboptimal control of turbulent channel flow for drag reduction. *J. Fluid Mech.*, 358:245–258, 1998.
12. D. K. Lilly. A proposed modification of the Germano subgrid-scale closure method. *Phys. Fluids A*, 4(3):633–635, 1992.
13. Parviz Moin and Thomas Bewley. Feedback control of turbulence. *Appl. Mech. Rev.*, 47(6-2):S3–S13, 1994.
14. Parviz Moin and Thomas Bewley. Application of control theory to turbulence. In *Twelfth Australian Fluid Mechanics Conference*, pages 109–117, Dec. 10–15 1995.
15. Ugo Piomelli. High Reynolds number calculations using the dynamic subgrid-scale stress model. *Phys. Fluids A*, 5(6), 1993.
16. Ugo Piomelli and Junhui Liu. Large-eddy simulation of rotating channel flows using a localized dynamic model. *Phys. Fluids*, 7(4):839, April 1995.
17. W. H. Press, S. A. Teukolsky, W. T. Vetterling, and B. P. Flannery. *Numerical Recipes*. Cambridge University Press, 1996.
18. J. Smagorinsky. General circulation experiments with the primitive equations. I. The basic experiment. *Mon. Weather Rev.*, 91:99–165, 1963.
19. R. Teman, T. Bewley, and P. Moin. Control of turbulent flows. In *Proceedings of the 18th IFIP TC7. Conference on System Modelling and Optimization*, 1997.

ROBUSTNESS OF FLOW PHENOMENA IN A SPATIALLY DEVELOPING TURBULENT MIXING LAYER

I.C.C. DE BRUIN, B.J. GEURTS AND C.H. DRIESEN
*Faculty of Mathematical Sciences, University of Twente,
P.O. Box 217, 7500 AE Enschede, The Netherlands*

AND

J.G.M. KUERTEN
*Faculty of Mechanical Eng., Eindhoven Univ. of Technology,
P.O. Box 513, 5600 MB Eindhoven, The Netherlands*

Abstract. Direct numerical simulations of transitional and developed turbulent flow in a mixing layer are performed. We discuss reference results of a numerical simulation using inflow perturbations derived from linear stability theory. Furthermore a resolution study is done. Robustness of flow phenomena is studied by applying an alternative inflow forcing which uses random perturbations. The results are discussed and compared with data from physical experiments.

1. Introduction

Already in the sixties Bradshaw (1966) concluded that many features of mixing layers are very sensitive to initial and boundary conditions while comparing experiments of a subsonic mixing layer developing either from a turbulent or a laminar boundary layer. Later on, the results of several more experiments were collected and compared by Brown *et al.* (1974), establishing a linear relation between the vorticity thickness and a velocity-difference parameter. Some years thereafter Browand *et al.* (1979) investigated the growth of the two-dimensional mixing layer from a laminar and turbulent boundary layer and found the momentum thickness growing slower when initiated from the turbulent boundary layer. A review of the very extensive literature on the topic of instabilities and their sensitivity to upstream perturbations is given in Ho *et al.* (1984). Summarized in Mehta *et al.* (1986), several mixing layer properties like *e.g.* turbulent intensities and growth

rate seem to be very sensitive to small changes in the state and thickness of the initial boundary layer, in the free-stream turbulence intensity and maybe in the trailing edge thickness. These studies all concern physical experiments. No numerical simulation study is known that considers this dependence on the inflow boundary condition in particular.

Recently, the generation of turbulent inflow data for spatially-developing boundary layer simulations was discussed in Lund *et al.* (1998). The physics of a mixing layer yields a more unstable flow compared to a boundary layer. Therefore, the costs of a calculation starting from a laminar profile plus some disturbances at the inflow and a natural transition to turbulence downstream are within the limits of todays supercomputers. So, the adaptations to generate turbulence that are required in boundary layer simulations are not necessary in mixing layer simulations. Furthermore, a simulation with inflow perturbations containing only Linear Stability Theory (LST) modes is described in Wasistho *et al.* (1997). There, a turbulent state was reached in a relatively short streamwise extent due to an applied adverse pressure gradient. Another alternative for the generation of inflow perturbations of the flat plate is described in Ducros *et al.* (1996) where the most unstable 2D mode is combined with 3D random white noise. The use of different initial perturbations was also considered in the temporal setting. In Rogers *et al.* (1994), simulations for the temporal mixing layer were initialized with velocity fields obtained from a DNS of a turbulent boundary layer computation. Finally we mention the temporal mixing layer described in Vreman *et al.* (1997) where the DNS is initialized by perturbations based on LST modes. There the LST modes had to be combined carefully in order to generate an efficient transition to turbulence.

In the rest of this paper we consider two quite different cases. First, we use the most unstable modes arising from Linear Stability Theory (LST) at the inflow boundary to generate a turbulent mixing layer further downstream. Several combinations of both two and three dimensional modes were used. Moreover, a grid refinement in all three directions has been done in order to study the quality of the solution. Next, the spatial development from random perturbations at the inflow is considered. The evolution of characteristic thicknesses in the streamwise direction for both simulations is compared with results from physical experiments. A suitable quantity used for comparison purposes is the momentum thickness as well as its growth rate (Rogers *et al.*, 1994).

Conclusions regarding the robustness of the spatially developing mixing layer depend on the quantities that are considered. For example, the location of transition is changed considerably when using different inflow perturbations. However, *e.g.* the process of streamwise evolution from transition to turbulence is roughly unchanged. The momentum thickness exhibits a

linear growth which makes it a suitable quantity for *e.g.* similarity studies. The robustness of the resulting growth rate with respect to changes in the inflow perturbations points towards the existence of a single state of similarity. This is in contrast to other studies mentioned before that report the existence of several similarity states although it is remarked that a longer streamwise distance (physical experiments) or computation time (temporal DNS) might result in a single similarity state. The outline of this paper is as follows. In Section 2 we will introduce the numerical method and pay attention to the treatment of the outflow boundary. Next, the numerical results are presented and compared with data from physical experiments in Section 3. Finally, in Section 4 we will formulate the conclusions.

2. Numerical method

We consider direct numerical simulations of subsonic spatially developing turbulent free shear flows. Previously, the temporal mixing has been investigated with DNS and the results were used *e.g.* for the assessment of the quality of several subgrid models in large eddy simulations (LES) (Vreman *et al.*, 1997). However, the temporal simulation is only a crude approximation of physical reality since periodic conditions are applied in the streamwise direction. Therefore, we extended this approach to enable spatial simulations containing inflow and outflow boundaries.

In the spatial setting, the computational domain is limited through the introduction of artificial boundaries. For the flow studied here, especially the outflow boundary requires careful attention since no simple physical boundary condition is available in case of turbulent flow. A buffer domain is introduced in order to damp the reflections that may occur in the vicinity of the numerical outflow boundary. This procedure is combined with characteristic wave relations (Poinsot *et al.*, 1992). In the buffer domain, the turbulent solution which enters the buffer is gradually forced towards a steady mean flow near the end of the buffer. The damping function used here is formulated such that its effect is approximately grid independent and is found to be robust and with minimal upstream influence in both boundary- and mixing layer (Wasistho *et al.*, 1997; de Bruin *et al.*, 1998).

We focus on direct numerical simulations in a rectangular computational domain. An efficient spatial discretization which includes a fourth order finite volume technique suited for both uniform and stretched grids is employed. The time-integration method uses a second order four-stage Runge-Kutta scheme.

Previously, the numerical method and boundary conditions were validated by superimposing small perturbations on a base flow at the inflow boundary and comparing the results with Linear Stability Theory (Wa-

sistho *et al.*, 1997; de Bruin *et al.*, 1998). These perturbations provide a time dependent forcing of the flow at the inflow boundary. We observed a good agreement between DNS and LST results at sufficient resolution. Furthermore, it could be inferred that the upstream influence of the buffer domain was very small indeed.

3. Numerical results

We consider a mixing layer flow with a Reynolds number of 200 and a Mach number of 0.8 based on the upper free stream velocity and viscosity and half the vorticity thickness at the inflow. Temperature is scaled by a reference value of 276 K. The dimensionless lower stream velocity is equal to 0.5, and both the upper- and lower stream dimensionless temperatures are equal to one. In the normal direction the domain size is 60 which was found adequate.

We use a uniform grid in all directions. Because the width of the layer increases and transition to turbulence arises, a fine resolution is needed. Guided by previous results for the flat plate, (Wasistho *et al.*, 1997) we use a reference resolution of 25 points per perturbation wavelength of the most unstable mode in the streamwise and 128 points in the normal direction respectively. This resolution was fine enough for the turbulent mixing layer as well. Furthermore, we take 16 points in the spanwise direction which extends half a wavelength using the symmetry as described in Sandham *et al.* (1992). This reduces the computer time and storage requirements by a factor of two. Summarizing, the total numerical domain is covered by $450 \times 128 \times 16$ grid points for the reference case. In the rest of this section we will study the robustness of the momentum thickness growth rate in the turbulent regime.

3.1. LINEAR STABILITY THEORY PERTURBATIONS

We selected the most unstable 2D mode from a linear stability analysis as point of reference in the construction of a suitable inflow perturbation. In this particular case we have a streamwise wave number $\alpha = \alpha_r + i\alpha_i = 0.392 - i0.0532$ and circular frequency $\omega = 0.296$. These data result in a phase velocity which is very close to the mean velocity of the two free streams.

Previous investigations in a domain 10 times the wavelength of the dominant 2D mode showed that this extent was too short to reach a turbulent state downstream (de Bruin *et al.*, 1998). Here, a streamwise domain of 18 wavelengths is used, of which the buffer length consists of two wavelengths. We observed no transition when only the most unstable fundamental 2D and 3D modes were used at the inflow, which shows the importance of the

subharmonic modes. The well-known pairing process was observed with the inclusion of the first two subharmonic modes of the fundamental 2D mode (with wavelengths two and four times the fundamental mode). For full transition to turbulence additional subharmonic 3D modes were needed as well. We observed that both the relative amplitudes of the 3D modes and the total amplitude of all modes together should be large enough in order to generate turbulence further downstream well within the computational domain while retaining a laminar and a transitional region. A suitable total amplitude of the perturbations imposed at the inflow boundary is 0.2. In total, we have three 2D modes (fundamental and the first two subharmonics) and three pairs of 3D oblique modes, resulting in the following total perturbation v at the inflow boundary:

$$v(x_2, x_3, t) = \epsilon \sum_{j=1}^N A^j \left(\Psi_r^j(x_2) \cos(\gamma^j) - \Psi_i^j(x_2) \sin(\gamma^j) \right), \quad (1)$$

with ϵ and A^j the total and j -th relative amplitude and Ψ^j the complex eigenfunction (consisting of a r(eal) and i(maginary) part) that is multiplied with a goniometric function of $\gamma^j = \alpha_r^j x_1 + \beta_r^j x_3 - \omega^j t + \phi^j$ with α, β the complex streamwise and real spanwise wavenumbers, ω the real frequency and ϕ the phase. The number of modes, N , equals 9 for this reference case. This simple perturbation leads to a DNS containing turbulence far downstream. The values for all these arguments are collected in Table 1. We take no phase differences for the 3D modes since that may violate the symmetry condition in the spanwise direction. The phase of the 2D subharmonics (relative to the 2D fundamental) was chosen differently from the 2D fundamental mode in order to minimize the distance between pairings (Moser *et al.*, 1993; Colonius *et al.*, 1997).

In Figure 1, the spanwise vorticity is shown in the plane $x_3 = \pi/2$. We can distinguish the different stages from laminar through transitional to

	2D				3D			
	α_r	α_i	ϕ	ω_r	α_r	α_i	β_r	ω_r
F	0.392	-0.0532	0.125 π	0.296	0.391	-0.0310	± 0.391	0.296
S1	0.196	-0.0405	0.375 π	0.151	0.196	-0.0208	± 0.391	0.149
S2	0.0980	-0.0235	0.5 π	0.0772	0.0978	-0.0093	± 0.391	0.0745

TABLE 1. Wavenumbers $\alpha = (\alpha_r, \alpha_i)$, $\beta = \beta_r$, phases ϕ and frequencies $\omega = \omega_r$ from the fundamental mode (F) and its first two subharmonics (S1, S2) for the 2D and 3D perturbations. Together this results in three 2D modes and three pairs of 3D modes.

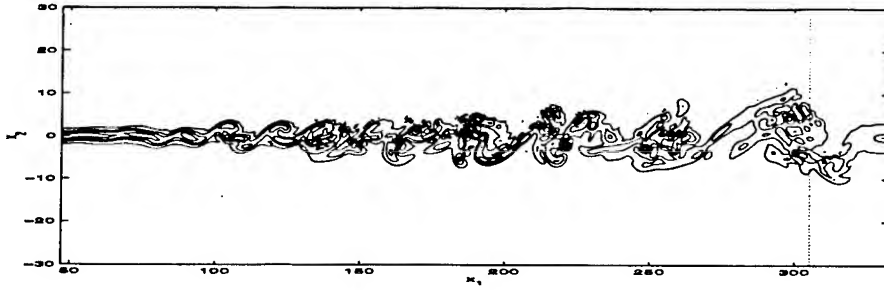


Figure 1. Contourplot of the spanwise vorticity at 10 iso-values equally distributed in the interval $[-0.25, 0.25]$ in the plane $x_3 = \pi/2$. The streamwise extent consists of 16 perturbation wavelengths in the physical domain and 2 perturbation wavelengths in the buffer (after the dashed line). The perturbations at inflow consist of modes from Linear Stability Theory.

turbulent flow. Furthermore, we performed a grid refinement in all three directions. This was done at a resolution of $900 \times 192 \times 32$ points. The results were quite close to the coarse grid solution as illustrated by Figure 2 where the time evolution of the streamwise momentum is compared for both resolutions at a location in the laminar and turbulent regime respectively starting from a fluid at rest at time $t = 0$. It is clear from these figures that the time evolution of both streamwise momenta coincides in the laminar regime and deviates somewhat in the turbulent regime while the main features remain the same: the mean value deviates 1% and the standard deviation 4%.

3.2. RANDOM PERTURBATIONS

In order to study the downstream dependence of the flow on the inflow condition, we next consider the case where the perturbations at the inflow are random variables multiplied with a Gaussian distribution in the normal coordinate to locate the perturbations near the centerline. Three-dimensionality was introduced by including a sinusoidal perturbation in the spanwise direction. The perturbations v imposed at the inflow have the following form:

$$v(x_2, x_3, t) = \epsilon \exp(-x_2^2) (A_{2D} R_{2D}(t) + A_{3D} g(\beta x_3) R_{3D}(t)) \quad (2)$$

with β the real spanwise wavenumber taken as the value computed with LST. Furthermore, g is either a sine or a cosine and R_{2D} and R_{3D} are random functions according to the following differential equation in time:

$$\frac{dR}{dt}(t) = \frac{R(t)}{\tau} + \chi(t). \quad (3)$$

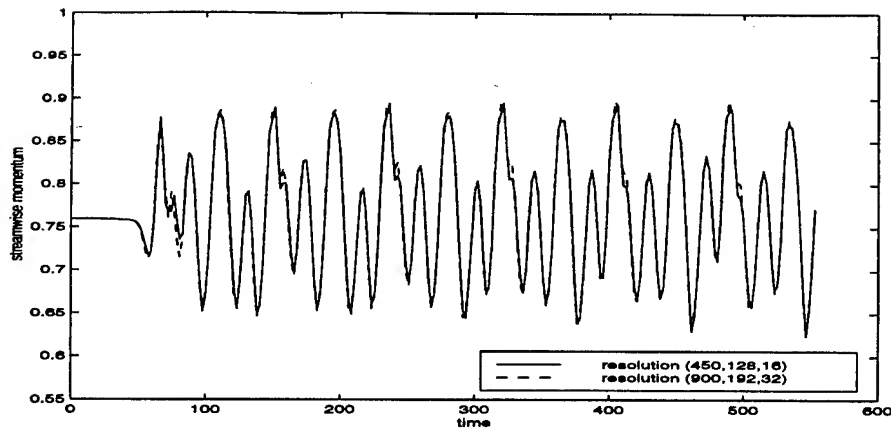
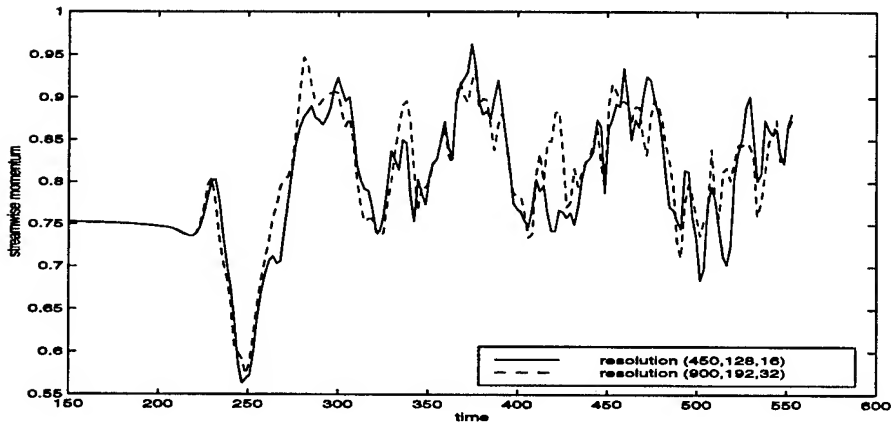
a: $x_1 = 100$ b: $x_1 = 250$

Figure 2. Time evolution of the midline streamwise momentum.

The relaxation time, τ , is taken equal to 1.2 which is about ten times the time step. Furthermore, $\chi(t)$ is a random function with a Gaussian distribution around zero with standard deviation 3.0 and being updated each time stage. For all four 2D and five 3D components of the perturbations, this random function is computed independently. These perturbations are added to the similarity solution of the boundary layer equations. The value of the amplitude ϵ is taken equal to 0.2 as in the reference run with perturbations from LST. The differential equation is solved simultaneously during the simulation with the four-stage Runge-Kutta method.

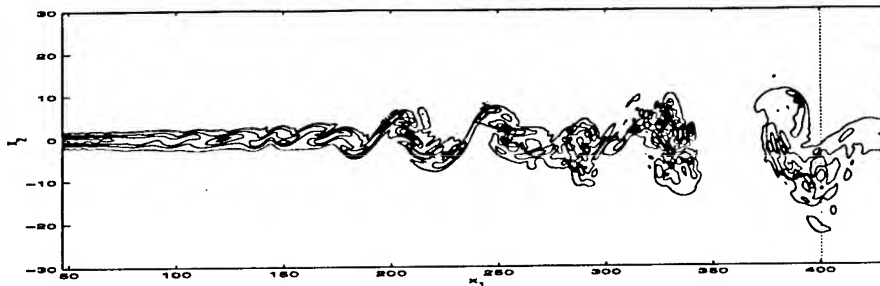


Figure 3. Contourplot of the spanwise vorticity at 10 iso-values equally distributed in the interval $[-0.25, 0.25]$ in the plane $x_3 = \pi/2$. The streamwise extent consists of 22 perturbation wavelengths in the physical domain and 2 perturbation wavelengths in the buffer (after the dashed line). The perturbations at inflow consist of random perturbations.

In this case, with the same streamwise extent of the domain as before, the flow does not become turbulent downstream, since some extra streamwise distance is required to allow the most unstable modes to arise from the noise imposed at the inflow. Extending the streamwise domain by about 25% resulted in a simulation in which a turbulent state evolves and *e.g.* the momentum thickness growth rate compares well with the results arising from the LST case described in the previous section. In Figure 3 the spanwise vorticity is shown at the same time as in Figure 1. It is clear that the flow remains longer near the laminar state and transition arises further downstream compared to the LST case.

In Figure 4 the momentum thickness, averaged over 2600 units of time and the spanwise direction, is plotted as a function of the streamwise coordinate for both inflow perturbations. The computed thickness is compared with the thickness of the laminar field which is proportional to the square root of the streamwise coordinate. Because the solution is damped towards the local laminar solution at the end of the buffer, it is clear why all lines coincide near the inflow as well as the outflow boundary. If we compare the momentum thickness from the LST and random perturbation case, it is clear that the final growth rate in the turbulent regime is about equal for both cases. More details on the convergence of the momentum thickness and its growth rate can be found in de Bruin *et al.* (1999).

3.3. COMPARISON WITH PHYSICAL EXPERIMENTS

We next compare the growth rate with physical experiments. As stated in Rogers *et al.* (1994), it is more common in experiments to use the vorticity thickness for self-similar scaling instead of the momentum thickness, because the momentum thickness is an integral quantity while the vorticity thickness is obtained from the derivative of the mean velocity. Con-

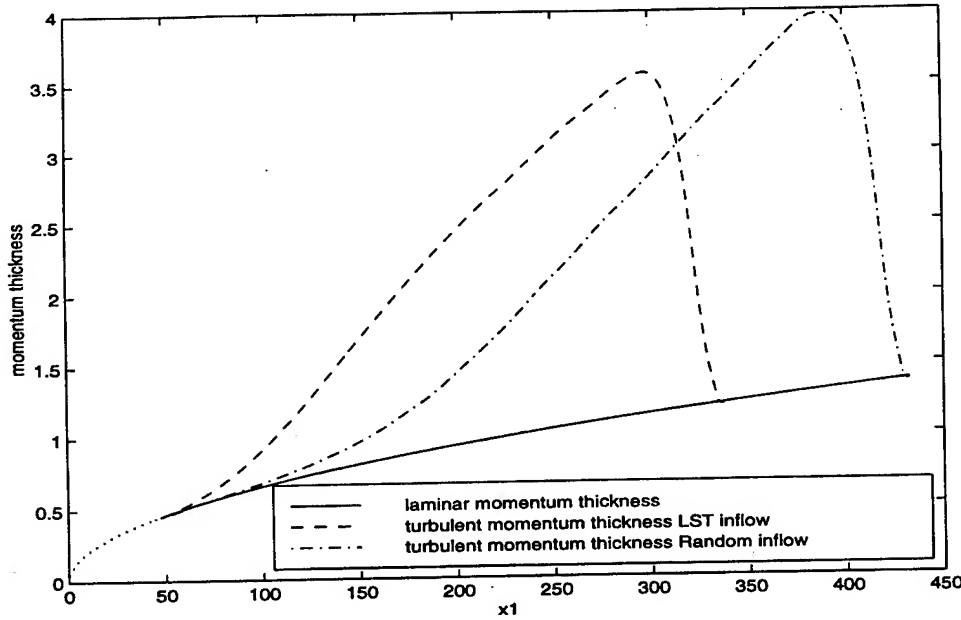


Figure 4. Streamwise evolution of the momentum thickness.

sequently, the momentum thickness evolves smoothly while the vorticity thickness may not. From Dimotakis (1991), for incompressible shear layers with equal freestream densities, we have a relation for the vorticity thickness δ_ω :

$$\frac{\delta_\omega}{x_1} = C \frac{U_1 - U_2}{U_1 + U_2}$$

where U_1 and U_2 denote the upper and lower free stream velocities respectively. Results from various physical experiments give a range $[0.125, 0.225]$ for the constant C . For the present case, in which compressibility effects are small, the vorticity thickness growth rate should be in the range $[0.042, 0.075]$ since the dimensionless free stream velocities are equal to $U_1 = 1$ and $U_2 = 0.5$ respectively. The computed vorticity thickness growth rate is equal to 0.055 in the reference DNS and falls well in this range.

4. Conclusion

The robustness of averaged quantities in a spatially evolving mixing layer flow has been tested from two perspectives. First, a grid refinement in all three directions showed acceptable deviations, even in the turbulent regime. Second, we used a totally different set of perturbations at the inflow which,

far enough downstream, yield a flow that can be compared well with the results involving LST perturbations. The location of transition shifted further downstream in the random perturbation case. The robustness of the momentum thickness growth rate with respect to changes in the inflow perturbations suggests the existence of only one similarity state. Future studies involve other statistical properties such as *e.g.* the Reynolds stress as well as the dependence on the remaining boundaries in the computational domain. The results presented here encourage the application of the numerical method to evaluate Reynolds Averaged Navier-Stokes modelling and Large Eddy Simulations which will be considered in the nearby future.

References

- Bradshaw P., The effect of initial conditions on the development of a free shear layer, *J. Fluid Mech.*, 26, pp. 225-236, 1966.
- Browand F.K. & Latigo B.O., Growth of the two-dimensional mixing layer from a turbulent and nonturbulent boundary layer, *Phys. Fluids*, 22(6), pp. 1011-1019, 1979.
- Brown G.L. & Roshko A., Density effects and large structures in turbulent mixing layers, *J. Fluid Mech.*, 64, pp. 775-816, 1974.
- Colonius T., Lele S.K. & Moin P., Sound generation in a mixing layer, *J. Fluid Mech.*, 330, pp. 375-409, 1997.
- de Bruin I.C.C., Wasistho B., Geurts B.J., Kuerten J.G.M. & Zandbergen P.J., Simulation of Subsonic Spatially Developing Turbulent Shear Flows, *Lecture Notes in Physics*, 515, pp. 147-152, Springer, Berlin, 1998.
- de Bruin I.C.C., Geurts B.J., & Kuerten J.G.M., Statistical Analysis of the Turbulent Mixing Layer, *Proceedings of the 3rd workshop on DNS and LES*, Cambridge, 1999.
- Dimotakis P.E., Turbulent Free Shear Layer Mixing and Combustion, *Progress in Astronautics and Aeronautics*, 137, pp. 265-340, 1991.
- Ducros F., Comte P. & Lesieur M., Large-eddy simulation of transition to turbulence in a boundary layer developing spatially over a flat plate, *J. Fluid Mech.*, 326, pp. 1-36, 1996.
- Ho C.-M. & Huerre P., Perturbed free shear layers, *Ann. Rev. Fluid Mech.*, 16, pp. 365-424, 1984.
- Lund T.S., Wu X. & Squires K.D., Generation of Turbulent Inflow Data for Spatially-Developing Boundary Layer Simulations, *J. Comp. Phys.*, 140, pp. 233-258, 1998.
- Mehta R.D. & Westphal R.V., Near-field turbulence properties of single- and two-stream plane mixing layers, *Exp. Fluids*, 4, pp. 257-266, 1986.
- Moser R.D. & Rogers M.M., The three-dimensional evolution of a plane mixing layer: pairing and transition to turbulence *J. Fluid Mech.*, 247, pp. 275-320, 1993.
- Rogers R.D. & Moser M.M., Direct simulation of a self-similar turbulent mixing layer, *Phys. Fluids*, 6(2), 1994.
- Poinsot T.J. & Lele S.K., Boundary Conditions for Direct Simulations of Compressible Viscous Flows, *J. Comp. Phys.*, 101, pp. 104-129, 1992.
- Sandham N. & Kleiser L., The late stages of transition to turbulence in channel flow, *J. Fluid Mech.*, 245, pp. 319-348, 1992.
- Vreman B., Geurts B.J. & Kuerten J.G.M., Large-Eddy Simulation of the Turbulent Mixing Layer, *J. Fluid Mech.*, 339, pp. 357-390, 1997.
- Wasistho B., Geurts B.J. & Kuerten J.G.M., Simulation techniques for spatially evolving instabilities in compressible flow over a flat plate, *Computers and Fluids*, 26, pp. 713-739, 1997.

THE SUBGRID-SCALE ESTIMATION MODEL

J. ANDRZEJ DOMARADZKI AND KUO-CHIEH LOH
*Department of Aerospace and Mechanical Engineering,
University of Southern California,
Los Angeles, CA 90089-1191, U.S.A.*

Abstract.

The subgrid scale estimation procedure provides an estimate of unfiltered quantities appearing in the definitions of the subgrid-scale tensors and consists of two steps. In the deconvolution step an approximate inversion of the filtering operation is performed. Subsequently, the nonlinear step is used to generate a range of subgrid scales on a mesh two times smaller than the mesh employed for a discretization of the resolved quantities. The subgrid scale stresses are then computed directly from the definitions using the estimated fields. The modeling procedure is described and evaluated by comparing results of large eddy simulations of turbulent channel flow with the corresponding results of direct numerical simulations and experiments.

1. Introduction

The large eddy simulation equations for an incompressible flow are conventionally written as

$$\frac{\partial}{\partial t} \bar{u}_i + \frac{\partial}{\partial x_j} \bar{u}_i \bar{u}_j = -\frac{1}{\rho} \frac{\partial}{\partial x_i} \bar{p} + \nu \frac{\partial^2}{\partial x_j \partial x_j} \bar{u}_i - \frac{\partial}{\partial x_j} \tau_{ij} \quad (1)$$

$$\frac{\partial}{\partial x_i} \bar{u}_i = 0. \quad (2)$$

The overbar denotes spatial filtering which, for a quantity $f(\mathbf{x})$, is defined by the integral

$$\bar{f}(\mathbf{x}) = \int G(\mathbf{x}, \mathbf{x}') f(\mathbf{x}') d\mathbf{x}', \quad (3)$$

where G is a given kernel function. In Eq. (1), u_i , p , and ν are the velocity, pressure, and the kinematic viscosity, respectively, and the effects of subgrid-scale quantities on the resolved velocity are described by a subgrid-scale stress tensor

$$\tau_{ij} = \overline{u_i u_j} - \overline{u_i} \overline{u_j}, \quad (4)$$

which must be modeled in terms of the resolved quantities to close Eq. (1). Recent reviews of SGS modeling procedures are given by Piomelli [1] and Lesieur [2] and many applications are described in the Proceedings edited by Galperin and Orszag [3].

The continuing work in the field of SGS modeling is motivated by the known deficiencies of the traditional models. For instance, SGS quantities predicted by the eddy viscosity models correlate poorly with the exact quantities. The eddy viscosity assumption also implies separation of scales between interacting eddies, contrary to the observed locality (in scale) of the energy transfer. The Smagorinsky model, by design, is unable to account for backscatter, i.e. the energy flux from the unresolved to the resolved scales. The backscatter is present in the dynamic model but may cause numerical instabilities if it is not controlled by averaging procedures. Similarity models have been developed to cure such deficiencies but were found to lack sufficient SGS dissipation. The traditional models also face difficulties if new physical phenomena are encountered. For instance, in convective and compressible flows SGS effects involving temperature must be modeled. In general, the modeling principles optimized for the velocity field offer very little guidance how to best model the temperature effects and new modeling assumptions must be developed and validated.

An alternative approach to SGS modeling was proposed recently by Domaradzki *et al.* [4, 5] with the goal of overcoming the shortcomings of the traditional approaches.

1.1. SUBGRID-SCALE ESTIMATION MODEL

In the proposed method the primary modeled quantity is the unfiltered velocity field appearing in the definition of the subgrid-scale stress tensor (4). An estimate u_i^e of the unfiltered velocity is obtained by expanding the resolved large scale velocity field, $\overline{u_i}$, to subgrid-scales two times smaller than the grid scale. Once the estimate u_i^e of the full field u_i is known the SGS stress tensor is computed directly from the definition

$$\tau_{ij} = \overline{u_i u_j} - \overline{u_i} \overline{u_j} \approx \overline{u_i^e u_j^e} - \overline{u_i^e} \overline{u_j^e}. \quad (5)$$

The estimation procedure was implemented first in the spectral representation [4] and extended later to the physical space representation on

uniform [5] and non-uniform [6] meshes. The physical space version is described briefly below.

Consider a velocity field u_i which is a continuous function of a variable x on the interval $[0, L_x]$. For the purpose of numerical simulations u_i may be approximated in terms of its values at discrete points using sufficiently small mesh size Δ_{DNS} . Assume that the continuous function u_i is filtered with a top hat filter with the width Δ . In general, the filtered velocity \bar{u}_i is smoother than the unfiltered field u_i and it can be accurately represented by sampling it on a coarser mesh $\Delta_{LES} \approx \Delta \gg \Delta_{DNS}$. Specifically, we will choose $\Delta_{LES} = \Delta/2$ and the computational LES mesh points are $x_n = n\Delta_{LES}$, ($n = 0, 1, \dots, N$).

The SGS estimation procedure consists of two steps. In the kinematic step we seek a function $u_i^0(x)$ such that

$$\bar{u}_i^0(x_n) = \bar{u}_i^{(N)}(x_n), \quad (6)$$

on the LES mesh points x_n , where on the right hand side of Eq. (6) are the known values of the resolved field on the LES mesh. Assuming that $u_i^0(x)$ may be accurately represented by N nodal values, $u_i^0(x_n)$, the top hat filtering on the left hand side of Eq. (6) involves integration over interval Δ spanning three neighboring points. Using the Simpson's rule for the integration results in a tridiagonal system of equations for the values of $u_i^0(x_n)$

$$\frac{1}{6} [u_i^0(x_{n-1}) + 4u_i^0(x_n) + u_i^0(x_{n+1})] = \bar{u}_i^{(N)}(x_n). \quad (7)$$

The system can be solved if values for the end points are provided. Note that the l.h.s. of (7) is a discrete filter based on the continuous top hat filter and the procedure to obtain the nodal values of $u_i^0(x)$ is an approximate, numerical inversion of the filtering operation, often called the deconvolution. The deconvolution is frequently encountered in image processing and its properties are discussed in many textbooks on this subject, e.g. [7, 8]. In the context of SGS modeling approximate deconvolutions were investigated recently by Geurts [9] and Stolz and Adams [10].

The deconvolution is followed by the nonlinear step which generates the subgrid scales twice smaller than the smallest scales resolved on the original LES mesh. In order to be able to capture these subgrid scales a finer mesh is required. The fine mesh is constructed by halving the LES mesh in each Cartesian direction, e.g. in the homogeneous directions the fine mesh spacing is $\Delta_{LES}/2$. Previously computed u_j^0 is first interpolated from the coarse LES mesh to the fine mesh. In actual numerical simulations we have employed interpolation through cubic splines. Next, the small scales are produced as a result of nonlinear interactions among large scales. The

details of the procedure are explained in ref. [5]. Briefly, the estimated velocity is obtained as a sum of u_j^0 and a perturbation velocity u'_i

$$u'_i = \theta N'_i. \quad (8)$$

In the above formula N'_i is the growth rate of subgrid scales due to the nonlinear interactions among resolved scales. It is computed as

$$N'_i = N_i^0 - \overline{N_i^0}, \quad (9)$$

where N_i^0 is the nonlinear term from which the advection effects by the large scales are removed

$$N_i^0 = -(u_j^0 - \overline{u_j^0}) \frac{\partial}{\partial x_j} u_i^0. \quad (10)$$

The time scale θ can be interpreted as the large eddy turnover time and its value may vary with the position in a flow to reflect local conditions of turbulence. It is estimated assuming that locally in space the energy of subgrid scales is proportional to the energy of the smallest resolved scales. This provides the following expression

$$\theta = C \sqrt{\frac{(u_i^0 - \overline{u_i^0})^2}{N_i'^2}} \quad (11)$$

where the constant of proportionality C is found to be approximately 1/2 for the inertial range spectral form. All calculations in the nonlinear step are performed on the fine mesh. In particular the top hat filtering is performed by integrating over intervals spanning five mesh points using the Simpson's rule. Once the estimated field $u_i^e = u_i^0 + u'_i$ is found the SGS stress tensor is computed on the fine mesh directly from the definition (4) and then sampled on the coarse mesh for use in the LES solver.

For the sake of simplicity the estimation procedure was described above for the uniform mesh. Its extension to an arbitrary non-uniform mesh is straightforward. Consider a non-uniform mesh in z direction. In such a case the top hat filtering of function $f(z)$ is defined using a variable filter width $\Delta(z)$

$$\overline{f}(z) = \frac{1}{\Delta(z)} \int_{z-\frac{\Delta(z)}{2}}^{z+\frac{\Delta(z)}{2}} f(z') dz'. \quad (12)$$

The discrete version of (12) is constructed as follows. Let z_{n-1} , z_n , and z_{n+1} be three neighboring grid points for which $(z_n - z_{n-1}) < (z_{n+1} - z_n)$. We define the filter width at the mid-point z_n as $\Delta(z_n) = 2(z_n - z_{n-1})$.

The limits of integration in formula (12) are then z_{n-1} and $z_{n+1}^* = z_{n-1} + \Delta(z_n) < z_{n+1}$. The numerical integration using the Simpson's rule requires a value of $u_i^0(z_{n+1}^*)$ which is obtained by a quadratic interpolation on the mesh points z_{n-1} , z_n , and z_{n+1} . The tridiagonal system for the non-uniform mesh equivalent to (7) for the uniform mesh has then the form

$$a_n u_i^0(z_{n-1}) + b_n u_i^0(z_n) + c_n u_i^0(z_{n+1}) = \bar{u}_i^{(N)}(z_n), \quad (13)$$

where the coefficients a_n , b_n , and c_n depend only on the mesh spacings $(z_n - z_{n-1})$ and $(z_{n+1} - z_n)$.

Formulas (7) and (13) involve one dimensional filtering and deconvolution operations. In two and three dimensions the filtering and inversion are performed as a sequence of one dimensional operations.

As demonstrated recently the modeling principle used for incompressible turbulence is immediately applicable to compressible flows [11]. The LES equations are obtained by spatial filtering of compressible flow equations. The result is rewritten in terms of Favre (or density-weighted) filtering, which for a function f is defined as

$$\tilde{f} = \frac{\overline{\rho f}}{\bar{\rho}}, \quad (14)$$

where the overbar denotes spatial filtering with a top-hat filter with the filter width Δ and ρ is the density. We follow Moin *et al.* [12] and Erlebacher *et al.* [13] in neglecting several terms in the equations that are considered small. Resulting continuity and momentum equations for spatially filtered density $\bar{\rho}$ and Favre filtered velocity \tilde{u}_i are

$$\frac{\partial \bar{\rho}}{\partial t} + \frac{\partial}{\partial x_i} (\bar{\rho} \tilde{u}_i) = 0, \quad (15)$$

$$\frac{\partial \bar{\rho} \tilde{u}_i}{\partial t} + \frac{\partial}{\partial x_j} (\bar{\rho} \tilde{u}_i \tilde{u}_j + \bar{\rho} \tilde{\sigma}_{ij}) = \frac{\partial \tilde{\sigma}_{ij}}{\partial x_j} - \frac{\partial \tau_{ij}}{\partial x_j}. \quad (16)$$

In Eq. (16) $\tilde{\sigma}_{ij}$ is the viscous stress, that is

$$\tilde{\sigma}_{ij} = \bar{\mu} \left(\frac{\partial \tilde{u}_i}{\partial x_j} + \frac{\partial \tilde{u}_j}{\partial x_i} - \frac{2}{3} \frac{\partial \tilde{u}_k}{\partial x_k} \delta_{ij} \right), \quad (17)$$

where μ is the viscosity and τ_{ij} represents the subgrid-scale (SGS) stress,

$$\tau_{ij} = \bar{\rho} (\widetilde{u_i u_j} - \tilde{u}_i \tilde{u}_j) = \overline{\rho u_i u_j} - \overline{\rho u_i} \overline{\rho u_j} / \bar{\rho}. \quad (18)$$

The energy equation can be written as follows:

$$\frac{\partial E_T}{\partial t} + \frac{\partial}{\partial x_i} [(E_T + p) u_i] = \frac{\partial}{\partial x_j} (u_i \sigma_{ij}) - \frac{\partial}{\partial x_i} \left(\kappa \frac{\partial T}{\partial x_i} \right), \quad (19)$$

where the total energy is given by $E_T = \rho C_v T + \rho u_k u_k / 2$, κ is the thermal conductivity, and C_v is the specific heat at constant volume. The filtered total energy equation is

$$\frac{\partial \bar{E}_T}{\partial t} + \frac{\partial}{\partial x_i} \left((\bar{E}_T + \bar{\rho} R \bar{T}) \tilde{u}_i \right) = - \frac{\partial}{\partial x_i} (C_p q_i) + \frac{\partial}{\partial x_i} \left(\bar{\kappa} \frac{\partial \bar{T}}{\partial x_i} \right) + \frac{\partial}{\partial x_i} (\bar{\sigma}_{ij} \tilde{u}_i), \quad (20)$$

where q_i is the subgrid-scale heat flux

$$q_i = \bar{\rho} \left(\overline{T u_i} - \bar{T} \tilde{u}_i \right) = \overline{\rho u_i T} - \overline{\rho u_i} \overline{\rho T} / \bar{\rho}. \quad (21)$$

In deriving (20) the filtered equation of state was used, $\bar{p} = \bar{\rho} R \bar{T}$, and the relation $C_p = C_v + R$, where C_p is the specific heat at constant pressure. The resolved temperature and total energy are related by

$$\bar{E}_T = \bar{\rho} C_v \bar{T} + \frac{1}{2} \bar{\rho} \tilde{u}_k \tilde{u}_k + \frac{1}{2} \tau_{kk}. \quad (22)$$

To close the above equations for the primitive variables $\bar{\rho}$, \tilde{u}_i , \bar{T} the SGS stress (18) and the SGS heat flux (21) must be expressed in terms of those variables using the model. The SGS estimation model is applied as follows. First, the deconvolution for $\bar{\rho}$ is performed providing unfiltered ρ^0 . To avoid violating the conservation of mass no attempt is made to use the nonlinear correction for SGS density scales. Next the deconvolution is performed for spatially filtered velocities, $\overline{\rho u_i} = \bar{\rho} \tilde{u}_i$. The resulting quantities are divided by ρ^0 to provide u_i^0 for use in the nonlinear correction step. Similarly, the deconvolution for \bar{E}_T is performed and the relation for E_T^0 in terms of ρ^0 , u_i^0 and T^0 is solved for the temperature T^0 . The nonlinear correction to T^0 is found as for the velocity by replacing the nonlinear term for the velocity by the nonlinear term for the temperature. Estimated density $\rho^e = \rho^0$, velocity $u_i^e = u_i^0 + u_i'$, and temperature $T^e = T^0 + T'$ are used to calculate the SGS stress and the SGS heat flux from formulas (18) and (21), respectively. In *a priori* tests for spatially evolving compressible turbulence and shock/turbulence interaction the estimation model showed correlations over 90% with the exact DNS values and it performed very well also in actual LES [11].

2. Numerical simulations

The model is evaluated in LES of turbulent channel flow. The fluid is contained between two parallel rigid walls separated by a distance L_z in the vertical direction z . The horizontal dimensions of the computational domain are L_x in the streamwise direction x and L_y in the spanwise direction y .

TABLE 1. Parameters in the numerical simulations

Case	Grid	$L_x \times L_y \times L_z$	Re_τ
hiDNS	$160 \times 160 \times 129$	$3.6\pi \times 1.9\pi \times 2$	210
loDNS1	$32 \times 32 \times 33$	$4\pi \times 2\pi \times 2$	205
EPZ1	$32 \times 32 \times 33$	$4\pi \times 2\pi \times 2$	184
loDNS2	$48 \times 64 \times 49$	$2.5\pi \times 0.5\pi \times 2$	1302
EPZ2	$48 \times 64 \times 49$	$2.5\pi \times 0.5\pi \times 2$	998

The details of the simulations are described by Domaradzki and Loh [5]. We employ a numerical Navier-Stokes code developed by Chan [14] which uses a pseudo-spectral numerical method for spatial discretization with Fourier expansions in the streamwise and spanwise directions, and Legendre polynomials in the wall normal direction. The equations are integrated in time using a second order predictor-corrector method introduced by Kim and Moin [15]. The model is applied using top hat filtering in all three Cartesian directions, including the wall normal direction in which a non-uniform mesh is used. LES were performed for two different Reynolds numbers based on shear velocity $Re_\tau \approx 200$ and $Re_\tau \approx 1000$. The parameters used in the simulations are gathered in Table 1. In addition to the LES runs EPZ1 and EPZ2 runs loDNS1 and loDNS2 with the same spatial resolution but without the model were performed. The performance of the model was further evaluated by comparing the LES results from the low Reynolds number case EPZ1 with the results of well resolved DNS of Gilbert [16] (run hiDNS). For the high Reynolds number case EPZ2 comparisons were made with the experimental results of Wei and Willmarth [17] and the results of the large eddy simulations of Piomelli [18] performed with the dynamic model. All simulations were performed with the constant mass flux through the channel until steady state was reached and were continued in the steady state to collect turbulence statistics.

A number of quantities were computed from DNS data and in actual LES. Without exception the LES results were in a very good agreement with the exact DNS data and the experiments [5, 6]. In particular, the SGS stresses were predicted accurately and the model was found to give SGS dissipation comparable to the Smagorinsky model and sufficient to guarantee the correct evolution of the flow. The new model also predicted local backscatter without any adverse effects on the numerical stability of the simulations. As an illustration consider the mean LES velocity $U_i = <$

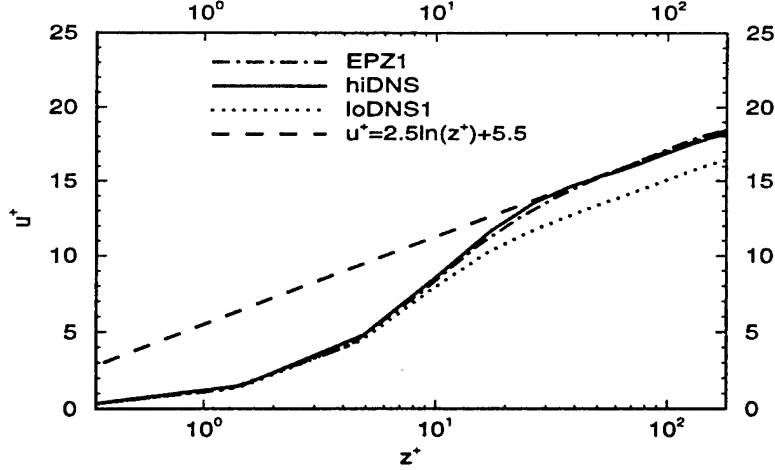


Figure 1. Mean velocity profile for low Reynolds number cases. Solid line: case hiDNS; dotted line: case loDNS1; dashed-dotted line: case EPZ1; broken line: the log law $u^+ = 2.5 \ln(z^+) + 5.5$.

\bar{u}_i where $\langle \dots \rangle$ denotes an average over horizontal planes and over several datasets in the steady state. In figure 1 we plot the mean velocity in wall coordinates for the well resolved DNS data (hiDNS), under-resolved case loDNS1 and case EPZ1. The velocity in the case hiDNS satisfies the standard linear law of the wall for $z^+ < 5$ and the logarithmic law with the additive constant 5.5 for $z^+ > 30$. For the case EPZ1 we get rather good agreement with these DNS data, with slight under prediction in the buffer region $10 < z^+ < 40$. For the case loDNS1 the mean velocity in the log region has the correct slope but the additive constant of 4.0 is too small. The mean velocity for the higher Reynolds number cases EPZ2 and loDNS2 are shown in figure 2 where they are compared with the corresponding results of the large eddy simulations of Piomelli [18] and the experimental results of Wei and Willmarth [17]. As for the low Reynolds number case the estimation model gives very good results and the low resolution DNS significantly under predict the experimental data, by about 21% in the midchannel.

The primary reason for good predictions of turbulent quantities provided by the estimation model is that it correctly represents the SGS stress

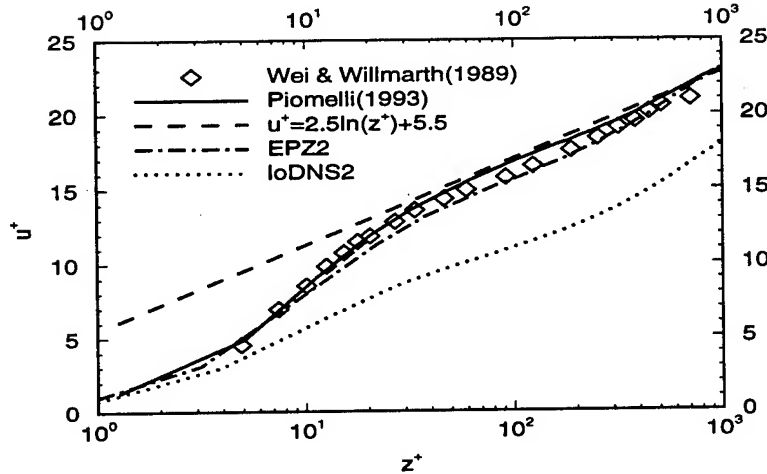


Figure 2. Mean velocity profile for high Reynolds number cases. Solid line: Piomelli (1993); \diamond : Wei and Willmarth (1989); dotted line: case loDNS2; dashed-dotted line: case EPZ2; broken line: the log law $u^+ = 2.5 \ln(z^+) + 5.5$.

tensor and its correlations with other physical quantities. Indeed, the modeled SGS shear stress component τ_{13} shown in Fig. 3 is in an excellent agreement with the exact DNS result. In Fig. 4 we plot the correlation coefficient between τ_{13} and the negative resolved rate-of-strain S_{ij} . Note that this correlation is uniformly close to unity for the eddy viscosity models which assume that both quantities are proportional. This assumption is contradicted by the DNS data that show the correlation between 0.2 and 0.4 in the core flow and a sign reversal at the wall. It is seen that the estimation model represents all features of the actual correlation very well.

Acknowledgments

This work was supported by the NSF Grant CTS-9704728 and the Contract No. B347850 from the Lawrence Livermore National Laboratory.

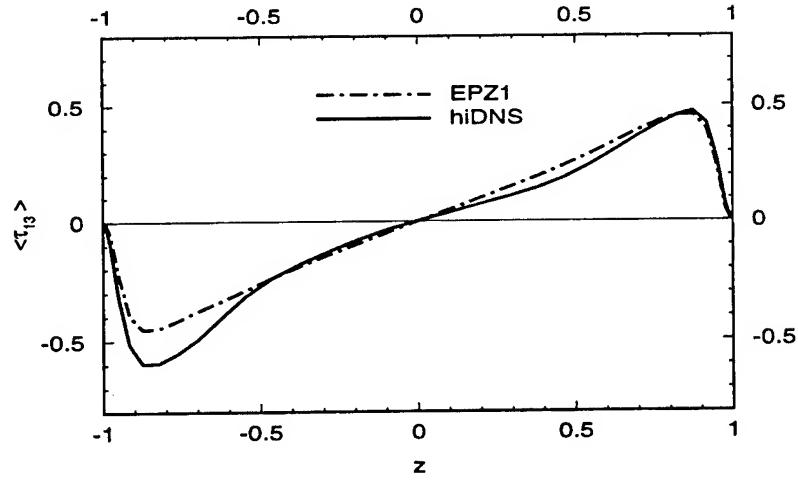


Figure 3. The plane averaged component of the SGS stress tensor $\langle \tau_{13} \rangle$.

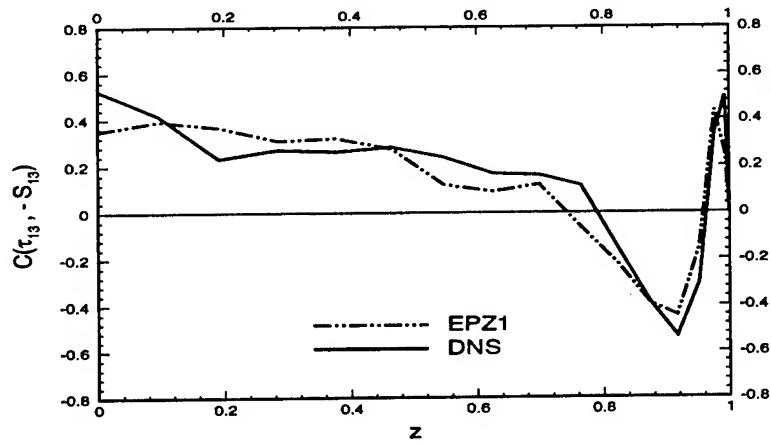


Figure 4. The plane correlation coefficient between τ_{13} and $-S_{13}$.

References

1. U. Piomelli, "Large-eddy simulations of turbulent flows", TAM Report No. 767, University of Illinois, Urbana-Champaign, 1994.
2. M. Lesieur, "New trends in large-eddy simulations of turbulence", *Annu. Rev. Fluid Mech.* **28**.
3. "Large eddy simulation of complex engineering and geophysical flows", B. Galperin and S.A. Orszag, eds., (Cambridge University Press, Cambridge, 1993).
4. J.A. Domaradzki and E.M. Saiki, "A subgrid-scale model based on the estimation of unresolved scales of turbulence", *Phys. Fluids* **9**, 2148 (1997).
5. J.A. Domaradzki and K.C. Loh, "The subgrid-scale estimation model in the physical space", in press, *Phys. Fluids* (1999).
6. K.C. Loh and J.A. Domaradzki, "The subgrid-scale estimation model on non-uniform grids", submitted, *Phys. Fluids* (1999).
7. "Digital Image Restoration", H.C. Andrews and B.R. Hunt, (Prentice-Hall, Englewood Cliffs, New Jersey, 1977).
8. "Image Restoration and Reconstruction", R.H.T. Bates and M.J. McDonnell, (Clarendon Press, Oxford (1986).
9. B.J. Geurts, "Inverse modeling for large-eddy simulation", *Phys. Fluids* **9**, 3585 (1997).
10. S. Stolz and N.A. Adams, "An approximate deconvolution procedure for large-eddy simulation", in press, *Phys. Fluids* (1999).
11. J.A. Domaradzki, T. Dubois, and A. Honein, "The Subgrid-Scale Estimation Model Applied to Large Eddy Simulations of Compressible Turbulence", *Proceedings of the 1998 Summer Program, Center for Turbulence Research, NASA Ames/Stanford*, 351, (1998).
12. P. Moin, K. Squires, W. Cabot, and S. Lee, "A dynamic subgrid-scale model for compressible turbulence and scalar transport", *Phys. Fluids A* **3**, 2746-2757 (1991).
13. G. Erlebacher, M.Y. Hussaini, C.G. Speziale, and T.A. Zang, "Toward the large-eddy simulation of compressible turbulent flows", *J. Fluid Mech.* **238** 155-185 (1992).
14. D.C. Chan, "Effects of rotation on turbulent convection: direct numerical simulation using parallel computers", Ph.D. Thesis, University of Southern California, 1996.
15. J. Kim and P. Moin, "Application of a fractional-step method to incompressible Navier-Stokes equations", *J. Comput. Phys.* **59**, 308 (1985).
16. N. Gilbert, "Numerische Simulation der Transition von der laminaren in die turbulente Kanalströmung", DFVLR-Forschungsbericht 88-55, (DLR Göttingen, Germany, 1988).
17. T. Wei and W.W. Willmarth, "Reynolds-number effects on the structure of a turbulent channel flow", *J. Fluid Mech.* **204**, 57 (1989).
18. U. Piomelli, "High Reynolds number calculations using the dynamic subgrid-scale model", *Phys. Fluids A* **5**, 1484 (1993).

DIRECT NUMERICAL SIMULATION OF TRANSITIONS TOWARD TURBULENCE IN COMPLEX CHANNEL FLOWS*

B.D. Duncan** and K.N. Ghia
Computational Fluid Dynamics Research Laboratory
Department of Aerospace Engineering and Engineering Mechanics
University of Cincinnati
Cincinnati, OH 45219

Abstract

A numerical tool for the direct numerical simulation (DNS) of instability and transition to turbulence is presented and applied to problems of secondary instability of complex channel flows. The Navier-Stokes equations for incompressible flow are solved in generalized curvilinear coordinates so that channel flows may be investigated in which the walls of the channel are both curved and wavy. The channel geometry and the flow solution are assumed to be periodic in the streamwise and spanwise directions. A spectral collocation method is employed, in which the periodic directions are discretized using the Fourier collocation method, and the transverse direction is discretized using the Chebyshev collocation method. The time integration is performed with implicit coupling of velocity and pressure at each time step. Both fully- and semi-implicit second-order integration schemes were developed in this study. For the fully-implicit method, Newton's method is directly applied to the solution of the nonlinear system of equations. The large linear algebra system obtained from the linearization of the spatial discretization and coupled velocity and pressure is solved using a preconditioned iteration scheme based on the Generalized Minimal Residual (GMRES) method. Preconditioning is performed through an approximate factorization of the linearized Navier-Stokes operator which decouples the solutions of the velocity and pressure updates during the iterative algorithm. The velocity and pressure sub-iterations are both solved using preconditioned GMRES as well. The velocity system is preconditioned by a block Jacobi (line-implicit) approximation. The pressure system is preconditioned by left and right Fourier transform operators followed by a block Jacobi approximation.

This numerical technique was applied to several problems of instability and transition in curved channel flows and in curved channel flows with wall waviness. The numerical methodology was validated by carefully comparing the present results with those of Finlay, Keller and Ferziger (*JFM*, vol. 194, 1988) and Ligrani *et al.* (*Phys. Of Fluids A*, vol. 4, no. 4, 1992) for two- and three-dimensional Dean vortex flows in a curved channel. Also, new results were obtained for curved channel flows with two-dimensional small amplitude wall waviness. The waviness significantly altered the evolution of both Dean vortex and Tollmien-Schlichting wave instabilities. The traveling wave twisting Dean vortex solution of Ligrani *et al.* for Reynolds number 409 was repeated with wall waviness, and resulted in a highly oscillatory state. Waviness also modified the secondary instability of Tollmien-Schlichting waves at Reynolds number 5000 by forcing asymmetry in the three-dimensional Λ -vortex structures near the upper and lower walls of the channel. Finally, highly unsteady and complex results were obtained for saturated Tollmien-Schlichting waves in two-dimensional channel flow with large amplitude wall waviness at Reynolds number 5000. These cases were used to demonstrate the capabilities of the computational tool for DNS of instability and transition in complex channel flows.

Introduction

The present method has been discussed by [1] and [2] and is a new numerical technique based on a spectral collocation discretization of the incompressible Navier-Stokes equations in generalized curvilinear coordinates. A numerical approach was selected that allows non-constant coefficients in the governing equations, while retaining the requirements of periodicity in the streamwise and spanwise directions. The discretization yields a coupled set of nonlinear or linear algebraic equations for the velocity and pressure at each time step. The resulting algebraic equations and solution approach are described in the following section.

* This work is supported in part by AFOSR Grant No. F49620-93-1-0393, NSF Grant No. CTS-9512450 and Ohio Supercomputer Center Grant No. PES070-5.

** Presently affiliated with Automotive Aerodynamics, Inc., Charlotte, NC

$$\frac{\partial \mathbf{U}}{\partial t} + \mathbf{N}(\mathbf{U}) = -\mathbf{G}(P) + \mathbf{L}(\mathbf{U}) + \mathbf{Q}, \text{ and}$$

$$D(\mathbf{U}) = 0, \text{ where}$$

$$\mathbf{N}(\mathbf{U}) = \frac{1}{2\sqrt{g}} \mathbf{D}^i (\sqrt{g} U^i \mathbf{U}) + \frac{1}{2} U^i \mathbf{D}^i (\mathbf{U}), \quad (7)$$

$$\mathbf{L}(\mathbf{U}) = \frac{1}{\text{Re} \sqrt{g}} \mathbf{D}^i (\sqrt{g} g^{ij} \mathbf{D}^j (\mathbf{U})),$$

$$\mathbf{G}(P) = \bar{e}_i g^{ij} \mathbf{D}^j (A^i(P)), \text{ and}$$

$$D(\mathbf{U}) = A^0 \left(\frac{1}{\sqrt{g}} \mathbf{D}^i (\sqrt{g} U^i) \right).$$

The momentum equation is integrated in time, with the continuity equation as a constraint, using either the fully-implicit (FI) or semi-implicit (SI) second-order scheme. To facilitate numerical solution and incorporate boundary conditions, the momentum and continuity equations are written as the residual functions \mathbf{F}_m and F_c , respectively:

$$\mathbf{F}_m = \begin{cases} \mathbf{U}^{n+1} - \mathbf{u}_{upper} & \text{if } \xi^3 = -1 \\ \mathbf{U}^{n+1} - \mathbf{u}_{lower} & \text{if } \xi^3 = 1 \\ \mathbf{F}_m^* & \text{otherwise} \end{cases} = 0, \quad F_c = D(\mathbf{U}^{n+1}) = 0, \quad (8)$$

where for the FI scheme:

$$\mathbf{F}_m^* = \mathbf{U}^{n+1} - \mathbf{U}^n + \frac{\Delta t}{2} \{-\mathbf{L}(\mathbf{U}^{n+1}) + \mathbf{N}(\mathbf{U}^{n+1}) - \mathbf{Q}^{n+1}\} + \frac{\Delta t}{2} \{-\mathbf{L}(\mathbf{U}^n) + \mathbf{N}(\mathbf{U}^n) - \mathbf{Q}^n\} + \Delta t \mathbf{G}(P^{n+1/2}), \quad (9)$$

and for the SI scheme:

$$\begin{aligned} \mathbf{F}_m^* = & \mathbf{U}^{n+1} - \mathbf{U}^n + \frac{\Delta t}{2} \{-\mathbf{L}(\mathbf{U}^{n+1}) - \mathbf{Q}^{n+1}\} + \frac{\Delta t}{2} \{-\mathbf{L}(\mathbf{U}^n) - \mathbf{Q}^n\} \\ & + \frac{\Delta t}{2} \{3\mathbf{N}(\mathbf{U}^n) - \mathbf{N}(\mathbf{U}^{n-1})\} + \Delta t \mathbf{G}(P^{n+1/2}). \end{aligned} \quad (10)$$

Iterative Approach

The above algebraic system is solved using a multiple-level iteration method which produces a solution to a specified tolerance. For the system obtained from the FI discretization, the system is nonlinear, and Newton's method is used on the outer level. Each Newton iteration requires the solution of a linear algebraic system, in which the coefficient matrix is the linearized Navier-Stokes operator. This linear system is solved using a generalized minimum residual (GMRES) method[6][7]. An approximate factorization similar to those shown in [8] and [9] is used to precondition the system. The Jacobian, \mathbf{A} , of the residual function is:

$$\mathbf{A} = \frac{\partial(\mathbf{F}_m, F_c)}{\partial(\mathbf{U}^{n+1}, P^{n+1/2})} = \begin{Bmatrix} \mathbf{I} + \mathbf{Z}\mathbf{E} & \Delta t \mathbf{Z}\mathbf{G} \\ \mathbf{D} & 0 \end{Bmatrix}, \quad (11)$$

where $\mathbf{Z} = \begin{cases} 0 & \text{if } \xi^3 = 1 \text{ or } -1 \\ \mathbf{I} & \text{otherwise} \end{cases}$ and $\mathbf{E} = \frac{\Delta t}{2} \{-\mathbf{L} + \mathbf{N}^*(\mathbf{U}^{n+1})\}.$

In the above, \mathbf{D} , \mathbf{G} and \mathbf{L} are matrices representing the application of the discrete divergence, gradient, and viscous stress functions, and $\mathbf{N}^*(\mathbf{U}^{n+1})$ is a matrix containing the linearized convective terms, evaluated at the most recent guess for the velocity solution.

In the GMRES method, the Jacobian is preconditioned using the approximate factorization:

$$\tilde{\mathbf{A}} = \begin{Bmatrix} \mathbf{I} + \mathbf{Z}\mathbf{E} & 0 \\ \mathbf{D} & -\Delta t \mathbf{D}\mathbf{Z}\mathbf{G} \end{Bmatrix} \begin{Bmatrix} \mathbf{I} & \Delta t \mathbf{Z}\mathbf{G} \\ 0 & \mathbf{I} \end{Bmatrix} = \begin{Bmatrix} \mathbf{I} + \mathbf{Z}\mathbf{E} & \Delta t (\mathbf{I} + \mathbf{Z}\mathbf{E})\mathbf{Z}\mathbf{G} \\ \mathbf{D} & 0 \end{Bmatrix}, \quad (12)$$

which differs from the original system at order Δt^2 in the momentum equation pressure coefficient. This approximate factorization decouples the velocity and pressure in the solution procedure.

$$\frac{\partial \mathbf{U}}{\partial t} + \mathbf{N}(\mathbf{U}) = -\mathbf{G}(P) + \mathbf{L}(\mathbf{U}) + \mathbf{Q}, \text{ and}$$

$$D(\mathbf{U}) = 0, \text{ where}$$

$$\mathbf{N}(\mathbf{U}) = \frac{1}{2\sqrt{g}} \mathbf{D}^i (\sqrt{g} U^i \mathbf{U}) + \frac{1}{2} U^i \mathbf{D}^i (\mathbf{U}), \quad (7)$$

$$\mathbf{L}(\mathbf{U}) = \frac{1}{\text{Re} \sqrt{g}} \mathbf{D}^i (\sqrt{g} g^{ij} \mathbf{D}^j (\mathbf{U})),$$

$$\mathbf{G}(P) = \bar{e}_i g^{ij} D^j (A^+(P)), \text{ and}$$

$$D(\mathbf{U}) = A^0 \left(\frac{1}{\sqrt{g}} D^i (\sqrt{g} U^i) \right).$$

The momentum equation is integrated in time, with the continuity equation as a constraint, using either the fully-implicit (FI) or semi-implicit (SI) second-order scheme. To facilitate numerical solution and incorporate boundary conditions, the momentum and continuity equations are written as the residual functions F_m and F_c , respectively:

$$\mathbf{F}_m = \begin{cases} \mathbf{U}^{n+1} - \mathbf{u}_{upper} & \text{if } \xi^3 = -1 \\ \mathbf{U}^{n+1} - \mathbf{u}_{lower} & \text{if } \xi^3 = 1 \\ \mathbf{F}_m^* & \text{otherwise} \end{cases} = 0, \quad F_c = D(\mathbf{U}^{n+1}) = 0, \quad (8)$$

where for the FI scheme:

$$\mathbf{F}_m^* = \mathbf{U}^{n+1} - \mathbf{U}^n + \frac{\Delta t}{2} \{-\mathbf{L}(\mathbf{U}^{n+1}) + \mathbf{N}(\mathbf{U}^{n+1}) - \mathbf{Q}^{n+1}\} + \frac{\Delta t}{2} \{-\mathbf{L}(\mathbf{U}^n) + \mathbf{N}(\mathbf{U}^n) - \mathbf{Q}^n\} + \Delta t \mathbf{G}(P^{n+1/2}), \quad (9)$$

and for the SI scheme:

$$\mathbf{F}_m^* = \mathbf{U}^{n+1} - \mathbf{U}^n + \frac{\Delta t}{2} \{-\mathbf{L}(\mathbf{U}^{n+1}) - \mathbf{Q}^{n+1}\} + \frac{\Delta t}{2} \{-\mathbf{L}(\mathbf{U}^n) - \mathbf{Q}^n\} \\ + \frac{\Delta t}{2} \{3\mathbf{N}(\mathbf{U}^n) - \mathbf{N}(\mathbf{U}^{n-1})\} + \Delta t \mathbf{G}(P^{n+1/2}). \quad (10)$$

Iterative Approach

The above algebraic system is solved using a multiple-level iteration method which produces a solution to a specified tolerance. For the system obtained from the FI discretization, the system is nonlinear, and Newton's method is used on the outer level. Each Newton iteration requires the solution of a linear algebraic system, in which the coefficient matrix is the linearized Navier-Stokes operator. This linear system is solved using a generalized minimum residual (GMRES) method [6][7]. An approximate factorization similar to those shown in [8] and [9] is used to precondition the system. The Jacobian, \mathbf{A} , of the residual function is:

$$\mathbf{A} = \frac{\partial(\mathbf{F}_m, F_c)}{\partial(\mathbf{U}^{n+1}, P^{n+1/2})} = \begin{Bmatrix} \mathbf{I} + \mathbf{Z}\mathbf{E} & \Delta t \mathbf{Z}\mathbf{G} \\ \mathbf{D} & 0 \end{Bmatrix}, \quad (11)$$

where $\mathbf{Z} = \begin{cases} 0 & \text{if } \xi^3 = 1 \text{ or } -1 \\ \mathbf{I} & \text{otherwise} \end{cases}$ and $\mathbf{E} = \frac{\Delta t}{2} \{-\mathbf{L} + \mathbf{N}^*(\mathbf{U}^{n+1})\}$.

In the above, \mathbf{D} , \mathbf{G} and \mathbf{L} are matrices representing the application of the discrete divergence, gradient, and viscous stress functions, and $\mathbf{N}^*(\mathbf{U}^{n+1})$ is a matrix containing the linearized convective terms, evaluated at the most recent guess for the velocity solution.

In the GMRES method, the Jacobian is preconditioned using the approximate factorization:

$$\tilde{\mathbf{A}} = \begin{Bmatrix} \mathbf{I} + \mathbf{Z}\mathbf{E} & 0 \\ \mathbf{D} & -\Delta t \mathbf{D}\mathbf{Z}\mathbf{G} \end{Bmatrix} \begin{Bmatrix} \mathbf{I} & \Delta t \mathbf{Z}\mathbf{G} \\ 0 & \mathbf{I} \end{Bmatrix} = \begin{Bmatrix} \mathbf{I} + \mathbf{Z}\mathbf{E} & \Delta t (\mathbf{I} + \mathbf{Z}\mathbf{E})\mathbf{Z}\mathbf{G} \\ \mathbf{D} & 0 \end{Bmatrix}, \quad (12)$$

which differs from the original system at order Δt^2 in the momentum equation pressure coefficient. This approximate factorization decouples the velocity and pressure in the solution procedure.

The innermost iteration level consists of iterative solution procedures for the velocity and pressure corrections. The velocity correction is obtained using GMRES with simple block-diagonal preconditioning. The pressure correction is obtained through a two-dimensional Fourier transform of the system, and GMRES with block-diagonal preconditioning is used to solve the transformed system. For the SI integration scheme, the same multi-level procedure is used, except that Newton's method on the outer level is replaced with a single step in which the solution is updated based on the solution of the linear algebraic system.

The multiple-level iteration method differs considerably from the solution procedures used in the time-splitting, or fractional step, method that has been used in many previous studies, see [5][10][11]. However, the approximate factorization strategy produces a linear system that is very similar to that used in the time-splitting approach[9]. Also, the transformation of the pressure problem into Fourier wave-number space produces a linear algebra problem for pressure similar to that obtained in previous studies, yet flexible enough to handle the non-constant coefficients that are present due to metric terms.

Results

Previous studies on the effects of various types of geometric variations on the stability of channel and boundary layer flows are reviewed in [2]. These variations include distributed and localized surface roughness, wall waviness, grooves, compliant boundaries and flow obstructions such as cylinders, spheres and vertical baffles. Wall blowing and suction has been used to imitate the effects of surface roughness and waviness. Small geometric variations can have the effect of forcing or controlling the dominant modes of instability, see [12][13][14] for examples. Larger variations can bypass the dominant instability mode and can alter the route to turbulence by activating an instability at lower Re which would not have occurred without the geometric disturbance. For examples, see [15][16][17].

The direct numerical simulation code for periodic channel flows was used to study the effect of wall waviness on the instabilities leading to transition to turbulence in curved channel flows. Two competing instability mechanisms were studied for 3-D flows: the secondary instability of Dean vortices, and the secondary instability of Tollmien-Schlichting (TS) waves. Also, instability leading to a possibly chaotic 2-D flow was examined for flow in a 2-D curved channel with large-amplitude wall waviness.

The formation and breakdown of Dean vortices is the dominant transition mechanism in channel flows with significant streamwise curvature. In this study, a 3-D twisting Dean vortex state was computed for $Re=409$ for comparison with the experimental and numerical results of [18]. This state occurs as a supercritical bifurcation (as Re is increased) from 2-D axisymmetric Dean vortex flow, as the 2-D flow encounters secondary instability to streamwise disturbances above a critical Re which depends on the curvature. As the instability grows, nonlinear effects cause the wave to saturate at a finite amplitude, and eventually a constant-amplitude traveling wave results. This wave can be seen experimentally as a twisting of the vortices near the channel centerline, and can be measured quantitatively as an oscillation in velocity time histories. The sample of the results for this case is shown in Figs. 1-3. The time history of streamwise velocity at three locations is shown in Fig. 1, demonstrating the periodic variation of the flow due to the traveling wave. The results were averaged in the streamwise direction for comparison with the results of [18] in Fig. 2. Contours of vorticity magnitude on the centerline plane are shown in Fig. 3.

The effect of wall waviness on twisting Dean vortex flow was examined for the same case. The waviness that was selected was quite small, with amplitude, 0.01 times the channel height. The wave pattern is made up of a combination of streamwise, spanwise, and oblique waves, all at the fundamental streamwise and spanwise wavenumbers, as shown in Fig. 4. It was found that the waviness had a significant effect on the twisting Dean vortex flow. For the same Re used in the curved channel case, $Re=409$, the simulation produced an oscillatory state in contrast to the traveling-wave result for curved channel flow. A snapshot of this state is shown in Fig. 5. Further results will be shown in the presentation.

The route to turbulence more common in plane flows is the secondary instability of TS waves. Though they are less dominant in flows with streamwise curvature when assuming a disturbance environment capable of exciting either TS or Dean modes, they offer a possible route to turbulence in the absence of Dean vortices. For this study, a fully-developed saturated TS wave was perturbed with a small-amplitude spanwise disturbance. It was found that the growth of the spanwise disturbance occurred very rapidly and caused the formation of Λ -vortices near both walls just as in plane channel studies such as [11]. The simulation was continued partially through the transition process, and revealed a complex vortex stretching and reconnection structure. The Λ -vortex on the upper wall formed and collapsed twice, while the Λ -vortex on the lower wall formed and collapsed once during the simulation. The vorticity on the lower wall is shown in Fig. 6 for three time levels.

The effect of small-amplitude wall waviness on the secondary instability of TS waves was investigated. The wall waviness was the same as in the Dean vortex case, and was used to trigger the secondary instability. In this case, growth of the secondary instability was even more rapid. Also, the Λ -vortex pattern was altered

significantly due to the pressure gradient variations caused by the wall waviness. The wall waviness pattern is highly asymmetric and oblique. It enhanced the growth of one leg of the Λ -vortex on each wall and inhibited the growth of the other. The simulation contained one cycle of formation and collapse of the asymmetric Λ -vortex on the top wall and the formation of the first asymmetric Λ -vortex on the lower wall. The vorticity on the lower wall is shown in Fig. 7.

The first two studies examined the effect of wall waviness on the two secondary instability mechanisms which occur in curved channel flows. The third study that was performed was the examination of the primary instability, that is, the evolution of a saturated TS wave, in a 2-D curved channel with larger wall waviness amplitude. As reviewed in [2], previous studies have examined the temporal development of the flow in 2-D channels with obstructions, grooves, and wall waviness. Such obstructions or large wall variations can cause flow separation and unsteady vortex shedding. These interesting flow phenomena, when coupled with streamwise instabilities in the form of TS waves, greatly alter the stability of the flow and create more complicated 2-D states such as quasi-periodic or chaotic flows. Thus, the process of transition to turbulence occurring through 3-D secondary instability of these flows would be greatly altered. In this study, a new 2-D state was examined at $Re=4000$ in a curved channel with large-amplitude upper and lower wall waviness such that the channel periodically diverges and converges, creating regions of significant adverse and favorable pressure gradient, and causing unsteady separation and vortex shedding. The flow increases in complexity in time for the duration of the simulation, and it appears as if the flow becomes chaotic. However, this could not be quantified without longer simulation time. Snapshots of the vorticity are shown in Fig. 8.

Conclusion

The results presented here and in [2] validate the numerical tool developed for simulations of transition and turbulence in complex channel flows. The tool was used for an initial study of the effects of wall waviness on secondary instability of curved channel flows, and showed significant modifications to the evolution of Dean vortex and Tollmien-Schlichting wave instabilities.

References

- [1] Duncan, B. D., and Ghia, K. N., "An Iterative Approach for Solving the Incompressible Navier-Stokes Equations for Simulation of Transition and Turbulence in Complex Geometries," First AFOSR International Conference on DNS/LES, Louisiana Tech University, Louisiana, August, 1997.
- [2] Duncan, B. D., Direct Numerical Simulation of Transitions Toward Turbulence in Complex Channel Flows, Ph.D. Dissertation, University of Cincinnati, 1998.
- [3] Finlay, W. H., Keller, J. B., and Ferziger, J. H., "Instability and Transition in Curved Channel Flow," *J. Fluid Mech.*, 194, pp. 417-456, 1988.
- [4] Zang, T. A., "On the Rotation and Skew-Symmetric Forms for Incompressible Flow Simulations," *Appl. Numer. Math.*, Vol. 6, 1990.
- [5] Canuto, C., Hussaini, M. Y., Quarteroni, A., and Zang, T. A., *Spectral Methods in Fluid Dynamics*, Springer-Verlag, 1988.
- [6] Axelsson, O., *Iterative Solution Methods*, Cambridge U. Press, 1996.
- [7] Saad, Y., and Schultz, M. H., "GMRES: A Generalized Minimal Residual Algorithm for Solving Nonsymmetric Linear Systems," *SIAM J. Sci. Stat. Comp.*, 7, pp. 856-869, 1986.
- [8] Perot, J. B., "An Analysis of the Fractional Step Method," *J. Comp. Phys.*, 108, pp. 51-58, 1993.
- [9] Dukowicz, J. K., and Dvinsky, A. S., "Approximate Factorization as a High Order Splitting for the Implicit Incompressible Flow Equations," *J. Comp. Phys.*, 102, pp. 336-347, 1992.
- [10] Karniadakis, G. E., and Triantafyllou, G. S., "Three-Dimensional Dynamics and Transition to Turbulence in the Wake of Bluff Objects," *J. Fluid Mech.*, 238, pp. 1-30, 1992.
- [11] Zang, T. A., and Hussaini, M. Y., "A Three-Dimensional Spectral Algorithm for Simulations of Transition and Turbulence," ICASE Report No. 85-19, 1985.
- [12] Choudhari, M., "Boundary-Layer Receptivity due to Distributed Surface Imperfections of a Deterministic or Random Nature," *Theoret. Comput. Fluid Dynamics*, 4, pp. 101-117, 1993.
- [13] Corke, T. C., and Knasiak, K. F., "Stationary-Travelling Cross-Flow Mode Interactions with Periodic Distributed Roughness," AIAA Paper No. 96-2016, 27th AIAA Fluid Dynamics Conference, New Orleans, LA, June 17-20, 1996.
- [14] Karniadakis, G. E., Mikic, B. B., and Patera, A. T., "Minimum-Dissipation Transport Enhancement by Flow Destabilization: Reynolds' Analogy Revisited," *J. Fluid Mech.*, 192, pp. 365-391, 1988.

- [15] Carlson, H. A., Berkooz, G., and Lumley, J. L., "Direct Numerical Simulation of Flow in a Channel with Complex Time-Dependent Wall Geometries: A Pseudospectral Method," *J. Comp. Phys.*, 121, pp. 155-175, 1995.
- [16] Amon, C. H., and Patera, A. T., "Numerical Calculation of Stable Three-Dimensional Tertiary States in Grooved-Channel Flow," *Phys. Fluids A*, 1(12), pp. 2005-2009, 1989.
- [17] Sahan, R. A., Liakopoulos, A., and Gunes, H., "Reduced Dynamical Models of Nonisothermal Transitional Grooved-Channel Flow," *Phys. Fluids*, 9(3), pp. 551-565, 1997.
- [18] Ligrani, P. M., Finlay, W. H., Fields, W. A., Fuqua, S. J., and Subramanian, C. S., "Features of Wavy Vortices in a Curved Channel from Experimental and Numerical Studies," *Phys. Fluids A*, 4(4), pp. 695-709, 1992.

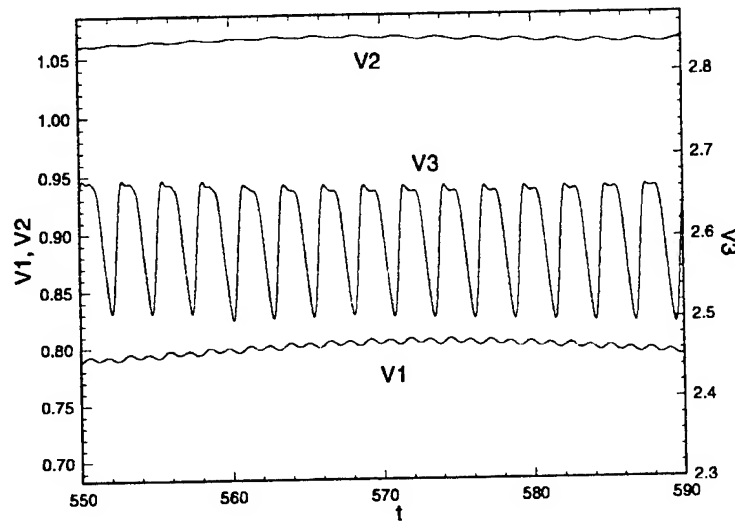


Figure 1. Here, the streamwise (contravariant) velocity component is shown at three arbitrary points in the flow, for the twisting Dean vortex. Locations V1 and V2 are near the walls, while location V3 is in the center of the channel. The time trace of these velocities, sampled every time step, shows both the low frequency transient, and the high frequency oscillation representing the traveling wave. In b), the final 40 characteristic time is shown.

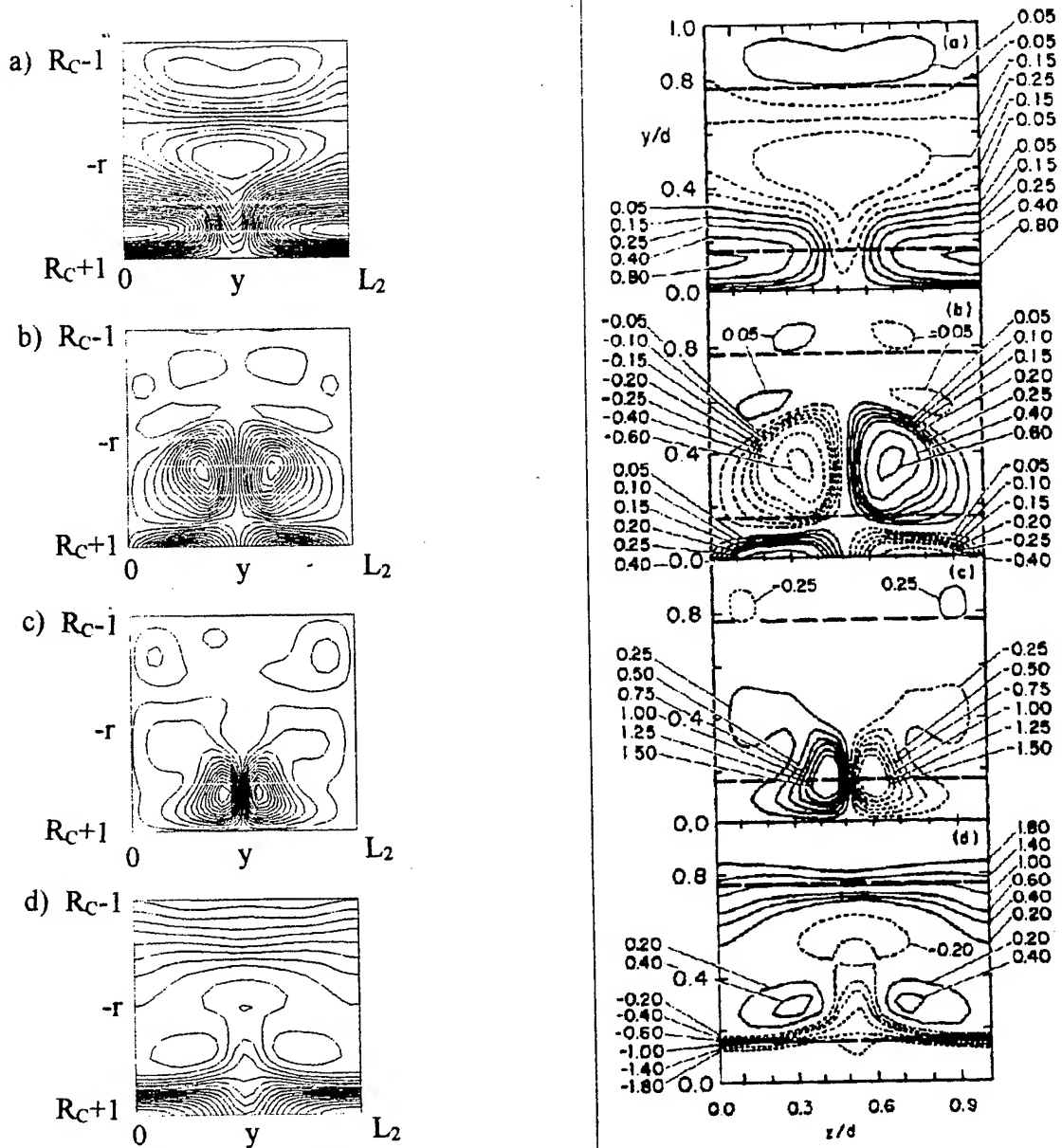


Figure 2. Left: The results from the twisting Dean vortex simulation were averaged in the streamwise direction, and are shown here in the cross-sectional y - r plane. For direct comparison with Ligrani *et al.* (1992), the direction of the r axis is reversed. CCPE was subtracted from the average streamwise velocity, and the perturbation streamwise velocity is shown in a). The three components of vorticity are shown: streamwise in b), transverse in c) and spanwise in d). Spectral resolution=24x24x32 (streamwise x spanwise x transverse), $\Delta t=0.001$ with the SI method.

Right: DNS results are shown from Ligrani *et al.* (1992) for comparison with the present results. Between their heavy dashed lines is the region corresponding to their photographs of twisting Dean vortices. The flow quantities are a) streamwise velocity, b) streamwise vorticity, c) transverse vorticity, and d) spanwise vorticity.

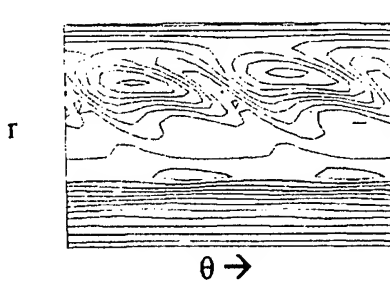


Figure 3 (caption below)

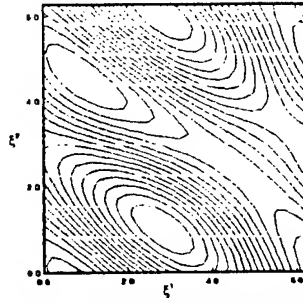


Figure 4 (caption below)

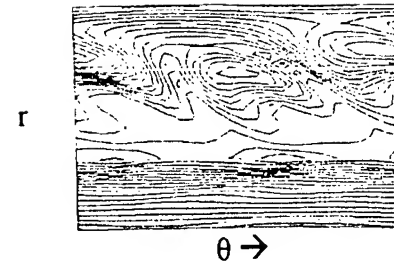


Figure 5 (caption below)

Figure 3. The twisting Dean vortex flow field is shown in the θ - r plane in the center of the domain, at $y=L^2/2$. Flow is from left to right. Contours of vorticity magnitude are shown. The twisting of the Dean vortex pair can be seen in this plane as streamwise variations.

Figure 4. Contours of surface displacement for the lower wall of the curved channel with streamwise and spanwise waviness. The combined streamwise, spanwise, and oblique waviness yields a rippled, asymmetric surface.

Figure 5. The twisting Dean vortex result, with wall waviness, is shown here in a θ - r plane in the center of the domain, at $y=L^2/2$. Contours of vorticity magnitude are shown. Spectral resolution= $8 \times 16 \times 32$, $\Delta t=0.001$ with the SI method.

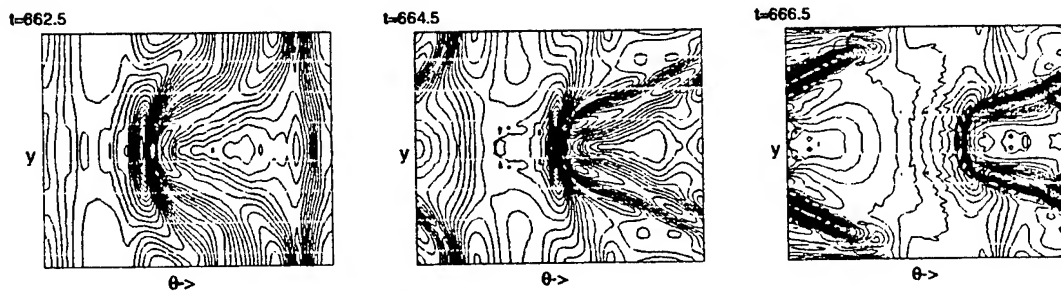


Figure 6. Contours of vorticity magnitude on the lower wall are shown for three time levels for a Tollmien-Schlichting wave in a curved channel. The surface is projected onto the x - y plane. Spectral resolution= $64 \times 64 \times 64$, $\Delta t=0.001$ with the SI method.

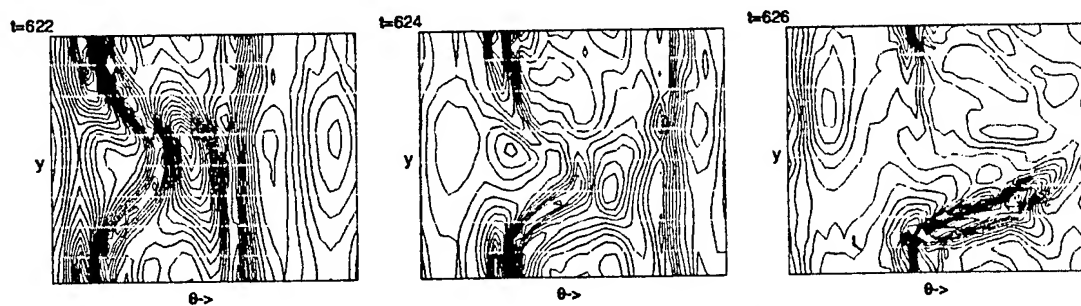


Figure 7. Contours of vorticity magnitude on the lower wall are shown for three time levels for a Tollmien-Schlichting wave in a curved channel with wall waviness. The surface is projected onto the x - y plane. Spectral resolution= $32 \times 32 \times 64$, $\Delta t=0.001$ with the SI method.

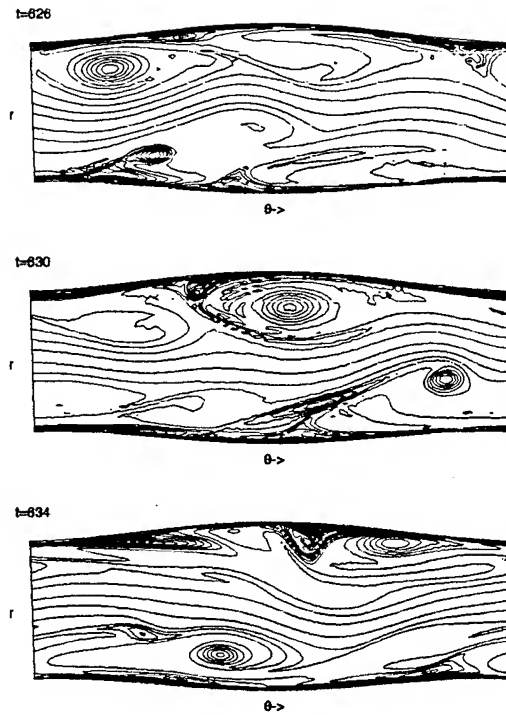


Figure 8. Contours of vorticity magnitude for three time levels for 2-D flow in a curved wavy channel. The vorticity shows the complicated vortex shedding events, and the interactions between vortical structures and the walls. Spectral resolution= $128 \times 1 \times 128$, $\Delta t=0.0005$ with the SI method.

IMPLEMENTATION OF AN SGS MODEL IN A B-SPLINE SPECTRAL METHOD AND LES OF A TURBULENT AXIAL VORTEX

B. ESHPUNIYANI AND G.A. BLAISDELL
School of Aeronautics and Astronautics
Purdue University
West Lafayette, IN 47907-1282

Abstract.

The dynamic SGS model is implemented into a b-spline/Fourier spectral DNS code. The entire SGS term (minus the divergence of the SGS stress) is computed in physical space and then expressed in terms of a b-spline expansion. The inner product operation on this term leads to four integrals involving double products of b-splines. Two of these already are part of the formulation of the other terms in the weak form of the Navier-Stokes equation and are being computed in the original code using Gaussian quadrature. This approach thus leads to only two additional integrations. An LES of a turbulent axial vortex is currently being performed.

1. Introduction

The work presented includes a description of the implementation of the dynamic SGS model into a b-spline/Fourier spectral DNS code. This effort is part of an on-going project on the DNS and LES of turbulent axial vortices with and without the effect of an external strain field. The overall project is motivated by the wake hazard problem for commercial aircraft where the wing-tip vortices behind large aircraft present a serious safety concern for the following aircraft. In order for progress to be made in the prediction and control of these vortices, it will be helpful to have a better understanding of how turbulence within these vortices behaves and how the turbulence affects the distribution of vorticity. Also, current turbulence models do not perform well for strongly rotating flows and the current study

provides needed data for the improvement of turbulence models for such flows.

There have been several experimental studies of turbulent vortices, which are discussed in the papers^{3,4} by Devenport *et al.* (1996) and Leweke and Williamson (1998). Numerical simulations of an isolated turbulent axial vortex have been presented in a series of papers by Ragab *et al.* (1995). More recently, DNS have been done by Coppens (1998), Qin (1998) and Blaisdell and Qin (1999), who considered the effects of an external strain field. The effect of strain was included because each vortex of a trailing vortex pair induces a strain field on the opposite vortex. The strain creates an instability (the short wavelength instability is known as the Widnall instability) which affects the development of turbulence within the vortex. A DNS has been done by Orlandi *et al.* (1998) of a trailing vortex pair corresponding to the experiment of Leweke and Williamson

The objective of the current study is to extend the simulations of Qin to higher Reynolds numbers by using LES. The appropriate Reynolds number is $Re_\Gamma = \Gamma/\nu$, where Γ is the circulation of the vortex and ν is the kinematic viscosity. The DNS have a Reynolds number $Re_\Gamma = 16,500$ which is about three orders of magnitude smaller than that found in the wakes of large commercial aircraft. While LES still cannot reach full scale Reynolds numbers, it will allow the effects of varying Reynolds number to be studied. Also, Reynolds number is particularly important for the case with strain, because viscosity creates a high wave number cut-off for unstable modes. The current DNS are barely able to capture the instability due to strain because the smallest unstable mode has a length scale comparable to the vortex core size. It is desirable to have a wider range of unstable length scales, and this should be achievable with LES.

2. Governing Equations

The incompressible Navier-Stokes equations can be written as

$$\vec{\nabla} \cdot \vec{u} = 0 \quad (1)$$

$$\frac{\partial \vec{u}}{\partial t} + \vec{u} \cdot \vec{\nabla} \vec{u} + \vec{\nabla} p = \frac{1}{Re} \vec{\nabla} \cdot \vec{\nabla} \vec{u}, \quad (2)$$

where \vec{u} = velocity and p = pressure. Here all quantities are normalized using the radius of the computational domain (see figure 1), R , as the length scale and the initial axial velocity deficit, $V_o = V_z(r = \infty) - V_z(r = 0)$, as the velocity scale, where $V_z(r)$ is the mean axial velocity. $Re = V_o R / \nu$ is the computational Reynolds number.

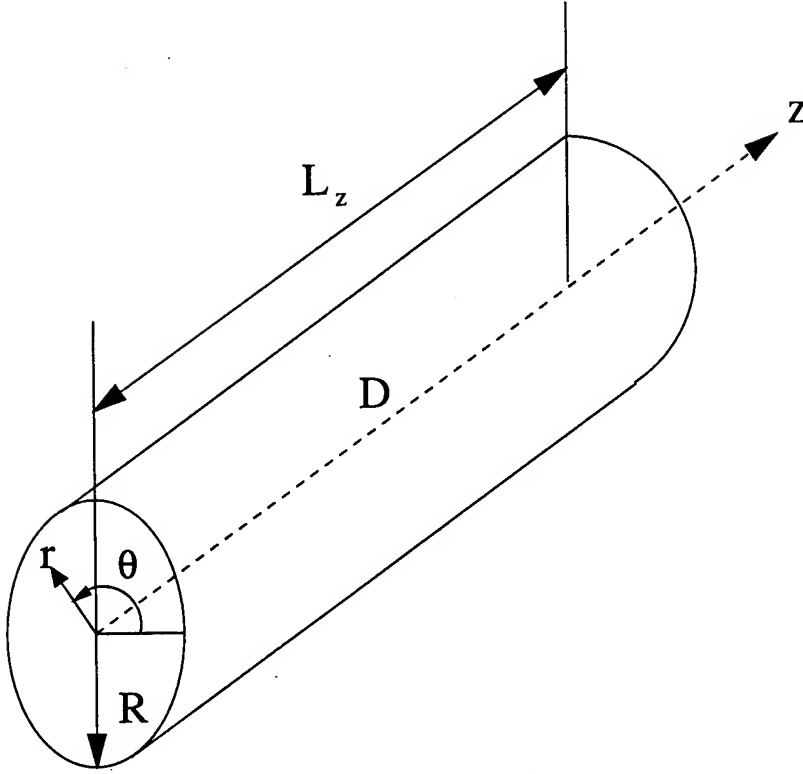


Figure 1. The coordinate system and the computational domain.

Upon applying a spatial filter to the above, assuming that the filter commutes with differentiation, we get the governing equations for LES

$$\vec{\nabla} \cdot \vec{u} = 0 \quad (3)$$

$$\frac{\partial \vec{u}}{\partial t} + \vec{u} \cdot \vec{\nabla} \vec{u} + \vec{\nabla} \bar{p} = \frac{1}{Re} \vec{\nabla} \cdot \vec{\nabla} \vec{u} + \vec{T}, \quad (4)$$

where the overbar denotes the filtering operation and $\vec{T} = -(\overline{\vec{u} \cdot \vec{\nabla} \vec{u}} - \vec{u} \cdot \vec{\nabla} \vec{u}) = -\vec{\nabla} \cdot (\overline{\vec{u} \vec{u}} - \vec{u} \vec{u})$ is minus the divergence of the SGS stress.

Now we can use the identity $\vec{u} \cdot \vec{\nabla} \vec{u} = -\vec{u} \times \vec{\omega} + \frac{\vec{\nabla}(\vec{u} \cdot \vec{u})}{2}$ to write the filtered momentum equation as

$$\frac{\partial \vec{u}}{\partial t} + \vec{\nabla} \bar{P} = \vec{u} \times \vec{\omega} + \frac{1}{Re} \vec{\nabla} \cdot \vec{\nabla} \vec{u} + \vec{T}, \quad (5)$$

where $\vec{\omega} = \vec{\nabla} \times \vec{u}$ is the filtered vorticity and $\bar{P} = \bar{p} + \frac{\vec{u} \cdot \vec{u}}{2}$ is the modified pressure.

3. Numerical Method

The vortex under consideration is time developing and, therefore, homogeneous in the axial (z) direction. This corresponds to a vortex far downstream, under the approximation that the flow changes slowly in the streamwise direction. Also, the azimuthal direction is naturally periodic. This enables the use of a Fourier spectral method in the streamwise and azimuthal directions. Basis spline polynomials (b-splines) are used in the radial direction. These provide spectral-like accuracy and are C^{k-2} continuous, where k is the order of the splines being used. Also, since b-splines have local support on a given interval (see figure 2), they lead to sparse matrices that can be efficiently stored and solved.

Loulou (1996) developed a computer program to study turbulent pipe flow that solves the incompressible Navier-Stokes equations in cylindrical coordinates using a Galerkin formulation with a Fourier spectral method in z and θ and a b-spline method in r . The program was modified by Qin (Qin *et al.* 1998) to solve the vortex problem and to run on an IBM SP2 parallel computer. This code has been further modified to perform large eddy simulations of a turbulent axial vortex using the dynamic SGS model which is implemented using the approach described below.

Before solving the filtered Navier-Stokes equations, they are transformed to a form that is better suited to numerical computation. Let \vec{v} be a numerical approximation to \vec{u} that consists of a truncated expression in terms of divergence free vector functions (Moser *et al.* (1983)). Thus equation (3) drops out by construction. Also, let $\vec{\xi}$ be any vector function representable by an additional set of divergence free vector functions such that it is homogeneous at the domain boundary. Now the standard weighted residual technique is used, with $\vec{\xi}$ as the weight function, to get the weak form of the Navier-Stokes equation

$$(\vec{\xi}, \frac{\partial \vec{v}}{\partial t}) = \frac{1}{Re} (\vec{\xi}, (\vec{\nabla} \cdot \vec{\nabla} \vec{v})) + (\vec{\xi}, (\vec{v} \times \vec{\omega})) + (\vec{\xi}, \vec{T}), \quad (6)$$

where $(\vec{a}, \vec{b}) = \int_D \vec{a} \cdot \vec{b} dV$ is an inner product. $\vec{\xi}$ being divergence free and homogeneous at the boundary results in the pressure term dropping out.

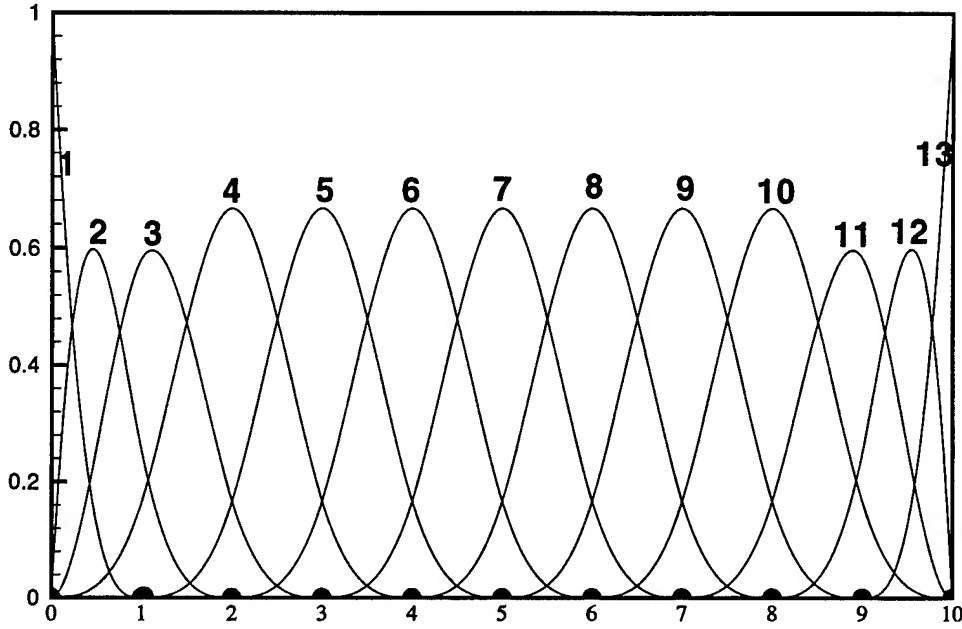


Figure 2. Cubic B-splines on an 11-knot uniform grid

The continuity constraint results in the velocity vector having only two independent components. Hence two distinct classes of divergence free vectors are required to represent \vec{v} . For the current problem, since homogeneity is assumed in the streamwise direction and the azimuthal direction is periodic, \vec{v} is represented as

$$\vec{v} = \sum_{jml} [\alpha_{jml}^+(t) \vec{u}_l^+(r, k_\theta, k_z) + \alpha_{jml}^-(t) \vec{u}_l^-(r, k_\theta, k_z)] e^{i(k_\theta \theta + k_z z)}, \quad (7)$$

where α^\pm are the expansion coefficients, $k_z = 2\pi m/L_z$ ($-N_z/2 \leq m \leq N_z/2 - 1$) are the streamwise wave numbers, $k_\theta = j$ ($-N_\theta/2 \leq j \leq N_\theta/2 - 1$) are the azimuthal wave numbers and \vec{u}_l^\pm ($1 \leq l \leq N_r$) are the expansion vectors. Since a Galerkin formulation is used, the weight functions are essentially the same as the expansion functions used to represent the velocity.

Upon using the expansion and weight functions chosen and performing the required integrations, a system of ODEs is obtained for the expansion coefficients. For details regarding the above, and the treatment of the linear

viscous term, the reader is directed to Loulou (1996) and Qin (1998). The present work focuses on computing the non-linear terms.

4. Non-Linear Terms

The following two non-linear terms have to be evaluated

$$f_{nl_1}^{\pm} = \frac{1}{2\pi L_z} \int_0^{L_z} \int_0^{2\pi} \int_0^{R_2} w_{\mu}^{\pm} (\vec{v} \times \vec{\omega}) e^{-i(k'_\theta \theta + k'_z z)} r dr d\theta dz \quad (8)$$

$$f_{nl_2}^{\pm} = \frac{1}{2\pi L_z} \int_0^{L_z} \int_0^{2\pi} \int_0^{R_2} w_{\mu}^{\pm} \cdot \vec{T} e^{-i(k'_\theta \theta + k'_z z)} r dr d\theta dz \quad (9)$$

The first term, $f_{nl_1}^{\pm}$, is present in the original DNS formulation and is computed using a pseudo-spectral approach. Fast Fourier transforms are used to compute the product $w_{\mu}^{\pm} (\vec{v} \times \vec{\omega})$ in physical space. The vorticity is directly related to the velocity, and so can be determined from the velocity expansion. The integrals in the radial direction, involving triple products of b-spline functions, are computed to machine accuracy using Gaussian quadrature. The final result is obtained by using the Fourier transform. For a complete description see Loulou (1996).

A similar approach cannot be used for $f_{nl_2}^{\pm}$, the nonlinear term arising from using an SGS model (eddy viscosity times the resolved strain rate). The eddy viscosity cannot be expressed in terms of the expansion of the velocity field as the vorticity can. One approach is to compute the eddy viscosity in physical space using a pseudo-spectral approach. Once defined in physical space, the eddy viscosity can be expanded in terms of b-spline functions, but with coefficients that are not directly related to the velocity field. Unfortunately, this leads to a large set of additional integrals involving triple products of b-spline functions, which would greatly increase the cost of the simulation.

An alternate approach is to compute the entire SGS term, \vec{T} , in physical space and to express this quantity in terms of a b-spline expansion. This leads to four integrals involving double products of b-splines. Two of these already are part of the formulation of the other terms in the weak form of the Navier-Stokes equation and are computed in the original code using Gaussian quadrature. This approach thus leads to only two additional integrations. This is the approach chosen, and is implemented in the following steps.

4.1. STEP 1

We start by computing the resolved strain rate tensor. In cylindrical coordinates this is given by

$$\begin{aligned}\bar{S}_{rr} &= \frac{\partial \bar{v}_r}{\partial r}, \quad \bar{S}_{r\theta} = \frac{1}{2} \left(\frac{1}{r} \frac{\partial \bar{v}_r}{\partial \theta} + \frac{\partial \bar{v}_\theta}{\partial r} - \frac{\bar{v}_\theta}{r} \right), \quad \bar{S}_{rz} = \frac{1}{2} \left(\frac{\partial \bar{v}_z}{\partial r} + \frac{\partial \bar{v}_r}{\partial z} \right) \\ \bar{S}_{\theta\theta} &= \left(\frac{1}{r} \frac{\partial \bar{v}_\theta}{\partial \theta} + \frac{\bar{v}_r}{r} \right), \quad \bar{S}_{\theta z} = \frac{1}{2} \left(\frac{\partial \bar{v}_\theta}{\partial z} + \frac{1}{r} \frac{\partial \bar{v}_z}{\partial \theta} \right), \quad \bar{S}_{zz} = \frac{\partial \bar{v}_z}{\partial z}\end{aligned}\quad (10)$$

The velocity components are computed as

$$\begin{aligned}\bar{v}_r(r, \theta, z, t) &= K_l g_l(r) \\ \bar{v}_\theta(r, \theta, z, t) &= J_l r g_l'(r) + I_l g_l(r) \\ \bar{v}_z(r, \theta, z, t) &= -G_l g_l'(r) - F_l \frac{g_l(r)}{r}\end{aligned}\quad (11)$$

where g_l are the b-spline polynomials (see figure 2) and the summation convention is used for repeated indices. K_l, J_l, I_l, G_l and F_l are functions of (θ, z, t) and are defined in Loulou (1996), for example

$$F_l(\theta, z, t) = \sum_{k_\theta, k_z} (k_\theta - 1) \alpha_l^-(t) e^{i(k_\theta \theta + k_z z)} \quad (12)$$

Expressions for the derivatives of the velocity components can be obtained by differentiating the relations given in (11). At the origin, a transformation to the Cartesian coordinate system is used to handle the singularity problems.

4.2. STEP 2

Next the eddy viscosity, ν_T , is computed using the Smagorinsky model

$$\nu_T = C(\Delta_f)^2 \bar{S}_M \quad (13)$$

where,

$$\bar{S}_M = (2\bar{S}_{mn}\bar{S}_{nm})^{1/2}$$

and

$$\Delta_f = (r\Delta\theta\Delta z)^{1/2}$$

is the filter width. The coefficient C is found using the dynamic procedure (Germano *et al.* (1991)) and is given by

$$C = \frac{\langle (\widehat{\bar{u}_i \bar{u}_j} - \widehat{\bar{u}_i} \widehat{\bar{u}_j}) M_{ij} \rangle}{\langle M_{ij} M_{ij} \rangle}$$

where,

$$M_{ij} = -2\widehat{\Delta}_f^2 \widehat{\overline{S}_M}(\widehat{\overline{S}_{ij}}) + 2\Delta_f^2 \widehat{\overline{S}_M}(\widehat{\overline{S}_{ij}})$$

Here the hat denotes test filtering with the test filter width $\widehat{\Delta}_f$ and $\langle \rangle$ denotes averaging over the homogeneous directions. Note that test filtering is performed only in the z and θ directions, which is analogous to the approach used in LES of channel flows where the test filter is applied in planes parallel to the wall. A sharp cut off filter is used in (k_θ, k_z) wave space.

4.3. STEP 3

The SGS stress tensor is computed as

$$\begin{aligned} T_{rr} &= 2\nu_T \overline{S}_{rr}, & T_{r\theta} &= 2\nu_T \overline{S}_{r\theta}, & T_{rz} &= 2\nu_T \overline{S}_{rz} \\ T_{\theta\theta} &= 2\nu_T \overline{S}_{\theta\theta}, & T_{\theta z} &= 2\nu_T \overline{S}_{\theta z}, & T_{zz} &= 2\nu_T \overline{S}_{zz} \end{aligned} \quad (14)$$

where the resolved scale strain rates are given in equation(10). The isotropic part of the SGS stress tensor is absorbed in the modified pressure term.

4.4. STEP 4

The SGS term \overrightarrow{T} is now put together as

$$\overrightarrow{T} = [T_r, T_\theta, T_z], \quad (15)$$

where

$$\begin{aligned} T_r &= \frac{\partial(T_{zr})}{\partial z} + \frac{1}{r} \frac{\partial(rT_{rr})}{\partial r} + \frac{1}{r} \frac{\partial(T_{r\theta})}{\partial \theta} - \frac{1}{r} (T_{\theta\theta}) \\ T_\theta &= \frac{\partial(T_{z\theta})}{\partial z} + \frac{1}{r} \frac{\partial(rT_{\theta r})}{\partial r} + \frac{1}{r} \frac{\partial(T_{\theta\theta})}{\partial \theta} + \frac{1}{r} (T_{r\theta}) \\ T_z &= \frac{\partial(T_{zz})}{\partial z} + \frac{1}{r} \frac{\partial(rT_{zr})}{\partial r} + \frac{1}{r} \frac{\partial(T_{z\theta})}{\partial \theta} \end{aligned}$$

Here derivatives in the θ and z directions are evaluated using FFTs while derivatives in the r direction are evaluated using b-splines. At the origin, a transformation to the Cartesian coordinate system is used to handle singularity problems.

4.5. STEP 5

The SGS term is expanded in terms of b-splines as

$$\vec{T} = [T_r, T_\theta, T_z] = \sum_{k=1}^{N_r} [a_k, b_k, c_k] g_k(r), \quad (16)$$

4.6. STEP 6

Upon performing the inner product operation on the b-spline representation of the SGS stress, we get the nonlinear term $f_{nl_2}^\pm$ as

For $k_z = k_\theta = 0$:

$$\begin{aligned} f_{nl_2}^+ &= \frac{1}{2\pi L_z} \int_0^{L_z} \int_0^{2\pi} \left[\sum_{k=1}^{N_r} b_k m_3 \right] e^{-i(k'_\theta \theta + k'_z z)} d\theta dz \\ f_{nl_2}^- &= \frac{1}{2\pi L_z} \int_0^{L_z} \int_0^{2\pi} \left[\sum_{k=1}^{N_r} c_k m_{15} \right] e^{-i(k'_\theta \theta + k'_z z)} d\theta dz \end{aligned} \quad (17)$$

For $k_z = 0, k_\theta > 0$:

$$\begin{aligned} f_{nl_2}^+ &= ik_\theta \frac{1}{2\pi L_z} \int_0^{L_z} \int_0^{2\pi} \left[\sum_{k=1}^{N_r} a_k m_3 \right] e^{-i(k'_\theta \theta + k'_z z)} d\theta dz \\ &\quad + \frac{1}{2\pi L_z} \int_0^{L_z} \int_0^{2\pi} \left[\sum_{k=1}^{N_r} b_k m_3 \right] e^{-i(k'_\theta \theta + k'_z z)} d\theta dz \\ &\quad + \frac{1}{2\pi L_z} \int_0^{L_z} \int_0^{2\pi} \left[\sum_{k=1}^{N_r} b_k m_6 \right] e^{-i(k'_\theta \theta + k'_z z)} d\theta dz \\ f_{nl_2}^- &= \frac{1}{2\pi L_z} \int_0^{L_z} \int_0^{2\pi} \left[\sum_{k=1}^{N_r} c_k m_{16} \right] e^{-i(k'_\theta \theta + k'_z z)} d\theta dz \\ &\quad + (1 - k_\theta) \frac{1}{2\pi L_z} \int_0^{L_z} \int_0^{2\pi} \left[\sum_{k=1}^{N_r} c_k m_{15} \right] e^{-i(k'_\theta \theta + k'_z z)} d\theta dz \end{aligned} \quad (18)$$

For $k_z \neq 0, k_\theta = 0$:

$$\begin{aligned} f_{nl_2}^+ &= k_z \frac{1}{2\pi L_z} \int_0^{L_z} \int_0^{2\pi} \left[\sum_{k=1}^{N_r} b_k m_3 \right] e^{-i(k'_\theta \theta + k'_z z)} d\theta dz \\ f_{nl_2}^- &= ik_z \frac{1}{2\pi L_z} \int_0^{L_z} \int_0^{2\pi} \left[\sum_{k=1}^{N_r} a_k m_3 \right] e^{-i(k'_\theta \theta + k'_z z)} d\theta dz \\ &\quad + k_z \frac{1}{2\pi L_z} \int_0^{L_z} \int_0^{2\pi} \left[\sum_{k=1}^{N_r} b_k m_3 \right] e^{-i(k'_\theta \theta + k'_z z)} d\theta dz \end{aligned}$$

$$\begin{aligned}
& + \frac{1}{2\pi L_z} \int_0^{L_z} \int_0^{2\pi} \left[\sum_{k=1}^{N_r} c_k m_{15} \right] e^{-i(k'_\theta \theta + k'_z z)} d\theta dz \\
& + \frac{1}{2\pi L_z} \int_0^{L_z} \int_0^{2\pi} \left[\sum_{k=1}^{N_r} c_k m_{16} \right] e^{-i(k'_\theta \theta + k'_z z)} d\theta dz \quad (19)
\end{aligned}$$

For $k_z \neq 0$, $k_\theta > 0$:

$$\begin{aligned}
f_{nl_2}^+ &= ik_\theta k_z \frac{1}{2\pi L_z} \int_0^{L_z} \int_0^{2\pi} \left[\sum_{k=1}^{N_r} a_k m_3 \right] e^{-i(k'_\theta \theta + k'_z z)} d\theta dz \\
& + k_z \frac{1}{2\pi L_z} \int_0^{L_z} \int_0^{2\pi} \left[\sum_{k=1}^{N_r} b_k m_3 \right] e^{-i(k'_\theta \theta + k'_z z)} d\theta dz \\
& + k_z \frac{1}{2\pi L_z} \int_0^{L_z} \int_0^{2\pi} \left[\sum_{k=1}^{N_r} b_k m_6 \right] e^{-i(k'_\theta \theta + k'_z z)} d\theta dz \\
f_{nl_2}^- &= ik_z \frac{1}{2\pi L_z} \int_0^{L_z} \int_0^{2\pi} \left[\sum_{k=1}^{N_r} a_k m_3 \right] e^{-i(k'_\theta \theta + k'_z z)} d\theta dz \\
& + k_z \frac{1}{2\pi L_z} \int_0^{L_z} \int_0^{2\pi} \left[\sum_{k=1}^{N_r} b_k m_3 \right] e^{-i(k'_\theta \theta + k'_z z)} d\theta dz \\
& + \frac{1}{2\pi L_z} \int_0^{L_z} \int_0^{2\pi} \left[\sum_{k=1}^{N_r} c_k m_{16} \right] e^{-i(k'_\theta \theta + k'_z z)} d\theta dz \\
& + (1 - k_\theta) \frac{1}{2\pi L_z} \int_0^{L_z} \int_0^{2\pi} \left[\sum_{k=1}^{N_r} c_k m_{15} \right] e^{-i(k'_\theta \theta + k'_z z)} d\theta dz \quad (20)
\end{aligned}$$

Here m_3, m_6, m_{15} and m_{16} are elemental matrices defined as

$$\begin{aligned}
m_3 &= \int_0^R g_l g_k r dr, \quad m_6 = \int_0^R g'_l g_k r^2 dr \\
m_{15} &= \int_0^R g_l g_k dr, \quad m_{16} = \int_0^R g'_l g_k r dr \quad (21)
\end{aligned}$$

m_3 and m_6 are already being computed in the original code. m_{15} and m_{16} are the two additional integrations added into the code. These integrals are computed to machine accuracy using Gaussian quadrature. The following are computed in physical space

$$\begin{aligned}
I_1 &= \sum_{k=1}^{N_r} a_k m_3, \quad I_2 = \sum_{k=1}^{N_r} b_k m_3, \quad I_3 = \sum_{k=1}^{N_r} c_k m_{15} \\
I_4 &= \sum_{k=1}^{N_r} c_k m_{16}, \quad I_5 = \sum_{k=1}^{N_r} b_k m_6 \quad (22)
\end{aligned}$$

Now, since $\frac{1}{2\pi L_z} \int_0^{L_z} \int_0^{2\pi} (\dots) e^{-i(k'_\theta \theta + k'_z z)}$ is the definition of a Fourier transform, I_1 through I_5 are transformed to wave space using FFTs to obtain $\hat{I}_1(k_\theta, k_z)$ through $\hat{I}_5(k_\theta, k_z)$ and $f_{nl_2}^\pm$ is obtained in wave space as

For $k_z = k_\theta = 0$:

$$\begin{aligned} f_{nl_2}^+ &= \hat{I}_2 \\ f_{nl_2}^- &= \hat{I}_3 \end{aligned} \quad (23)$$

For $k_z = 0, k_\theta > 0$:

$$\begin{aligned} f_{nl_2}^+ &= ik_\theta \hat{I}_1 + \hat{I}_2 + \hat{I}_5 \\ f_{nl_2}^- &= \hat{I}_4 + (1 - k_\theta) \hat{I}_3 \end{aligned} \quad (24)$$

For $k_z \neq 0, k_\theta = 0$:

$$\begin{aligned} f_{nl_2}^+ &= k_z \hat{I}_2 \\ f_{nl_2}^- &= ik_z \hat{I}_1 + k_z \hat{I}_2 + \hat{I}_3 + \hat{I}_4 \end{aligned} \quad (25)$$

For $k_z \neq 0, k_\theta > 0$:

$$\begin{aligned} f_{nl_2}^+ &= ik_\theta k_z \hat{I}_1 + k_z \hat{I}_2 + k_z \hat{I}_5 \\ f_{nl_2}^- &= ik_z \hat{I}_1 + k_z \hat{I}_2 + \hat{I}_4 + (1 - k_\theta) \hat{I}_3 \end{aligned} \quad (26)$$

5. Conclusions

The dynamic SGS model has been implemented into a b-spline/Fourier spectral code. Since the eddy viscosity cannot be expressed in terms of the expansion of the velocity field, as the vorticity can, the new non-linear term arising from using the SGS model cannot be obtained exactly within the framework of a Galerkin formulation. A pseudo spectral approach is taken in which the entire SGS term is computed in physical space and expressed in terms of a b-spline expansion. This leads to four integrals involving double products of b-splines, two of which already are part of the formulation of the other terms in the weak form of the Navier-Stokes equation and are computed in the original code. Only two additional integrations are thus required to be performed. This approach is much more efficient computationally in comparison to an alternate approach which would involve expanding just the eddy viscosity in terms of b-spline functions.

An LES of a turbulent axial vortex is currently under progress. The case parameters are chosen to be the same as STRN2 in Qin (1998). This

simulation serves the purposes of code validation and an evaluation of the quality of LES results. This shall be followed by large eddy simulations of a turbulent axial vortex at higher Reynolds numbers. This will allow the effects of varying Reynolds numbers to be studied and provide much needed data for the improvement of turbulence models for strongly rotating flows.

References

- Blaisdell, G.A. and Qin, J.H. (1999) Numerical simulation of a strained turbulent axial vortex, to be presented at the *First International Symposium on Turbulence and Shear Flow Phenomenon*, Santa Barbara, CA, September 12-15 1999.
- Coppens, F. (1998) Simulations Numeriques Sur Le Developpement De La Turbulence Dans Un Tourbillon *Ph.D. thesis, L'Institut Polytechnique De Toulouse, 3 June 1998*.
- Devenport, W.J., Rife, M.C., Liapis, S.I. and Follin, G.J. (1996) The structure and development of a wing-tip vortex, *J. Fluid Mech.* Vol. no. 312, pp. 67-106.
- Germano, M., Piomelli, U., Moin, P. and Cabot, W. (1991) A dynamic subgrid scale eddy-viscosity model *Physics of Fluids* Vol. no. 3, pp. 1760-1765.
- Leweke, T. and Williamson, C.H.K. (1998) Cooperative elliptic instability of a vortex pair *J. Fluid Mech.* Vol. no. 360, pp. 85-119.
- Loulou, P. (1996) Direct Numerical Simulation of Incompressible Pipe Flow Using a B-spline Spectral Method *Ph.D. thesis, Department of Aeronautics and Astronautics, Stanford University, June 1996*.
- Moser, R.D., Moin, P. and Leonard, A. (1983) A spectral numerical method for the Navier-Stokes equations with applications to Taylor-Couette flow *J. Comp. Phys.* Vol. no. 52(3), pp. 524-544.
- Orlandi, P., Carnevale, G.F., Lele, S.K. and Shariff, K. (1998) DNS study of stability of trailing vortices *Center for Turbulence Research, Proceedings of the Summer Program 1998*
- Qin, J.H. (1998) Numerical Simulations of a Turbulent Axial Vortex *Ph.D. thesis, Department of Aeronautics and Astronautics, Purdue University, December 1998*.
- Qin, J.H. and Blaisdell, G.A. (1998) Numerical simulation of a turbulent axial vortex, *American Physical Society/Division of Fluid Dynamics meeting, Philadelphia, PA, November 22-24 1998*.
- Ragab, S.A. and Sreedhar, M.K. (1995) Numerical simulation of vortices with axial velocity deficits, *Phys. Fluids.* Vol. no. 7, pp. 549-558.

LARGE EDDY SIMULATION OF SCALAR TRANSPORT IN A TURBULENT JET FLOW

S.C. GARRICK

*Department of Mechanical Engineering
University of Minnesota
Minneapolis, MN 55455-0111*

AND

F.A. JABERI AND P. GIVI

*Department of Mechanical & Aerospace Engineering
State University of New York - Buffalo
Buffalo, NY 14260-4400*

1. Introduction

Large eddy simulation (LES) of turbulent reacting flows has been the subject of widespread investigation (McMurtry *et al.*, 1992; Galperin and Orszag, 1993; Menon *et al.*, 1993; McMurtry *et al.*, 1993; Gao and O'Brien, 1993; Madnia and Givi, 1993; Frankel *et al.*, 1993; Cook and Riley, 1994; Givi, 1994; Fureby and Lofstrom, 1994; Möller *et al.*, 1996; Branley and Jones, 1997; Cook *et al.*, 1997; Jiménez *et al.*, 1997; Mathey and Chollet, 1997; Colucci *et al.*, 1998; DesJardin and Frankel, 1998; Jaber and James, 1998; Réveillon and Vervisch, 1998; Vervisch and Poinso, 1988). Amongst these, recently Colucci *et al.* (1998) developed a methodology, termed the "filtered density function" (FDF). The fundamental property of the FDF is to account for the effects of subgrid scale (SGS) scalar fluctuations in a probabilistic manner. This is similar to probability density function (PDF) methods which have proven to be very useful in Reynolds averaging procedures (Libby and Williams, 1980; Libby and Williams, 1994; O'Brien, 1980; Pope, 1985; Dopazo, 1994). Colucci *et al.* (1998) developed a transport equation for the FDF in constant density flows in which the effects of unresolved convection and subgrid mixing are modeled similarly to those in "conventional" LES, and Reynolds averaging procedures. This transport equation was solved numerically by a Lagrangian Monte Carlo

procedure and the results were compared with those obtained by direct numerical simulation (DNS) and by a conventional finite difference LES in which the effects of SGS scalar fluctuations are ignored (LES-FD). It was shown that in non-reacting flows, the first two SGS moments of the FDF, as obtained by the Monte Carlo solution, are close to those obtained by LES-FD. The advantage of the FDF was demonstrated in reacting flows in which its results were shown to deviate significantly from those obtained by LES-FD but compare favorably with DNS data. The encouraging results generated by FDF warrant its extension and application to more complex flows. Further assessment of its predictive capability is also in order. The primary objective in this work is to extend the FDF methodology for LES of three-dimensional (3D) turbulent reacting jet flows. The FDF deals only with scalar quantities; the hydrodynamic field is obtained via conventional LES.

2. Formulation

We consider constant density turbulent reacting jet flows involving N_s species. The primary transport variables are the velocity vector $u_i(\underline{x}, t)$, ($i = 1, 2, 3$), the fluid pressure $p(\underline{x}, t)$, and the species' mass fractions $\phi_\alpha(\underline{x}, t)$ ($\alpha = 1, 2, \dots, N_s$). These variables are governed by the conservation equations:

$$\frac{\partial u_j}{\partial x_j} = 0, \quad (1)$$

$$\frac{\partial u_i}{\partial t} + \frac{\partial u_i u_j}{\partial x_j} = -\frac{\partial p}{\partial x_i} + \frac{\partial \tau_{ij}}{\partial x_j}, \quad (2)$$

$$\frac{\partial \phi_\alpha}{\partial t} + \frac{\partial \phi_\alpha u_j}{\partial x_j} = -\frac{\partial J_j^\alpha}{\partial x_j} + \omega_\alpha, \quad (3)$$

where ω_α is the chemical source term. Assuming a Newtonian fluid and Fickian diffusion,

$$\tau_{ij} = \nu \left(\frac{\partial u_i}{\partial x_j} + \frac{\partial u_j}{\partial x_i} \right), \quad J_j^\alpha = -\Gamma \frac{\partial \phi_\alpha}{\partial x_j}, \quad (4)$$

where ν is the kinematic viscosity, $\Gamma = \frac{\nu}{Sc}$ is the molecular diffusivity and Sc is the molecular Schmidt Number. Large eddy simulation involves the use of the spatial filtering operation (Aldama, 1990; Moin, 1991)

$$\langle \phi(\underline{x}, t) \rangle_L = \int_{-\infty}^{+\infty} h_s(\underline{x} - \underline{x}') \phi(\underline{x}', t), d\underline{x}' \quad (5)$$

where $h_s(\underline{x})$ denotes the filter function of width Δ_H , and $\langle \phi(\underline{x}, t) \rangle_L$ represents the filtered value of the transport variable $\phi(\underline{x}, t)$. We consider

spatially & temporally invariant, localized and "positive" filter functions (Vreman *et al.*, 1994). The application of the filtering operation to the transport equations yields:

$$\frac{\partial \langle u_j \rangle_L}{\partial x_j} = 0 \quad (6)$$

$$\frac{\partial \langle u_i \rangle_L}{\partial t} + \frac{\partial \langle u_i \rangle_L \langle u_j \rangle_L}{\partial x_j} = -\frac{\partial \langle p \rangle_L}{\partial x_i} + \frac{\partial \langle \tau_{ij} \rangle_L}{\partial x_j} - \frac{\partial T_{ij}}{\partial x_j} \quad (7)$$

$$\frac{\partial \langle \phi_\alpha \rangle_L}{\partial t} + \frac{\partial \langle u_j \rangle_L \langle \phi_\alpha \rangle_L}{\partial x_j} = -\frac{\partial \langle J_j^\alpha \rangle_L}{\partial x_j} - \frac{\partial M_j^\alpha}{\partial x_j} + \langle \omega_\alpha \rangle_L \quad (8)$$

where $T_{ij} = \langle u_i u_j \rangle_L - \langle u_i \rangle_L \langle u_j \rangle_L$ and $M_j^\alpha = \langle u_j \phi_\alpha \rangle_L - \langle u_j \rangle_L \langle \phi_\alpha \rangle_L$ denote the SGS stress and the SGS mass flux, respectively.

The closure problem in LES of non-reacting flows is essentially one of representing the unresolved terms T_{ij} and M_j^α . In reacting flows, the problem is compounded by the presence of the chemical source term $\langle \omega_\alpha \rangle_L$, for which an additional model is required. For closure of the hydrodynamic SGS stresses, the gradient-diffusion approximation is invoked:

$$T_{ij} - (\delta_{ij}/3)T_{kk} = -2\nu_t \langle \mathcal{S}_{ij} \rangle_L \quad (9)$$

where $\langle \mathcal{S}_{ij} \rangle_L$ is the resolved strain rate tensor and ν_t is the SGS viscosity modeled via the modified kinetic energy model (MKEV) (Colucci *et al.*, 1998):

$$\nu_t = C_k \Delta_H \sqrt{|\langle u_i^* \rangle_L \langle u_i^* \rangle_L - \langle \langle u_i^* \rangle_{L'} \rangle_L \langle \langle u_i^* \rangle_{L'} \rangle_{L'}|}, \quad (10)$$

where $u_i^* = u_i - \mathcal{U}_i$ and \mathcal{U}_i is a reference velocity in the x_i direction. The subscript L' denotes the filter at the secondary level which has a characteristic size (denoted by $\Delta_{H'}$) larger than that of grid level filter. The gradient-diffusion approximation is also used for closure of the SGS mass fluxes (Eidson, 1985):

$$M_j^\alpha = -\Gamma_t \frac{\partial \langle \phi_\alpha \rangle_L}{\partial x_j} \quad (11)$$

where $\Gamma_t = \nu_t / Sc_t$, and Sc_t is the SGS Schmidt number and is assumed constant.

The filtered density function (FDF) is utilized to represent the scalars in a probabilistic manner. For the scalar array $\underline{\phi}(\underline{x}, t) = [\phi_1, \phi_2, \dots, \phi_{N_s}]$, the FDF, denoted by f_L , is defined as (Pope, 1990):

$$f_L(\underline{\psi}; \underline{x}, t) \equiv \int_{-\infty}^{+\infty} \varepsilon[\underline{\psi}, \underline{\phi}(\underline{x}', t)] h_s(\underline{x}' - \underline{x}) d\underline{x}', \quad (12)$$

$$\varepsilon[\underline{\psi}, \underline{\phi}(\underline{x}, t)] = \delta[\underline{\psi} - \underline{\phi}(\underline{x}, t)] \equiv \prod_{\alpha=1}^{N_s} \delta[\psi_\alpha - \phi_\alpha(\underline{x}, t)], \quad (13)$$

where δ denotes the delta function and $\underline{\psi}$ denotes the composition domain counterpart of the scalar vector $\underline{\phi}$. The term $\varepsilon[\underline{\phi} - \underline{\psi}(\underline{x}, t)]$ is the “fine-grained” density (Lundgren, 1967; O’Brien, 1980), and Eq. (12) states that the FDF is the spatially filtered, fine-grained density. Thus, f_L gives the density in the composition space around \underline{x} , weighted by the filter h_s . With a positive definite filter (Vreman *et al.*, 1994), f_L has all the properties of the PDF. For further development, it is useful to define the “conditional filtered value” of the variable $Q(\underline{x}, t)$ by

$$\langle Q(\underline{x}, t) | \underline{\psi} \rangle_L \equiv \frac{\int_{-\infty}^{+\infty} Q(\underline{x}', t) \varepsilon[\underline{\psi}, \underline{\phi}(\underline{x}', t)] h_s(\underline{x}' - \underline{x}) d\underline{x}'}{f_L(\underline{\psi}; \underline{x}, t)} \quad (14)$$

where $\langle \alpha | \beta \rangle_L$ denotes the filtered value of α conditioned on β . Equation (14) implies

$$\begin{aligned} (i) \quad & \text{For } Q(\underline{x}, t) = c, \quad \langle Q(\underline{x}, t) | \underline{\psi} \rangle_L = c \\ (ii) \quad & \text{For } Q(\underline{x}, t) \equiv \hat{Q}(\underline{\phi}(\underline{x}, t)), \quad \langle Q(\underline{x}, t) | \underline{\psi} \rangle_L = \hat{Q}(\underline{\psi}) \\ (iii) \quad & \text{Integral property:} \quad \langle Q(\underline{x}, t) \rangle_L = \int_{-\infty}^{+\infty} \langle Q(\underline{x}, t) | \underline{\psi} \rangle_L f_L(\underline{\psi}; \underline{x}, t) d\underline{\psi} \end{aligned} \quad (15)$$

where c is a constant, and $\hat{Q}(\underline{\phi}(\underline{x}, t)) \equiv Q(\underline{x}, t)$ denotes the case where the variable Q can be completely described by the compositional variable $\underline{\phi}(\underline{x}, t)$. These properties, in conjunction with the FDF, facilitate the calculation of the moments involving the scalar variables via integration over composition space,

$$\langle Q(\underline{x}, t) \rangle_L = \int_{-\infty}^{+\infty} \hat{Q}(\underline{\psi}) f_L(\underline{\psi}; \underline{x}, t) d\underline{\psi}. \quad (16)$$

The FDF transport equation is obtained by taking the time derivative of Eq. (12) and making use of Eq. (3):

$$\begin{aligned} \frac{\partial f_L}{\partial t} + \frac{\partial \langle u_j \rangle_L f_L}{\partial x_j} &= - \frac{\partial [\langle u_j | \underline{\psi} \rangle_L - \langle u_j \rangle_L] f_L}{\partial x_j} \\ &+ \frac{\partial}{\partial \psi_\alpha} \left[\left\langle \frac{\partial J_j^\alpha}{\partial x_j} | \underline{\psi} \right\rangle_L f_L \right] - \frac{\partial [\hat{\omega}_\alpha(\underline{\psi}) f_L]}{\partial \psi_\alpha}. \end{aligned} \quad (17)$$

This is an exact transport equation for the FDF. The last term on the RHS is due to chemical reaction and is in a closed form. The second term on the left hand side represents the filtered convection of the FDF in physical space and is also closed (provided $\langle u_i \rangle_L$ is known). The unclosed terms are the first two terms on the RHS which represents the transport of the FDF

via SGS convection and the effects of diffusion in composition space. The SGS convective flux is modeled via the gradient-diffusion approximation,

$$[\langle u_j | \psi \rangle_L - \langle u_j \rangle_L] f_L = -\Gamma_t \frac{\partial f_L}{\partial x_j}. \quad (18)$$

The closure for the conditional SGS diffusion is based on the linear mean square estimation (LMSE) model (O'Brien, 1980), which is also known as the interaction by exchange with the mean, or the IEM model (Borghi, 1988). Implementation of this model together with Eq. (18) yields the modeled FDF transport equation:

$$\begin{aligned} \frac{\partial f_L}{\partial t} + \frac{\partial [\langle u_i \rangle_L f_L]}{\partial x_i} &= \frac{\partial}{\partial x_i} \left[(\Gamma + \Gamma_t) \frac{\partial f_L}{\partial x_i} \right] \\ &+ \frac{\partial}{\partial \psi_\alpha} [\Omega_m (\psi_\alpha - \langle \phi_\alpha \rangle_L) f_L] - \frac{\partial [\hat{\omega}_\alpha(\psi) f_L]}{\partial \psi_\alpha}. \end{aligned} \quad (19)$$

In the second term on the RHS, Ω_m is the frequency of scalar mixing within the subgrid and is modeled via $\Omega_m = C_\Omega (\Gamma + \Gamma_t) / \Delta_H^2$. This equation may be integrated to obtain transport equations for the SGS moments. For example, the first moment, $\langle \phi_\alpha \rangle_L$, or the filtered mean is governed by:

$$\frac{\partial \langle \phi_\alpha \rangle_L}{\partial t} + \frac{\partial \langle u_j \rangle_L \langle \phi_\alpha \rangle_L}{\partial x_j} = \frac{\partial}{\partial x_j} \left[(\Gamma + \Gamma_t) \frac{\partial \langle \phi_\alpha \rangle_L}{\partial x_j} \right] + \langle \omega_\alpha \rangle_L, \quad (20)$$

3. Numerical Formulation

The numerical solution of the hydrodynamic and the scalar fields involves a two step explicit procedure. The first involves the advancement of the hydrodynamic variables and is accomplished via a compact finite difference scheme (Kennedy and Carpenter, 1994). The second involves the time advancement of the FDF for which a Lagrangian Monte Carlo procedure is used. This procedure is based on the idea of "equivalent systems" by considering the random process $X_i(t)$,

$$dX_i(t) = D_i(\underline{X}(t), t)dt + E^{1/2}(\underline{X}(t), t)dW_i(t), \quad (21)$$

where $D_i(\underline{X}, t)$ is the drift vector, $E(\underline{X}, t)$ is the diffusion coefficient and W_i represents the Wiener-Lévy process (Karlin and Taylor, 1981). With the equivalence:

$$E \equiv 2(\Gamma + \Gamma_t), \quad D_i \equiv \langle u_i \rangle_L + \frac{\partial (\Gamma + \Gamma_t)}{\partial x_i}. \quad (22)$$

the Fokker Planck equation corresponding to stochastic differential equation (21) becomes equivalent to the spatial transport equation of the modeled FDF equation (19).

In the numerical solution, the FDF is represented with a set of scalars $\phi_\alpha^{(n)}(\underline{X}^{(n)}(t), t)$ assigned on the particles throughout the flow-field. The location of the notional particles are given by $\underline{X}^{(n)}$ and Eq. (21) is integrated via the Euler-Maruyama scheme:

$$X_i^{(n)}(t_{k+1}) = X_i^{(n)}(t_k) + D_i^{(n)}(t_k)\Delta t + \left(E^{(n)}(t_k)\Delta t\right)^{1/2} \xi_i^{(n)}(t_k), \quad (23)$$

where $D_i^{(n)}(t_k) = D_i(\underline{X}^{(n)}(t_k), t)$, $E^{(n)}(t_k) = E(\underline{X}^{(n)}(t_k), t)$ and $\xi_i^{(n)}$ is a random variable with the standard Gaussian PDF. This scheme preserves the Markovian character of the diffusion process (Gardiner, 1990) and facilitates affordable computations. The coefficients D_i and E require the knowledge of the filtered mean velocity and the diffusivity (molecular and SGS). These are provided by the solution of Eqs. (6)-(7) by a finite difference procedure and then is interpolated to the particle location.

The scalar composition of each particle changes due to the effects of chemical reaction, and mixing (SGS and molecular). Both mechanisms are implemented deterministically and the scalars evolve according to

$$\frac{d\phi_\alpha^+}{dt} = -\Omega_m(\phi_\alpha^+ - \langle\phi_\alpha\rangle_L) + \omega_\alpha, \quad (24)$$

where ϕ_α^+ denotes the scalar value of a particle.

4. Results

Both FDF and LES-FD are employed for simulations of 3D turbulent round jets under both non-reacting and reacting conditions similar to those considered in the experiments of Shea (1977). In the nonreactive case, the configuration consists of a jet of ozone (O_3) diluted in nitrogen (N_2) issuing into a coflowing stream of N_2 . In the reacting flow, the surrounding fluid consists of nitric oxide (NO) diluted in N_2 . The chemistry is modeled via the one-step reaction of $O_3 + NO \rightarrow O_2 + NO_2$. The ratio of the reactants' concentration to that of the carrier gas is of order $\mathcal{O}(10^{-4})$. With such dilute reactants, the effects of reaction exothermicity can be neglected (Shea, 1977). In reacting flow simulations via LES-FD, the SGS scalar correlations are neglected.

The streamwise velocity at the inflow boundary is initialized with an approximate top-hat radial distribution. The initial velocity is U_o in the jet, and U_∞ in the co-flow, with a velocity ratio of $U_o/U_\infty = 4$. The Reynolds number based on the jet diameter (D) and the inner jet velocity is $Re_D =$

4,000. The space coordinates are $\underline{x} = [x, y, z]$, where x is the streamwise direction, and y & z are the radial/cross-stream directions. A mesh consisting of $101 \times 61 \times 61$ grid points in the x, y, z directions, respectively, is used to cover a domain of size $8D \times 4D \times 4D$. The ratio of the secondary filter size to the grid filter size is $\Delta_{H'}/\Delta_H = 3$. The values of the other parameters are: $Sc = 1$, $Sc_t = 0.7$, $C_k = 0.045$, $C_\Omega = 2$. No attempt was made to find the optimum, or the "dynamically" determined (Germano *et al.*, 1991; Germano, 1996) values of the model constants.

The simulation results are statistically analyzed via time averaging over 16,000 samples. In the FDF simulations, the filtered values of the scalar quantities are determined by performing local averaging. The volume from which an ensemble of particles is constructed is Δ_E^3 . By increasing Δ_E , the number of particles in the ensemble increases. This improves the statistical accuracy but increases dispersion. First, LES results of the non-reacting jet flow are considered in which the FDF simulations are conducted with $\Delta_E = 2\Delta_H$. This size facilitates the use of fewer particles while still retaining a large enough sample for reliable statistics. The instantaneous density of the number of the Monte Carlo particles is presented in Fig. 1. This figure provides a visual demonstration of the basic methodology and the flow structure, as captured by the FDF. To establish the consistency of the FDF, its results are compared with those of LES-FD. Shown in Fig. 2 are the contour plots of the filtered ozone mass fraction at planes normal to the streamwise coordinate. The results via FDF are very similar to those obtained by LES-FD; the latter contain slight numerical oscillations which are not present in the Lagrangian Monte Carlo simulations. The comparison between the filtered values as predicted by FDF and LES-FD is quantified by performing a linear regression analysis of data at all the points. This analysis yields a correlation coefficient of 0.99 between the two sets of results which indicates a very good agreement between the LES-FD and the FDF in predicting the filtered mean values.

The radial distributions of the time-averaged, filtered, normalized ozone mass fractions $\overline{\langle Y_{O_3}^* \rangle}_L = \overline{\langle Y_{O_3} \rangle}_L / \overline{\langle Y_{O_3} \rangle}_L (x = y = z = 0)$ are shown in Fig. 3. In the non-reacting case, expectedly, the FDF results agree well with those via LES-FD. Both simulations predict a similar rate of decay for the centerline values of the mass fraction as the flow evolves. In the reacting case, however, there is a significant difference between the results of the two simulations. It is noted that LES-FD predicts a much larger rate of reactant conversion in comparison with FDF. This difference is due to the neglect of the SGS scalar fluctuations in the LES-FD. This trend was observed in all the cases considered and is consistent with that observed in Reynolds-averaged simulations (Bilger, 1980). An attempt was made to compare the results with experimental data of Shea (1977). But there are

not sufficient detailed data reported in regard to the initial conditions in this experiments. Also, because of numerical concerns some of the simulation parameters are different from those considered experimentally. Work is in progress to generate DNS data for 3D, turbulent reacting jet flows with simple chemistry schemes of the type considered here. Such data are needed for further assessment of the methodology before it is implemented for simulations of more complex reacting flows.

Although the FDF methodology is presented here for isothermal, constant density, reacting flows with a simple kinetics scheme, the extension to variable density flows, with exothermic reactions imposes no serious mathematical difficulties (Jaberi *et al.*, 1999). For LES of variable density flows, it is convenient to use the filtered mass density function (FMDF), denoted by F_L , defined as

$$F_L(\underline{\psi}; \underline{x}, t) \equiv \int_{-\infty}^{+\infty} \rho(\underline{x}', t) \varepsilon[\underline{\psi}, \underline{\phi}(\underline{x}', t)] h_s(\underline{x}' - \underline{x}) d\underline{x}', \quad (25)$$

where ρ is the fluid density. The integral property of the FMDF is such that

$$\int_{-\infty}^{+\infty} F_L(\underline{\psi}; \underline{x}, t) d\underline{\psi} = \int_{-\infty}^{+\infty} \rho(\underline{x}', t) h_s(\underline{x}' - \underline{x}) d\underline{x}' = \langle \rho(\underline{x}, t) \rangle_L. \quad (26)$$

Jaberi *et al.* (1999) developed a transport equation for the FMDF and applied it for LES of several reacting flows. All the results as compared with DNS and laboratory data show significant advantages over LES-FD. With inclusion of efficient numerical integration routines for the treatment of complex chemistry mechanisms (Pope, 1997), it is conceivable that LES of reactive flows with realistic chemical kinetics may be conducted for engineering applications in the near future. In this regard, the scalar FDF methodology is attractive in that the present Monte Carlo solver can be used directly in available CFD codes. Similar to PDF methods, the closure problems associated with the FDF (and FMDF) are the correlations involving the velocity field (such as SGS stresses and mass fluxes). This may be overcome by considering the joint velocity-scalar FDF (FMDF) similar to that in PDF methods (Pope, 1994b). This issue is currently under investigation.

The computational requirement for FDF simulations with 2×10^6 particles is about 2.5 times that of LES-FD. This overhead appears tolerable in view of the attractiveness of the methodology. Also, the computational requirements for FDF is significantly less than that of DNS. But the range of flow parameters (such as the Reynolds and the Damköhler numbers) that can be considered by FDF is significantly larger than can be treated by DNS, and the results are more accurate than those by LES-FD. Colucci *et*

al. (1998) and Jaber *et al.* (1999) report a comparison of the computational requirements of LES-FD, FDF and DNS for several flow configurations. This comparison could be made only in flows for which DNS was possible, *i.e.* low Damköhler and Reynolds numbers. At higher values of these parameters, the computational cost associated with DNS would be exceedingly higher than that of FDF. Thus for practical flows for which DNS is currently impossible, the FDF would be a good alternative. Several means of reducing the FDF's computational requirements are possible and should be considered. These could be useful in future applications in complex flows. The FDF method will benefit from ongoing and future improvements in PDF and other LES schemes (Pope, 1994a; Subramaniam and Pope, 1997; Pierce and Moin, 1998) from both modeling and computational standpoints.

5. Acknowledgment

The first author acknowledges the support of HBECC Fellowship provided by the U.S. Office of Naval Research under Grant N000014-92-J-1252-NY-001. This work is part of a research program sponsored by the NASA Langley Research Center under Grant NAG-1-1122 to SUNY-Buffalo, with Dr. J. Philip Drummond serving as the Technical Monitor. Acknowledgment is also made to the Donors of the Petroleum Research Funds administered by the American Chemical Society for their support under Grant ACS-PRF 32892-AC9. Computational resources are provided by the Minnesota Supercomputing Institute, and the National Center for Supercomputing Applications at the University of Illinois at Urbana.

References

- Aldama, A. A. (1990). Filtering techniques for turbulent flow simulations. volume 49 of *Lecture Notes in Engineering*. Springer-Verlag, New York, NY.
- Bilger, R. W. (1980). Turbulent flows with nonpremixed reactants. In Libby and Williams (1980), chapter 3, pages 65–113.
- Borghi, R. (1988). Turbulent combustion modeling. *Prog. Energy Combust. Sci.* 14, 245–292.
- Branley, N. and Jones, W. P. (1997). Large eddy simulation of a turbulent non-premixed flame. In *Proceedings of the Eleventh Symposium on Turbulent Shear Flows*, pages 21.1–21.6, Grenoble, France.
- Colucci, P. J., Jaber, F. A., Givi, P., and Pope, S. B. (1998). Filtered density function for large eddy simulation of turbulent reacting flows. *Phys. Fluids* 10, 499–515.
- Cook, A. W. and Riley, J. J. (1994). A subgrid model for equilibrium chemistry in turbulent flows. *Phys. Fluids* 6, 2868–2870.
- Cook, A. W., Riley, J. J., and Kosály, G. (1997). A laminar flamelet approach to subgrid-scale chemistry in turbulent flows. *Combust. Flame* 109, 332–341.
- DesJardin, P. E. and Frankel, S. H. (1998). Large eddy simulation of a turbulent non-premixed reacting jet: Application and assessment of subgrid-scale combustion models. *Phys. Fluids* 10, 2298–2314.
- Dopazo, C. (1994). Recent developments in pdf methods. In Libby and Williams (1994),

- chapter 7, pages 375–474.
- Eidson, T. M. (1985). Numerical simulation of the turbulent rayleigh-benard problem using subgrid modelling. *J. Fluid Mech.* **158**, 245–268.
- Frankel, S. H., Adumitroaie, V., Madnia, C. K., and Givi, P. (1993). Large eddy simulations of turbulent reacting flows by assumed PDF methods. In Ragab, S. A. and Piomelli, U., editors, *Engineering Applications of Large Eddy Simulations*, pages 81–101. ASME, FED-Vol. 162, New York, NY.
- Fureby, C. and Lofstrom, C. (1994). Large-eddy simulations of bluff body stabilized flames. In *Proceedings of 25th Symp. (Int.) on Combustion*, pages 1257–1264. The Combustion Institute, Pittsburgh, PA.
- Galperin, B. and Orszag, S. A., editors. (1993). *Large Eddy Simulations of Complex Engineering and Geophysical Flows*. Cambridge University Press, Cambridge, England.
- Gao, F. and O'Brien, E. E. (1993). A large-eddy simulation scheme for turbulent reacting flows. *Phys. Fluids A* **5**, 1282–1284.
- Gardiner, C. W. (1990). *Handbook of Stochastic Methods*. Springer-Verlag, New York, NY.
- Germano, M., Piomelli, U., Moin, P., and Cabot, W. H. (1991). A dynamic subgrid-scale eddy viscosity model. *Phys. Fluids A* **3**, 1760–1765.
- Germano, M. (1996). A statistical formulation of dynamic model. *Phys. Fluids* **8**, 565–570.
- Givi, P. (1994). Spectral and random vortex methods in turbulent reacting flows. In Libby and Williams (1994), chapter 8, pages 475–572.
- Jaberi, F. A. and James, S. (1998). A dynamic similarity model for large eddy simulation of turbulent combustion. *Phys. Fluids* **10**, 1775–1777.
- Jaberi, F. A., Colucci, P. J., James, S., Givi, P., and Pope, S. B. (1999). Filtered mass density function for large eddy simulation of turbulent reacting flows. *J. Fluid Mech.* submitted.
- Jiménez, J., Liñán, A., Rogers, M. M., and Higuera, F. J. (1997). *A Priori* testing of subgrid models for chemically reacting non-premixed turbulent flows. *J. Fluid Mech.* **349**, 149–171.
- Karlin, S. and Taylor, H. M. (1981). *A Second Course in Stochastic Processes*. Academic Press, New York, NY.
- Kennedy, C. A. and Carpenter, M. H. (1994). Several new numerical methods for compressible shear-layer simulations. *Appl. Num. Math.* **14**, 397–433.
- Libby, P. A. and Williams, F. A., editors. (1980). *Turbulent Reacting Flows*, volume 44 of *Topics in Applied Physics*. Springer-Verlag, Heidelberg.
- Libby, P. A. and Williams, F. A., editors. (1994). *Turbulent Reacting Flows*. Academic Press, London, England.
- Lundgren, T. S. (1967). Distribution functions in the statistical theory of turbulence. *Phys. Fluids* **10**, 969–975.
- Madnia, C. K. and Givi, P. (1993). Direct numerical simulation and large eddy simulation of reacting homogeneous turbulence. In Galperin and Orszag (1993), chapter 15, pages 315–346.
- Mathey, F. and Chollet, J. P. (1997). Large eddy simulation of turbulent reactive flows. In *Proceedings of the Eleventh Symposium on Turbulent Shear Flows*, pages 16.19–16.24, Grenoble, France.
- McMurtry, P. A., Menon, S., and Kerstein, A. R. (1992). A linear eddy sub-grid model for turbulent reacting flows: Application to hydrogen-air combustion. In *Proceedings of 24th Symp. (Int.) on Combustion*, pages 271–278. The Combustion Institute, Pittsburgh, PA.
- McMurtry, P. A., Menon, S., and Kerstein, A. R. (1993). Linear eddy modeling of turbulent combustion. *Energy & Fuels* **7**, 817–826.
- Menon, S., McMurtry, P. A., and Kerstein, A. K. (1993). A linear eddy subgrid model of turbulent combustion. In Galperin and Orszag (1993), chapter 14, pages 287–314.
- Moin, P. (1991). Towards large eddy and direct numerical simulations of complex turbu-

- lent flows. *Computer Methods in Applied Mechanics and Engineering* **87**, 329–334.
- Möller, S. I., Lundgren, E., and Fureby, C. (1996). Large eddy simulations of unsteady combustion. In *Proceedings of 26th Symp. (Int.) on Combustion*, page 241. The Combustion Institute, Pittsburgh, PA.
- O'Brien, E. E. (1980). The probability density function (PDF) approach to reacting turbulent flows. In Libby and Williams (1980), chapter 5, pages 185–218.
- Pierce, C. D. and Moin, P. (1998). A dynamic model for subgrid-scale variance and dissipation rate of a conserved scalar. *Phys. Fluids* **10**, 3041–3044.
- Pope, S. B. (1985). PDF methods for turbulent reactive flows. *Prog. Energy Combust. Sci.* **11**, 119–192.
- Pope, S. B. (1990). Computations of turbulent combustion: Progress and challenges. In *Proceedings of 23rd Symp. (Int.) on Combustion*, pages 591–612. The Combustion Institute, Pittsburgh, PA.
- Pope, S. B. (1994a). Lagrangian pdf methods for turbulent flows. *Ann. Rev. Fluid Mech.* **26**, 23–63.
- Pope, S. B. (1994b). On the relation between stochastic Lagrangian models of turbulence and second-moment closures. *Phys. Fluids* **6**, 973–985.
- Pope, S. B. (1997). Computationally efficient implementation of combustion chemistry using *in situ* adaptive tabulation. *Combust. Theo. Modelling* **1**, 41.
- Réveillon, J. and Vervisch, L. (1998). Subgrid-scale turbulent micromixing: Dynamic approach. *AIAA J.* **36**, 336–341.
- Shea, J. R. (1977). A chemical reaction in a turbulent jet. *J. Fluid Mech.* **81**, 317–333.
- Subramaniam, S. and Pope, S. B. (1997). Comparison of PDF mixing models for non-premixed turbulent reacting flow. Technical Report FDA 97-03, Cornell University, Ithaca, NY.
- Vervisch, L. and Poinso, T. (1988). Direct numerical simulation of non-premixed turbulent flames. *Annu. Rev. Fluid Mech.* **30**, 655–691.
- Vreman, B., Geurts, B., and Kuerten, H. (1994). Realizability conditions for the turbulent stress tensor in large-eddy simulation. *J. Fluid Mech.* **278**, 351–362.

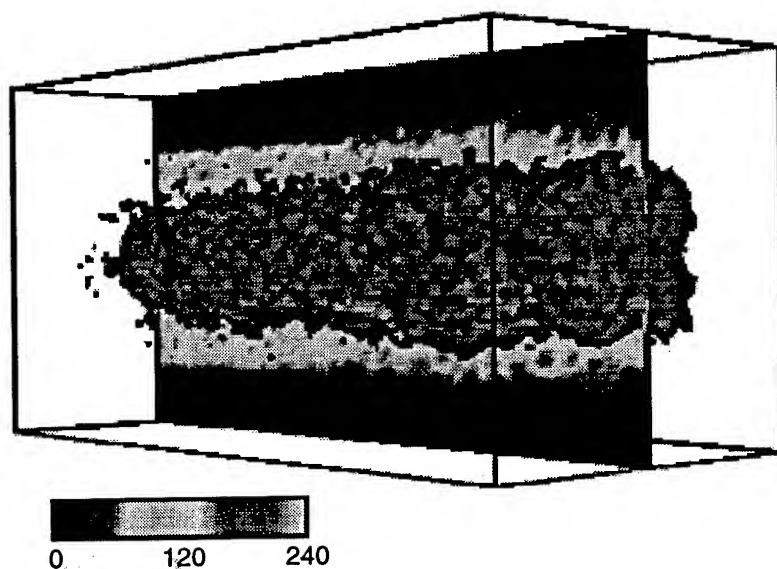


Figure 1. Monte Carlo particle number density.

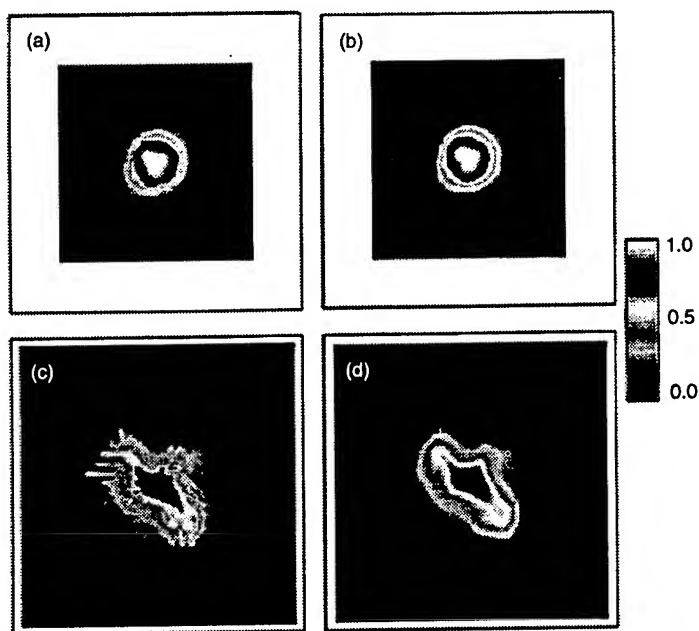


Figure 2. Instantaneous filtered mean ozone mass fraction contours at streamwise planes: (a) LES-FD, $x/D = 2.5$; (b) FDF, $x/D = 2.5$; (c) LES-FD, $x/D = 7.5$; (d) FDF, $x/D = 7.5$.

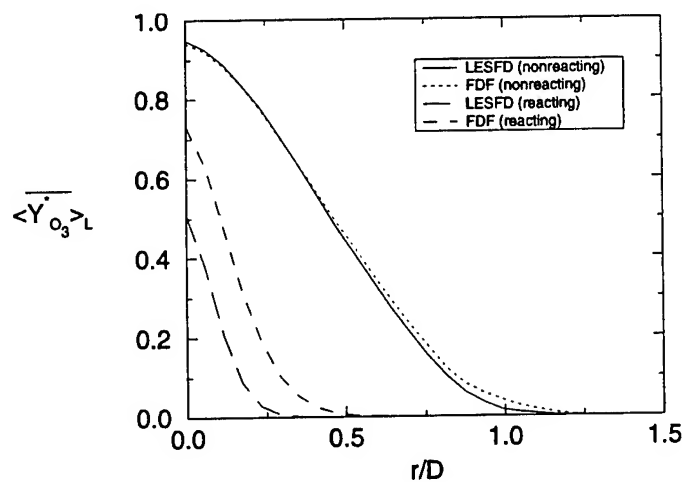


Figure 3. Time-averaged filtered mean ozone mass fraction.

DNS AND MODELING OF SPRAY TURBULENT MIXING

RAPHAËL HAUGUEL*, JULIEN RÉVEILLON* AND LUC VERVISCH⁺

* *Université de Rouen*

⁺ *Institut National des Sciences Appliquées de Rouen*

LMFN / UMR CNRS / CORIA 6614

Avenue de l'Université - BP 8

FR-76801 Saint Etienne du Rouvray Cedex, France

e-mail: reveillon@coria.fr

1. Introduction

The injection of liquid fuel is a common procedure in turbulent combustion devices operating in the non-premixed regime. In these systems, dispersion, vaporization of the fuel droplets and turbulent combustion strongly interact. The understanding and modeling of these complex phenomena are important issues when optimizing combustion processes, to improve the economical and ecological output of the device.

Various numerical models may be found in the literature to calculate turbulent flames, using either Reynolds Averaged Navier-Stokes equations (RANS) or Large Eddy Simulation (LES). The typical inputs of non-premixed turbulent combustion modeling are the mean and the fluctuations of the mixture fraction. In this paper, we study the effect on the gaseous mixture fraction of a vaporizing liquid fuel. To this end, Direct Numerical Simulation (DNS) is utilized. Previous works have shown the ability of DNS to study the dispersion of solid particles (or non-vaporizing droplets) in a turbulent environment (Elgobashi and Truesdell, 1989; Squires and Eaton, 1990). Similarly, DNS is now a standard tool for studying premixed and non-premixed single phase turbulent combustion (Givi, 1989; Poinot et al., 1996; Vervisch and Poinot, 1998).

In this work, a two way coupling (Elgobashi and Truesdell, 1992) between the droplets and the turbulent flow has been utilized to simulate 3-D homogeneous freely decaying turbulence and 2-D mixing layers. The first part of this paper presents the physical and numerical features of the study. A Lagrangian/Eulerian formulation for disperse sprays has been selected.

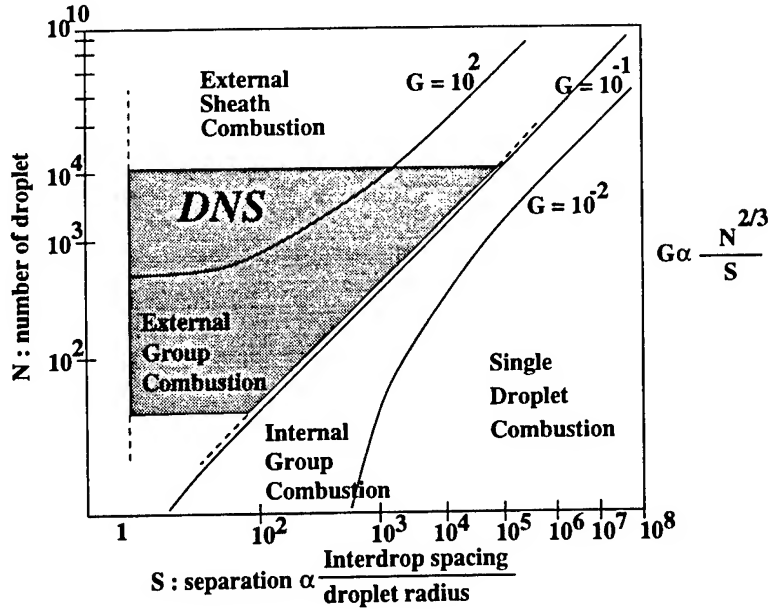


Figure 1. Classification of spray combustion regime, group combustion diagram of Chiu *et al.*

Then, a special attention is given to the effects of the vaporization source terms on the mean fluctuations of the mixture fraction.

2. Eulerian/Lagrangian formulation for DNS

Direct numerical simulation, in theory, allows for a model-free simulation, however the resources required to perform the simulation of both the turbulent gas phase motion and the detailed properties of the liquid phase are too great. In our simulations, the flows around an individual drop and inside the drop are not fully resolved. Instead, closures discussed below are introduced for the liquid phase along with its vaporization rate (Faeth, 1983; Law, 1982; Sirignano, 1983). These simulations are restricted to droplets that are smaller than the Kolmogorov length scale. Therefore, in the group combustion diagram of Chiu *et al.* (Chiu *et al.*, 1982) classifying different combustion regimes (fig. 1), the present simulations are limited to problems observed in external combustion around clusters of droplets.

The spray is composed of a collection of individual droplets convected by the turbulent flow, and it is natural to follow these droplets in a Lagrangian context. Then, two major issues emerge: the description of the droplets

themselves and their coupling with the turbulent carrier phase that is solved in an Eulerian context.

2.1. GOVERNING EQUATIONS

In the Lagrangian context, we solve for the position (X_i), the diameter (Θ), and, the velocity (V_i) of N droplets. This system (Faeth, 1983; Kuo, 1986) may be written for each k droplet as:

$$\begin{aligned}\frac{dX_i^k}{dt} &= V_i^k, \\ \frac{d(\Theta^k)^3}{dt} &= -A\dot{\omega}_v^k, \\ \frac{d(\Theta^k)^3 V_i^k}{dt} &= A(D_i^k - \dot{\omega}_v^k V_i^k),\end{aligned}$$

with the mass evaporation rate and drag force given by:

$$\begin{aligned}\dot{\omega}_v^k &= \pi S_{hc}^k \rho D^* \ln(1 + B_Y) \Theta^k, \\ D_i^k &= \frac{\pi}{8} \rho (\Theta^k)^2 C_D^k |\underline{U}^k - \underline{V}^k| (U_i^k - V_i^k),\end{aligned}$$

with $D^* = (\mu/\rho Re Sc)$. S_{hc}^k is the convective Sherwood number taking a value of 2 in a quiescent atmosphere and depending in the turbulent simulations on the Reynolds number of the droplet $Re_D^k = Re(|\underline{U}^k - \underline{V}^k| \Theta^k)/\nu$, as

$$S_{hc}^k = 2 + \frac{0.55 Re_D^k Sc}{(1.232 + Re_D^k Sc^{4/3})^{1/2}},$$

C_D^k is the drag force coefficient,

$$C_D^k = \frac{24}{Re_D^k} \left(1 + \frac{Re_D^k^{2/3}}{6} \right).$$

$A = 6/(\pi \rho_l)$ is a constant parameter in which ρ_l is the liquid constant density. The properties of the gas (μ viscosity, ρ density and U_i velocity) are obtained at the droplet position from the grid nodes using a third order interpolation algorithm (Guichard et al., 1998). These equations have been made dimensionless with Re_e as the acoustic Reynolds number of the DNS problem. Sc and Pr are the Schmidt number of the fuel and the Prandtl number, where $Pr = Sc = 0.7$.

The Spalding number is defined as $B_Y = (Y_F^s - Y_F^\infty)/(1 - Y_F^s)$, where Y_F^s and Y_F^∞ are the gaseous fuel concentrations at the surface of the drop and in the pure gas respectively (Kuo, 1986). In a first approximation B_Y is assumed constant, corresponding to situations where the temperature of the spray is close to saturation.

The Eulerian view of the Lagrangian sources is constructed by cumulating sources of all the droplets found in a particular mesh volume, \mathcal{V} defined in the vicinity of the Eulerian grid point (Crowe et al., 1977). The flow is described in the Eulerian context by solving the following equations accounting for the two-way coupling:

$$\begin{aligned} \frac{\partial \rho}{\partial t} + \frac{\partial \rho U_j}{\partial x_j} &= \frac{1}{\mathcal{V}} \sum_k \dot{\omega}_v^k, \\ \frac{\partial \rho U_i}{\partial t} + \frac{\partial \rho U_i U_j}{\partial x_j} &= -\frac{\partial P}{\partial x_i} + \frac{1}{Re} \frac{\partial \sigma_{ij}}{\partial x_j} - \frac{1}{\mathcal{V}} \sum_k (D_i^k - \dot{\omega}_v^k V_i^k), \\ \frac{\partial \rho e_t}{\partial t} + \frac{\partial \rho e_t U_j}{\partial x_j} &= -\frac{\partial p U_j}{\partial x_j} + \frac{\partial}{\partial x_i} \left(\lambda^* \frac{\partial T}{\partial x_i} \right) + \frac{1}{Re} \frac{\partial \sigma_{ij} U_j}{\partial x_i} \\ &\quad - \frac{1}{\mathcal{V}} \sum_k \left[V_i^k \left(D_i^k - \frac{1}{2} w_v^k V_i^k \right) \right], \\ \frac{\partial \rho Y_F}{\partial t} + \frac{\partial \rho Y_F U_j}{\partial x_j} &= \frac{\partial}{\partial x_i} \left(\rho D^* \frac{\partial Y_F}{\partial x_i} \right) + \frac{1}{\mathcal{V}} \sum_k w_v^k, \\ \frac{\partial \rho Y_O}{\partial t} + \frac{\partial \rho Y_O U_j}{\partial x_j} &= \frac{\partial}{\partial x_i} \left(\rho D^* \frac{\partial Y_O}{\partial x_i} \right), \end{aligned}$$

with $\lambda^* = \frac{\mu C_p}{Re Pr}$. A third order Runge-Kutta scheme with a minimal data storage method (Wray, 1990) is used for time stepping. Spatial derivatives are estimated using the sixth order Lele's PADE scheme (Lele, 1992).

2.2. DNS PARAMETERS

2.2.1. Homogeneous and Isotropic turbulence

The droplets are organized in clusters (or clouds) homogeneously embedded in a 3D freely decaying turbulence, with an initial integral length scale that is twice the mean radius of the clusters. The density of droplets is chosen to reproduce, in the mean, a near-stoichiometric dilute spray of n-heptane with the stoichiometric value $Z_{st} = 0.0625$, the spray is initially monodispersed. Table 1 summarizes the parameters used in the four different simulations, featuring various Spalding numbers and therefore different mean vaporization time. To compare the time evolution of $\widetilde{Z''^2}$ with and

TABLE 1. Parameters of the simulations ($65 \times 65 \times 65$ Eulerian nodes, 10800 droplets organized in 9 clusters): The turbulence is characterized by its integral length scale l_t , the eddy turnover time τ_t , the Kolmogorov time τ_k , and, the Reynolds number $Re_{lt} = (u' l_t / \nu) \approx (\tau_t / \tau_k)^2$. The properties of the spray are: Θ_0 the initial diameter of the droplets, B_Y the Spalding number and its related vaporization time τ_v . All the presented results are normalized using l_t and τ_t .

Case	B_Y	Θ_0/l_t	τ_t/τ_v	τ_v/τ_k	Re_{lt}
TV_G	∞	0.014	∞	0	104
TV_1	4	0.014	1.37	7.5	104
TV_2	2.7	0.014	1.18	8.66	104
TV_3	1.9	0.014	0.94	10.97	104

without droplets vaporization, a simulation with an infinite value of the Spalding number B_Y was also performed. This case corresponds to pure mixing between fuel and oxidizer, the mass of fuel being instantaneously released by the droplets at the initial time of the simulation.

2.2.2. Temporal mixing layer

A hyperbolic tangent velocity profile (fig. 3-top)

$$U(\underline{x}, t = 0) = \frac{1}{2}(S_1 + S_2) + \frac{1}{2}(S_1 - S_2) \tanh\left(\frac{2y}{\delta_0}\right)$$

has been chosen to initialize the mixing layer. S_1 and S_2 are the two stream velocities. Data are made dimensionless with the convective velocity $S_0 = (S_1 - S_2)/2$, the thickness of the mixing layer δ_0 , and, $t_0 = \delta_0/S_0$. To help in the generation of large-scale instabilities, small perturbations issued from a white noise spectrum are superimposed to this initial velocity field. The streamwise direction has periodic boundary conditions and non-reflecting boundaries are applied on the spanwise direction.

A Gaussian function centered at the position of the maximum shear is used for the droplets repartition (fig. 3-top). The mean droplet density is 8000, the droplets diameter is 0.02 and the Spalding number takes on the value 0.06, allowing to observe vaporizing droplets during the development of the instabilities.

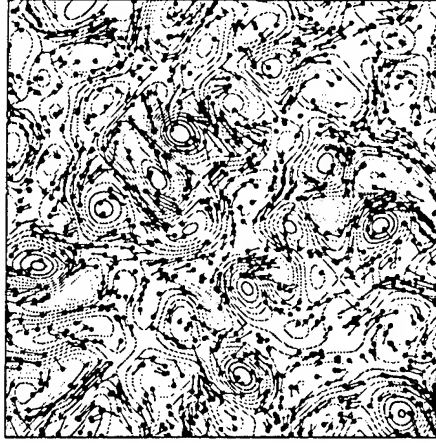


Figure 2. 2D snapshot of droplets turbulent dispersion. Isolines: isovorticity contours, vector: droplet velocity.

3. Mixture fraction analysis

3.1. MIXTURE FRACTION PROPERTIES

The mixture fraction is defined as $Z = (\Phi Y_F / Y_{F,o} - Y_O / Y_{O,o} + 1) / (\Phi + 1)$ (Linán and Williams, 1993). The mass fractions in pure fuel and pure oxidizer are denoted by $Y_{F,o}$ and $Y_{O,o}$, respectively, and the stoichiometric point is $Z_{st} = 1 / (1 + \Phi)$. The equivalence ratio of the mixture is $\Phi = (\nu_O \mathcal{M}_O Y_{F,o}) / (\nu_F \mathcal{M}_F Y_{O,o})$, with the molecular weights \mathcal{M}_O , \mathcal{M}_F and the stoichiometric coefficients ν_O , ν_F , ν_P would correspond to the chemical reaction $\nu_F Y_F + \nu_O Y_O \rightarrow \nu_P Y_P$, here only mixing between fuel and air is considered.

The transport equation for Z may be written:

$$\frac{\partial \rho Z}{\partial t} + \frac{\partial \rho Z U_j}{\partial x_j} = \frac{\partial}{\partial x_i} \left(\rho D^* \frac{\partial Z}{\partial x_i} \right) + \frac{1}{(1 + \Phi)} \left(\frac{\Phi + Y_{F,o}}{Y_{F,o}} \right) \rho \dot{W}_v ,$$

where $\rho \dot{W}_v = \frac{1}{V} \sum_k \dot{\omega}_v^k$ is the Eulerian vaporization rate. From this equation, and by setting $Y_{F,o} = 1$, the balance equation for the fluctuations $\widetilde{Z''^2}$

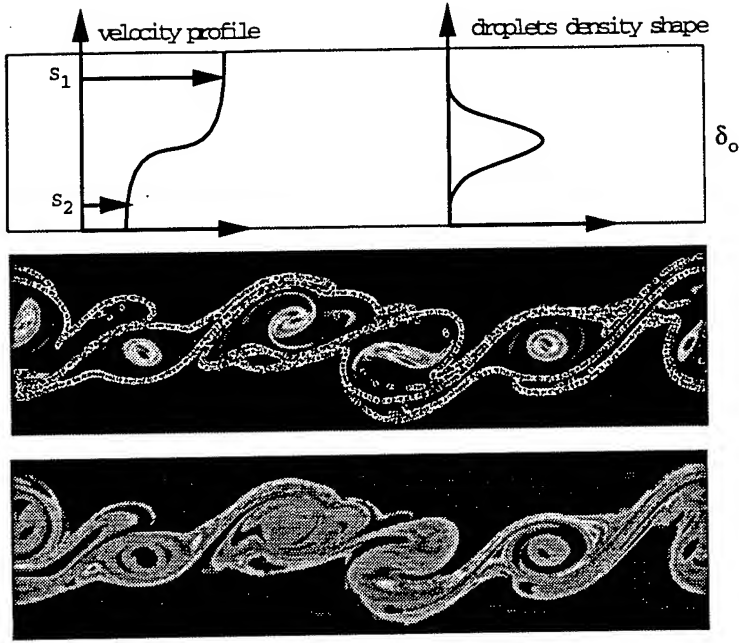


Figure 3. Temporal mixing layer, top: initial configuration, middle: isovorticity contours and droplets (*time* = 240), bottom: mixture fraction field (*time* = 240).

is derived:

$$\begin{aligned} \frac{\partial \bar{\rho} \tilde{Z}''^2}{\partial t} + \frac{\partial \bar{\rho} \tilde{Z}''^2 \tilde{U}_i}{\partial x_i} &= \overbrace{-\frac{\partial}{\partial x_i} (\bar{\rho} \tilde{Z}''^2 \tilde{U}_i'')}^{\text{Turbulent convection}} \underbrace{- 2 \bar{\rho} \tilde{Z}'' \tilde{U}_i' \frac{\partial \tilde{Z}}{\partial x_i}}_{\text{Production}} \\ &- \overbrace{2 \rho D^* \frac{\partial \tilde{Z}''}{\partial x_i} \frac{\partial \tilde{Z}''}{\partial x_i}}^{\text{Dissipation rate}} + \underbrace{2 \bar{\rho} \tilde{Z}'' \tilde{W}_v (1 - \tilde{Z}) - \bar{\rho} \tilde{Z}''^2 \tilde{W}_v}_{\text{Vaporization sources}} , \end{aligned}$$

in which the dissipation rate

$$\bar{\rho} \tilde{\chi} = \overline{\rho D^* |\nabla \tilde{Z}''|^2} ,$$

appears with two unclosed source terms directly representative of spray vaporization:

$$\bar{\rho} \tilde{S}^+ = 2 \bar{\rho} \tilde{Z}'' \tilde{W}_v (1 - \tilde{Z}) ,$$

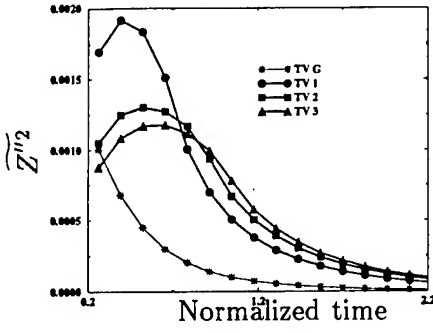


Figure 4. Time evolution of the fluctuations $\widetilde{Z''^2}$.

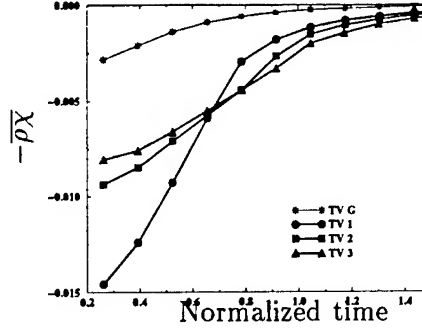


Figure 5. Time evolution of the scalar dissipation rate $\overline{\rho\chi}$.

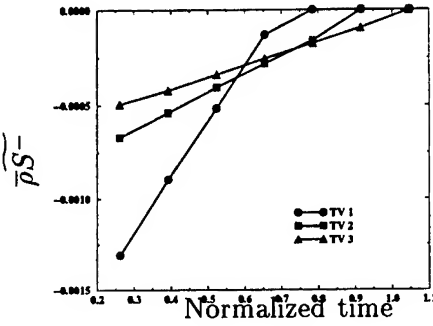


Figure 6. Time evolution of $\overline{\rho S^-}$.

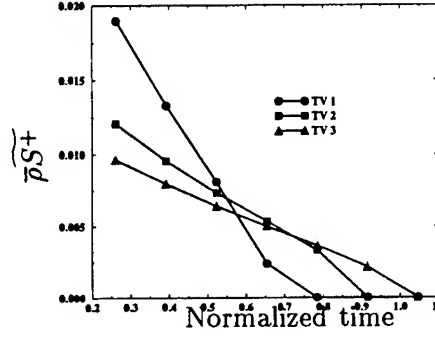


Figure 7. Time evolution of $\overline{\rho S^+}$.

and

$$\overline{\rho S^-} = -\overline{\rho Z''^2 \dot{W}_v} \quad .$$

In a previous work (Réveillon et al., 1998), it has been shown that the mean turbulent mixing time and related quantities are dramatically affected by vaporization of the liquid phase. In dilute spray, this is due to the impact of vaporization sources on the small scales of the turbulent fuel distribution. Practically speaking, because of the source of fuel localized at the surface of the drop, the value taken by $|\nabla Y_F|$ when $Y_F \rightarrow 1$, tends to be larger in the case of droplets than for a pocket of a pure diffusing gas without local source of fuel. One consequence of this is the increase in dissipation rate $\overline{\rho\chi}$ following the introduction of the spray. Using the DNS data, the time evolution of the various terms and quantities related to the fluctuations of mixture fraction are now studied.

3.2. ANALYSIS OF $\widetilde{Z''^2}$ SOURCE TERMS

When vaporization and turbulent mixing compete, for a fixed turbulent Reynolds number, different behaviors may be observed depending on the Spalding number. The vaporization of the discrete phase tends to generate fluctuations of mixture fraction, turbulent mixing in counterpart tends to reduce $\widetilde{Z''^2}$ through $\overline{\rho\chi}$. This is observed for the homogeneous flows in fig. 4, where the fluctuations of mixture fraction are first generated by the local sources of fuel, and $\widetilde{Z''^2}$ increases quickly to reach a maximum point. The value of $\widetilde{Z''^2}$ at its maximum depends on the characteristic vaporization time (fig. 4), when the shorter the vaporization time, the larger this value. After reaching this maximum, turbulent micro-mixing overcomes vaporization and an exponential-like decay representative of mixing is recovered. Since the initial total volume of liquid and Reynolds number are fixed in the simulations, the time required to vaporize all the liquid decreases when increasing B_Y , and the decay of $\widetilde{Z''^2}$, significative of an evolution controlled by fuel/air pure mixing, appears sooner. When vaporization and mixing times are of the same order (TV3), after increasing, $\widetilde{Z''^2}$ reaches a plateau before mixing dominates leading to the decay of the fluctuations.

The vaporization terms $\overline{\rho S^+}$ and $\overline{\rho S^-}$ are also extracted from DNS. In fig. 7, $\overline{\rho S^+}$ is identified as a production term, that is of the same order as the dissipation rate $\overline{\rho\chi}$. In opposition, $\overline{\rho S^-}$ is negative, small, almost negligible compared to the dissipation rate and to the source $\overline{\rho S^+}$ (fig. 6). Therefore when $\overline{\rho S^+} > \overline{\rho\chi}$, the generation of fluctuations due to vaporization dominates and $\widetilde{Z''^2}$ increases. An equilibrium condition would correspond to $\overline{\rho S^+} \approx \overline{\rho\chi}$, this is observed in fig. 4 when $\widetilde{Z''^2}$ reaches its maximum. The situation $\overline{\rho S^+} < \overline{\rho\chi}$ leads to the decay of $\widetilde{Z''^2}$. Notice that $\overline{\rho S^+} = 0$ when all the fuel is in the gas phase, this occurs before reaching the point where $\widetilde{Z''^2} = 0$, and since $\overline{\rho\chi} \rightarrow 0$ only when $\widetilde{Z''^2} = 0$, the end of the simulations is always mixing controlled.

Similar trends are observed in the mixing layer (fig. 8), and the DNS results confirm that it is difficult to neglect the effects of spray evaporation on the fluctuations of mixture fraction. In the performed simulations, for the same initial condition, different interactions are observed between the term $\overline{\rho S^+}$ and the scalar dissipation rate $\overline{\rho\chi}$. The results depend on the Spalding parameter of the spray, leading to various time evolutions of $\widetilde{Z''^2}$ during the coupled vaporization-mixing process.

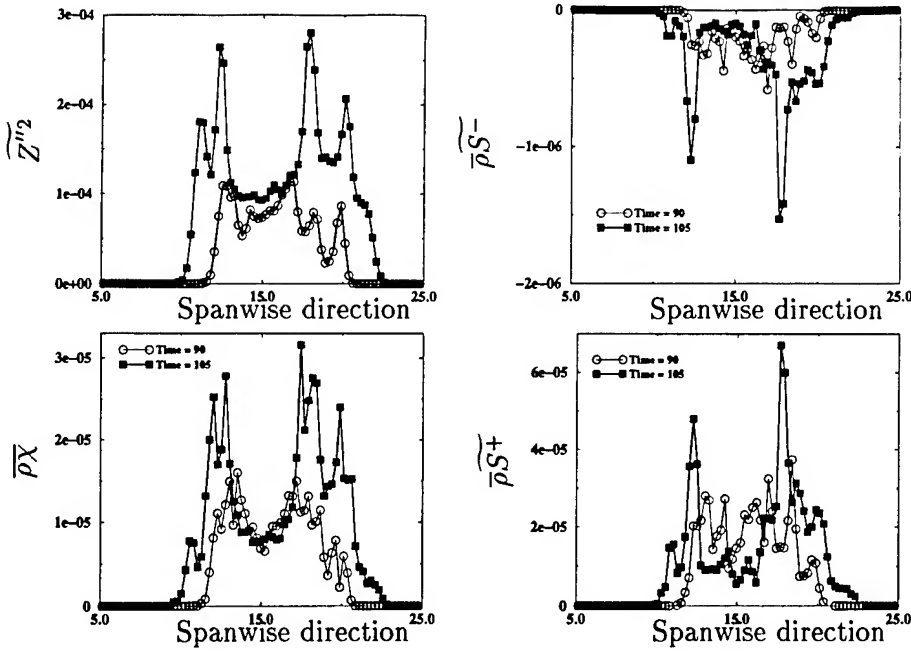


Figure 8. Time evolution of quantities averaged along the streamwise direction of the mixing layer: mixture fraction variance $\overline{Z''^2}$, dissipation $-\overline{\rho\chi}$, and vaporization source terms $\overline{\rho S^+}$ and $\overline{\rho S^-}$.

4. Conclusion

Spray modeling is one of the greatest challenge in the calculations of non-premixed turbulent combustion chambers. A Lagrangian model for two-phase flows has been applied with a DNS code to describe mixture fraction evolution during the vaporization and dispersion of droplet clouds. It has been shown that turbulent micro-mixing of the gas phase as well as mean dissipation rate are strongly affected by the liquid phase parameters (droplets volume and distribution, fuel physical properties, etc) during the whole vaporization period.

The mean source of fuel due to liquid phase vaporization leads to a mean source of mixture fraction that can be provided via an Euler-Lagrange model for the spray. These terms in the case of a dilute spray have been studied with the help of DNS, and it was found that they cannot be neglected, models for these terms are under development (Réveillon and Vervisch, 1999).

Acknowledgement

This work was supported by the Center for Turbulence Research Stanford and Nasa-Ames 1998 Summer Program. The authors have benefited from many stimulating and exciting discussions with the members of CTR.

References

- Chiu, H. H., Kim, H. Y., and Croke, E. J. (1982). Internal group combustion of liquid droplets. In combustion institute, T., editor, *Proceedings of the nineteenth Symposium (International) on combustion*.
- Crowe, C. T., Sharma, M. P., and Stock, D. E. (1977). The particle-source in cell (psi cell) model for gas droplet flows. *Journal of Fluids Engineering*, pages 325-332.
- Elgobashi, S. and Truesdell, G. (1989). Direct simulation of particle dispersion in a decaying isotropic turbulence. In *Seventh symposium on turbulent shear flows*, Stanford. Stanford University.
- Elgobashi, S. and Truesdell, G. (1992). Direct numerical simulation of particle dispersion in a decaying isotropic turbulence. *J. Fluid Mech.*, 242:655-700.
- Faeth, G. (1983). Evaporation and combustion of sprays. *Prog. Energy Combust. Sci.*, 9:1-76.
- Givi, P. (1989). Model free simulations of turbulent reactive flows. *Prog. Energy Combust. Sci.*, 15:1-107.
- Guichard, L., Lecordier, B., and Réveillon, J. (1998). Evaluation des algorithmes utilisés en piv grâce à la simulation numérique directe. In *6ieme Congrès francophone de Vélocimétrie Laser, F-5*. Saint-Louis, France.
- Kuo, K., editor (1986). *Principles of combustion*. John Wiley and sons.
- Law, C. (1982). Recent advances in droplet vaporization and combustion. *Prog. Energy Combust. Sci.*, 8:171-201.
- Lele, S. K. (1992). Compact finite difference schemes with spectral like resolution. *J. Comput. Phys.*, (103):16-42.
- nán, A. L. and Williams, F. (1993). *Fundamentals aspects of combustion*. Oxford University Press.
- Poinsot, T., Candel, S., and Trouvé, A. (1996). Direct numerical simulation of premixed turbulent combustion. *Prog. Energy Combust. Sci.*, 12:531-576.
- Réveillon, J., Bray, K., and Vervisch, L. (1998). Dns study of spray vaporization and turbulent micro-mixing. In *AIAA 98-1028*, 36th Aerospace Sciences Meeting and Exhibit, January 12-15, Reno NV.
- Réveillon, J. and Vervisch, L. (1999). Accounting for spray vaporization in non-premixed turbulent combustion modeling: A single droplet model (sdm). *submitted*.
- Sirignano, W. A. (1983). Fuel droplet vaporization and spray combustion theory. *Prog. Energy Combust. Sci.*, 8:291-322.
- Squires, K. D. and Eaton, J. (1990). Measurements of particle dispersion obtained from direct numerical simulations of isotropic turbulence. *J. Fluid Mech.*, 226:1-35.
- Vervisch, L. and Poinsot, T. (1998). Direct numerical simulation of non-premixed turbulent flame. *Annu. Rev. Fluid Mech.*, (30):655-692.
- Wray, A. A. (1990). Minimal storage time-advancement schemes for spectral methods. Technical report, Center for turbulence research Report, Stanford University.

ASSESSMENT OF THE GENERALIZED SCALE-SIMILARITY MODEL IN HOMOGENEOUS TURBULENCE SUBJECTED TO ROTATION

KIYOSI HORIUTI

*Department of Mechano-Aerospace Engineering,
Tokyo Institute of Technology,
2-12-1 O-okayama, Meguro-ku, Tokyo 152, Japan*

1. Introduction

In LES, a coarse graining of the small scales is performed by using a filtering procedure, i.e. the resolved or grid scale component of f , \bar{f} , is derived via the convolution integral of f with the filter function, $\bar{G}(\mathbf{x})$ ($\mathbf{x} = (x_1, x_2, x_3)$). In the present study, the spherically symmetric Gaussian filter function was used, in which the characteristic filter width, $\bar{\Delta}$, was set equal to 2Δ . Δ is the grid interval for the LES mesh. We consider the flow which is homogeneous in the x , y , and z directions. The subgrid-scale (SGS) component is denoted as $f' = f - \bar{f}$.

The SGS stress tensor, $\tau_{ij} = \overline{u_i u_j} - \bar{u}_i \bar{u}_j$, results from filtering the Navier-Stokes equations. The SGS models for τ_{ij} commonly used are divided into two groups: SGS eddy viscosity coefficient model (Smagorinsky 1963) and scale-similarity model (Bardina 1983). These SGS models generally require proper optimization of the parameters contained in the models. Remarkable progress was made for the determination of the model parameter value by the dynamic procedure proposed by Germano *et al.* (1991). An alternative theoretical approach to determine the parameter values is the utilization of the invariance constraints on the SGS stress under a change of frame (Speziale 1985 *a*). In Speziale (1985 *b*), the constraints on the SGS stresses in non-inertial frames of reference which undergo rotations were explored for some class of filter functions. It was shown that the SGS stress tensor depends on the motion of the frame of reference, but the divergence of the SGS stress is a frame-indifferent vector. Consistency of the linear

combination models of Clark *et al.* (1979) (the nonlinear model) as

$$\tau_{ij} \simeq \frac{\overline{\Delta}^2}{12} \frac{\partial \overline{u}_i}{\partial x_l} \frac{\partial \overline{u}_j}{\partial x_l} - 2C_S \overline{\Delta}^2 |\overline{S}| \overline{S}_{ij}, \quad (1)$$

with these constraints was discussed. Fureby and Tabor (1997) showed that the total summation of the Leonard and cross terms is invariant. The purpose of the present work is to assess the consistency of the recent dynamic SGS models with the constraints in turbulence subjected to rotation.

2. Subgrid-scale stress tensor in a rotating frame

We explore the transformation properties of the SGS stress tensor in a non-inertial frame of reference which is undergoing rotation. We obtain the transformation rule for the filtered velocity as (Speziale 1985 *b*)

$$\overline{u}_i = \overline{u}_i^* + \epsilon_{imn} \Omega_m x_n^*, \quad (2)$$

where Ω_k denotes the angular velocity of the non-inertial frame of reference relative to an inertial framing, and ϵ_{ijk} the alternating tensor. Quantities in an inertial frame of reference are denoted as f , and those in a non-inertial frame of reference as f^* . We assume $(\Omega_1, \Omega_2, \Omega_3) = (0, 0, \Omega)$ and Ω is set to a time-independent constant. Here, we utilized the relation, $\overline{x}_i^* = x_i^*$, which is true for isotropic filter functions (Speziale 1985 *b*; Fureby & Tabor 1997). From (2), we derive the following relations:

$$u_i' = u_i - \overline{u}_i = u_i^* - \overline{u}_i^*, \quad \overline{u}_i - \overline{u}_i^* = \overline{u}_i^* - \overline{u}_i^*. \quad (3)$$

Subsequently, when the Gaussian filter function is used, the SGS stress tensor, τ_{ij} , is transformed as

$$\overline{u_i u_j} - \overline{u}_i \overline{u}_j = (\overline{u_i^* u_j^*} - \overline{u}_i^* \overline{u}_j^*) + \tau_{ij}^c, \quad (4)$$

$$\tau_{ij}^c = \epsilon_{ikl} \Omega_k \frac{\overline{\Delta}^2}{12} \frac{\partial \overline{u}_j^*}{\partial x_l^*} + \epsilon_{jkl} \Omega_k \frac{\overline{\Delta}^2}{12} \frac{\partial \overline{u}_i^*}{\partial x_l^*} + \frac{\overline{\Delta}^2}{12} (\Omega_k \Omega_k \delta_{ij} - \Omega_i \Omega_j). \quad (5)$$

The τ_{ij} term is not indifferent to frame rotation (Speziale 1985 *b*), but the characteristic feature of the correction terms, τ_{ij}^c , in (5) is that it is solenoidal, i.e.

$$\frac{\partial \tau_{ij}^c}{\partial x_j^*} = 0. \quad (6)$$

The SGS stress tensor depends on the motion of the frame of reference. However, this is not of any serious consequence because only its divergence enters into the filtered momentum equation.

The modeled SGS stress tensor must have the same properties as the exact SGS stress tensor, and the rotational constraints must be satisfied by any reliable SGS model. The SGS stress tensor, τ_{ij} , consists of three terms

$$\tau_{ij} \equiv \overline{u_i u_j} - \bar{u}_i \bar{u}_j = L_{ij}^m + C_{ij}^m + R_{ij}^m, \quad (7)$$

where

$$L_{ij}^m = \overline{u_i u_j} - \bar{u}_i \bar{u}_j, C_{ij}^m = \overline{u_i u_j'} + \overline{u_j' u_i} - (\bar{u}_i \bar{u_j'} + \bar{u_j'} \bar{u}_i), R_{ij}^m = \overline{u_i' u_j'} - \bar{u_i'} \bar{u_j'}.$$

L_{ij}^m denotes the modified Leonard term, C_{ij}^m the modified cross term, and R_{ij}^m the modified SGS Reynolds stress. These three terms are transformed as

$$L_{ij}^m = L_{ij}^{m*} + \epsilon_{ikl} \Omega_k \frac{\bar{\Delta}^2}{12} \frac{\partial \bar{u}_j^*}{\partial x_l^*} + \epsilon_{jkl} \Omega_k \frac{\bar{\Delta}^2}{12} \frac{\partial \bar{u}_i^*}{\partial x_l^*} + \frac{\bar{\Delta}^2}{12} (\Omega_k \Omega_k \delta_{ij} - \Omega_i \Omega_j), \quad (8)$$

$$C_{ij}^m = C_{ij}^{m*} + \epsilon_{ikl} \Omega_k \frac{\bar{\Delta}^2}{12} \frac{\partial (\bar{u}_j - \bar{u}_j)^*}{\partial x_l^*} + \epsilon_{jkl} \Omega_k \frac{\bar{\Delta}^2}{12} \frac{\partial (\bar{u}_i - \bar{u}_i)^*}{\partial x_l^*}, \quad (9)$$

and R_{ij}^m is invariant under this transformation. Note that the correction terms for the L_{ij}^m and the C_{ij}^m terms are solenoidal. The order of the correction terms for the L_{ij}^m and C_{ij}^m terms are $\bar{\Delta}^2$ and $\bar{\Delta}^4$, respectively.

3. Formulation of the generalized scale-similarity model

In the generalized scale-similarity model, the velocity, u_i , is approximated by a representative velocity, \hat{u}_i , and substituted into τ_{ij} as

$$\tau_{ij} = (\overline{u_i u_j} - \bar{u}_i \bar{u}_j) \simeq (\overline{\hat{u}_i \hat{u}_j} - \bar{\hat{u}}_i \bar{\hat{u}}_j). \quad (10)$$

We propose to approximate \hat{u}_i as

$$\hat{u}_i = [I - (I - \bar{G})^n] u_i, \quad (11)$$

where I denotes the identity operator, \bar{G} the operator corresponding to application of the Gaussian filter. We term the model (10) with (11) as the multilevel filtered model. As n is increased, the amplitude of the truncation errors is reduced.

When $n = 2$, we obtain the following model as (Horiuti 1997):

$$\tau_{ij} \simeq C_L L_{ij}^m + C_C L_{ij}^C + C_B L_{ij}^R, \quad (12)$$

where

$$L_{ij}^C = L_{ij}^m - (\bar{\bar{u}}_i \bar{\bar{u}}_j - \bar{\bar{u}}_i \bar{\bar{u}}_j), \quad (13)$$

$$L_{ij}^R = \overline{\overline{u_i^l u_j^l}} - \overline{\overline{u_i^l}} \overline{\overline{u_j^l}} = \overline{(\overline{u_i} - \overline{\overline{u_i}})(\overline{u_j} - \overline{\overline{u_j}})} - \overline{(\overline{u_i} - \overline{\overline{u_i}})} \overline{(\overline{u_j} - \overline{\overline{u_j}})}. \quad (14)$$

We allowed the dependence of the model terms on the parameters C_L , C_C and C_B , because these parameters cannot be determined using only the Galilean invariance constraint (Horiuti 1997).

As a subset of a linear combination of the scale-similarity model (12) and the Smagorinsky model, the following models are derived.

When $C_L = C_C = C_B = 0$, the dynamic Smagorinsky model (DSM, Germano *et al.* 1991) is derived. When $C_L = 1$, $C_C = C_B = 0$, the mixed model (Bardina 1983) is derived. The nonlinear model ((1)) (Clark *et al.* 1979) can be derived using the Taylor expansion for the L_{ij}^m term in Bardina's mixed model (Horiuti 1993). Zang, Street & Koseff (1993) proposed the dynamic mixed model (DMM). As an extension of DMM, Liu, Meneveau & Katz (1994) proposed the dynamic two-parameter mixed model (DTM). When $C_C = C_B = 0$, we derive the DTM proposed by Salvetti and Banerjee (1995) ($C_L - C_S$ model). When $C_L = 1$ and $C_C = 0$, we derive the DTM ($C_B - C_S$ model (Horiuti 1997)).

4. Compatibility of the models with rotational constraints

A linear combination model of the scale-similarity (12) with $C_C = 0$ and Smagorinsky models yields the transformation of the exact and modeled SGS stress tensor as

$$(\overline{u_i^* u_j^*} - \overline{u_i^*} \overline{u_j^*}) + \epsilon_{ikl} \Omega_k \frac{\overline{\Delta^2}}{12} \frac{\partial \overline{u_j^*}}{\partial x_l^*} + \epsilon_{jkl} \Omega_k \frac{\overline{\Delta^2}}{12} \frac{\partial \overline{u_i^*}}{\partial x_l^*} + \frac{\overline{\Delta^2}}{12} (\Omega_k \Omega_k \delta_{ij} - \Omega_i \Omega_j) \quad (15)$$

$$\simeq C_L^* \left\{ L_{ij}^{m*} + \epsilon_{ikl} \Omega_k \frac{\overline{\Delta^2}}{12} \frac{\partial \overline{u_j^*}}{\partial x_l^*} + \epsilon_{jkl} \Omega_k \frac{\overline{\Delta^2}}{12} \frac{\partial \overline{u_i^*}}{\partial x_l^*} + \frac{\overline{\Delta^2}}{12} (\Omega_k \Omega_k \delta_{ij} - \Omega_i \Omega_j) \right\} \quad (16)$$

$$+ C_B^* L_{ij}^{R*} - 2C_S^* \overline{\Delta^2} |\overline{S^*}| \overline{S_{ij}^*}.$$

Although the modeled SGS stress is not form invariant (Speziale 1979), when constant values are assumed for the model parameters, this non-invariance does not cause any serious consequence, because the constraint (6) is satisfied. When the model parameters are determined using the dynamic procedure, the non-invariance of the L_{ij}^m term generates an inconsistency of the model with the constraints.

In the DSM, by comparison of (15) and (16), we notice that there is no constant term in the modeled stress tensor corresponding to that in the exact stress tensor. This modeled stress tensor is inconsistent with the exact SGS stress tensor in the limit of $\Omega \rightarrow \infty$, or when $\overline{u_i^*}$ is set equal to a constant value, unless the additional condition, $\tilde{\Delta} \ll 1/\Omega$, is satisfied. This

discrepancy is also reflected in the equation for the dynamical parameter C_S in the DSM as

$$C_S = \frac{\mathcal{L}_{ij}(\bar{\mathbf{u}})\mathcal{E}_{ij}}{\mathcal{E}_{ij}\mathcal{E}_{ij}}, \quad (17)$$

where

$$\mathcal{L}_{ij}(\mathbf{u}) = (\widetilde{u_i u_j} - \widetilde{u_i} \widetilde{u_j}), \quad \mathcal{E}_{ij} = 2\{\bar{\Delta}^2 |\widetilde{\bar{S}}| \widetilde{\bar{S}_{ij}} - \widetilde{\bar{\Delta}}^2 |\widetilde{\bar{S}}| \widetilde{\bar{S}_{ij}}\}.$$

The tildes ($\widetilde{\quad}$) denote the 'test' filter, \widetilde{G} (Germano *et al.* 1991), the characteristic width $\widetilde{\Delta}$ of which was chosen as $\widetilde{\Delta}^2 = 3\bar{\Delta}^2$ in the present study. $\mathcal{E}_{ij} = \mathcal{E}_{ij}^*$, but the $\mathcal{L}_{ij}(\bar{\mathbf{u}})$ term is not indifferent because

$$\mathcal{L}_{ij}(\bar{\mathbf{u}}) = \mathcal{L}_{ij}(\bar{\mathbf{u}})^* + \epsilon_{ikl}\Omega_k \frac{\bar{\Delta}^2}{12} \frac{\partial \widetilde{u_j^*}}{\partial x_l^*} + \epsilon_{jkl}\Omega_k \frac{\bar{\Delta}^2}{12} \frac{\partial \widetilde{u_i^*}}{\partial x_l^*} + \frac{\bar{\Delta}^2}{12} (\Omega_k \Omega_k \delta_{ij} - \Omega_i \Omega_j), \quad (18)$$

which is of the order of $\Omega^2 \bar{\Delta}^2$, and the contribution of this correction term is large when Ω is large.

In the $C_L - C_S$ model, the constant terms in (15), $(\bar{\Delta}^2/12(\Omega_k \Omega_k \delta_{ij} - \Omega_i \Omega_j))$, and (16), $(C_L^* \bar{\Delta}^2/12(\Omega_k \Omega_k \delta_{ij} - \Omega_i \Omega_j))$, must be identical because these constant terms become predominant, when $\Omega \rightarrow \infty$, or when \bar{u}_i^* is set equal to a constant value. To equate these two terms, we find that C_L is not arbitrary, but must be set equal to unity. The same result for the value of C_L can be obtained when the dynamic procedure is actually used to determine C_L . When (18) is inserted into the dynamical equation for C_L , we find that C_L is dependent on x_i^* , implying that the constraint (6) is not satisfied. Thus, C_L must be a constant independent of x_i^* . When Ω was large, the dominant term in the equation for C_L became

$$\left(\frac{\bar{\Delta}^2}{12}\right)^2 [2(\Omega_k \Omega_k \Omega_l \Omega_l)(\mathcal{E}_{pq}\mathcal{E}_{pq}) - (\Omega_p \Omega_q \mathcal{E}_{pq})(\Omega_k \Omega_l \mathcal{E}_{kl})], \quad (19)$$

in both the denominator and the numerator of the equation. Thus, C_L tends to be equal to unity when Ω is large. The constant value for C_L must be equal to unity. It is interesting to note that the present value of 1.0 for C_L is close to the previous estimate obtained using the dynamic procedure (C_L is approximately in the range of 1.0 ~ 1.4 with its variance ≈ 0.2 (e.g. Salvetti & Banerjee 1995; Horiuti 1997)).

In the DTM proposed by Liu *et al.* (1994), the proportionality coefficient for the scale-similarity part had to be set equal to 1/3 to equate the modeled and exact constant terms. The estimated value obtained using experimental analysis was close to this theoretical estimate (in the range of 0.45 ± 0.15 (Liu *et al.* 1994)).

In the following, we consider the models in which C_L is set equal to unity. The relation, $C_S \approx C_S^*$, should be satisfied for the models to be compatible with the constraint (6).

In the DMM, the model parameter C_S is determined as

$$C_S = \frac{[\mathcal{L}_{ij}(\bar{\mathbf{u}}) - \mathcal{L}_{ij}(\bar{\bar{\mathbf{u}}})]\varepsilon_{ij}}{\varepsilon_{ij}\varepsilon_{ij}}. \quad (20)$$

The constant terms found in the DSM ((18)) and the $C_L - C_S$ model ((19)) were eliminated in the DMM. The correction terms became of the order of $\Omega\tilde{\Delta}^4$. A similar result was obtained for the $C_B - C_S$ model.

It should be emphasized that the correction term for the DSM in (18) was similar to that for the L_{ij}^m term in (8), while the correction term for the DMM and $C_B - C_S$ model was similar to that for the C_{ij}^m term (equation not shown). These results indicate that, when the dynamic procedure is used, an accurate model must be implemented at each level of decomposition for the SGS stress tensor; the L_{ij}^m , C_{ij}^m and R_{ij}^m terms.

Accordingly, we need to implement accurate models for the C_{ij}^m term. Thus, we restore the L_{ij}^C term in (12). Due to the constraint for the correction term, the value for parameter C_C should be set equal to unity. Then, in the correction term arising in the L_{ij}^C term, the magnitude of the correction term was reduced to the order of $\Omega\tilde{\Delta}^6$. We consider the incorporation of the L_{ij}^C term with $C_C = 1$ into the DMM (modified DMM) and into the $C_B - C_S$ model (modified $C_B - C_S$ model).

For the analysis shown above, we have utilized the formulation for the test-filtered stress tensor proposed by Zang *et al.* (1993). The same conclusion was drawn when the formulation by Vreman *et al.* (1994) was used.

All dynamic models assessed above are only approximately compatible with the rotational constraints, whereas in the nonlinear model (1), the exact and modeled correction terms become identical (Speziale 1985 b). When the proportionality coefficient for the first term in the nonlinear model was determined using the dynamic procedure, its asymptotic value in the limit of $\Omega \rightarrow \infty$ was unity, as similarly shown for C_L in the $C_L - C_S$ model. In the dynamic equation for C_S contained in the nonlinear model, the correction terms were eliminated, and $C_S^* = C_S$.

5. Assessment in homogeneous turbulence subjected to rotation

We directly assess the SGS models using the DNS database for incompressible homogeneous turbulence which was subjected to rotation, and generated using 128, 128 and 128 grid points in the x , y , and z directions, respectively. The size of the computational domain was 2π in each direction, the initial rms turbulent velocity was set equal to 1.0, and the kinematic

viscosity, ν , was set equal to 0.005. Ω was chosen equal to 0.0, 1.0, 4.0 and 10.0. The SGS stresses computed by filtering the DNS data are compared with those calculated using the SGS models. The SGS models were assessed at $t = 0.5$ for the case with $\Omega = 10.0$. The DNS flow field was filtered to $32 \times 32 \times 32$ in the x , y and z directions, respectively.

In the '*a priori*' test, the SGS stresses computed by filtering the DNS data were compared with those calculated using the SGS models. In the correlation coefficients, $\phi(\tau_{11}, f)$, shown in table 1, the DSM results had the lowest correlation with the filtered DNS data. This poor correlation improved considerably in the DMM, but further improvement was achieved using the modified DMM. The correlation coefficient was rather low in the $C_B - C_S$ model, but it was improved in the modified $C_B - C_S$ model. The ratios of the rms values for modeled and exact SGS stresses, $R_{rms}(\tau_{11}, f)$, were generally close to unity except for the DSM. Note that the result obtained using the $C_L - C_S$ model is similar to that obtained using the DMM. High correlation was achieved in the nonlinear model because the correction term for this model is identical to the exact correction term.

The temporal variations of the grid-scale energy obtained using the DSM in the '*a posteriori*' test for $\Omega = 10.0$, when the correction terms were implemented, showed very large deviation from the exact DNS data, indicating that the DSM is inconsistent with the rotational constraints. The temporal variations calculated using the DMM and the $C_L - C_S$ model, in which the correction terms were implemented, were almost identical. In fact, the average value of C_L was close to unity (≈ 1.02), with its rms value being very small (≈ 0.02) in accordance with the theoretical estimate that $C_L = 1$.

Figure 1 shows the temporal variations of the grid-scale energy, K_G , for the cases with $\Omega = 10.0$, obtained using DNS and that calculated using the DMM and the modified DMM. In all tested cases, the results obtained using the modified DMM yielded better agreement with the filtered DNS data than those obtained using the DMM. Also contained in figure 1 are the results obtained by implementing the correction terms. The difference

TABLE 1. Correlation coefficients and ratio of root-mean-square values between the exact SGS stress, τ_{11} , and those obtained using the different models. DMM' denotes the modified DMM, and $C_B - C_S'$ the modified $C_B - C_S$ model. The correction terms were implemented into both exact and modeled terms.

f	DSM	DMM	(1)	DMM'	$C_L - C_S$	$C_B - C_S$	$C_B - C_S'$
$\phi(\tau_{11}, f)$	0.033	0.66	0.85	0.94	0.64	0.71	0.95
$R_{rms}(\tau_{11}, f)$	9.84	1.06	1.18	0.93	1.14	1.19	0.98

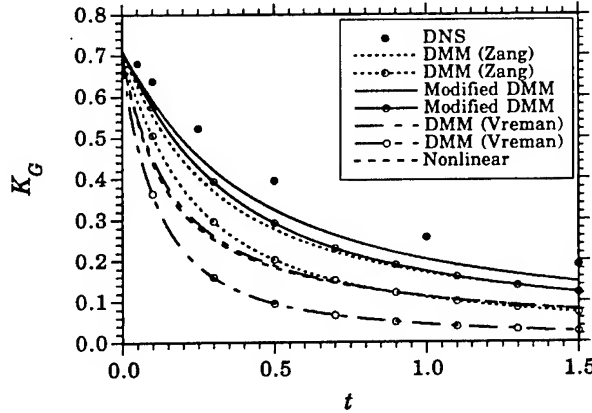


Figure 1. Temporal variations of the grid-scale energy, K_G , obtained using DNS and those calculated using the DMM, modified DMM and nonlinear models for $\Omega = 10.0$. The lines with the blank circles (\circ) denote the results obtained by implementing the correction terms. DMM (Zang) and DMM (Vreman) denote the results obtained using the DMM in conjunction with Zang *et al.*'s and Vreman *et al.*'s formulations, respectively.

between those obtained without and with implementation was significantly large. The difference was considerably reduced for the results obtained using the modified DMM, i.e. an inclusion of the L_{ij}^C term is crucial. When the correction terms were implemented into the $C_B - C_S$ model, the result was inferior to those obtained using the modified DMM, but the modified $C_B - C_S$ model improved the prediction accuracy, implying that the SGS models with a low accuracy for modeling the C_{ij}^m term may even yield incorrect results for a rotating turbulence.

6. Higher-order models for the modified cross term

In the previous section, it was shown that the correction terms for the SGS models in rotating turbulence can be better approximated by incorporating the L_{ij}^C term. However, even in the modified DMM and modified $C_B - C_S$ models, differences between the results obtained with and without implementation of the correction terms were still large. The truncation error for the correction term can be reduced as n is increased in the multilevel filtered model. We propose a linear combination model of the multilevel filtered model (10) and the Smagorinsky model (the dynamic multilevel mixed model (DMLM)). In the dynamic equation for the model parameter C_S in the DMLM, the truncation error for the correction term became of the order of $\Omega \tilde{\Delta}^{2(n+1)}$ when (11) was used with n .

It was found that the correlation coefficients between the exact τ_{11} term and modeled τ_{11} term estimated using the DMLM with $n = 6$ and 8 , as well as the ratios of the rms values between them, were very close to unity. In the temporal variations of the grid-scale energy, the difference between the results obtained with and without implementation of the correction terms was reduced with an increase of n : they were almost identical when $n = 8$, and were close to the filtered DNS data.

We examined the behavior of the multilevel filtered model in the limit of $n \rightarrow \infty$. In the profiles for the Fourier transform of the operator $[1 - (1 - \bar{G})^n]$, it was found that as $n \rightarrow \infty$, the filter function tends to converge to the identity operator, 1 . Thus, the multilevel filtered model converges to the defiltered (deconvoluted) model as

$$\hat{u}_i = [1 - (1 - \bar{G})^n] u_i \rightarrow 1 u_i = \bar{G}^{-1} \bar{u}_i = u_i^<, \quad (21)$$

where $u_i^<$ is the component of u_i , the Fourier transform of which resides in the resolved wave number range. The defiltered model possesses an advantage in that the correction term for a frame rotation is identical to the exact correction term, i.e. $C_S = C_S^*$ and this model is form invariant.

The temporal variations of the grid-scale energy obtained using the defiltered model were generally close to that obtained using the DMLM with $n = 8$, confirming that the multilevel filtered model actually converges to the defiltered model. The defiltered model, however, tended to underestimate the decay rate of the grid-scale energy, i.e. the defiltered model possesses a drawback in that the dissipation of the grid-scale energy into the SGS caused by this model is insufficient.

In the profiles of the volume-averaged production terms, $P = -\tau_{ij} \bar{S}_{ij}$, it was found that P was overestimated in the DMLM with $n = 2$ and underestimated in the DMLM with $n = 8$. This difference between the cases with $n = 2$ and $n = 8$ was due to the difference in the magnitude of the Smagorinsky model part in the modeled SGS stress, i.e. the contribution of the Smagorinsky model part was substantially reduced as n was increased. The scale-similarity model shows high correlation with the exact τ_{ij} term, whereas the strain rate tensor possesses very low correlation with the exact τ_{ij} term. Therefore, when the model parameters are determined using the dynamic procedure for the mixed model, the solution tends to align more with the scale-similarity model part than with the eddy viscosity model part. Thus, the contribution of the Smagorinsky model part is reduced, and the net energy flux from the grid scale to the SGS is underestimated.

The estimation of the P term, however, was found to be dependent on the formulations for the test-filtered SGS stress. When Vreman *et al.*'s formulation was used, the reduction of the Smagorinsky model part contribution

occurred considerably gradually as n was increased. Its complete convergence was achieved when n was increased to ≈ 500 , but the contribution of the Smagorinsky model part was still significantly large. Therefore, the Smagorinsky model caused a significant contribution to the dissipation of the grid-scale energy into the SGS. When Zang *et al.*'s formulation was used, its convergence was very fast, and was complete when $n = 8$.

In figure 1, we contained the results for the temporal variations of the grid-scale energy, K_G , calculated using the DMM and the nonlinear model, in which Vreman *et al.*'s formulation was used. The decay rate of the grid-scale energy was overestimated when Vreman *et al.*'s formulation was used, in comparison to the result obtained using Zang *et al.*'s formulation. The result obtained using the nonlinear model was close to that obtained using the DMM with Vreman *et al.*'s formulation without the implementation of the correction term. The advantage of the nonlinear model is that the result calculated with the implementation of the correction terms is identical to that calculated without the implementation.

In the defiltered model, the average P term even became negative. As a result, the decay rate of the grid-scale energy was underpredicted when using the defiltered model. This insufficient drain of the grid-scale energy into the SGS for the defiltered model was previously reported by Domaradzki & Loh (1998), who showed that the fields derived by a simple deconvolution for the resolved wave number range do not yield sufficiently high SGS dissipation, and the inclusion of SGS with sizes below the LES mesh size is necessary to achieve sufficiently high dissipation.

7. Conclusions

Theoretical consideration is presented for the constraints on the subgrid-scale (SGS) models for the SGS stress tensor in a non-inertial frame of reference undergoing rotation. We derived the exact expression for the correction term for the SGS stress tensor in a rotating frame relative to an inertial framing so that the transformed SGS stress tensor became compatible with the transformation of the frame for the spherical Gaussian filter function. Conformity of the modeled SGS stress tensor estimated using the previous dynamic SGS models (the dynamic Smagorinsky, dynamic mixed, dynamic two-parameter mixed and nonlinear models) with the constraints imposed by these correction terms is examined. It is shown that values for certain model parameters contained in the mixed models can be theoretically determined by imposing these constraints. The nonlinear model was compatible with the constraints, but other dynamic models were found to violate the constraints when the angular velocity of a rotating frame was large. Failure of previous models was attributable to insufficient accuracy

in approximating the modified cross term in the decomposition of the SGS stress tensor. A new dynamic mixed model is proposed to improve the approximation accuracy for the modified cross term, in which multilevel filtering of the velocity field was utilized to systematically eliminate the truncation error for the modeled correction term. In both the *a priori* and *a postepriori* numerical assessment of the SGS models in decaying homogeneous turbulence which is subjected to rotation, the proposed model performed better than the previous models, when the level of the multifiltering operation was large. The difference between the results obtained with and without implementation of the correction terms into the proposed model was negligible as it should be for a SGS model which is compatible with the constraints. Formulations for the test-filtered SGS stress in the dynamic procedure were compared, and it was shown that the results are dependent on the formulation. The relationship of the proposed model with the defiltered model is discussed in the limit of the infinite level of multifiltering, showing that the defiltered model is compatible with the constraints.

This work was partially supported by a Grant-in-Aid for Scientific Research from the Ministry of Education of Japan (No.10650162).

REFERENCES

- BARDINA, J. 1983 , *Ph.D. dissertation*. Stanford University, Stanford
- CLARK, R.A., FERZIGER, J.H. & REYNOLDS, W.C. 1979 , *J. Fluid Mech.* **91**, 1.
- DOMARADZKI, J. A. & LOH, K.-C. 1998 , . , Submitted to *Phys. Fluids*.
- FUREBY, C. & TABOR, G. 1997 , *Theoret. Comput. Fluid Dynamics*. **9**, 85.
- GERMANO, M., PIOMELLI, U., MOIN, P. & CABOT, W.H. 1991 , *Phys. Fluids*. **A3**, 1760.
- GEURTS, B. J. 1997 , *Phys. Fluids*. **9**, 3585.
- HORIUTI K. 1993 , *Phys. Fluids*. **A5**, 146.
- HORIUTI, K. 1997 , *Phys. Fluids*. **9**, 3443.
- LIU, S., MENEVEAU, C. & KATZ, J. 1994 , *J. Fluid Mech.* **275**, 83.
- SALVETTI, M.V. & BANERJEE, S. 1995 , *Phys. Fluids*. **7**, 2831.
- SMAGORINSKY, J. 1963 , *Monthly Weather Review*. **91**, 99.
- SPEZIALE, C.G. 1979 , *Phys. Fluids*. **22**, 1033.
- SPEZIALE, C.G. 1985 *a* , *J. Fluid Mech.* **156**, 55.
- SPEZIALE, C.G. 1985 *b* , *Geophys. Astrophys. Fluid Dynamics*. **33**, 199.
- VREMAN, B., GEURTS, B. & KUERTEN, H. 1994 , *Phys. Fluids*. **6**, 4057.
- ZANG, Y., STREET, R.L. & KOSEFF, J. 1993 , *Phys. Fluids*. **A5**, 3186.

DIRECT NUMERICAL SIMULATION OF TURBULENT FLAME KERNELS

KARL.W.JENKINS AND R.STEWART.CANT

*University of Cambridge
CFD Laboratory
Department of Engineering
Trumpington Street
Cambridge
CB2 1PZ
United Kingdom*

June 1999

Abstract. A combustion DNS code has been developed to solve a fully compressible reacting flow and applied to studying the effects of a turbulent flame kernel. High accuracy numerical techniques have been employed which are 10th order explicit in space and a third order explicit Runge Kutta method in time. Parallel coding is achieved using the Message Passing Interface (MPI) and a performance test is presented showing efficiency and speed up factors. Turbulence is generated numerically for 64 independent simulations using the same laminar flame as an initial condition. Each initial turbulence field has been tested as a simulation of decaying isotropic turbulence without the inclusion of a flame. Initial results for the turbulent reacting simulations on a grid of 96^3 points are presented along with a laminar flame on a grid of 384^3 points.

1. Introduction

A physical problem of practical interest is the growth of a flame kernel in a turbulent environment. The early flame once established is laminar and propagates spherically outwards. Its motion is accelerated by flow divergence due to thermal expansion and it begins to interact with the surrounding turbulence becoming wrinkled and increasing in surface area. A difficulty that arises in this kind of combustion problem involves the strong coupling between the turbulence, the chemical kinetics and the heat release. The interactions are generally three dimensional and time dependent, and are not easily accessible to experimental investigation.

A combustion DNS code called SENGAs has been developed at Cambridge to extract information on flame structure which is obtainable by no other means. This information can be extracted in the form of statistics (such as mean turbulent kinetic energy) or data sets for post-processing, and time dependent data may be obtained "on the fly" if the quantities of interest are known in advance. The code solves a fully compressible reacting flow. In combustion DNS this implies that density is a function of pressure as well as temperature and all acoustic activity is fully resolved (Cant, 1994). A fully compressible scheme enables complex boundary conditions to be implemented (Poinso *et al.*, 1996) using the Navier Stokes characteristic boundary condition (NSCBC) formalism (Poinso and Lele, 1992). Inflow and outflow conditions are of particular interest, and the formulation allows the inclusion of realistic heat release in a thermodynamically open system.

The computational requirements for combustion DNS are very large due to the conflicting demands of resolution at the smallest scales and the need to include a reasonable range of turbulence length scales. Therefore, to simulate physically relevant problem sizes parallel supercomputers need to be employed. Bearing this in mind, the code was designed from the outset to run in a parallel environment.

Due to the computational requirements of combustion DNS, two approaches to simulation have been followed. The first is two dimensional DNS with complex chemistry (Baum *et al.*, 1992), while the second is three dimensional DNS with heat release adopting simple chemistry. Three dimensional DNS with heat release has been used by (Rutland and Cant, 1994) to study turbulent transport. However boundary conditions to incorporate heat release were applied in the streamwise direction only, the other directions incorporating Fourier pseudo spectral methods. (Troune and Poinso, 1994) have also used three dimensional DNS with heat release to investigate flame surface density. Again only one direction incorporates inflow and outflow boundaries with two periodic boundaries. The study of ignition and early flame kernel growth using DNS has been undertaken by (Poinso, 1991). However, this study involved two dimensional simulation

Three dimensional simulations are chosen in preference to two dimensional due to the differing dynamics of turbulence (Batchelor, 1953), (Bradshaw, 1971), (Herring *et al.*, 1974). In two dimensions, the vortex stretching mechanism for the cascade of energy to progressively smaller scales of motion is absent and the smallest scales of motion do not follow the Kolmogorov scaling laws. Therefore to capture the Kolmogorov scales, SENGAs uses three dimensional DNS with heat release, incorporating outflow boundaries in all directions. The advantage of the present work is that it enables the investigation of a flame away from all boundaries, thus removing any statistical skewness from numerical interaction at the boundary.

The objective of this research is to study flame kernels in a turbulent environment. In the following, a fully compressible, three dimensional, parallel combustion DNS code is used to get basic information on flame structure. The paper is organised as follows. The equations governing the simulation of this flow problem are outlined with the non dimensionalisation procedure. The theoretical background and numerical method of generating an initial turbulent field which satisfies the conditions of continuity, homogeneity and isotropy is given. The main numerical procedures are outlined along with parallel implementation. Finally results are presented for

DNS OF TURBULENT FLAME KERNELS

a single laminar flame simulation of 384^3 points, and for sixty four turbulent simulations of 96^3 points.

2. Problem Definition

The motion and reaction of gases in a combustion system are governed by conservation equations which describe the transport of properties of the flow (Kuo, 1986). These are partial differential equations describing conservation of overall mass, momentum, energy and a conservation equation for each individual species. It is convenient to non dimensionalise these governing equations with respect to reference values. There are many possible choices for the reference values depending on the exact problem under consideration. The form adopted here begins with time scales that are non dimensionalised with respect to domain size x_0 and laminar flame speed S_i .

$$u_0 = S_i; \quad t_0 = \frac{x_0}{u_0}$$

Density and pressure are non dimensionalised using reference values (in the unburned state) ρ_0 and P_0 , and following the same, viscosity, thermal conductivity and diffusion are non dimensionalised using μ_0 , λ_0 and D_0 . Finally the physical temperature T^* is non dimensionalised using

$$T = \frac{T^* - T_0}{T_{ad} - T_0}$$

which has values between zero and one for an adiabatic combustion process with a starting temperature T_0 and flame temperature T_{ad} . Substituting these definitions into the governing equations yields the following set of equations for overall conservation, momentum, energy and species conservation. All variables are non dimensional terms and standard tensor notation is applied.

$$\frac{\partial \rho}{\partial t} + \frac{\partial \rho u_k}{\partial x_k} = 0 \quad (1)$$

$$\frac{\partial \rho u_i}{\partial t} + \frac{\partial \rho u_k u_i}{\partial x_k} = -\frac{\partial P}{\partial x_k} + \frac{1}{Re} \frac{\partial \tau_{ki}}{\partial x_k} \quad (2)$$

$$\frac{\partial \rho E}{\partial t} + \frac{\partial \rho u_k E}{\partial x_k} = -(\gamma - 1) M^2 \frac{\partial P u_k}{\partial x_k} \quad (3)$$

$$\begin{aligned} & + \frac{1}{Re} (\gamma - 1) M^2 \frac{\partial \tau_{ki} u_i}{\partial x_k} \\ & + \frac{\tau}{Re P_r} \frac{\partial}{\partial x_k} \left(\lambda \frac{\partial T}{\partial x_k} \right) \\ & + \frac{\tau}{Re S_c} \frac{\partial}{\partial x_k} \left(\rho D \frac{\partial c}{\partial x_k} \right) \end{aligned}$$

$$\frac{\partial \rho c}{\partial t} + \frac{\partial \rho u_k c}{\partial x_k} = w_\alpha + \frac{1}{Re S_c} \frac{\partial}{\partial x_k} \left(\rho D \frac{\partial c}{\partial x_k} \right) \quad (4)$$

where c is a reaction progress variable or normalised mass fraction, γ is the ratio of specific heat capacities and τ_{ki} represents the viscous stress tensor, given by

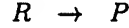
$$\tau_{ij} = \mu \left(\frac{\partial u_i}{\partial x_j} + \frac{\partial u_j}{\partial x_i} - \frac{2}{3} \frac{\partial u_m}{\partial x_m} \delta_{ij} \right)$$

The symbol τ without subscripts, denotes a heat release parameter defined as

$$\tau = \frac{T_{ad} - T_0}{T_0}$$

Note that in the governing equations above, the non-dimensional forms μ , λ and ρD are retained explicitly. Therefore each form may be specified as a known function of temperature if required.

For combustion DNS, it is usually necessary to limit the number of chemical species by using reduced kinetic mechanisms due to equation 4. Therefore the flame is considered premixed with a simple, single step reaction mechanism controlled by Arrhenius kinetics. This one step mechanism has a single reaction



where R represents the reactants and P the products. Assuming species diffusivities are equal the reaction progress variable c , can be used to describe the chemical state of the system. The non dimensional reaction progress variable has values between zero and one, representing an unburned gas and a fully burned gas respectively.

The non dimensional parameters appearing in the above equations are the Reynolds, Prandtl, Schmidt and Mach numbers given by

$$Re = \frac{\rho_0 u_0 x_0}{\mu_0}; \quad Pr = \frac{\mu_0 C p_0}{\lambda_0}; \quad Sc = \frac{\mu_0}{\rho_0 D_0}; \quad M = \frac{u_0}{a_0}$$

where a_0 is the speed of sound in the unburned gas

To solve the problem numerically, the six differential equations above must be supplemented by the thermal and caloric equations of state. These two equations of state in non dimensional form are given by

$$P = \frac{\rho(1 + \tau T)}{\gamma M^2} \quad (5)$$

$$E = \frac{(1 + \tau T)}{\gamma} + \frac{1}{2} u_k u_k (\gamma - 1) M^2 + \tau(1 - c) \quad (6)$$

Finally to close the problem, a non dimensional reaction rate term ω_α is required. This reaction rate represents the rate at which the reaction progress variable is produced and is given by

$$\omega_\alpha = B \rho (1 - c) \exp \left(-\frac{\beta(1 - T)}{1 - \alpha(1 - T)} \right) \quad (7)$$

DNS OF TURBULENT FLAME KERNELS

where B is the pre-exponential factor, β is the non-dimensional activation energy or Zel'dovich number:

$$\beta = \frac{E(T_{ad} - T_0)}{R^0 T_{ad}^2}$$

and α is the heat release parameter

$$\alpha = \frac{\tau}{1 + \tau} = \frac{T_{ad} - T_0}{T_{ad}}$$

3. Numerical Procedure

In combustion DNS, the most popular method of spatial discretisation has been the 6th order compact scheme developed by (Lele, 1992). This method produces spectral like accuracy in finite difference form and removes the restriction of spectral methods with respect to the treatment of boundary conditions. In the present case, explicit methods are used in three dimensional space and time with parallel implementation achieved through the Message Passing Interface (MPI). The explicit method for space was chosen over the more traditional compact method to improve efficiency in a parallel environment, since compact schemes require a tridiagonal solver.

First and second spatial derivatives are discretised using a central 10th order explicit scheme. This scheme provides accuracy comparable to that of the compact schemes and allows boundary conditions to be implemented more easily. To produce a solution in time, all time derivatives are discretised using the third order compact Runge-Kutta method (Wray, 1990). This requires three sub steps for each main time advancement step and requires only two storage locations, one for the time derivative and one for the dependent variable.

An initial field of isotropic homogeneous turbulence is generated numerically to satisfy the continuity constraint for incompressible flow. The central requirement for this turbulent field is the specification of an energy spectrum $E(k)$, where k is a wavenumber in the Fourier-space representation of the turbulent velocity field. Fourier modes having random phase angles but satisfying continuity, homogeneity and isotropy are generated to produce the initial turbulent field. The energies contained in these modes were selected from a curve known to be representative of the energy spectrum of isotropic turbulence. The energy spectrum used here is that of (Lee and Reynolds, 1985), given by

$$E(k) = \begin{cases} \gamma k^2 & k_0 \leq k \leq k_p \\ \gamma k_p^{\frac{11}{3}} k^{-\frac{5}{3}} & k_p \leq k \leq k_c \\ 0 & \text{otherwise} \end{cases}$$

where k_0 , k_p and k_c are the minimum, peak and cut off wavenumbers, identifying portions of the spectrum corresponding to the energy containing eddies, inertial subrange and the dissipation range (Tennekes and Lumley, 1972) and γ is a magnitude factor. k_p and γ are variables which control the form and magnitude of the

energy spectrum and thus predetermine the total kinetic energy and other properties of the initial turbulent flow.

Boundary conditions are implemented using the Navier Stokes characteristic boundary conditions (NSCBC) (Poinsot and Lele, 1992). The tenth order finite differences are evaluated over an eleven point stencil. Therefore for outflowing boundary conditions 5 grid points are required outside the domain. To accommodate this problem, the code uses explicit schemes of increasing accuracy away from the boundary. These schemes starting at point 1, the boundary, for the first and second derivatives are given in table 1

TABLE 1. SENGAs Outflow Numerical Boundary Schemes

Grid point	Numerical Scheme	1st deriv Stencil	2nd deriv stencil
1	2nd order one sided	3	4
2	2nd order centered	3	3
3	4th order centered	5	5
4	6th order centered	7	7
5	8th order centered	9	9

Various boundary schemes have been used in relation to the main body schemes in SENGAs. These methods have included a interior sixth order compact scheme with boundaries treated using a sixth order compact scheme over points 5,4 and 3 with points 2 and 1 treated using a fourth order Pade scheme and a third or fourth order compact boundary scheme of (Lele, 1992). Explicit interior schemes using the above boundary treatment have also been used. Using explicit schemes for both the interior and the boundaries, as shown above, yielded a most satisfactory result. Instability and reflection was not a problem, especially at the corner points if all three boundaries are specified as outflow. Therefore the present method requires no extra features such as filtering, thus maintaining a minimum computational effort.

4. Parallel Implementation

SENGAs was developed with modular "plug in" differentiators, thus enabling different numerical schemes and parallel transfer interfaces to be implemented with ease. For a full description of the code, numerics and parallel methodology see (Jenkins and Cant, 1999).

Parallel implementation is achieved by domain decomposition in three dimensions for $1 \rightarrow N_p$, where N_p represents the number of processors available. Initially, the global initial parameters are distributed together with boundary conditions on to all N_p processors. Then for each time advancement sub-step, subroutines transfer

DNS OF TURBULENT FLAME KERNELS

the parallel data.

In order to calculate all spatial derivative relationships in parallel, six variables (ρ , E , c , u , v and w) are transferred across neighbouring processors which do not have a boundary constraint. The transfer operations require a halo width of five grid points to accommodate the stencil width of the explicit schemes discussed in section 3.

Second cross derivative terms in the viscous stress tensor were initially calculated using successive first derivatives. Using this method, a 64 processor job required an extra 288 transfers on top of the 1728 passes required from the data transfer subroutines. Therefore to eliminate the extra transfers and improve parallel efficiency, cross derivatives are now calculated directly. This requires corner data which is easily obtained by transferring x , y and z direction data in succession and avoids more than one face of a processor being in transfer mode at the same time. A rigorous parallel performance test for $1 \rightarrow 64$ processors on a Hitachi SR2201 was undertaken to demonstrate speed up values $S_p = \frac{t_1}{t_p}$ and parallel efficiency $E_p = \frac{S_p}{p}$, where t_1 and t_p represent the wall clock times on one and number of processors p respectively. Performance tests are normally carried out with the same number of grids on each processor. However, SENGAs was tested with a constant global domain size of 60^3 as the number of processors increases. Increasing the number of processors reduces the local computational domain size on each processor which is 60^3 for 1 processor and 15^3 for 64 processors. Therefore, for each test, the number of communications remain constant compared with the local domain sizes, giving a clear indication of the parallel benefits. Results for 1, 2, 4, 8, 27 and 64 processors are shown in Figure 1. For 1728 send and receives using 64 processors, a parallel efficiency of nearly 60 % is achieved with a speed up factor of over 30 for a constant global domain. (Emerson, 1996) gives reasons for not achieving perfect efficiency and speed up.

5. Simulation Method and Parameters

Results from two problem definitions will be shown, one for a laminar flame on a grid size of 384^3 points and the other for a turbulent flame on a grid size of 96^3 points. For each case, the same problem parameters were used as shown in table 2.

TABLE 2. Problem Parameters

B	α	τ	β	Re	Pr	Sc	M
1225.0	0.83	5.0	6.0	30	0.7	0.7	0.00142

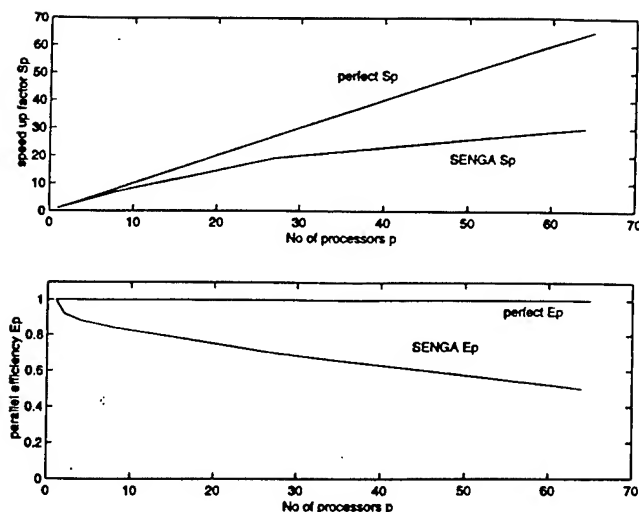


Figure 1. Parallel Speed up and Efficiency

Method one was initialised by setting up a Gaussian distribution of the progress variable c decomposed onto 64 processors, each with a grid size of 96^3 . Results obtained using the numerical schemes described above with six outflowing boundaries are shown in Figure 2 as profiles of temperature, density, velocity and reaction rate. Note that the profiles are taken through the flame along the centre x -axis which shows the left and right flame front of the kernel. These profiles were obtained by allowing the flame to evolve from the initial condition in a time dependent computation with a fully resolved acoustic field.

This test was undertaken to demonstrate the stability and symmetry obtained from the code and to use this 384^3 laminar solution as a data base comparison to the turbulent 384^3 case, which is in progress. The density and temperature profiles shows there is a significant heat release due to the left and right flame front. The figures also show the preheat zone ahead of the thin reaction zone, a rapid change in velocity behind the flame, and the slope of the temperature profile to equilibrium (fully burned) is well captured. Figure 3 shows contours of progress variable ranging from 0.1 to 0.9 at the centre x - y plane. The reaction progress variable shows the stages of the combustion process from the unburned case ($c=0$) to the fully burned case ($c=1$) with a non dimensional flame thickness of 0.36. The simulation was run over 4000 time steps with a non dimensional laminar flame speed of 0.401 and an initial mass fraction burned of 0.0719 ($t=0$).

Method two employs a 64 processors in parallel to simulate 64 turbulent cases,

DNS OF TURBULENT FLAME KERNELS

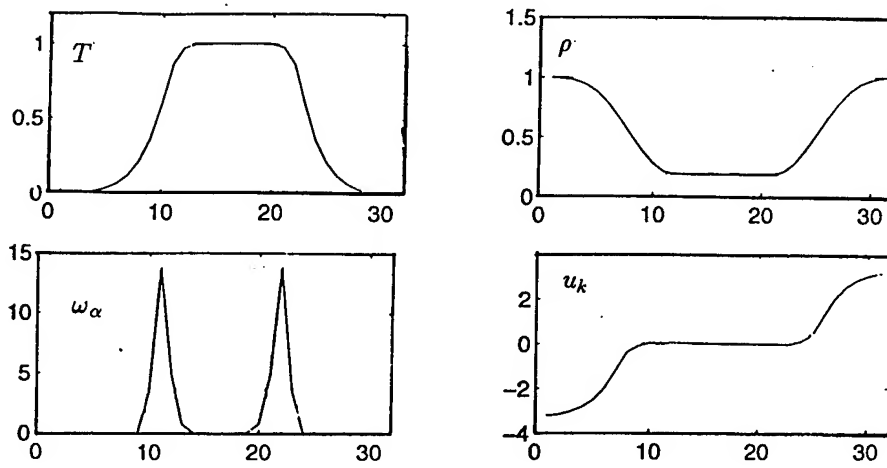


Figure 2. Profiles along centre x-axis

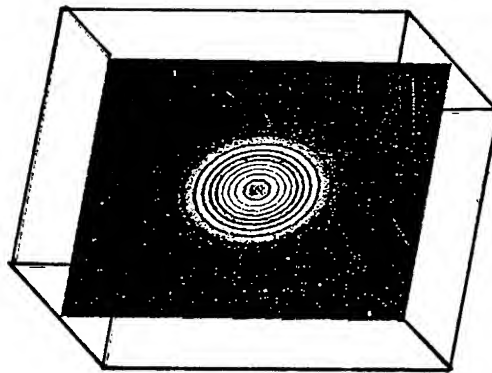


Figure 3. Progress variable contours at the centre x-y plane

each with a different initial turbulent field. Each simulation takes place on a 96^3 grid with outflowing boundaries on each face, and since there is no passing of data a parallel efficiency of 100 % is achieved. Initially 64 different turbulent fields were generated with initial $\frac{u'}{S_L}$ values ranging from 0.516 to 15.96 and large eddy turn over times $\frac{L}{u'}$ ranging from 0.10 to 3.19, where L is the turbulent integral length scale. A laminar flame evolved over 100 time steps was then centred in each de-

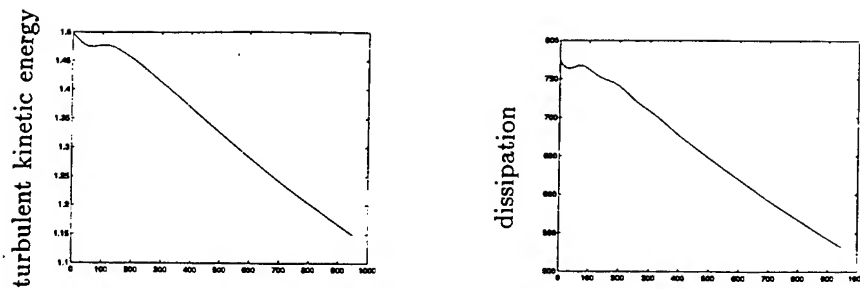


Figure 4. Turbulent kinetic energy and dissipation decay from processor 0

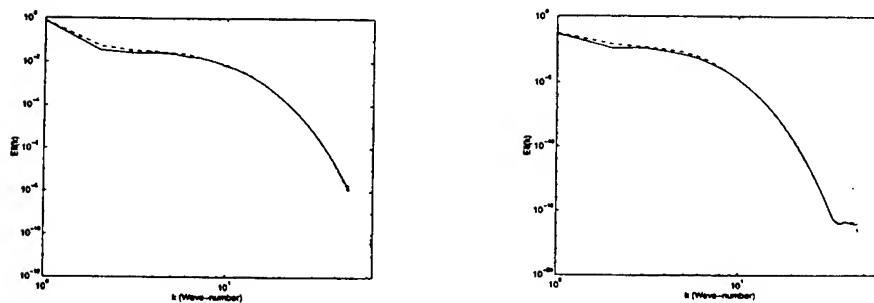


Figure 5. Radial energy spectra after 300 and 1500 time steps

caying turbulent field to start the flame turbulence interactions.

In the absence of any source of energy the initial turbulence described in section 2 should decay to isotropic turbulence with time. This decay was checked on each processor before any flame inclusion following the work of (Lee and Reynolds, 1985). First, the turbulent kinetic energy and dissipation were calculated to ensure isotropic decay on each processor. Figure 4 shows the results from processor 0, note the first 100 time steps shows a non decaying section due to the approximation of the initial turbulence. Therefore the turbulent field in each case was allowed to run 200 time steps before the inclusion of the flame. Also, the diagonal component of energy tensor $E_{ii}(k)$ at two time intervals was calculated. Figure 5 show clear evidence of isotropy at 300 and 1500 time steps for all wave numbers

Finally, Figure 6 shows a three dimensional surface plot of the progress variable c , ranging from 0.15 to 0.75 from processor 10 after 4000 time steps. The figure indicates the initial period from the laminar flame ($t=0$) to the onset of flame

DNS OF TURBULENT FLAME KERNELS

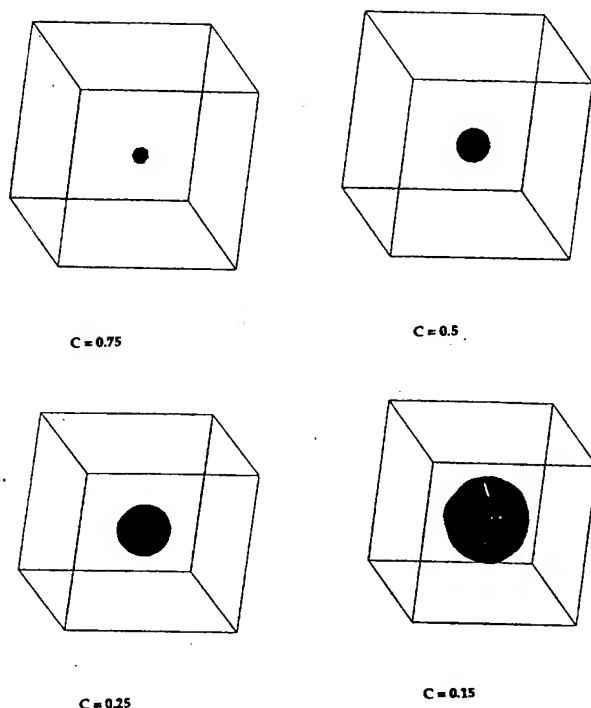


Figure 6. 3D surface plots of progress variable after 4000 time steps

wrinkling, more noticeable at the lower value of progress variable.

6. Conclusions

Initial results up to 4000 time steps for a wide variety of turbulent simulations indicate that the flame is still stabilising with an almost linear increase in mass fraction burned. Considering that two weeks of cpu time was used to reach this stage, up to three months of elapsed time may be needed to see extensive flame wrinkling.

However the code has shown excellent performance for such a robust test and isotropic decaying turbulence has been achieved. Therefore further turbulent results will emerge in due course.

Acknowledgements

This work has been supported by EPSRC under research grant numbers GR/K96519 and GR/M18256. The authors would also like to thank the High Performance Computing Centre at Cambridge University for their assistance and access to the Hitachi SR2201.

References

- Batchelor, G.K. (1953) The theory of homogeneous turbulence, *Cambridge University Press*.
- Baum, M., Poinso, T.J., Haworth, D.C. (1992) Numerical simulations of turbulent premixed $H_2/O_2/N_2$ flames with complex chemistry, *Proc. 1992 Summer Program* pp. 345-366. Centre for Turbulence Research, Stanford University and NASA Ames.
- Bradshaw, P. (1971) An introduction to turbulence and its measurement, *Pergamon Press*.
- Cant, R.S. (1994) Direct numerical simulations in combustion, *ERCOFTAC Summer School on Turbulent Combustion and its Computation*, Cambridge, Sept 1994.
- Emerson, D.R. (1996) Introduction to parallel computers, in *High Performance Computing in Fluid Dynamics*, ERCOFTAC Summer School, Delft University, The Netherlands June 24-28, *Kluwer Academic Press*.
- Herring, J.R., Orszag, S.A., Kraichnan, R.H., Fox, D.G. (1974) Decay of two dimensional homogeneous turbulence, *J.Fluid Mech* 66 pp. 417-444.
- Jenkins, K.W., Cant, R.S. (1999) Parallel Combustion DNS results, *Cambridge University Engineering Dept Technical Report*, In print.
- Kuo, K.K. (1986) Principles of Combustion, *Wiley Interscience Publication*.
- Lee, M.J., Reynolds, W.C. (1985) Numerical experiments on the structure of homogeneous turbulence. *Technical report TF-24* Dept of Mech Eng, Stanford University.
- Lele, S.K. (1992) Compact finite difference schemes with spectral like resolution, *J.Comp.Phys* 103, 16-42.
- Poinso, T.J. (1991) Flame ignition in premixed turbulent flow, *Centre for Turbulence Research Annual Research Briefs* Stanford University and NASA Ames. Centre for Turbulence Research 1-22.
- Poinso, T., Lele, S.K. (1992) Boundary conditions for direct simulations of compressible viscous flows, *J.Comp.Phys* 101, 104-129.
- Poinso, T.J., Candel, S., Trounev, A. (1996) Applications of direct numerical simulation to premixed turbulent combustion, *Prog Energy Comb Sci*, Vol 21, pp. 531-576.
- Rutland, C.J., Cant, R.S. (1994) Turbulent transport in premixed flames, *Centre for Turbulence Research Summer School*, Stanford University and NASA Ames. Centre for Turbulence Research.
- Tennekes, H., Lumley, J.L. (1972) A first course in turbulence, *MIT Press* Cambridge, Mass.
- Trove, A., Poinso, T. (1994) The evolution equation for the flame surface density in turbulent premixed combustion, *J.Fluid Mech* 278, 1-31.
- Wray, A.A. (1990) Minimal storage time advancement schemes for spectral methods, *unpublished report*, NASA Ames.

DIRECT NUMERICAL SIMULATION OF BOUNDARY-LAYER RECEPTIVITY FOR SUBSONIC FLOW AROUND AIRFOIL

LI JIANG, HUA SHAN, CHAOQUN LIU
*Center for Numerical Simulation and Modeling,
Louisiana Tech University, Ruston, LA*

Abstract

Direct numerical simulation is used to study leading edge receptivity to free-stream disturbance. The full compressible Navier-Stokes equations in generalized curvilinear coordinates are solved by LU-SGS implicit scheme, which requires no tridiagonal inversion and is capable of being completely vectorized and parallelized. A fourth-order centered compact scheme is used for spatial derivatives and second-order Euler Backward scheme is applied for temporal discretization. A sixth-order implicit filter is employed to reduce the numerical oscillation. The non-reflecting boundary conditions are imposed at the far-field and outflow boundaries to avoid possible non-physical wave reflection. The code is developed in a form of total flow and no base flow with perturbation assumption is needed. The code also does not need buffer or sponge domain for DNS. The leading-edge receptivities of the compressible boundary-layer over the flat plate and the Joukowski airfoil to free-stream disturbances are simulated.

1. Introduction

The boundary-layer receptivity is the process by which the external disturbances enter the boundary-layer and excite instability waves. These disturbances include environmental sound, vorticity, and free-stream turbulence. In the process of transition from laminar to turbulent flow, receptivity is the initial stage. Investigation of the receptivity mechanism contributes to understanding of where and how the instability waves are generated. Obviously, it plays an important role in transition prediction.

The receptivity problem is different from the stability problem, which is an eigenvalue problem. The receptivity is modeled as an initial value problem. The boundary-layer receptivity to free-stream disturbance has

been investigated theoretically, experimentally and numerically, and much progress has been made during the past decades.

Theoretical analyses based on asymptotic solutions of the Navier-Stokes equation [1] have shown that the boundary-layer receptivity to free-stream long-wave disturbance is generated by wavelength adjustment mechanism. This adjustment can be attributed to the rapid streamwise variations in the mean boundary-layer flow and/or sudden changes in surface boundary condition. Therefore, many different factors can be regarded as to introduce a disturbance into the boundary-layer, for example, leading-edge, discontinuity in surface curvature, and strong pressure gradient. Though theoretical study has made much progress in understanding receptivity mechanism, it is still a long way from practical application for complex flow.

In recent years, numerical study is becoming more appealing because of the development of powerful computers and efficient numerical techniques. As far as computational approaches are concerned, the numerical scheme must have high resolution and high accuracy in order to resolve a wide range of physical waves, such as the free-stream disturbances with long wavelength and the generated instability waves with short wavelength. Low dissipation is required to accurately predict the development of the instability waves which have much smaller amplitudes compared to the mean flow. The treatment of boundary conditions is also important to prevent waves from reflecting on the boundary which may contaminate the actual instability waves. So receptivity calculation is a great challenge to DNS code. However, some encouraging results have appeared in literatures. Most work has been concerned with leading-edge receptivity to free-stream sound and vorticity. For incompressible flow, Lin *et al.* [2] simulated the receptivity to free-stream sound of the flat-plate boundary-layer over a semi-infinite flat plate with an elliptic leading edge. In their simulation, the full incompressible Navier-Stokes equations in the form of vorticity and stream function were solved with a second-order finite difference scheme. Spatial and temporal developments of Tollmien-Schlichting (T-S) waves in the boundary-layer were observed. The effects of the leading-edge shape (ellipse ratio $AR = 3, 6, 9$) and juncture continuity were studied. The results showed that the sharper leading edge is less receptive and the contribution of the discontinuity in curvature to receptivity is substantial. The same geometry and flow parameters as [2] were chosen by Buter and Reed [3], but the external disturbance was free-stream vorticity. The Modified Strongly Implicit Procedure was used to solve incompressible Navier-Stokes equation in the form of vorticity and stream function with a second-order finite difference scheme. On the outflow boundary the second-order derivatives were specified. To avoid wave reflection, the unsteady simulations were terminated before the disturbance wave front reached the downstream boundary. Their

results showed distinct development of T-S waves in the boundary-layer along the flat-plate. The effects of disturbance amplitude, orientation, the shape of the leading edge, and the surface curvature were also investigated. Some valuable conclusions were achieved. Osamah *et al.* [4] studied the receptivity to free-stream sound of boundary-layer over a slender body with a parabolic leading edge. The incompressible Navier-Stokes equations in the stream function and vorticity form were converted to two systems of equations describing the basic flow and perturbation flow. These two systems were solved separately using a second-order finite difference scheme. To avoid wave reflection, a buffer domain is used near the outflow boundary, where the governing equations are parabolized. The effects of leading edge nose radius and angle of attack were investigated. Both two- and three-dimensional leading-edge receptivity have been simulated by Liu *et al.* [6]. The geometries include the flat-plate with elliptic leading edge and the Joukowski airfoil. The total flow was divided into two parts: the base flow and the disturbance flow, which were solved separately with different equations. The buffer domain is used to damp the possible reflecting waves on the outflow boundary. The vortical disturbance was introduced at upstream. T-S waves were observed developing along the flat-plate and airfoil. For compressible flow, Collis and Lele's [5] worked on the numerical simulation of the boundary-layer receptivity of a flat-plate with a super-elliptic leading-edge to the free-stream acoustic wave at Mach number $M = 0.1$ and $M = 0.8$ respectively. The total flow and the disturbance flow were solved with different equations, which were discretized using the hybrid finite difference and the spectral approximation. For the base flow, a non-reflecting boundary condition with viscous correction was used on the outflow boundary, while a first-order Reimann extrapolation was performed on the inflow boundary. For the disturbance flow, in addition to these boundary conditions, extra terms were added to the Navier-Stokes equations at the sponge domains near the inflow, outflow and far-field boundaries to absorb the out-going waves. The T-S wave growth was clearly presented by their results. The results also showed that the disturbance amplitude significantly increases with Mach number, which suggests that the flow is more unstable at higher Mach numbers.

In summary, there are two kinds of numerical approaches to simulate the boundary-layer receptivity to free-stream disturbance. One is to solve the base flow and the disturbance flow separately, the other is to solve the total flow. The advantage of the first approach lies in the fact that high accuracy is more likely preserved when the disturbance flow is solved separately, because the perturbation is several orders smaller than the base flow. But this approach becomes impractical when the flow with complex geometry is concerned, where the base flow does not exist or is hard to estimated.

In this case, from the physical point of view, the second approach is more reasonable. Because of the huge amplitude difference between the base flow and the perturbation, the second approach needs more effective numerical techniques. In this work, a compressible Navier-Stokes solver for total flow is developed to simulate the leading edge receptivity of boundary-layer over complex geometry to free-stream sound and vorticity. The numerical method and computational results are presented in the following sections.

2. Governing Equations

The three-dimensional compressible Navier-Stokes equations in generalized curvilinear coordinates (ξ, η, ζ) can be written in conservative forms:

$$\frac{1}{J} \frac{\partial Q}{\partial t} + \frac{\partial(E - E_v)}{\partial \xi} + \frac{\partial(F - F_v)}{\partial \eta} + \frac{\partial(G - G_v)}{\partial \zeta} = 0 \quad (1)$$

The flux vectors for compressible flow are

$$\begin{aligned} Q &= \begin{pmatrix} \rho \\ \rho u \\ \rho v \\ \rho w \\ e \end{pmatrix} \quad E = \frac{1}{J} \begin{pmatrix} \rho U \\ \rho U u + p \xi_x \\ \rho U v + p \xi_y \\ \rho U w + p \xi_z \\ U(e + p) \end{pmatrix} \quad F = \frac{1}{J} \begin{pmatrix} \rho V \\ \rho V u + p \eta_x \\ \rho V v + p \eta_y \\ \rho V w + p \eta_z \\ V(e + p) \end{pmatrix} \\ G &= \frac{1}{J} \begin{pmatrix} \rho W \\ \rho W u + p \zeta_x \\ \rho W v + p \zeta_y \\ \rho W w + p \zeta_z \\ W(e + p) \end{pmatrix} \quad E_v = \frac{1}{J} \begin{pmatrix} 0 \\ \tau_{xx}\xi_x + \tau_{yx}\xi_y + \tau_{zx}\xi_z \\ \tau_{xy}\xi_x + \tau_{yy}\xi_y + \tau_{zy}\xi_z \\ \tau_{xz}\xi_x + \tau_{yz}\xi_y + \tau_{zz}\xi_z \\ q_x\xi_x + q_y\xi_y + q_z\xi_z \end{pmatrix} \\ F_v &= \frac{1}{J} \begin{pmatrix} 0 \\ \tau_{xx}\eta_x + \tau_{yx}\eta_y + \tau_{zx}\eta_z \\ \tau_{xy}\eta_x + \tau_{yy}\eta_y + \tau_{zy}\eta_z \\ \tau_{xz}\eta_x + \tau_{yz}\eta_y + \tau_{zz}\eta_z \\ q_x\eta_x + q_y\eta_y + q_z\eta_z \end{pmatrix} \quad G_v = \frac{1}{J} \begin{pmatrix} 0 \\ \tau_{xx}\zeta_x + \tau_{yx}\zeta_y + \tau_{zx}\zeta_z \\ \tau_{xy}\zeta_x + \tau_{yy}\zeta_y + \tau_{zy}\zeta_z \\ \tau_{xz}\zeta_x + \tau_{yz}\zeta_y + \tau_{zz}\zeta_z \\ q_x\zeta_x + q_y\zeta_y + q_z\zeta_z \end{pmatrix} \end{aligned}$$

where J is Jacobian of the coordinate transformation, and $\xi_x, \xi_y, \xi_z, \eta_x, \eta_y, \eta_z, \zeta_x, \zeta_y, \zeta_z$ are coordinate transformation metrics.

$$U = u\xi_x + v\xi_y + w\xi_z, \quad V = u\eta_x + v\eta_y + w\eta_z, \quad W = u\zeta_x + v\zeta_y + w\zeta_z \quad (2)$$

$$e = \frac{p}{\gamma - 1} + \frac{1}{2}\rho(u^2 + v^2 + w^2) \quad (3)$$

The components of the viscous stress and heat flux are denoted by $\tau_{xx}, \tau_{yy}, \tau_{zz}, \tau_{xy}, \tau_{xz}, \tau_{yz}$, and q_x, q_y, q_z , respectively. All the equations are cast in

nondimensional forms, and the resulting parameters are defined as:

$$M_r = \frac{U_r^*}{\sqrt{\gamma R T_r^*}}, \quad Re = \frac{\rho_r^* U_r^* L^*}{\mu_r^*}, \quad Pr = \frac{C_p \mu_r^*}{\kappa_r^*}, \quad \gamma = \frac{C_p}{C_v} \quad (4)$$

The superscript * represents the reference value. R , C_p and C_v are the ideal gas constant, the specific heat at constant pressure and constant volume, respectively. The viscosity is derived from the Sutherland's law in dimensionless form:

$$\mu = T^{\frac{3}{2}} \frac{1+S}{T+S}, \quad S = \frac{110.3}{T_r^*} \quad (5)$$

3. Numerical Method

In Eq. (1), the second-order Euler Backward scheme is used for time discretization. The fully implicit form of the difference equation is:

$$\begin{aligned} & \frac{3Q^{n+1} - 4Q^n + Q^{n-1}}{2J\Delta t} + \frac{\partial(E^{n+1} - E_v^{n+1})}{\partial\xi} \\ & + \frac{\partial(F^{n+1} - F_v^{n+1})}{\partial\eta} + \frac{\partial(G^{n+1} - G_v^{n+1})}{\partial\zeta} = 0 \end{aligned} \quad (6)$$

Q^{n+1} is estimated iteratively as:

$$Q^{n+1} = Q^p + \delta Q^p \quad (7)$$

$$\delta Q^p = Q^{p+1} - Q^p \quad (8)$$

At step $p = 0$, $Q^p = Q^n$. As δQ^p is driven to zero, Q^p approaches Q^{n+1} . The flux vectors are linearized as following:

$$E^{n+1} \approx E^p + A^p \delta Q^p, \quad F^{n+1} \approx F^p + B^p \delta Q^p, \quad G^{n+1} \approx G^p + C^p \delta Q^p \quad (9)$$

So that Eq. (6) can be written as:

$$\left[\frac{3}{2}I + \Delta t J (D_\xi A + D_\eta B + D_\zeta C) \right] \delta Q^p = R \quad (10)$$

where R is the residual:

$$\begin{aligned} R = & -\left(\frac{3}{2}Q^p - 2Q^n + \frac{1}{2}Q^{n-1}\right) \\ & - \Delta t J [(D_\xi(E - E_v) + D_\eta(F - F_v) + D_\zeta(G - G_v))]^p \end{aligned} \quad (11)$$

D_ξ, D_η, D_ζ represent partial differential operators, A, B, C are the Jacobian matrices of flux vectors:

$$A = \frac{\partial E}{\partial Q}, \quad B = \frac{\partial F}{\partial Q}, \quad C = \frac{\partial G}{\partial Q} \quad (12)$$

The right hand side of Eq. (10) is discretized using a fourth-order compact scheme [7] for spatial derivatives, and the left hand side of the equation is discretized following the LU-SGS [8] method. In this method, the Jacobian matrices of flux vectors are split as:

$$A = A^+ + A^-, \quad B = B^+ + B^-, \quad C = C^+ + C^- \quad (13)$$

where,

$$A^\pm = \frac{1}{2}[A \pm r_A I], \quad B^\pm = \frac{1}{2}[B \pm r_B I], \quad C^\pm = \frac{1}{2}[C \pm r_C I] \quad (14)$$

where,

$$\begin{aligned} r_A &= \kappa \times \max[|\lambda(A)|] + \tilde{\nu} \\ r_B &= \kappa \times \max[|\lambda(B)|] + \tilde{\nu} \\ r_C &= \kappa \times \max[|\lambda(C)|] + \tilde{\nu} \end{aligned} \quad (15)$$

where $\lambda(A)$, $\lambda(B)$, $\lambda(C)$ are eigenvalues of A , B , C respectively, κ is a constant greater than 1. $\tilde{\nu}$ is associated to the effects of viscous terms.

$$\tilde{\nu} = \max \left[\frac{\mu}{(\gamma - 1)M_r^2 R_e P_r}, \frac{4}{3} \frac{\mu}{R_e} \right] \quad (16)$$

The first-order upwind finite difference scheme is used for the split flux terms in the left hand side of Eq. (10). As the left hand side is driven to zero by iteration, the discretization error will also be driven to zero. So the first-order upwind scheme will not destroy the accuracy of the approach. The finite difference representation of Eq. (10) can be written as:

$$\begin{aligned} \left[\frac{3}{2}I + \Delta t J(r_A + r_B + r_C)I \right] \delta Q_{i,j,k}^p &= R_{i,j,k}^p \\ &- \Delta t J [A^- \delta Q_{i+1,j,k}^p - A^+ \delta Q_{i-1,j,k}^p \\ &+ B^- \delta Q_{i,j+1,k}^p - B^+ \delta Q_{i,j-1,k}^p \\ &+ C^- \delta Q_{i,j,k+1}^p - C^+ \delta Q_{i,j,k-1}^p] \end{aligned} \quad (17)$$

In LU-SGS scheme, Eq. (17) is solved by three steps. First, δQ^0 is initialized using

$$\delta Q_{i,j,k}^0 = \left[\frac{3}{2}I + \Delta t J(r_A + r_B + r_C)I \right]^{-1} R_{i,j,k}^p \quad (18)$$

In the second step, $\delta Q_{i,j,k}^*$ is obtained by

$$\begin{aligned} \delta Q_{i,j,k}^* &= \delta Q_{i,j,k}^0 + \left[\frac{3}{2}I + \Delta t J(r_A + r_B + r_C)I \right]^{-1} \\ &\times [\Delta t J (A^+ \delta Q_{i-1,j,k}^* + B^+ \delta Q_{i,j-1,k}^* + C^+ \delta Q_{i,j,k-1}^*)] \end{aligned} \quad (19)$$

In the last step, δQ^p is obtained by

$$\begin{aligned} \delta Q_{i,j,k}^p &= \delta Q_{i,j,k}^* - \left[\frac{3}{2}I + \Delta t J(r_A + r_B + r_C) \right]^{-1} \\ &\times [\Delta t J(A^- \delta Q_{i+1,j,k}^p + B^- \delta Q_{i,j+1,k}^p + C^- \delta Q_{i,j,k+1}^p)] \quad (20) \end{aligned}$$

The sweeping is performed along the planes of $i + j + k = \text{const}$, i.e. in the second step, sweeping is performed from the low-left corner of the grid to the high-right corner, and then vice versa in the third step.

To depress numerical oscillation caused by numerical scheme, spatial filtering is used instead of artificial dissipation. Implicit sixth-order compact scheme for space filtering [7] is applied for primitive variables u, v, w, ρ, p after each time step.

For subsonic flow, u, v, w, T are prescribed at upstream boundary, ρ is obtained by solving modified N-S equation based on characteristic analysis. On the far field and out flow boundary, non-reflecting boundary conditions are applied. The adiabatic and the non-slipping conditions are used for the wall boundary. All equations of boundary conditions are solved implicitly with interior points. Specific details of boundary treatment can be found in [9].

4. Numerical Result

4.1. NUMERICAL VERIFICATION

Based on the numerical methods and boundary conditions discussed in the previous section, the corresponding computer code has been developed. The flat plate flow of $M = 0.5$, $Re_\delta = 1000$ is selected as the testing case for code validation. δ is the displacement thickness at the inlet of the computational domain. The similarity solution of the flat plate flow is used as the initial value to obtain a steady solution, which will be used as the initial field of unsteady problems.

The spatial evolutions of small disturbance imposed at the inlet are simulated. At the inlet boundary, the eigenfunction obtained from the Linear Stability Theory (LST) is enforced. The eigenfunction has a frequency of $\omega = 0.114$, and a space wavenumber of $\alpha = 0.29919 - i5.09586 \times 10^{-3}$. The streamwise length of the computational domain includes 8 T-S wavelengths, and the inlet height is 40δ . A uniform mesh is used in the streamwise direction x and a stretched mesh is used in the wall normal direction y . The corresponding grid spacing at the wall in y direction is $\Delta y = 0.03774\delta$. The overall grid size is of 128×41 .

At the far-field and the outflow boundaries, non-reflecting boundary conditions [9] are used. The number of time steps used per time period is 500. After 10 time period of calculation, the T-S wave has been fully

established over the entire domain, and the disturbances are picked out for analysis. The distributions of disturbance amplitude of the streamwise velocity u , the wall normal velocity w , the pressure p , and the temperature T are shown in Fig. 1 by solid lines, while the linear stability theory (LST) results are shown by symbols in the same figure. The computational results are in good agreement with the LST results. In Fig. 2, the growth rate α_i from the computation and the linear theory are displayed. Deviation only appears near the outflow boundary, and no reflecting wave influences upstream field.

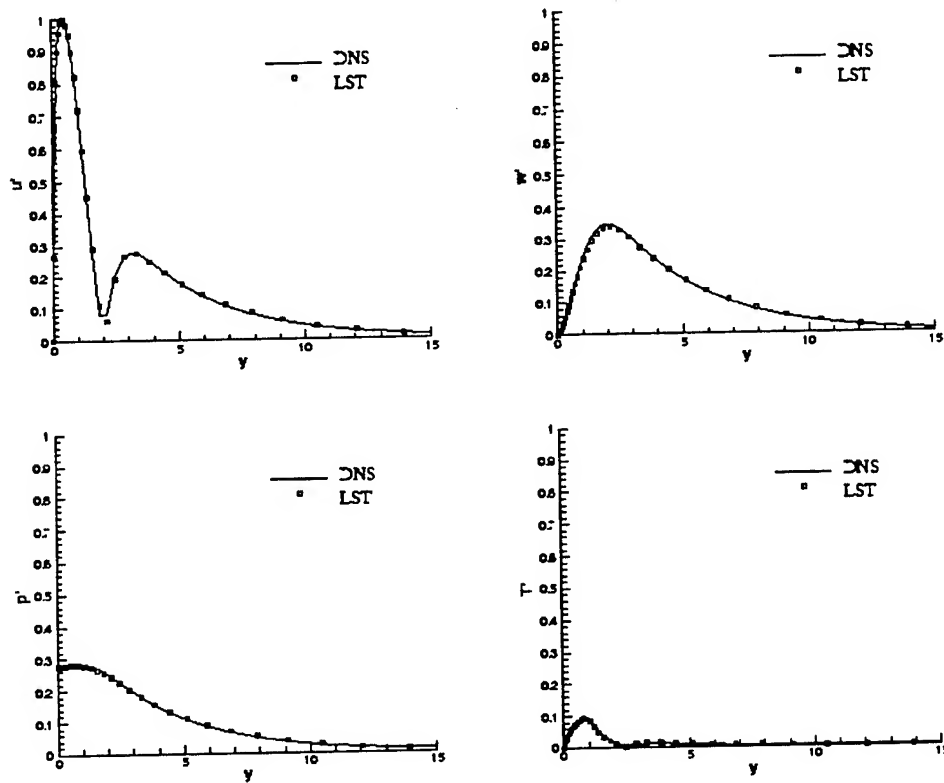


Figure 1. Amplitude distributions in the wall-normal direction at $Re_x = 339,200$

4.2. LEADING EDGE RECEPTIVITY OF BOUNDARY LAYER OVER THE FLAT-PLATE

Direct numerical simulations of leading edge receptivity of boundary layer over the flat-plate to free-stream disturbance are presented in this section.

The leading edge geometry is described by the following formula:

$$\left(1 - \frac{x}{AR}\right)^m + y^n = 1 \quad (21)$$

Two different geometries are chosen. One is the super-ellipse with $AR = 6$, $m = 4$, and $n = 2$, which was used by Lin *et al.* [2] and Collis *et al.* [5], and the other is the ordinary ellipse with $AR = 6$, $m = 2$, and $n = 2$, which was used by Lin *et al.* [2], Buter *et al.* [3] and Liu *et al.* [6]. The difference between these two geometries is that the super ellipse has continuous curvature at the juncture of leading edge with flat-plate, while the curvature at the juncture is discontinuous for the ordinary ellipse, which is also sharper than the super ellipse. The half thickness of the flat-plate h is selected as the reference length. For all calculations, the Reynolds number, based on h and the free-stream velocity U is $Re = 2400$. The Mach number is $M = 0.1$. The angle of attack is zero.

The C-type grids are generated using an elliptic grid generation method based on a composite mapping, which is consisted of an algebraic- and an elliptic-transformation [10]. Meshes are clustered near the leading edge and near the wall. For the ordinary ellipse, meshes are also clustered at the juncture. Grids of 741×121 and 801×121 are used for the super-ellipse and the ordinary ellipse geometry, respectively. These meshes have more than 20 grid points in the streamwise direction for each T-S wave. Fig. 3 shows the grids for the super-ellipse geometry.

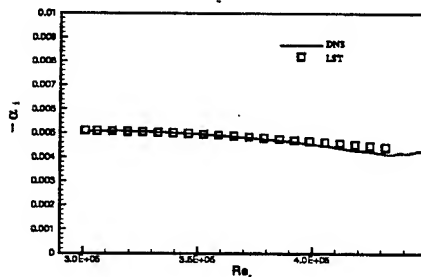


Figure 2. Evolution of spatial growth rate of T-S wave

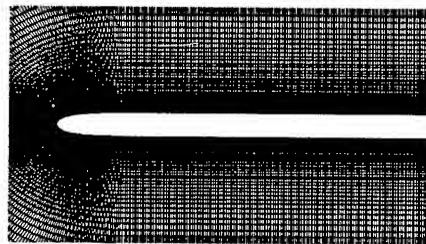


Figure 3. Computational mesh for the flat-plate with super-ellipse leading-edge

Steady state solutions are first obtained by advancing unsteady flow computation to convergence. Fig. 4 and Fig. 5 show the results for the super-ellipse leading-edge. Fig. 4 gives the distribution of pressure gradient with respect to arc length s along the flat-plate, where the maximum adverse pressure gradient appears in the region of the leading-edge. Downstream of the pressure-recovery region, the pressure gradient becomes very

small and tends to be constant downstream. Fig. 5 shows the streamwise velocity profile at the streamwise location of $x = 22.7$, where η is the Blasius variable. In these two figures, the results from [5] are also depicted for comparison, and both the results are in good agreement. Fig. 6 and Fig. 7 show the the steady state results for the ordinary ellipse leading-edge. In Fig. 6 the maximum adverse pressure gradient appears exactly at the juncture point, where the discontinuity of surface curvature occurs. Because the ellipse leading-edge is sharper than the super-ellipse leading edge, the maximum magnitude of the adverse pressure gradient is smaller. The streamwise velocities at the juncture ($x = 6$) and downstream of the juncture ($x = 22.7$) are shown in Fig. 7, where the non-parallel characteristic of the boundary-layer flow is observed. In these two cases, rapid streamwise variations of pressure distribution appear in the region of the leading-edge and the juncture, which is considered as one of the motivations of the wavelength-adjustment mechanism in the receptivity problem.

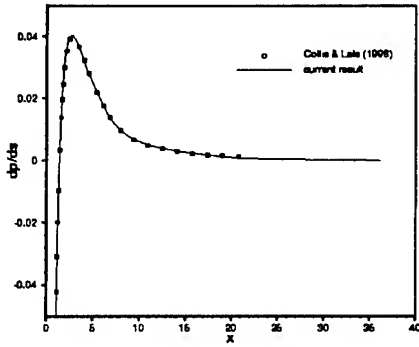


Figure 4. Pressure gradient along the flat-plate with super-ellipse leading-edge

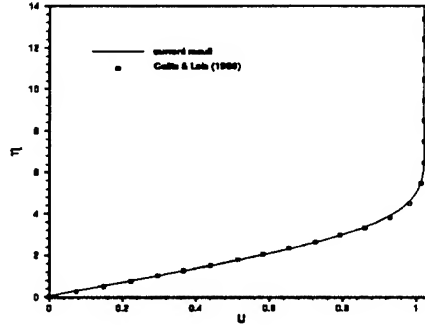


Figure 5. Streamwise velocity profile at $x = 22.7$ of flat-plate with super-ellipse leading-edge

4.2.1. Receptivity to Acoustic Wave

The super-ellipse leading-edge receptivity to acoustic wave is simulated. Starting from the steady flow solution as the initial condition, unsteady flow computation is performed by imposing an acoustic wave with the amplitude of 0.001 in the free-stream, which is similar to [11]. The non-dimensional frequency is chosen as $F = 230$ which is the same as used by Collis *et al.* [5]. After enough periods of forcing, a periodic solution is attained for the entire flow field. Fig. 8 shows the contours of vertical disturbance velocity v' . Because the Stokes-wave has nearly no effect on the vertical direction, the

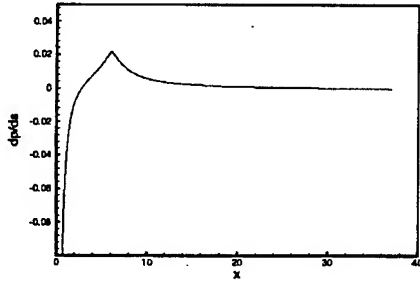


Figure 6. Pressure gradient along the flat-plate with ellipse leading-edge

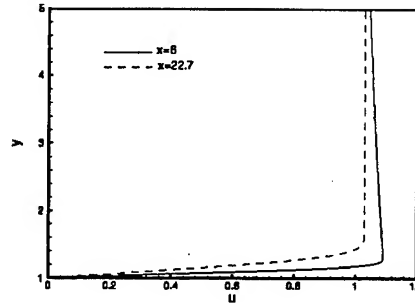


Figure 7. Streamwise velocity profile at different locations of flat-plate with ellipse leading-edge

contours of the vertical disturbance velocity clearly shows the generation of the instability wave from the leading edge and the its development along the flat-plate. The ratio of the T-S wavelength to the forced acoustic wavelength is about 1:30, which agrees with the result of Collis *et al.* [5]. The vertical disturbance velocity near the wall at $y = 0.2$ is displayed as a function of the streamwise coordinate x in Fig. 9, where the growth of the disturbance is obvious.

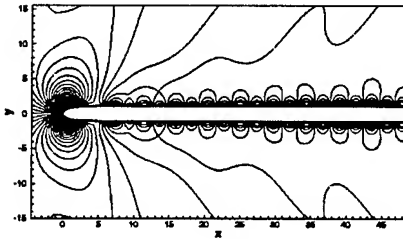


Figure 8. Contours of vertical disturbance velocity

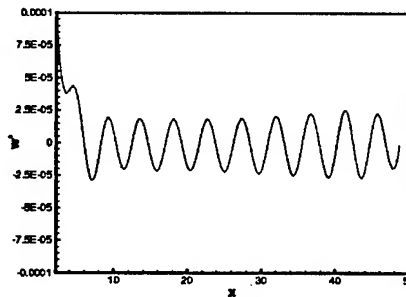


Figure 9. Vertical disturbance velocity distribution along the flat-plate at $y = 0.2$

The development of the forced acoustic wave is depicted in Fig. 10 as the contours of streamwise disturbance velocity u' . There is no evident distortion in the far field and the outlet boundary. That means the non-reflecting boundary condition works well. Near the flat-plate, because of the existence of the Stokes-wave, the development of the instability waves is obscured. Decomposition processing described in [3] is carried out to subtract the Stokes-wave from the total disturbance. Fig. 11 shows the contours of

the Fourier amplitude of the streamwise disturbance velocity u' after the Stokes-wave has been subtracted. The T-S wave is clearly growing along the plate. A comparison of the T-S wave amplification factor N along the flat plate with that obtained by Collis *et al.* [5] is presented in Fig. 12. The Branch-I locations from both the results are in good agreement. Fig. 13 shows the profile of streamwise disturbance velocity u' at different streamwise locations downstream of the juncture. These profiles are found to agree well with the typical T-S wave mode shape functions.

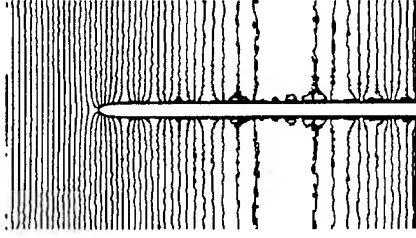


Figure 10. Contours of the streamwise disturbance velocity



Figure 11. Contours of the Fourier amplitude of the streamwise disturbance velocity after the Stokes-wave is subtracted

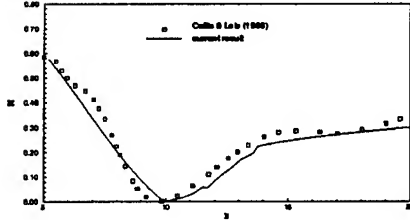


Figure 12. Amplification factor of T-S wave along flat-plate

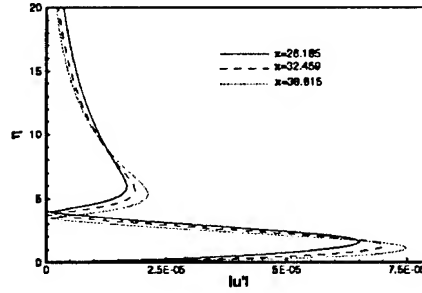


Figure 13. Amplitude profile of streamwise disturbance velocity after Stokes-wave is subtracted

4.2.2. Receptivity to Vortical Disturbance

Receptivity to free-stream vortical disturbance of boundary-layer over flat-plate with an ellipse leading-edge is calculated. The discontinuity of the surface curvature is another receptivity source apart from leading-edge. The free-stream vortical disturbance is written in the following form [6]:

$$u'(x_0, y, t) = \epsilon A(|y| - y_c) e^{-\frac{(|y| - y_c)^2}{k}} \cos(\omega t) \quad (22)$$

where A is a parameter for normalizing the amplitude, ω is the frequency, k is a constant to define the profile. The parameters used in this case are as follows: $\omega = 0.552$, $k = 0.0075$, $y_c = 0.05$, $\epsilon = 0.001$. The non-dimensional frequency is the same as used in the previous case, i.e. $F = 230$. After enough periods of forcing, the solutions of all field reach a periodic state. Fig. 14 shows the contours of streamwise disturbance velocity u' . This figure is enlarged in the y direction by three times to make a better display. In the streamwise direction, shortly after the juncture, the short wave disturbance is generated near the wall beneath the imposed long wave perturbation. Fig. 15 gives the streamwise distribution of the disturbance velocity u' at two different vertical locations. It is evident that the signal near the wall ($y = 0.0665$) has a shorter wavelength compared with that far from the wall ($y = 0.3577$). The computational results indicate that the short wave dominates near the wall, and in the middle of the boundary-layer, the wave is longer than the near wall wave and shorter than the free-stream wave. It is pointed out by [3] that the nature of the signal near the wall is influenced almost exclusively by the generated T-S waves. Fig. 15 also shows the growth of the T-S wave near the wall, while the long wave decays along the plate.

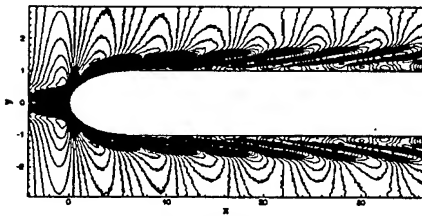


Figure 14. Contours of streamwise disturbance velocity

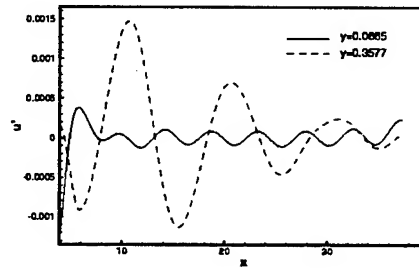


Figure 15. Distribution of streamwise disturbance velocity along the plate at different vertical locations

4.3. LEADING EDGE RECEPTIVITY OF AIRFOIL

The receptivity of boundary-layer over an airfoil to the free-stream vorticity is also simulated. The Joukowski airfoil is modified such that the ratio of the half-thickness to the chord-length is 1:45. Reynolds number based on the half-thickness and the free-stream velocity is $Re = 2400$, and Mach number is $M = 0.1$. The nondimensional frequency of free-stream disturbance is $F = 230$, and the amplitude is 0.01. These parameters are similar to those used in the previous cases for flat-plate simulation.

The C-type grids of 741×121 are plotted in Fig. 16. The shape of the leading edge of this Joukowski airfoil is sharper than that of the flat-plate used in previous two cases, and the surface curvature is smooth. It is predictable from the characteristics of this geometry that the boundary-layer over the airfoil is less receptive compared with the flat-plate. Fig. 17 shows the pressure gradient along the airfoil surface at the steady state. There is a rapid change of pressure gradient near the leading edge, but the maximum amplitude of the adverse pressure gradient is much smaller compared with the results from the flat-plate. In addition, most part of the airfoil locates in the region with an adverse pressure gradient. The pressure gradient decreases rapidly near the trailing edge.

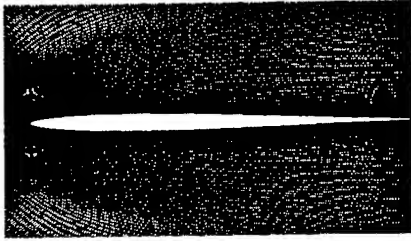


Figure 16. Grid distribution around the airfoil

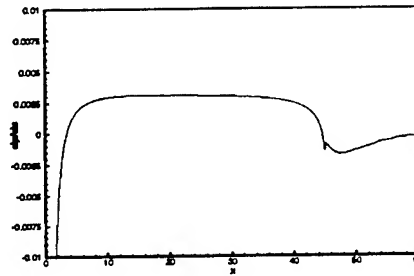


Figure 17. Pressure gradient along the airfoil

The unsteady calculation is carried out by introducing symmetric vortical disturbance at the upstream of the airfoil. After enough periods of forcing, the entire domain attains a periodic solution. Fig. 18 depicts the streamwise disturbance velocity at different wall-normal locations as a function of the streamwise coordinate x . At the location far from the wall ($j = 40$), the external perturbations dominate and decay while propagating downstream. In the near wall region ($j = 14$), instability waves with shorter wavelength can be observed in the rear part of the airfoil. The wavelength of the instability waves is almost the same as the wavelength of the T-S waves generated in the boundary-layer over the flat-plate. Compared with Fig. 15, where the T-S waves become visible shortly after the juncture between the leading edge and the flat-plate, in this case for the airfoil, the point where the T-S waves start to grow moves further downstream from the juncture of the leading edge with the rest part of the airfoil. The T-S waves generated in the region of the leading edge experience a longer distance of decaying followed by a growth in the rear part of the airfoil. The T-S waves keep growing for a while after passing the trailing edge, and then begin to decay in the wake. Fig. 19 shows the contours of the streamwise disturbance velocity. This figure is enlarged by three times in the y direction

to obtain better visual effect near the wall. The T-S waves can be clearly observed in the rear part of the airfoil. Because the wave length of the T-S waves is close to that of the external waves, it is difficult to subtract the external waves from the total disturbance. As we are currently working on the decomposition technique, more result will be given in the future.

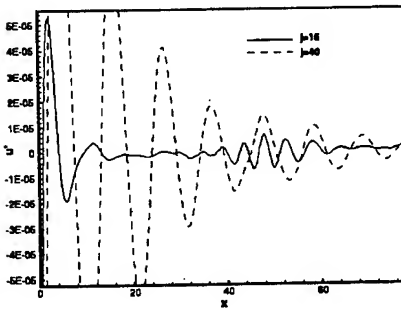


Figure 18. Distributions of the streamwise disturbance velocity versus x

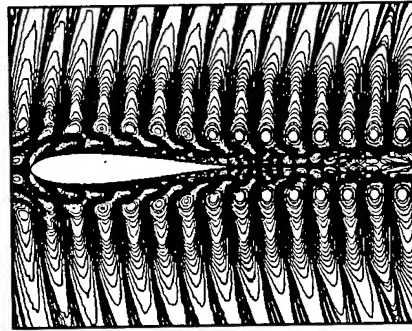


Figure 19. Contours of the streamwise disturbance velocity u'

5. Conclusion

The leading-edge receptivity to the free-stream disturbance is simulated by direct numerical simulation. The numerical calculation is performed by solving the full compressible Navier-Stokes equations in the generalized curvilinear coordinates. The second-order LU-SGS implicit scheme is applied for time integration. This scheme requires no tridiagonal inversion and is capable of being completely vectorized, provided the corresponding Jacobian matrices are properly selected. A fourth-order centered compact scheme is used for spatial derivatives. In order to reduce numerical oscillation, a sixth-order implicit filter is employed. The non-reflecting boundary conditions are imposed at the far-field and outflow boundaries to prevent possible non-physical wave reflection and avoid the using of buffer or sponge technique.

Linear growth of Tollmien-Schlichting waves along the flat-plate is calculated as the test case for code validation. The computational results agree well with the linear stability theory. The leading-edge receptivity of the compressible boundary-layer over the flat plate to the free-stream acoustic and the vortical disturbances is investigated. For both cases, the generation and distinct growth of the Tollmien-Schlichting waves are clearly observed along the flat-plate. Attempt has also been made to simulate the flow with more complex geometry, such as the leading-edge receptivity of

the boundary-layer around a modified Joukowski airfoil to the free-stream vortical disturbance. The instability waves is generated near the leading edge followed by a rapid decay and then begin to grow in the rear part of the airfoil. The onset point of amplification of T-S wave is further downstream than that of the flat-plate. More calculations will be carried out to investigate the effects of the geometry and the angle of attack on the onset point of the T-S wave amplification.

Acknowledgment

This work was supported by Air Force Office of Scientific Research Grant F49620-97-1-0033 monitored by Dr. L. Sakell. The authors are grateful for AFOSR's sponsorship of this research work. The authors would like to thank DoD HPCC for providing computer resources of the Cray and other supercomputers.

References

1. Goldstein, M. E., Hultgren, L. S. (1989) Boundary-Layer receptivity to long-wave free-stream disturbances. *Ann. Rev. Fluid Mech.*, **21**, pp.137-166
2. Lin, N., Reed, H. L., Saric, W. S. (1992) Effect of leading-edg geometry on boundary-layer receptivity to free-stream sound. In *Instability, Transition, and Turbulence*, edited by Hussaini, M., Kumar, A., Streett, C., Springer-Verlag, New York.
3. Buter, T. A., Reed, H. L. (1994) Boundary layer receptivity to free-stream vorticity, *Phys. Fluids*, **6**(10), pp.3368-3379
4. Haddad, O. M., Corke, T. C. (1998) Boundary layer receptivity to free-stream sound on parabolic bodies, *J. Fluid Mech.*, **368**, pp.1-26
5. Collis, S. S., Lele, S. K. (1996) A computational approach to swept leading-edge receptivity. *AIAA Paper*, **96-0180**
6. Liu, Z., Liu, C., Xiong, G. (1998) A contravariant velocity based implicit multilevel method for simulating the whole process of incompressible flow transition around Joukowski airfoils, *Applied Mechanics and Engineering*, **3**, pp.111-161
7. Lele, S. K. (1992) Compact finite difference schemes with spectral-like resolution. *J. Comput. Phys.* **103**, pp.16-42
8. Yoon, S., Kwak D. (1992) Implicit Navier-Stokes solver for three-dimensional compressible flows, *AIAA Journal*, **30**, pp.2653-2659
9. Jiang, L., Shan, H., Liu, C., Visbal, M. R. (1999) Non-reflecting boundary condition in curvilinear coordinates, *Second AFOSR International Conference on DNS/LES*, Rutgers, New Jersey, June 7-9.
10. Spekreuse, S. P. (1995) Elliptic grid generation based on laplace equation and algebraic transformations, *J. Comput. Phys.*, **118**, pp.38-61.
11. Zhong, X. L. (1997) Direct numerical simulation of Hypersonic boundary-layer transition over blunt leading edges, *AIAA Paper*, **97-0755**

NON-REFLECTING BOUNDARY CONDITIONS FOR DNS IN CURVILINEAR COORDINATES

LI JIANG, HUA SHAN, CHAOQUN LIU
*Center for Numerical Simulation and Modeling,
Louisiana Tech University, Ruston, LA*

AND

MIGUEL R. VISBAL
Wright Patterson Air Force Base, Dayton, OH

Abstract

High-order non-reflecting boundary conditions in a generalized curvilinear coordinate system for solving the time-dependent Navier-Stokes equations in complex geometry have been developed based on the characteristic analysis and the modified Navier-Stokes equation. Viscous terms are taken into account to include the viscous effect near the wall. All boundary conditions are added implicitly to the equations of interior points to ensure the stability of this scheme. The computational results show that the non-reflecting boundary conditions are compatible to the sixth- or fourth-order compact central difference scheme and maintain a high-order accuracy for the global solution. The non-reflecting boundary conditions work surprisingly well without any artificial buffer or sponge. No visible reflected wave was found from either inflow, outflow, far-field, or solid surface. The computational solution is found quite accurate comparing with valid data.

1. Introduction

Most important flows, such as transition, turbulence, vortex dynamics, etc. which Air Force is interested in, are involved in a time-dependent process that requires a time-accurate numerical prediction, such as direct numerical simulation (DNS) or large eddy simulation (LES). As well-understood now, DNS and LES are required to have minimum errors in wave magnitude and phase. However, in the field of finite-difference methods, low order upwinding, hybrid, or other schemes can introduce serious dissipation and dispersion even for a single wave and are therefore not encouraged to use for DNS or LES. High-order schemes with spectral-like resolution and low numerical dissipation (Lele, 1992) are necessary. DNS/LES for complex geometry was criticized, but now an increasing number of researchers (Liu,

et al., 1993, 1995, 1997, 1998; Visbal *et al.*, 1998) are working on this direction. The fundamental problem with DNS/LES seems to be solved and our experience shows DNS can be used for flow transition and LES can be used for fully developed turbulent flow for a spectrum of engineering applications.

In DNS/LES for compressible flow, especially for complex geometry, the properly imposed boundary condition is required to prevent the wave from reflecting at the boundary and contaminating the inner region of a computational domain. Realistic transition study often requires spatial evolution simulation. Periodic assumption is not valid when complex geometry is involved. In these cases, the specification of the outflow boundary conditions becomes one of the major difficulties. To avoid reflection of outgoing waves, a buffer domain (Street & Macaraeg, 1989) was introduced adding to the original computational domain at the outflow boundary. The governing equations in the buffer domain has been modified by increasing diffusion in certain direction. Alternatively, a sponge layer approach has been used by Israeli & Orszag (1981), Fasel (1990), Givoli (1991), Kloker *et al.* (1993), Collis & Lele (1996). The sponger layer is put outside the outflow or far-field boundary, where a dumping function is used to depress the flow fluctuations. It is reported by Guo *et al.* (1996) that combination of the sponge and buffer approach is needed to attain good effectiveness. Liu & Liu (1993) have developed an efficient buffer technique, which requires small buffer domain. In the previous work of Shan *et al.* (1999), the sponge approach has been successfully applied to a LES of supersonic boundary layer transition. Both buffer or sponge zones are capable of absorbing the outward moving waves, and have been used in many DNS/LES computations. But these methods have some shortages. First, extra sponge or buffer areas have to be added to the original domain, which will increase the the number of grid points and computational cost. Second, the sponge approach can only be applied when the equations of perturbation are considered, which may not be applicable when the so-called "base flow" does not exist or can hardly be defined.

An alternative approach to the buffer or sponge method is the non-reflecting boundary condition based on the characteristic analysis. The characteristic boundary conditions for Euler system can be found in a number of literatures (Whitfield, 1983; Thompson, 1987, 1990). The concept of non-reflecting boundary conditions was proposed by Thompson (1987, 1990), where the idea of specifying the boundary conditions according to the inward and outward propagating waves has been introduced. Usually the outgoing waves have their behavior defined entirely by the solution at and within the boundary, and no boundary conditions are needed. Therefore, the number of boundary conditions is equal to the number of incoming

waves. In Thompson's paper, boundary conditions of Euler equations are given for different situations without considering the viscosity effect. The characteristic boundary conditions for Euler system cannot be directly used for Navier-Stokes equations. Actually, there is no characteristic relation in Navier-Stokes system. However, in some circumstances, such as free stream, far field, etc. where the viscosity is less important, the characteristic relation can still be used. Poinso and Lele (1992) have extended Thompson's method to specify the boundary conditions for the Navier-Stokes equations, where the effect of viscous has been taken into account. However, they only give the expression of boundary conditions in the Cartesian coordinates.

The present work focuses on the application of high-order non-reflecting boundary conditions in a generalized curvilinear coordinate system for DNS/LES of time-dependent Navier-Stokes equations in complex geometry. A sixth- or fourth-order centered compact scheme is used for spatial derivatives. In order to reduce numerical oscillation, a sixth-order implicit filter is employed. The non-reflecting boundary conditions are imposed at the far-field and outlet boundaries to avoid possible non-physical wave reflection. No buffer or sponge zone is used in this computation. The computational results show that the non-reflecting boundary conditions are compatible to the compact central difference scheme and maintain a high-order accuracy for the solution. The non-reflecting boundary conditions which are presented in this paper work surprisingly well and no visible reflected wave was found from either inflow, outflow, far-field, or solid surface. The computational solution is found quite accurate comparing with valid data.

2. Non-reflecting Boundary Condition

The three-dimensional Navier-Stokes equations in generalized curvilinear coordinates (ξ, η, ζ) can be written as

$$\frac{1}{J} \frac{\partial Q}{\partial t} + \frac{\partial(E - E_v)}{\partial \xi} + \frac{\partial(F - F_v)}{\partial \eta} + \frac{\partial(G - G_v)}{\partial \zeta} = 0 \quad (1)$$

Detailed expressions for flux terms are as follows:

$$Q = \begin{pmatrix} \rho \\ \rho u \\ \rho v \\ \rho w \\ e \end{pmatrix} \quad E = \frac{1}{J} \begin{pmatrix} \rho U \\ \rho U u + p \xi_x \\ \rho U v + p \xi_y \\ \rho U w + p \xi_z \\ U(e + p) \end{pmatrix} \quad F = \frac{1}{J} \begin{pmatrix} \rho V \\ \rho V u + p \eta_x \\ \rho V v + p \eta_y \\ \rho V w + p \eta_z \\ V(e + p) \end{pmatrix}$$

$$\begin{aligned}
G &= \frac{1}{J} \begin{pmatrix} \rho W \\ \rho W u + p \zeta_x \\ \rho W v + p \zeta_y \\ \rho W w + p \zeta_z \\ W(e + p) \end{pmatrix} & E_v &= \frac{1}{J} \begin{pmatrix} 0 \\ \tau_{xx}\xi_x + \tau_{yx}\xi_y + \tau_{zx}\xi_z \\ \tau_{xy}\xi_x + \tau_{yy}\xi_y + \tau_{zy}\xi_z \\ \tau_{xz}\xi_x + \tau_{yz}\xi_y + \tau_{zz}\xi_z \\ q_x\xi_x + q_y\xi_y + q_z\xi_z \end{pmatrix} \\
F_v &= \frac{1}{J} \begin{pmatrix} 0 \\ \tau_{xx}\eta_x + \tau_{yx}\eta_y + \tau_{zx}\eta_z \\ \tau_{xy}\eta_x + \tau_{yy}\eta_y + \tau_{zy}\eta_z \\ \tau_{xz}\eta_x + \tau_{yz}\eta_y + \tau_{zz}\eta_z \\ q_x\eta_x + q_y\eta_y + q_z\eta_z \end{pmatrix} & G_v &= \frac{1}{J} \begin{pmatrix} 0 \\ \tau_{xx}\zeta_x + \tau_{yx}\zeta_y + \tau_{zx}\zeta_z \\ \tau_{xy}\zeta_x + \tau_{yy}\zeta_y + \tau_{zy}\zeta_z \\ \tau_{xz}\zeta_x + \tau_{yz}\zeta_y + \tau_{zz}\zeta_z \\ q_x\zeta_x + q_y\zeta_y + q_z\zeta_z \end{pmatrix}
\end{aligned}$$

where J is the Jacobian of the coordinate transformation, and $\xi_x, \xi_y, \xi_z, \eta_x, \eta_y, \eta_z, \zeta_x, \zeta_y, \zeta_z$ are the coordinate transformation metrics. U, V, W , and e are defined as follows:

$$U = u\xi_x + v\xi_y + w\xi_z, \quad V = u\eta_x + v\eta_y + w\eta_z, \quad W = u\zeta_x + v\zeta_y + w\zeta_z \quad (2)$$

$$e = \frac{p}{\gamma - 1} + \frac{1}{2}\rho(u^2 + v^2 + w^2) \quad (3)$$

The components of the viscous stress and heat flux are denoted by $\tau_{xx}, \tau_{yy}, \tau_{zz}, \tau_{xy}, \tau_{xz}, \tau_{yz}$, and q_x, q_y, q_z , respectively.

Using the characteristic analysis [15], hyperbolic terms in ξ direction of Eq. (1) are modified, can be recast as

$$\begin{aligned}
&\frac{\partial \rho}{\partial t} + d_1 + V \frac{\partial \rho}{\partial \eta} + \rho \left(\eta_x \frac{\partial u}{\partial \eta} + \eta_y \frac{\partial v}{\partial \eta} + \eta_z \frac{\partial w}{\partial \eta} \right) + W \frac{\partial \rho}{\partial \zeta} \\
&\quad + \rho \left(\zeta_x \frac{\partial u}{\partial \zeta} + \zeta_y \frac{\partial v}{\partial \zeta} + \zeta_z \frac{\partial w}{\partial \zeta} \right) + vis_1 = 0 \\
&\frac{\partial u}{\partial t} + d_2 + V \frac{\partial u}{\partial \eta} + \frac{1}{\rho} \eta_x \frac{\partial p}{\partial \eta} + W \frac{\partial u}{\partial \zeta} + \frac{1}{\rho} \zeta_x \frac{\partial p}{\partial \zeta} + vis_2 = 0 \\
&\frac{\partial v}{\partial t} + d_3 + V \frac{\partial v}{\partial \eta} + \frac{1}{\rho} \eta_y \frac{\partial p}{\partial \eta} + W \frac{\partial v}{\partial \zeta} + \frac{1}{\rho} \zeta_y \frac{\partial p}{\partial \zeta} + vis_3 = 0 \\
&\frac{\partial w}{\partial t} + d_4 + V \frac{\partial w}{\partial \eta} + \frac{1}{\rho} \eta_z \frac{\partial p}{\partial \eta} + W \frac{\partial w}{\partial \zeta} + \frac{1}{\rho} \zeta_z \frac{\partial p}{\partial \zeta} + vis_4 = 0 \\
&\frac{\partial p}{\partial t} + d_5 + V \frac{\partial p}{\partial \eta} + \gamma p \left(\eta_x \frac{\partial u}{\partial \eta} + \eta_y \frac{\partial v}{\partial \eta} + \eta_z \frac{\partial w}{\partial \eta} \right) + W \frac{\partial p}{\partial \zeta} \\
&\quad + \gamma p \left(\zeta_x \frac{\partial u}{\partial \zeta} + \zeta_y \frac{\partial v}{\partial \zeta} + \zeta_z \frac{\partial w}{\partial \zeta} \right) + vis_5 = 0
\end{aligned} \quad (4)$$

where vector \mathbf{d} is obtained from the characteristic analysis,

$$\begin{pmatrix} d_1 \\ d_2 \\ d_3 \\ d_4 \\ d_5 \end{pmatrix} = \begin{pmatrix} \frac{1}{c^2}[\frac{1}{2}(\mathcal{L}_1 + \mathcal{L}_5) + \mathcal{L}_2] \\ \frac{\xi_x}{2\beta\rho c}(\mathcal{L}_5 - \mathcal{L}_1) - \frac{1}{\beta^2}(\xi_y\mathcal{L}_3 + \xi_z\mathcal{L}_4) \\ \frac{\xi_y}{2\beta\rho c}(\mathcal{L}_5 - \mathcal{L}_1) + \frac{1}{\beta^2\xi_x}[(\xi_x^2 + \xi_z^2)\mathcal{L}_3 - \xi_z\xi_y\mathcal{L}_4] \\ \frac{\xi_z}{2\beta\rho c}(\mathcal{L}_5 - \mathcal{L}_1) - \frac{1}{\beta^2\xi_x}[\xi_y\xi_z\mathcal{L}_3 - (\xi_x^2 + \xi_y^2)\mathcal{L}_4] \\ \frac{1}{2}(\mathcal{L}_1 + \mathcal{L}_5) \end{pmatrix} \quad (5)$$

where c is the sound speed, and

$$\beta = \sqrt{\xi_x^2 + \xi_y^2 + \xi_z^2} \quad (6)$$

\mathcal{L}_i 's represent the amplitude variations of the characteristic waves corresponding to the characteristic velocities λ_i 's, which are given by

$$\lambda_1 = U - C_\xi \quad (7)$$

$$\lambda_2 = \lambda_3 = \lambda_4 = U \quad (8)$$

$$\lambda_5 = U + C_\xi \quad (9)$$

where $C_\xi = c\beta$, and \mathcal{L}_i 's can be expressed as

$$\begin{aligned} \mathcal{L}_1 &= (U - C_\xi) \left[-\frac{\rho c}{\beta} \left(\xi_x \frac{\partial u}{\partial \xi} + \xi_y \frac{\partial v}{\partial \xi} + \xi_z \frac{\partial w}{\partial \xi} \right) + \frac{\partial p}{\partial \xi} \right] \\ \mathcal{L}_2 &= U \left(c^2 \frac{\partial \rho}{\partial \xi} - \frac{\partial p}{\partial \xi} \right) \\ \mathcal{L}_3 &= U \left(-\xi_y \frac{\partial u}{\partial \xi} + \xi_x \frac{\partial v}{\partial \xi} \right) \\ \mathcal{L}_4 &= U \left(-\xi_z \frac{\partial u}{\partial \xi} + \xi_x \frac{\partial w}{\partial \xi} \right) \\ \mathcal{L}_5 &= (U + C_\xi) \left[\frac{\rho c}{\beta} \left(\xi_x \frac{\partial u}{\partial \xi} + \xi_y \frac{\partial v}{\partial \xi} + \xi_z \frac{\partial w}{\partial \xi} \right) + \frac{\partial p}{\partial \xi} \right] \end{aligned} \quad (10)$$

The terms vis_i 's in Eq. (4) represent the viscous terms, which are given by transformation of the initial viscous terms in Eq. (1)

$$\begin{pmatrix} vis_1 \\ vis_2 \\ vis_3 \\ vis_4 \\ vis_5 \end{pmatrix} = -J\hat{P}^{-1} \left(\frac{\partial E_v}{\partial \xi} + \frac{\partial F_v}{\partial \eta} + \frac{\partial G_v}{\partial \zeta} \right) \quad (11)$$

where \hat{P} is the Jacobian matrix, and $\hat{P} \equiv \frac{\partial \tilde{Q}}{\partial \tilde{Q}}$. \tilde{Q} is the vector of primitive variables, i.e. $\tilde{Q} = \rho, u, v, w, p^T$.

$$\hat{P}^{-1} = \begin{pmatrix} 1 & 0 & 0 & 0 & 0 \\ -\frac{u}{\rho} & \frac{1}{\rho} & 0 & 0 & 0 \\ -\frac{v}{\rho} & 0 & \frac{1}{\rho} & 0 & 0 \\ -\frac{w}{\rho} & 0 & 0 & \frac{1}{\rho} & 0 \\ \frac{\gamma-1}{2}(u^2 + v^2 + w^2) & (1-\gamma)u & (1-\gamma)v & (1-\gamma)w & \gamma-1 \end{pmatrix} \quad (12)$$

The analogous definitions can be made for the other two directions. In ζ direction, the modified N-S equations should be

$$\begin{aligned} \frac{\partial \rho}{\partial t} + d_1 + V \frac{\partial \rho}{\partial \eta} + \rho(\eta_x \frac{\partial u}{\partial \eta} + \eta_y \frac{\partial v}{\partial \eta} + \eta_z \frac{\partial w}{\partial \eta}) + U \frac{\partial \rho}{\partial \xi} \\ + \rho(\xi_x \frac{\partial u}{\partial \xi} + \xi_y \frac{\partial v}{\partial \xi} + \xi_z \frac{\partial w}{\partial \xi}) + vis_1 = 0 \\ \frac{\partial u}{\partial t} + d_2 + V \frac{\partial u}{\partial \eta} + \frac{1}{\rho} \eta_x \frac{\partial p}{\partial \eta} + U \frac{\partial u}{\partial \xi} + \frac{1}{\rho} \xi_x \frac{\partial p}{\partial \xi} + vis_2 = 0 \\ \frac{\partial v}{\partial t} + d_3 + V \frac{\partial v}{\partial \eta} + \frac{1}{\rho} \eta_y \frac{\partial p}{\partial \eta} + U \frac{\partial v}{\partial \xi} + \frac{1}{\rho} \xi_y \frac{\partial p}{\partial \xi} + vis_3 = 0 \\ \frac{\partial w}{\partial t} + d_4 + V \frac{\partial w}{\partial \eta} + \frac{1}{\rho} \eta_z \frac{\partial p}{\partial \eta} + U \frac{\partial w}{\partial \xi} + \frac{1}{\rho} \xi_z \frac{\partial p}{\partial \xi} + vis_4 = 0 \\ \frac{\partial p}{\partial t} + d_5 + V \frac{\partial p}{\partial \eta} + \gamma p(\eta_x \frac{\partial u}{\partial \eta} + \eta_y \frac{\partial v}{\partial \eta} + \eta_z \frac{\partial w}{\partial \eta}) + U \frac{\partial p}{\partial \xi} \\ + \gamma p(\xi_x \frac{\partial u}{\partial \xi} + \xi_y \frac{\partial v}{\partial \xi} + \xi_z \frac{\partial w}{\partial \xi}) + vis_5 = 0 \end{aligned} \quad (13)$$

$$\begin{pmatrix} d_1 \\ d_2 \\ d_3 \\ d_4 \\ d_5 \end{pmatrix} = \begin{pmatrix} \frac{1}{c^2} [\frac{1}{2}(\mathcal{L}_1 + \mathcal{L}_5) + \mathcal{L}_2] \\ \frac{\zeta_x}{2\beta\rho c}(\mathcal{L}_5 - \mathcal{L}_1) + \frac{1}{\beta^2 \zeta_x} [(\zeta_y^2 + \zeta_z^2)\mathcal{L}_3 - \zeta_x \zeta_y \mathcal{L}_4] \\ \frac{\zeta_y}{2\beta\rho c}(\mathcal{L}_5 - \mathcal{L}_1) - \frac{1}{\beta^2 \zeta_y} [(\zeta_x \zeta_y \mathcal{L}_3 - (\zeta_x^2 + \zeta_z^2)\mathcal{L}_4] \\ \frac{\zeta_z}{2\beta\rho c}(\mathcal{L}_5 - \mathcal{L}_1) - \frac{1}{\beta^2 \zeta_z} [\zeta_x \zeta_z \mathcal{L}_3 + \zeta_y \mathcal{L}_4] \\ \frac{1}{2}(\mathcal{L}_1 + \mathcal{L}_5) \end{pmatrix} \quad (14)$$

$$\begin{aligned} \mathcal{L}_1 &= (W - C_\zeta) \left[-\frac{\rho c}{\beta} (\zeta_x \frac{\partial u}{\partial \zeta} + \zeta_y \frac{\partial v}{\partial \zeta} + \zeta_z \frac{\partial w}{\partial \zeta}) + \frac{\partial p}{\partial \zeta} \right] \\ \mathcal{L}_2 &= W(c^2 \frac{\partial \rho}{\partial \zeta} - \frac{\partial p}{\partial \zeta}) \\ \mathcal{L}_3 &= W(-\zeta_x \frac{\partial w}{\partial \zeta} + \zeta_z \frac{\partial u}{\partial \zeta}) \end{aligned} \quad (15)$$

$$\begin{aligned}
\mathcal{L}_4 &= W(-\zeta_y \frac{\partial w}{\partial \zeta} + \zeta_z \frac{\partial v}{\partial \zeta}) \\
\mathcal{L}_5 &= (W + C_\zeta) \left[\frac{\rho c}{\beta} (\zeta_x \frac{\partial u}{\partial \zeta} + \zeta_y \frac{\partial v}{\partial \zeta} + \zeta_z \frac{\partial w}{\partial \zeta}) + \frac{\partial p}{\partial \zeta} \right] \\
\beta &= \sqrt{\zeta_x^2 + \zeta_y^2 + \zeta_z^2} \\
C_\zeta &= c\beta
\end{aligned} \tag{16}$$

In η direction, the modified N-S equations are

$$\begin{aligned}
\frac{\partial \rho}{\partial t} + d_1 + W \frac{\partial \rho}{\partial \zeta} + \rho (\zeta_x \frac{\partial u}{\partial \zeta} + \zeta_y \frac{\partial v}{\partial \zeta} + \zeta_z \frac{\partial w}{\partial \zeta}) + U \frac{\partial \rho}{\partial \xi} \\
+ \rho (\xi_x \frac{\partial u}{\partial \xi} + \xi_y \frac{\partial v}{\partial \xi} + \xi_z \frac{\partial w}{\partial \xi}) + vis_1 &= 0 \\
\frac{\partial u}{\partial t} + d_2 + W \frac{\partial u}{\partial \zeta} + \frac{1}{\rho} \zeta_x \frac{\partial p}{\partial \zeta} + U \frac{\partial u}{\partial \xi} + \frac{1}{\rho} \xi_x \frac{\partial p}{\partial \xi} + vis_2 &= 0 \\
\frac{\partial v}{\partial t} + d_3 + W \frac{\partial v}{\partial \zeta} + \frac{1}{\rho} \zeta_y \frac{\partial p}{\partial \zeta} + U \frac{\partial v}{\partial \xi} + \frac{1}{\rho} \xi_y \frac{\partial p}{\partial \xi} + vis_3 &= 0 \\
\frac{\partial w}{\partial t} + d_4 + W \frac{\partial w}{\partial \zeta} + \frac{1}{\rho} \zeta_z \frac{\partial p}{\partial \zeta} + U \frac{\partial w}{\partial \xi} + \frac{1}{\rho} \xi_z \frac{\partial p}{\partial \xi} + vis_4 &= 0 \\
\frac{\partial p}{\partial t} + d_5 + W \frac{\partial p}{\partial \zeta} + \gamma p (\zeta_x \frac{\partial u}{\partial \zeta} + \zeta_y \frac{\partial v}{\partial \zeta} + \zeta_z \frac{\partial w}{\partial \zeta}) + U \frac{\partial p}{\partial \xi} \\
+ \gamma p (\xi_x \frac{\partial u}{\partial \xi} + \xi_y \frac{\partial v}{\partial \xi} + \xi_z \frac{\partial w}{\partial \xi}) + vis_5 &= 0
\end{aligned} \tag{18}$$

$$\begin{pmatrix} d_1 \\ d_2 \\ d_3 \\ d_4 \\ d_5 \end{pmatrix} = \begin{pmatrix} \frac{1}{c^2} [\frac{1}{2}(\mathcal{L}_1 + \mathcal{L}_5) + \mathcal{L}_2] \\ \frac{\eta_x}{2\beta\rho c} (\mathcal{L}_5 - \mathcal{L}_1) + \frac{1}{\beta^2 \eta_y} [(\eta_y^2 + \eta_z^2) \mathcal{L}_3 - \eta_x \eta_z \mathcal{L}_4] \\ \frac{\eta_y}{2\beta\rho c} (\mathcal{L}_5 - \mathcal{L}_1) - \frac{1}{\beta^2} [\eta_x \mathcal{L}_3 + \eta_z \mathcal{L}_4] \\ \frac{\eta_z}{2\beta\rho c} (\mathcal{L}_5 - \mathcal{L}_1) - \frac{1}{\beta^2 \eta_y} [\eta_x \eta_z \mathcal{L}_3 - (\eta_x^2 + \eta_y^2) \mathcal{L}_4] \\ \frac{1}{2} (\mathcal{L}_1 + \mathcal{L}_5) \end{pmatrix} \tag{19}$$

$$\begin{aligned}
\mathcal{L}_1 &= (V - C_\eta) \left[-\frac{\rho c}{\beta} (\eta_x \frac{\partial u}{\partial \eta} + \eta_y \frac{\partial v}{\partial \eta} + \eta_z \frac{\partial w}{\partial \eta}) + \frac{\partial p}{\partial \eta} \right] \\
\mathcal{L}_2 &= V (c^2 \frac{\partial \rho}{\partial \eta} - \frac{\partial p}{\partial \eta}) \\
\mathcal{L}_3 &= V (-\eta_x \frac{\partial v}{\partial \eta} + \eta_y \frac{\partial u}{\partial \eta}) \\
\mathcal{L}_4 &= V (-\eta_z \frac{\partial v}{\partial \eta} + \eta_y \frac{\partial w}{\partial \eta}) \\
\mathcal{L}_5 &= (V + C_\eta) \left[\frac{\rho c}{\beta} (\eta_x \frac{\partial u}{\partial \eta} + \eta_y \frac{\partial v}{\partial \eta} + \eta_z \frac{\partial w}{\partial \eta}) + \frac{\partial p}{\partial \eta} \right]
\end{aligned} \tag{20}$$

$$\beta = \sqrt{\eta_x^2 + \eta_y^2 + \eta_z^2} \quad (21)$$

$$C_\eta = c\beta \quad (22)$$

2.1. SUBSONIC INFLOW BOUNDARY CONDITION

For uniform subsonic inflow at $\xi = 1$, four quantities should be specified, i.e. u, v, w, T , while the density ρ is obtained by solving Eq. (4). This arrangement is made based on the fact that the four characteristic waves $\mathcal{L}_2, \mathcal{L}_3, \mathcal{L}_4, \mathcal{L}_5$ are entering the computational domain, while \mathcal{L}_1 is going outward. Therefore, \mathcal{L}_1 is calculated from interior points using Eq. (10), where the spatial derivatives are calculated using the compact finite difference scheme, and $\mathcal{L}_2, \mathcal{L}_3, \mathcal{L}_4, \mathcal{L}_5$ are given in (23)–(26) which are similar to those in [15] [1].

$$\mathcal{L}_3 = \xi_y \frac{\partial u}{\partial t} - \xi_x \frac{\partial v}{\partial t} \quad (23)$$

$$\mathcal{L}_4 = \xi_z \frac{\partial u}{\partial t} - \xi_x \frac{\partial w}{\partial t} \quad (24)$$

$$\mathcal{L}_5 = \mathcal{L}_1 + \frac{2\beta\rho c}{\xi_x} \left[\frac{1}{\beta^2} (\xi_y \mathcal{L}_3 + \xi_z \mathcal{L}_4) - \frac{\partial u}{\partial t} \right] \quad (25)$$

$$\mathcal{L}_2 = \frac{\rho}{M_r^2} \frac{\partial T}{\partial t} + \frac{1}{2} (\mathcal{L}_1 + \mathcal{L}_5) \quad (26)$$

2.2. SUBSONIC OUTFLOW BOUNDARY CONDITION

For subsonic outflow at $\xi = N_x$, the static pressure p_∞ of far field is given. At this boundary, four characteristic waves $\mathcal{L}_2, \mathcal{L}_3, \mathcal{L}_4, \mathcal{L}_5$ are going out the computational domain, while \mathcal{L}_1 is entering the field. Therefore, $\mathcal{L}_2, \mathcal{L}_3, \mathcal{L}_4, \mathcal{L}_5$ can be calculated from the interior points using Eq. (10) with the compact finite difference scheme, while the \mathcal{L}_1 is given by [1]

$$\mathcal{L}_1 = K(p - p_\infty) \quad (27)$$

and $K = \delta(1 - M_{max}^2)c/l$, where M_{max} is the maximum Mach number, l is the characteristic length scale, δ is a constant.

2.3. FAR FIELD BOUNDARY CONDITION

For far field boundary at $\zeta = N_z$, the directions of characteristic waves are determined automatically by local field values, and \mathcal{L}_i of the outgoing

waves are calculated from the interior points using Eq. (15). Those inward going waves are set to zero. i.e.

$$\mathcal{L}_i = \begin{cases} \mathcal{L}_i, & \text{for } \lambda_i > 0 \\ 0, & \text{for } \lambda_i < 0 \end{cases} \quad (28)$$

2.4. NO-SLIP WALL BOUNDARY CONDITION

For no-slip wall at $\zeta = 1$, velocities u, v, w are set to zero, $\mathcal{L}_3, \mathcal{L}_4$ are given by

$$\mathcal{L}_3 = \frac{1}{\rho} [(\eta_z \zeta_x - \eta_x \zeta_z) \frac{\partial p}{\partial \eta} + (\xi_z \zeta_x - \xi_x \zeta_z) \frac{\partial p}{\partial \xi}] \quad (29)$$

$$\mathcal{L}_4 = \frac{1}{\rho} [(\eta_z \zeta_y - \eta_y \zeta_z) \frac{\partial p}{\partial \eta} + (\xi_z \zeta_y - \xi_y \zeta_z) \frac{\partial p}{\partial \xi}] \quad (30)$$

The characteristic wave \mathcal{L}_1 is going outward, so it can be calculated from the interior points, while the inward wave \mathcal{L}_5 is given by

$$\mathcal{L}_5 = \mathcal{L}_1 + \frac{2\rho\beta c}{\zeta_z} \left[\frac{1}{\beta^2} (\zeta_x \mathcal{L}_3 + \zeta_y \mathcal{L}_4) - \frac{1}{\rho} (\eta_z \frac{\partial p}{\partial \eta} + \xi_z \frac{\partial p}{\partial \xi}) \right] \quad (31)$$

\mathcal{L}_2 is determined by

$$\mathcal{L}_2 = \begin{cases} 0, & \text{for adiabatic wall} \\ \frac{1}{2}(\gamma - 1)(\mathcal{L}_1 + \mathcal{L}_5), & \text{for isothermal wall} \end{cases} \quad (32)$$

When all \mathcal{L}_i 's at each boundary are obtained, d_i can be easily calculated from Eq. (5), (14), and (19). All the terms other than d_i in Eq. (4), (13), and (18) are calculated in the same way as the interior points. Eq. (4), (13), and (18) are solved implicitly together with interior points.

3. Computational results

The non-reflecting boundary conditions are plugged in the DNS/LES code, which uses high order compact scheme and fully implicit method. Details of the numerical method and code verification can be found in [4]. The calculations of unsteady flow passing a semi-infinite flat-plate with a super-ellipse leading edge are carried out for validation. The Reynolds number based on the half thickness and the free-stream velocity is $Re = 2400$, and the Mach number is $M = 0.1$. A C-type grid is produced using elliptic grid generation method. The steady state solution is obtained by advancing unsteady flow computation to convergence. Starting from the steady state solution as the initial field, unsteady computation has been carried out by

introducing periodic disturbance in the free-stream with a nondimensional frequency of $F = 230$.

The first case is the direct numerical simulation of the response of flow to the acoustic waves imposed in the free-stream. After a certain time of forcing, a periodic solution is obtained. Fig. 1 shows the contours of streamwise disturbance velocity. The acoustic waves pass through the flat-plate and propagate down stream. There is no noticeable distortion in the far field and outflow boundary, as the waves smoothly pass over the boundary.

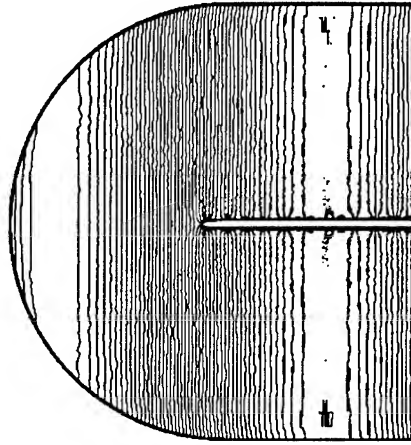


Figure 1. Contours of streamwise disturbance velocity

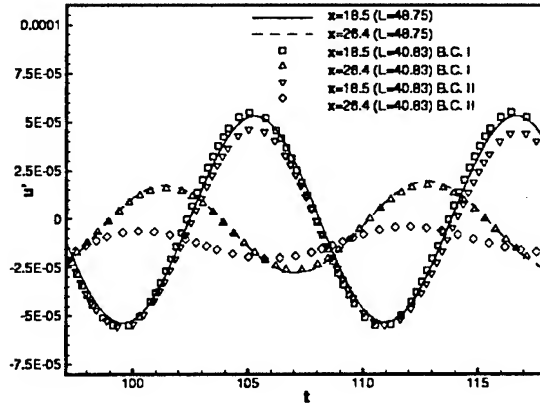


Figure 2. Streamwise disturbance velocity versus time at $y = 0.197$

The second case is the direct numerical simulation of the response of flow to the vortical disturbance, which is imposed at 2.5 plate thickness upstream of the leading edge. The outflow non-reflecting condition is tested by comparing the results obtained from two computational domain with different streamwise length. Fig. 2 shows the streamwise disturbance velocity at different downstream locations as a function of time under different boundary configuration. The long computational domain with a length of $L = 48.75$ is considered as the standard configuration. The previously introduced non-reflecting boundary condition is imposed at the outflow boundary. In Fig. 2, the results corresponding to the this standard configuration are displayed with solid line (at $x = 18.5$) and broken line (at $x = 26.4$). In the second configuration, a short domain with a streamwise length of $L = 40.83$ is used. The same non-reflecting boundary condition as in the first configuration is imposed at the outflow boundary. In Fig. 2, the second configuration is denoted as B.C.I, where the streamwise disturbance velocity at $x = 18.5$ and $x = 26.4$ are drawn as a function of time. It is clear that the results from the first and the second configuration agree well. In the third configuration which is denoted by B.C.II in Fig. 2, the computational domain is the same as in the second configuration. But at the outflow boundary, instead of using the non-reflecting condition, an extrapolation condition is imposed, i.e. the boundary values are defined as the extrapolation of the interior points. Compare the result with the standard configuration, at $x = 18.5$ the difference in streamwise disturbance velocity is visible, where the disturbance wave is slightly damped. The result deviates dramatically from the standard configuration at $x = 26.4$, where the disturbance wave is severely damped, and the difference in wavelength and phase angle is also observed. It is also found out that the nearer the location is to the outflow boundary, the larger the error is. The results indicate the failure of the extrapolation condition because of the reflection of wave from the outlet boundary and the contamination of the solution in the domain. It is noticeable that the mesh size and grid distribution are the same for all these configurations.

In order to show that non-reflecting boundary condition works successfully, the distribution of streamwise and vertical disturbance velocity along the longitudinal direction of the plate are depicted in Fig. 3 and Fig. 4. Results from both the first (long domain) and the second (short domain) configurations are displayed for comparison. It is observed that the waves propagate along the plate and pass smoothly through the exit boundary without any visible reflection. The results from long domain and short domain agree well except some deviation close to the exit boundary of the short domain.

Fig. 5 shows the contours of vertical disturbance velocity of the first

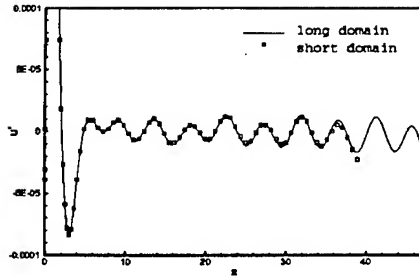


Figure 3. Distribution of streamwise disturbance velocity along the plate at $y = 0.042$

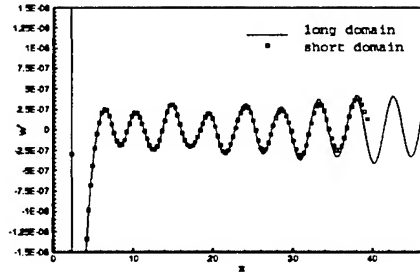


Figure 4. Distribution of vertical disturbance velocity along the plate at $y = 0.042$

(long domain) and the second (long domain) configurations. There is no distortion at the exit boundary. Therefore, the short domain with non-reflecting boundary condition achieves acceptable results and the length of the domain has little effect on the upstream solution.

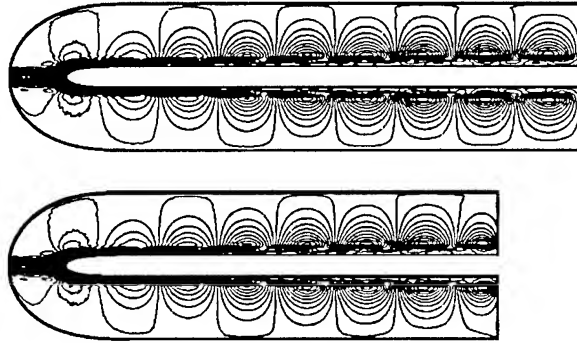


Figure 5. Contours of vertical disturbance velocity in different domains

The examples of the applications of the non-reflecting boundary condition to two- and three-dimensional flow with complex geometry are also given to show that the non-reflecting condition is fully compatible with high-order compact schemes in curvilinear coordinates. Fig. 6 shows the DNS results of the spanwise vorticity around a NACA 0012 airfoil at a 12° angle of attack, where the fluid flow around the airfoil becomes unstable and eddy structures are formed in the vicinity of the airfoil. Eddy structures shedding from the leading edge of the airfoil and the induced vortices have been brought downstream by the mean flow, and eventually move out of the computational domain through the outflow boundary without distortion and reflection. The computational domain of a three-dimensional

delta wing is shown in Fig. 7, where the outflow boundary is at the downstream end of the delta wing. The contours of the streamwise vorticity on selected cross sections are displayed in Fig. 8. A pair of co-rotating vortices appear over the suction side of the delta wing. Even at the outflow boundary, these vortical structures are also quite clear without any distortion. These examples served as an evidence show that the non-reflecting boundary conditions work well in DNS/LES of flow with complex geometry. The detailed description about the DNS/LES results for flow around two-dimensional airfoil and three-dimensional delta wing will be reported in upcoming papers.

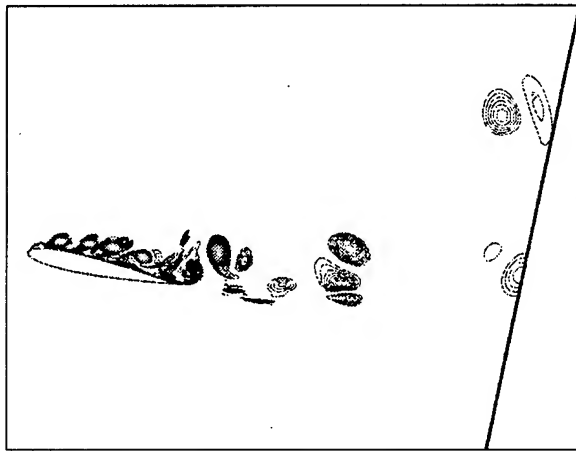


Figure 6. Contours of spanwise vorticity around a NACA 0012 airfoil with a 12° angle of attack, $Re = 5 \times 10^5$, $M = 0.4$

4. Conclusion

Non-reflecting boundary conditions for complex geometry in a generalized curvilinear coordinates are developed based on the characteristic analysis and the modified Navier-Stokes equation. Viscous terms are taken into account to include the viscous effect near the wall. All the boundary conditions are solved implicitly with the equations of interior points to ensure that the scheme is stable. Several cases are chosen to test the non-reflecting boundary conditions. With non-reflecting boundary conditions at the far field and outflow boundary, the unsteady waves can smoothly pass the boundaries without visible reflecting waves.

Acknowledgment

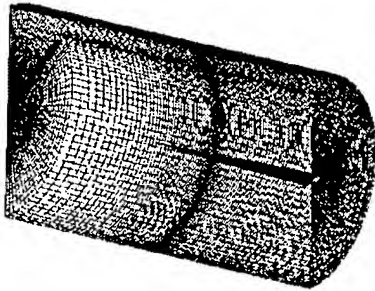


Figure 7. Computational domain of a three-dimensional delta wing

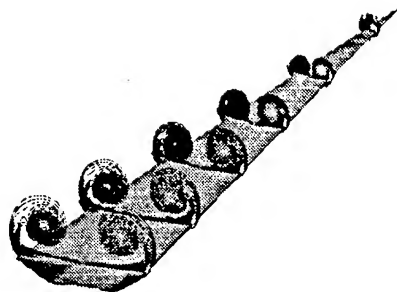


Figure 8. Contours of the streamwise vorticity on selected cross sections, angle of attack $\alpha = 12.5^\circ$, $Re = 5 \times 10^4$, $M = 0.1$

This work was supported by Air Force Office of Scientific Research Grant F49620-97-1-0033 monitored by Dr. L. Sakell and Summer Visiting Faculty Program. The authors are grateful for AFOSR's sponsorship of this research work. The authors would like to thank DoD HPCC for providing computer resources of the Cray and other supercomputers.

References

1. Collis, S.S. and Lele, S.K. (1996) A computational approach to swept leading-edge receptivity, *AIAA Paper* 96-0180
2. Fasel, H. (1990) Numerical investigation of the three-dimensional development in boundary-layer transition, *AIAA Journal*, **28**, pp.29-37
3. Guo, Y., Kleiser, L., and Adams, N. (1996) Comparison of temporal and spatial direct numerical simulation of compressible boundary-layer transition, *AIAA Journal*, **34**(4), pp.683-690
4. Jiang, L., Shan, H., Liu, C. (1999) Direct numerical simulation of boundary-layer receptivity for subsonic flow around airfoil, *The Second AFOSR International Conference on DNS/LES*, Rutgers, New Jersey, June 7-9.
5. Kloker, M., Konzelmann, U., and Fasel, H. (1993) Outflow boundary conditions for spatial Navier-Stokes simulations of transition boundary layers, *AIAA Journal*, **31**, pp.620-628
6. Lele, S. K. (1992) Compact finite difference schemes with spectral-like resolution.

- J. Comput. Phys.*, **103**, pp.16-42
7. Liu, C., Liu, Z., and McCormick, S. (1993) Multigrid methods for flow transition in three-dimensional boundary layers with surface roughness, NASA Contractor Report 4540.
 8. Liu, Z., and Liu, C. (1993) High order finite difference and multigrid methods for spatially evolving instability in a planar channel, *J. Comp. Phys.*, **106**, pp.92-100
 9. Liu, C., and Liu, Z. (1995) Multigrid mapping and box relaxation for simulation of the whole process of flow transition in 3-D boundary layers, *J. Comput. Phys.*, **119**, pp.325-341
 10. Liu, C. and Liu, Z. (1997) Direct Numerical Simulation for Flow Transition Around Airfoils, *Proceedings of First AFOSR International Conference on DNS/LES*, Louisiana Tech University, Ruston, Louisiana, August 4-8, 1997, pp.13-28, Edited by C. Liu, Z. Liu and L. Sakell.
 11. Liu, Z., Xiong, G., and Liu, C. (1998) A contravariant velocity based implicit multilevel method for simulating the whole process of incompressible flow transition around Joukowski airfoils, *J. of Applied Mechanics and Engineering*, **3**(1), pp.111-161
 12. Poinso, T. J., Lele, S. K. (1992) Boundary conditions for direct simulations of compressible viscous flows, *J. Comput. Phys.*, **101**, pp 104-129
 13. Shan, H., Jiang, L., Zhao, W., and Liu, C. (1999) Large eddy simulation of flow transition in a supersonic flat-plate boundary layer. *AIAA Paper* 99-0425
 14. Street, C. L., and Macaraeg, M. G. (1989) Spectral multi-domain for large-scale fluid dynamics simulations, *Appl. Num. Math.*, **6**, pp.123.
 15. Thompson, K. W. (1987) Time dependent boundary conditions for hyperbolic systems, I, *J. Comput. Phys.*, **68**, pp.1-24
 16. Thompson, K. W. (1990) Time dependent boundary conditions for hyperbolic systems, II, *J. Comput. Phys.*, **89**, pp.439-461
 17. Visbal, M. R. and Gaitonde, D. V. (1998) High-order accurate methods for unsteady vortical flows on curvilinear meshes, *AIAA Paper* 98-0131
 18. Whitfield, D. (1983) Three-dimensional unsteady Euler equation solutions using flux vector splitting, *Mississippi State University Report*.

MODULATION AND SUBGRID SCALE MODELING OF GAS-PARTICLE TURBULENT FLOW

T. KAJISHIMA, S. TAKIGUCHI AND Y. MIYAKE
Department of Mechanical Engineering, Osaka University
2-1 Yamadaoka, Suita, Osaka, 565-0871 Japan

Abstract. Turbulence modulation in particle-laden fluid flow, especially the influence of vortex shedding, was investigated based on the direct numerical simulation. To this end, we developed a finite-difference scheme to resolve the flow around each particle moving in turbulence. Energy budget around a sphere suggested that the energy production due to vortex shedding was about 20% of work by the particle. Homogeneous turbulence including many particles showed a modulation in background turbulence; namely, energy transfer from larger to smaller scale through wavenumber region corresponding to the mean spacing of particles. Taking these findings into account, a one-equation model for subgrid scale turbulence was suggested for the large-eddy simulation of particle-laden turbulence.

1. Introduction

Turbulent flows including dispersed particles, bubbles or droplets are characterized by the multiple scale interactions between phases. The large-eddy simulation (LES) may be suitable for the practical tool to predict them since LES defines the scales to be resolved and to be modeled. To improve a model for the particle motion in turbulence as well as the subgrid scale (SGS) model in LES, the direct numerical simulation (DNS) could allow us useful information. However, previous "direct" simulations of two-phase turbulence (Elghobashi and Truesdell, 1993; Pan and Banerjee, 1996; Maxey et al., 1997) represented particles by point source models (Maxey and Riley, 1983).

Recently, more complete DNS of multiphase turbulence were conducted. Pan and Banerjee(1997) used a body-force model at the grid points inside

particle in couple with the spectral method for fluid turbulence. Particle Reynolds numbers in their DNS were 133 for stationary particles and 15 for moving particles. The present authors proposed an another approach by the finite-difference method (Kajishima et al., 1998; Takiguchi et al., 1999). We directly integrated the fluid stress on the particle surface and successfully simulated the vortex shedding up to $Re = 600$. Though the relatively low resolution for each particle, these DNS efficiently reproduced the flow including a number of particles.

In the present paper, we improve our two-way coupling scheme for solid-fluid two-phase flow. The reliability is examined by simulating the flow around a sphere. The energy budget is evaluated especially for the case of vortex shedding at high Reynolds number. In addition, DNS of homogeneous turbulence including many particles is shown. Finally, some suggestions for SGS models of particle-laden turbulence will be given on the basis of our findings by DNS.

2. Numerical Method

The incompressible flow of Newtonian fluid including rigid particles is considered. The fluid turbulence is solved by the finite-difference method using the fixed Cartesian coordinate system.

The basic equations are the continuity equation

$$\nabla \cdot \mathbf{u} = 0 \quad (1)$$

and the equation of motion

$$\frac{\partial \mathbf{u}}{\partial t} + \mathbf{u} \cdot \nabla \mathbf{u} = -\frac{\nabla p}{\rho} + \nu \nabla^2 \mathbf{u} + \mathbf{g} + \mathbf{f}_p, \quad (2)$$

where \mathbf{g} is body force such as gravity. \mathbf{u} is a representative velocity at the grid defined by

$$\mathbf{u} = (1 - \alpha)\mathbf{u}_f + \alpha\mathbf{u}_p, \quad (3)$$

where α denotes the volumetric fraction of particle in the grid, \mathbf{u}_f the fluid velocity and \mathbf{u}_p the velocity inside the particle defined by

$$\mathbf{u}_p = \mathbf{v}_p + \mathbf{r} \times \boldsymbol{\omega}_p. \quad (4)$$

\mathbf{v}_p is the velocity, $\boldsymbol{\omega}_p$ the angular velocity, \mathbf{r} the relative position from the momentum center of particle. A time-marching scheme for Eq.(2) may be

$$\mathbf{u}^{n+1} = \mathbf{u}^n + \Delta t \mathbf{H} + \Delta t \mathbf{f}_p \quad (5)$$

where \mathbf{H} contains the all other terms in Eq.(2) and Δt is the time-increment. Suppose that \mathbf{u}^{n+1} is equal to $(1 - \alpha)\mathbf{u}_f + \alpha\mathbf{u}_p$ at $(n + 1)$ -th time-step and also that \mathbf{H} is much smaller than \mathbf{f}_p at the interface grid. We can derive

$$\mathbf{f}_p = \alpha (\mathbf{u}_p - \mathbf{u}) / \Delta t. \quad (6)$$

Thus \mathbf{f}_p is interpreted as a particle force on the fluid at the interface grid. Equation (2) automatically reverts to the equation of fluid motion in the region $\alpha = 0$. This approach is similar to the fortified solution algorithm (Fujii, 1995) used in the data exchange between grid systems in different zones for single-phase flow.

Equations for momentum and angular momentum of each particle are

$$\frac{d(m_p \mathbf{v}_p)}{dt} = - \int_{V_p} \mathbf{f}_p dV + \mathbf{G}_p \quad (7)$$

$$\frac{d(I_p \cdot \boldsymbol{\omega}_p)}{dt} = - \int_{V_p} \mathbf{r} \times \mathbf{f}_p dV + \mathbf{T}_p \quad (8)$$

where m_p denotes the mass, I_p the inertia tensor, V_p the volume of particle. \mathbf{G}_p and \mathbf{T}_p represent the external force and the external moment, respectively. Particles are tracked in Lagrangian frame of reference without any models for drag force, lift force, memory effect and so on.

In our DNS, the particle scale D_p is several times larger than the width of computational grid Δ , as shown in Fig.1(a). The particle surface is assumed to be plane in the cell as shown in Fig.1(b), allowing us an efficient evaluation of α . The over estimation in total volume was less than 2% for sphere of $D_p/\Delta = 8$, for example.

The staggered arrangement of variables is adopted for the fluid motion. The spatial derivative is approximated by the forth-order consistent scheme (Kajishima et al., 1998). The basic equations, Eqs.(1) and (2), are spatially discretized as

$$\delta_{x_i} u_i = 0, \quad (9)$$

$$\frac{\partial u_i}{\partial t} + \overline{u_j^{x_i} \delta_{x_j} u_i^{x_j}} = - \frac{\delta_{x_i} p}{\rho} + \nu \delta_{x_j} (\delta_{x_j} u_i) + g_i + f_{p,i}. \quad (10)$$

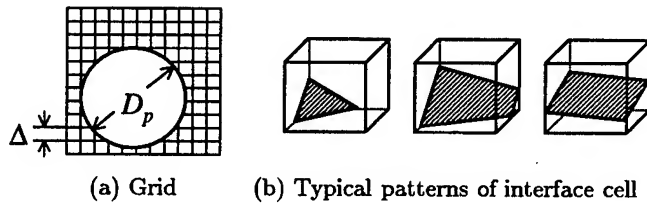


Figure 1. Computational grid and particle

The finite-difference and interpolation are represented as the forth-order central schemes:

$$\delta_x f|_i = (f_{i-\frac{3}{2}} - 27f_{i-\frac{1}{2}} + 27f_{i+\frac{1}{2}} - f_{i+\frac{3}{2}})/24\Delta x, \quad (11)$$

$$\bar{f}^x|_i = (-f_{i-\frac{3}{2}} + 9f_{i-\frac{1}{2}} + 9f_{i+\frac{1}{2}} - f_{i+\frac{3}{2}})/16. \quad (12)$$

We proved the reliability of this method by applying it to the turbulent channel flow (Kajishima et al., 1998).

The time-marching procedure is the fractional-step method based on the 2nd-order Adams-Bashforth method. It is summarized as follows:

1. The fractional-step velocity is obtained as

$$\tilde{\mathbf{u}} = \mathbf{u}^n + \Delta t(3\mathbf{H}_u^n - \mathbf{H}_u^{n-1})/2, \quad (13)$$

where $\mathbf{H}_u = -\mathbf{u} \cdot \nabla \mathbf{u} + \nu \nabla^2 \mathbf{u} + \mathbf{g}$.

2. The Poisson equation for pressure $P = p/\rho$

$$\nabla^2 P^{n+1} = (\nabla \cdot \tilde{\mathbf{u}})/\Delta t. \quad (14)$$

is solved by the residual cutting method (Tamura et al., 1997).

3. To satisfy the continuity equation, the flow field is corrected as

$$\hat{\mathbf{u}} = \tilde{\mathbf{u}} - \Delta t \nabla P^{n+1}. \quad (15)$$

4. The interaction force is evaluated as

$$\mathbf{f}_p = \alpha(\mathbf{u}_p^n - \hat{\mathbf{u}})/\Delta t \quad (16)$$

and the time marching is completed by

$$\mathbf{u}^{n+1} = \hat{\mathbf{u}} + \Delta t \mathbf{f}_p. \quad (17)$$

5. The velocity and angular velocity of a particle at the new step are obtained as

$$\mathbf{v}_p^{n+1} = \mathbf{v}_p^n + \Delta t(3\mathbf{H}_v^n - \mathbf{H}_v^{n-1})/2, \quad (18)$$

$$\boldsymbol{\omega}_p^{n+1} = \boldsymbol{\omega}_p^n + \Delta t(3\mathbf{H}_\omega^n - \mathbf{H}_\omega^{n-1})/2. \quad (19)$$

(Refer to Eqs.(7),(8) for \mathbf{H}_v and \mathbf{H}_ω .)

6. The location of a particle is moved by

$$\mathbf{x}_p^{n+1} = \mathbf{x}_p^n + \Delta t(\mathbf{v}_p^n + \mathbf{v}_p^{n+1})/2. \quad (20)$$

Then the velocity \mathbf{u} inside the particle ($|\mathbf{x} - \mathbf{x}_p| < D_p/2$ and $\alpha = 1$) is replaced by $\mathbf{u}_p^{n+1} = \mathbf{v}_p^{n+1} + \mathbf{r} \times \boldsymbol{\omega}_p^{n+1}$.

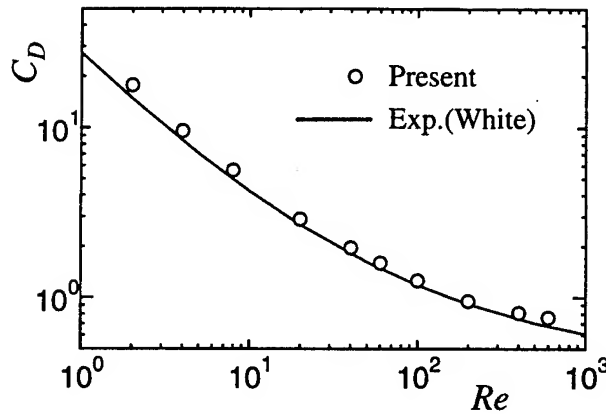


Figure 2. Drag coefficient of a sphere fixed in a uniform stream



Figure 3. Instantaneous flow around a sphere particle at $Re = 400$

3. Results and Discussion

3.1. ENERGY BUDGET AROUND A SPHERE

The three-dimensional flow around a sphere fixed in a uniform stream is simulated. The computational grid is cubic of the width Δ . In our prior work (Takiguchi et al., 1999), three steps of grid resolution, $D_p/\Delta = 11$, 8 and 5 were examined where D_p denotes the particle diameter. Finer cases $D_p/\Delta = 11$ and 8 reproduced wavy wake for $Re > 130$ as well as vortex shedding for $Re > 300$ (Sakamoto and Haniu, 1990). Coarser case $D_p/\Delta = 5$, however, could not reproduce the unsteady flow in high Reynolds number region. Thus the desirable resolution of grid is $D_p/\Delta \geq 8$ for our analysis. Figure 2 shows the drag coefficient C_D obtained by the grid resolution $D_p/\Delta = 10$. Our numerical result agrees acceptably with experimental data (White, 1991) up to the Reynolds number 600.

Figure 3 shows an instantaneous flow around a sphere at Reynolds number 400 visualized by the iso-surfaces of $\nabla^2 p$. Hairpin-like vortices as shown in Fig.3 are shed intermittently. Details have been reported in Takiguchi et al.(1999).

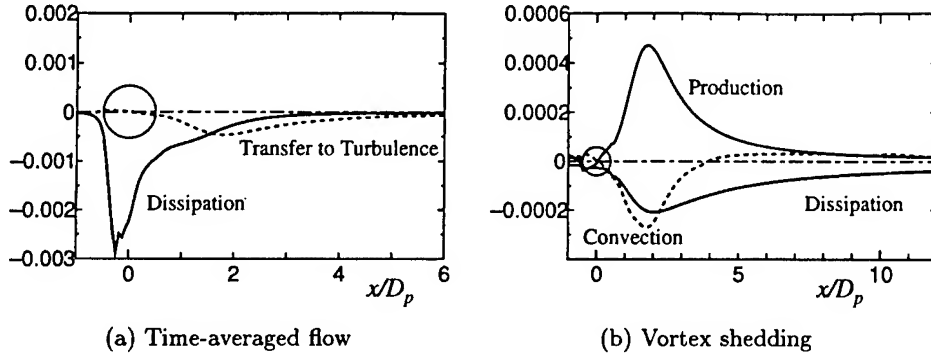


Figure 4. Kinetic energy budget around a sphere ($Re = 400$)

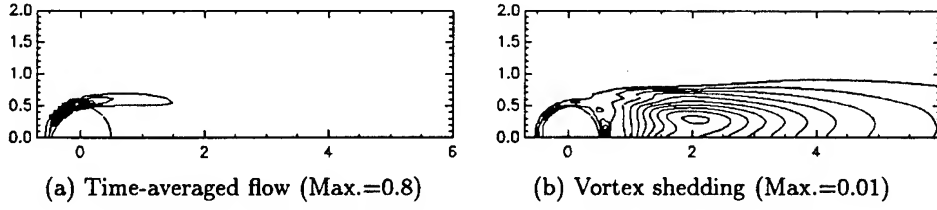


Figure 5. Energy dissipation in flow around a sphere at $Re = 400$

The smallest scale turbulence to be accounted for in modeling of particle-laden flows are eddies due to particle motion. To evaluate the energy budget around a particle, we obtained the time averaged flow field at $Re = 400$ by an improved grid resolution $D_p/\Delta = 16$. The time averaged budget of mean flow energy $K = \bar{u}_i \bar{u}_i / 2$ is

$$-F_p U = -\frac{1}{Re} \frac{\partial \bar{u}_i}{\partial x_j} \frac{\partial \bar{u}_i}{\partial x_j} + \overline{u'_i u'_j} \frac{\partial \bar{u}_i}{\partial x_j} + \text{diffusion} \quad (21)$$

where F_p is a time-averaged drag force and U is the uniform stream. The right hand side consists of the dissipation by time-averaged flow and energy transfer to turbulence. The budget of turbulence energy $k = \overline{u'_i u'_i} / 2$, on the other hand, is

$$-\bar{u}_j \frac{\partial k}{\partial x_j} - \overline{u'_i u'_j} \frac{\partial \bar{u}_i}{\partial x_j} - \frac{1}{Re} \frac{\partial \overline{u'_i u'_j}}{\partial x_j} + \text{diffusion} = 0. \quad (22)$$

Main terms represent convection, production and dissipation, respectively.

Figure 4 shows the profiles of Eqs.(21) and (22) averaged in the cross section perpendicular to the main stream. Distributions of dissipation rate are also shown in Fig.5. Particle-induced energy $F_p U$ is dissipated in the high-shear region close to the particle as shown in Fig.5(a). Integration of

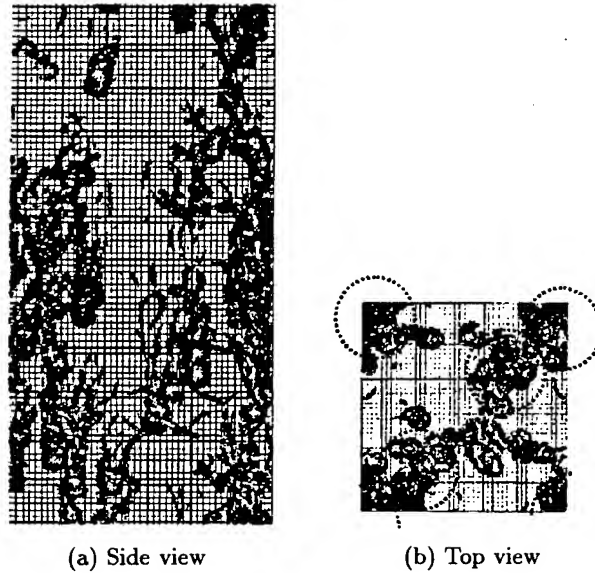


Figure 6. Flow field including 40 particles falling down at $Re = 380$ (iso-surface of $\nabla^2 p$)

the dissipation in Eq.(21) in the whole domain is about 80% of supply. Whether this portion should be included in grid scale or subgrid scale depends on the grid width of LES. The residual of energy is transferred into the turbulence component in the wake region, mainly in $0 \leq x/D_p \leq 5$ as shown in Fig.4(a). It indicates that at least 20% of particle-induced energy should be accounted for the production in SGS energy. It is dissipated in the downstream of the particle as shown in Fig.5(b). However, the SGS energy due to the vortex shedding is not in locally equilibrium as shown in Fig.4(b). The residual is transformed to far downstream.

3.2. MODULATION IN PARTICLE-LADEN TURBULENCE

3.2.1. Case A: Homogeneous Turbulence with Particle Clusters

For the first application of our method to particle-laden turbulence, we simulated a homogeneous flow field in which particles are falling down by gravity. The computational grid for fluid flow is cubic. The numbers of them are 256 in vertical direction and 128 in horizontal directions. Periodic boundary condition is assumed in each direction. The number of loaded particles is 40. They are rigid spheres. The ratio between particle-diameter and grid-width is 8. The particle-particle collisions are assumed to be elastic. As the volumetric fraction of particles is 0.25%, we guess the influence of collision is not important. The density ratio between solid particle and

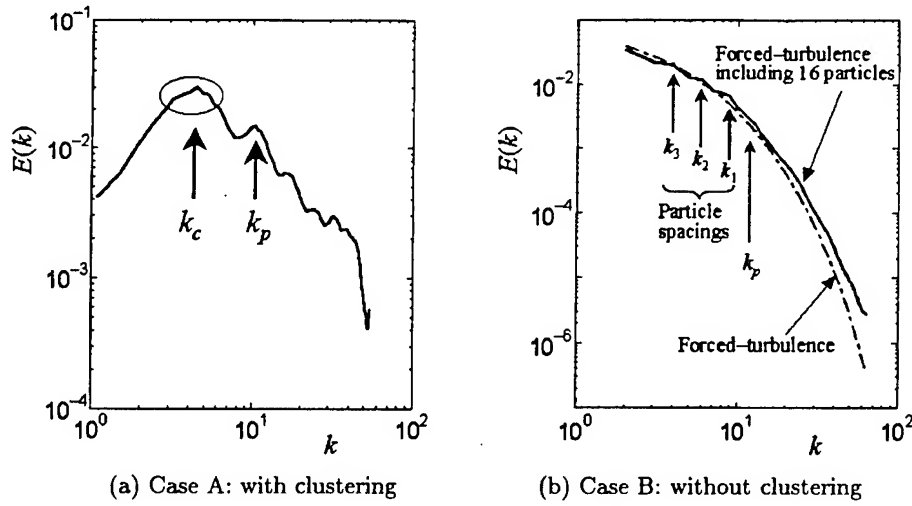


Figure 7. Energy spectra of particle-laden turbulence

fluid has been adjusted so that the mean Reynolds number is about 400.

Figure 6 shows an instantaneous flow field visualized by $\nabla^2 p$ iso-surfaces. Each particle sheds hair-pin like vortices. The fluid drag on a particle in the wake of other particles is smaller than the gravity. So some particles tend to approach ones in under side, resulting in the formation of particle clusters. At the moment shown in Fig.6, 4~5 clusters are observed. Figure 7(a) shows the energy spectrum of fluid turbulence caused by the particle. A local maximum is observed at the wavenumber corresponding to the particle diameter, $k_p = 10$. The dominant part of energy, however, is in the scale of lower wavenumber. The wavenumber range of it is corresponding to the horizontal spacing of clusters as shown in Fig.6(b).

3.2.2. Case B: Homogeneous Turbulence without Particle Clusters

To consider the influence of particle spacing on the background turbulence, relative position between particles are fixed in this setup. Particles are arranged in a horizontal matrix and moved down by a constant velocity in a homogeneous turbulence. The particle Reynolds number is 300. The background turbulence is kept statistically steady by random forcing (Eswaran and Pope, 1988). The fluid turbulence is directly simulated by 128^3 cubic grids. The number of particles is 4×4 in one periodic domain. The ratio between particle-diameter and grid-width is 8.

Figure 7(b) compares energy spectra between single-phase turbulence and modulated one. The wavenumbers corresponding to the particle spacing, k_m for m pitches, as well as k_p for the particle diameter are indicated

in the figure. The energy is reduced by the particles in the wavenumber region lower than $k_1 \sim k_3$, while it is increased in higher wavenumber region. Thus the turbulence is modulated to be more dissipative. The Reynolds number of particle-laden turbulence is $Re(= k^2/\varepsilon\nu) = 970$, which is lower than $Re = 1440$ of single phase turbulence. Though an additional energy was supplied through the vortex shedding, array of wake divide background eddies into smaller ones than the particle spacing. The reduction in length scale due to wakes made turbulence more dissipative.

4. Conclusions

We have shown the energy budget around a sphere particle and turbulence modulation by particles by means of newly developed method for DNS. Non-equilibrium feature was pointed out in the wake of sphere with vortex shedding. The vortex shedding from each particle as well as wakes of particle clusters supplied additional energy into fluid turbulence. But the length scale of turbulence was reduced due to the array of wake when particles did not form the larger structures such as clusters, resulting in more dissipative turbulence.

On the basis of these observations, we consider the large-eddy simulation for particle-laden turbulence. The filtered Navier-Stokes equation with SGS eddy viscosity model is

$$\frac{\partial \bar{u}_i}{\partial t} + \bar{u}_j \frac{\partial \bar{u}_i}{\partial x_j} = -\frac{1}{\rho} \frac{\partial \bar{p}}{\partial x_i} + \frac{\partial}{\partial x_j} [2(\nu + \nu_S) \bar{S}_{ij}] + g_i + \sum F_{pi}, \quad (23)$$

where F_p is the force due to particles in the computational cell, ν_S the SGS eddy viscosity, $\bar{S}_{ij} = (\partial \bar{u}_i / \partial x_j + \partial \bar{u}_j / \partial x_i) / 2$ the rate of strain of the resolved flow. The particle diameter is supposed to be much smaller than the computational cell in an actual LES for engineering application. Considering the non-equilibrium in particle-induced eddies as described in Sec.3.1, a one-equation model for SGS kinetic energy is appropriate for LES of particle-laden turbulence, especially with vortex shedding. The statistically-derived equation for SGS energy k_S (Yoshizawa and Horiuti, 1985) could be modified as

$$\frac{\partial k_S}{\partial t} + \bar{u}_j \frac{\partial k_S}{\partial x_j} = 2\nu_S \bar{S}_{ij} \bar{S}_{ij} + P_S - C_\varepsilon \frac{k_S^{3/2}}{\Delta'} + \frac{\partial}{\partial x_j} \left[(C_k \nu_S + \nu) \frac{\partial k_S}{\partial x_j} \right]. \quad (24)$$

where $\nu_S = C_\nu \Delta \sqrt{k_S}$ is the SGS eddy viscosity, Δ the filter length. C_ν , C_ε and C_k are non-dimensional constants. Based on the energy budget shown in Sec.3.1, SGS portion of particle-induced turbulence energy could be modeled as

$$P_S = 0.2 f_1 \sum \bar{u}_i F_{pi}. \quad (25)$$

In addition, the length scale in dissipation rate term should be modified as $\Delta' = f_2 \Delta$ to represent the change in length scale suggested in Sec.3.2. The modification in energy transfer from resolved scale to subgrid scale ($2\nu_S \bar{S}_{ij} \bar{S}_{ij}$) is then realized through the change in ν_S . The functions $f_1 (\leq 1)$ and $f_2 (\leq 1)$ depend on the strength of vortex shedding, or particle Reynolds number. We need further DNS to evaluate them.

References

- Elghobashi, S. and Truesdell, G.C. (1993) On the Two-Way Interaction between Homogeneous Turbulence and Dispersed Solid Particles. I: Turbulence modification, *Phys. Fluids*, A5-7, pp.1790-1801
- Eswaran, W. and Pope, S.B. (1988) An Examination of Forcing in Direct Numerical Simulations of Turbulence, *Comput. Fluids*, 16-3, pp.257-278
- Fujii, K. (1995) Unified Zonal Method based on the Fortified Solution Algorithm, *J. Comput. Phys.*, 118 pp.92-108.
- Kajishima, T., Takiguchi, S. and Miyake, Y. (1998) Direct Numerical Simulation of Interaction between Turbulence and Particles, *Proc. ASME Fluids Engineering Division Summer Meeting, Washington, DC*, No.FEDSM98-5021 (CD-ROM)
- Kajishima, T., Ohta, T., Okazaki, K. and Miyake, Y. (1998) High-Order Finite-Difference Method for Incompressible Flows using Collocated Grid System, *JSME Int. J., Ser.B*, 41-4, pp.830-839
- Maxey, M.R. and Riley, J.J (1983) Equation of Motion for a Small Rigid Sphere in a Nonuniform Flow, *Phys. Fluids*, 26-4, pp.883-889
- Maxey, M.R., Patel, B.K., Chang, E.J. and Wang, L.-P. (1997) Simulations of Dispersed Turbulent Multiphase Flow, *Fluid Dynamics Res.*, 20, pp.143-156
- Pan, Y. and Banerjee, S. (1996) Numerical Simulation of Particle Interactions with Wall Turbulence, *Phys. Fluids*, 8-10, pp.2733-2755
- Pan, Y. and Banerjee, S. (1997) Numerical Investigation of the Effects of Large Particles on Wall-Turbulence, *Phys Fluids*, 9-2, pp.3786-3807
- Sakamoto, H. and Haniu, H. (1990) A Study on Vortex Shedding from Spheres in a Uniform Flow, *Trans ASME, J. Fluid Eng.*, 112, pp.386-392
- Takiguchi, S., Kajishima, T. and Miyake, Y. (1999) Numerical Scheme to Resolve the Interaction between Solid Particles and Fluid Turbulence, *to appear in JSME Int. J., Ser.B*, 42
- Tamura, A., Kikuchi, K. and Takahashi, T. (1997) Residual Cutting Method for Elliptic Boundary Value Problems, *J. Comput. Phys.*, 137, pp.247-264
- White, F.M. (1991) *Viscous Fluid Flow*, McGraw-Hill, New York.
- Yoshizawa, A. and Horiuti, K. (1985) A Statistically-Derived Subgrid-Scale Kinetic Energy Model for the Large-Eddy Simulation of Turbulent Flows, *J. Phys. Soc. Jpn.*, 54-8, pp.2834-2839.

LARGE EDDY SIMULATION USING UNSTRUCTURED SPECTRAL/*HP* ELEMENTS

G-S KARAMANOS

*Brown University, Division of Applied Mathematics, Box F,
Providence, R.I. 02912.*

S.J. SHERWIN

*Imperial College of Science, Technology & Medicine, Department
of Aeronautics, Prince Consort Road, SW7 2BY, U.K.*

AND

J.F. MORRISON

*Imperial College of Science, Technology & Medicine, Department
of Aeronautics, Prince Consort Road, SW7 2BY, U.K.*

Abstract. The suitability of spectral/*hp* elements for large eddy simulation (LES) and the performance of the Smagorinsky eddy-viscosity model are investigated. The two-dimensional spectral/*hp* elements discretisation of Sherwin & Karniadakis (1995) is applied with a Fourier series expansion in the third direction. Muschinski's (1996) concept of an LES-fluid is tested through numerical experiments by considering isotropic turbulence decay at an initial Reynolds number $Re_\lambda = 245$ and cylinder flow at $Re = 3900$. Considering the Smagorinsky length scale, $\eta_{LES} = c_s \Delta$, as the LES-fluid counterpart of Kolmogorov's dissipation length scale, it is shown that for a Smagorinsky length scale larger than the implicit (or explicit) filter width, the subfilter model damps motions smaller than η_{LES} . If the filter width is larger than η_{LES} , then the numerical discretisation determines the length scale of the model. This is often associated with a reduction of the Smagorinsky length scale in the wall region of channel flow simulations.

It is concluded that the spectral element method may be successfully applied to LES, if the filter width is not based just on the grid size, but rather on the grid size and polynomial order of the expansion basis used. A new definition of the filter width is proposed and tested, which is dependent on the polynomial order as well as the cell dimensions. It is shown that spectral elements may then be used in LES in a manner equivalent

to any other discretisation. The added advantage of the method lies in the unstructured nature of the mesh, which allows flexibility in simulating complex geometries, and the arbitrary nature of the order of the discretisation.

1. Introduction

The main areas of research in LES have been the definition and simulation of the large scales, and the modelling techniques of the small scales. For the latter, various techniques have been proposed, with the majority of the models using the eddy-viscosity hypothesis. The most common model is the Smagorinsky model, and this is the one also adopted in this work. For the simulation of the large scales, finite-volume/finite-difference and global spectral methods have traditionally been used. Spectral methods are very accurate, but cannot usually cope with complex geometries. Finite-volume/finite-difference schemes are low-order methods that are capable of efficiently handling complex geometries. Most of these discretisations, have been based upon structured meshes, where the separation of the large from the small scales (a procedure defined as filtering) is normally associated with the convolution of the velocity field with a filter function in Fourier space. As more and more complex geometries are simulated, the use of numerical discretisations that are efficient and flexible in complex geometries is important. Dailey *et al.* (1998), Knight *et al.* (1998) and Jansen (1995) have faced this challenge using finite-volume and finite elements. Recent work, though, by Ghosal (1995), Blaisdell *et al.* (1995), Kravchenko & Moin (1997) indicate a considerable effect of the truncation and aliasing error on low-order simulations, and advocate the use of high-order schemes.

Unstructured spectral/*hp* element method (Sherwin & Karniadakis 1995, Warburton 1999) is a high-order scheme with the capability of efficient discretisation of complex geometries. The fundamental concept consists of discretising the computational domain with triangular cells, and approximating the solution within each cell using a series of polynomials (expansion basis), the order of which may be chosen arbitrarily. Convergence may, therefore, be achieved either by increasing the number of cells, or by increasing the order of polynomials.

The aim of this paper is to investigate the applicability of the unstructured spectral element method in LES. A 2-dimensional spectral element discretisation using triangular subdomains is applied, extended in the third direction with Fourier series. The time-stepping scheme is based on the splitting scheme of Karniadakis *et al.* (1991), extended to account for the variable viscosity introduced by the Smagorinsky model (Karamanos &

Sherwin 1998). Using the Smagorinsky model, the paper will focus on the implementation of the model within this numerical scheme, investigating the effect of the polynomial order, and proposing a new definition for the model length scale, based on the element size and polynomial order.

The paper focuses on the definition of a Smagorinsky length scale as a function of cell size and polynomial order for a triangular high-order cell, and the evaluation of the Smagorinsky eddy-viscosity model and its filtering capabilities under different flow conditions.

2. Definitions

The theory of LES has been well described in the reviews of Rogallo & Moin (1984), Ciofalo (1994), Lesieur & Metais (1996), among others. It is important, though, to stress the distinction between subfilter, subgrid, filtered and resolved scales. A *subgrid* motion is one which is smaller than the grid size, while a *subfilter* scale (SFS) motion is one removed by a filter (implicit or explicit). If the filter width is equal to the mesh width, then the subfilter and subgrid scales are the same. It follows that a *resolved* motion is one resolved by the numerical discretisation, while a *filtered* motion is a motion remaining from filtering of the resolved motions. With a high-order scheme, subgrid and subfilter scales are therefore different, with the SFS model representing the subfilter scales and not the subgrid scales. Filtering the Navier-Stokes equations, the equations of motion for a large eddy simulation may be derived as

$$\frac{\partial(\tilde{u}_i)}{\partial x_i} = 0, \quad \frac{\partial(\tilde{u}_i)}{\partial t} + \frac{\partial(\tilde{u}_i \tilde{u}_j)}{\partial x_j} = -\frac{\partial \tilde{p}}{\partial x_i} + \frac{\partial}{\partial x_i} \left\{ (\nu + \nu_s) \left[\frac{\partial \tilde{u}_i}{\partial x_j} + \frac{\partial \tilde{u}_j}{\partial x_i} \right] \right\}. \quad (1)$$

The term ν_s represents the Smagorinsky eddy-viscosity model, defined as $\nu_s = l_s^2 |\tilde{S}|$, where $|\tilde{S}| = (2\tilde{S}_{ij}\tilde{S}_{ij})^{1/2}$ is the magnitude of the filtered strain-rate tensor. l_s is a length scale, called *Smagorinsky length scale* or *subfilter length scale*. It is equal to $l_s = c_s \Delta$, where c_s is a constant, called the *Smagorinsky constant*, and Δ is the filter width. Deardorff (1970) suggested $\Delta = (\Delta_x \Delta_y \Delta_z)^{1/3}$, where $\Delta_x, \Delta_y, \Delta_z$ are the filter widths in each direction. For spectral elements with triangles, the filter width Δ has to be redefined to consider the triangular high-order nature of the cell. According to Gottlieb & Orszag (1977), the polynomial order, P , and the resolved half-wave number, k , are related by $P = k\pi$. A new definition of Δ is thus proposed, based on the area of the triangle, A , and the grid spacing, Δz , in the Fourier direction, of the form

$$\Delta = \left(A \left(\frac{\pi}{P} \right)^2 \Delta z \right)^{1/3}. \quad (2)$$

In the literature, c_s varies between 0.065 and 0.23, depending on the numerical discretisation, the definition of Δ and the flow conditions. There is currently no optimum value or relationship for the length scale $l_s = c_s \Delta$. Muschinski (1996) proposed an elementary physical picture of the definition of l_s . The ideas provide a rational basis for the determination of an optimum value of c_s . Muschinski (1996) argues that the LES equations, in essence, describe a non-Newtonian Smagorinsky fluid, called ‘Smagorinsky fluid’ or an ‘LES-fluid’, in which the viscosity is proportional to a deformation tensor amplitude, i.e. $\nu_{LES} = l_s^2 |S|$. He shows that the length scale, $l_s = \eta_{LES}$, is the equivalent Kolmogorov dissipation length scale $\eta = \frac{\nu^{3/4}}{\epsilon^{1/4}}$. Assuming an isotropic turbulent flow at a high Reynolds number, a Kolmogorov-type similarity theory is put forward, leading to a turbulent kinetic energy spectrum of the form

$$E(k) = \alpha_{LES}(c_s) \epsilon^{-2/3} k^{-5/3} f_{LES}(x, c_s), \quad (3)$$

where α_{LES} is an LES-generated Kolmogorov coefficient and is a function of c_s . f_{LES} is a dimensionless function of the dimensionless wave number, $x = kl_s$, and specifies an effective spatial filter. For large c_s , the asymptote of f_{LES} is physically the Smagorinsky-fluid counterpart of Kolmogorov’s damping-function, $f(x)$, which describes the drop-off of the turbulence kinetic energy spectrum at wave numbers in the vicinity of η^{-1} . The value of c_s also controls the ratio of the SFS length scale, l_s , to the resolved length scale of the numerical discretisation. Large c_s imply that the effective spatial filter is determined by the model, while a small c_s implies that the numerical resolution determines the spatial filter.

It will be shown that, by matching l_s with standard values from the literature, even if the cell size and discretisation are different, similar behaviour is obtained as suggested by the theory of homogeneous turbulence (Batchelor, 1967). Also, for l_s greater than the discretisation length scale, the SFS model acts as a filter.

3. Test Cases

3.1. ISOTROPIC TURBULENCE DECAY

The theory of homogeneous turbulence has been well summarised by Lesieur (1995) and Batchelor (1967). The simplest possible case is a cubic box of sides, $L = 1$, with periodic boundary conditions. The flow is isotropic and fully turbulent, decaying over time. According to Batchelor (1967), if a power-law decay of kinetic energy for each velocity component, $\frac{1}{2} \overline{u_i^2} \propto t^{-n}$, is assumed with n an integer, then the Taylor microscale λ is given by $\lambda^2 = \frac{10 \nu t}{n}$. If the value of $n = 1.2$ is considered (Saffman 1967), then

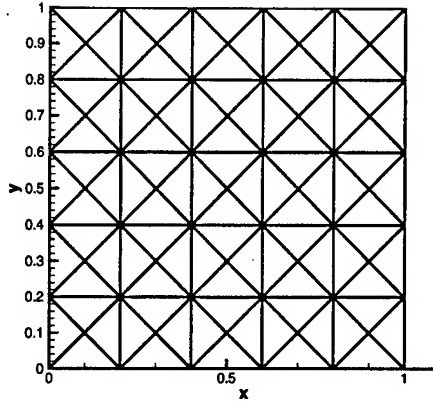


Figure 1. Mesh in the spectral element plane.

$\overline{q^2} = \frac{1}{2}\overline{u_i^2} \propto t^{-1.2}$ and $\lambda^2 = 10\nu t$. It follows that the Reynolds number, $Re_\lambda = \frac{\sqrt{\overline{q^2}}\lambda}{\nu}$, should decrease with time as $Re_\lambda \propto t^{-0.1}$, and as a consequence of the isotropy, $3\frac{1}{2}\overline{u_i^2} = \overline{q_i^2}$. Also, Re_λ in each direction and the power spectral densities of each velocity component against wave number should be equal to each other. This is, therefore, a good test of the effect of the triangular shape of the cells on the isotropy of the flow. The initial properties of the flow are isotropic, therefore, any anisotropy developed during the simulation will most likely be due to the triangular shape of the cells.

Experimental data for grid turbulence decay by Comte-Bellot & Corrsin (1971) is used for setting the initial conditions, using the computer program of J.H. Morrison (1998). The objective of the simulations is to calibrate the Smagorinsky length scale $l_s = c_s\Delta$, by ensuring the SFS model dissipates enough energy for the turbulent kinetic energy decay rate to be $n \approx -1.2$. The filtering and resolution capabilities of the spectral element discretisation and its interaction with the SFS model are also evaluated.

A Smagorinsky coefficient is considered for the mesh of Figure 1, with a polynomial order $P=11$. The resolution is equivalent to having 16 Fourier modes resolved, according to equation, $P = k\pi$, discussed earlier. In the classical LES theory, Lilly (1967) defined the Smagorinsky length scale as $\eta_{LES}^L = l_s = c_s^L \Delta^L$, where c_s^L is the value suggested by Lilly's (1967) theory ($c_s^L = 0.165$) for a filter width $\Delta^L = \frac{1}{32}$, based on the grid spacing for a structured grid of 32 points. Under the current numerical scheme, the filter width, Δ , is defined according to equation (2), so if c_s^L were used, then η_{LES}

Case	P	$c_s = \frac{\eta_{LES}}{\Delta}$	η_{LES}/L
1	11	0.196	5.156×10^{-3}
2	11	0.237	6.25×10^{-3}
3	11	0.303	7.974×10^{-3}
4	9	0.196	6.589×10^{-3}
5	7	0.129	5.156×10^{-3}
6	4	0.089	5.156×10^{-3}

TABLE 1. Summary of simulations.

would be different from that used by Lilly (1967). In order for the Smagorinsky model to behave in a similar manner to the traditional structured-grid-low-order schemes, the same Smagorinsky length scale has to be used,

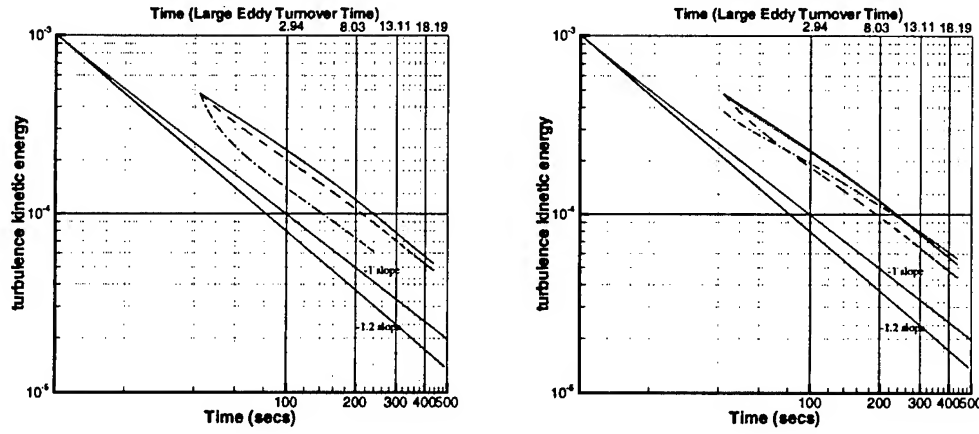


Figure 2. Turbulence kinetic energy decay: Left: solid line, Case 1; dashed line, Case 2; dash dot line, Case 3. Right: solid line, Case 1; dashed line, Case 4; dotted line, Case 5; dash dot line, Case 6.

which can only be done by modifying the Smagorinsky constant c_s . A new value is therefore proposed, derived from the equality $c_s \Delta = c_s^L \Delta^L$, producing $c_s = 0.196$ for $P = 11$. This value is valid if the Kolmogorov constant is $\alpha = 1.6$. If $\alpha = 1.5$ is assumed, then $c_s^L = 0.202$ and $c_s = 0.237$.

Six test cases are studied (Table 1), with varying polynomial order and SFS length scales. All the simulations ran for 20 large eddy turnover times, starting from the same velocity field. Figure 2 shows the decay of the turbulent kinetic energy. At the initial development time, Case 3 is excessively dissipative, while Cases 1 and 2 retain approximately a decay rate of -1.2, indicating the correct model dissipation. It is clear, also, that the

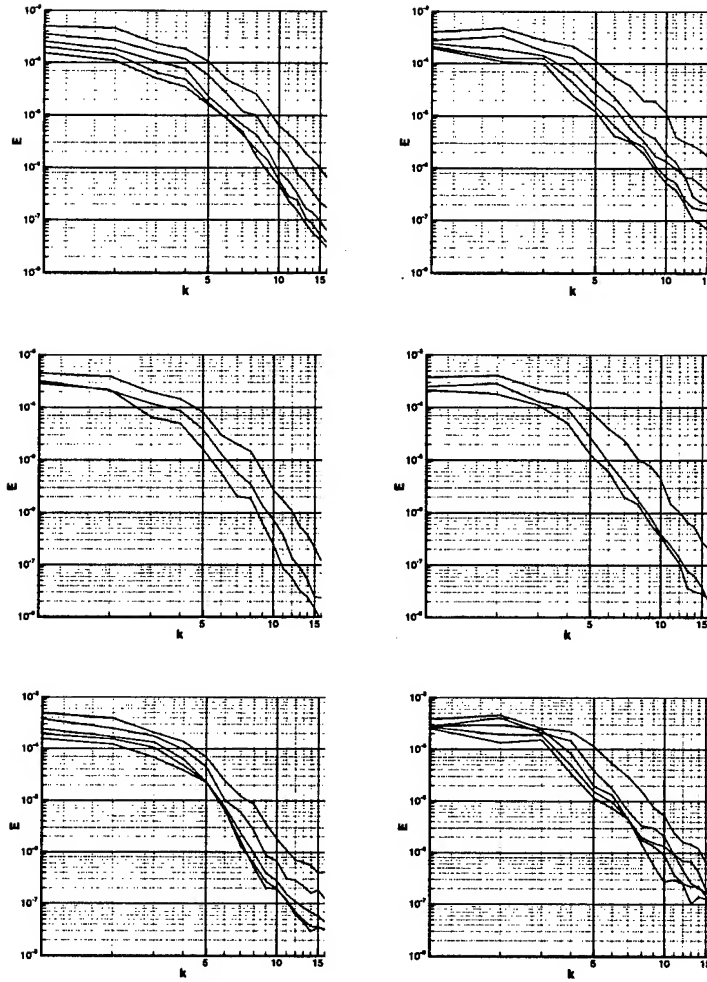


Figure 3. Evolution with time (top to bottom line) of energy spectra E_{uu} v.s. k_x (left), E_{wv} v.s. k_z (right): Top set: Case 2; Middle set: Case 3; Bottom set: Case 6.

resolved-scale energy decreases as c_s increases, as expected. With the resolution reduced, as in Case 4, and the Smagorinsky coefficient fixed (i.e. an increase in the Smagorinsky length), the energy decay will increase. However, if the resolution is decreased with the Smagorinsky length scale fixed, then less energy is dissipated, (Figure 2, Case 5), due to fewer energy carrying wave numbers being resolved. Case 6 is different. The resolution has been reduced to very low levels, that are not fine enough to give a correct behaviour, so the results of this case should be treated with caution. Power

spectral density plots will also show that this case is also affected by aliasing. Due to fewer wave numbers being captured, the subfilter dissipation is lower, resulting to a lower rate of energy decay. Later in the simulation, the behaviour of the energy curve reaches levels comparable to the other simulations, probably due to the length scales having increased, and becoming comparable to the discretisation length scales. Another explanation may be that aliasing increases the energy in the high wave numbers. Combined with a gradual decrease in the energy of the low wave numbers due to dissipation, this leads to a lower rate of decay of the energy.

Figure 3 shows the development of the one dimensional power spectral densities with time. On the left, the energy spectra as calculated in the spectral element plane are plotted, while on the right, the energy spectra as calculated on the $y-z$ plane. Case 3 has a higher Smagorinsky coefficient, and it is clear that the higher wave numbers decay in a smoother manner than, say, Case 2 which has a lower Smagorinsky length scale. Also, the higher wave numbers have a higher reduction of energy with increasing Smagorinsky length scale due to the higher dissipation inherent in the use of the larger Smagorinsky length scale. As the resolution in the spectral element plane is reduced, the high wave numbers are polluted and aliasing appears, especially with Case 6. Wave number 6 is the largest wave number correctly resolved in Case 6, while the Smagorinsky length scale corresponds to a wave number of 16. Therefore, the Smagorinsky model neither filters nor damps any motions below the discretisation scale, which is probably one of the reasons for aliasing and incorrect behaviour of the decay.

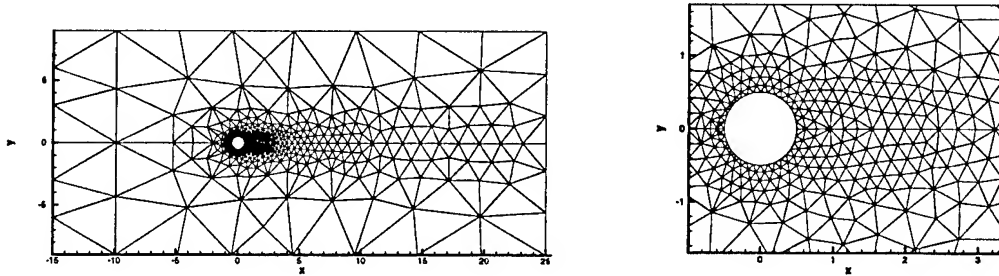


Figure 4. Mesh used on cylinder simulations: Left, full domain; Right, near the cylinder.

3.2. CYLINDER FLOW AT $Re = 3900$.

LES, using the Smagorinsky coefficients derived from the isotropic turbulence decay, and channel flow simulations (Karamanos 1999) are presented, using the mesh shown in Figure 4. Three cases are tested: Case 1,

without any SFS model (simulation provided by Ma, 1998); Case 2, using the Smagorinsky coefficient derived from channel flow simulations (Karanos 1999), $c_s = 0.032$, based on the Moin & Kim (1981) simulation; and Case 3, using the Smagorinsky coefficient of isotropic turbulence decay, i.e. $c_s = 0.196$. Over a computational domain of 40 by 20 by 1.5π , 902 elements are used with a polynomial order, $P = 8$, and 32 Fourier modes, i.e.

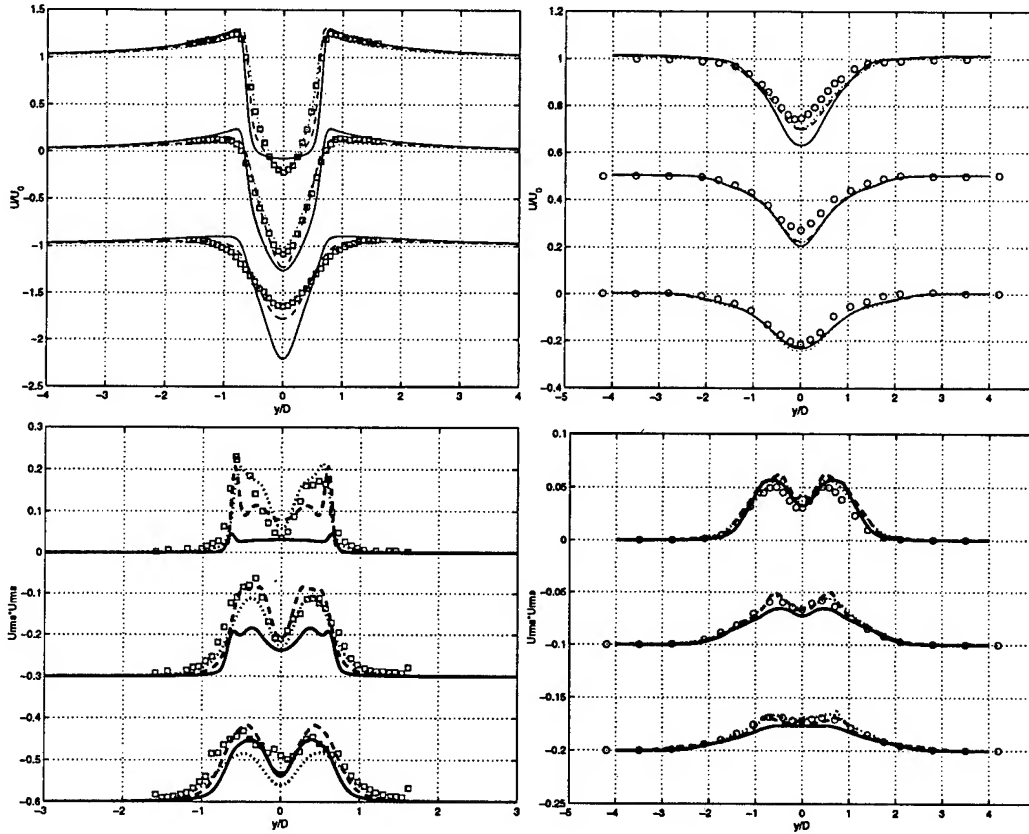


Figure 5. Top Set: Time Averaged streamwise velocity. Left: Top, $x/D = 1.06$; Middle, $x/D = 1.54$; Bottom, $x/D = 2.02$. Right: Top, $x/D = 4$; Middle, $x/D = 7$; Bottom, $x/D = 10.0$. Bottom Set: Turbulence Intensities of streamwise velocity. Left: Top, $x/D = 1.06$; Middle, $x/D = 1.54$; Bottom, $x/D = 2.02$. Right: Top, $x/D = 4$; Middle, $x/D = 7$; Bottom, $x/D = 10.0$. Dotted lines, Case 1; dashed line, Case 2; solid line, Case 3; circles, Ong & Wallace (1996); squares, Lourenco & Shih (1993).

64 Fourier planes, in the spanwise direction. De-aliasing is applied using the 3/2 rule, and the Panton (1997) wall damping function is used in the near-wall region.

Since the simulations use the same resolution, any difference is due to the effect of the Smagorinsky model. The velocity profiles (Figure 5) indi-

cate a change from a V -type profile to a U -type profile with increasing c_s at $x/D = 1.06$, while further away from the cylinder, Case 3 is underestimating the streamwise velocity. At $x/D > 4$, the average velocities are fairly insensitive to the subfilter scale model. At $x/D = 1.06$, the turbulence intensities are lowered with increasing c_s . This indicates a relationship between a U -type profile and reduced turbulence intensity. An extreme case is Case 3, which has the highest dissipation, lowest turbulence intensity and a clear U -type profile, while Case 2 is an intermediate stage. Case 1 has a V -type profile, with the highest turbulence intensity and the least dissipation. The effect of the SFS model is decreasing away from the cylinder.

4. Conclusion

Although not presented, further quantities have also been investigated, such as the skewness, flatness, dissipation rates and Taylor microscales, for the isotropic turbulence, and the average velocities and turbulence intensities for v , and energy spectra, among others for the cylinder flow. Together with LES performed on channel flows, at $Re_\tau = 180$ and 640 (Karamanos 1999), they provide the same conclusions, indicating good performance of the new filter width.

- Because of the different discretisation scheme, comparison with other Smagorinsky constants used is not strictly valid. Instead, comparisons should be made between Smagorinsky length scales $c_s\Delta$, which determines the energy drain from the resolved scales. The older definition of the Smagorinsky length scale would not take the polynomial order into account. A new definition of Δ is proposed, based on polynomial order and cell size. Simulations performed with the new length scale showed consistent behaviour of the model with the established SFS model behaviour. Increasing or decreasing resolution by varying the cell size or the polynomial order is now reflected in the SFS length scale.
- In the isotropic turbulence decay flow, an insensitivity of the turbulence kinetic energy decay and resolved dissipation to the Smagorinsky length scale was noted after long time integration, also observed by Chasnov & Piomelli (1996).
- The Smagorinsky eddy viscosity model is not designed to improve the properties of the cylinder flow. It is considered, though, a good model in order to understand the role of the SFS model in a transitional flow. The effect of the SFS model is most pronounced in the $x/D < 3$ region, with the near wake ($x/D > 4$) not drastically influenced. Energy spectra, though not presented, indicate a filtering effect of the SFS model, which is consistent with Muschinski's (1996) ideas, and

the energy spectra presented in the isotropic turbulence decay case.

Overall, it is concluded that the spectral element method may successfully be applied to LES, using the established LES theory, if the subfilter length scale is not based just on the grid size, but rather on the grid size and polynomial order. With this qualification, spectral elements may be used in LES in a manner equivalent to any other discretisation.

The authors would like to acknowledge the use of the Imperial College Computing Centre, and the Maui High Performance Computing Centre.

References

1. G.K. Batchelor 1967, The theory of homogeneous turbulence, Cambridge University Press.
2. G.A. Blaisdell, E.T. Spyropoulos and J.H. Qin 1996, The effect of the formulation of non-linear terms on aliasing errors in spectral methods, *Appl. Numer. Math.*, **20**: 62.
3. J.R. Chasnov and U. Piomelli 1996, Large-Eddy Simulations: theory and applications, Turbulence and Transition Modelling, ed. by M.Hallback, D.S.Henningson, A.V.Johansson and P.H.Alfredsson, Kluwer Academic Publishers.
4. M. Ciofalo 1994, Large-Eddy Simulation: a critical survey of models and applications, *Advances in Heat Transfer*, **25**: 321.
5. G. Comte-Bellot and S. Corrsin 1971, Simple Eulerian time correlation of full- and narrow-band velocity signals in grid-generated, isotropic turbulence, *Journal of Fluid Mechanics*, **48**: 273.
6. L.D. Dailey, T.A. Simons and R.H. Pletcher, 1998, Large eddy simulation of isotropic decaying turbulence with structured and unstructured grid finite methods, <http://www.public.iastate.edu/~dailey/homepage.html>.
7. J.W. Deardorff 1970, A numerical study of three-dimensional turbulent channel flow at large Reynolds numbers, *Journal of Fluid Mechanics*, **41**(2): 453.
8. S. Ghosal 1995, Analysis of discretization errors, Centre for Turbulence Research, *Annual Research Briefs*, NASA Ames/ Stanford University, Centre for Turbulence Research.
9. D. Gottlieb and S.A. Orszag 1977, Numerical analysis of spectral methods: theory and applications. SIAM-CMBS, Philadelphia.
10. P. Moin and J. Kim 1982, Numerical investigation of turbulent channel flow, *Journal of Fluid Mechanics*, **188**: 341.
11. K. Jansen 1996, Large-Eddy simulation of flow around a NACA 4412 airfoil using unstructured grids, *Annual Research Briefs*, NASA Ames/ Stanford University, Center for Turbulence Research.
12. G-S Karamanos 1999, Large Eddy Simulation using Unstructured Spectral/*hp* Finite Elements, Ph.D thesis, Imperial College of Science Technology & Medicine, Department of Aeronautical Engineering.
13. G-S Karamanos and S.J. Sherwin 1998, A high-order splitting scheme for the Navier-Stokes equations with variable viscosity, Herzliya, Israel.
14. G.E. Karniadakis, M. Israeli and S.A. Orszag 1991, High-order splitting methods for incompressible Navier-Stokes equations, *J. of Comp. Phys.*, **97**: 414.
15. D. Knight, G. Zhou, N. Okong'o and V. Shukla 1998, Compressible Large Eddy Simulation Using Unstructured Grid, 36th Aerospace Sciences Meeting and Exhibit, *AIAA 98-0535*.
16. A.G. Kravchenko and P. Moin 1997, On the effect of numerical errors in LES of turbulent flows, *J. of Comp. Phys.*, **131**: 310.

17. M. Lesieur and O. Metais 1996, New trends in large-eddy simulation, *Ann. Rev. Fluid Mech.*, **28**: 45.
18. D.K. Lilly 1967, The representation of small-scale turbulence in numerical simulation experiments, Proc. IBM Scientific Computing Symposium on Environmental Sciences, White Plains, N.Y., 195.
19. X. Ma 1998, Brown University, Private Communication.
20. J.H. Morrison 1998, NASA, Private Communication.
21. A. Muschinski 1996, A similarity theory of locally homogeneous and isotropic turbulence generated by a Smagorinsky-type LES, *Journal Fluid Mechanics*, **325**: 239.
22. R.L. Panton 1997, A Reynolds stress function for wall layers, *Journal of Fluids Engineering*, **119**: 325.
23. R.S. Rogallo 1981, Numerical experiments in homogeneous turbulence, NASA TM-81315.
24. P.G. Saffman 1967, The large-scale structure of homogeneous turbulence, *Journal of Fluid Dynamics*, **27**: 581.
25. P.G. Saffman, 1967, Note on decay of homogeneous turbulence, *Phys. Fluids*, **10**: 1349.
26. S. J. Sherwin and G.E. Karniadakis 1995, A Triangular Spectral Element Method; Applications to the Incompressible Navier- Stokes Equation, *Comp. Meth. in Applied Mech. and Eng.*, **123**: 189.
27. T. Warburton 1999, Spectral/hp methods on polymorphic multi-domain algorithms and applications, Ph.D. thesis, Division of Applied Mathematics, Brown University.

NUMERICAL MODELING OF FUEL/AIR MIXING IN A DRY LOW-EMISSION PREMIXER

W.-W. KIM AND S. MENON

*School of Aerospace Engineering
Georgia Institute of Technology
Atlanta, GA 30332-0150
U.S.A*

Abstract

Large-eddy simulation of turbulent fuel/air mixing in a combustor that is a close approximation of a full-scale General Electric gas turbine combustor has been carried out to quantify the efficiency of the premixer of this combustor. Experimental studies show that the swirling fuel/air mixture generated by the dual annular counter-rotating premixer has significant spatial variation in the local equivalence ratio in the near field. This unmixedness can impact the emission characteristics of the combustor. The present study focuses on determining if this observed phenomenon can be simulated using a large-eddy simulation methodology that captures the dynamics of scalar mixing within the context of a new linear-eddy subgrid mixing model as well as a gradient-diffusion based subgrid closure. Results demonstrate that unmixedness observed in the experiments can be simulated with reasonable accuracy on a relatively coarse grid.

1. Introduction

Turbulent mixing of species involves two separate physical processes that work concurrently. The first process is turbulent stirring and the second is molecular diffusion. In turbulent stirring, the interface between (initially separate) reactants is convoluted by the action of turbulent eddies. These eddies distort the interfacial surface on length scales which range from the largest scale of turbulence to the smallest Kolmogorov microscale. Surface distortions results in large increase in the interfacial area and in the local species gradients. This process of turbulent stirring does not mix the reactant species but only distorts the surface between them. Molecular diffusion, on the other hand, is the process by which species are mixed at the molecular level. In turbulent flows, molecular diffusion is dominated by inertial forces and is essentially negligible except at the smallest scales where species gradients become sufficiently large so that molecular diffusion becomes important.

In this paper, the mixing process in a gas turbine combustor which is (in terms of dimensions and flow conditions) part of an operational LM-6000 lean premixed combustor being developed by General Electric Aircraft Engine (GEAE) Company is investigated using Large-Eddy Simulation (LES). The mixing caused by the dual annular counter-rotating

swirler premixer of this combustor is also being evaluated experimentally [5]. Measurements indicate that there is a significant spatial and temporal variation in the fuel/air unmixedness in the combustor. For example, data show a maximum spatial variation on the order of 50% of the known overall equivalence ratio and a temporal unmixedness in peak equivalence ratio 2.4 times larger than the overall stoichiometry. This spatio-temporal variation is very important to quantify from design standpoint since variation in the local equivalence ratio can adversely impact NO_x emission levels [6] and, especially in the lean case, result in combustion instability [21].

To determine if this unmixedness can be numerically predicted, the experimental configuration [5] is simulated here using LES methodology. The underlying philosophy behind LES is to explicitly calculate the large energy-containing scales of motion which are directly affected by boundary conditions while modeling only the small scales of the flow. The large scales are difficult to model due to their variability from one problem geometry to the next. The smaller scales are presumed to be more universal in nature and therefore, more amenable to modeling. The LES equations of motion describe the evolution of the large scales and are derived by applying a *spatial* filter function to the conservation equations. The effect of the unresolved small scales appear as additional terms in the large-scale or resolved field equations. These *subgrid* terms must be modeled or additional equations for these terms derived in order to close the LES equations.

One attractive aspect of LES is that the dynamics of most of the turbulent motion are captured without modeling. LES is, therefore, expected to provide a more realistic picture of turbulent interactions than is obtained from Reynolds-Averaged Navier-Stokes (RANS) calculation where all turbulence scales are modeled. LES is also not restricted by temporal and spatial resolution requirements as is Direct Numerical Simulation (DNS) where all turbulence scales are directly resolved without employing any models. LES may, therefore, be applied to high Reynolds number flows of general interest which are unattainable using DNS provided the subgrid terms are determined using physically accurate models. As a recent study [16] of premixed reacting flow in GEAE's LM6000 combustor demonstrated, engineering solutions (i.e., turnaround in a few days) are feasible if relatively coarse grid resolution (e.g., half a million grid points) is used and the solver is executed on massively parallel systems. However, it was also determined that in order to obtain results accurate enough for engineering analysis a higher order subgrid model is required to allow for non-equilibrium effects in the subgrid scales. Since the present mixing study is also an engineering analysis of a full-scale hardware a similar philosophy is employed, i.e., only coarse grid is employed and the ability of the subgrid closure for such a resolution is evaluated within the computational constraint of getting full LES simulation completed within 48-72 hours (albeit on a 120-processor Cray T3E).

For LES of scalar mixing some fundamentally different issues need to be considered. Stirring by the turbulent eddies must be accompanied by molecular diffusion to achieve mixing of species. Both these features must be modeled or simulated accurately to predict local mixedness. However, in conventional LES when eddy-diffusivity closure (using arguments analogous to those used for the closure of the subgrid stresses based on eddy viscosity) is employed, then it is implicitly assumed that both small-scale turbulent stirring *and* molecular diffusion can be modeled using an effective eddy diffusivity that scales with the subgrid eddy viscosity. This assumption is obviously not justifiable in general. However, it has not yet been established what are the quantifiable errors inherent in this approach when employed to study engineering flows of interest, especially when only fuel/air unsteady mixing at very high Reynolds number is of interest. Note that reacting flows with

realistic heat release enforce additional constraints that may not be adequately captured by an eddy-diffusivity subgrid closure. Since the present study is limited to non-reacting high Re scalar mixing this issue is not relevant. However, it is worth noting that for fully premixed reactants in high-Re flow (and for appropriate Damköhler number) a front propagation model based on the G -equation approach (with a closure for the turbulent flame speed) can be used for engineering predictions as recently demonstrated [16]. Therefore, it is of interest to determine if there is a similar regime of validity where conventional fuel/air mixing closures can be utilized (with verifiable estimate of error) for engineering design studies. Failure of this type of closure would indicate the need for (and, in fact demand) a subgrid scalar closure that accounts for both small-scale turbulent stirring and molecular diffusion processes even if the associated computational cost increases. An evaluation of a new subgrid mixing model is also carried out here.

This paper attempts to address some of these issue using a flow configuration of engineering interest. The ability of the subgrid closure within the constraints of a coarse grid resolution and computational turn-around time acceptable from engineering standpoint is also addressed.

2. Conventional Subgrid Mixing Model

To solve the LES equations of motion for the resolved scale quantities, accurate subgrid models must be specified to close the system of equations. The filtered momentum and energy equations requires closure for the subgrid stress tensor and total enthalpy flux, respectively. These unclosed terms are parameterized using the localized dynamic model [14, 15]. The subgrid eddy viscosity in this model is determined based on a one-equation model for the subgrid kinetic energy, k^{sgs} . Moreover, the eddy viscosity model coefficients are dynamically and locally (both in space and time) determined by using similarity between the subgrid stress tensor and the test-scale Leonard stress tensor which has been observed in experiments [17].

The filtered species equations contain unknown subgrid terms representing a turbulent species flux, a diffusive mass flux, and the filtered mass production or reaction rate term. Accurate modeling of these terms comprises most of the difficulty in applying LES to reacting flows. A popular closure for the species transport terms due to turbulence is the gradient-diffusion assumption which results in

$$\Phi_{k,j}^{sgs} = \bar{\rho}(\widetilde{Y_k u_j} - \widetilde{Y_k} \widetilde{u_j}) = -\bar{\rho} \frac{\nu_T}{Sc_t} \frac{\partial \widetilde{Y_k}}{\partial x_j} \quad (1)$$

where $\widetilde{Y_k}$, $\widetilde{u_j}$ and $\bar{\rho}$ are, respectively, the k th species mass fraction, the fluid velocity component in the j th direction and the mixture density. Here, ν_T and Sc_t are, respectively, the turbulent eddy viscosity and the turbulent Schmidt number. Also, $\widetilde{}$ and $\bar{}$ denote application of the spatial filter and the spatial Favre filter, respectively. Use of this type of assumption for reactive species is dubious. Earlier, this closure was attributed as a source of errors in a comparison of reacting LES simulations with DNS data [4].

The magnitude of $\Phi_{k,j}^{sgs}$, as modeled in equation (1), is expected to dominate molecular diffusion at high Reynolds numbers when the subgrid turbulent kinetic energy is large. The effect of molecular diffusion in the filtered species equation results from the terms involving the diffusion velocities $U_{k,j}$. When $\Phi_{k,j}^{sgs}$ swamps the molecular diffusion terms, the final solution can be expected to be invariant with the diffusion process. This was

found to be the case in this study for simulations of high Reynolds number jet flows modeled using equation (1). Molecular diffusion is thereby effectively neglected in the resolved scale equation. This results in a serious problem for reacting flow simulations because the combustion process is strongly dependent on molecular diffusion at the small scales. Improperly accounting for molecular diffusion may result in significant errors. An alternative subgrid modeling approach which avoids this difficulty has been proposed [18]. This approach uses the *Linear-Eddy Model* (LEM) as a subgrid model in LES of turbulent premixed and diffusion flames. The LEM model is discussed in the following section.

3. Linear-Eddy Subgrid Mixing Model

The LEM model was originally developed as a stand-alone model for scalar mixing in turbulent flows. The most important feature of this model is that it distinguishes between turbulent convection and molecular diffusion. These two mechanisms are treated separately. Thus, turbulent diffusion is the result of a combination of convection and molecular diffusion. This is in contrast to earlier models (including the model described in the previous section) that assume turbulent diffusion to be primarily due to turbulent advection in the direction of gradient diffusion. However, these models were unable to explain the Schmidt number dependency of mixing processes observed in numerous experiments. It is now accepted that even in high Reynolds number flows molecular diffusion processes cannot be neglected and must be included.

In a series of papers [8, 9, 11] Kerstein developed the linear-eddy model to address the above issues and described how it could be used to predict mixing phenomena. Studies included mixing of a passive scalar in a turbulent wake, the fractal nature of scalar interfaces, mixing in turbulent jets and shear layer, and mixing and reaction in turbulent jets.

In combustion, mixing and chemical reactions are closely coupled. Thus, a natural extension of the original LEM was to include finite-rate reactions. The result is a model for turbulent combustion that treats reaction-diffusion processes and mixing processes within a single unifying framework [11].

The applications of the LEM model within LES (hereafter, this will be called the LEM subgrid model) have demonstrated good characteristics of this approach both in qualitative and quantitative comparisons [18, 1, 23, 19, 2]. This subgrid model has several advantages over other conventional closure approaches. First, the LEM subgrid model provides for a more fundamentally correct picture of the turbulent mixing process. Second, the LEM model is formulated to avoid the use of gradient-diffusion assumption for species transport.

The strategy within the LEM subgrid model is to resolve all relevant fluid mechanical length scales of the flow (as in DNS) inside each LES cell. As a result, the effect of subgrid species fluctuations is directly resolved. Resolving all the length scales of the flow, however, will in general be computationally intractable. Therefore, the LEM subgrid model is implemented in only one spatial dimension to keep the simulations affordable. And, in this sense, the LEM model is considered one-dimensional approximation of DNS. As details of the LEM formulation are available in the aforementioned literature, only a brief overview follows.

Molecular diffusion is treated deterministically by the one-dimensional species equation which is reduced from the three-dimensional continuity and species equations for constant

pressure:

$$\frac{\partial Y_k}{\partial t} = -\frac{1}{\rho} \frac{\partial \rho Y_k V_k}{\partial x} \quad k = 1, \dots, N \quad (2)$$

If Fick's law is assumed, the diffusion velocity V_k is obtained from

$$V_k = (-D_k/Y_k)(\partial Y_k/\partial x) \quad (3)$$

where D_k is the mixture averaged molecular diffusion coefficient. Using backward-Euler time integration and second-order-accurate finite-differencing for the derivatives, the equation is marched time accurately at the diffusion time step until it reaches the next LES physical time level. The diffusion time step is determined from linear stability of backward Euler time integration,

$$\Delta t_{diff} = C_{diff} \Delta x_{LEM}^2 / D_k \quad (4)$$

where Δx_{LEM} is the width of the spacing between two discretized cells in the LEM domain, and C_{diff} is a constant set equal to 0.25 for explicit integration.

Turbulent stirring is modeled stochastically by a series of instantaneous rearrangement events of the species fields. These rearrangement events correspond to turbulent convection induced by turbulent eddies smaller than the LES grid size. The length scale and frequency of these eddies are determined to conform to three-dimensional inertial range turbulence scaling laws [12]. Each rearrangement event is interpreted as the action of a single eddy on the species field and is numerically implemented as a mapping process called the triplet map [10]. This mapping first creates three copies of the selected segment and then increases the spatial gradients of the copies by compressing each segment by a factor of three and reversing the middle segment. Finally, the original segment is replaced by the newly mapped segments. Due to its triplet nature, each mapping event requires at least six LEM cells so that on a discretized domain, the Kolmogorov length scale η is resolved by six LEM cells.

The LEM triplet mappings have three stochastic parts: the segment (eddy) size to be mapped (or stirred), the location of the event, and the rate (or frequency) of the events. To determine these parameters, LEM determines the eddy size randomly from a pdf of eddy sizes,

$$f(l) = \frac{5}{3} \frac{l^{-8/3}}{\eta^{-5/3} - L^{-5/3}} \quad (5)$$

in the range $\eta < l < L$ (where L denotes the integral length scale) obtained from inertial range scaling [9]. The event location is randomly chosen from a uniform distribution within the one-dimensional domain.

To determine the event rate, LEM first relates fluid element diffusivity to the random walk of a marker particle and determines the total turbulent diffusion of a marker particle caused by eddies of size ranging from L to η based on triplet mapping [9] as,

$$D_T \approx \nu(L/\eta)^{4/3} = \frac{2}{27} \lambda \int_{\eta}^L l^3 f(l) dl \quad (6)$$

where ν is the kinematic viscosity. This expression is related to an equivalent expression $D_T = C_\lambda u' L$, [9], where C_λ is a model constant. Using the Renormalization Group (RNG) theory it can be shown that this constant has a value of 0.0614 which is close to the value

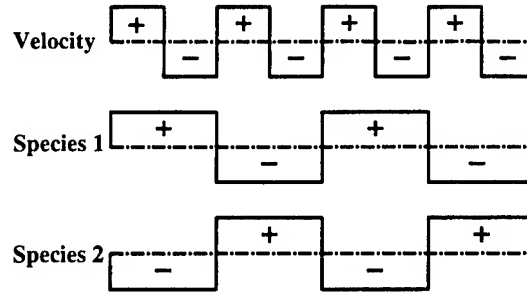


Figure 1. Schematic illustration of the initial LEM velocity and species fields used in every LES cell. Both fields have zero initial mean and the LEM simulation in each LES cell evolves the correlation $\Phi_{k,j}^{sgs}$.

obtained earlier [22] using premixed flame experimental data. The event frequency λ per unit length is determined from the diffusivity relations as [9],

$$\lambda = \frac{54}{5} \frac{\nu Re C_\lambda [(L/\eta)^{5/3} - 1]}{L^3 [1 - (\eta/L)^{4/3}]} \quad (7)$$

where Reynolds number $Re = u' L / \nu$ and u' is subgrid turbulent fluctuation. Finally, the event rate is determined as $E = \lambda X_{LEM}$, where X_{LEM} is the length of the one-dimensional domain. The time interval between events is then given as $\Delta t_{stir} = 1/(\lambda X_{LEM})$. Here, η is determined from the familiar inertial range scaling law $\eta = N_\eta L Re^{-3/4}$ where N_η is another constant which is also evaluated to be 8.12 using the RNG theory.

In the present study, the LEM subgrid model is implemented to directly resolve the subgrid correlation $\Phi_{k,j}^{sgs} = \bar{\rho} \widetilde{Y'_k u'_j}$ (where $'$ denotes the fluctuating component and this relation implies that the cross terms are neglected) inside each LES cell at each time level. This is in contrast to the other LEM based subgrid method [3] where the entire scalar evolution is simulated in the subgrid and large-scale convective transport is carried out using a Lagrangian advection method (called splicing [18]). The present method is much more computationally efficient and focuses primarily on the subgrid closure of species-velocity correlation $\Phi_{k,j}^{sgs}$.

The present approach involves constructing an initial species and velocity fluctuation LEM fields in each LES cell at each LES time level. Figure 1 shows an initial field distribution (currently chosen rather simply with some constraints, as noted below). It is assumed that initially, all turbulent eddies in each LES cell are Kolmogorov eddies and that they are uniformly distributed. This assumption can be relaxed by using an appropriate eddy size distribution but is invoked here for simplicity. In the velocity fluctuation field initialization, each positive and negative velocity fluctuation region represents three LEM cells and one pair (i.e., six LEM cells) of “+” and “-” velocity fluctuations represents one (Kolmogorov) eddy. However, note that this simple approximation of eddies is consistent with the triplet mapping used for turbulent stirring. The magnitude of the velocity fluctuation is obtained from the subgrid kinetic energy (i.e., $u' = (2k^{sgs}/3)^{1/2}$). On the other hand, species fluctuations are assumed to be uniform in each Kolmogorov eddy (i.e., six LEM cells) and varies only from one eddy to the other eddy. Magnitude of species fluctuations is set to be as maximum as possible in global sense. The constraints in this initialization are that the (subgrid) mean of both species and velocity fluctuation is zero and in addition, the mean of velocity-species fluctuation is zero. As a result, any action of

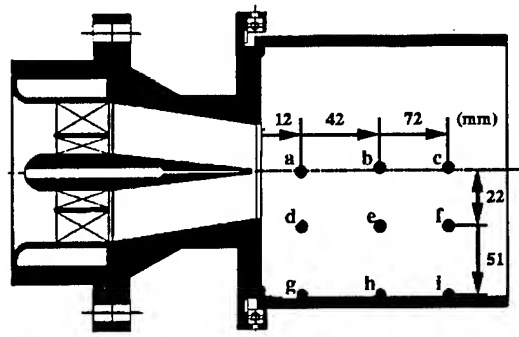


Figure 2. Centerline sectional view of the dry low NOx gas turbine combustor.

turbulent eddies (i.e., stirring and molecular diffusion) will increase the correlation (i.e., $\Phi_{k,j}^{sgs}$) from its initial zero value.

All subgrid turbulent processes evolve from this initial condition concurrently but at their own (i.e., local) characteristic time scales. Analogous to the scalar diffusion equation (2) a viscous diffusion equation is also solved within the LEM domain. However, the diffusion time scale for the velocity field is determined based on the kinematic viscosity instead of the molecular diffusion coefficient used for the scalar fields. This approach is similar to the One-Dimensional Turbulence (ODT) approach recently proposed by Kerstein [13]. The key difference is that the present approach only uses the subgrid velocity field to evolve the scalar-velocity correlations whereas in the original approach ODT was employed to evolve the entire turbulent flow field. Furthermore, in the present implementation some approximations have been used that need to further investigated.

Since the initialization is somewhat arbitrary, the $\Phi_{k,j}^{sgs}$ correlation that evolves needs to be calibrated since the initial evolution is from an unrealistic field and does not represent real physics. Thus, the LEM field must evolve till the correlation becomes realistic. This time scale may exceed the physical LES time step (again primarily due to the non-physical initialization). In the present study, the subgrid evolution was allowed to occur for a time scale an order of magnitude larger than the LES time step in order to evolve the correlation. Calibration is an issue still under investigation. In the present case, a scaling factor of 0.0005 was used to rescale the correlation based on parametric studies.

As a final note, the CPU time for the present LEM subgrid model was about 40 % higher than the conventional model. This cost is significantly lower than the effort required for the full subgrid LEM implementation (which involves Lagrangian transport of scalar fields using the "splicing" technique) and therefore, justifies this approach as an engineering LES approach. The memory overhead for the present LEM model was also not significant.

4. Results and Discussions

The domain studied is the combustor downstream of the dual annular counter-rotating swirler premixer that is being studied experimentally [5]. This configuration is part of the General Electric LM6000 dry, low-emission gas turbine combustor [7]. A centerline sectional view of the combustor is shown in Figure 2. Also shown are the locations where experimental data (primarily histograms) was obtained. The premixer exit (i.e., combustor

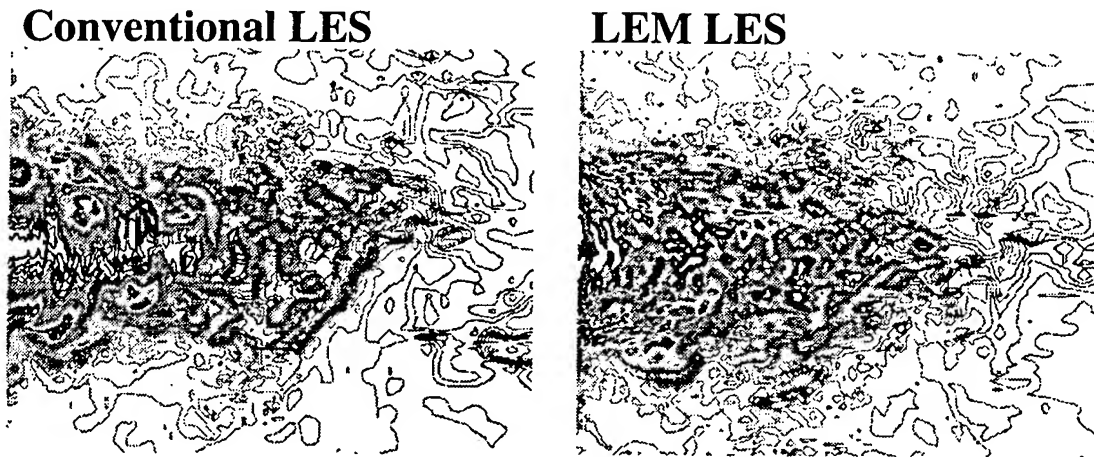


Figure 3. Comparison of instantaneous local equivalence ratio contours.

inlet) diameter is 48mm and the combustor diameter is 129mm. Therefore, the increase in the cross-sectional area over the backward facing step of the dump combustor is 7.2:1 which is quite large. A swirling jet is injected from the premixer at a pressure of 1.16×10^5 N/m² and a temperature of 350 K. The Reynolds number Re based on the inlet mean streamwise velocity and the inlet jet diameter D_0 is 180,000.

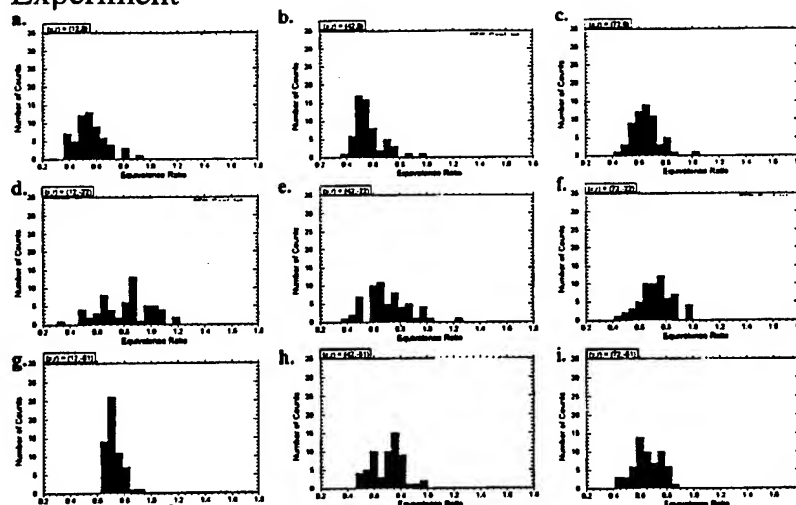
The computational domain is resolved in this study using a resolution of $121 \times 61 \times 81$ grid points along, the axial, the radial, and the azimuthal directions, respectively. The grid was clustered in regions of interest (such as the jet shear layer). Note that the present computational domain covers a full-scale gas turbine combustor including combustor nozzle which is extended up to 710 mm downstream from the premixer exit. In an earlier study of premixed reacting flow [16] the accuracy of this type of coarse grid was investigated and it was determined that this resolution is reasonably for engineering level accuracy. Therefore, we investigate the ability of a similar grid to capture fuel/air mixing.

The numerical algorithm solves the full, unsteady, compressible Navier-Stokes equations (and the k^{sgs} equation) using a finite-volume code that is fourth-order accurate in space and second-order accurate in time. The initial conditions were set approximately using turbulent jet profiles and, therefore, a period of time was required to wash the effect of the initial conditions out before accurate data can be collected. The inflow conditions (mean velocity profiles, turbulence intensity profile, and equivalence ratio profile) at the premixer exit were specified based on the information provided by University of Illinois at Urbana-Champaign (UIUC). At the combustor exit, characteristic outflow boundary conditions [20] were imposed.

The current simulations were carried out on a distributed memory parallel machine (the Cray T3E) using the Message-Passing Interface (MPI). The parallelization strategy has been reported elsewhere [16]. Typically, 120 Cray T3E processors were employed primarily to reduce the turn-around time. As demonstrated earlier [16], the present explicit LES code does scale-up very well on the Cray T3E.

In the following discussion we focus on the test conditions for which data was available for comparison. Arbitrarily chosen instantaneous contour plots of the fuel/air distribution (local equivalence ratio) obtained from the LES using both conventional and LEM subgrid

Experiment



Conventional LES

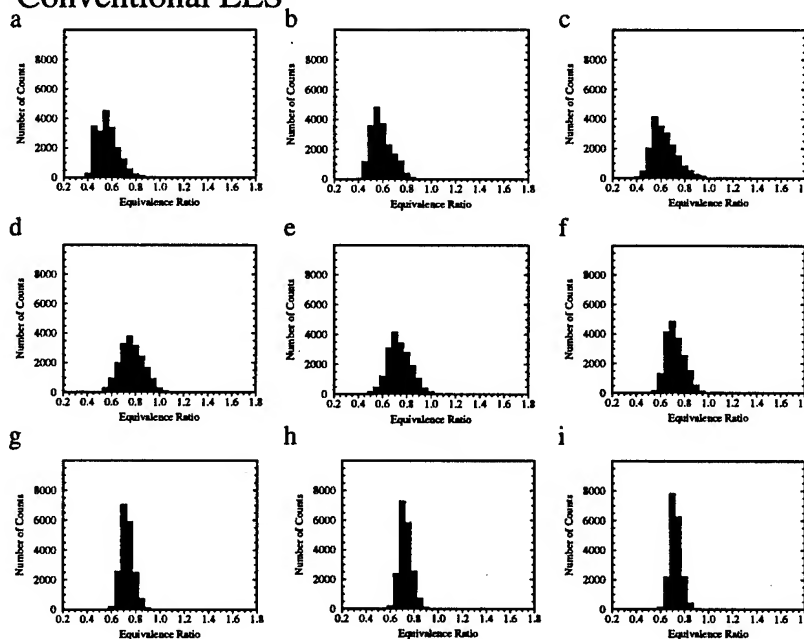


Figure 4. Comparison of the point histograms of equivalence ratio.

mixing models are compared in Figure 3. The plots show a plane perpendicular to z -axis through the combustor centerline (i.e., side view). This type of instantaneous flow field information is useful to understand how unmixedness affects NO_x generation and degrades flame stability. As expected, the LEM-LES is able to capture much smaller structures of species fluctuations which are mostly smeared out in the conventional LES based on the gradient-diffusion assumption. It is also observed that the LEM-LES predicts that the species fluctuations spreads out more radially than the conventional LES.

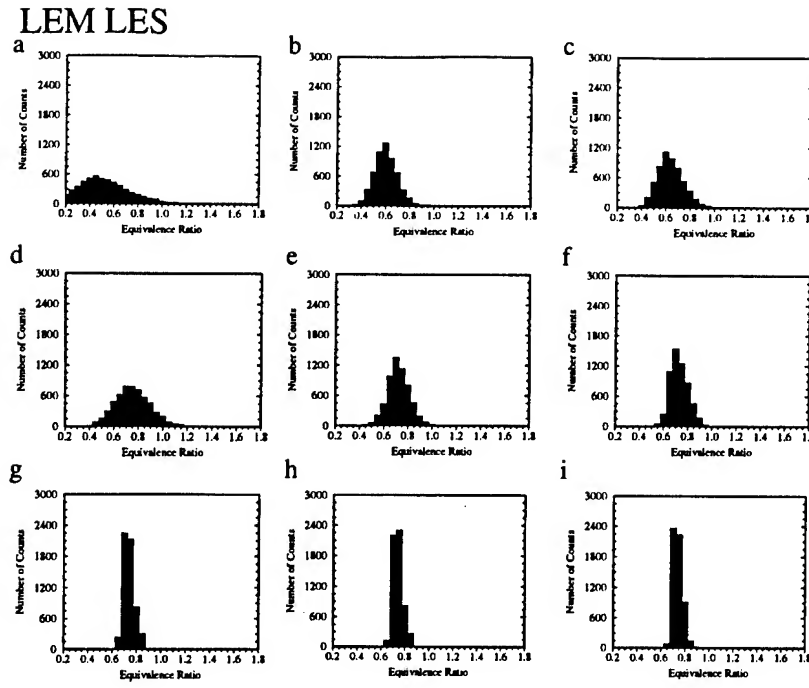


Figure 5. Comparison of the point histograms of equivalence ratio.

Figures 4 and 5 compare the point histograms of equivalence ratio measured by Frazier *et al.* [5] (see Fig. 2), the prediction by the conventional LES and by the LEM based LES. Note that only 60 samples were used to determine the experimental histogram and therefore, the data may be insufficient to obtain statistically stationary data. On the other hand, the LES histograms are computed using 19200 samples for the conventional LES and 5760 for the LEM LES at each location and is considered to have reached statistical stationary state. Therefore, the peaks of the histogram (number of counts) are not expected to be similar and only the extent of variation in the equivalence ratio can be compared.

As mentioned earlier, pockets containing fuel-rich mixtures emanate from the outer regions of the premixer exit. The broad equivalence ratio distributions of the point histogram along the edge of the premixer exit (location “d”) exemplify the fluctuating nature of these pockets. Flow reversal and turbulent mixing was sufficient to produce a uniform mixture concentration in the recirculation regions near the premixer exit surface corner (location “g”). Major differences between the experimental and the LES histograms appear downstream of this location (i.e., locations “h” and “i”). Both LES results show that this uniform mixture concentration persists at the downstream locations while the histograms from the experiment are broadened. This discrepancy needs to be revisited when additional experimental data becomes available for more reliable estimates. In spite of this difference there is a reasonable agreement between experimental and LES data at the other locations. Comparing the gradient diffusion closure based LES and the LEM based LES shows that the latter method predicts broader histograms, especially in locations “a” and “d”, than the conventional LES. This implies that the LEM subgrid closure results in more unmixedness than the conventional LES and its results appear to be closer to the experimental data.

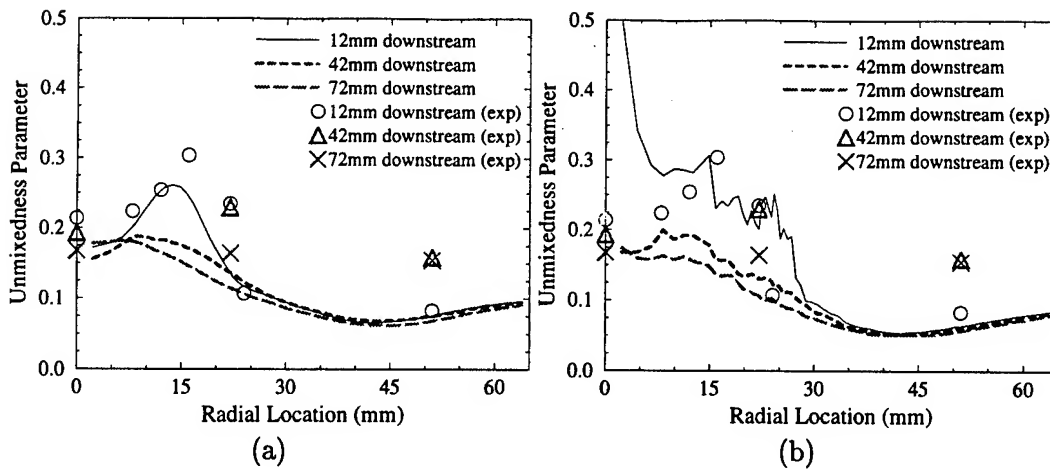


Figure 6. Radial profiles of the unmixedness parameter; (a) conventional LES (b) LEM LES.

Temporal fluctuations of the local equivalence ratio (i.e., broadness of the histogram) can be quantified using the unmixedness parameter s :

$$s = \frac{\sigma_{\Phi}}{\mu_{\Phi}} \quad (8)$$

where μ_{Φ} and σ_{Φ} are the time-averaged mean and standard deviation of the local equivalence ratio, respectively. Figure 6a and 6b show, respectively, the conventional LES and the LEM-LES predictions of the radial variation of the unmixedness parameter s at three downstream locations. The LEM-LES result shows a more fluctuating behavior. As observed in the histograms, the agreement between both LES results and the experimental data is quite reasonable at the first downstream locations (i.e., $x=12\text{mm}$). In particular, the LEM-LES predicts the unmixedness both in shape and magnitude except for near centerline region. However, at the other two locations, there are some significant differences and this is an issue that needs to be revisited when more data becomes available.

5. Conclusions

The application of LES to turbulent fuel/air mixing in a full-scale gas turbine combustor is discussed using two different closure models for subgrid species transport. The present effort is directed towards developing a reacting flow LES methodology for engineering applications and as such, many computationally efficient simplifications were used. Key simplification of coarse grid LES has been offset by using higher order subgrid closure models for both momentum and scalar transport. The LES methodology has been used to predict the unmixedness observed in experiments in a full-scale GE combustor. Results show that the experimentally observed spatial variation in the local equivalence ratio in the near field has been well captured by the LES. The subgrid LEM based closure shows significant promise to deal with subgrid mixing without invoking conventional gradient diffusion closure. Further development of this approach with a more appropriate subgrid turbulence initialization is currently underway.

Acknowledgments

We wish to thank Professor J. E. Peters for providing the experimental data. This work was supported in part by the Army Research Office Multidisciplinary University Research Initiative and by the Air Force Office of Scientific Research under the Focussed Research Initiative. Computations were carried out under the DoD HPC Grand Challenge Project at NAVO, Stennis Space Center and ARC, Huntsville.

References

1. Calhoon, W. H. and Menon, S. (1997). Linear-eddy subgrid model for reacting large-eddy simulations: Heat release effects. *AIAA-97-0368*.
2. Chakravarthy, V. K. and Menon, S. (1999a). Large eddy simulation of stationary premixed flames using a subgrid flamelet approach. Second AFOSR International Conference on DNS and LES, Rutgers University, June 7-9, 1999.
3. Chakravarthy, V. K. and Menon, S. (1999b). Modeling of turbulent premixed flames in the flamelet regime. In *First International Symposium on Turbulence and Shear Flow Phenomena*.
4. Frankel, S. H., Adumitroaie, V., Madnia, C. K., and Givi, P. (1993). Large eddy simulation of turbulent reacting flows by assumed pdf methods. In Piomelli, U. and Ragab, S., editors, *Engineering Applications of Large Eddy Simulations*, volume 162 of *FED*, pages 81-101. ASME.
5. Frazier, T. R., Foglesong, R. E., Coverdill, R. E., Peters, J. E., and Lucht, R. P. (1998). An experimental investigation of fuel/air mixing in an optically accessible axial premixer. *AIAA-98-3543*.
6. Fric, T. F. (1993). Effects of fuel-air unmixedness on nox emissions. *Journal of Propulsion and Power*, 9(5):708-713.
7. Joshi, N. D., Mongia, H. C., Leonard, G., Stegmaier, J. W., and Vickers, E. C. (1998). Dry low emissions combustor development. *ASME-98-GT-310*.
8. Kerstein, A. R. (1988). Linear-eddy model of turbulent scalar transport and mixing. *Combustion Science and Technology*, 60:391-421.
9. Kerstein, A. R. (1991a). Linear-eddy modeling of turbulent transport. part 6. microstructure of diffusive scalar mixing fields. *Journal of Fluid Mechanics*, 231:361-394.
10. Kerstein, A. R. (1991b). Linear-eddy modeling of turbulent transport. part v: Geometry of scalar interfaces. *Physics of Fluids A*, 3(5):1110-1114.
11. Kerstein, A. R. (1992a). Linear-eddy modeling of turbulent transport. 7. finite-rate chemistry and multi-stream mixing. *Journal of Fluid Mechanics*, 240:289-313.
12. Kerstein, A. R. (1992b). Linear-eddy modeling of turbulent transport. part 4. structure of diffusion-flames. *Combustion Science and Technology*, 81:75-86.
13. Kerstein, A. R. (1999). One-dimensional turbulence: Model formulation and application to homogeneous turbulent shear flows and buoyant stratified flows. *Journal of Fluid Mechanics* (to appear).
14. Kim, W.-W. and Menon, S. (1995). A new dynamic one-equation subgrid-scale model for large-eddy simulations. *AIAA-95-0356*.
15. Kim, W.-W. and Menon, S. (1999). An unsteady incompressible navier-stokes solver for large-eddy simulation of turbulent flows. *International Journal for Numerical Methods in Fluids* (to appear).
16. Kim, W.-W., Menon, S., and Mongia, H. C. (1999). Large-eddy simulation of a gas turbine combustor flow. *Combustion Science and Technology* (to appear).
17. Liu, S., Meneveau, C., and Katz, J. (1994). On the properties of similarity subgrid-scale models as deduced from measurements in a turbulent jet. *Journal of Fluid Mechanics*, 275:83-119.
18. Menon, S., McMurtry, P., and Kerstein, A. R. (1993). A linear eddy mixing model for large eddy simulation of turbulent combustion. In Galperin, B. and Orszag, S., editors, *LES of Complex Engineering and Geophysical Flows*. Cambridge University Press.
19. Pannala, S. and Menon, S. (1998). Large eddy simulations of two-phase turbulent flows. *AIAA-98-0163*.
20. Poinso, T. and Lele, S. (1992). Boundary conditions for direct simulations of compressible viscous flow. *Journal of Computational Physics*, 101:104-129.
21. Shih, W. P., Lee, J. G., and Santavica, D. A. (1996). Stability and emissions characteristics of a lean premixed gas turbine combustor. *Twenty-Sixth Symposium (International) on Combustion*.
22. Smith, T. M. and Menon, S. (1996). Model simulations of freely propagating turbulent premixed flames. *Twenty-sixth Symposium (International) on Combustion*, pages 299-306.
23. Smith, T. M. and Menon, S. (1998). Subgrid combustion modeling for premixed turbulent reacting flows. *AIAA-98-0242*.

DYNAMIC INVERSE MODELLING IN LES OF THE TEMPORAL MIXING LAYER

J.G.M. KUERTEN

*Department of Mechanical Engineering, J.M. Burgers Center
Eindhoven University of Technology, P.O. Box 513
5600 MB Eindhoven, The Netherlands*

AND

B.J. GEURTS AND R. VAN BUUREN

*Faculty of Mathematical Sciences, J.M. Burgers Center
University of Twente, P.O. Box 217
7500 AE Enschede, The Netherlands*

Abstract. We applied dynamic inverse modelling to large-eddy simulation of the temporal mixing layer. Smagorinsky's model is adopted as base model and the results are compared to the standard dynamic eddy-viscosity model as well as filtered DNS results. The difference between the results of the two models for the present application is found to be small. This is explained by performing a detailed sensitivity analysis with respect to the dynamic coefficient, which appears to hint towards a 'self-restoring' response underlying the observed robustness.

1. Introduction

Modelling of transitional and turbulent flow forms a field of considerable interest, although developments in numerical methods and computer resources enable the use of direct numerical simulation (DNS) for increasingly complex flows. In large-eddy simulations (LES) the modelling process starts with the application of a spatial convolution filter to the Navier-Stokes equations. Filtering of the nonlinear convective terms gives rise to the turbulent stress tensor

$$\tau_{ij} = \overline{u_i u_j} - \bar{u}_i \bar{u}_j \quad ; \quad i, j = 1, 2, 3, \quad (1)$$

which contains contributions from the filtered (\bar{u}_i) and the unfiltered (u_i) velocity components. Since in an LES only the filtered velocity components are calculated, the turbulent stress tensor has to be modelled. Various modelling strategies have been proposed. The dynamic modelling approach (Germano *et al.*, 1991) has shown to give rise to quite accurate LES predictions (Vreman *et al.*, 1997). This approach involves the introduction of a second ‘explicit’ filter and is aimed at an appropriate optimisation of parameters contained in an assumed base model. The optimisation is performed in accordance with an exact algebraic identity involving τ at different filter levels, and yields dynamically determined solution dependent model parameters.

Recently, it has been proposed to extend this approach and introduce apart from the explicit filter also its inverse (Kuerten *et al.*, 1999). This implies new algebraic identities which involve the base model at various filter levels. In one of the extensions proposed these filter levels involve only the smallest resolved scales in the LES as well as yet smaller scales. Hence, inaccuracies arising from the use of a larger filter width associated with the explicit filter in the traditional dynamic approach can be partially compensated and basic modelling assumptions can be maintained more strictly. This especially refers to the similarity assumption related to different filter levels in an inertial range of the energy spectrum.

In this paper we will apply this dynamic inverse modelling strategy to LES of the temporal mixing layer at low Mach number. As base model we adopt the Smagorinsky eddy-viscosity subgrid model. The results will be compared with filtered DNS results and results from LES using the traditional dynamic eddy-viscosity model. In section 2 we will briefly recapitulate the dynamic modelling approach and its extension to dynamic inverse modelling. Numerical realizations of the explicit filter and their inverse will be shown in section 3. The temporal mixing layer is introduced in section 4 and the results will be presented in section 5. Finally, in section 6 some conclusions will be drawn.

2. Dynamic inverse modelling

In large-eddy simulation of turbulence the flow quantities are decomposed into a large-scale contribution and a small-scale contribution by a spatial filter. The large-scale contributions are explicitly calculated, whereas only the effects of the small-scale contributions on the large-scale flow are described by a so-called subgrid model. The main term to be modelled is the turbulent stress tensor (1). In the widely used Smagorinsky model (Smagorinsky, 1963) the turbulent stress tensor is modelled by a viscous term:

$$\tau_{ij} = -C_S^2 \Delta^2 |\bar{S}| \bar{S}_{ij}, \quad (2)$$

where Δ is the filter width, \bar{S}_{ij} is the strain rate tensor based on the filtered velocity and

$$|\bar{S}|^2 = \frac{1}{2} \bar{S}_{ij} \bar{S}_{ij}. \quad (3)$$

For the Smagorinsky constant C_S various values have been used. A major drawback of this model is the excessive dissipation in laminar regions of the flow (Vreman *et al.*, 1997).

In order to overcome this problem Germano *et al.* proposed the dynamic procedure, where C_S^2 is replaced by a coefficient C_d which is dynamically adjusted to the local structure of the flow (Germano *et al.*, 1991). The main assumption in the dynamic procedure is that the coefficient C_d is independent of the filter width (Carati *et al.*, 1997). To specify C_d the Smagorinsky model is substituted in Germano's identity, which reads

$$T_{ij} - \widehat{\tau_{ij}} = \widehat{\bar{u}_i \bar{u}_j} - \widehat{\bar{u}_i} \widehat{\bar{u}_j}, \quad (4)$$

where the hat ($\widehat{}$) denotes the explicit filter operation and T_{ij} is the turbulent stress tensor corresponding to the consecutive application of the two filters:

$$T_{ij} = \widehat{\widehat{\bar{u}_i \bar{u}_j}} - \widehat{\bar{u}_i} \widehat{\bar{u}_j}. \quad (5)$$

The right-hand side in identity (4) contains only resolved flow quantities and is known in an LES, whereas the terms on the left-hand side involve the turbulent stress tensors at different filter levels. If the base model is substituted for these tensors, the only unknown in the identity is the coefficient C_d , which can, for example, be calculated with a least-squares approach as a function of space and time (Lilly, 1992).

It is clear that the independence of C_d of the filter width can only hold within certain bounds and is approximately valid if the model is adopted at filter levels inside the inertial range. In order to save calculation time the filter width in an LES is usually chosen as large as possible. In this situation the validity of the model on the test filter level may become questionable and it would be preferable if the base model is only applied at smaller scales. This can be achieved by using a generalisation of Germano's identity (4) to any combination of filters. In order to illustrate this generalisation it is convenient to introduce a new notation (Kuerten *et al.*, 1999), in which we use the notation L for a filter operator, and define the product operator S by

$$S(f, g) = fg. \quad (6)$$

Further the commutator of two operators is written as

$$[L, S](u_i, u_j) = L(S(u_i, u_j)) - S(L(u_i, u_j)). \quad (7)$$

Now the turbulent stress tensor can be written as

$$\tau_{ij} = [L, S](u_i, u_j) \quad (8)$$

and Germano's identity reads:

$$[\mathcal{L}_1 \mathcal{L}_2, S] = [\mathcal{L}_1, S] \mathcal{L}_2 + \mathcal{L}_1 [\mathcal{L}_2, S], \quad (9)$$

where both \mathcal{L}_1 and \mathcal{L}_2 denote any filter operator. In the standard dynamic models \mathcal{L}_2 is the common LES filter and \mathcal{L}_1 is the test filter. However, as (9) holds for any two filters we can also take $\mathcal{L}_2 = \mathcal{H}^{-1}L$ and $\mathcal{L}_1 = \mathcal{H}$, where L is the LES filter, \mathcal{H} is any explicit filter and \mathcal{H}^{-1} its inverse. This choice for the two filters leads to the identity

$$\tau_{ij} - \mathbb{T}_{ij} = \mathbb{L}_{ij}, \quad (10)$$

where

$$\mathbb{T}_{ij} = \mathcal{H}(\mathcal{H}^{-1}(\overline{u_i u_j}) - \mathcal{H}^{-1}(\overline{u_i})\mathcal{H}^{-1}(\overline{u_j})) \quad (11)$$

and

$$\mathbb{L}_{ij} = \mathcal{H}(\mathcal{H}^{-1}(\overline{u_i})\mathcal{H}^{-1}(\overline{u_j})) - \overline{u_i u_j}. \quad (12)$$

If Smagorinsky's eddy viscosity model is adopted for the terms on the left-hand side, we find the following relation for the coefficient C_d :

$$C_d M_{ij} = \mathbb{L}_{ij}, \quad (13)$$

where

$$M_{ij} = -\Delta^2 |\bar{S}| \bar{S}_{ij} + ((\kappa \Delta)^2 |\tilde{S}| \tilde{S}_{ij})^\wedge. \quad (14)$$

Here $\kappa \Delta$ is the effective filter width of $\mathcal{H}^{-1}L$, to which we will return later and \tilde{S} is the strain rate tensor based on the velocity $\mathcal{H}^{-1}L(\mathbf{u})$. The hat after the last term on the right-hand side implies that the whole term between parentheses is filtered with \mathcal{H} . In the actual LES shown here the coefficient C_d is calculated with a least squares approach (Lilly, 1992). Furthermore, in order to prevent numerical instability caused by negative values of C_d , averaging over homogeneous directions is performed and the coefficient is artificially set to zero at locations where it would otherwise be negative. In (14) the model is applied at level L and at level $\mathcal{H}^{-1}L$, which thus involves scales smaller than resolved in the LES. Hence, this form of dynamic inverse modelling provides the best guarantee that the model is applied only in the inertial range.

In the next section we will first discuss the explicit filters \mathcal{H} and \mathcal{H}^{-1} which appear in the dynamic inverse model. After that we will apply the model in a large-eddy simulation of the compressible temporal mixing layer.

3. Numerical filters

In LES the roles of the filters L and \mathcal{H} differ essentially. Whereas L is central in the theoretical development and does not appear explicitly in an LES calculation, the test filter \mathcal{H} and its inverse \mathcal{H}^{-1} are explicitly applied in case dynamic modelling based on the identity derived in the previous section is adopted. In an LES the resolved fields are known only at grid points ($\{x_m\}_{m=0}^N$). Therefore, the explicit filter and its inverse can only be applied as finite dimensional operators.

The numerical approximation of a one-dimensional convolution filter is written as

$$\mathcal{H}(u)(x_m) = \sum_{j \in \mathbb{Z}} \alpha_j u(x_{m+j}), \quad (15)$$

where for consistency $\sum_j \alpha_j = 1$. To satisfy the realizability conditions (Vreman *et al.*, 1994) we require the coefficients α_j to be non-negative. As an example consider the numerical filters with $\alpha_0 = 1 - \alpha$, where $0 < \alpha < 1$, $\alpha_1 = \alpha_{-1} = \alpha/2$ and $\alpha_j = 0$ if $|j| \geq 2$. A special case arises with $\alpha = 1/3$ which corresponds to Simpson quadrature applied to the top-hat filter with $\delta = 2h$ where h is the grid spacing and δ the width of \mathcal{H} . The effect of a numerical filter on a Fourier mode $u = \exp(ikx)$ is given by

$$\mathcal{H}(u)(x_m) = (1 - \alpha + \alpha \cos(kh)) \exp(ikx_m) = H_\alpha(kh) u(x_m). \quad (16)$$

This filter can only be inverted if the 'characteristic' function H_α is strictly positive, which implies that $\alpha < 1/2$. The inverse is then given by

$$\mathcal{H}^{-1}(\exp(ikx)) = \frac{1}{H_\alpha(kh)} \exp(ikx). \quad (17)$$

The application of \mathcal{H}^{-1} to a general solution which is known only by its grid-values $\{u(x_m)\}$ can be specified using discrete Fourier transforms between grid- and wavenumber space. The result is

$$\mathcal{H}^{-1}(u)(x_m) = \frac{1}{N} \sum_{j=0}^{N-1} \sum_k H_\alpha^{-1}(kh) \cos(kh(m-j)) u(x_j), \quad (18)$$

where the inner summation extends over $k = 2\pi k^*/hN$ with k^* all integers between $-N/2$ and $N/2$. In practice the double summation makes application of the inverse filter inefficient if N becomes large. However, for values of N larger than about 10 the result hardly depends on N . Taking the limit $N \rightarrow \infty$ in the summation over k we find

$$\mathcal{H}^{-1}(u)(x_m) = \sum_{j=0}^{N-1} \left(\frac{\alpha - 1 + \sqrt{1 - 2\alpha}}{\alpha} \right)^{|m-j|} \frac{u(x_j)}{\sqrt{1 - 2\alpha}} \quad (19)$$

For all positive values of α smaller than $1/2$ the power series in this expression converges and the convergence rate increases if α decreases. Hence, for small values of α an accurate and efficient approximation of the inverse filter can be obtained with only a few terms. Extension of the numerical filter and its inverse to three spatial dimensions is straight forward.

Before we turn to a description of the temporal mixing layer in the next section we will first spend some time on the effective filter width of the numerical filter \mathcal{H} and its inverse. If \mathcal{H} is a numerical filter, it can be seen as the discrete approximation of a continuous filter and its filter width can be defined as the width of the corresponding continuous filter. As an example, the numerical filter with $\alpha = 1/3$ described above is an approximation of the top-hat filter with filter width equal to $2h$. So, we define the width of the numerical filter as $\delta = 2h$.

In dynamic models which use Smagorinsky's model as a base model, the effective filter width of the composition of two filters is also needed. In Vreman *et al.* (1997) it has been shown that the composition of two top-hat filters is not a top-hat filter, and that the top-hat filter which is the best approximation has a width given by

$$\Delta_{\mathcal{H}L}^2 = \Delta_{\mathcal{H}}^2 + \Delta_L^2. \quad (20)$$

A problem still remains in the definition of the effective filter width of $\mathcal{H}^{-1}L$. The composition $\mathcal{H}^{-1}\mathcal{H}$ equals the identity operator, which is the limit of the top-hat filter for $\Delta \rightarrow 0$ and thus has a filter width equal to zero. If we now consider (20) as a definition of the effective filter width for any filter operator or its inverse, we find

$$\Delta_{\mathcal{H}^{-1}}^2 = -\Delta_{\mathcal{H}}^2. \quad (21)$$

As a final step we can define the effective width of $\mathcal{H}^{-1}L$ by using (20) again. An interesting case arises when \mathcal{H} is a numerical approximation of L . Then $\mathcal{H}^{-1}L$ has effective width $\kappa\Delta$ equal to zero. It follows that the second term on the right-hand side of (14) is absent. This makes this particular dynamic inverse model very cost effective.

4. Temporal mixing layer

In this section we will describe the test case of a compressible temporal mixing layer adopted in this paper. The computational domain is a cube. Periodic boundary conditions are imposed in the streamwise and spanwise directions, whereas the boundaries in the normal direction are free-slip walls. As initial condition a hyperbolic tangent velocity profile is taken as the mean streamwise velocity, the other mean velocity components are zero, the mean pressure is uniform and the mean temperature is obtained from

the Busemann-Crocco law. In order to initiate turbulence, perturbations consisting of eigenfunctions provided by linear stability theory (LST) are superimposed on the mean profile. The length of the domain equals four times the wavelength of the most unstable mode according to LST. In this way two subsequent pairings of the rollers are allowed. Subharmonic and oblique modes are added to initiate the vortex pairings and to introduce three-dimensionality. The Mach number is 0.2, which makes the simulation practically incompressible. The Reynolds number is 50, based on the upper velocity and half the initial vorticity thickness.

The initial condition is prepared on a uniform grid with 192^3 grid points. On this grid a direct numerical simulation (DNS) is performed for comparison purposes. The initial condition is filtered onto a uniform grid with 32^3 grid points, on which the LES is carried out. The filter width equals $D/16$, where D is the length of the computational domain, i.e. $\Delta = 2h$. The filter used is the top-hat filter. The numerical method for both the DNS and the LES is a fourth order accurate finite volume method without artificial dissipation for the spatial discretization and a second order four-stage compact-storage Runge-Kutta method for the time integration. More details on the test case and on the numerical method can be found in Vreman *et al.* (1997).

5. Results

In this section we will present LES results for both the traditional dynamic (DSM) and the dynamic inverse model (DIM) using Smagorinsky's eddy viscosity model as base model. The results will be compared with filtered DNS results. In the DSM the explicit test filter has a width equal to 2Δ . In the DIM we use the numerical explicit with $\alpha = 1/3$. This implies that $\kappa\Delta = 0$ in (14). In (19) the sum is taken over $j = m - 5, \dots, m + 5$. Since the sum of the coefficients should be equal to 1, the coefficient of the term $j = m$ has been slightly changed. The simulation results with the sum taken over $j = m - 10, \dots, m + 10$ are indistinguishable.

The LES for both dynamic models reproduce the large-scale roller structures found in the DNS and undergo a transition to turbulence. Figure 1 displays the spanwise vorticity at $t = 80$ in a plane in spanwise direction for both dynamic models and for the filtered DNS results. Both dynamic models are qualitatively in good agreement with the filtered DNS results: the peak values of the vorticity are quite well predicted and roughly the correct amount of small structures is present. The differences between the results of the two models are quantitatively very small. This holds for mean quantities, but also for turbulence intensities. As an example we show the momentum thickness as a function of time in Fig. 2. In Fig. 3 the dynamic

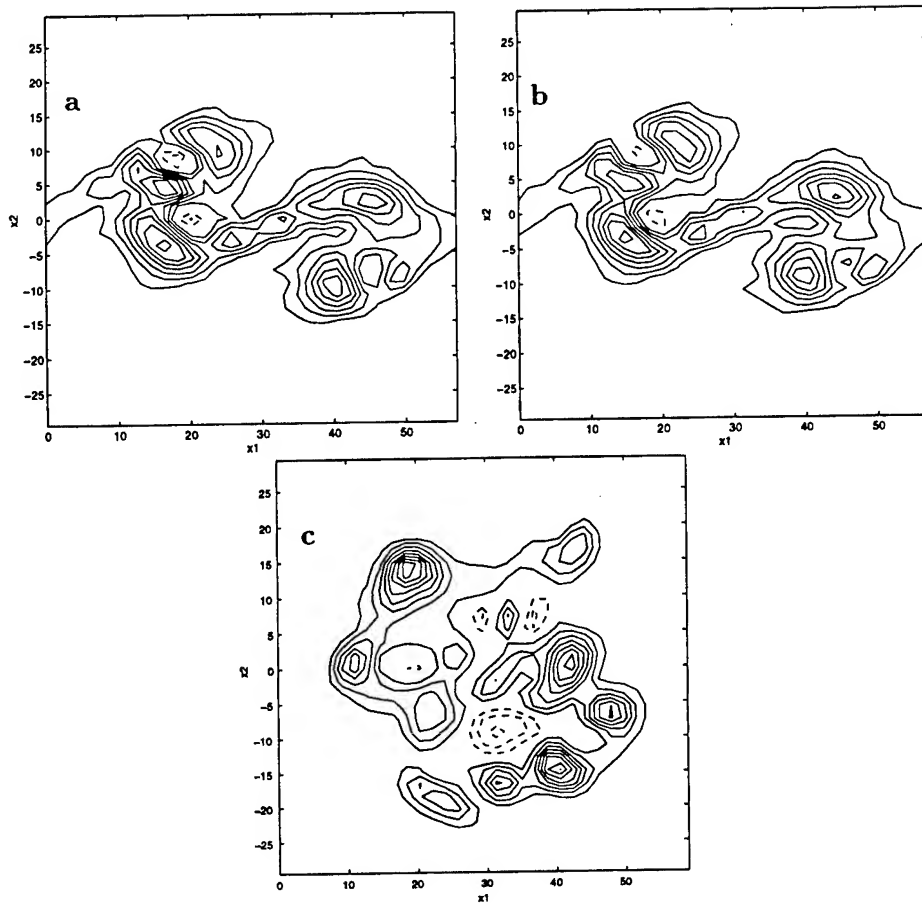


Figure 1. Contours of spanwise vorticity in a plane perpendicular to the spanwise direction at $t = 80$. Solid and dotted contours indicate negative and positive vorticity respectively. a: DSM, b: DIM, c: filtered DNS

coefficient C_d is plotted as a function of time at the centre-line of the mixing layer. We see that there is a sizeable difference in the value of the dynamic coefficient of 20–50%, which apparently hardly influences the simulation results. In order to study the sensitivity of the simulation results on the value of C_d we performed another simulation in which we determined the value of C_d in the same way as in the DSM, but multiplied it afterwards by a factor of 2 (DSM2). In the initial stages of the simulation the resulting subgrid dissipation turns out twice as large as in the DSM. However, this reduces the amount of small scales present, and thus decreases the strain rate tensor. Hence, in the later stages of the simulation the molecular dissipation is smaller and the subgrid dissipation is only roughly 20% larger

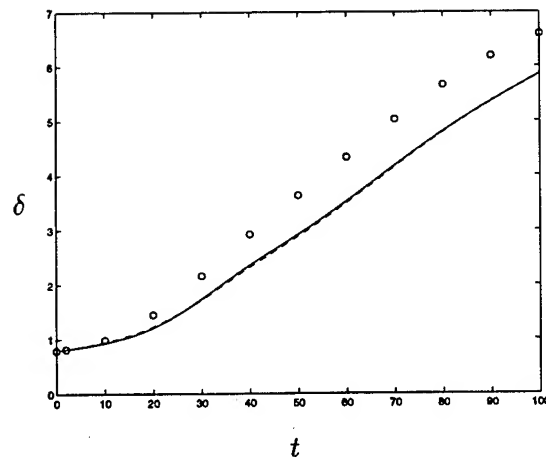


Figure 2. Momentum thickness as a function of time; solid: DSM, dashed: DIM, \circ : filtered DNS

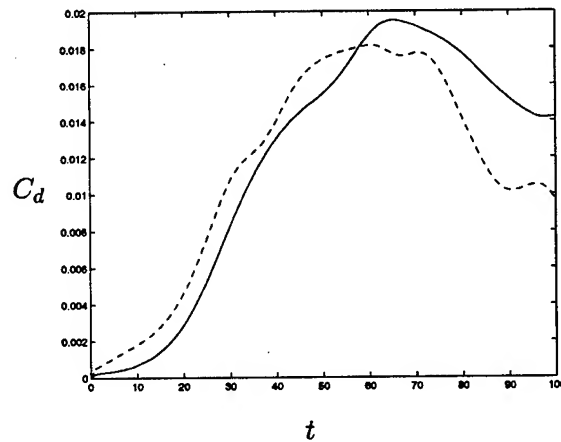


Figure 3. Dynamic coefficient as a function of time at the centre-line; solid: DSM, dashed: DIM

than in the DSM as can be seen in Fig. 4. The effect on mean quantities is therefore very small and even turbulent intensities change by only some 10%. This is consistent with the results for DSM and DIM.

Finally, we compare the efficiency of both subgrid models. The only difference between the two models is the way in which the coefficient C_d is calculated. Since in the DIM the second term in (14) equals zero, the amount of work is less than in the DSM, resulting in a decrease in calculation time of approximately 15%.

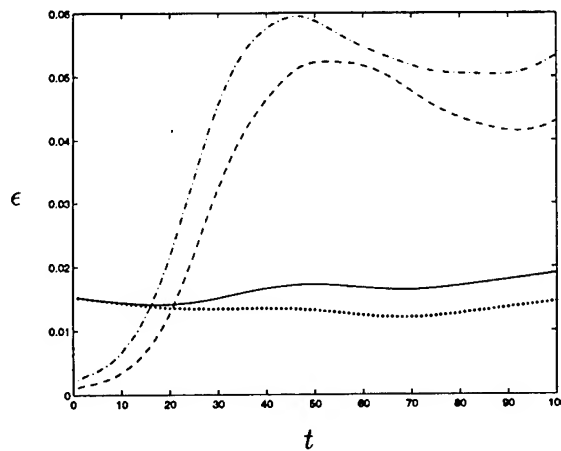


Figure 4. Subgrid dissipation and molecular dissipation as function of time; solid: DSM-molecular, dashed: DSM-subgrid, dotted: DSM2-molecular, dash-dotted: DSM2-subgrid

6. Conclusion

We applied dynamic inverse modelling to LES of a temporal mixing layer, using Smagorinsky's model as a base model and compared the results with the standard dynamic eddy-viscosity model. To this end we introduced a numerical filter and its exact inverse. The quantitative simulation results are almost the same. It is argued that this is caused by the insensitivity of the simulation to relatively small changes in the dynamic coefficient. A sensitivity analysis revealed that even a large change in the value of the dynamic coefficient hardly influences mean flow quantities.

References

- Carati, D. and Vanden Eijnden, E. (1997) On the self-similarity assumption in dynamic models for large eddy simulations, *Phys. Fluids*, **9**, 2165–2167
- Germano, M., Piomelli, U., Moin, P. and Cabot, W.H. (1991) A dynamic subgrid-scale eddy viscosity model, *Phys. Fluids A*, **3**, 1760–1765
- Kuerten, J.G.M., Geurts, B.J., Vreman, A.W. and Germano, M. (1999) Dynamic inverse modelling and its robustness in LES of the mixing layer, *to be published*
- Lilly, D.K. (1992) A proposed modification of the Germano subgrid-scale closure method, *Phys. Fluids A*, **4**, 633–635
- Smagorinsky, J. (1963) General circulation experiments with the primitive equations, *Mon. Weather Rev.*, **91**, 99–164
- Vreman, A.W., Geurts, B.J. and Kuerten, J.G.M. (1994) Realizability conditions for the turbulent stress tensor in Large Eddy Simulation, *J. Fluid Mech.*, **278**, 351–362
- Vreman, A.W., Geurts, B.J. and Kuerten, J.G.M. (1997) Large-eddy simulation of the turbulent mixing layer, *J. Fluid Mech.*, **339**, 357–390

COMPARISON OF THE ENO AND COMPACT SCHEMES FOR DNS/LES OF TURBULENCE

FOLUSO LADEINDE AND XIAODAN CAI

*Aerospace Research Corporation, L.I.
Stony Brook, Long Island, NY*

AND

MIGUEL R. VISBAL AND DATTA V. GAITONDE

*Air Vehicles Directorate
Air Force Research Laboratory
Wright-Patterson AFB, OH*

Abstract. The comparative ability of ENO and compact schemes to correctly calculate homogeneous compressible turbulence is investigated in this work. Also included in the analysis are the weighted essentially nonoscillatory (WENO) scheme and a third-order, upwind-biased scheme. The ability of the various schemes to represent certain single-point statistics and the spectra energy distribution is compared. The compact scheme requires filters for numerical stability. The effects of an adjustable parameter in the filter formulation on the computed results are discussed, as are the roles of filters in the ability of the ENO code to dissipate turbulence energy. The effect of grid refinement on the relative spectra energy dissipation by ENO and compact schemes are presented.

1. Introduction

The comparative evaluation of the computational speed, accuracy, and robustness of the ENO and compact schemes is investigated in a systematic manner in this work. The objective of this study is to determine the characteristics of the methods for compressible DNS and LES. The computer program FDL3DI, with its two-dimensional version, FDL2DI, both developed by the authors from Wright-Patterson, was used for the compact calculations, whereas the ENO program came from procedures developed

at Aerospace Research Corporation, Long Island. Both codes are used with a *curvilinear* coordinate transformation, in order to treat the irregular geometries that are of interest in application. Previous applications of the ENO and compact schemes to DNS include Ladeinde *et al.* (1995) and Lee *et al.* (1997), respectively. We will focus on Mach number M_1 values of 0.1, 0.5 and 0.7, where M_1 is the sonic Mach number of the initial flow, or $M_1 = (u_{rms}/c_s(\mathbf{x}))_0$, where $u_{rms} = (\overline{|\mathbf{u}(\mathbf{x})|^2})^{1/2}$ is the root-mean-square value of the velocity at any instant in time, $c_s(\mathbf{x})$ is the local sound speed, an overline means spatial averaging and the subscript "0" implies the initial value in time. The instantaneous turbulence Mach number M_s is also used in this paper, where $M_1 = (M_s)_0$.

There are potential problems with the compact schemes that have not received enough attention. This includes the computational burden of the coupling between nodal gradients, the dissipative effect of filtering that is often required for numerical stability of Navier-Stokes calculations, anisotropy issues (numerical, not turbulence), and the evaluation of the viscous terms, particularly in curvilinear coordinate situations. The spectral-like resolution and the relative ease of implementation of the compact schemes are the overriding reasons for the interest in them.

The ENO approach also has potential problems, such as the possibility of overdiffusion from upwind-like procedures, which depends on grid refinement and the particular implementation (Roe, Lax-Friedrich, etc.) and the cost of the adaptive stencil. The nonlinearity of the stencil adaptation process is also potentially harmful in terms of numerical oscillations. The high-order resolution and the suitability for high Mach numbers are the overriding reasons for the interest in the ENO schemes.

2. Governing Equations

The problem chosen for the comparison study is the decaying homogeneous turbulence problem of Ghosh and Matthaeus(1992), hereafter referred to as GM, who employed the pseudospectral method. The GM problem was chosen because of the thorough theoretical and numerical treatment. The problem is two-dimensional which, compared to its three-dimensional counterpart, makes it more affordable, and hence, more suitable for the kind of parametric study undertaken in this paper. Note that the reference pseudospectral results were generated in GM. The unsteady, two-dimensional, viscous Navier-Stokes equations are solved in strong conservation form using the generalized curvilinear coordinates (ξ, η) :

$$\frac{\partial}{\partial t} \left(\frac{U}{J} \right) + \frac{\partial F}{\partial \xi} + \frac{\partial G}{\partial \eta} = \frac{1}{\text{Re}} \left[\frac{\partial F_v}{\partial \xi} + \frac{\partial G_v}{\partial \eta} \right] \quad (1)$$

where $U = \{\rho, \rho u, \rho v, \rho E_t\}$ is the solution vector, J is the Jacobian of the transformation, F, G are the inviscid fluxes and F_v, G_v are the viscous fluxes.

The initial condition for this problem is of the pseudosound type and is obtained by first solving for the fluctuating pressure p' from the Poisson equation for the incompressible component of the initial velocity field:

$$\nabla^2 p' = -\gamma M_1^2 \nabla(\mathbf{u}^I \cdot \nabla \mathbf{u}^I),$$

where the right-hand side of this equation is due solely to the solenoidal velocity component \mathbf{u}^I from random numbers. The pseudosound density fluctuation is obtained from the relation $\delta \rho_{PS} = \frac{1}{\gamma} p'$ and the initial pressure and density fields are $P = 1 + p'$ and $\rho = 1 + \delta \rho_{PS}$. The imposed turbulence spectrum is chosen to match that in GM:

$$E_i = \begin{cases} 1, & 1 \leq k \leq \sqrt{12}, \\ 0, & \text{otherwise} \end{cases}$$

where "i" is an index defined by $i - \frac{1}{2} \leq k \leq i + \frac{1}{2}$, with $k = \sqrt{k_x^2 + k_y^2}$ and k_x, k_y are the turbulence wavenumbers in the x - and y -directions respectively. The Mach numbers investigated are $M_1 = 0.1, 0.5$, and 0.7 ; the Reynolds number is 250. As in GM, a grid of 64^2 is sufficient to resolve the important scales of flow although results for 256^2 are also analyzed for grid dependence. The computational length of the domain runs from 0.0 to 7.081 units in both x and y . The gas is assumed to be polytropic, with $P = \rho^\gamma$ and T (temperature) $= \rho^{\gamma-1} \gamma M_1^2$.

3. Numerical Schemes

3.1. COMPACT DIFFERENCING

The derivative u' for any generic variable u in the transformed coordinate frame is represented as:

$$\alpha u'_{i-1} + u'_i + \alpha u'_{i+1} = b \frac{u_{i+2} - u_{i-2}}{4\Delta\xi} + a \frac{u_{i+1} - u_{i-1}}{2\Delta\xi} \quad (2)$$

where α, a , and b are constants which determine the spatial properties of the algorithm. The base compact differencing schemes used in this paper are the three-point, fourth-order scheme, C4, with $(\alpha, a, b) = (\frac{1}{4}, \frac{3}{2}, 0)$, the five-point, sixth-order scheme, C6, with $(\alpha, a, b) = (\frac{1}{3}, \frac{14}{9}, \frac{1}{9})$. Also used is the five-point, fourth-order scheme, O5, with $(\alpha, a, b) = 0.430816, 1.6205440$, and 0.2410880. This scheme minimizes the dispersion error over the entire range of wavenumbers up to 2 points per wave.

Equation (2) is used to calculate the various derivatives in the (ξ, η) plane, as well as the metrics from coordinate transformation. The inviscid fluxes in the Navier-Stokes equations are formed in the transformed coordinates at each nodal point and the components differentiated using equation (2). The same coefficients (α, a, b) are used for both the metrics and the fluxes, which is useful in reducing the error on stretched meshes (Visbal and Gaitonde, 1998; Gaitonde and Visbal, 1998). To calculate the viscous and heat conduction terms, the primitive variables $u = \{\rho, \rho u, \rho v, \rho E_t\}$ are first compact differentiated to form the stress tensor and heat flux vector. The viscous and heat conduction terms of the flow equations are then computed by another application of equation (2). The use of second derivative compact formulations, as in Lele (1992), has some advantages but could lead to excessive computational penalty on curvilinear coordinates.

The compact formulas for the domain boundary points are well known; the present work is based on the boundary formulas in Gaitonde and Visbal (1998). Time integration of the ODE that results from the spatial discretization was based on the classical fourth order Runge Kutta scheme.

Numerical instability is often encountered in the solution of the Navier-Stokes equations with compact differencing. The calculations are stabilized with numerical filters (Lele, 1992). In the formulation, the filtered values \tilde{u} for any quantity u in the transformed plane is represented as:

$$\alpha_f \tilde{u}_{i-1} + \tilde{u}_i + \alpha_f \tilde{u}_{i+1} = \sum_{n=0}^N \frac{a_n}{2} (u_{i+n} + u_{i-n}) \quad (3)$$

This representation provides a non-dispersive, $2N$ th-order filter with $2N+1$ point stencil. The spectral function F for this scheme can be represented as

$$F(\omega) = \frac{\sum_{n=0}^N a_n \cos(n\omega)}{1 + 2\alpha_f \cos(\omega)}$$

where ω is the normalized wavenumber $\omega = \frac{2\pi k}{N}$, $N = \frac{L}{h}$, and k is the physical wave number, L is domain length and h is the grid spacing. The eighth- and tenth-order filters are used in the present work, for which the coefficients are:

$$\begin{aligned} a_0 &= \left(\frac{93 + 70\alpha_f}{128}, \frac{193 + 126\alpha_f}{256} \right), & a_1 &= \left(\frac{7 + 18\alpha_f}{16}, \frac{105 + 302\alpha_f}{256} \right), \\ a_2 &= \left(\frac{-7 + 14\alpha_f}{32}, \frac{15(-1 + 2\alpha_f)}{64} \right), & a_3 &= \left(\frac{1}{16} - \frac{\alpha_f}{8}, \frac{45(1 - 2\alpha_f)}{512} \right), \\ a_4 &= \left(-\frac{1}{128} + \frac{\alpha_f}{64}, \frac{5(1 - 2\alpha_f)}{512} \right), & a_5 &= \left(0, \frac{1 - 2\alpha_f}{512} \right) \end{aligned} \quad (4)$$

The foregoing filters are a subset of the more elaborate ones proposed by Gaitonde and Visbal (1998). For convenience, we will refer to their filters as VG filters. The boundary treatments in VG filters are available in the reference.

The notations used in Gaitonde and Visbal (1999) will be adopted to simplify the specification of the compact difference schemes. The homogeneous turbulence results presented in this paper are based on periodic boundary conditions. In this case, the notation C_n will be used to denote an n th order compact differencing scheme. For the filter scheme, the interior order will be designated with its order of accuracy superscripted with the value of a parameter, α_f . For example, $F10^{0.3}$ represents a tenth-order filter with $\alpha_f = 0.3$. The compact differencing schemes used are C4, O5, and C6, whereas the filter schemes are $F8^{0.4}$ and $F10^{0.4}$.

3.2. ENO AND WENO SCHEMES

The ENO and WENO schemes presented in Shu (1997) were used. The ENO/WENO procedure pertains to the differencing of the convective terms of the Navier-Stokes equations in a way that avoids discretization across very strong gradients. (The viscous terms are discretized with explicit fourth order schemes.) Thus, based on the Navier-Stokes equations in (1), the ENO problem can be written as:

$$u_t(\xi, \eta, t) + f_\xi(u(\xi, \eta, t)) + g_\eta(u(\xi, \eta, t)) = 0, \quad (5)$$

where it is apparent that u , f , and g are vector functions. The convective terms are reconstructed to accuracy k , which is taken as 3 or 4 in the present work. The basic ENO differencing problem is:

$$\begin{aligned} \frac{du_{ij}}{dt} &= -\frac{1}{\Delta\xi} (\hat{f}_{i+\frac{1}{2},j} - \hat{f}_{i-\frac{1}{2},j}) - \frac{1}{\Delta\eta} (\hat{g}_{i,j+\frac{1}{2}} - \hat{g}_{i,j-\frac{1}{2}}) \\ &= f' + g' + O(\Delta\xi^k, \Delta\eta^k) \equiv L(u). \end{aligned} \quad (6)$$

Many options are possible with the ENO or WENO schemes. The base ENO scheme in the present paper focuses on the characteristic-wise high order finite differencing with Roe speed and Lax-Friedrichs flux-splitting. The stencils for $\hat{f}_{i\pm\frac{1}{2},j}$ and $\hat{g}_{i,j\pm\frac{1}{2}}$ are adaptively selected from the relatively smooth part of the flow and constructed to be of the desired order via Lagrange-type interpolation. For WENO, one uses a convex combination of all the candidate stencils, instead of using just one of these. Details of the procedures are available in Shu (1997). Note that for WENO, the leading order truncation error is $O(\Delta\xi^{2k-1})$ compared to $O(\Delta\xi^k)$ for ENO, where

k is the order of the scheme. The calculations reported in this paper were carried out with $k = 3$.

In addition to the ENO and compact differencing schemes, the suitability of popular engineering CFD schemes for DNS/LES is also investigated using the third-order, upwind-biased Roe scheme, hereafter referred to as the “Roe” scheme.

4. Results and discussions

For the Navier-Stokes equations, the compact differencing schemes in the current formulation require filters for numerical stability. Without them, the results were either unphysical or the calculations divergent. Therefore, all the compact results presented in this paper were generated with filters.

In general, for $M_1 = 0.1, 0.5$, the ENO (using the center stencil-biased scheme at the lower Mach number and the fully adaptive scheme at the higher Mach number) and compact results for certain single-point quantities show good agreement. This is the case for the temporal evolution of ρ, u' , and p at selected points in the domain. The results for $M_1 = 0.1$ are indistinguishable for the two schemes, and only slight deviations have appeared at $M_1 = 0.5$. The differences between the results for the two schemes are more pronounced at $M_1 = 0.7$. Qualitative agreement in the whole field is also evident in the density contour map of figure 1 ($M_1 = 0.5$).

It is important to note that some tuning of the ENO scheme is often required in order to handle a wide range of Mach numbers. That is, when the Mach number is low (i.e., smooth field), the stencil adaptation process in the standard ENO procedure becomes unreliable, leading to inaccurate results. The temporal kinetic energy decay in figure 2 ($M_1 = 0.1$) illustrates this problem, where figure 2 (a) is the result for the standard adaptive ENO whereas, in figure 2 (b), the stencil is biased toward a centered one, following the suggestion in Shu (1990). This difficulty was first reported in Rogerson and Meiburg (1990), albeit for a simple analytical function. Application of the same biasing technique to $M_1 = 0.5$ gave results that were similar to those for the standard, unbiased formulation for E_{kin} (total kinetic energy), E_{int} (total internal energy) and M_s^2 (turbulence Mach number squared). However, the turbulence energy spectra (P_k and P_i) are poorly represented at high wave numbers, compared to the standard adaptive stencil scheme (figure 3). The foregoing results suggest that, with ENO, for non-reacting calculations, it might be necessary to bias the stencil toward a centered one when $(M_1)_{max} \leq 0.3$ and to use the standard stencil adaptation process for $(M_1)_{max} > 0.3$. (The maximum Mach number is taken over all the nodal points in the domain.) The cut-off of 0.3 is obviously not strict, and is only a guide. Moreover, other factors, such as chemical reactions, could introduce

other sources of strong gradients and hence reduce the Mach number limit for the use of the centered stencil.

The basic difficulty with the upwind-biased scheme is excessive dissipation, which is apparent in figure 1(c) and the turbulence kinetic energy (E_{kin}) and internal energy (E_{int}) plots in figure 2.

Using the same filter schemes (i.e., $F8^{0.4}$ and $F10^{0.4}$), no significant differences were found for E_{kin} , E_{int} , U^L/U^T (the ratio of the longitudinal and transverse velocity components), and M_s^2 when the differencing scheme was C4, O5, or C6 (figure 4 (a)). The spectra of the turbulence kinetic and internal energy were also the same. For the same compact differencing scheme, a small effect on the spectra distribution is observable when the filter scheme is changed from $F8^{0.4}$ to $F10^{0.4}$ (figure 4 (b)). The single-point variables listed above remained essentially unaffected by the change in filter order.

The choice of the parameter α_f within $0.2 \leq \alpha_f \leq 0.499$ did not affect the magnitude and temporal evolution of E_{kin} to any observable level (not shown) and has only a minor effect on E_{int} (figure 5 (a)). However, the effects are quite significant at the high wave number end of the turbulence kinetic and internal energy spectra. Increasing α_f moves the wave number cut off to the right (figure 5(b)). The spectral distribution of P_k (not shown) is similar to that of P_i in figure 5 (b), except for the different magnitudes at $\kappa = 1$ and the absence of the wiggles at the high wave number end of the profile for $\alpha_f = 0.499$.

Figure 6 (a) and (b) compare the performance of WENO with that of ENO and compact scheme for $M_1 = 0.5$. A slight reduction in E_{kin} is noticeable in the WENO results. The spectra decay for WENO (figure 6 (b)) is also much smoother than that for ENO and compact. For the same grid, the WENO results tend to be slightly more dissipative, while the results for ENO and compact show better agreement (Table 1). One interesting feature of the WENO results compared to those for ENO is the absence of energy accumulation at high wave numbers (figure 6 (b)).

The combination of VG filters with the standard ENO scheme causes an enhanced dissipation at high wave numbers (figure 7), thereby eliminating the energy accumulation that is characteristic of the spectra from standard ENO. The effect on E_{kin} and E_{int} is not significant.

The E_k and E_{int} results are reasonably close for 64^2 and 256^2 (not shown). The spectral energy decay results for the two grids are compared in figure 7 for P_k , $M_1 = 0.5$. The effect on P_i is similar (not shown). For the compact scheme, grid refinement extends the dissipation range wave number, similar to the effect of increasing α_f . For ENO, energy accumulation at the high wave numbers is eliminated with grid refinement. However, unlike the compact results, the decay rate for unfiltered ENO is roughly

the same for 64^2 and 256^2 . For the compact scheme, the decay rates for the two grids depart significantly after $\kappa = 10$, suggesting that the high wave number dissipation for 64^2 is numerically forced. Note that the addition of filters to ENO, at 64^2 , also lead to differences in the decay rate compared to the case for 256^2 .

The relative CPU consumption of ENO and compact schemes was investigated for 64^2 . On average, the compact code runs faster by a factor of 1.6. Preliminary work also indicates that this factor increases for increasing grid size, with an estimate of 3 to 6 for 1024^3 . It should be noted, however, that neither code was optimized, so that the numbers are good only as a rough guide.

5. Concluding Remarks

The main findings from the present investigation can be summarized as follows:

- 1) Engineering CFD schemes such as the third-order, upwind-biased scheme may not be suitable for DNS/LES because of the excessive dissipation reflected in the single-point statistics and the energy spectra.
- 2) A stencil-biasing parameter must be adjusted for the ENO scheme in order to promote a centered stencil when the Mach number is low. However, the parameter must not promote a centered stencil for high Mach numbers.
- 3) For the same filter scheme ($F8^{0.4}$ or $F10^{0.4}$), the compact differencing schemes C4, O5, and C6 produce similar results for single-point statistics and spectral energy decay. For the same compact differencing scheme (C4, O5, and C6), the filter schemes $F8^{0.4}$ and $F10^{0.4}$ produce similar single-point statistics but slightly different spectra.
- 4) The filter parameter α_f , within $0.2 \leq \alpha_f \leq 0.499$, does not affect the single-point data investigated but has a significant effect on the spectral decay of turbulence energy. Larger α_f values shift the cut-off wave number to the right of the spectrum.
- 5) The compact differencing schemes require filters for numerical stability whereas ENO does not. However, the standard ENO results produce spectra that accumulate energy at the high wave numbers. The use of VG filters alleviates this problem.
- 6) WENO results do not accumulate energy at high wave numbers and are generally slightly more dissipated compared to both the compact and standard ENO results.
- 7) Grid refinement (64^2 versus 256^2) shifts the high wave number cut-off to the right for both ENO and compact and, for both schemes, grid refinement changes the decay rate (at the high wave number end)

- relative to the filtered 64^2 results. The decay rate for the unfiltered 64^2 ENO results is roughly the same as that for 256^2 .
- 8) Energy accumulation (by ENO) or possible premature dissipation in wave number space (by WENO or compact) might undermine DNS results if not prevented.
 - 9) The findings in this paper are potentially significant for SGS modeling. Not only do we have to worry about the dependence of the Smagorinsky constant on the SGS model in terms of the subgrid scale cutoff wave number and energy accumulation, we also need to include the differential effects of the numerical schemes on these high wave number phenomena.
 - 10) The present paper suggests that single-point statistics may fail to reveal important numerical difficulties. It is therefore advisable to also examine the energy spectra for possible numerical difficulties.

Acknowledgments

The authors are grateful for AFOSR sponsorship under tasks monitored by Drs. M. Jacob, L. Sakell, and S. Walker. This work was also supported in part by a grant of HPC time from the DoD HPC Shared Resource Centers at CEWES and NAVO. The Aerospace Research Corporation, Long Island is a Division of Thaerocomp Technical Corporation and a Corporate Partner of Cornell University.

References

- Gaitonde, D. & Visbal, M.R. 1998. *Report # AFRL-VA-WP-TR-1998-3060*, AFRL, WPAFB
- Gaitonde, D. & Visbal, M.R. 1999. *Paper AIAA-99-0557*, Reno, NV.
- Ghosh, S. & Matthaeus, 1992. *Phys. Fluids A*, 4(1), pp. 148.
- Ladeinde, F., O'Brien, E. E., Cai, X., & Liu, W. 1995. *Phys. Fluids*, 48 (11), pp. 2848.
- Lee, S., Lele, S.K. & Moin, P. 1997. *J. Fluid Mech.* 340, pp. 225-247.
- Lele, S.K. 1992. *J. of Computational Physics*, 103, 16-42.
- Rogerson, A.M. & Meiburg, E. *J. of Scientific Computing*, 5(2), 151-167.
- Shu, C.-W. 1997. *ICASE Report No. 97-65* (1997) 1-78.
- Shu, C.-W. 1990. *J. of Scientific Computing*, 5(2), 127-149.
- Visbal, M.R. & Gaitonde, D.V. 1998. *Paper AIAA-98-0131*, Reno, NV.

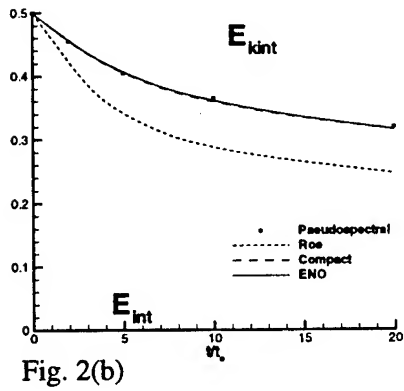
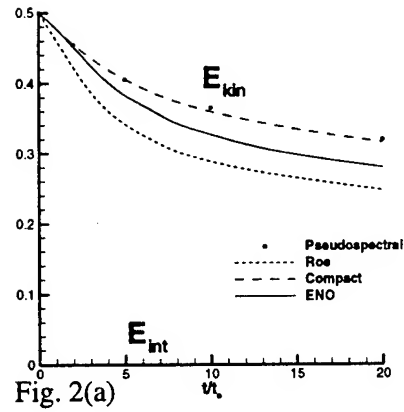
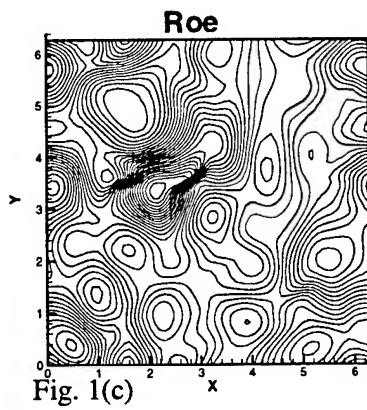
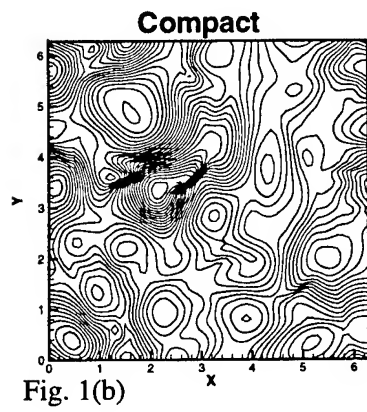
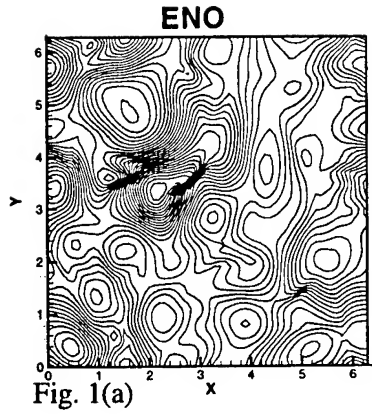


Fig. 1 Density contour maps for ENO, compact, and third-order upwind-biased schemes. $M_1=0.5$, $t/t_c=1.0$.

Fig.2 Time evolution of total kinetic energy and internal energy for $M_1=0.1$. ENO in Fig.2(a) uses adaptive stencil, in Fig.2(b) it uses centrally-biased stencil.

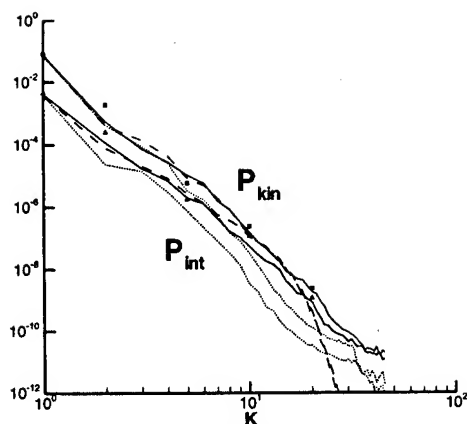


Fig. 3(a) Spectra for $M_1=0.5$. Symbols: pseudospectral; dots: Roe; dash: compact; solid line: adaptive stencil ENO. $t/t_c=20$.

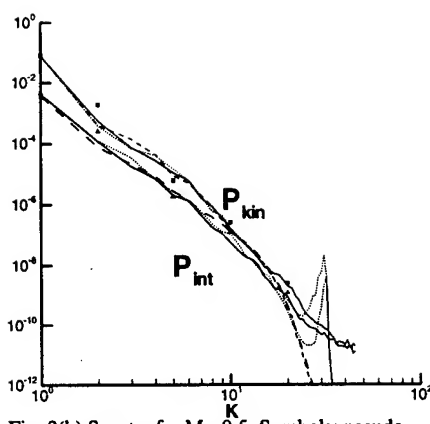


Fig. 3(b) Spectra for $M_1=0.5$. Symbols: pseudo-spectral; dots: fixed stencil ENO; dash: compact; solid line: adaptive stencil ENO. $t/t_c=20$.

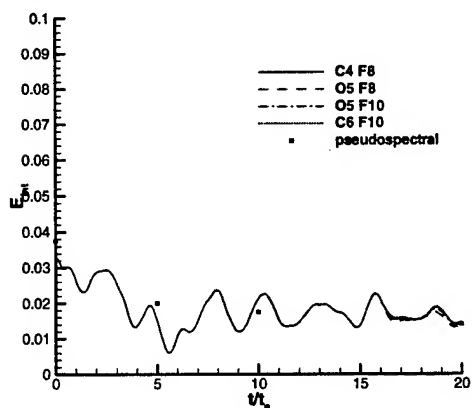


Fig. 4(a) Time evolution of internal energy for different compact and filter schemes, $M_1=0.5$.

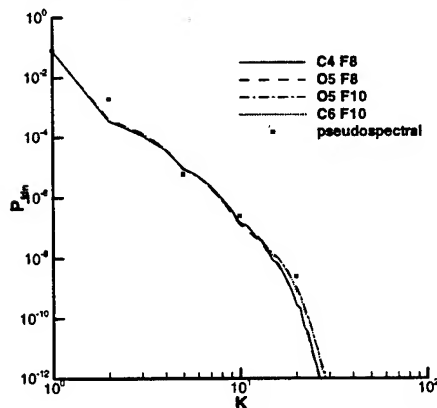


Fig. 4(b) Kinetic energy spectra for different compact and filter schemes, $M_1=0.5$, $t/t_c=20$.

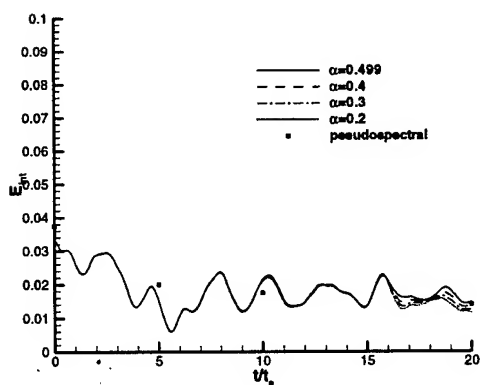


Fig. 5(a) Time evolution of kinetic energy for different filter parameter values in compact scheme, $M_1=0.5$.

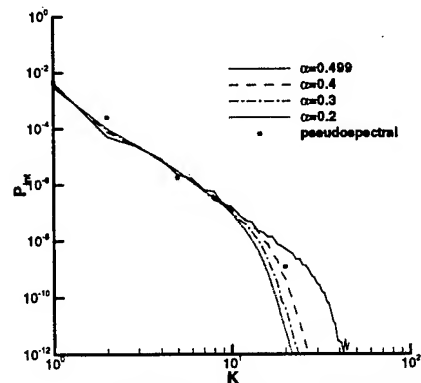


Fig. 5(b) Internal energy spectra for different filter parameter values in compact scheme, $M_1=0.5$, $t/t_c=20$.

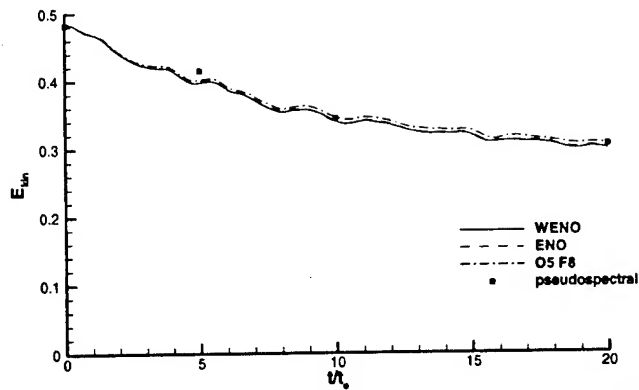


Fig. 6(a) Time evolution of total internal energy for different schemes, $M_1=0.5$.

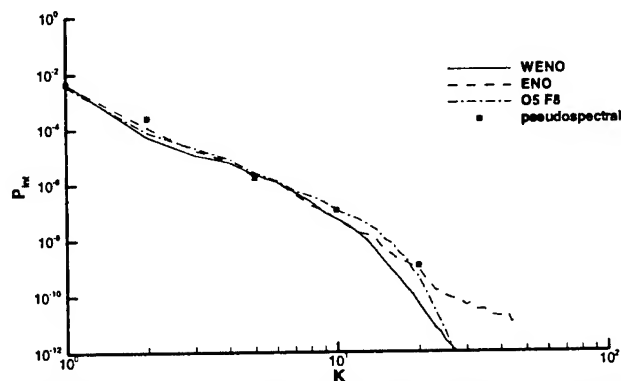


Fig. 6(b) Internal energy spectra for different schemes, $M_1=0.5$, $t/t_c=20$.

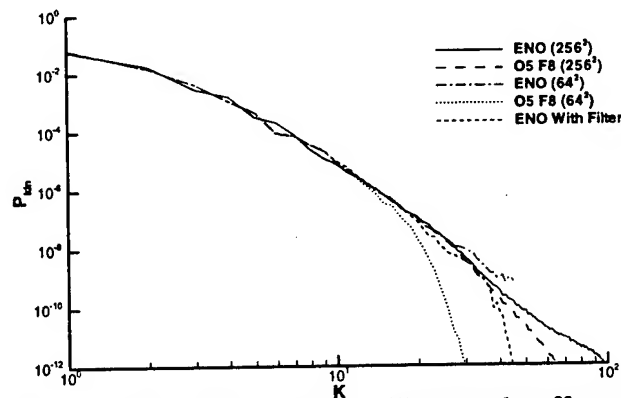


Fig. 7 Kinetic energy spectra to illustrate the effects of grid refinement, $M_1=0.5$, $t/t_c=20$.

DNS FOR FLOW PAST A 3D FLEXIBLE WING

I. LOMTEV, R.M. KIRBY AND G.E. KARNIADAKIS

Division of Applied Mathematics, Brown University

Abstract. We will present a matrix-free discontinuous Galerkin method for simulating compressible viscous flows on two- and three-dimensional moving domains. To this end, we solve the Navier-Stokes equations in an Arbitrary Lagrangian Eulerian (ALE) framework. Spatial discretization is based on standard structured and unstructured grids but using an orthogonal spectral hierarchical basis. The method is third-order accurate in time, and converges exponentially fast in space for smooth solutions. A novelty of the method is the use of a force-directed algorithm from graph theory that requires no matrix inversion to efficiently update the grid while minimizing distortions. We present several simulations using the new method, including validation using published results from a pitching airfoil, and new results for flow past a three-dimensional wing subject to large flapping insect-like motion.

1. Introduction

Despite great research efforts in designing good unstructured grids for aerodynamic flows, especially for three-dimensional simulations, most finite element and finite volume solutions depend strongly on the quality of the grid. For highly distorted grids convergence is questionable, and in most cases convergence rates are typically less than second-order. Moreover, efforts to increase the accuracy of finite volume methods to higher than second-order have not been very successful as conservativity in the formulation or monotonicity of the solution have to be compromised. These difficulties are particularly pronounced for simulations in moving computational domains involving aeroelastic motion and other flow-structure interaction problems [1],[2].

In the current work we extend the standard flux-based finite volume to high-order by employing: (1) An appropriate flux-based formulation in a new discontinuous Galerkin framework; and (2) A tensor-based spectral basis appropriate for polymorphic sub-domains. Specifically, we use a *discontinuous Galerkin* approach that allows the use of an *orthogonal* polynomial basis of different order in each element. This in turn, allows multi-domain representation with a discontinuous (i.e. globally L^2) trial basis. This discontinuous basis is orthogonal, hierarchical, and maintains a tensor-product property even for non-separable domains [3], [4]. Moreover, in the proposed method the conservativity property is maintained automatically in the element-wise sense by the discontinuous Galerkin formulation, while monotonicity is controlled by varying the order of the spectral expansion and by performing h-refinement around discontinuities.

We have followed the Arbitrary Lagrangian Eulerian (ALE) framework as in previous works, e.g. [5, 6], but with an important difference on computing the grid velocity. Specifically, we developed a modified version of the force-directed method [7] to compute the grid velocity via incomplete iteration. We then update the location of the vertices of the elements using the known grid velocity. In addition to the ALE treatment, the proposed method is new both in the formulation (e.g. construction of inviscid and viscous fluxes, use of characteristic variables, no need for limiters) as well as in the discretization as it uses *polymorphic* subdomains. We will demonstrate this flexibility in the context of simulating viscous flows that require accurate boundary layer resolution.

The paper is organized as follows: We first present the ALE discontinuous Galerkin formulation for an advection and diffusion scalar equations separately for clarity. We then present simulations of subsonic and supersonic viscous flows in stationary and moving domains.

2. Numerical Formulation

We consider the non-dimensional compressible Navier-Stokes equations, which we write in compact form in an Eulerian reference frame as

$$\bar{\mathbf{U}}_t + \nabla \cdot \mathbf{F} = Re_\infty^{-1} \nabla \cdot \mathbf{F}'' \quad \text{in } \Omega \quad (1)$$

where \mathbf{F} and \mathbf{F}'' correspond to inviscid and viscous flux contributions, respectively, and Re_∞ is the reference Reynolds number. Here the vector $\bar{\mathbf{U}} = [\rho, \rho u_1, \rho u_2, \rho u_3, \rho e]^t$ with $\mathbf{u} = (u_1, u_2, u_3)$ the local fluid velocity, ρ the fluid density, and e the total energy. Splitting the Navier-Stokes operator in this form allows for a separate treatment of the inviscid and viscous contributions, which, in general, exhibit different mathematical properties.

In the following, we will solve the Navier-Stokes equations in a time-dependent domain $\Omega(t)$ by discretizing on a grid whose points may be moving with velocity U^g , which is, in general, *different* than the local fluid velocity. This is the so-called Arbitrary Lagrangian Eulerian (or ALE) formulation which reduces to the familiar Eulerian and Lagrangian framework by setting $U^g = 0$ and $U^g = u$, respectively [8, 5]. In this context, we will review briefly the discontinuous Galerkin formulation employed in the proposed method. In the proposed formulation, no flux limiters are necessary as the entropy condition is satisfied in the L_2 -norm as has been shown theoretically in [9].

2.1. DISCONTINUOUS GALERKIN FOR ADVECTION

Using the Reynolds transport theorem we can write the Euler equations in the ALE framework following the formulation proposed in [5] as

$$\vec{U}_t + G_{i,i} = -U_i^g \vec{U}_{,i}, \quad (2)$$

where the ALE flux term is defined as

$$G_i = (u_i - U_i^g) \vec{U} + p[0, \delta_{1i}, \delta_{2i}, \delta_{3i}, u_i], \quad i = 1, 2, 3.$$

We can recover the *Euler flux* F (see equation 1) by simply setting $U^g = 0$, and in general we have that $G_i = F_i - U_i^g \vec{U}$. Now if we write the ALE Euler equations in terms of the *Euler flux* then the source term on the right-hand-side of equation (2) is eliminated and we obtain:

$$\vec{U}_t + F_{i,i} - U_i^g \vec{U}_{,i} = 0, \quad (3)$$

which can then be recasted in the standard quasi-linear form

$$\vec{U}_t + [A_i - U_i^g I] \vec{U}_{,i} = 0,$$

where $A_i = \partial F_i / \partial U$ ($i = 1, 2, 3$) is the flux Jacobian and I is the unit matrix. In this form it is straightforward to obtain the corresponding characteristic variables since the ALE Jacobian matrix can be written

$$A_i^{ALE} \equiv [A_i - U_i^g I] = R_i \cdot [\Lambda_i - U_i^g I] \cdot L_i,$$

where brackets denote matrix. Here the matrix Λ contains in the diagonal the eigenvalues of the original Euler Jacobian matrix A , and R and L are the right- and left-eigenvector matrices, respectively, containing the corresponding eigenvectors of A . Notice that the shifted eigenvalues of the ALE Jacobian matrix do not change the corresponding eigenvectors in the

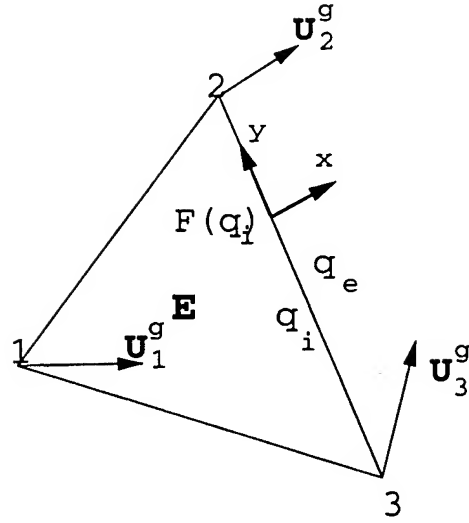


Figure 1. Notation for a triangular element.

characteristic decomposition.

To explain the discontinuous Galerkin ALE formulation we consider the two-dimensional equation for advection of a conserved scalar q in a region $\Omega(t)$

$$\frac{\partial q}{\partial t} + \nabla \cdot \mathbf{F}(q) - \mathbf{U}^g \cdot \nabla q = 0.$$

In the discontinuous Galerkin framework, we test the equation above with discontinuous test functions v separately on each element (e) (see also [10, 11]) to obtain

$$\begin{aligned} & (v, \partial_t q)_e + (v, \nabla \cdot \mathbf{F}(q))_e - (v, \mathbf{U}^g \cdot \nabla q)_e \\ & + \int_{\partial T_e} v [\tilde{f}(q_i, q_e) - \mathbf{F}(q) - (q_{up} - q_i) \cdot \mathbf{U}^g] \cdot \hat{n} ds = 0. \end{aligned} \quad (4)$$

Here (\cdot, \cdot) denotes inner product evaluated over each element, and \tilde{f} is a numerical boundary flux [10]; the notation is explained in figure 1. Notice that this form is different than the form used in the work of [12] and [13] where the time derivative is applied to the inner product, i.e.

$$\begin{aligned} & \partial_t (v, q)_e + (v, \nabla \cdot \mathbf{F}(q))_e - (v, \mathbf{U}^g \cdot \nabla q)_e - (v, q \nabla \cdot \mathbf{U}^g)_e \\ & + \int_{\partial T_e} v [\tilde{f}(q_i, q_e) - \mathbf{F}(q) - (q_{up} - q_i) \cdot \mathbf{U}^g] \cdot \hat{n} ds = 0. \end{aligned} \quad (5)$$

Note that from Reynolds transport theorem we have that

$$\partial_t \int_{\Omega(t)} d\Omega = \int_{\Omega(t)} (q_t + q \nabla \cdot \mathbf{U}^g) d\Omega,$$

where the partial time derivative on the right-hand-side is with respect to the moving ALE grid. The difference between the forms in equations 4 and 5 is that the different treatment of the time derivative introduces a term in the second case (equation (5)) that involves the divergence of the grid. While the two forms are equivalent in the continuous case, they are not necessarily equivalent in the discrete case.

To compute the boundary terms, we follow an upwind treatment based on *characteristics* similar to the work in [10], including here the term representing the grid motion. To this end, we need to linearize the ALE Jacobian *normal to the surface*, i.e. $[A - U_n^g I] = R[\Lambda - U_n^g I]L$, where U_n^g is the velocity of the grid in the *bfn* direction. The term $(q_{up} - q_i)$ expresses a jump in the variable at inflow edges of the element resulted from an upwind treatment. In the case of a system of conservation laws the numerical flux \tilde{f} is computed from an approximate Riemann solver [10].

In this formulation, the space of test functions may contain formally discontinuous functions, and thus the corresponding discrete space contains polynomials within each "element" but zero outside the element. Here the "element" is, for example, an individual triangular region T_i in the computational mesh applied to the problem. Thus, the computational domain $\Omega = \bigcup_i T_i$, and T_i, T_j overlap only on edges. In the current work, we employ a spectral polynomial basis as a trial basis which is orthogonal and has tensor-product form on triangles and quadrilaterals in two-dimensions as well as on tetrahedra, hexahedra, prisms and pyramids in three-dimensions (see [4] for details).

The diffusion part is not altered by the moving grids and we refer the reader to [14]; also details on the new grid velocity algorithm can be found in [15].

2.2. DISCONTINUOUS GALERKIN FOR DIFFUSION

The viscous contributions do not depend on the grid velocity \mathbf{U}^g , and therefore we can apply the following discontinuous Galerkin formulation. Let us consider as a model problem the parabolic equation with variable coefficient $\nu(\mathbf{x})$ to demonstrate the treatment of the viscous contributions:

$$\begin{aligned} u_t &= \nabla \cdot (\nu \nabla u) + f, \quad \text{in } \Omega, \quad u \in L^2(\Omega) \\ u &= g(\mathbf{x}, t), \quad \text{on } \partial\Omega \end{aligned}$$

We then introduce the flux variable

$$\mathbf{q} = -\nu \nabla u \quad (6)$$

with $\mathbf{q}(\mathbf{x}, t) \in \mathbf{L}^2(\Omega)$, and re-write the parabolic equation

$$u_t = -\nabla \cdot \mathbf{q} + f, \quad \text{in } \Omega$$

$$1/\nu \mathbf{q} = -\nabla u, \quad \text{in } \Omega$$

$$u = g(\mathbf{x}, t), \quad \text{on } \partial\Omega,$$

The weak formulation of the problem is then as follows:

Find $(\mathbf{q}, u) \in \mathbf{L}^2(\Omega) \times L^2(\Omega)$ such that

$$(u_t, w)_e = (\mathbf{q}, \nabla w)_e - \langle w, \mathbf{q}_b \cdot \mathbf{n} \rangle_e + (f, w)_e, \quad \forall w \in L^2(\Omega)$$

$$1/\nu(\mathbf{q}^m, \mathbf{v})_e = (u, \nabla \cdot \mathbf{v})_e - \langle u_b, \mathbf{v} \cdot \mathbf{n} \rangle_e, \quad \forall \mathbf{v} \in \mathbf{L}^2(\Omega)$$

$$u = g(\mathbf{x}, t), \quad \text{on } \partial\Omega$$

where the parentheses denote standard inner product in an element (e), as before, and the angle brackets denote boundary terms on each element, with \mathbf{n} denoting the unit outwards normal. The boundary terms contain weighted boundary values of u_b, q_b , which can be chosen as the arithmetic mean of values from the two sides of the boundary, i.e. $u_b = 0.5(u_i + u_e)$, and $q_b = 0.5(q_i + q_e)$ [16], where the subscript (i) denotes contributions evaluated at the interior side of the element boundary, and (e) on the exterior side of the element boundary (see Figure 1).

Upon integrating by parts once more, we obtain an equivalent formulation which is easier to implement, and it is actually used in the computer code. The new variational problem is

$$(u_t, w)_e = (-\nabla \cdot \mathbf{q}, w)_e - \langle w, (\mathbf{q}_b - \mathbf{q}_i) \cdot \mathbf{n} \rangle_e + (f, w)_e, \quad \forall w \in L^2(\Omega)$$

$$1/\nu(\mathbf{q}, \mathbf{v})_e = (-\nabla u, \mathbf{v})_e - \langle u_b - u_i, \mathbf{v} \cdot \mathbf{n} \rangle_e, \quad \forall \mathbf{v} \in \mathbf{L}^2(\Omega)$$

$$u = g(\mathbf{x}, t), \quad \text{in } \partial\Omega.$$

This method is element-wise conservative, a property which is particularly difficult to preserve in high-order finite elements. A similar conservative discontinuous Galerkin method for diffusion problems but using a *single* variational statement, i.e. without the introduction of the auxiliary flux variable (equation 6), has been developed by Oden et al. [17] (see also [18] and [19]). We refer the interested reader to these works and to [17] in particular for a theoretical treatment of the diffusion problem including

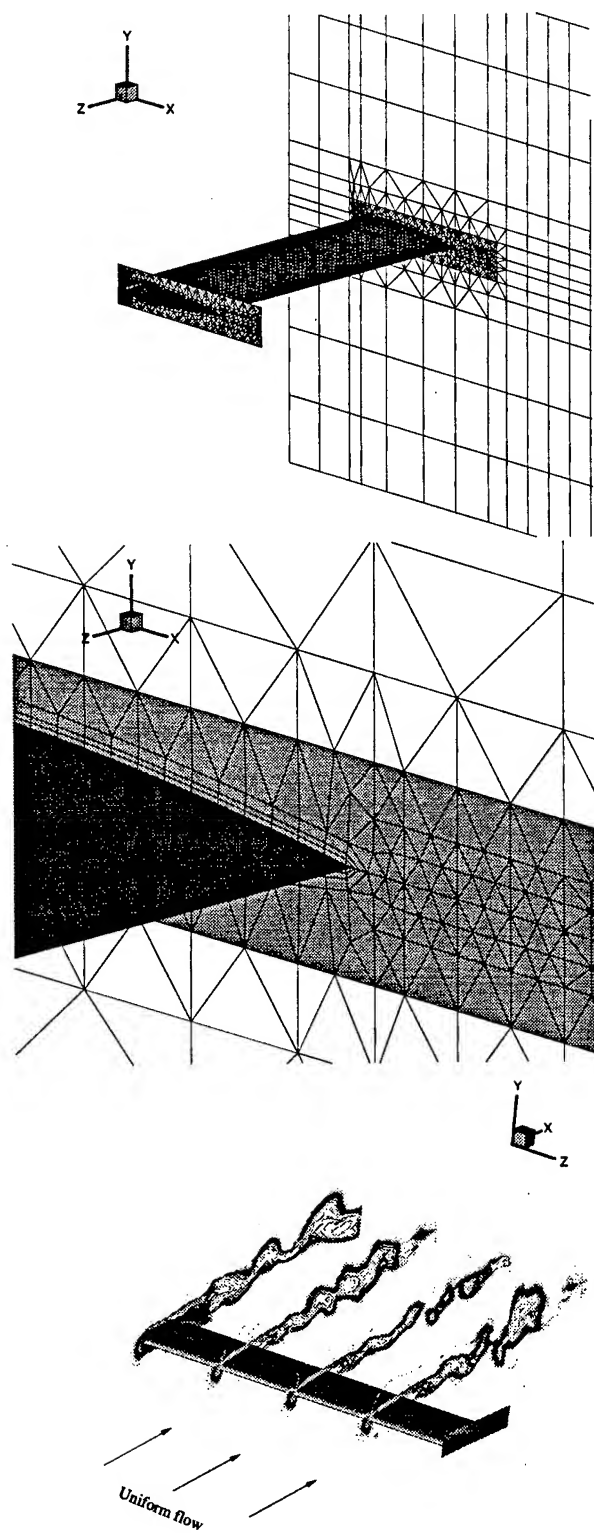


Figure 2. Skeleton mesh for flow past a three-dimensional NACA0012 airfoil with endplates (top and middle). Iso-contours for x-component of momentum for $M = 0.5$ flow past a three-dimensional NACA0012 airfoil with endplates (bottom).

a more rigorous definition of discrete spaces (the so-called broken Sobolev spaces) as well as derivation of *a priori* error estimates.

3. Subsonic Flow Simulations

We consider flow past a NACA 0012 airfoil with plates attached to each end as a simple model of a wing between an engine and fuselage. We impose uniform upwind boundary conditions at inflow and outflow, and the domain is periodic from one end of the airfoil to the other. A thin layer of hexahedra was used on the surface of the wing, and a combination of both hexahedra and prisms were used in the remainder of the computational domain. The simulation was run with up to 4th order expansion at $Re = 2000$ (based on chord length). A summary of the simulation parameters is given in table 1, and the hybrid grid and representative results are shown in 2.

Parameter	Value
Dimension	3d
Re	2000 base on chord length
Mach	0.5
Δt	1e-4
P-Range	1 to 4
K_{Prisms}	1960
K_{Hex}	2095
Method	Discontinuous Galerkin

TABLE 1. Simulation parameters for compressible flow past a NACA0012 airfoil with endplates.

At low-order the simulation ran to steady state. This is due to a reduced effective Reynolds number achieved because of numerical dissipation. As we increased the order we saw unsteadiness developing in the wake of the wing, and what appears to be oblique shedding. This is only a marginally three-dimensional domain but it does demonstrate the ability of *NekTar* to direct resolution into boundary layers and to fill out a domain with larger elements.

4. Supersonic Flow Simulations

We first show results from a 2D simulation of supersonic viscous flow around a pitching wing. In particular, we consider a NACA4420 airfoil with periodic pitching about a pivot axis at $\frac{1}{2}$ chord length. The temporal variation of the pitch is given by:

$$\begin{pmatrix} x \\ y \end{pmatrix} = \begin{pmatrix} x_c \\ y_c \end{pmatrix} + R \cdot \begin{pmatrix} \cos(\Omega(t)) \\ \sin(\Omega(t)) \end{pmatrix}.$$

The angle of attack Ω is changing according to:

$$\Omega(t) = \Omega_0 + \alpha \cdot \sin(t\omega),$$

where α is a magnitude of the pitch (we performed 2 sets of simulations with α equal to 0.1 and 0.15). ω is the frequency, its nondimensional value was taken $\frac{\pi}{3}$. The initial angle of attack Ω_0 is 20 degrees. The computational domain is shown in 3. 1582 triangular elements were used in the discretization. The pivot axis is at $x_c = 0.$, $y_c = 0.1$. The Mach number is 2, and the chord Reynolds number is 1,200.

The main objective here is to show the possibility of computing supersonic flows in moving or deforming domains without remeshing. In order to accomplish that, we used comparatively thick layer of h-refinement around the shock wave, again, $p = 0$ order polynomials were used there in order to avoid oscillation. This thick layer is needed in order to capture the shock wave which is not stationary, but is moving periodically with the pitching airfoil. The magnitude of pitching α is restricted not only by mesh deformation considerations but by the fact that the shock wave should be confined within $p = 0$ elements. If the shock wave gets in the area of high order elements, we can expect the computation to blow up. As it turned out the algorithm allowed comparatively large deformations; the simulations were stable even for $\alpha = 0.15$, which correspond to angle of attack variations from 11.4 to 28.6 degrees. Figures 4 show the position of the airfoil and density contours for those two cases.

Figure 5 shows plots of the drag and lift coefficients for the two cycles of the pitching movement. In the plot we present separately the forces due to pressure and due to viscosity. We see that the viscous forces contribute a non-negligible amount to the drag force and they decrease the lift by some amount. In figure 6 we plot total lift and drag coefficients for $\alpha = 0.15$, 0.1 pitching and for the stationary airfoil. The drag coefficient increases by almost 50% while the lift is increased by 30% when the angle of attack is maximal if compared to the stationary airfoil. Even for the stationary airfoil the drag/lift ratio is about 0.735. This is a aerodynamic stall, as

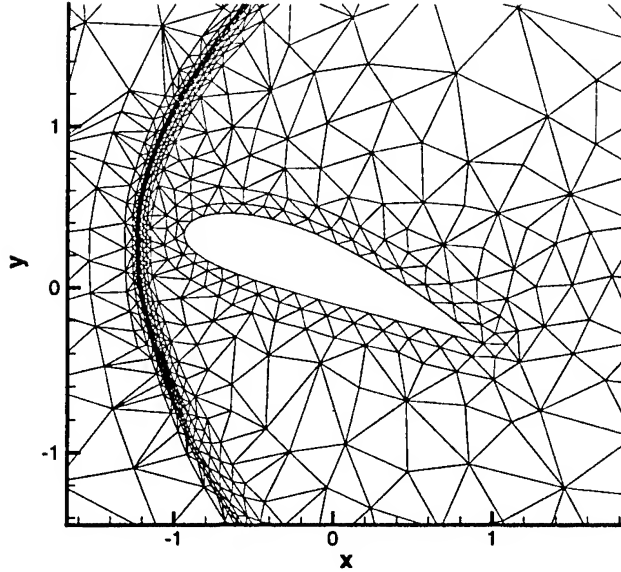


Figure 3. The computational domain for $Ma = 2$ flow around a pitching airfoil. Thick layer of $p = 0$ elements is used around the shock wave to capture its movement. High order elements are used around and in the wake of the airfoil.

there is a large area of separated flow on the upper surface near the trailing edge.

The last simulation is a supersonic 3D flow past a deforming NACA 4420 airfoil. The computational grid was obtained by 3D extrusion of the two dimensional grid used in the previous simulation. Six layers of tetrahedra have been built on the top of the mesh shown in 3, the width of each layer is 0.5, so the domain extends in z -direction from 0. to 3. As in 2D, it is Mach number 2., Reynolds number 1,200 flow. 28,476 elements have been used in this simulation. Variable order polynomials were used in this simulation: $p = 0$ (constants) at the shock wave and up to $p = 5$ around and in the wake of the airfoil. The movement of the wing was prescribed by the following formula:

$$\begin{pmatrix} x \\ y \\ z \end{pmatrix} = \begin{pmatrix} x_c \\ y_c \\ z \end{pmatrix} + R \cdot \begin{pmatrix} \cos(\Omega(t, z)) \\ \sin(\Omega(t, z)) \\ 0 \end{pmatrix}$$

where

$$\Omega(t, z) = \Omega_0 + \alpha_1 \sin(t\omega_1) + \alpha_2 \sin(t\omega_2)(1. - \sin(\pi/3z))$$

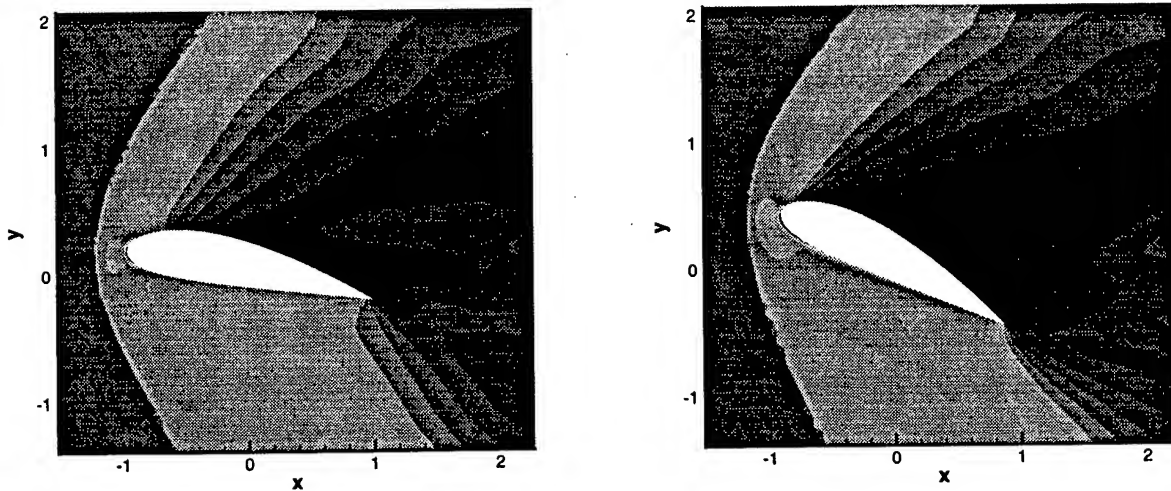


Figure 4. Mach number 2, Reynolds number 1,200 flow. Density contours. Shown on the left is the minimal angle of attack position 11.4 degrees, and on the right: 28.6 degrees.

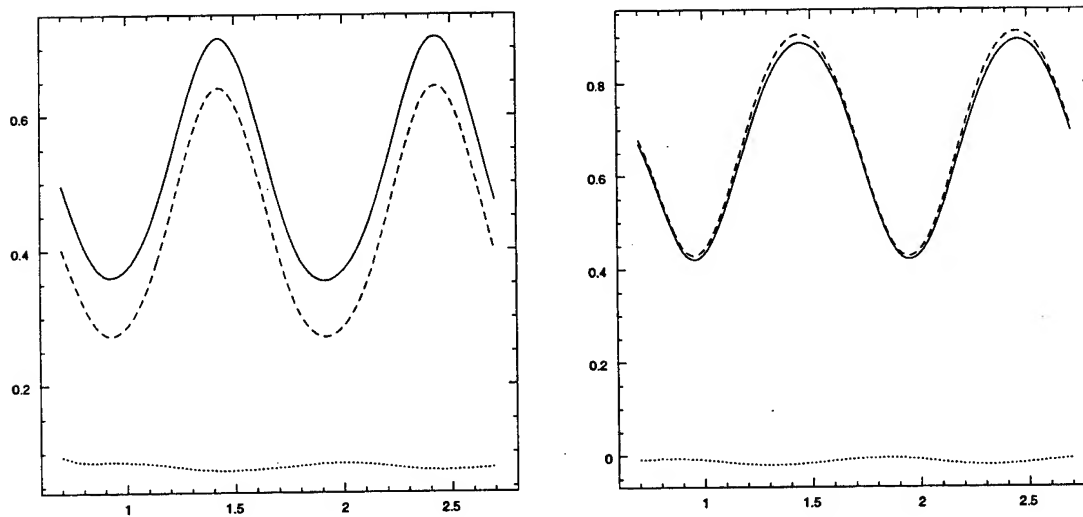


Figure 5. Drag (left) and lift (right) coefficients versus time for the supersonic pitching 2D wing. The dash line denotes contribution from pressure forces, and the dot line denotes contributions from viscous forces; the solid line is the total force.

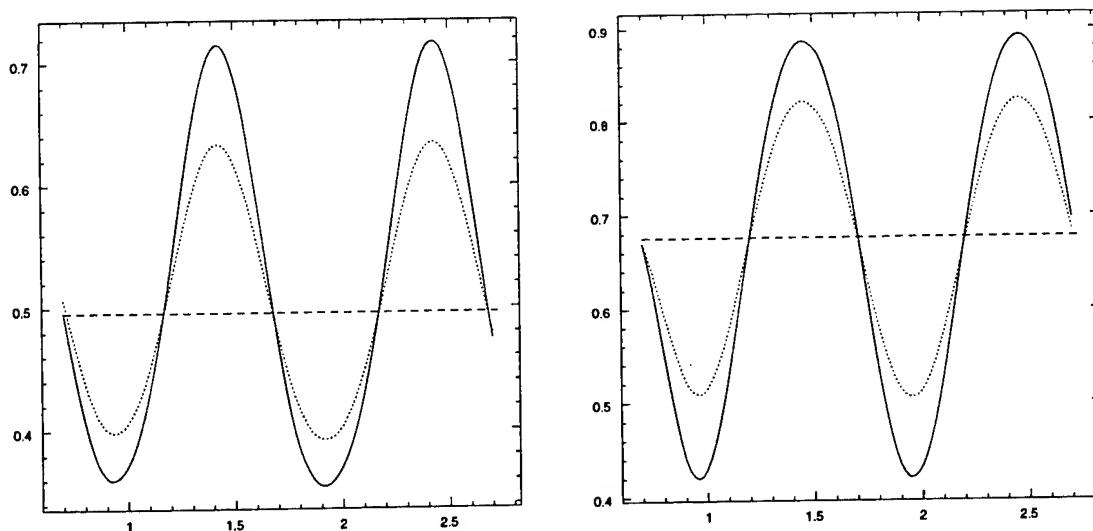


Figure 6. Drag (left) and lift (right) coefficients versus time for the 3D flapping wing. The solid line corresponds to $\alpha = 0.15$, the dot line - $\alpha = 0.1$ pitching amplitude, and the dash line denotes the stationary airfoil.

This motion combines two dimensional pitch with the deformation along the z -axis. α_1, ω_1 define the two dimensional pitch, those values have been taken equal to $0.1, \frac{\pi}{6}$. Values of α_2, ω_2 ($0.07, \frac{\pi}{3}$) are the parameters of 3D deformation. The center of rotation is the point $(x_c, y_c) = (0., 0.1)$. Figure 7 shows two snapshots of the shape of the airfoil. Figure 7 plots the isosurface of density equal to 0.5 and the shock wave that was visualized by computing the value of $\text{grad}(\rho) \cdot \vec{V}$. One can see 3D structures developing in the wake of the wing.

Finally, we conclude this section by commenting on the computational cost of the simulations. All the two-dimensional and the three-dimensional simulations were run using an MPI-based parallel version of the method presented here with the partitioning based on a multi-level graph approach provided by the METIS software [20]. Specifically, The three-dimensional supersonic simulation was run for 25,000 time steps on 32 processors of SGI O2000 at NCSA for a total of 65 CPU hours.

Acknowledgments

This work was supported by AFOSR monitored by Dr. L. Sakell, and computations were done on the IBM SP2 at CFM and NPACI, and on the SGI O 2000 at NCSA.

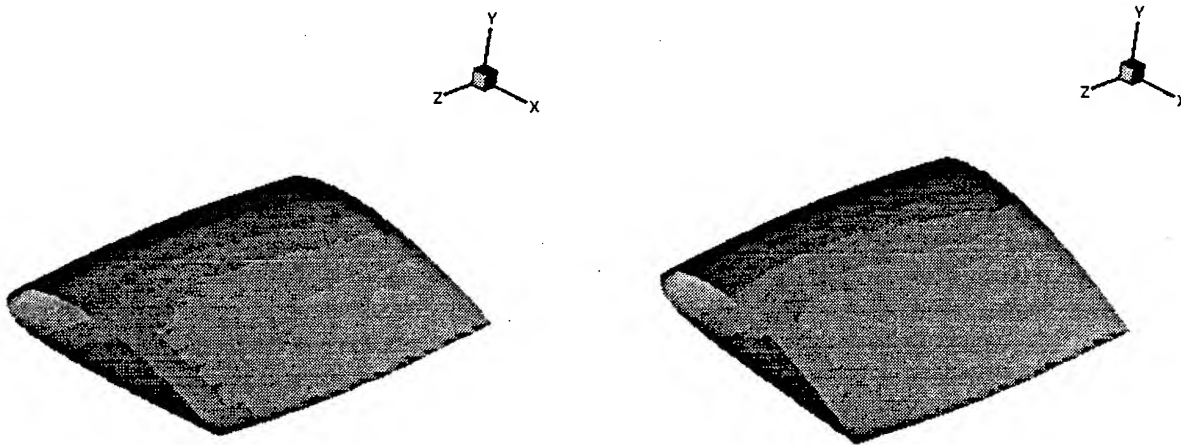


Figure 7. Deformation of the 3D NACA 4420 prismatic wing.

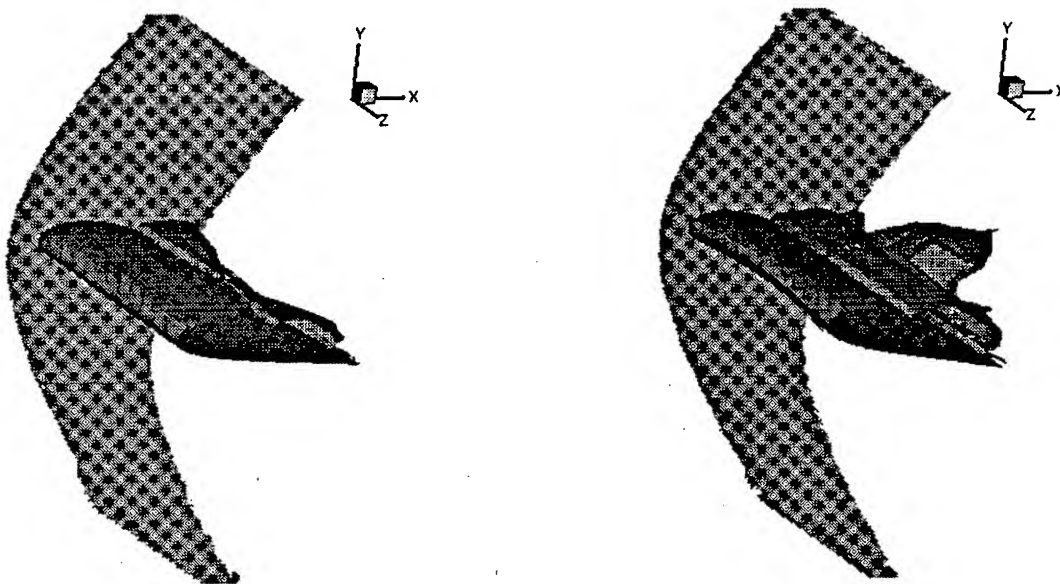


Figure 8. Shock wave and density $\rho = 0.5$ contour for the Ma 2., Re 1,200 flow past deforming wing.

References

1. C. Farhat, M. Lesoinne, and P. LeTallec. Load and motion transfer algorithms for fluid/structure interaction problems with non-matching discrete interfaces: Momentum and energy conservation, optimal discretization and application to aeroelasticity. *Comp. Meth. Appl. Mech. Eng.*, 157:95–114, 1998.
2. T. Tezduyar, M. Behr, and J. Liu. A new strategy for finite element computations involving moving boundaries and interfaces - The deforming spatial domain/space-time procedure: I. The concept and the preliminary numerical tests. *Comp. Meth. Appl. Mech. Eng.*, 94:339–351, 1992.
3. M. Dubiner. Spectral methods on triangles and other domains. *J. Sci. Comp.*, 6:345, 1991.
4. G.E. Karniadakis and S.J. Sherwin. *Spectral/hp Element Methods for CFD*. Oxford University Press, 1999.
5. C.S. Venkatasubban. A new finite element formulation for ALE Arbitrary Lagrangian Eulerian compressible fluid mechanics. *Int. J. Engng Sci.*, 33 (12):1743–1762, 1995.
6. R. Lohner and C. Yang. Improved ale mesh velocities for moving bodies. *Comm. Num. Meth. Eng. Phys.*, 12:599–608, 1996.
7. G. Di Battista, P. Eades, R. Tamassia, and I.G. Tollis. *Graph Drawing*. Prentice Hall, 1998.
8. T.J.R. Hughes, W.K. Liu., and T.K. Zimmerman. Lagrangian-Eulerian finite element formulation for incompressible viscous flows. *Comput. Methods Appl. Mech. Eng.*, 29:329, 1981.
9. G. Jiang and C.W. Shu. On a cell entropy inequality for discontinuous Galerkin methods. *Math. Comp.*, 62:531, 1994.
10. I. Lomtev, C. Quillen, and G.E. Karniadakis. Spectral/hp methods for viscous compressible flows on unstructured 2D meshes. *J. Comp. Phys.*, 144:325–357, 1998.
11. K.S. Bey, A. Patra, and J.T. Oden. hp version discontinuous Galerkin methods for hyperbolic conservation laws. *Comp. Meth. Appl. Mech. Eng.*, 133:259–286, 1996.
12. L.-W. Ho. *A Legendre spectral element method for simulation of incompressible unsteady free-surface flows*. PhD thesis, Massachusetts Institute of Technology, 1989.
13. B. Koobus and C. Farhat. Second-order schemes that satisfy GCL for flow computations on dynamic grids. In *AIAA 98-0113, 36th AIAA Aerospace Sciences Meeting and Exhibit, Reno, NV*, January 12-15, 1998.
14. I. Lomtev and G.E. Karniadakis. A discontinuous Galerkin method for the Navier-Stokes equations. *Int. J. Num. Meth. Fluids*, 29:587–603, 1999.
15. I. Lomtev, R.M. Kirby, and G.E. Karniadakis. A discontinuous Galerkin ALE method for viscous compressible flows in moving domains. *J. Comp. Phys.*, to appear, 1999.
16. I.G. Giannakouros. *Spectral element/Flux-Corrected methods for unsteady compressible viscous flows*. PhD thesis, Princeton University, Dept. of Mechanical and Aerospace Engineering, 1994.
17. J.T. Oden, I. Babuska, and C.E. Baumann. A discontinuous hp finite element method for diffusion problems. *J. Comp. Phys.*, 146:491–519, 1998.
18. C.E. Baumann and J.T. Oden. A discontinuous hp finite element method for the solution of the Euler and Navier-Stokes equations. *Int. J. Num. Meth. Fluids*, in press, special issue edited by J. Heinrich.
19. C.E. Baumann and J.T. Oden. A discontinuous hp finite element method for convection-diffusion problems. *Comp. Meth. Appl. Mech. Eng.*, in press, special issue on Spectral, Spectral Element, and hp Methods in CFD, edited by G.E. Karniadakis, M. Ainsworth and C. Bernardi.
20. G. Karypis and V. Kumar. METIS: Unstructured graph partitioning and sparse matrix ordering system version 2.0. Technical report, Department of Computer Science, University of Minnesota, Minneapolis, MN 55455, 1995.

DNS OF A MACH 4 REACTING TURBULENT BOUNDARY LAYER

M.P. MARTIN AND G.V. CANDLER

University of Minnesota

Department of Aerospace Engineering and Mechanics

Army High Performance Computing Research Center

110 Union St. SE, Minneapolis, MN 55455

Abstract. A direct numerical simulation approach is used to study a Mach 4, $Re_\theta = 8200$ turbulent boundary layer. The conditions chosen represent a 26° wedge at a Mach number of 20 and 20 km altitude. In this case, the boundary layer temperature is high enough to induce chemical reactions. It is found that endothermic reactions result in a reduction in the magnitude of the temperature fluctuations. However, when the reactions are exothermic, the temperature and the reaction rate fluctuations are enhanced.

1. Introduction

The boundary layers on proposed air-breathing hypersonic cruise vehicles will be hot, turbulent and chemically reacting. To design these hypersonic vehicles, we need a clear understanding of the physical processes that govern these flows. For this reason, we perform direct numerical simulations (DNS) of hypersonic reacting turbulent boundary layers.

Thus far, our understanding of the interaction between turbulent motion and chemical reactions in hypersonic flows is somewhat limited. With the very high energies present in hypersonic flows, the temperature fluctuations will be very large. The reaction rate depends exponentially on temperature, and temperature fluctuations result in large increases in the reaction rates. Also, the chemical source term can either damp or amplify turbulent fluctuations. Recent linear stability analysis by Johnson *et al.* (1998) has shown that hypersonic boundary layers tend to be stabilized by endothermic reactions and destabilized by exothermic reactions.

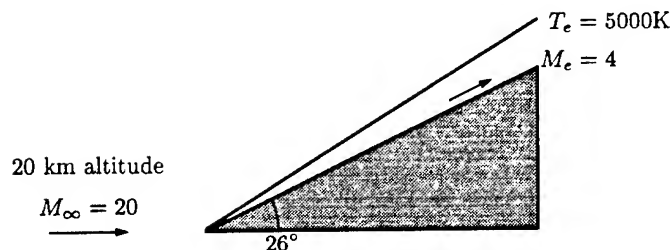


Figure 1. Flow conditions for the direct numerical simulations of boundary layers.

Martín and Candler (1998) use DNS to perform a fundamental study of isotropic turbulence interacting with finite-rate chemical reactions at conditions typical of a hypersonic boundary layer. They find that the turbulent motion is fed from the energy provided by the exothermic reactions, while the reaction rate is increased by the turbulent temperature fluctuations. This is a feedback process that takes place through the pressure-strain term in the Reynolds stress equation. The feedback is negative for endothermic reactions, resulting in a reduction in the turbulent motion.

To generalize the findings from the isotropic simulations, DNS of turbulent reacting boundary layers are presented. The conditions chosen are $Re_\theta = 8200$, $M_\infty = 4.0$, $T_\infty = 5000$ K, and $\rho_\infty = 0.5$ kg/m³. These conditions represent a 26° wedge at a Mach number of 20 and 20 km altitude and are illustrated in Fig. 1. In this case, the boundary layer temperature is high enough to induce chemical reactions. We use a single model reaction, $S1 + M \rightleftharpoons S2 + M$, where species S1 and S2 have the same molecular weight, that of diatomic nitrogen, M_{N_2} . The dissociation reaction rate corresponds to a nitrogen dissociation reaction.

The remainder of the paper is organized as follows. We first discuss the numerical method and initial condition for the simulations. We describe results for the non-reacting turbulent boundary layer. Finally, we compare the non-reacting, endothermic, and exothermic simulation results.

2. Numerical method and initial conditions

The numerical method combines an ENO scheme for the inviscid fluxes with an implicit time advancement technique. The ENO scheme was designed for low dissipation by Weirs *et al.* (1997) and provides shock-capturing, which is necessary at the Mach numbers considered. The time advancement technique is based on the DPLU relaxation method of Candler *et al.* (1994) and was extended to second-order accuracy by Olejniczak and Candler (1997). The derivatives required for the viscous terms are evaluated using 4th-order central differences.

The implementation of the numerical scheme has been successfully validated in Martín *et al.* (1998) by performing a DNS of a non-reacting turbulent boundary layer at $Re_\theta = 740$, $M = 0.3$, $T_w = T_\infty = 300$ K, and $\rho_\infty = 1$ kg/m³, and by comparing the results to experimental data.

The initial conditions chosen for the supersonic boundary layer simulations are $Re_\theta = 7000$, $M_\infty = 4.0$, $T_\infty = 5000$ K, and $\rho_\infty = 0.5$ kg/m³. The size of the domain in both homogeneous directions needs to be long enough to enclose a good statistical sample of the large structures. It is found that the lengths of 4δ , and 2δ in the streamwise and spanwise directions, respectively, are adequate. In the wall-normal direction, the length of the domain is determined so that acoustic disturbances originating in the upper boundary do not interact with the boundary layer on the lower wall. The x , y , and z coordinates correspond to the streamwise, spanwise, and wall-normal directions, respectively. The number of grid points is $192 \times 128 \times 128$. The resolution for this grid is $15\Delta x^+ \times 11\Delta y^+$ in the homogeneous directions. The grid is stretched in the wall-normal direction and the grid-stretching factor is 1.069. The first point away from the wall is located at $z^+ = 0.13$, and there are 28 grid points below $z^+ = 10$.

The boundary condition in the streamwise direction is periodic. Thus, the outflow conditions are used as in flow conditions and the boundary layer is allowed to grow in time as the simulation progresses. Low speed simulations with these type of boundary conditions are jeopardized, since the amount of kinetic energy at the boundary layer edge may not be sufficient to maintain the turbulence levels in the boundary layer. However, this is not an issue in the present simulations, since the kinetic energy at the boundary layer edge is substantial. The boundary condition in the spanwise direction is periodic, and the boundary condition at the boundary layer edge is supersonic.

The initialization of compressible turbulence is the art of making an educated guess. In the following simulations, the mean velocity, density, and temperature turbulent profiles, and the inner parameters, u_τ and z_τ , at desired Mach number are obtained from a $k - \epsilon$ Reynolds-averaged Navier-Stokes simulation (Jones and Launder, 1992). The fluctuating velocity fields are obtained by normalizing the Mach 0.3 velocity fluctuations (Martín *et al.*, 1998) by the ratio of the inner parameters at the high Mach number to that at $M = 0.3$. In this way, the initial fluctuating fields are scaled in proportion to the Mach number, and the initial turbulence structures and energy spectra resemble those of a realistic turbulent boundary layer. The initial fluctuations in the thermodynamic variables are estimated using the strong Reynolds analogy (Morkovin, 1962).

The chemical reactions are turned on after the boundary layer simulation reaches a stationary state based on a constant distribution of the turbulent kinetic energy scaled on inner variables. The binary reaction

$S1 + M \rightleftharpoons S2 + M$ is used, and both species have the same molecular weight, M_{N_2} , and internal degrees of freedom, so that the gas constant and specific heat do not change during the simulation. The species mass fractions are initialized to their equilibrium values at the mean temperature and density. Although the chemical composition in typical hypersonic boundary layers is not in equilibrium, this initialization serves to isolate the effect of turbulent fluctuations in the turbulence-chemistry interaction. For the conditions chosen, the reaction is endothermic. To achieve exothermicity for the purpose of comparison, we change the sign of the heat of formation.

3. Non-reacting simulations

After initializing the flow, the turbulent kinetic energy is found to be out of equilibrium. The non-reacting adiabatic boundary layer simulation reaches a stationary state near $t/\tau_\Lambda = 12$, where t is the time and $\tau_\Lambda = \delta/U_\infty$. The Reynolds number increases during the simulation, the results are shown for $t/\tau_\Lambda = 12$, and $Re_\theta = 8200$.

Figure 2 plots the two-point correlations, showing that the turbulent structures are not correlated in the middle of the box. Thus, the size of the box remains large enough to perform a DNS at the conditions chosen. Figure 3 plots the energy spectra for various quantities in the logarithmic region, $z^+ = 110$, and in the viscous sublayer, $z^+ = 4.25$. The Reynolds number for the simulation is large enough so that the energy spectra develop an inertial range. Furthermore, there are about 4 decades of decay, showing that the turbulence is well resolved.

Figure 4 plots the mean velocity profile scaled on the inner variables. The data agree with the theoretical values in the viscous region. However, the data fail to match the empirical law in the logarithmic region. Recent experimental data (Konrad and Smits, 1998) show that a Mach 3 adiabatic boundary layer matches the Van-Driest law in the logarithmic region. Note that the adiabatic wall temperature increases by 47% in going from $M = 3$ to $M = 4$. Also, the temperatures in the DNS are much higher than those in the experiment because the experiment was conducted with a cold free-stream (total temperature of approximately 265 K). It is uncertain whether there is an edge temperature effect that modifies the scaling of the law of the wall.

Figure 5 plots the temperature contours along planes perpendicular to the flow direction. Since the wall temperature is very high, the bursting events are clearly seen as the hot fluid from the near-wall region mixes into the cold fluid above. We observe the typical mushroom-shaped structures associated with turbulent boundary layers. However, these structures are

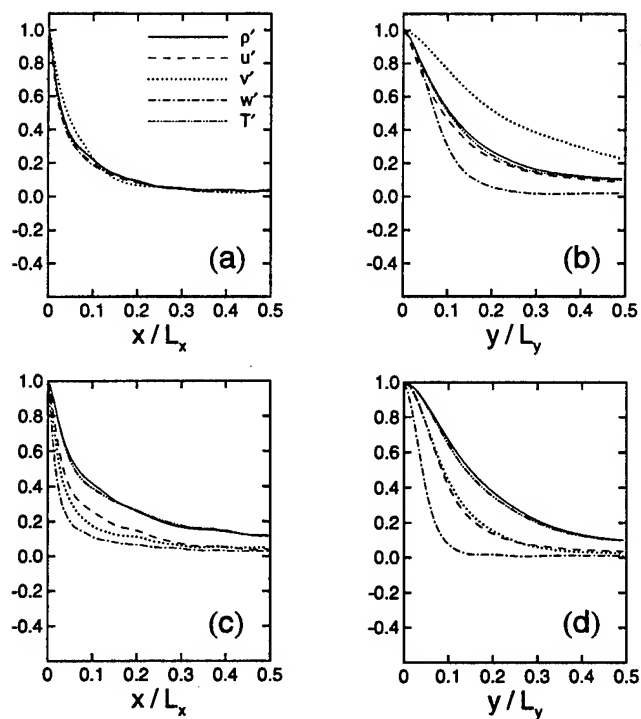


Figure 2. Two-point correlations for the non-reacting simulation, (a)-(b) $z^+ = 110$, and (c)-(d) $z^+ = 4.25$.

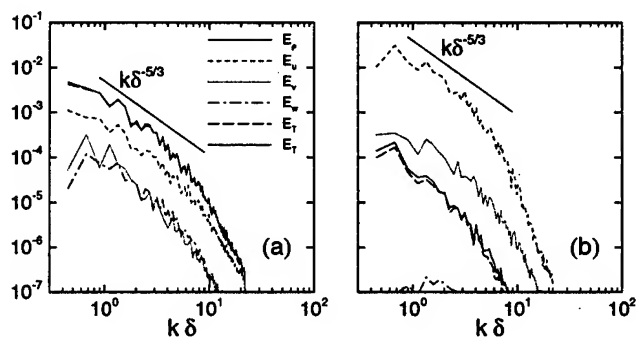


Figure 3. Two-dimensional energy spectra at (a) $z^+ = 110$, and (b) $z^+ = 4.25$, for the non-reacting simulation.

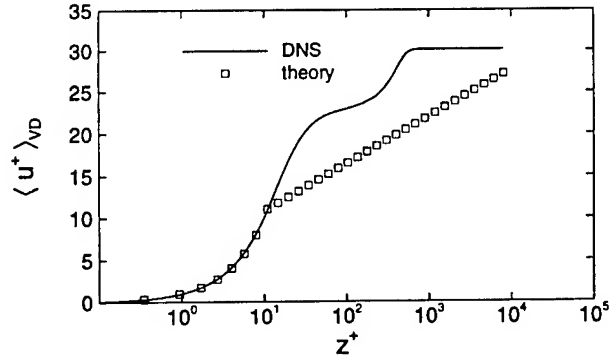


Figure 4. Mean velocity profile scaled on inner variables, and compared to the theoretical $u^+ = z^+$, and Van-Driest empirical $u^+ = 2.44 \log z^+ + 5.2$ scaling laws for non-reacting simulation.

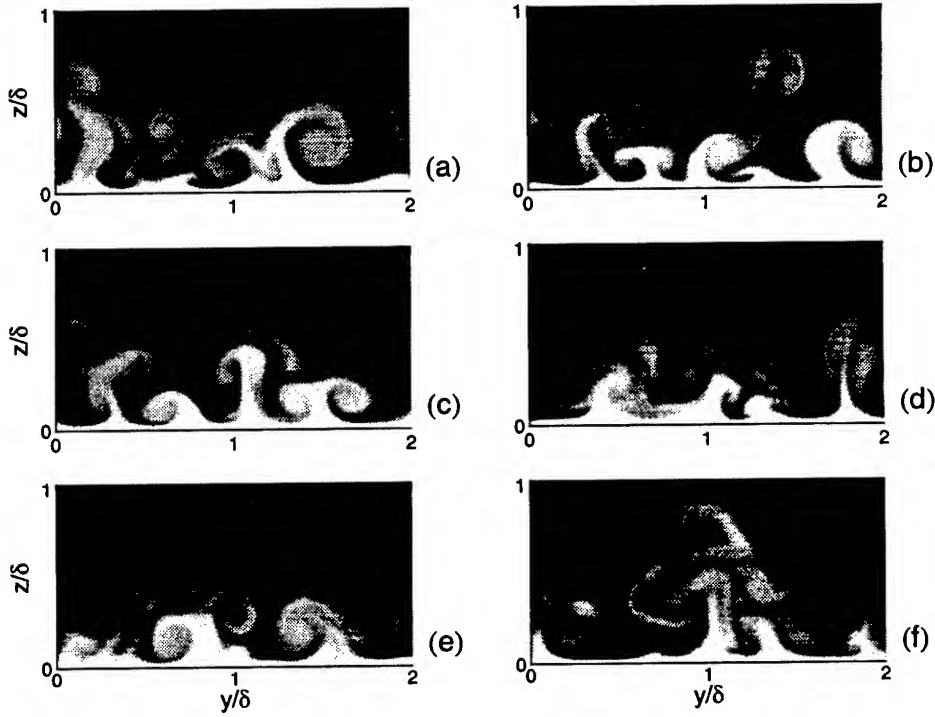


Figure 5. Temperature contours along the spanwise direction for the non-reacting simulation, (a) $x = \delta/8$, (b) $x = \delta/4$, (c) $x = 3\delta/8$, (d) $x = \delta/2$, (e) $x = \delta$, and (f) $x = 3\delta/2$. For a color version visit our web site at www.arc.umn.edu/martin/research.html.

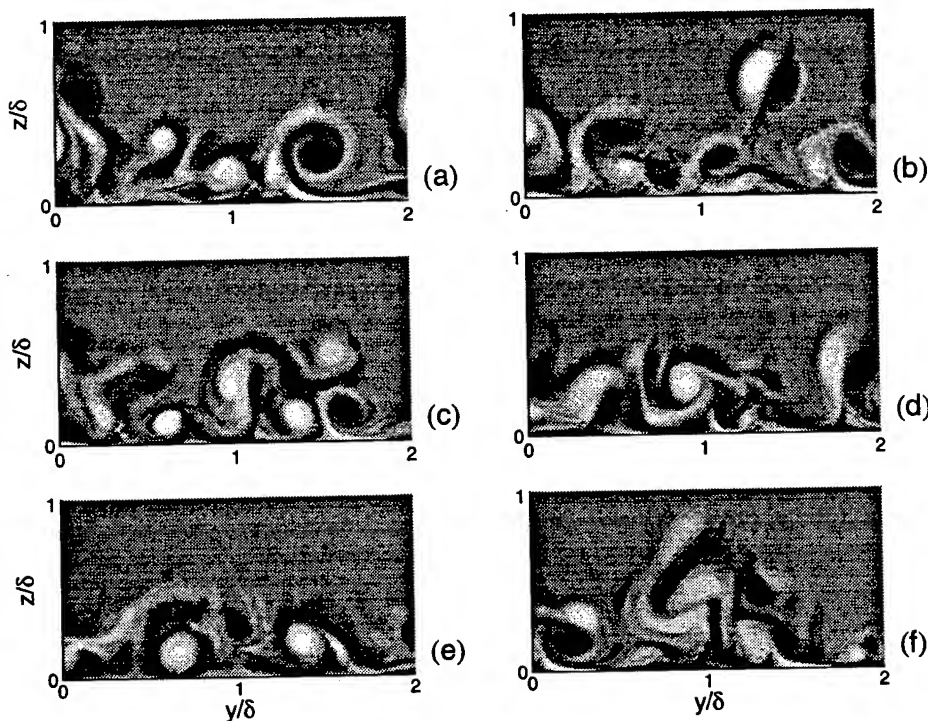


Figure 6. Streamwise vorticity contours along the spanwise direction for the non-reacting simulation. (a) $x = \delta/8$, (b) $x = \delta/4$, (c) $x = 3\delta/8$, (d) $x = \delta/2$, (e) $x = \delta$, and (f) $x = 3\delta/2$.

significantly larger than previously observed in experiments with lower compressibility levels and temperature fields.

Figure 6 plots the streamwise component of vorticity along the spanwise direction. We observe that the eddy structures are composed of counter-rotating vortices that enhance mixing. Although these structures comprise large portions of the boundary layer, it is found that they dissipate in less than 70 wall units in the streamwise direction.

4. Reacting simulations

As a preliminary analysis of the turbulent-chemistry interaction in the boundary layer, the reacting adiabatic simulation is considered. Under the temperature conditions chosen, the reaction $S1 + M \rightleftharpoons S2 + M$ is endothermic across the boundary layer. To achieve exothermic reactions, the sign of the heat of formation is changed. In this section, the non-reacting, endothermic, and exothermic simulations for the adiabatic boundary layer are compared.

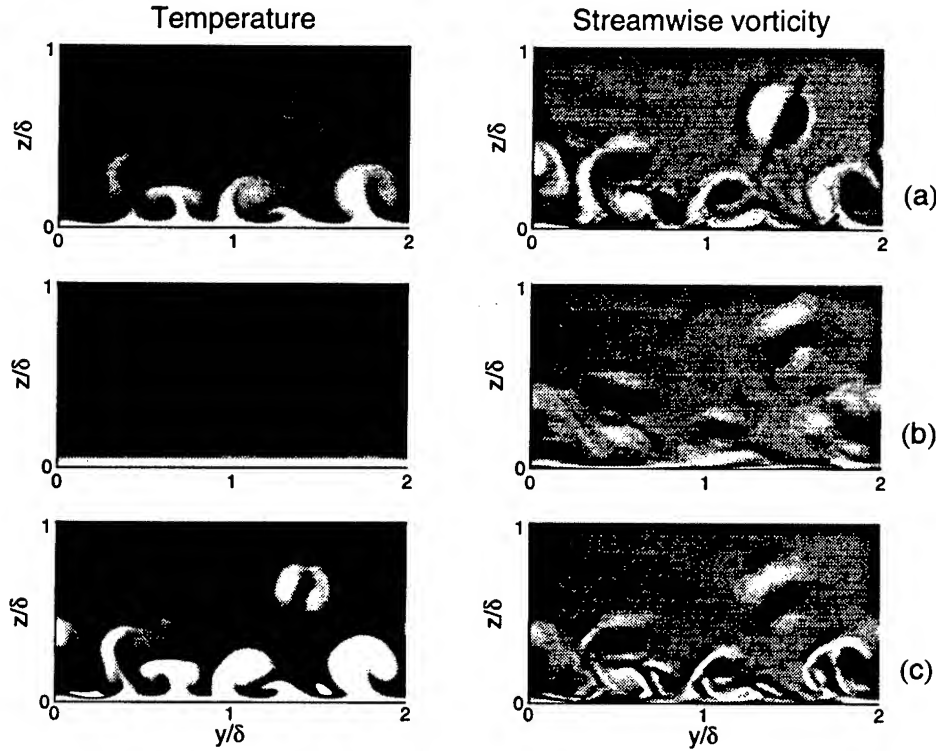


Figure 7. Temperature (left) and streamwise vorticity (right) contours along the spanwise direction for the (a) non-reacting, (b) endothermic, and (c) exothermic simulations, $x = \delta/4$.

Figure 7 plots temperature contours along the spanwise direction. We observe that for the endothermic simulation, the vortical structures are annihilated. Thus, the temperature increases continuously from the boundary layer edge to the wall. In contrast, for the exothermic simulation, the temperature at the core of the mushroom-shaped structures increases. Thus, the exothermic reactions occur locally, and in regions of the flow where the temperature is highest. Figure 7 also plots the streamwise vorticity along the spanwise direction for the same simulations. For the endothermic simulation, the magnitude of vorticity decreases. However, for the exothermic simulation, the vorticity magnitude increases at the cores of the vortex pairs. The localized addition of energy causes compressions and expansions that flatten and elongate the cores of the vortex pairs.

Figure 8 plots the product mass-fraction contours for the reacting simulations. For the endothermic simulation, the chemical composition does not differ significantly from the initial condition. In contrast, for the exother-

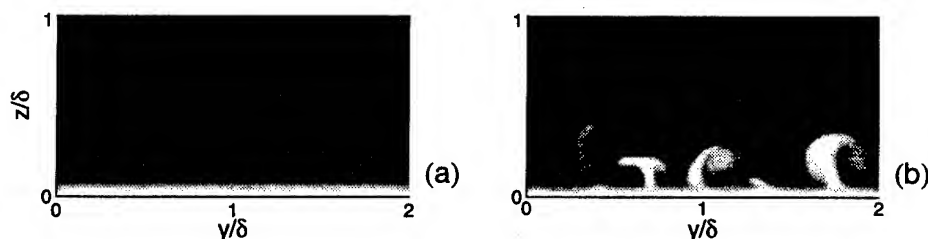


Figure 8. Product mass-fraction contours along the spanwise direction for the (a) endothermic, and (b) exothermic simulations, $x = \delta/4$.

mic simulation, the product mass fraction increases in regions where the magnitude of the temperature fluctuations is high.

Figure 9 plots the magnitude of the temperature fluctuations for the three simulations. We observe that the magnitude decreases when the reactions are endothermic. In contrast, when the reaction is exothermic, the magnitude increases up to 110% of the average temperature. Finally, Fig. 10 plots the mass fraction of species S2 normal to the surface. The solid line represents the initial mass fraction. For the endothermic simulation, there is very little activity in the production or destruction of S2. However, there is significant production for the exothermic simulation.

5. Summary

The initialization and resolution requirements for a Mach 4, $Re_\theta = 8200$ boundary layer have been presented. It is found that the domain size and grid resolution are adequate to perform the direct numerical simulations. The preliminary results for an adiabatic boundary layer have been discussed.

For the non-reacting simulation, it is found that the turbulent mixing of hot and cold fluid is substantial. This process generates large mushroom-shaped structures that comprise large portions of the boundary layer. The cores of these structures are composed of counter-rotating vortex pairs. It is found that these structures observed in the spanwise planes dissipate quickly in the streamwise direction. A possible explanation for this is the increase in dissipation due to the presence of shocks. However, a careful shock detection study has not been performed yet. The mean velocity with Van-Driest transformation given by the DNS and the empirical prediction were not in agreement. For the conditions chosen, the adiabatic wall temperature was nearly 18500 K. It is not clear whether the significantly higher adiabatic wall temperature simulation should reproduce the theoretical results, which are predicted for much lower temperature fields. Further analy-

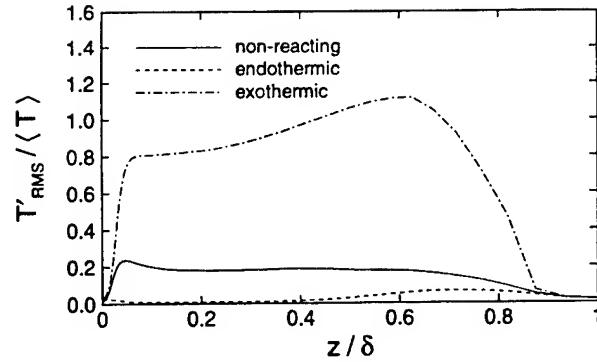


Figure 9. Normalized magnitude of the temperature fluctuations for the non-reacting, endothermic, and exothermic simulations.

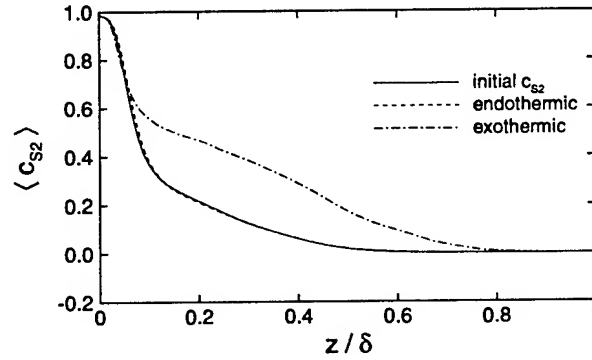


Figure 10. Mass fraction of S2 species for the endothermic and exothermic simulations.

sis is required to assess whether there is an edge temperature effect that may explain the stronger mixing and modified mean velocity profile that are predicted by the DNS.

For the endothermic reacting simulations, the energy removed by the reaction results in annihilation of the vortical structures in the temperature field and weakening of the vortex dipoles. In contrast, the heat released by the exothermic reaction increases the strength of the vortices. The energy release induces localized expansions and compressions that elongate the cores of the vortex pairs.

As in the case of the reacting isotropic turbulence (Martín and Candler, 1998), it is found that the exothermic reactions increase the magnitude of the temperature fluctuations, while the reaction rate is increased by the

turbulent temperature fluctuations. The opposite occurs when the reaction is endothermic.

Acknowledgments

We would like to acknowledge the support from the Air Force Office of Scientific Research Grant number No. AF/F49620-98-1-0035. This work was also sponsored by the Army High Performance Computing Research Center under the auspices of the Department of the Army, Army Research Laboratory cooperative agreement number DAAH04-95-2-0003 / contract number DAAH04-95-C-0008, the content of which does not necessarily reflect the position or the policy of the government, and no official endorsement should be inferred. A portion of the computer time was provided by the University of Minnesota Supercomputing Institute.

References

- Candler, G.V., Wright, W.J., and McDonald, J.D. (1994) Data-Parallel Lower-Upper Relaxation method for reacting flows, *AIAA Journal*, **32**, pp. 2380-86.
- Johnson, H., Seipp, T., & Candler, G.V. (1998) Numerical study of hypersonic reacting boundary layer transition on cones. *Physics of Fluids*, **10**, pp. 2676-85.
- Jones, W.P., and Launder, B.E. (1992) The prediction of laminarization with a two-equation model of turbulence, *International Journal of Heat and Mass Transfer*, **15**, pp. 301-14.
- Konrad, W., and Smits, A.J. (1998) Turbulence measurement in a three-dimensional boundary layer in supersonic flow, *Journal of Fluid Mechanics*, **372**, pp. 1-23.
- Martín, M.P., and Candler, G.V. (1998) Effect of Chemical reactions on decaying isotropic turbulence. *Physics of Fluids*, **10**, pp. 1715-24.
- Martín, M.P., Olejniczak, D.J., Weirs, V.G., and Candler, G.V. (1998) DNS of reacting hypersonic turbulent boundary layers, *AIAA Paper No. 98-2917*.
- Morkovin, M.V. (1962) Effects of compressibility on turbulent flows, A.J. (ed) of *Mécanique de la Turbulence*, pp. 367-80, CNRS.
- Olejniczak, D.J., and Candler, G.V. (1997) A Data-Parallel LU relaxation method for DNS of compressible flows, *Proceedings of the First AFOSR International Conference on DNS and LES*, Ruston, LA, Paper No. N-03, Aug. 1997.
- Weirs, V.G., and Candler, G.V. (1997) Optimization of weighted ENO schemes for DNS of compressible turbulence, *AIAA Paper No. 97-1940*.

ACCOUNTING FOR SCALE-DEPENDENCE IN THE DYNAMIC SMAGORINSKY MODEL

CHARLES MENEVEAU

*Department of Mechanical Engineering
Johns Hopkins University, Baltimore MD 21218*

AND

FERNANDO PORTÉ-AGEL AND MARC B. PARLANGE

*Department of Geography and Environmental Engineering
Johns Hopkins University, Baltimore MD 21218*

Abstract.

The dynamic model has been very successful in Large-Eddy Simulation of a variety of turbulent flows. The model makes the crucial assumption that the coefficient is scale-invariant, which is reasonable in the inertial range of turbulence. Surprisingly, the dynamic model's success has occurred even in flows where the grid-scale is not in an ideal inertial range. It turns out that the most well-known successful applications (such as transitional flows, the viscous sublayer, etc..) are those where the true SGS stress is only a small contribution to the dynamics, and where the errors induced by the deviations from scale-invariance are of minor consequence. However, there are important flows in which the errors can have large effects, such as in LES of wall-bounded flows that do not resolve the viscous sublayer. Near the wall, the grid-scale is on the order of the local integral scale (the distance to the wall) and the SGS shear stress contributes significantly to the mean momentum balance. In this paper we show that the traditional dynamic model yields coefficients that are too small, which translates into high wavenumber pile-up of the longitudinal energy spectra near the wall. In order to correct for this problem in a dynamic fashion, a new scale-dependent dynamic model is proposed. It involves a secondary test-filter operation that allows one to probe from the simulated resolved field how the coefficient depends on scale. Applications to LES of a wall-bounded flow that does not resolve the viscous sublayer are presented, showing much improved longitudinal energy spectra and better mean velocity profiles.

1. Introduction

The dynamic model (Germano *et al.*, 1991) has had a significant impact in improving the accuracy of LES of turbulent flows in a number of geometries and flow conditions. In principle, the dynamic model allows us to circumvent the need for a-priori specification and consequent tuning of the coefficient because it is evaluated directly from the resolved scales in an LES (see Meneveau & Katz, 2000, for a review on the use of scale-invariance based turbulence models in LES).

However, the traditional dynamic model makes the crucial assumption that the coefficient does not depend on scale. While this is a reasonable assumption if the filter scale Δ pertains to an idealized inertial range of turbulence, it is not expected to hold if Δ falls near a transition scale (denoted below by Δ_t) where more complicated physics may occur. For instance, in certain flow regions the grid scale may approach the integral scale of turbulence, ℓ . This limit is of considerable relevance for applications in which LES approaches the Reynolds-averaged Navier-Stokes (RANS) formulation, sometimes called VLES. In particular, it can be important in LES of wall-bounded flows, where in general the integral scale is on the order of the distance to the wall, z . If the simulation does not resolve the viscous sublayer, the first few cells near the wall have a grid-scale on the order of the local integral scale. Thus, at a scale $\Delta \sim z$ one expects a transition behavior. When LES approaches direct numerical simulation (DNS), the model coefficient decreases when the grid-scale approaches the Kolmogorov scale η , i.e. the transition occurs near $\Delta_t \sim \eta$ (Voke, 1996; Meneveau & Lund, 1997). In each one of these applications, possible scale-dependencies of the model coefficient near Δ_t occur which violate the central assumption of the dynamic model. Further, one does not necessarily know a-priori how the coefficient changes with scale, e.g. whether it decreases or increases with decreasing scale.

In this work, we present a generalization of the dynamic model that relaxes the assumption of strict scale invariance. Briefly, the methodology is based on introducing a secondary test filter that, in addition to the traditional test filter, is used to determine both the coefficient *and* how it changes across scales. It thus allows applying the dynamic model to cases where the model coefficient changes with scale. This is the case in large-eddy simulation of very high-Reynolds number boundary layers such as the atmospheric boundary layer. The scale-dependent model is tested in such simulations, and the results are compared with those from (a) the traditional Smagorinsky model that requires specification of the coefficient and of parameters for a wall damping function, and (b) the traditional dynamic model that assumes scale invariance of the coefficient.

2. Smagorinsky and standard dynamic model

The traditional Smagorinsky model (Smagorinsky, 1963) for the deviatoric part of the subgrid-scale stress reads

$$\tau_{ij} - \frac{1}{3} \tau_{kk} \delta_{ij} = -2 \nu_T \tilde{S}_{ij}, \quad (1)$$

where $\tilde{S}_{ij} = \frac{1}{2} (\partial \tilde{u}_i / \partial x_j + \partial \tilde{u}_j / \partial x_i)$ is the resolved strain rate tensor and ν_T is the eddy viscosity given by $\nu_T = (C_s^\Delta \Delta)^2 |\tilde{S}|$. Here $|\tilde{S}| = 2 (\tilde{S}_{ij} \tilde{S}_{ij})^{\frac{1}{2}}$ is the magnitude of the resolved strain-rate tensor, Δ is the filter width, and C_s^Δ is the Smagorinsky coefficient (a non-dimensional parameter). For isotropic turbulence with a cutoff scale Δ in the inertial subrange, Lilly (1967) determined that $C_s \approx 0.17$, independent of Δ . However, it is well-known that this value is not universal. In non-turbulent regions it should vanish (Piomelli & Zang, 1991), and in the presence of mean shear it should be lower (Moin & Kim 1982). The dynamic model (Germano *et al.* 1991) avoids, in principle, the need for a-priori specification and consequent tuning of the coefficient because it is evaluated directly from the resolved scales during an LES. The approach is based on the Germano identity

$$L_{ij} \equiv \overline{\tilde{u}_i \tilde{u}_j} - \tilde{u}_i \tilde{u}_j = T_{ij} - \tau_{ij}, \quad (2)$$

where $T_{ij} = \overline{\tilde{u}_i \tilde{u}_j} - \tilde{u}_i \tilde{u}_j$ is the stress at a test-filter scale (typically 2Δ). For the Smagorinsky model applied at scale 2Δ we may write

$$T_{ij} - \frac{1}{3} T_{kk} \delta_{ij} = -2 (C_s^{2\Delta} 2\Delta)^2 |\tilde{S}| \tilde{S}_{ij}. \quad (3)$$

Substitution of Eqs. 1 and 3 into 2, in addition to the crucial assumption of scale invariance

$$C_s^{2\Delta} = C_s^\Delta \equiv C_s, \quad (4)$$

leads to the system

$$L_{ij} - \frac{1}{3} \delta_{ij} L_{kk} = C_s^2 M_{ij}, \quad \text{where} \quad (5)$$

$$M_{ij} = 2\Delta^2 (\overline{|\tilde{S}| \tilde{S}_{ij}} - 4|\tilde{S}| \tilde{S}_{ij}). \quad (6)$$

(It has also been assumed that the coefficient can be extracted from the test-filtering operation, Ghosal *et al.*, 1995). Minimizing the error $\langle (L_{ij} - C_s^2 M_{ij})^2 \rangle$ (Lilly 1992), where the averaging is over directions of statistical homogeneity (Ghosal *et al.* 1995) or fluid pathlines (Meneveau *et al.* 1996), results in

$$C_s^2 = \frac{\langle L_{ij} M_{ij} \rangle}{\langle M_{ij} M_{ij} \rangle}. \quad (7)$$

However, as anticipated in section 1, there are situations in which the assumption of scale-invariance (Eq. 4) may not hold, such as in high-Reynolds number LES of wall-bounded flows in which the viscous sublayer is not resolved. To illustrate the difficulties encountered we begin with an implementation of the traditional Smagorinsky and the standard dynamic models in the simulation of a rough-wall, pressure-driven channel flow which does not resolve the viscous sublayer.

3. Simulations with traditional models

LES of a rough-wall, pressure-driven channel flow is performed, using the traditional Smagorinsky and standard dynamic Smagorinsky model.

3.1. NUMERICAL PROCEDURE

A modified version of the LES code described in Albertson & Parlange (1999) is used. The code solves the filtered Navier-Stokes equations for incompressible flow, driven by a constant pressure gradient in the streamwise direction. The convective term is written in rotational form, and the gradient of resolved kinetic energy is included in the pressure gradient. Horizontal directions are discretised pseudo-spectrally, while wall-normal derivatives are approximated with second-order central differences. The grid planes are staggered in the vertical with the first vertical velocity plane at a distance $\Delta_z = L_z/(N_z - 1)$ from the surface, and the first horizontal velocity plane at $\Delta_z/2$ from the surface.

The $\tilde{w}\partial\tilde{u}/\partial z$ convective term at the first node $z = \Delta_z/2$ is treated in a special fashion. Since \tilde{w} and $\partial\tilde{u}/\partial z$ are obtained at $z = \Delta_z$ (w nodes in the staggered grid), $\tilde{w}\partial\tilde{u}/\partial z$ at $z = \Delta_z/2$ is computed by averaging its value at $z = 0$ (where it is zero) and at $z = \Delta_z$. For a logarithmic mean velocity profile the finite-difference approximation of the derivative, $[\partial\tilde{u}/\partial z]_{fd}$, becomes inaccurate near $z = 0$. In order to account for this problem, the value of the derivative $\partial\tilde{u}/\partial z$ at $z = \Delta_z$ is corrected using $\partial\tilde{u}/\partial z = [\partial\tilde{u}/\partial z]_{fd} + \partial U/\partial z(1 - f)$, where U is the mean resolved velocity at $z = \Delta_z$ and $f = (\ln(3))^{-1} \simeq 0.91$ is the ratio between the finite-difference approximation and the exact value of the derivative based on the logarithmic velocity profile. This correction only affects the mean flow near the wall, leaving rms profiles and spectra unchanged.

The pseudospectrally evaluated convective terms are dealiased by zero padding and truncation using the 3/2 rule (Orszag, 1970). A rigorous dealiasing of these terms is necessary since aliasing errors affect the smallest resolved scales, which are used by the dynamic procedure to compute the model coefficient. The upper boundary has a stress-free condition, i.e. $\partial\tilde{u}/\partial z = \partial\tilde{w}/\partial z = 0$. At $z = 0$, the instantaneous wall stress, $\tau_{i3}|_w$, must

be prescribed. It is related to the velocity at the first vertical node through the application of a log-layer condition (see e.g. Schumann 1975, Balaras *et al.* 1995) as follows

$$\tau_{i3}|_w = -u_*^2 [\tilde{u}_i(z)/U(z)] = - \left[\frac{U(z) \kappa}{\ln(z/z_o)} \right]^2 [\tilde{u}_i(z)/U(z)] \quad (i = 1, 3). \quad (8)$$

Here u_* is the friction velocity, z_o is the roughness length, and κ is von Karman's constant ($\kappa=0.4$). $U(z)$ is the mean resolved horizontal velocity that is evaluated from the simulation by averaging over wall parallel planes. $\tilde{u}_i(z)$ is the instantaneous local resolved velocity at a height z (in our case, we use $z = \Delta_z/2$).

The computational domain size is $L_x = L_y = 2\pi L_z$. The simulations are for "infinite Reynolds number", i.e. the equations are solved with the eddy-viscosity but without a molecular viscosity term. A wall roughness of $z_o = L_z \times 10^{-4}$ is prescribed. The time advancement is by a second-order accurate Adams-Bashforth scheme. The numerical parameters of the simulation are $L_z = 10^3$, $u_* = 0.45$, and $z_o = 0.1$. Simulations with the traditional Smagorinsky model use a coefficient equal to $C_s = 0.17$ with a wall-damping function as proposed in Mason & Thomson (1992) that include a damping parameter set to $n = 1$. Simulations with the standard dynamic model do not prescribe arbitrary parameters, except for using 2Δ as a test-filter scale. Test-filtering is done in wall-parallel planes using a spectral cutoff filter.

The domain is divided into $N_x \times N_y \times N_z = 54 \times 54 \times 54$ nodes, and additional simulations are carried out with resolutions of $N_x \times N_y \times N_z = 16 \times 16 \times 16$, $24 \times 24 \times 24$, and $36 \times 36 \times 36$, in order to study the dependence on filter (grid) scale. In order to significantly reduce computational overload, the dynamic coefficients at every horizontal plane are computed only once every 10 time steps. We have found no significant differences in the results by reducing this interval. Where needed, an equivalent filter scale is computed according to $\Delta = (\Delta_x \Delta_y \Delta_z)^{1/3}$ (Deardorff 1974, Scotti *et al.* 1993).

3.2. RESULTS

Mean velocity distributions are reported in Porté-Agel *et al.* (1999). In this paper, we concentrate on the spectral characteristics of the flow, and on the coefficients returned by the dynamic model. As a summary, in terms of the mean flow an overall reasonable agreement with the log-law is observed (not shown). Looking in detail, however, the traditional Smagorinsky model slightly overpredicts the log-law profile, while the dynamic model slightly underpredicts it. These trends are typically indicative of excessively damped

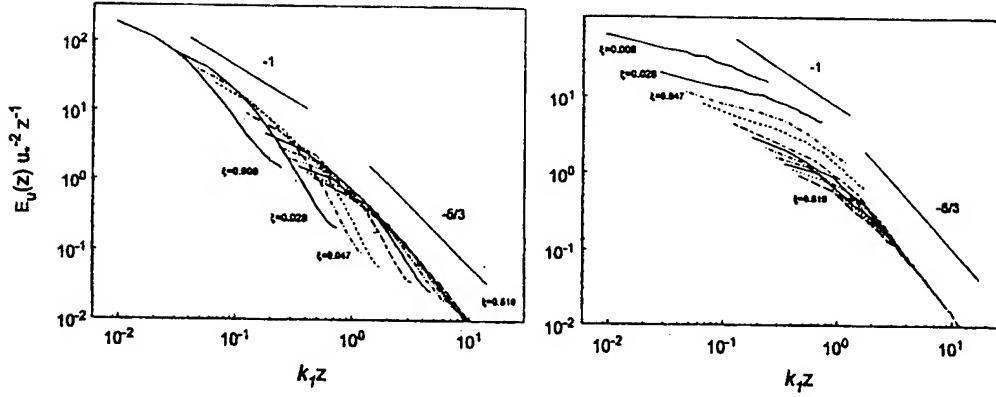


Figure 1. Normalized streamwise velocity spectra versus $k_1 z$ at different heights (a): computed from the traditional Smagorinsky model with $C_s = 0.17$ and a wall-damping parameter $n = 1$. (b) Spectra computed from the standard dynamic model which assumes $C_s^\Delta = C_s^2 \Delta$. From top to bottom, the curves are for $\xi = z/L_z = 0.009, 0.028, 0.047, 0.066, 0.123, 0.179, 0.235, 0.292, 0.349, 0.406, 0.462, 0.519$.

or excessively elevated resolved Reynolds stresses, respectively, which points to excessive SGS energy dissipation by the traditional Smagorinsky model, and to insufficient SGS dissipation by the dynamic model.

Figure 1(a) shows longitudinal energy spectra for the traditional Smagorinsky model, in units of u_* and z , the height above the wall. Different curves correspond to different non-dimensional heights above the wall, $\xi = z/L_z$. In these units, previous laboratory (Perry *et al.*, 1986) and atmospheric (Kader & Yaglom, 1991) measurements show full collapse of the various curves, with a $k_1^{-5/3}$ behavior at small scales ($k_1 z > 1$) and a k_1^{-1} behavior at larger scales ($k_1 z < 1$). These sets provide useful data for comparing LES-generated spectra at various heights to experimental data in wall-bounded flows. As is evident from Fig. 1(a), the Smagorinsky model does not produce the desired collapse, and it causes the spectra to decay too quickly at high wavenumbers, i.e. the model is too dissipative. This is a well-known problem of the Smagorinsky model in non-viscous sublayer resolving LES, even using wall-damping functions.

Figure 1(b) shows longitudinal energy spectra for the standard dynamic Smagorinsky model, which assumes scale-invariance. There is good collapse at high wavenumbers (i.e. the model appears to give the correct behavior in the bulk of the channel). However, in the near-wall region (i.e. at wavenumbers $k_1 z < 1$), the spectra do not collapse, and they appear too flat, i.e. there is 'pile-up' of energy at small scales. This behavior is indicative that

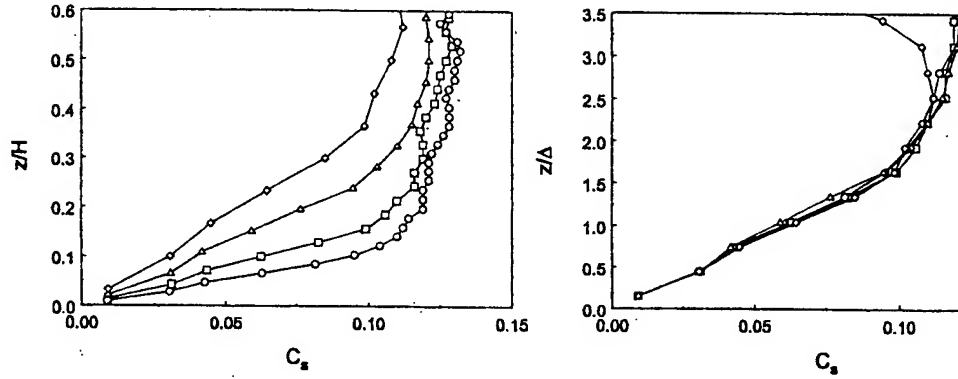


Figure 2. (a) Dynamic Smagorinsky coefficients as obtained from the scale-invariant traditional dynamic model in LES of channel flow that does not resolve the viscous sublayer. Different symbols denote results for different resolutions. Circles: $N_z = 16$, squares: $N_z = 24$, triangles: $N_z = 36$, and rhombs: $N_z = 54$. In all cases $N_x = N_y = N_z$. (b) Same as (a), plotted as function of z/Δ .

the dynamic coefficient is too low. These trends are consistent with the mean velocity profile results described above.

In order to understand why the dynamic model yields too low a coefficient, it is instructive to repeat the calculation at various resolutions. Figure 2(a) shows the resulting coefficient profiles for the four resolutions used. As can be seen, the damping near the wall is indeed captured by the dynamic procedure. A decrease near the wall was also observed in high (but finite) Reynolds number simulations of Balaras *et al.* (1995). When replotted as function of z/Δ (Fig. 2(b)), our results show that there is an excellent collapse with (z/Δ) .

While the results confirm that the dynamic model is able to automatically capture wall-damping in non-resolved wall layers, the observed scaling with z/Δ is problematic because it implies that at any fixed z , the coefficient is a function of Δ . This contradicts the fundamental scale-invariance assumption of the dynamic model (Eq. 4). As pointed out before, the dependence of C_s on Δ is not surprising since the grid scale near the wall approaches the local integral scale. These observations raise the possibility that the results of Fig. 2(b) are incorrect since they have been obtained from a procedure with an internal inconsistency. In fact, if one believes that the coefficient obtained from the standard dynamic procedure may be appropriate at a scale larger than Δ (but not at Δ , see Meneveau & Lund, 1997), and since in the present flow C_s is a decreasing function of Δ , it is plausible that the coefficient obtained here is too low. This trend would be

consistent with the observed spectral pile-up.

4. The scale-dependent dynamic model

Next, we present a generalization of the dynamic model that can be used in applications in which the assumption of Eq. 4 (scale invariance) is not justified. More technical details can be found in Porté-Agel *et al.* (1999).

4.1. FORMULATION

Without assuming that $C_s^\Delta = C_s^{2\Delta}$, we can still write down the Germano identity for the Smagorinsky model (Eq. 5) where

$$M_{ij} = 2\Delta^2 \left(|\tilde{S}| \tilde{S}_{ij} - 2^2 \beta |\tilde{S}| \tilde{S}_{ij} \right). \quad (9)$$

This expression contains a new unknown, $\beta \equiv (C_s^{2\Delta}/C_s^\Delta)^2$. When scale-invariance holds, $\beta = 1$. In order to obtain a dynamic value for β , we use a second test-filter at a larger scale. For simplicity we take 4Δ . Variables filtered at scale 4Δ are denoted by a caret. Writing the Germano identity between scale Δ and 4Δ yields

$$Q_{ij} - \frac{1}{3} Q_{kk} \delta_{ij} = (C_s^\Delta)^2 N_{ij}, \quad \text{where} \quad (10)$$

$$Q_{ij} = \widehat{\tilde{u}_i \tilde{u}_j} - \tilde{u}_i \tilde{u}_j, \quad \text{and} \quad (11)$$

$$N_{ij} = 2\Delta^2 \left(|\hat{\tilde{S}}| \hat{\tilde{S}}_{ij} - 4^2 \theta |\hat{\tilde{S}}| \hat{\tilde{S}}_{ij} \right), \quad (12)$$

where $\theta \equiv (C_s^{4\Delta}/C_s^\Delta)^2$. Again minimizing the error $\langle (Q_{ij} - C_s^2 N_{ij})^2 \rangle$, we obtain

$$(C_s^\Delta)^2 = \frac{\langle Q_{ij} N_{ij} \rangle}{\langle N_{ij} N_{ij} \rangle}. \quad (13)$$

Setting Eq. 7 equal to Eq. 13 yields

$$\langle Q_{ij} N_{ij} \rangle \langle M_{ij} M_{ij} \rangle - \langle L_{ij} M_{ij} \rangle \langle N_{ij} N_{ij} \rangle = 0, \quad (14)$$

This expression has two unknowns, β and θ . In order to solve Eq. 14 they must be related. This goal can be achieved by postulating a functional form for the scale dependence of the coefficient, valid at least in the vicinity of the scale Δ . A natural choice is to assume a power law of the form, $C_s^\Delta = \gamma \Delta^\phi$, or, in a dimensionally more appropriate way,

$$C_s^{\alpha\Delta} = C_s^\Delta(\Delta) \alpha^\phi. \quad (15)$$

For such power-law behavior, $\beta = \alpha^\phi$, independent of scale. This assumption is far weaker than the standard dynamic model, which corresponds to the special case $\phi = 0$. For the assumed local power-law behavior, one can show that $\theta = \beta^2$. With this substitution Eq. 14 only contains the unknown β , and can be rewritten as follows:

$$A_0 + A_1\beta + A_2\beta^2 + A_3\beta^3 + A_4\beta^4 + A_5\beta^5 = 0. \quad (16)$$

Above,

$$\begin{aligned} A_0 &= b_2c_1 - b_1c_2, & A_1 &= a_1c_2 - b_2e_1, \\ A_2 &= b_2d_1 + b_1e_2 - a_2c_1, & A_3 &= a_2e_1 - a_1e_2, \\ A_4 &= -a_2d_1 - b_1d_2, & \text{and } A_5 &= a_1d_2, \quad \text{where} \\ a_1 &= -2\Delta^2 4 \langle |\bar{S}| \bar{S}_{ij} L_{ij} \rangle, & b_1 &= -2\Delta^2 \langle |\bar{S}| \bar{S}_{ij} L_{ij} \rangle, \\ c_1 &= (2\Delta^2)^2 \langle |\bar{S}| \bar{S}_{ij} |\bar{S}| \bar{S}_{ij} \rangle, & d_1 &= (2\Delta^2)^2 4^2 \langle |\bar{S}|^2 \bar{S}_{ij} \bar{S}_{ij} \rangle, \\ & \text{and } e_1 &= (2\Delta^2)^2 4 \langle |\bar{S}| \bar{S}_{ij} |\bar{S}| \bar{S}_{ij} \rangle \end{aligned} \quad (17)$$

are also already needed for the traditional dynamic model, and

$$\begin{aligned} a_2 &= -2\Delta^2 4^2 \langle |\hat{S}| \hat{S}_{ij} Q_{ij} \rangle, & b_2 &= -2\Delta^2 \langle |\hat{S}| \hat{S}_{ij} Q_{ij} \rangle, \\ c_2 &= (2\Delta^2)^2 \langle |\hat{S}| \hat{S}_{ij} |\hat{S}| \hat{S}_{ij} \rangle, & d_2 &= (2\Delta^2)^2 (4^2)^2 \langle |\hat{S}|^2 \hat{S}_{ij} \hat{S}_{ij} \rangle, \\ & \text{and } e_2 &= (2\Delta^2)^2 (4)^2 \langle |\hat{S}| \hat{S}_{ij} |\hat{S}| \hat{S}_{ij} \rangle, \end{aligned} \quad (18)$$

are new requirements for the scale-dependent model.

4.2. RESULTS

The scale-dependent model is implemented in the simulation described in §3.1. The additional test-filtered quantities at scale 4Δ are obtained by spectral filtering in the x-z planes. As in the traditional dynamic model, tensor contractions are averaged over such planes, corresponding to a minimization of the error in the modeled Germano identity over these regions of statistical homogeneity (Ghosal *et al.* 1995). Having evaluated the required tensor contractions, we must find the appropriate root of the polynomial of Eq. 16. Detailed analysis of the polynomial (see Porté-Agel *et al.* 1999) shows that of the five roots for β , only the largest one is physically meaningful. The other values of β imply changes in sign of $\langle L_{ij} M_{ij} \rangle$ and/or $\langle Q_{ij} N_{ij} \rangle$, which is unphysical (on average). In order to solve the

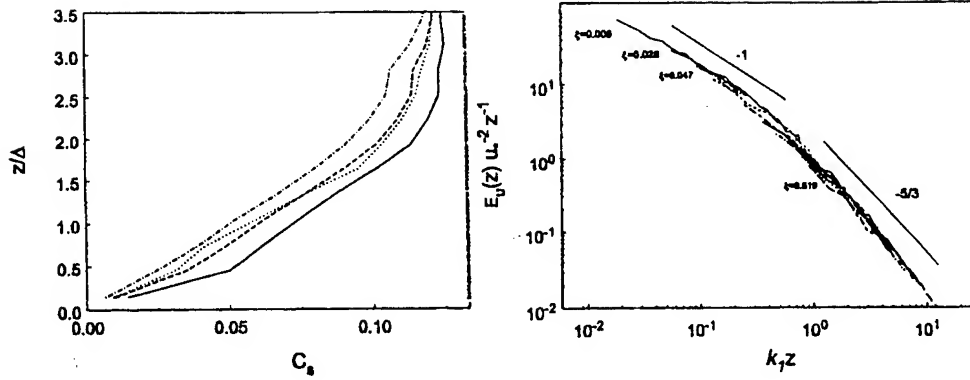


Figure 3. (a): Vertical distribution of the time-averaged coefficient C_s^Δ (solid line), $C_s^{2\Delta} = \beta^{1/2} C_s^\Delta$ (dashed line), and $C_s^{4\Delta} = \beta C_s^\Delta$ (dot-dashed line) obtained using the scale-dependent dynamic model. The dotted line is the coefficient obtained using the traditional dynamic model that assumes $C_s^{2\Delta} = C_s^\Delta$. (b): Normalized streamwise velocity spectra versus $k_1 z$ at different heights, computed from the scale-dependent dynamic model. From top to bottom, the curves are for the same $\xi = z/L_x$ as in previous figures.

polynomial equation, a Newton-Raphson technique is employed. In terms of computational expense, with the dynamic procedure applied every 10 time steps, the scale-dependent dynamic model takes only an insignificant amount more CPU time than the traditional dynamic model. Once β has been found, it is replaced into Eq. 9 and C_s^Δ is obtained from Eq. 7.

Fig. 3(a) shows the distribution of the average value of the coefficients C_s^Δ obtained using the scale-dependent procedure (solid line). Comparing this result to the average value of the coefficient that results from the traditional dynamic model (dotted line, replotted from Fig. 2(b)), it can be seen that the present result is higher. This trend is as expected: The traditional dynamic model underestimates the coefficient since it is based on scales larger than Δ (which are near the local integral scale). By properly extrapolating the trend, the scale-dependent dynamic model gives a coefficient which is appropriate at the true grid-scale Δ where the coefficient should be larger. Also shown in the figure are the coefficients at the larger scales, also determined dynamically from the scale-dependent approach: the dashed line is $C_s^{2\Delta} = \beta^{1/2} C_s^\Delta$, and the dot-dashed line is $C_s^{4\Delta} = \beta C_s^\Delta$.

Figure 3(b) shows the longitudinal spectra at various heights above the wall obtained from the scale-dependent dynamic model. Comparisons with Figs. 1(a) and 1(b) confirms that this model yields much improved predictions of the turbulence structure at all scales, and at all heights above the wall. No 'pile-up' of energy is observed near the wall, which is consistent

with a higher model coefficient. Mean velocity profiles (not shown) also indicate improved agreement with the law of the wall.

5. Conclusions

It has often been argued that the main strength of the dynamic model is manifested in flows in which the grid-scale is outside of the inertial range (e.g. improved predictions in transitional flows, in the viscous sublayer, or in the transition to the viscous range), where indeed the assumption of scale-invariance should not hold. As has been shown before (Meneveau & Lund, 1997), even if the assumption does not hold the dynamic model is able to reproduce the main trends of changing coefficient. And, in the cases mentioned (transitional flows, in the viscous sublayer, or in the viscous subrange), the SGS stresses are small to begin with. In those cases it does not matter too much if the dynamic model gives an overestimate of the coefficient, since the SGS stresses contribute only a negligible part of the dynamics. However, in applications where the SGS stress becomes a significant part of the dynamics, such as in the near-wall region of non-sublayer resolving simulations, it matters a great deal whether the coefficient is underestimated.

For such cases, we have developed a generalization of the dynamic model that allows the coefficient to change with Δ in a self-consistent fashion. The new model involves a secondary test filter that, together with the traditional test filter, is used to determine both the coefficient and how it changes across scales. This model has been applied to LES of a non-sublayer resolving LES of wall-bounded flow. Simulations with such a model are stable and robust, and yield expected trends of the coefficient as function of scale. Predictions of energy spectra near the wall are significantly improved. The mean velocity profiles are also improved over those that use the standard dynamic model. This new, more general, dynamic model should be tested in other applications in which scale-dependence of the coefficient is suspected and important. Examples include rapidly distorted turbulence, stratified flows, etc...

ACKNOWLEDGMENT

The authors gratefully acknowledge the financial support of NSF-ATM-9726270. CM is also supported by the Office of Naval Research (grant N00014-98-1-0221, Dr. Patrick Purtell, program manager).

References

J.D. Albertson and M.B. Parlange. Surface length-scales and shear stress: implications

- for land-atmosphere interaction over complex terrain. *Water Resour. Res.*, in press, (1999a).
- E. Balaras, C. Benocci, and U. Piomelli. Finite-difference computations of high Reynolds-number flows using the dynamic subgrid-scale model. *Theor. Comp. Fluid Dyn.*, 7:207-216, (1995).
- J. W. Deardorff. Three-dimensional numerical study of the height and mean structure of a heated planetary boundary layer. *Bound. Layer Meteor.*, 7:81, (1974).
- M. Germano, U. Piomelli, P. Moin, and W.H. Cabot. A dynamic subgrid-scale eddy viscosity model. *Phys. Fluids A*, A 3:1760, (1991).
- S. Ghosal, T.S. Lund, P. Moin, and K. Akselvoll. A dynamic localization model for large eddy simulation of turbulent flow. *J. Fluid Mech.*, 286:229-255, (1995).
- B. Kader and A.M. Yaglom. Spectra and correlation functions of surface layer atmospheric turbulence in unstable thermal stratification. *Turbulence and coherent structures (O. Métais and M. Lesieur, editors)*, Kluwer Academic, Norwell Mass. 450pp, (1991).
- D.K. Lilly. The representation of small-scale turbulence in numerical simulation experiments. In *Proc. IBM Scientific Computing Symposium on Environmental Sciences*, page 195, (1967).
- D.K. Lilly. A proposed modification of the Germano subgrid scale closure method. *Phys. Fluids A*, 4:633, (1992).
- S. Liu, J. Katz, and C. Meneveau. Evolution and modeling of subgrid scales during rapid straining of turbulence. *J. Fluid Mech.*, 387:281-320, (1999).
- P.J. Mason and D.J. Thomson. Stochastic backscatter in large-eddy simulations of boundary layers. *J. Fluid Mech.*, 242:51-78, (1992).
- C. Meneveau and J. Katz. Scale-invariance and turbulence models for large-eddy simulation. *Annu. Rev. Fluid Mech.*, in press, (2000).
- C. Meneveau, T. Lund, and W. Cabot. A Lagrangian dynamic subgrid-scale model of turbulence. *J. Fluid Mech.*, 319:353-385, (1996).
- C. Meneveau and T.S. Lund. The dynamic Smagorinsky model and scale-dependent coefficients in the viscous range of turbulence. *Phys. Fluids*, 9:3932-3934, (1997).
- P. Moin and J. Kim. Numerical investigation of channel flow. *J. Fluid Mech.*, 118:341-377, (1982).
- A.E. Perry, S. Henbest, and M.S. Chong. A theoretical and experimental study of wall turbulence. *J. Fluid Mech.*, 165:163-199, (1986).
- U. Piomelli and T. A. Zang. Large-eddy-simulation of transitional channel flow. *Comp. Phys. Comm.*, 65:224, (1991).
- F. Porté-Agel, C. Meneveau, and M.B. Parlange. Dynamic model for large-eddy-simulations near the limits of the inertial range of turbulence. *ASME FED 1999, FEDSM99-7835*, (1999).
- F. Porté-Agel, C. Meneveau, and M.B. Parlange. A scale-dependent dynamic model for large-eddy simulation: application to the atmospheric boundary layer. *J. Fluid Mech.*, submitted, (1999).
- U. Schumann. Subgrid scale model for finite difference simulations of turbulent flows in plane channels and annuli. *J. Comp. Phys.*, 18:376, (1975).
- A. Scotti, C. Meneveau, and D.K. Lilly. Generalized Smagorinsky model for anisotropic grids. *Phys. Fluids A*, 5:2306, (1993).
- J. Smagorinsky. General circulation experiments with the primitive equations. i. the basic experiment. *Mon. Weather Rev.*, 91:99, (1963).
- L. M. Smith and V. Yakhot. Short- and long-time behavior of eddy-viscosity models. *Theoret. Comput. Fluid Dynamics*, 4:197, (1993).
- P.R. Voke. Subgrid-scale modeling at low mesh Reynolds number. *Theor. Comp. Fluid Dyn.*, 8:131-143, (1996).

DIRECT NUMERICAL SIMULATION OF HIGH SUBSONIC JETS

FAROUK OWIS* P. BALAKUMAR†

*Old Dominion University
Aerospace Engineering Department
Norfolk, VA 23529*

Abstract

The stability of spatially developing high subsonic jets at low and high Reynolds number is investigated using direct numerical simulation of the unsteady full Navier-Stokes equations. High order accurate numerical scheme with minimum dispersion error is used for the simulation and a perfectly matching layer technique is applied for the treatment of the outflow boundaries. The sound radiated by the vortex pairing process is studied by introducing the inflow disturbances at the fundamental frequency and its first two subharmonics. The results are in general agreement with the observations.

1. Introduction

This research is motivated by the need to understand the mechanism of jet development into turbulence and the noise generation process in jet mixing layers. Understanding the noise generation process represents the key to find noise suppression methods. Recently, there have been many studies on supersonic and subsonic jet noise radiation. Mankabadi and et al. (1993) studied the structure of supersonic jet and the noise radiated to the far field using Lighthill's acoustic analogy. Mitchel, Lele and Moin (1995) investigated the sound generation of subsonic and supersonic jets due to the vortex pairing process in the mixing layer and Colonius and et al. reported that the vortex pairing process is responsible for noise radiation from the shear layers.

Experiments by Laurence (1956) and Laufer and Yen (1983) have shown that the sound radiated from the jet is greatest within 4-6 diameters downstream and then decays through a transition region. This region is characterized by large vortical structures and the size of these structures is of the flow geometry size. For this reason, the unsteady flow equations can be solved in the near field using direct numerical simulation to provide the sound source for acoustic computations of the far field noise.

Evaluation of the sound source using the direct numerical simulation of Navier-Stokes equations requires using numerical techniques with minimum distortion and diffusive characteristics. The numerical errors get worth for high Reynolds number flow simulation. Typically, free shear layers of interest have very high Reynolds numbers. Therefore high order accurate numerical schemes with minimum dissipation and dispersion errors are needed. One of the well-tested numerical schemes is the extension

* Graduate research assistant

† Associate Professor

of the second order MacCormack scheme, which is known as 2-4 scheme and is developed by Gottlieb and Turkel (1976). This scheme has been used successfully by Farouk and Oran (1991), and by Ragab and Sheen (1991) for studying the nonlinear instability problems in plane shear layers. The scheme is fourth-order accurate in space and second order accurate in time. It has been extended to sixth-order spatial accuracy by Bayliss (1985). A new family of MacCormack schemes has been developed by Hixon (1997) to increase the accuracy of 2-4 scheme and to minimize the dispersion error. In addition, the accuracy of the time integration for these schemes is increased to fourth order using Runge Kutta method. These schemes have been tested on benchmark problems. One of the these schemes, which is MacCormack scheme based on the finite difference of the optimized dispersion relation preserving scheme, is employed in this work to study the sound radiated from subsonic jets by the vortex roll-up and pairings.

A special attention to the boundary treatment is required since the numerical boundaries can generate spurious waves that may render the computed solution entirely unacceptable. Several boundary conditions have recently been proposed for computational aeroacoustics. These boundary conditions include characteristic methods such as Thompson (1987) and Giles (1990), asymptotic analysis of the governing equations [Bayliss and Turkel (1982)], buffer domain technique [Street and Macaraeg (1989)] and matching layer developed by Hu (1995). In the current study, the perfectly matching layer technique is adopted since it produces minimum reflections at the boundaries.

In order to directly compute the fluctuation quantities of the jet flow, the laminar boundary layer equations are solved using two-point compact scheme to obtain the jet mean flow. An initial hyperbolic axial velocity profile, equation (1), is assumed for the laminar flow computations and the initial temperature profile is obtained using Crocco's relation (2).

$$U = 0.5[(1 + U_\infty) - (1 - U_\infty) \tanh\{\beta(r - 1)\}] \quad (1)$$

$$T = T_\infty + (T_j - T_\infty) \frac{(U - U_\infty)}{(U_j - U_\infty)} + 0.5 T_j (\gamma - 1) M^2 (U_j - U) \frac{(U - U_\infty)}{(U_j - U_\infty)^2} \quad (2)$$

The fundamental frequency and the eigenfunction are obtained using the linear stability analysis of the jet laminar flow.

2. Governing Equations

The governing equations are the unsteady full Navier-Stokes equations in polar coordinates and the equations are written in conservative form for two-dimensional axis-symmetric jet. The equations are normalized with respect to the jet exit conditions.

$$\frac{\partial Q}{\partial t} + \frac{\partial F}{\partial x} + \frac{1}{r} \frac{\partial rG}{\partial r} = S \quad (3)$$

$$Q = \begin{bmatrix} \rho \\ \rho u \\ \rho v \\ \rho E \end{bmatrix}, F = \begin{bmatrix} \rho u \\ p + \rho u^2 - \sigma_{xx} \\ \rho u v - \sigma_{xr} \\ (\rho E + p)u - u\sigma_{xx} - v\sigma_{xr} - k \frac{\partial T}{\partial x} \end{bmatrix}$$

$$G = \begin{bmatrix} \rho v \\ \rho u v - \sigma_{xr} \\ p + \rho v^2 - \sigma_{rr} \\ (\rho E + p)v - u\sigma_{xr} - v\sigma_{rr} - k \frac{\partial T}{\partial r} \end{bmatrix}, S = \frac{1}{r} \begin{bmatrix} 0 \\ 0 \\ p - \sigma_{\theta\theta} \\ 0 \end{bmatrix}$$

$$p = (\gamma - 1)\rho \left[E - \frac{1}{2}(u^2 + v^2) \right] \quad (4)$$

$$T = \frac{p}{\gamma M_j^2 \rho} \quad (5)$$

$$\text{where, } Re = \frac{\rho_j u_j r_j}{\mu_j}, \quad M_j = \frac{u_j}{\sqrt{\gamma R T_j}} \quad (6)$$

The viscosity is calculated using Sutherland's law and the thermal conductivity is obtained from this equation

$$k = \frac{\mu}{(\gamma - 1)M_j^2 Pr Re} \quad (7)$$

3. Numerical Discretization

MacCormack type schemes developed by Hixon (1997) with operator splitting are used for the numerical discretization. The operators are applied in the following symmetric way:

$$Q^{n+2} = L_{2x} L_{2r} L_{1r} L_{1x} Q^n \quad (8)$$

Where L_x and L_r are one-dimensional operators in x and r directions that are applied to the following one-dimensional equations

$$Q_t = -F_x \quad (9)$$

$$Q_t = -G_r + S \quad (10)$$

Using Rung-Kutta method for the time integration, the operator L_x is written as follows:

$$Q_t = -\frac{d}{dx}[F(Q)] \quad (11)$$

$$\begin{aligned}
h_1 &= -\Delta t \frac{d^f}{dx} [F(Q^n)] & h_2 &= -\Delta t \frac{d^b}{dx} [F(Q^n + \alpha_2 h_1)] \\
h_3 &= -\Delta t \frac{d^f}{dx} [F(Q^n + \alpha_3 h_2)] & h_4 &= -\Delta t \frac{d^b}{dx} [F(Q^n + \alpha_4 h_3)] \\
h_5 &= -\Delta t \frac{d^f}{dx} [F(Q^n + \alpha_5 h_4)] & h_6 &= -\Delta t \frac{d^b}{dx} [F(Q^n + \alpha_6 h_5)] \\
Q^{n+1} &= Q^n + \beta_1 h_1 + \beta_2 h_2 + \beta_3 h_3 + \beta_4 h_4 + \beta_5 h_5 + \beta_6 h_6
\end{aligned} \tag{12}$$

Table (1) Coefficients of fourth order Runge-Kutta

Accuracy	α_2	α_3	α_4	α_5	α_6	β_1	β_2	β_3	β_4	β_5	β_6
Fourth order	1/2	1/2	1	0	0	1/6	1/3	1/3	1/6	0	0

For the forward and backward differencing, the fluxes are discretized using the optimized dispersion relation-preserving scheme as follow:

$$\begin{aligned}
\left(\frac{dF}{dx} \right)^f &= a_{-1} F_{i-1} + a_0 F_i + a_1 F_{i+1} + a_2 F_{i+2} + a_3 F_{i+3} \\
\left(\frac{dF}{dx} \right)^b &= a_{-1} F_{i+1} + a_0 F_i + a_1 F_{i-1} + a_2 F_{i-2} + a_3 F_{i-3}
\end{aligned} \tag{13}$$

Table (2) Coefficients of flux discretization using MacCormack schemes

Scheme	a_{-1}	a_0	a_1	a_2	a_3
DRP/opt	$-\frac{.30874}{\Delta x}$	$-\frac{.63254}{\Delta x}$	$\frac{1.2330}{\Delta x}$	$-\frac{.3334}{\Delta x}$	$\frac{.04168}{\Delta x}$

4. Boundary conditions

Inflow B.CS:

For supersonic flow, all the flow variables are specified at the inflow boundary as mean flow and perturbations as:

$$\begin{aligned}
Q &= Q_m + \varepsilon Q_{dist} \\
Q_{dist} &= \sum_{k=1}^3 \text{Real}[Q_k(r) e^{-i\omega t/2^{k-1}}]
\end{aligned} \tag{14}$$

where $Q_k(r)$ are the eigenfunctions of the flow variables which are obtained from the linear stability analysis for the most unstable frequency ω and its subharmonics $\omega/2$ and $\omega/4$ and ε is the amplitude of the disturbance at the inflow boundary.

For subsonic flow, one flow variable is obtained from the interior points using the continuity equation and the rest of the flow variables are specified at the boundary as follow:

$$\frac{\partial \rho}{\partial t} + [\lambda_2 + \frac{1}{2}(\lambda_1 + \lambda_5)]/c^2 + \frac{\partial \rho v}{\partial r} = -\frac{\rho v}{r} \quad (15)$$

$$\lambda_1 = (u - c) \left(\frac{\partial p}{\partial x} - \rho u \frac{\partial u}{\partial x} \right), \quad \lambda_2 = u \left(c^2 \frac{\partial \rho}{\partial x} - \frac{\partial p}{\partial x} \right), \quad \lambda_5 = (u + c) \left(\frac{\partial p}{\partial x} - \rho c \frac{\partial u}{\partial x} \right)$$

For non-reflecting inflow boundary, $\lambda_2 = \lambda_5 = 0$ and λ_1 is calculated from the interior points.

Centerline Conditions:

A new set of equations is derived at the centerline using L'Hospital rule. These equations are applied with the following symmetric conditions:

$$\frac{\partial p}{\partial r} = \frac{\partial u}{\partial r} = \frac{\partial \rho}{\partial r} = 0 \quad (16)$$

$$v = 0$$

Perfectly Matching Layer:

The perfectly matching layer technique is applied at the outflow boundaries. This method is first proposed by Berenger (1994) for the absorption of electromagnetic waves and applied by Hu (1995) for Euler equations. In this technique, a region is attached to the computational domain at the boundaries as shown in figure (1) where exponential damping terms are added to the governing equation (3) to damp the disturbance.

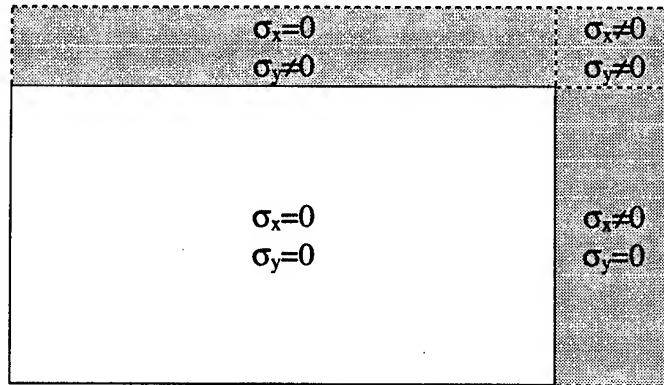


Figure (1) Computational Domain

For two-dimensional axisymmetric jet, the governing equations (3) are divided into two equations, one for the disturbance which is produced by the axial flux and the other for the radial flux.

$$\frac{\partial Q_1}{\partial t} + \frac{\partial (F - F_m)}{\partial x} + \sigma_x Q_1 = 0$$

$$\frac{\partial Q_2}{\partial t} + \frac{1}{r} \frac{\partial r (G - G_m)}{\partial r} + \sigma_y Q_2 = (S - S_m) \quad (17)$$

$$Q = Q_1 + Q_2 + Q_m$$

where, $\sigma_x = \sigma_{mx} \left(\frac{x-x^*}{L_b} \right)^{B_x}$

σ_{mx} is the maximum value of the absorption coefficient σ_x , L_b is the length of PML and x^* is the beginning of the Layer. Q_m, F_m, G_m and S_m denote the mean flow variables. In this technique, a region is added at the boundary as shown in figure (1) to damp the disturbance. In this region of the domain, exponential damping terms are added to the governing equations of the form:

5. Results

Two case cases are computed at different Reynolds numbers. The first simulation is done at Mach number 0.8 and Reynolds number 2500. An initial axial velocity profile with momentum thickness 0.08334 ($\beta=6$) is used for this simulation to obtain the jet mean flow. The fundamental frequency obtained using the linear stability theory is 1.3195 ($St=0.42$) and the first two subharmonics are 0.66 and 0.33. The amplitude of the inflow disturbance is assumed 0.0015 and the eigenfunctions of the inflow disturbances are normalized with respect to the maximum amplitude of the axial velocity disturbance. The dimensions of the domain and the grid parameters are summarized in table (3).

Table (3) Grid parameters for case 1 ($M=0.8$)

Parameter	Value
X_{max}/r_j (including matching layer)	55
R_{max}/r_j (including matching layer)	70
Maching layer in x-direction (L_{bx})	5
Maching layer in r-direction (L_{br})	8
Number of points in x-direction ($IMAX$)	1225
Number of points in r-direction ($JMAX$)	451
Number of points in axial matching layer	111
Number of points in radial matching layer	14
$\Delta x/r_j$	0.0449
$(\Delta r/r_j)_{min}$ at $r=1$	0.03
$(\Delta r/r_j)_{max}$ at $r=r_{max}$	0.611

The computations are run until the entire domain is settled into its nearly periodic steady state. Time history of the axial velocity at different downstream positions indicates that the flow becomes periodic at the outflow boundary after approximately 40 cycles of the fundamental frequency. The last 12 cycles of the computations are presented in figure (2). The axial velocity disturbances near the inflow boundary are dominated by all the excitation frequencies as shown in figure (2a) while the flow near the outflow boundary is dominated by the frequency of the first subharmonic which is the frequency of the vortex pairing process.

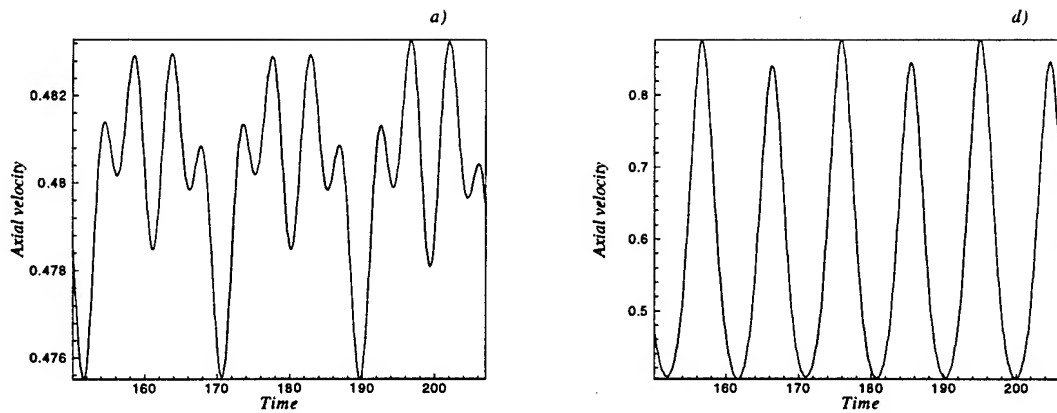


Figure (2) Time history of total axial velocity for $M_j=0.8$ at $r=1$ and a) $x=0$, b) $x=50$

The near field vorticity contours are plotted in figure (3) at five equally spaced instants within a periodic cycle of the second subharmonic of period (T). The jet shear layer roll-up is clear near the inflow and the vortex pairing is captured at two different downstream positions. As the flow moves downstream, the vorticity is reduced due to the effect of the viscosity.

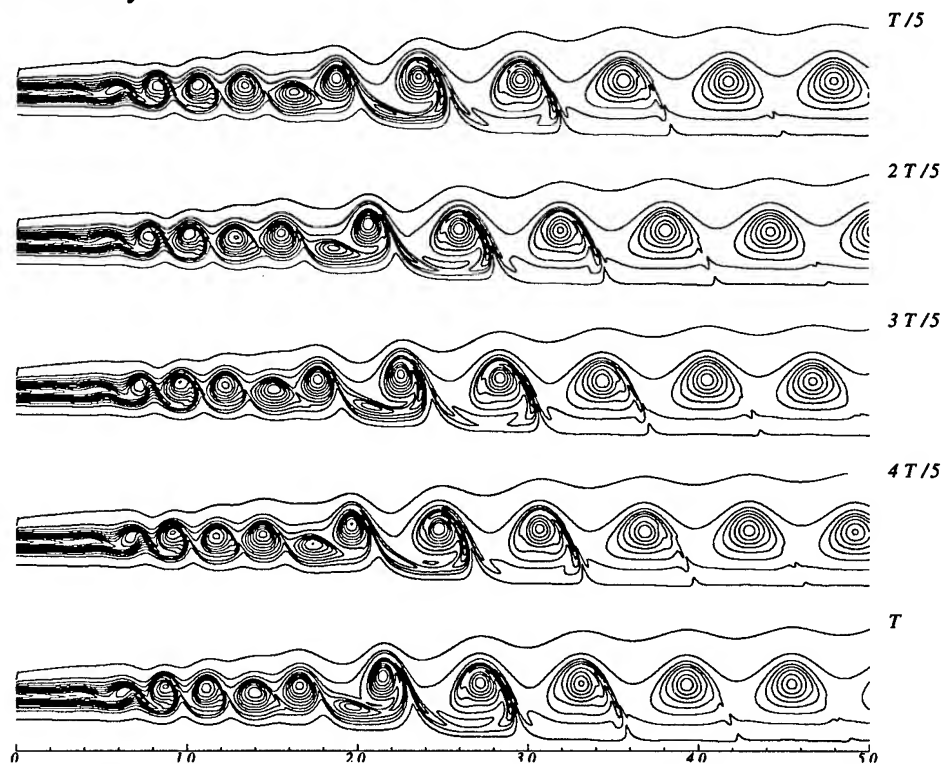


Figure (3) Evolution of vorticity with time at different equally spaced intervals ($M_j=0.8$). The contour levels range from 0 to $2.84 U_j/R_j$ with increment $0.236 U_j/R_j$ and 12 contour levels for each plot.

The amplitude of the axial velocity disturbance at different frequencies is computed from equation (18) using the Fourier transform of the time signal for the last cycle of the second subharmonic and the results are introduced in figure (4).

$$u'(\omega) = \left(\frac{1}{U_j^2 r_j^2} \int_{r=0}^{r_{\max}} 2\pi r u^2 dr \right)^{\frac{1}{2}} \quad (18)$$

One concludes from the figure that the maximum amplitude of the disturbance occurs at frequency $f/2$ which is the frequency of the first subharmonic. The amplitude of the first subharmonic grows until it peaks at downstream location ($x=22$) where the vortex pairing process is complete. The correspondence of the saturation position and the completion of the vortex pairing process is also observed by Mitchel, Lele and Moin (1995). Additionally, the amplitude of the disturbances at the fundamental frequency saturates in the region of the vortex roll-up and it grows again until it saturates at the end of the vortex pairing process. The multiple saturation is observed by Colonius and et al. (1997). The amplitude of the second subharmonic grows slowly and no saturation is observed for this frequency which means that a third pairing process may be obtained further downstream. Other frequencies are plotted but they have small amplitudes with respect to the fundamental frequency and the first subharmonic.

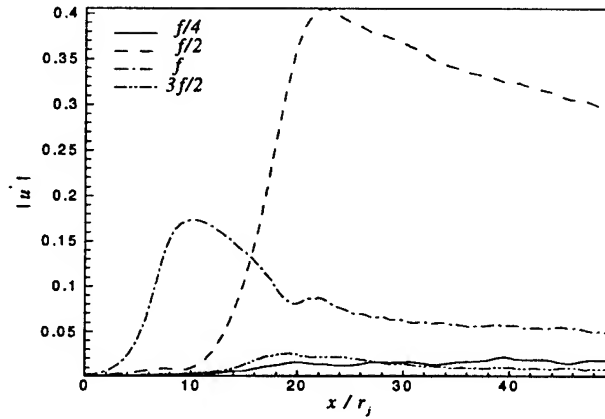


Figure (4) Amplitude of axial velocity disturbance versus downstream position at various frequencies ($M_f=0.8$)

Table (3) Source frequencies and saturation positions for ($M_f=0.8$)

Frequency	Saturation position	Maximum amplitude
$f/2$	22.5	0.406
f	12.5	0.245
$3f/2$	22.5	0.0405
$2f$	10	0.0269
$5f/2$	22.5	0.012
$3f$	10.5	0.0164

A list of the saturation positions of the different frequencies and their amplitudes is presented in table (4). Only even frequencies of the second subharmonic have considerable amplitudes. The fundamental frequency (f) and its multiple frequencies ($n f$), where n is integer, saturate at the same axial position where the first pairing process is complete while multiple frequencies of the first subharmonic ($n f/2$) reach their peak amplitude at the same location of the second vortex pairing.

The growth of the momentum thickness is plotted for both laminar and disturbed jet flows as shown in figure (5). In the region of vortex roll-up, the momentum thickness has nearly the same value as for the laminar jet. Following the region of the vortex roll-up, two steps-like increase in the momentum thickness are observed at various axial positions, which correspond to two different vortex-pairing processes. The first step like increase in the momentum thickness starts at $x=6$ and ends at $x=11$ which is the position of saturation for the fundamental frequency and another step increase resumes after the completion of the first pairing. The second vortex pairing is complete where the first subharmonic reaches its maximum value which means that this region is dominated by the frequency of the first subharmonic. As a result of the viscosity effect on the vorticity levels, the growth rate of the momentum thickness decreases after the completion of the second vortex pairing process.

The far field pressure disturbance contours are shown in figure (6) with an arrow indicating the position of the vortex pairing process. The domain shown in the graph is limited between 5 and 50 radius in the radial direction. It is evident that the pressure waves propagate to the far field in semi-circles and these waves emanate from the region of the vortex pairing where the instability waves saturate. This is similar to the observations of Laufer and Yen (1983) and Colonius, Lele and Moin (1997).

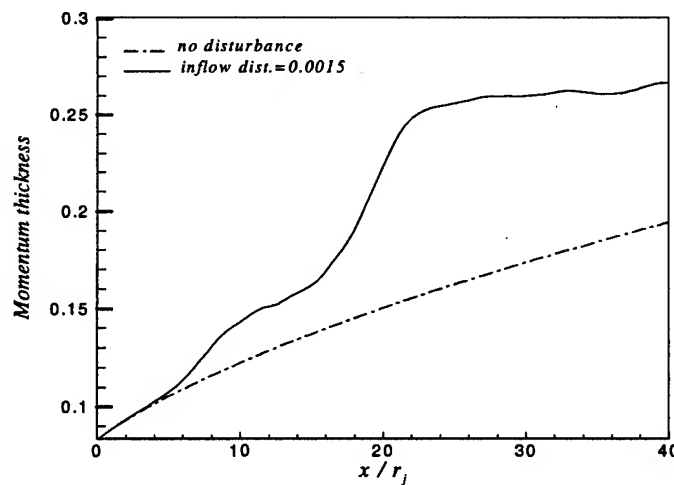


Figure (5) Variation of jet momentum thickness with downstream position ($M_j=0.8$)



Figure (6) Far field pressure disturbance contours for $M_f=0.8$ with maximum and minimum pressure levels $\pm 1.5 \times 10^3$ and 15 levels

The total radial velocity contours in the near field is presented in figure (7). The contours are presented in the region ($0 < r \leq 5$) with 16 contour levels. The maximum value of the levels is 0.236 and the minimum is -0.23 . High values of the total radial velocity exist where the vortices are located and these regions of high radial velocity are equally spaced near the outflow.

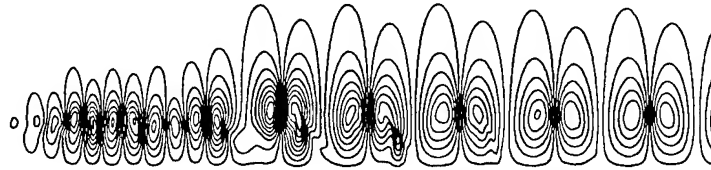


Figure (7) Contours of total normal velocity ($M_f=0.8$).

The second case is computed at higher Reynolds number ($Re=10^5$) and Mach number 0.85. The initial axial velocity profile used for the laminar flow computations has a momentum thickness 0.1 ($\beta=5$) and the temperature ratio of the jet is assumed to be one. Prandtl number is chosen to be 0.72 for this simulation. Linear stability analysis for this jet indicates that the most unstable frequency is 1.231 ($St=0.392$). The inflow for the jet simulation is also excited at the most unstable frequency and its first two subharmonics with an initial amplitude 0.014.

The computational domain is extended to 60 radius in the axial direction and 14 radius in the radial direction. The last 10 radius in the axial direction are used for the matching layer. The mesh size is 1336×151 and uniform grid is used in the axial direction while the grid is stretched in the radial direction with minimum grid spacing 0.029 at the shear layer.

The computations are continued until the flow becomes nearly periodic at the outflow boundary after 45 cycles of the fundamental frequency and the data of the last four cycles are analyzed using the discrete Fourier transform. The axial velocity disturbance amplitudes at different frequencies are presented in figure (8).

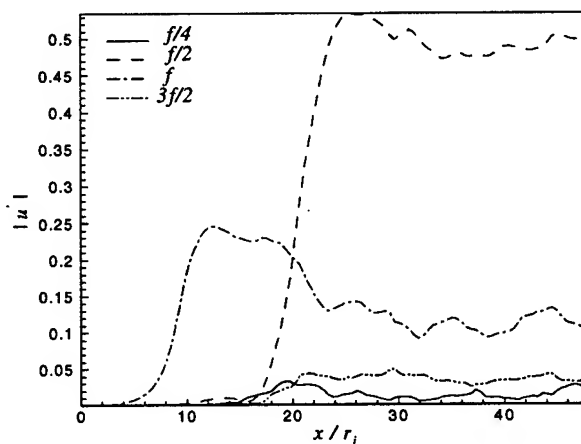


Figure (8) Amplitude of axial velocity disturbance versus downstream position at various frequencies ($M_f=0.85$ and $Re=10^5$)

As a result of increasing Reynolds number, the amplitude of the disturbance for the first subharmonic is higher than that of the low Reynolds number simulation. The same result is predicted by the linear stability analysis. The first subharmonic saturates approximately in the same downstream position of the lower Reynolds number simulation. Only one saturation is observed for the fundamental frequency at $x=11$ and the higher frequencies peaks near the saturation location of the first subharmonic.

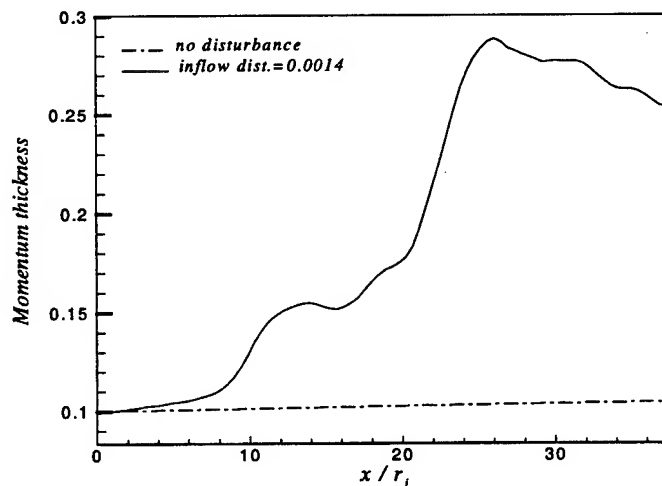


Figure (9) Variation of jet momentum thickness with downstream position ($M_f=0.85$ and $Re=10^5$)

The momentum thickness of the laminar flow grows very slowly with axial distance since the effect of the viscosity for high Reynolds number jet is very small. For the perturbed jet, the momentum thickness grows very quickly and two steps-like increase are observed at the vortex pairing positions.

References

- 1) Bayliss, A. and Turkel, E., 1982 "Far field boundary conditions for compressible flows" *Journal of Computational Physics*, Vol. 48, pp. 182-199.
- 2) Bayliss, A., Maestrello, L., Parikh, P., and Turkel, E., 1985 'A Fourth Order Scheme for the Unsteady Compressible Navier-Stokes Equations', *AIAA paper* 85-1694.
- 3) Berenger, J-P, "A perfectly matched layer for the absorption of electromagnetic waves" *Journal of Computational Physics*, Vol. 114, 1994, pp. 185-200.
- 4) Colonius, T., Lele, S.K. and Moin, P., 1997 'Sound Generation in Mixing layer', *Journal Of Fluid Mechanics*, Vol. 330, pp. 375-409.
- 5) Farouk, B., Oran, E.S., and Kailasanath, K. 1991, 'Numerical Simulation of the structure of supersonic shear layers', *Physics of Fluids*, Vol. 3, pp.2786-2798.
- 6) Giles, M.B., 1990 " Nonreflecting boundary conditions for Euler equation calculations" *AIAA Journal*, Vol. 28, No. 12, pp. 2050-2058.
- 7) Gottlieb, D. and Turkel, E., 1976 'Dissipative two-four method for time dependent problems', *Mathematics of computations*, Vol. 30, No. 136, pp. 703-723.
- 8) Hayder, M.E., Turkel, E. and Mankbadi, R.R., ' Numerical Simulations of a High Mach Number Jet Flow', *AIAA paper* 93-0653, 1993.
- 9) Hixon, R., 'On Increasing the Accuracy of MacCormack Schemes for Aeroacoustic Applications', *AIAA paper* 97-1586-CP, 1997.
- 10) Hu, F.Q, 1995 'On Absorbing Boundary Conditions for linearized Euler Equations by a Perfectly matching Layer', *ICASE Report* No. 95-70.
- 11) Laufer, J. and Yen, T-C., 1983 "Noise generation by a low-Mach-number jet" *Journal of Fluid Mechanics*, Vol. 134, pp.1-31.
- 12) Laurence, J. C., 1956 "Intensity scale and spectra of turbulence in mixing region of free subsonic jet" *NACA Rep.* No. 1292.
- 13) Mankabadi, R.R., Hayder, E. and Povinelli, L.A., 'The Structure of Supersonic Jet Flow and Its Radiated Sound', *AIAA paper* 93-0549, 1993.
- 14) Mitchel, B. E., Lele, S. K. and Moin, P., 1995 "Direct computation of the sound generated by vortex pairing in an axisymmetric jet" *AIAA* 95-0504.
- 15) Poinso, T.J., and Lele, S.K., 'Boundary Conditions for Direct Simulations of Compressible Viscous Reacting Flows', *Journal of Computations Physics*, Vol. 101, No.1, 1992, pp.104-129.
- 16) Ragab, S.A. and Sheen, S., 'The Nonlinear Development of Supersonic Instability Waves in a Mixing Layer', *Phiscs of Fluids*, Vol. 4, 1991, pp. 553-566.
- 17) Soh, W. Y., 1994 "Unsteady jet flow computation towards noise prediction" *AIAA* 94-0138.
- 18) Street, C. L., Macaraeg, M. G., 1989 "Spectral multi-domain for large-scale fluid dynamics simulations" *Int. Journal Appl. Numer. Math.*, Vol. 6, pp. 123-139, 1989.
- 19) Thompson, K.W, 'Time Dependent Boundary Conditions for hyperbolic Systems', *Journal of Computations Physics*, Vol. 68, No.1, 1987, pp.1-24.

GENERATION OF A ONE-PARAMETER FAMILY OF RESIDUALS FOR THE FILTERED EQUATIONS OF FLUID MOTION

G. PANTELIS

*Scientific Computing Group, Information Management Division,
A.N.S.T.O.*

PMB 1, Menai, NSW, 2234, Australia.

1. Introduction

Analysis based on Galilean invariance [1] and more recently of positive definiteness [2] are useful in approaching some kind of validation for proposed subgrid scale models used in large eddy simulations. In [3] an attempt is made to construct general formulae for the residual stress-strain in terms of the macroscale variables (equivalently the filtered fields) based on a model error. In [4] it was demonstrated how such formulae could form a template for the discretization scheme and how the differencing coefficients and empirical parameters of the model can be associated. It was suggestive of exploiting the degrees of freedom of the coupled system of empirical and numerical difference coefficients to investigate the possible employment of constraints which capture the dominant dissipative-dispersive characteristics of the application. The process also demonstrates how the subgrid scale model can be isolated from the discretization error.

The approach of [3, 4] involves a transformation from the systems of equations which govern the macroscale to those governing the microscale. As a result only general structures of the macroscale equations can be investigated with the necessity of incorporating into these equations a relatively large number of unknown empirical parameters. Applying tests such as Galilean invariance along with other physical constraints can considerably reduce the number of empirical parameters leading to an expression for the residual stress-strain which approaches practical application (see [3]). The same transformation technique applied to the inverse map, i.e. from the microscale to the macroscale systems, is less useful since relatively high frequency oscillations contained in the microscale solutions are not removed and useful definitions of the model error are more difficult to construct.

This difficulty can be overcome by effectively incorporating into the transformation the filtering process to remove the oscillations of relatively high frequencies. The result is a formulation for the residual stress-strain with much of the empiricism removed.

The filtering process generates a one-parameter family of filtered fields from exact solutions of the equations of fluid motion. One can examine the behaviour of the equations of motion under the action of this one-parameter family of filtered fields. This ultimately leads to useful definitions for the model error of the filtered or macroscale equations. The model error can be directly associated with the approximation of the residual stress-strain of the filtered equations of motion. By introducing the scale parameter as an independent variable along with the usual space and time coordinates it is found that the residuals satisfy a partial differential equation constraint through which the model error is related. Under this constraint the model error of the governing filtered equations can be estimated given any sub-grid scale model. In addition these derived identities suggest approximation schemes for the residual stress-strain.

A brief outline of the approach will be presented here in a relatively informal manner and for brevity the description is restricted to incompressible fluids. A more rigorous description of the approach starting from the equations of compressible fluids will be presented elsewhere.

2. Model Error

Let Ω denote the space domain with independent coordinates (x^a) ($a = 1, 2, 3$) which correspond to the usual cartesian coordinates $(x^1, x^2, x^3) = (x, y, z)$. Let $M = \Omega \times T$ denote the space of independent variables (x^a, t) , where T is the semi-infinite interval $t \geq 0$, and t is the time. Let N denote the space $M \times I$, where I is the semi-infinite interval $\eta \geq 0$, and η is some parameter associated with scale to be defined below. Let u^α ($\alpha = 1, \dots, 4$) denote the dependent variables on N , where $u^a = v^a$ ($a = 1, 2, 3$) is the filtered velocity and $u^4 = p$ is the filtered pressure. The Gaussian filter operating on space sections Ω of N (i.e. for t and η held constant) for a dependent variable $u^\alpha(x^a, t, \eta)$ is given by

$$u^\alpha(x^a, t, \eta) = \int_{\Omega} G(x^a - \hat{x}^a, \eta) u^\alpha(\hat{x}^a, t, 0) d\hat{\Omega} \quad (1)$$

where $d\hat{\Omega} = d\hat{x}d\hat{y}d\hat{z}$ is the spatial volume element and

$$G(x^a, \eta) = (4\pi\eta)^{-3/2} \exp[-\delta_{cd} x^c x^d / (4\eta)] \quad (2)$$

where $\delta_{cd} = \delta_c^d = \delta^{cd} = 1$ for $c = d$ and zero otherwise. Here and throughout we use nondimensional variables and for convenience the indices a, b, c, d, e, f, g will be used specifically for the range 1 to 3. The

Greek indices α, β will be used specifically for the range $1 \leq \alpha, \beta \leq 4$. The Einstein summation convention is used. The parameter η is associated with scale along which the smooth transitions of microscale to macroscale systems occurs. We can write

$$\eta = \beta \epsilon^2 / 2 \quad (3)$$

where $\epsilon = l/L$ represents the ratio of the microscopic length scale l (smallest resolvable characteristic length scale) and the macroscopic length scale L . The parameter β (> 0) is chosen to control the rate of damping of oscillations in the dependent variables.

If all dependent variables on N are smooth and vanish as each of $|x|$, $|y|$ and $|z|$ tend to infinity on the space section Ω then the filter (1) is a solution to the Cauchy problem satisfying

$$\frac{\partial u^\alpha}{\partial \eta} = \Delta u^\alpha \quad (4)$$

with the data $u^\alpha(x^a, t, 0)$ prescribed on the section $N|_{\eta=0}$. Here

$$\Delta = \delta^{cd} \frac{\partial^2}{\partial x^c \partial x^d} \quad (5)$$

and the Cauchy problem is defined such that the scale parameter replaces the role traditionally taken by the time t (t appears only as a parameter). Integration of the diffusion equation (4) with respect to the parameter η will generate a one-parameter family of fields $u^\alpha(x^a, t, \eta)$ on N from the initial data $u^\alpha(x^a, t, 0)$ prescribed on the section $N|_{\eta=0}$.

The motivation behind the introduction of the filter (1) is to damp out oscillations of relatively high frequencies that may exist in the $u^\alpha(x^a, t, 0)$. As a result of the special property of the diffusion equation the same type of damping can be effected as (4) is integrated along the scale parameter η . If the spatial domain is bounded this equation may be supplemented with boundary conditions with the same consequence of damping. Hence we may regard the filtering operation to be effected in the general sense by the integration of the partial differential equation (4) with respect to η and ignore the integral filter operator (1) altogether.

We define the functions $\tilde{f}^\alpha \in C^\infty(N)$ ($\alpha = 1, \dots, 4$)

$$\begin{aligned} \tilde{f}^a &= v_t^a + v^b v_b^a + \delta^{ab} p_b - \mu \delta^{cd} v_{cd}^a \\ \tilde{f}^4 &= v_b^b \end{aligned} \quad (6)$$

where the subscripts t and b , respectively, denote differentiation with respect to t and x^b , respectively. We are using nondimensional variables so

that μ is the inverse of the Reynolds number. Let $u^\alpha(x^a, t, 0)$ be a solution of

$$\tilde{f}^\alpha = 0, \quad \eta = 0 \quad (7)$$

i.e. $u^\alpha(x^a, t, 0)$ is an exact solution of the equations of fluid momentum and continuity. From the prescribed data $u^\alpha(x^a, t, 0)$ we can generate a one-parameter family of fields $u^\alpha(x^a, t, \eta)$ by the integration of (4) with respect to η . We now investigate the behaviour of the \tilde{f}^α of (6) under the action of these fields.

Differentiating (6) with respect to η , and noting (4), gives after some manipulation

$$\frac{\partial \tilde{f}^\alpha}{\partial \eta} = \Delta \tilde{f}^\alpha - s^\alpha \quad (8)$$

where

$$s^a = 2\delta^{cd}v_c^b v_{bd}^a, \quad s^4 = 0 \quad (9)$$

Let $e^\alpha \in C^\infty(N)$ such that

$$e^\alpha = \frac{\partial r^\alpha}{\partial \eta} - \Delta r^\alpha - s^\alpha \quad (10)$$

for some $r^\alpha \in C^\infty(N)$ such that

$$r^\alpha = 0, \quad \eta = 0 \quad (11)$$

Let

$$f^\alpha = \tilde{f}^\alpha + r^\alpha \quad (12)$$

We refer to the r^α as the residuals. It follows that

$$\frac{\partial f^\alpha}{\partial \eta} = \Delta f^\alpha + e^\alpha \quad (13)$$

By definition

$$f^\alpha = 0, \quad \eta = 0 \quad (14)$$

First, consider the case where Ω is unbounded and the flow vanishes as the $|x^a|$ tend to infinity. Then (13)-(14) defines a Cauchy problem for the f^α with formal solution given by

$$f^\alpha(x^a, t, \eta) = \int_0^\eta \int_\Omega G(x^a - \hat{x}^a, \eta - \hat{\eta}) e^\alpha(\hat{x}^a, t, \hat{\eta}) d\hat{\Omega} d\hat{\eta} \quad (15)$$

Here the definition of the Cauchy problem is used in the sense that η replaces the traditional role taken by the time t , and t appears only as a parameter. The right hand side of (15) defines the model error of the

filtered equations of fluid motion in an unbounded spatial domain Ω . The aim is to find the residual terms r^α which render the e^α sufficiently small. If the residuals r^α are known exactly, i.e. r^α satisfy (10) such that $e^\alpha = 0$, then the Cauchy problem (13)-(14) yields the trivial solution $f^\alpha = 0$ for $\eta \geq 0$.

If Ω is bounded then we have through the prescription of the u^α on the boundary $\partial\Omega$ of Ω the boundary conditions

$$f^\alpha = \psi^\alpha(x^\alpha, t, \eta), \quad (x^\alpha) \in \partial\Omega \quad (16)$$

where the ψ^α are given through the prescription of the u^α on the boundary $\partial\Omega$. The system (13), (14) and (16) can be regarded as an initial/boundary value problem for the f^α , where as above η replaces the traditional role taken by the time t , and t appears only as a parameter.

For the initial-boundary problem (13), (14) and (16) it follows from [5] (pp. 301-303) that, if for some $\eta_0 > 0$ and $\delta_0 > 0$,

$$|\psi^\alpha| < \delta_0/2, \quad |e^\alpha| < \delta_0/(2\eta_0); \quad 0 < \eta < \eta_0, \quad t \geq 0 \quad (17)$$

then

$$|f^\alpha| < \delta_0; \quad (x^\alpha) \in \Omega, \quad 0 < \eta < \eta_0, \quad t \geq 0 \quad (18)$$

The inequality (18) can be defined as the model error associated with the filtered equations of motion for the bounded Ω case. The aim is to find the residual terms r^α which render the e^α sufficiently small. The inequality on ψ^α is obtained by a suitable prescription of boundary conditions involving the velocity, and possibly the fluid pressure.

The derivations given above are important in that they demonstrate how the model error associated with the governing filtered equations can be estimated given any prescribed subgrid scale model r^α . On the other hand (10) is suggestive of possible approximations for the r^α . Without meaning to be exhaustive three are presented in the following section.

3. Approximation of the Residuals

3.1. ASYMPTOTIC APPROXIMATION

The right hand side of (10) suggests, for sufficiently small η , an expansion of the form

$$r^\alpha = \sum_{p=0}^P \eta^p r_{(p)}^\alpha(u^\beta, u_i^\beta, u_{ij}^\beta) \quad (19)$$

for some $P \geq 1$, where $r_{(p)}^\alpha \in C^\infty(N)$ depend only on the indicated arguments, i.e. they have no explicit dependence on the independent coordinates x^α, t, η . By construction

$$r_{(0)}^\alpha = 0 \quad (20)$$

We seek an approximate solution by substituting this expansion into the right hand side of (10) and collecting like terms in powers of η . The following identities are obtained:

$$\begin{aligned} r_{(1)}^\alpha &= s^\alpha \\ r_{(p)}^\alpha &= \frac{1}{p} [\Delta r_{(p-1)}^\alpha - \frac{\partial r_{(p-1)}^\alpha}{\partial \eta}], \quad 2 \leq p \leq P \end{aligned} \quad (21)$$

and

$$e^\alpha = -\eta^P [\Delta r_{(P)}^\alpha - \frac{\partial r_{(P)}^\alpha}{\partial \eta}] \quad (22)$$

For $P = 1$ we have

$$r^a = 2\eta \delta^{cd} v_c^b v_{bd}^a, \quad r^4 = 0 \quad (23)$$

The model error for the unbounded Ω case can be obtained by calculating e^α from (22) and substituting the result into (15) to obtain

$$\begin{aligned} f^a(x^g, t, \eta) &= -4 \int_0^\eta \hat{\eta} \int_\Omega G(x^g - \hat{x}^g, \eta - \hat{\eta}) \delta^{cd} \delta^{ef} (v_{ce}^b v_{bdf}^a)(\hat{x}^g, t, \hat{\eta}) d\hat{\Omega} d\hat{\eta} \\ f^4(x^a, t, \eta) &= 0 \end{aligned} \quad (24)$$

In balance form we can write

$$r^a = (r^{ab})_b \quad (25)$$

where

$$r^{ab} = 2\eta \delta^{cd} v_c^b v_d^a \quad (26)$$

and we have omitted terms involving v_b^b , v_{bi}^b , etc. The symmetric tensor r^{ab} represents the residual stress-strain which satisfies the requirement of Galilean invariance (see [1]). We also note that the above approximation of the residual is within the general structure derived in [3].

Higher order expressions could be obtained using this procedure. For $P = 2$ we obtain

$$r^a = 2\eta \delta^{cd} v_c^b v_{bd}^a + 2\eta^2 \delta^{cd} \delta^{ef} v_{ce}^b v_{bdf}^a \quad (27)$$

The residual stress-strain in this case is given by the symmetric tensor

$$r^{ab} = 2\eta \delta^{cd} v_c^b v_d^a + 2\eta^2 \delta^{cd} \delta^{ef} v_{ce}^b v_{df}^a \quad (28)$$

which also satisfies the required condition of Galilean invariance.

3.2. SCALE DISCRETIZATION

On some slice $N|_{\eta=\text{constant}}$, we seek to solve

$$f^\alpha = \tilde{f}^\alpha + r^\alpha \approx 0 \quad (29)$$

for some approximation of r^α . An implicit finite difference approximation of the right hand side of (10) across any two slices $N|_{\eta=\eta_1}$ and $N|_{\eta=\eta_0}$ can be written

$$(r^\alpha|_{\eta=\eta_1} - r^\alpha|_{\eta=\eta_0})/(\eta_1 - \eta_0) - (\Delta r^\alpha + s^\alpha)|_{\eta=\eta_1} \approx 0 \quad (30)$$

In view of (10) the term e^α is related to the truncation error of the difference approximation (30). If r^α and s^α are known exactly on the slice $N|_{\eta=\eta_0}$ then e^α is given by

$$e^\alpha = -\frac{1}{2}\eta \frac{\partial^2 r^\alpha}{\partial \eta^2} \quad (31)$$

where evaluation of the partial derivative with respect to η is taken at some point in the interval (η_0, η_1) . For the case $\eta_0 = 0$ (30) reduces to (recalling (11))

$$\Delta r^\alpha - \frac{1}{\eta} r^\alpha + s^\alpha \approx 0, \quad \eta = \eta_1 \quad (32)$$

Note that we have used a backward Euler scheme (with respect to η) which avoids the evaluation of s^α on the slice $N|_{\eta=\eta_0}$. On the slice $N|_{\eta=\eta_1}$, we iteratively solve the coupled system (29) and (32). The system (29) and (32) will be discretized in time and space and solved by iteration within each timestep.

The procedure could be extended by discretizing across more than one scale element, $0 = \eta_0 \leq \eta_1 \leq \dots \leq \eta_P$ for some $P \geq 1$. On each slice $N|_{\eta=\eta_p}$, $p = 1, \dots, P$, a grid system for the spatial discretization is required. For increasing scale a coarser spatial grid system is used. With present day computer hardware capacity it is likely that anything larger than $P = 2$ is not practical. In current dynamic modelling techniques the prescription for the residual r^α on the scale grid point $\eta = \eta_1$ is assumed to be known (usually the Smagorinsky model is assumed). In such a case the e^α for the first scale element would not be given by (31) since one must include the error associated with the prescribed subgrid scale model assumed on the slice $N|_{\eta=\eta_1}$. This error is obtained by first estimating the e^α by substituting the prescribed subgrid scale model into the right hand side of (10).

The problem here is prescribing a suitable model on the finer space grid system defined at $\eta = \eta_1$. Using only two spatial grid systems defined on the slices $N|_{\eta=\eta_1}$ and $N|_{\eta=\eta_2}$ we can avoid this difficulty if we can make the assumption that there exists some relationship of the form

$$r^\alpha|_{\eta=\eta_2} = F^\alpha(r^\beta|_{\eta=\eta_1}) \quad (33)$$

where F^α are some known functions of the indicated arguments. Using a trapezoidal scheme with respect to η for the approximation of (10) yields

$$\frac{r^\alpha|_{\eta=\eta_2} - r^\alpha|_{\eta=\eta_1}}{\eta_2 - \eta_1} - \frac{1}{2} \Delta (r^\alpha|_{\eta=\eta_2} + r^\alpha|_{\eta=\eta_1}) - \frac{1}{2} (s^\alpha|_{\eta=\eta_2} + s^\alpha|_{\eta=\eta_1}) \approx 0 \quad (34)$$

Such a formulation is especially advantageous since $e^\alpha = O((\eta_2 - \eta_1)^2)$. The systems (33) and (34) are coupled to (29), which are also solved on the slices $N|_{\eta=\eta_1}$ and $N|_{\eta=\eta_2}$. These are iterated within each timestep and the terms $s^\alpha|_{\eta=\eta_2}$ and $s^\alpha|_{\eta=\eta_1}$ updated from the velocity fields computed on the two grid systems.

References

1. Speziale, C.G. (1985) Galilean invariance of subgrid-scale stress models in large-eddy simulation of turbulence, *J. Fluid Mech.*, **Vol. 156**, pp. 55–62
2. Wang, L. (1997) Frame-indifferent and positive-definite Reynolds stress-strain relation, *J. Fluid Mech.*, **Vol. 352**, pp. 341–358
3. Pantelis, G. (1998) Derivation of macroscale equations for a class of physical applications, *Acta Applicandae Mathematicae*, **Vol. 54**, pp. 59–73
4. Pantelis, G. (1997) The construction of general structures of large eddy simulation models, in *Advances in DNS/LES*, C. Liu and Z. Lui (Eds.), Greydon Press, Columbus, pp. 393–400
5. Sobolev, S.L. (1964) *Partial Differential Equations of Mathematical Physics*, Pergamon Press

MULTI-BLOCK LARGE-EDDY SIMULATIONS OF TURBULENT BOUNDARY LAYERS

ANDREA PASCARELLI, UGO PIOMELLI

Department of Mechanical Engineering

University of Maryland, College Park, MD 20742

AND

GRAHAM V. CANDLER

Department of Aerospace Engineering and Mechanics

University of Minnesota, Minneapolis, MN

Abstract

Time-developing turbulent boundary layers over an isothermal flat plate at free-stream Mach numbers of 0.3 and 0.7 are computed using an explicit finite-difference method on structured multi-block grids. The size of each block is adjusted depending on the dimension of the largest structures present locally in the flow. This results in substantial savings of memory and CPU time, compared to standard single-block methods. The near-wall region is computed using a smaller domain, repeated periodically in the spanwise direction. The outer layer, which contains larger structures, is computed using a domain that is twice as wide. Although the flow at the interface between the blocks has a periodicity length determined by the inner-layer block, within a few grid points longer wavelengths are generated. The velocity statistics and rms intensities compare well with single-block calculations that use substantially more grid points.

1. Introduction

In applications that involve the interaction of a fluid stream with solid boundaries, the different length scales of the turbulent eddies in the inner and outer layers can pose a significant challenge for numerical simulations that resolve the energy-carrying structures, such as direct and large-eddy simulations of turbulence. Chapman [1] and Reynolds [2] studied the grid

requirements necessary to resolve the turbulent boundary layer. In the outer layer, the turbulent eddies scale with δ . To resolve such structures it is necessary to use a grid-spacing scaled in outer units, $\Delta x_i/\delta$. The number of grid points required to resolve the outer layer is proportional to $Re^{0.4}$ [1], (where $Re = U_\infty \ell/\nu$ is the Reynolds number based on the free-stream velocity, U_∞ , and a reference length, ℓ , of the same order as the computational domain size, L_i). On the other hand, since the inner-layer structures scale in wall units, the grid spacing in wall units, Δx_i^+ (where a plus indicates quantities normalized by the friction velocity u_τ and ν), must be kept constant. This results in a number of points in each direction given by

$$N_i = \frac{L_i}{\Delta x_i} = \frac{\nu}{\Delta x_i u_\tau} \frac{L_i \ell U_\infty}{\ell \nu} \frac{u_\tau}{U_\infty} = \frac{1}{\Delta x_i^+} \frac{L_i}{\ell} Re \sqrt{\frac{C_f}{2}} \sim Re^{1-\alpha}, \quad (1)$$

where it is assumed that $C_f \sim Re^{-2\alpha}$. For $\alpha \simeq 0.1 - 0.125$ this yields a total number of grid points that scales like $N \sim Re^{2.6}$.

These scaling arguments dictate the size of computational grids that must be used by numerical simulation methods that resolve the energy-carrying turbulent flow structures. In Direct Numerical Simulations (DNS) all of the relevant structures are resolved, down to the smallest scales of motion, and no modeling is used. In Large-Eddy Simulations (LES), only the energy-carrying structures are computed accurately; the small, subgrid, scales, which are more isotropic and drain energy from the large scales through the cascade process, are modeled. LES can result in significant savings over DNS, in terms of computational costs, especially when no solid boundaries are present: if the grid size corresponds to a wave-number in the inertial region of the spectrum, the resolution required by LES becomes independent of the Reynolds number. When the energy-carrying structures are Reynolds-number dependent, as is the case in the near-wall region of a boundary layer, the cost of the calculations is again affected by the Reynolds number, and is driven by the inner-layer resolution requirements. Although significant savings can be achieved over DNS, the application of LES to high Reynolds number external flows is still expensive.

The strong Reynolds-number dependence of the number of required grid points is due to the fact that the entire computational domain is discretized with a grid spacing that scales on the very small inner variables. In principle, the inner layer does not require a computational domain as large as the outer one. Jimenez and Moin [3] investigated the “minimal channel flow unit,” and concluded that a computational domain that spans approximately 250 – 350 wall units in the streamwise direction and 100 wall units in the spanwise direction is sufficient to sustain turbulence in plane-channel flow. Thus, a computational domain of these dimensions contains a sufficient number of turbulent structures (hairpins, quasi-streamwise vortices,

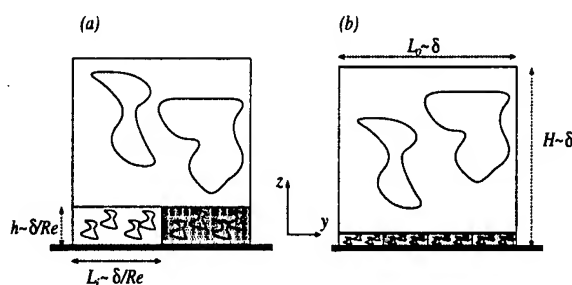


Figure 1. Sketch of the multi-block structure in the cross-plane with "inner-layer units". The flow is out of the paper. (a) Low Reynolds number; (b) high Reynolds number.

etc.) to allow the dynamic cycle of generation and destruction of such eddies to take its natural course.

Thus, a possible way to decrease the cost of the calculation of the inner layer in flows that are homogeneous in one direction, is to use a nearly minimal flow-unit in the near-wall region that is repeated periodically, and a larger computational domain in the outer region (Figure 1). In the spanwise and wall-normal directions, the "inner-layer unit" (ILU) would have constant dimensions in wall units. Therefore, its size (in outer variables) would scale like Re^{-1} , and it would require a constant number of grid points in the spanwise and wall-normal directions. The number of points required to resolve an ILU would be proportional to $Re^{0.9}$. The size of the outer-layer block, on the other hand, would depend on the boundary-layer thickness only, since the structures there scale like δ . As the Reynolds number increases, the physical dimensions of the inner-layer unit would decrease, and the unit would be replicated as many times as necessary to match the outer flow domain (Figure 1b). Thus, the cost of the calculation of the inner layer would be a relatively weak function of the Reynolds number, as the size of the ILU remains constant. The interface between the smaller inner-layer domains and the larger outer-layer ones may pose a problem, since the largest eddy present at the interface between layers is determined by the size of the ILU.

In this study the multi-block approach is proposed and tested in a wall-bounded flow with one direction of homogeneity, namely a temporally developing boundary layer. Single block LES calculations were performed at two Mach numbers, and the results are compared with those obtained using the inner-layer unit approach. In the next section, the problem formulation, numerical method and subgrid-scale model used are described. Then, computational results are presented and discussed. Finally, some conclusions are drawn in the last section.

2. Problem formulation

The governing equations for compressible LES are obtained through the application of spatial Favre-filtering [5, 6] to the Navier-Stokes equations to separate the effects of the (large) resolved scales from the (small) subgrid-scale motions. A Favre-filtered variable is defined as: $\tilde{f} = \overline{\rho f} / \bar{\rho}$. The Favre-filtered compressible Navier-Stokes equations of motion are given by

$$\frac{\partial \bar{\rho}}{\partial t} + \frac{\partial}{\partial x_j} (\bar{\rho} \tilde{u}_j) = 0, \quad (2)$$

$$\frac{\partial}{\partial t} (\bar{\rho} \tilde{u}_i) + \frac{\partial}{\partial x_j} (\bar{\rho} \tilde{u}_j \tilde{u}_i + \bar{p} \delta_{ij} - \tilde{\sigma}_{ji}) = - \frac{\partial \tau_{ji}}{\partial x_j} \quad (3)$$

$$\frac{\partial}{\partial t} (\bar{\rho} \tilde{E}) + \frac{\partial}{\partial x_j} [(\bar{\rho} \tilde{E} + \bar{p}) \tilde{u}_j - \tilde{\sigma}_{ji} \tilde{u}_i + \tilde{q}_j] = - \frac{\partial}{\partial x_j} (\gamma C_v Q_j). \quad (4)$$

Here,

$$\tilde{\sigma}_{ij} = 2\tilde{\mu}\tilde{S}_{ij} - \frac{2}{3}\tilde{\mu}\delta_{ij}\tilde{S}_{kk}, \quad \tilde{q}_j = -\tilde{k}\frac{\partial \tilde{T}}{\partial x_j}, \quad (5)$$

where $\tilde{\mu}$ is the molecular viscosity, and \tilde{k} is the thermal conductivity corresponding to the filtered temperature \tilde{T} , and $\tilde{S}_{ij} = (\partial \tilde{u}_i / \partial x_j + \partial \tilde{u}_j / \partial x_i) / 2$ is the resolved strain-rate tensor. The effect of the subgrid scales appears through the SGS stresses τ_{ij} , and the SGS heat flux Q_j :

$$\tau_{ij} = \bar{\rho} (\widetilde{u_i u_j} - \tilde{u}_i \tilde{u}_j) \quad (6)$$

$$Q_j = \bar{\rho} (\widetilde{u_j T} - \tilde{u}_j \tilde{T}). \quad (7)$$

It is also assumed here that $\overline{\mu(T)S_{ij}} \simeq \mu(\tilde{T})\tilde{S}_{ij}$, and an equivalent equality involving the thermal conductivity applies. Furthermore, the SGS contributions to turbulent and viscous diffusion are neglected. The subgrid-scale stresses were parametrized using the plane-averaged dynamic eddy-viscosity model [7, 8] in the form derived by Moin *et al.* [9] for compressible flows.

Equations (2–4) are solved in conservation form. The convective term is discretized using flux-vector splitting [10] with a fifth-order upwind-biased reconstruction; the diffusive terms are discretized using a fourth-order centered scheme. An explicit third-order low-storage Runge-Kutta method [11] was used for the temporal integration.

The initial condition was obtained from a single-block large-eddy simulation of the incompressible turbulent flat-plate boundary layer. The Reynolds number was $Re_{\delta_o^*} = \delta_o^* U_\infty / \nu \approx 1110$, where δ_o^* is the initial displacement thickness. The size of the computational domain was $120\delta_o^* \times 30\delta_o^* \times 22\delta_o^*$ in the streamwise, spanwise and wall-normal directions respectively; these dimensions corresponded to $6570 \times 1640 \times 1230$ wall units.

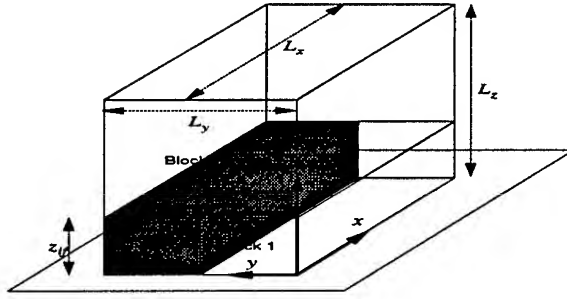


Figure 2. Multi-block arrangement for 3D turbulent boundary layer

Periodic boundary conditions were used in the streamwise and spanwise directions, and isothermal no-slip conditions were specified at solid surface, $z = 0$. The plate temperature T_w was set equal to the free-stream temperature T_∞ . The wall density was computed from conservation of mass at the wall, and, along with the specified wall temperature T_w , was used to calculate the wall pressure using the equation of state. At the top of the domain, the normal gradients of the conserved variables were set to zero.

Two types of calculations were performed; first, single-block computations were carried out as baseline cases; then, multi-block computations were performed to validate the proposed approach. In the single-block cases, $64 \times 48 \times 48$ grid points were used in the streamwise, spanwise and wall-normal directions, respectively, to discretize a domain whose size was equal to that of the initial field; resulted in an initial grid resolution $\Delta x_o^+ \approx 103$, $\Delta y_o^+ \approx 34$, and $\Delta z_{min,o}^+ = 0.15$ (a subscript "o" indicates that the initial friction velocity, $u_{\tau,o}$, and displacement thickness, δ_o^* , were used for the normalizations). The multi-block calculations were carried out using the arrangement shown in Fig. 2. Two rectangular subdomains were used, with conforming grids (the grid lines were continuous across the interfaces).

The inner layer was discretized using two subdomains, Blocks 1 and (1) in Fig. 2; the latter is purely virtual, and is periodic copy of Block 1. The inner-layer unit had the same dimension in the streamwise direction as the single-block calculation, and extended up to a height z_{if} , which could be varied. Its spanwise size was $L_{y,o}^+ = 820$. The dimensions of the ILU were significantly larger than those of the "minimal flow unit" of Jimenez and Moin [3], and were sufficient to contain several near-wall structures. The outer layer was discretized using a single block (Block 2 in the figure), whose dimensions were $L_{x,o}^+ = 6570$, $L_{y,o}^+ = 1640$; in the wall normal direction, it extended from z_{if}^+ to $L_{z,o}^+ = 1230$. Two values of z_{if} were tested: in one case, the interface was placed in the buffer region, at $z_o^+ = 30$, in the other, in the logarithmic layer at $z_o^+ = 104$.

For the multi-block calculations, the initial condition had to be modified to ensure regularity at the interface between the virtual inner-layer block and the outer block. This was achieved by assigning a generic variable q at point $y + L_y/2$ to be the average of the same variable in the single-block calculation, q_s , at points y and $y + L_y/2$. An exponentially decaying function of z was used to decrease the contribution of the point y as z increased:

$$q(y + \frac{L_y}{2}, 0) = [1 - g(z)]q_s(y, 0) + g(z)q_s(y + \frac{L_y}{2}, 0) \forall x, z; \quad (8)$$

$g(z)$ is defined as

$$g(z) = \frac{1}{\tanh(\beta)} \tanh \left[\frac{\beta(z - z_{if})}{L_z - z_{if}} \right] \quad (9)$$

The choice of the parameter β , which controls the thickness of the region over which the function transitions from 0 to 1, is crucial to the procedure, as will be shown later.

3. Results and discussion

Large-eddy simulations were carried out for two values of the Mach number, $M_\infty = 0.3$ and $M_\infty = 0.7$. The mean flow temperature and density were chosen to be $T_\infty = 300$ K and $\rho_\infty = 1$ kg/m³. In the viscosity law, $T_r = 273$ K, $T_s = 110.4$ K and the reference viscosity was $\mu_r = 1.71 \times 10^{-5}$ kg/(m · s) and $\mu_r = 3.99 \times 10^{-5}$ kg/(m · s) for the two calculations respectively [4]. The Reynolds numbers per unit length ($Re/l_r = 5.66 \times 10^6$ m⁻¹) was maintained constant while the Mach number was changed. The simulations were stopped after 2 large-eddy turnover times (LETOTs) $\delta_o^*/u_{\tau,o}$, since the boundary layer thickness was becoming comparable with the height of the computational domain. Several multi-block calculations were compared with the single-block calculations. The multi-block calculations differed by the height of the interface between the two layers, and by the thickness of the transition layer (*i.e.*, by the parameter β).

In Fig. 3 the mean velocity profiles after 0.4 LETOTs are shown. Practically no difference can be observed between the various cases at this time. The same behavior is obtained at later times for this case, as well as for the higher Mach-number case.

Figure 4 shows the rms turbulence intensities, $u_{i,rms} = \langle u_i'^2 \rangle^{1/2}$, for the low Mach-number case at $tu_{\tau,o}/\delta_o^* = 0.4$. Overall, the most accurate results were obtained when the interface was placed in the logarithmic region.

The resolved Reynolds shear stress, $-\langle \rho u''w'' \rangle$ normalized by τ_w is shown in Fig. 5 for the $M = 0.3$ calculation. The differences observed in the rms intensities are more evident here. The calculations in which the interface is

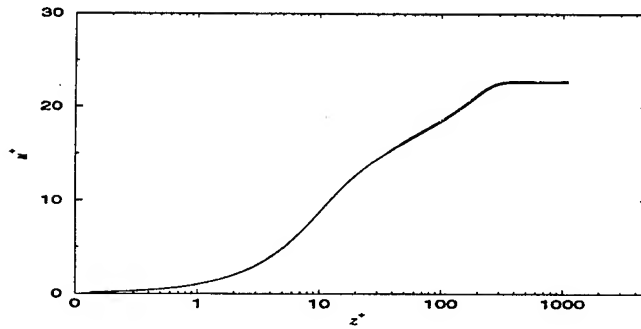


Figure 3. Mean velocity profiles at $tu_{\tau,o}/\delta_o^* = 0.4$ for $M = 0.3$. — Single block; $z_{if,o}^+ \approx 30$ wide transition; --- $z_{if,o}^+ \approx 30$ narrow transition; --- $z_{if,o}^+ \approx 104$ narrow transition.

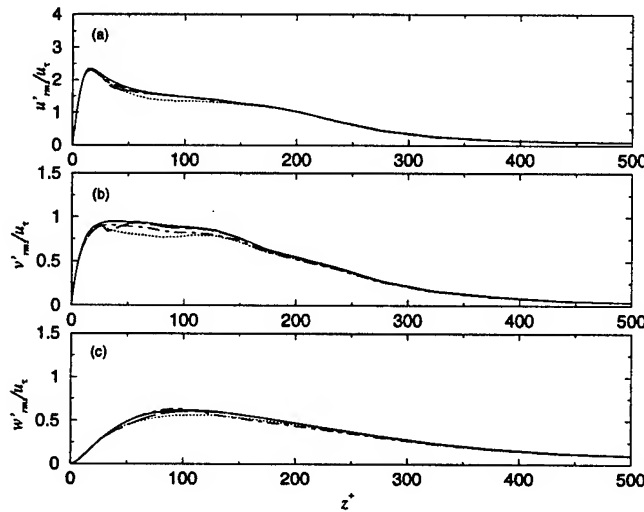


Figure 4. Turbulence intensities at $tu_{\tau,o}/\delta_o^* = 0.4$ and $M = 0.3$. (a) Streamwise, (b) spanwise, (c) wall normal. — Single block; $z_{if,o}^+ \approx 30$, wide transition; --- $z_{if,o}^+ \approx 30$, narrow transition; --- $z_{if,o}^+ \approx 104$, narrow transition.

in the buffer layer under-predict the stress throughout the buffer and logarithmic regions; more accurate prediction of the stresses is obtained when the interface is in the logarithmic region.

At the higher Mach number, better agreement was obtained. This result may be due to the fact that at higher Mach number the convection effects are more significant, and stronger non-linear interactions scramble the initial periodicity more rapidly.

The first- and second-order statistics obtained using the multi-block ap-

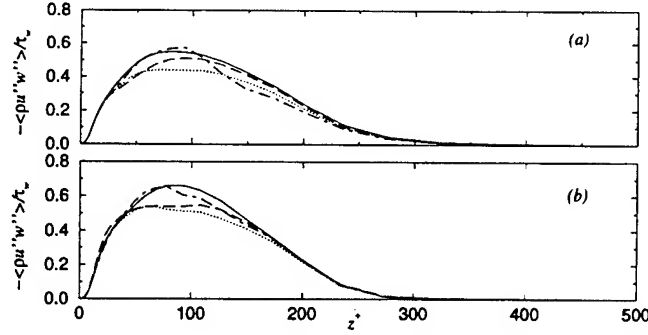


Figure 5. Resolved Reynolds shear stress for $M = 0.3$. (a) $tu_\tau/\delta^* = 0.4$; (b) $tu_\tau/\delta^* = 2$. — Single block; $z_{i,f,o}^+ \approx 30$, wide transition; --- $z_{i,f,o}^+ \approx 30$, narrow transition; -.- $z_{i,f,o}^+ \approx 104$ narrow transition.

proach with a periodic inner-layer unit compare well with those of single-block calculations at both Mach numbers examined. The main effect of the interface on the results is due to the initialization procedure, which results in a Reynolds-stress defect that was not recovered by the time the calculation was stopped. One could conjecture that, if the flow were statistically steady, and enough time were given for the nonlinear interactions, the defect would be completely filled in; the high-Mach number results support this argument. In any case, when the interface is located in the logarithmic layer this defect is rather small, and good agreement with the single-block calculations is achieved.

The effect of the interface periodicity on the turbulence structure in the outer layer remains to be investigated. To this end, define the two-point spanwise direction autocorrelation of an arbitrary fluctuating velocity component q'' :

$$R_{qq}(r, z; t) = \frac{\langle q''(x, y, z; t) q''(x, y + r, z; t) \rangle}{\langle q''(x, y, z; t)^2 \rangle}. \quad (10)$$

The streamwise velocity autocorrelation is shown in Fig. 6 at $tu_{\tau,o}/\delta_o^* = 0.4$, and at three distances from the wall (normalized using $u_{\tau,o}$). At $z_o^+ \approx 10$, the two-point correlation goes to zero well before half of the sub-domain width, showing that the width of the ILU is sufficient to include the widest structures present in the flow. At $z_o^+ \approx 35$ (one grid point above the interface), the periodicity of the interface condition results in a secondary peak of the two-point correlation at $L_y/2$ (i.e., $r/\delta^* \approx 14$). This secondary peak is higher (approximately 0.93) for the thick transition case; for the thin transition, it is reduced to 0.83. In the outer layer, at $z_o^+ \approx 167$ no correlation can be observed for either interface.

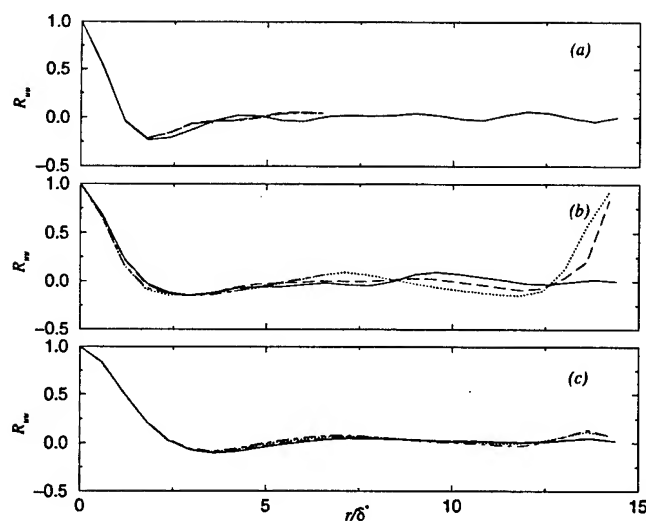


Figure 6. Two-point spatial autocorrelation function R_{uu} at $tu_{\tau,o}/\delta_o^* = 0.4$ for $M = 0.3$. (a) $z_o^+ \approx 10$, (b) $z_o^+ \approx 35$, (c) $z_o^+ \approx 167$. — Single block; $z_{if,o}^+ \approx 30$ wide transition; --- $z_{if,o}^+ \approx 30$ narrow transition; -.- $z_{if,o}^+ \approx 104$ narrow transition.

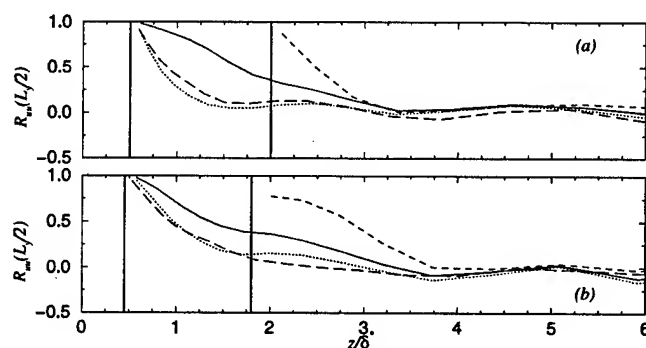


Figure 7. Two-point spatial autocorrelation function $R_{uu}(L_y/2)$. (a) $tu_{\tau}/\delta^* = 0.4$, (b) $tu_{\tau}/\delta^* = 2$. — $z_{if,o}^+ \approx 30$, wide transition, $M = 0.3$; $z_{if,o}^+ \approx 30$, narrow transition, $M = 0.3$; --- $z_{if,o}^+ \approx 104$, narrow transition, $M = 0.3$; -.- $z_{if,o}^+ \approx 30$, narrow transition, $M = 0.7$. The thick lines represent the two interfaces.

To determine the thickness over which the periodicity effects are felt, Fig. 7 plots the value of the secondary peak, $R_{uu}(L_y/2)$, as a function of z after 0.4 and 2 LETOTs. The narrow-transition calculations have a very rapid decrease of the secondary peak: within 4 grid points of the interface (about half a displacement thickness) the peak has decreased by 75%. Most of the outer layer is not affected at all by the periodicity introduced by the

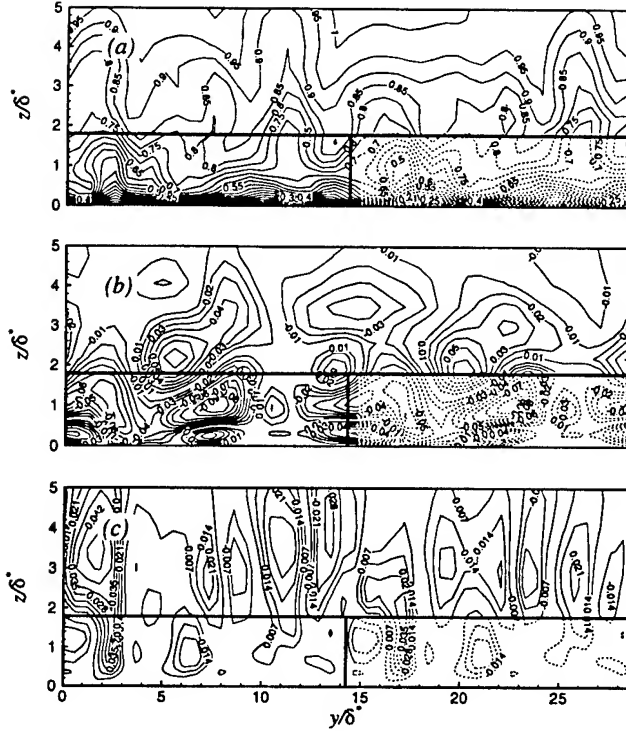


Figure 8. Instantaneous velocity iso-contours for $M = 0.3$, $tu_\tau/\delta^* = 1$. $z_{i,f,o}^+ \approx 104$, thin transition. (a) u ; (b) v ; (c) w . Dashed lines: virtual block.

ILU. The same behavior is observed in the correlations for the other velocity components.

The rapid loss of periodicity can also be illustrated through the instantaneous contours of the velocity fluctuations (Fig. 8). The difference in the structures between the two halves of the domain is quite remarkable. The large structure observed in the v contours at $y/\delta^* \approx 15$ and $z/\delta^* \approx 4$ in Fig. 8b is one example of a completely asymmetric eddy which must obviously result from the nonlinear interactions that occur above the interface.

4. Conclusions

An approach for the treatment of the near-wall layer in turbulence simulations has been presented that, in flows that have one direction of homogeneity, allows substantial savings of CPU time and memory over conventional methods. This method uses computational domains whose size is determined by the local scaling. The inner layer is resolved by a sub-domain (“inner-layer unit” or ILU) whose size is fixed in wall units. The ILU is

then repeated periodically as many times as required to match the dimensions of the outer layer sub-domain, which is determined by the size of the larger eddies present in the core of the flow.

Multi-block simulations with an ILU that is extended periodically give good agreement with single-block calculations for first- and second-order statistics, especially if the interface is located in the logarithmic layer. Placing the interface in the buffer layer, where much of the turbulent activity takes place, results in under-prediction of the Reynolds stress magnitudes and spurious pressure fluctuations. The periodicity introduced at the interface between the inner and outer layers does not spread outwards. Within a few grid points, larger structures are generated, and the correlation between the two halves of the domain is lost.

In the present study, only modest computational savings were achieved: the two multi-block calculations required only 25 and 33% fewer points than the single-block calculation. However with increased Reynolds number, the ratio of the near-wall periodic region thickness to the boundary-layer thickness decreases; this results in a dramatic increase in the number of grid points required to resolve the near wall region with a conventional method. With the present approach, the cost does not increase as rapidly since the ILU can be repeated as many times as necessary in the spanwise direction. If non-conforming meshes are used, such that the spanwise and streamwise spacings of the outer-layers can be increased over those of the inner-layer sub-domain, additional savings can be achieved.

Acknowledgments

The authors acknowledge the support from the Air Force Office of Scientific Research, under Grants No. AF/F49620-97-1-0244 (AP and UP) and AF/F49620-98-1-0035 (GVC), monitored by Dr. L. Sakell. Computer time was provided by the University of Minnesota Supercomputing Institute.

References

1. Chapman, D. R. *AIAA J.* **17**, 1293 (1979).
2. W. C. Reynolds. In *Whither turbulence? Turbulence at the crossroads*, edited by J. L. Lumley (Springer-Verlag, Heidelberg), 313 (1990).
3. J. Jimenez, and P. Moin. *J. Fluid Mech.* **225**, 213 (1991).
4. F. M. White. *Viscous Fluid Flow*. McGraw-Hill, second edition, (1991).
5. A. Favre. *J. de Mécanique* **4**, 361 (1965).
6. A. Favre. *J. de Mécanique* **4**, 391 (1965).
7. M. Germano, U. Piomelli, P. Moin, and W. H. Cabot. *Phys. Fluids A* **3**, 1760 (1991).
8. D. K. Lilly. *Phys. Fluids A* **4**, 633 (1992).
9. P. Moin, K. D. Squires, W. H. Cabot, and S. Lee. *Phys. Fluids A* **3**, 2746 (1991).
10. J. L. Steger and R. F. Warming. *J. Comput. Phys.* **40**, 263 (1981).
11. J. H. Williamson. *J. Comput. Phys.* **35**, 48 (1980).

EULERIAN TIME-DOMAIN FILTERING FOR SPATIAL LES

C. DAVID PRUETT

*Department of Mathematics
James Madison University
Harrisonburg, VA 22807*

Abstract. Eulerian time-domain filtering seems to be appropriate for LES of flows whose large coherent structures convect approximately at a common characteristic velocity; e.g., mixing layers, jets, and wakes. For these flows, we develop an approach to LES based on an explicit second-order digital Butterworth filter, which is applied in the time domain in an Eulerian context. The approach is validated through *a priori* and *a posteriori* analyses of the simulated flow of a heated, subsonic, axisymmetric jet.

1. Introduction

Historically, large-eddy simulation (LES) has relied upon spatial rather than time-domain filters. Conceptually, however, filtering in time would seem to enjoy certain advantages. First, the DNS-LES-RANS spectrum of numerical approaches would be self-consistent if time-domain filtering were exploited for LES as it is for RANS. Second, as observed by Frisch (1995) "Most experimental data on fully developed turbulence are obtained in the time domain and then recast into the space domain via the Taylor hypothesis." If time-domain analysis is natural for experiments, one wonders why spatial re-interpretation is necessary or desirable. Third, differentiation-operator/filter-operator commutation error is problematic for spatial filtering on finite domains (Blaisdell, 1997, and Vasilyev et al., 1998). Fourth, according to Moin and Jimenez (1993): "In LES, it is highly desirable for the filter width to be significantly larger than the computational mesh to separate the numerical and modeling errors. Practical considerations, however, usually require the filter width and mesh to be of the same order. In this case, there does not appear to be a necessity for higher than second order numerical methods for LES." In contrast, for the present temporally

filtered approach, the filter width is naturally an order of magnitude larger than the time step. Finally, it may be desirable in spatial LES of certain physical problems (e.g., jet flow) to manipulate the flow by localized (point) time-dependent sources for the purposes of control. Dakhoul and Bedford (1986) suggest that spatial filtering is fundamentally inconsistent with the introduction of point sources, whereas temporal filtering is not.

A few researchers (e.g., Dakhoul and Bedford, 1986) have developed space-time filters for LES, and recently, Meneveau et al. (1996) has implemented Lagrangian time-domain filtering. The author is unaware of any (solely) Eulerian time-filtered approach, the subject of this paper.

Given the possible advantages of temporal filtering, one wonders why the idea has received relatively little attention. Two possible reasons come to mind. First, time-domain filters for LES must be *causal*. That is, causal digital filters, which require past information, necessarily impose an overhead on memory requirements. Second, as intimated by Speziale (1987), temporally filtered approaches raise issues regarding Galilean invariance.

In the next section, we develop a causal digital filter that is well-suited to LES. Section 3 presents the filtered governing equations. In Section 4, the issue of Galilean invariance is addressed, and practical difficulties associated with temporal filtering are considered. The remaining sections comprise a “proof of concept” for Eulerian time-domain filtering. In Section 5, a jet-flow test case of interest in the field of aeroacoustics is defined. Section 6 reviews the numerical methodology exploited for the LES and reference DNS. In Section 7, *a priori* and *a posteriori* analyses of jet-flow data are presented. Finally, conclusions are offered in Section 8.

2. Time-Domain Filters

For LES, time-domain filters must be *causal*; that is, they cannot access future information.

2.1. CONTINUOUS CAUSAL FILTERS

In general, continuous causal filters assume the form

$$\overline{\phi}(t, \mathbf{x}) = \int_{-\infty}^t \phi(\tau, \mathbf{x}) G(\tau - t, \Delta) d\tau \quad (1)$$

where G is a kernel satisfying

$$\int_{-\infty}^0 G(\tau, \Delta) d\tau = 1 \quad \text{and} \quad \lim_{\Delta \rightarrow 0} G(\tau - t, \Delta) = \delta(\tau - t) \quad (2)$$

Here, an overline denotes a filtered field, $\delta(t)$ is the 1D Dirac delta function, and Δ is a variable temporal filter width. If G has bounded support (that

is, $\lim_{t \rightarrow -\infty} G(t, \Delta) = 0$), then partial differentiation and filtering commute. As an example of a kernel that satisfies these constraints, consider $G(t, \Delta) = H(t + \Delta)/\Delta$, where H is the Heaviside function, and whereby $\bar{\phi}(t) = \int_{t-\Delta}^t \phi(\tau) d\tau$. Because bounded support is the norm for time-domain filters, but not for spatial filters (Blaisdell, 1997), time-domain filtering enjoys a natural advantage with respect to commutation error.

2.2. DISCRETE CAUSAL FILTERS

The discrete analog of Eq. 1 is $\bar{\phi}_i = \sum_{j=0}^m p_j \phi_{i-j}$, where $\phi_i = \phi(i\Delta t, \mathbf{x})$ and Δt is a (fixed) time increment. In general, the coefficients p_j depend on the quadrature rule used to approximate the integral of Eq. 1, the specific kernel G , and the width Δ . Following Press et al. (1986), a more versatile digital filter-of *recursive* type-is given by

$$\bar{\phi}_i = \sum_{j=0}^m p_j \phi_{i-j} + \sum_{k=1}^n q_k \bar{\phi}_{i-k} \quad (3)$$

whereby $\bar{\phi}_i$ is a linear combination of previous unfiltered and filtered values. From Press et al. (1986), the frequency response of recursive filters of the form of Eq. 3 is

$$H(\Omega) = \frac{\sum_{j=0}^m p_j e^{-\iota j \Omega}}{1 - \sum_{k=1}^n q_k e^{-\iota k \Omega}} \quad (4)$$

where $\iota = \sqrt{-1}$, $\Omega = \omega^* \Delta t^*$ is the dimensionless frequency, and f^* and $\omega^* = 2\pi f^*$ are the dimensional physical and circular frequencies, respectively. (Throughout the paper, we denote dimensional quantities by asterisks.)

A class of recursive filters well-suited to LES is the "Butterworth" class. Low-pass digital Butterworth filters have the trait that p_0 vanishes in Eq. 3, which renders them fully explicit in time. The design of Butterworth filters of various order properties is discussed in Strum and Kirk (1988), to which the reader is referred. As our prototype, we adopt a second-order Butterworth filter, whose frequency response is shown in Fig. 1. The prototype, with a nominal cutoff frequency of $\Omega'_c \approx 1$, is rendered tunable by the introduction of a cutoff parameter, $R_c = \Omega_c/\Omega'_c = \Delta t/\Delta$, defined as the ratio of the actual cutoff to that of the prototype. The action of the filter on a harmonically rich signal is shown in Fig. 2 for selected values of R_c .

Time-domain filters suffer some disadvantages relative to spatial filters. First, they require storage of past information; the higher the order, the more storage. In particular, our second-order filter requires four fields of storage for each field filtered. However, relative to DNS, the net storage savings of temporally filtered LES remains substantial. Moreover, time-domain filtering, which is one-dimensional, results in less computational

effort than multi-dimensional spatial filtering. Second, unlike spatial filters, causal filters are necessarily one-sided; hence, they unavoidably introduce phase errors. Although space limitations foreclose a discussion of this point, the phase errors are predictable and usually modest. Third, digital Butterworth filters do not completely eliminate harmonics at the Nyquist frequency $\Omega = \pi$. However, in practical applications to LES, $R_c \ll 1$, in which case the amplitude at the Nyquist frequency is reduced several orders of magnitude (Fig. 1).

3. Governing Equations

Let $[\rho, p, T, u_1, u_2, u_3]^T$ be the fluid state vector comprised of the density ρ , pressure p , temperature T , and velocity components u_1 , u_2 , and u_3 . If the compressible Navier-Stokes equations (CNSE) are filtered in the time domain, the resulting system is formally identical to that of Eqs. (15), (16), and (34) of Erlebacher et al. (1992), where overlines and tildes distinguish conventionally filtered and Favre-filtered quantities, respectively. Favre (density-weighted) filtering arises naturally from the use of conservative variables and results in considerable simplification of the filtered CNSE. Specifically, for example, $\tilde{u}_i = \overline{\rho u_i} / \bar{\rho}$. For the filtered equations, the fluid state vector is comprised of a mixture of conventionally and Favre-filtered quantities, namely $[\bar{\rho}, \bar{p}, \bar{T}, \tilde{u}_1, \tilde{u}_2, \tilde{u}_3]^T$. The filtered equations contain residual [subgrid-scale (SGS)] stresses not present in the original equations, which require modeling. Several candidate SGS models are possible; however, for our present purpose, we adapt to temporal filtering the SEZHu model as detailed in Erlebacher et al. (1992). In tensor notation, and with modeled terms denoted by underlines, the dimensionless equations of state, continuity, momentum, and energy, respectively, are

$$\gamma M^2 \bar{p} = \bar{\rho} \bar{T} \quad (5)$$

$$\frac{\partial \bar{\rho}}{\partial t} + \frac{\partial (\bar{\rho} \tilde{u}_i)}{\partial x_i} = 0 \quad (6)$$

$$\begin{aligned} \frac{\partial (\bar{\rho} \tilde{u}_i)}{\partial t} + \frac{\partial}{\partial x_j} \left[\bar{\rho} \tilde{u}_i \tilde{u}_j + \bar{\rho} (\widetilde{\tilde{u}_i \tilde{u}_j} - \tilde{u}_i \tilde{u}_j) \right] = \\ - \frac{\partial \bar{p}}{\partial x_i} + \frac{\partial}{\partial x_j} \left[(\mu_v + \underline{\mu_T}) \tilde{S}_{ij} \right] \end{aligned} \quad (7)$$

$$\begin{aligned} \frac{\partial \bar{p}}{\partial t} + \frac{\partial}{\partial x_i} \left[\bar{p} \tilde{u}_i + \frac{\bar{p}}{\gamma M^2} (\widetilde{\tilde{u}_i \tilde{T}} - \tilde{u}_i \tilde{T}) \right] = \\ - (\gamma - 1) \bar{p} D + \frac{\partial}{\partial x_i} \left[(\kappa_v + \underline{\kappa_T}) \frac{\partial \tilde{T}}{\partial x_i} \right] + \frac{(\gamma - 1)}{Re} \bar{\Phi} \end{aligned} \quad (8)$$

where $D = \frac{\partial \tilde{u}_k}{\partial x_k}$ is the resolved-scale dilatation, $\tilde{S}_{ij} = 2(\tilde{e}_{ij} - \frac{1}{3}D\delta_{ij})$, δ_{ij} is the Kronecker delta, $\tilde{e}_{ij} = \frac{1}{2} \left[\frac{\partial \tilde{u}_i}{\partial x_j} + \frac{\partial \tilde{u}_j}{\partial x_i} \right]$ is the resolved-scale strain-rate tensor, and Φ is the dissipation function. For brevity, the physical viscosity and thermal conductivity are denoted, respectively, as $\mu_v = \tilde{\mu}/Re$ and $\kappa_v = \tilde{\mu}/(M^2 Re Pr)$, where Re , Pr , and M are the Reynolds, Prandtl, and Mach numbers, respectively. Similarly, the eddy viscosity and the eddy thermal conductivity are given, respectively, by $\mu_T = C_r l^2 \bar{\rho} \Pi^{1/2}$ and $\kappa_T = \mu_T/(\gamma M^2 Pr_T)$, where l is a length scale, Pr_T is the turbulent Prandtl number, γ is the ratio of specific heats, and $\Pi = \tilde{S}_{ij}\tilde{S}_{ij}$.

Of mixed type, the SEZHu model incorporates both scale-similarity and eddy-viscosity terms, which are underlined on the left and right sides of the equations above, respectively. In the momentum equation, for example, the underlined terms together model $\tau_{ij} = \bar{\rho}(\tilde{u}_i\tilde{u}_j - \underline{\tilde{u}_i\tilde{u}_j})$, the exact residual-stress tensor. The CNSE are recovered whenever the underlined terms are turned off, which renders the equations valid for either DNS or LES. For LES, the SGS model requires values for three constants. Following Erlebacher et al. (1992), we use $Pr_T = 0.5$, $C_r = 0.012$, and $l = 2\Delta x$.

For the axisymmetric jet-flow application, we exploit a cylindrical coordinate system, for which x (u_1) and z (u_1) are the axial and radial coordinates (velocities), respectively. Because of axisymmetry, the azimuthal coordinate (θ) does not come into play.

4. Galilean Invariance

Speziale (1987) raises issues regarding Galilean invariance and Eulerian time-domain filters. Ultimately, one can circumvent the issue by implementing temporal filtering in a Lagrangian frame of reference, as has been proposed by Meneveau et al. (1996). However, Lagrangian time-filtered approaches suffer at least one drawback, namely the introduction of additional closure equations, which renders SGS models potentially as computationally cumbersome as Reynolds-stress models. Thus, Eulerian time-domain filtering would be preferable whenever it is appropriate, which is the subject of this section.

4.1. DOPPLER EFFECT

Speziale (1985) shows that the spatially filtered part of a Galilean-invariant function is itself Galilean-invariant. Subsequently (Speziale, 1987), he implies that the same is not true of time-domain filters, which we have verified. In our words, although the governing equations themselves are Galilean invariant for time-domain filters, the individual terms of those equations are not. In essence, Eulerian temporally filtered quantities experience a Doppler

shift in the direction of the translational velocity of the reference frame, as illustrated below.

4.2. MODIFIED DISPERSION RELATION

We consider two reference frames, (t_M, x_M) and (t, x) , that are related by the Galilean transformation $t_M = t$, $x_M = x - vt$, and $u_M = u - v$, where v is the translational velocity of the moving frame (denoted by M) relative to the fixed one. We then consider as a model problem Burger's equation on an infinite domain,

$$\frac{\partial u}{\partial t} + u \frac{\partial u}{\partial x} = 0 \quad t > 0 ; -\infty < x < \infty \quad (9)$$

for which $u_0(t, x)$ is a known solution. If $u = u_0 + u'$ and $|u'|/|u_0| \ll 1$, then the linearized disturbance equation (LDE) holds for any small perturbation $|u'|$, namely

$$\frac{\partial u'}{\partial t} + u_0 \frac{\partial u'}{\partial x} + u' \frac{\partial u_0}{\partial x} \approx 0 \quad (10)$$

Normally the LDE arises in the context of stability theory, in which case u_0 is typically a time-independent basic state. However, in the context of LES, u_0 could be the time-dependent large-scale component of the velocity. The traveling-wave *ansatz* $u' = e^{i(kx - \omega t)}$ yields a time-asymptotic solution to Eq. 10 provided $\omega = u_0 k - i \frac{\partial u_0}{\partial x}$, which defines the dispersion relation between frequency ω and wavenumber k . A simple analysis shows that Eq. 9 is form-invariant under the Galilean transformation above. From this one infers that $\omega_M = \omega - kv$, which relates the frequencies in the fixed and the moving frames.

The practical effect of this Doppler shift is that, if the cutoff frequency ω_c is tuned to filter a particular region of the flow, that frequency may be ineffective at filtering other regions, an interpretation seemingly consistent with the experimental findings of Murray et al. (1996). This suggests that Eulerian time-domain filtering is most appropriate for flows whose large coherent structures move approximately at a common characteristic velocity u_0 ; for example, in free-shear flows such as mixing layers, jets, and wakes.

5. Test Case

We investigate a free-shear flow of relevance to the field of aeroacoustics, namely that of an axisymmetric jet. The problem is motivated by the potential of LES as a computational tool for the investigation of jet noise and its suppression. Specifically, we consider the evolution of a heated subsonic ($M_j = 0.8$) jet that exhausts into an atmosphere co-flowing at ten percent of the jet velocity. The specific parameters of the flow are as follows:

jet temperature $T_j^* = 600\text{F}$ (on which Mach number is based), ambient temperature $T_a^* = 70\text{F}$, nominal jet radius $R_j^* = 0.5$ in., ambient pressure $p_a^* = 216$ psf., and $Re = 10153$ (based on the jet conditions and the jet radius). The jet is assumed to be axisymmetric and fully expanded, in which case, in the absence of disturbances, the pressure is constant both radially and axially.

In the Results section to follow, lengths have been normalized by R_j^* , and the velocities, temperature, and density, have been normalized by U_j^* , T_j^* , and ρ_j^* , respectively.

6. Numerical Methodology

We view spatial DNS and LES as three-step processes. First, an unperturbed time-independent base state is obtained by boundary-layer techniques (Pruett, 1996). Second, the base state is subjected to temporally periodic perturbations; here, these are imposed through the streamwise velocity at the computational inflow boundary, as per Mankbadi et al., (1994). Numerical experimentation reveals most rapid development of the jet for a Strouhal number ($St = f_f^* R_j^* / U_j^*$) of 0.5, where f_f^* is the fundamental forcing frequency. An out-of-phase subharmonic is also included to enhance the pairing of adjacent vortices. The forcing amplitude is small—half a percent of U_j^* for the fundamental—and the forcing is ramped up slowly to minimize temporal transients. Third, the spatial evolution of the propagating disturbances is computed by numerical solution of the unfiltered (DNS) or filtered (LES) CNSE, as discussed below.

For both DNS and LES, we adapt the high-order numerical scheme of Pruett et al. (1995), to which the reader is referred for details. Briefly, this algorithm exploits fully explicit time advancement, high-order compact-difference methods (Lele, 1992) for aperiodic spatial dimensions, and spectral collocation methods for periodic spatial dimensions. Specifically, for the present axisymmetric-jet application, we use fourth- and sixth-order compact-difference schemes in the axial and radial dimensions, respectively. (The azimuthal dimension does not come into play because of the axisymmetry assumption.) The original method of Pruett et al. (1995) used a variable step for time advancement in the context of a third-order Runge-Kutta (RK3) scheme. However, the present LES application, which involves temporal filtering, requires a constant time step. Consequently, the original RK temporal integration has been replaced by a fixed-length, third-order Adams-Bashforth (AB3) technique.

Regarding boundary conditions, for both DNS and LES, symmetry conditions are imposed along the jet axis ($z = 0$). At the inflow boundary, we specify v , w , T , and the incoming Riemann invariants. At the far-field

boundary ($z = z_{\max}$), we adapt the non-reflecting boundary conditions of Thompson (1987) as modified by Pruett et al. (1995). At the outflow boundary, we exploit a buffer domain (Streett and Macaraeg, 1989/1990).

7. Results

For the DNS and LES results presented below, the computational domain is $0 \leq x \leq 20$ and $0 \leq z \leq 5$. The length of the domain was sufficient to allow one pairing of adjacent vortices. The final 16 percent of the domain comprises the buffer domain; results within the buffer region should be disregarded as unphysical. For later convenience, we define t_P to be the time in periods of oscillation at the fundamental disturbance frequency.

7.1. DNS

As a reference for the LES results to follow, well-resolved DNS results were obtained at a spatial resolution of 1280×512 and a temporal resolution of 4096 steps per fundamental disturbance period. The DNS required approximately 40 CPU hours on a Cray C90. Given the computational resources available, fully 3D jet flow or calculations at a higher Reynolds number were deemed impractical.

Figure 3, which presents instantaneous contours of constant density at $t_P = 18$ of the DNS, clearly shows the roll-up of the shear layer into a vortex street and the subsequent pairing of adjacent vortices, phenomena common to unbounded shear flows. It is interesting to note the fine detail of the density contours (hence the need for high resolution) and the similarity between the density and the vorticity contours (not shown due to space limitations). A similar comparison of vorticity and pressure contours (also not shown) is further revealing. Not unexpectedly, the centers of low pressure correspond with the centers of large vortices.

DNS data are further useful for *a priori* analysis of candidate SGS models. In *a priori* analysis of data obtained by particle velocimetry in the far field of a turbulent jet, Liu et al. (1994) observe high correlations between the residual-stress tensor τ_{ij} and the resolved-turbulent-stress tensor \mathcal{L}_{ij} , which is computed by *test* filtering the resolved velocity fields. Specifically, $\mathcal{L}_{ij} = \bar{\rho}(\hat{u}_i\hat{u}_j - \tilde{u}_i\tilde{u}_j)$ where conventional and Favre test-filtered quantities are denoted by checks and hats, respectively. In general, the test and grid filters have widths $\hat{\Delta}$ and Δ , respectively, whose ratio we denote as r . On the basis of their observations, Liu et al. (1994) propose the stress-similarity model $\tau_{ij} = c_L \mathcal{L}_{ij}$, where c_L is simply a constant. Does a similar result hold for time-domain filters?

Figure 4 presents instantaneous distributions of components of τ_{11} and \mathcal{L}_{11} , respectively, at $t_P = 18$. Here, we have used values of $R_c = 0.03125$ and

$R_c = 0.015625$ as cutoffs for the grid and test filters, respectively; hence, $r = 2$. (The grid-filter cutoff value is consistent with $R_c = 0.125$ for the LES calculation below, of coarser time resolution.) When adjusted for the phase lag of the test filter, correlations of 0.90 are obtained.

Following Liu et al. (1994), we also present results for $r = 1$. Whereas $r = 1$ is disallowed by conventional dynamic SGS models, Taylor-series analysis (Pruett, 1997) suggests that $r = 1$ is *optimal* for second-order filters in that the leading-order error term vanishes in the approximation of τ_{ij} by \mathcal{L}_{ij} . In this case, the correlation coefficients exceed 0.998 when corrected for the phase lag of the test filter. Moreover, coefficients on the order of 0.7 are obtained when the resolved and residual stresses are correlated at the same instant in time, without correction.

Present *a priori* tests suggests that strong correlations exist between the τ_{ij} and \mathcal{L}_{ij} , as observed also for spatial filters. We note that for $r = 1$, the stress-similarity model of Liu et al. (1994) is equivalent to the SEZHu model of Section 3 with its dissipative term turned off. It is well known, however, the similarity models alone are insufficiently dissipative for practical applications to LES. Hence, we consider an *a posteriori* test of the full SEZHu model.

7.2. LES

The SEZHu SGS model was implemented with no changes other than the incorporation of time-domain filtering in lieu of spatial filtering for the similarity term, which we evaluate in real time. Some numerical experimentation was necessary to find an appropriate level of dissipation. If the SGS model is insufficiently dissipative, the computation blows up. On the other hand, if the model is excessively dissipative, the instabilities that result in vortex shedding and pairing are suppressed. Because most model parameters were set for consistency with Erlebacher et al. (1992), dissipation was controlled by experimenting with grid resolution and with the test-filter cutoff R_c . Figure 5 presents instantaneous contours of constant density at $t_p = 18$ obtained from an LES computation of 432×192 spatial resolution, $R_c = 0.125$, and $r = 2$. Because fully explicit numerical schemes are typically over-resolved in time, it is natural that $\Delta \gg \Delta t$ ($R_c \ll 1$). Whereas the DNS calculation required 40 CPU hours, the coarser LES calculation required but two hours. Relative to the DNS results of Fig. 3, the shear-layer roll-up and pairing events of the LES computation are retarded but not prevented. Consequently, we believe that moderately resolved LES could serve as a computational platform for investigations of jet noise, and that a SGS model built on Eulerian time-domain filtering is well-suited for this task. To this end, we extract the compressible dilatation from the LES

computation, shown at $t_P = 18$ in Fig. 6. Each large vortex appears to be an acoustic quadrupole. These results suggest that significant acoustic radiation originates from the coherent structures.

8. Conclusions

An Eulerian time-filtered approach for LES has been developed, and the concept has been tested in *a priori* and *a posteriori* analyses of axisymmetric jet flow, from which we observe the following:

- Eulerian time-domain filtering is most applicable to flows whose large coherent structures convect at a common characteristic velocity, such as jets, wakes, and mixing layers.
- Time-domain filters have desirable properties in terms of operator commutivity.
- For LES with fully explicit time advancement, there is a naturally wide separation between the temporal discretization error and the dissipation of a time-domain filter.
- Butterworth filters, which are fully explicit in time and readily tunable, are well-suited to LES.
- Causal filters necessitate the storage of past information and unavoidably introduce phase errors; however, neither disadvantage is a “show stopper” for LES.
- Temporal filters, which are one-dimensional, require less computational effort than spatial filters, which are typically three-dimensional.
- In *a priori* analyses with time-domain filtering, we observe high correlations between corresponding components of the residual- and the resolved-turbulent-stress tensors, as observed by Liu et al. (1994) for spatial filters.

Acknowledgments

The author is especially grateful to Gordon Erlebacher of Florida State U., Ugo Piomelli of the U. of Maryland, Klaus Adams of ETH, Zurich, Garry Pantelis of the Scientific and Strategic Computing Group, ANSTO, Australia, Charles Meneveau of Johns Hopkins U., Jim Sochacki, his colleague at JMU, and to Kristine Meadows, Mark Carpenter, Craig Streett, Michele Macaraeg, and Bart Singer of NASA Langley Research Center, which supported this work through grants NAG1-1802 and NAG1-2033.

References

- Blaisdell, G.A. (1997) Computation of Discrete Filters and Differential Operators for Large-Eddy Simulation, in *Advances in DNS/LES*, Proceedings of the First AFOSR International Conference on DNS/LES, Louisiana Tech University, Ruston, LA, 4-8 August, 1997, pp. 333-340.
- Dakhoul, Y.M., and Bedford, K.W. (1986) Improved Averaging Method for Turbulent Flow Simulation. Part I: Theoretical Development and Application to Burgers' Transport Equation, *Int. J. Num. Meth. Fluids*, Vol. 6, pp. 49-64.
- Erlebacher, G., Hussaini, M.Y., Speziale, C.G., and Zang, T.A. (1992) Toward the Large-Eddy Simulation of Compressible Turbulent Flows, *J. Fluid Mech.*, Vol. 238, pp. 155-185.
- Frisch, U. (1995) *Turbulence*, Cambridge University Press, p. 59.
- Lele, S.K. (1992) Compact Finite Difference Schemes with Spectral-Like Resolution, *J. Comput. Phys.*, Vol. 103, pp. 16-42.
- Liu, S., Meneveau, C., and Katz, J. (1994) On the Properties of Similarity Subgrid-Scale Models as Deduced from Measurements in a Turbulent Jet, *J. Fluid Mech.*, Vol. 275, pp. 83-119.
- Mankbadi, R.R., Hayder, M.E., and Povinelli, L.A. (1994) Structure of Supersonic Jet Flow and Its Radiated Sound, *AIAA J.*, Vol. 32 no. 5, pp. 897-906.
- Meneveau, C., Lund, T.S., Cabot, W.H. (1996) A Lagrangian Dynamic Subgrid-Scale Model of Turbulence, *J. Fluid Mech.*, Vol. 319, pp. 353-385.
- Moin, P. and Jimenez, J. (1993) Large-Eddy Simulation of Complex Turbulent Flows, AIAA Paper No. 93-3099.
- Murray, J.A., Piomelli, U. and Wallace, J.M. (1996) Spatial and Temporal Filtering of Experimental Data for *A Priori* Studies of Subgrid-Scale Stresses, *Phys. Fluids A*, Vol. 8, no. 7, pp. 1978-1980.
- Press, W.H., Flannery, B.P., Teukolsky, S.A., and Vetterling, W.T. (1986) *Numerical Recipes: The Art of Scientific Computing*, Cambridge University Press, Cambridge, 1986.
- Pruett, C.D., Zang, T.A., Chang, C.-L., and Carpenter, M.H. (1995) Spatial Direct Numerical Simulation of High-Speed Boundary-Layer Flows-Part I: Algorithmic Considerations and Validation, *Theoret. Comput. Fluid Dynamics*, Vol. 7 no. 5, pp. 49-76.
- Pruett, C.D. (1996) A Semi-Implicit Method for Internal Boundary-Layer Flows, *Comp. Meth. Applied Mech. Eng.*, Vol. 137, pp. 379-393.
- Pruett, C.D. (1997) Toward Simplification of Dynamic Subgrid-Scale Models, in *Advances in DNS/LES*, Proceedings of the First AFOSR International Conference on DNS/LES, Louisiana Tech University, Ruston, LA, 4-8 August, 1997, pp. 291-298.
- Speziale, C.G. (1985) Galilean Invariance of Subgrid-Scale Stress Models in the Large-Eddy Simulation of Turbulence, *J. Fluid Mech.*, Vol. 156, pp. 55-62.
- Speziale, C.G. (1987) On the Decomposition of Turbulent Flow Fields for the Analysis of Coherent Structures, *Acta Mechanica*, Vol. 70, pp. 243-250.
- Streett, C.L., and Macaraeg, M.G. (1989/90) Spectral Multi-Domain for Large-Scale Fluid Dynamic Simulations, *App. Numer. Math.*, Vol. 6, pp. 123-139.
- Strum, R.D., and Kirk, D.E. (1988) *First Principles of Discrete Systems and Digital Signal Processing*, Addison-Wesley, New York.
- Thompson, K.W. (1987) Time Dependent Boundary Conditions for Hyperbolic Systems, *J. Comput. Phys.*, Vol. 68, pp. 1-24.
- Vasilyev, O.V., Lund, T.S., and Moin, P. (1998) A General Class of Commutative Filters for LES in Complex Geometries, submitted to *J. Comput. Phys.*

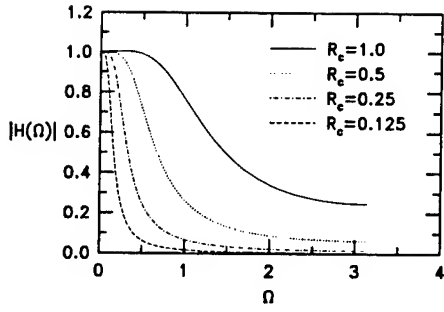


Figure 1. Transfer functions of 2nd-order digital Butterworth filters.

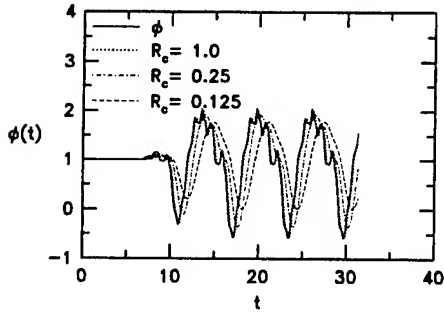


Figure 2. Time traces of unfiltered and causally filtered signals.

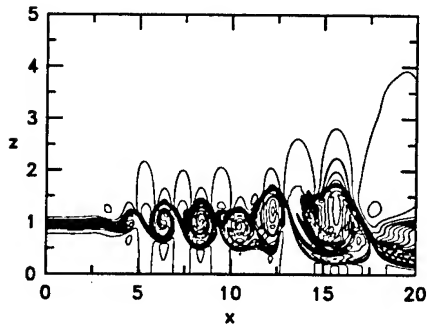


Figure 3. Contours of constant density from DNS at $t_P = 18$.

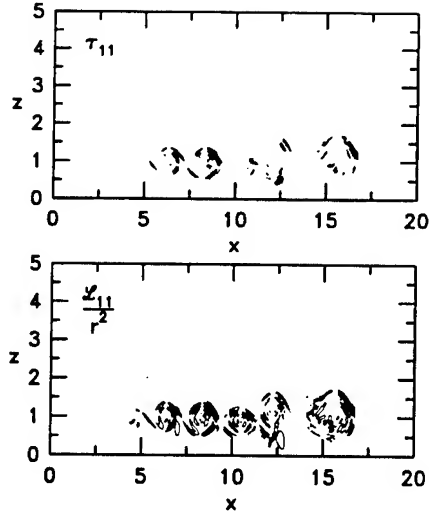


Figure 4. Comparison of residual and resolved stresses at $t_P = 18$.

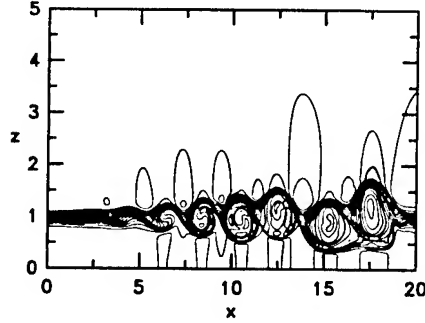


Figure 5. Contours of constant density from LES at $t_P = 18$.

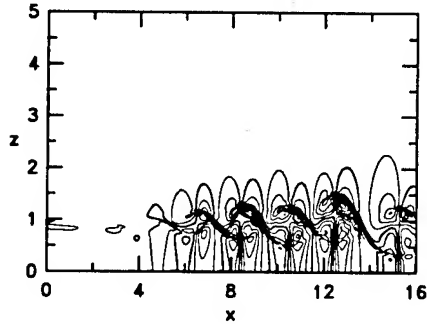


Figure 6. Isopleths of dilatation from LES at $t_P = 18$. Buffer domain not shown.

DNS OF A TURBULENT BOUNDARY LAYER UNDER A STRONG ADVERSE PRESSURE GRADIENT

MARTIN SKOTE AND DAN HENNINGSON

Department of Mechanics, KTH S-100 44 Stockholm Sweden.

Abstract.

Direct numerical simulation of a turbulent boundary layer under a strong pressure gradient has been performed. The flow considered is of equilibrium type which makes the analysis of the boundary layer equations simpler. Results from the analysis and the simulations are compared and the effects of the pressure gradient is discussed. The analysis can also be extended to the separated case, and evaluation of data from a simulation of a separated boundary layer of Na and Moin [8] is presented.

1. Introduction

In recent years direct numerical simulation (DNS) of turbulent boundary layers has become an important complement to experiments for obtaining turbulence data. The first DNS of turbulent boundary layers in an adverse pressure gradient (APG) were the temporal simulations performed by Spalart & Leonard [12] where they used a similarity coordinate system. Spalart & Watmuff [13] compared experiments and DNS of an APG turbulent boundary layer in a varying pressure gradient and they found good agreement. Skote et al. [10] performed simulations of turbulent boundary layers with moderately strong APG and compared with turbulence model predictions. Recent simulations have also been made past the point of separation. Spalart & Coleman [11] performed DNS of a separation bubble with heat transfer. Na & Moin [8] have performed DNS of a separation bubble from which data have been used in the present work.

The conditions needed for self-similarity as well as for the onset of separation have been the subject of several investigations. Clauser [2] performed experiments where he adjusted the pressure gradient such that a self-similar

turbulent boundary layer was obtained. A constant non-dimensional pressure gradient

$$\beta = \frac{\delta^*}{\tau_w} \frac{dP}{dx},$$

was shown to be a condition for self-similarity. Here δ^* is the displacement thickness, τ_w is the wall shear stress and $\frac{dP}{dx}$ is the pressure gradient. Mellor & Gibson [7] showed that self-similarity is obtained if the free stream velocity varies as $U \sim x^m$.

In the present work, direct numerical simulations (DNS) of the Navier-Stokes equations have been carried out with the objective of studying turbulent boundary layer flows in a strong adverse pressure gradient. First the numerical method will be described briefly and the implementation on different types of computers discussed. Then some results from the simulations will be discussed together with some basic theoretical considerations, and compared with a zero pressure gradient (ZPG) case. Also some data from the DNS performed by Na and Moin [8] will be presented and discussed in connection with separation.

2. Numerics and computers

The simulation is spatial and the inflow condition is a laminar profile calculated from the Falkner-Skan equation. The laminar boundary layer is then disturbed in the beginning of the computational box by a random volume force near the wall. The pressure gradient is applied through the variation of the free stream velocity, U , which is described by a power law, $U \sim x^m$. The code used for the DNS is developed at KTH and FFA [4], [5]. The program uses spectral methods with Fourier discretization in the horizontal directions and Chebyshev discretization in the normal direction. Since the boundary layer is developing in the downstream direction, it is necessary to use non-periodic boundary conditions in the streamwise direction. This is possible while retaining the Fourier discretization if a fringe region is added downstream of the physical domain. In the fringe region the flow is forced from the outflow of the physical domain to the inflow. In this way the physical domain and the fringe region together satisfy periodic boundary conditions. The fringe region is implemented by the addition of a volume force which form is designed to minimize the upstream influence. Time integration is performed using a third order Runge-Kutta method for the advective and forcing terms and Crank-Nicholson for the viscous terms.

All quantities are non-dimensionalized by the free stream velocity (U) and the displacement thickness (δ^*) at the starting position of the simulation ($x = 0$) where the flow is laminar. At that position $R_{\delta^*} = U\delta^*/\nu = 400$. The length (including the fringe), height and width of the computation box

were $700 \times 60 \times 48$ in these units. The number of modes was $512 \times 193 \times 192$. In the useful region of the computational box R_{δ^+} varies between 1000 and 3000.

Earlier the code could run on parallel computers with shared memory, e.g. the Cray C90. The code was changed to also parallelize on distributed memory machines using MPI. At each iteration, parallel FFT's are performed in the spatial directions. The data needed for each FFT is kept locally at the processor performing the FFT. This requires that large data sets are moved between the different processors when the direction of the FFT's are changed.

The FFT package used on the super-scalar processors is different from the vector counterpart. For vector machines (e.g. C90) it is important that a lot of data is processed at the same time in the vector registers. The memory is fast, and the crucial point is to avoid memory bank conflicts. For the scalar processors it is necessary to use the cache, thus smaller pieces of data should be processed. The communication with the memory is slower, so the most important point is to finish processing the data in the cache before fetching new data from memory. The performance of the code is compared for two different problem sizes and different number of processors. Two super-scalar computers are compared, a CRAY T3E at NSC in Linköping and an IBM SP2 at PDC, KTH in Stockholm. In figures 1 and 2 the performance of the code is shown as Mflop/s together with the optimal speed up, calculated from the performance on the lowest number of processors and considering that not the whole code can be parallelized. The speed up is better for case two than case one on both machines. The scaling is better on the T3E for both cases. We actually obtain an optimal performance for the larger case on the T3E. However, the overall performance is better on the SP2, which is approximately twice as fast as the T3E. Hence, for both the large and small cases, the scaling is better for the T3E associated with the higher performance of the message passing, and the overall performance is better for the SP2, mainly due to the higher performance of the FFT.

For the vector machines it is important that the vector registers are used efficiently. The vectorization is dependent on the size of the problem, a large problem will in a natural way contain long vectors. For small problems the size of the vectors can be increased by arranging the arrays in the code in a proper way. It is thus possible to optimize the code in this aspect. For case one, the performance on various CRAY vector based machines (J90 at PDC, C90 at NSC and T90 at SDSC, San Diego) has been checked for one processor computation with and without vector length optimization, see table 1.

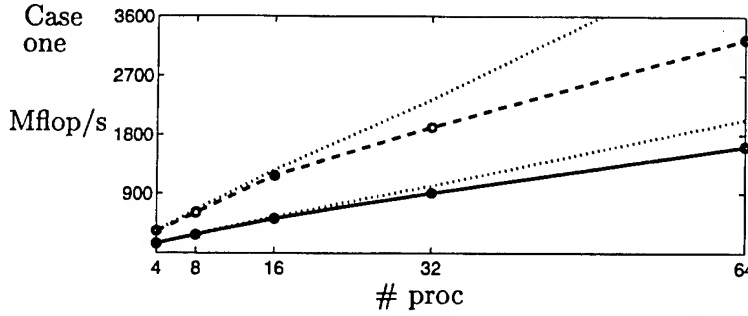


Figure 1. Mflop/s rates for different number of processors. — T3E ··· SP2. Case one: $128 \times 97 \times 128 = 1.6 \cdot 10^6$ points.

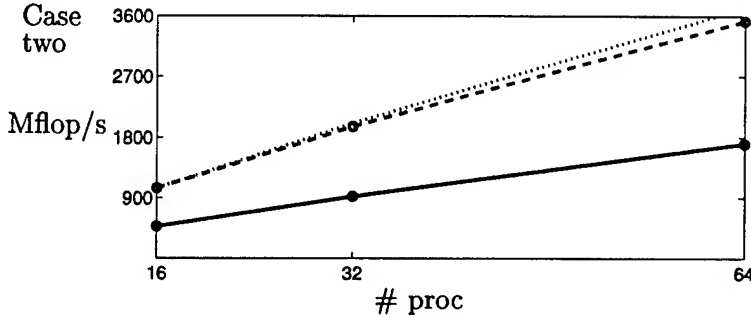


Figure 2. Mflop/s rates for different number of processors. — T3E ··· SP2. Case two: $512 \times 193 \times 256 = 25.3 \cdot 10^6$ points.

2.1. SIMULATION OF THE SEPARATED BOUNDARY LAYER

The simulation evaluated here was performed by Na and Moin [8], using a second-order finite difference method. The computational box was $350 \times 64 \times 50$ based on the δ^* at the turbulent inflow. The number of modes was $513 \times 193 \times 129$. The inflow condition was taken from Spalart's ZPG simulation. It consists of a mean turbulent velocity profile with superimposed turbulence with randomized amplitude factors while the phase was unchanged.

3. Results

In this chapter both theory and data from DNS will be presented in four different sections. First the mean flow parameters and their relations will be discussed. The outer and inner part of the boundary layer are discussed next, followed by a presentation of some data from the separated case together with a discussion of some recent theories.

	J90	C90	T90
peak processor performance	220	952	1700
performance of the code	93	361	501
with optimized vector length	100	522	710

TABLE 1. The speed on different vector machines for one processor for case one: $128 \times 97 \times 128 = 1.6 \cdot 10^6$ points.

3.1. MEAN FLOW PARAMETERS

The relation between the pressure gradient parameter β and the exponent for the free stream velocity variation m obtained from the equations of motions under the assumption of a constant ratio between the friction velocity and free stream velocity is

$$m = -\frac{\beta}{H(1 + \beta) + 2\beta} \quad (1)$$

where H is the shape factor. For details see [10], available as a free sample on <http://www.kap.nl/jrnllist.htm/JRNLHOME>. That the assumption of a constant u_τ/U can be considered as a well motivated approximation can be seen from Figure 3, where C_f for the APG and ZPG cases is plotted together with the free stream variation.

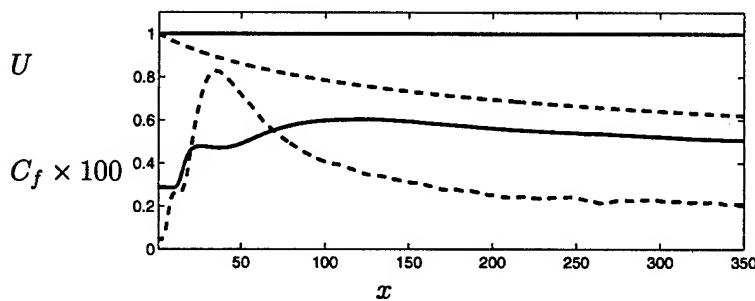


Figure 3. The free stream velocity and friction coefficient for — ZPG; - - APG

3.2. THE OUTER PART

If the viscous term is neglected in the equations describing the mean flow of a two-dimensional, incompressible, turbulent boundary layer, the equation governing the outer part of the layer is obtained. The equation can be formulated in the velocity defect F and an outer variable η ,

$$-2\beta F - (1 + 2\beta)\eta \frac{dF}{d\eta} - \frac{u_\tau}{U} \left\{ -\beta F^2 + \int_0^\infty F^2 d\eta (1 + \beta)\eta \frac{dF}{d\eta} - (1 + 2\beta) \frac{dF}{d\eta} \int_0^\eta F d\eta \right\} = \frac{dR}{d\eta} \quad (2)$$

where

$$(u - U)/u_\tau = F(\eta), \quad -\langle u'v' \rangle / u_\tau^2 = R(\eta) \\ \eta = y/\Delta(x), \quad \Delta = U\delta^*/u_\tau \quad (3)$$

If either the infinite Reynolds number limit, or the approximation of a constant u_τ/U is considered, it follows from equation (2) that a condition for self-similarity is that β is constant. In the present APG simulation the Reynolds stress profiles at different positions are not self-similar, due to the small variation in u_τ/U . For large Reynolds numbers, the profiles tend to a self-similar state. This can be seen from experiments, e.g. in Skåre and Krogstad's [9] experiments with a strong pressure gradient, or from calculations with turbulence models, [3].

In the simulation presented here, the value of the exponent m is -0.23 and the pressure gradient parameter β becomes 4.5. The shape factor is 1.9 and approximately constant. With these values on β and H obtained from the simulation, the relation (1) gives a value of $m = -0.23$, i.e. the same value given in the simulation to define the pressure gradient. From the boundary layer equation (2) it follows, see [10], that if m and β are constants, then

$$U = U_0(1 - \frac{x}{x_0})^m, \quad \Delta = (1 - \frac{x}{x_0})\Delta_0 \quad (4)$$

Note that both the virtual origin x_0 and the exponent m are parameters in the free stream velocity distribution. Thus, there is an ambiguity in the choice of m and x_0 . To obtain the true value of m , x_0 is first found by fitting the DNS data to equation 4b. Subsequently equation 4a is used to obtain m . The value of m became -0.23 at the downstream position where β was observed to be constant.

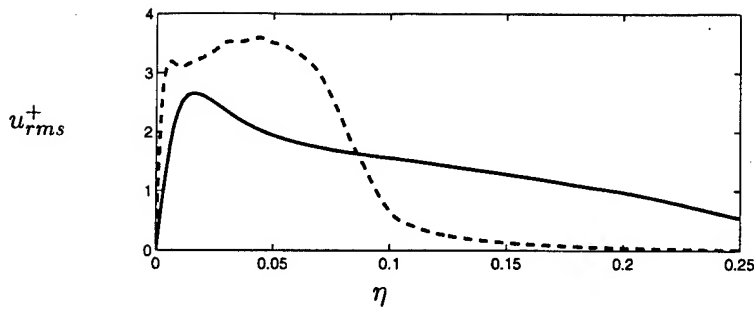


Figure 4. u_{rms} — ZPG; -- APG

In the outer part the behavior of turbulent statistics is different from the ZPG case. As an example, in the APG case a second peak develops in the u_{rms} profile as seen in Figure 4.

3.3. THE INNER PART

When neglecting the non-linear, advective terms in the equations describing the mean flow, the equation governing the inner part of the boundary layer is obtained. This equation can, when using the inner length and velocity scales ν/u_τ and u_τ be written,

$$0 = -\frac{\beta}{Re_*} + \frac{\partial^2 u^+}{\partial y^{+2}} - \frac{\partial}{\partial y^+} \langle u'v' \rangle^+ \quad (5)$$

where $Re_* = \frac{u_\tau \delta^*}{\nu}$ and $\langle u'v' \rangle$ is the Reynolds shear stress. If the ratio $\frac{\beta}{Re_*}$ is smaller than the other terms, the equation reduces to the equation governing the inner part of a ZPG boundary layer. However, for the APG case considered here this term can not be neglected. Equation (5) can be integrated to give an expression for the total shear stress,

$$\tau^+ \equiv \frac{\partial u^+}{\partial y^+} - \langle u'v' \rangle^+ = 1 + \frac{\beta}{Re_*} y^+. \quad (6)$$

The total shear stress, τ^+ , from the DNS and the curve $\tau^+(y^+)$ represented by equation (6) are shown in Figure 5. For the ZPG case, equation (6) predicts a constant shear stress of unity. The term

$$\frac{\beta}{Re_*} = \frac{\nu}{u_\tau^3} \frac{1}{\rho} \frac{dP}{dx} = \left(\frac{u_p}{u_\tau} \right)^3 \quad (7)$$

is evidently important for the shear stress distribution in the inner part of the boundary layer. The velocity scale

$$u_p = \left(\nu \frac{1}{\rho} \frac{dP}{dx} \right)^{1/3} \quad (8)$$

has to be used if the term (7) becomes very large which happens if $u_\tau \ll u_p$, i.e. the boundary layer is close to separation.

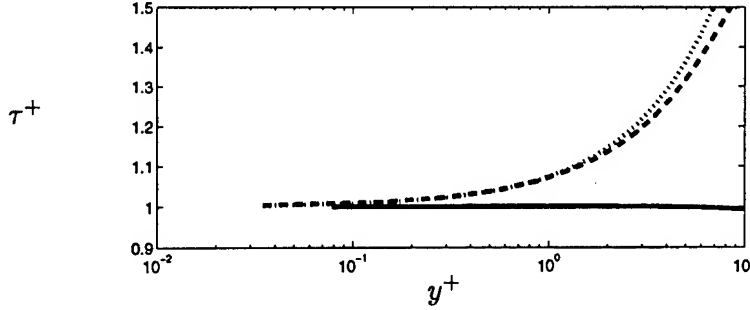


Figure 5. — ZPG; - - APG; ··· shear stress evaluated from equation (6).

When multiplying equation (6) by $\frac{\partial u^+}{\partial y^+}$ we get the mean energy budget.

$$\left(\frac{\partial u^+}{\partial y^+} \right)^2 - \langle u'v' \rangle^+ \frac{\partial u^+}{\partial y^+} = \frac{\partial u^+}{\partial y^+} + \frac{\beta}{Re_*} y^+ \frac{\partial u^+}{\partial y^+}. \quad (9)$$

The same equation is obtained if equation (5) is multiplied by u^+ . The terms are noted from left to right: direct dissipation, production, transport and pressure gradient term. The mean budget for the APG case in the inner region is shown in Figure 6. The largest contribution in the near wall region comes from the direct dissipation which is balanced by the transport term. At $y^+ = 7$ the pressure gradient term has reached its maximum and then decays to a constant value. The production of turbulent energy has its maximum at $y^+ = 8$, close to where the production and direct dissipation are equal in magnitude. All the terms balance each other, though the total sum deviates from zero at large values of y^+ . If the advective terms also are included in the total budget, the sum becomes zero but these terms are small compared to the others.

The mean budget for the ZPG case is shown in Figure 7. The dissipation and transport do not show the peaks close to the wall that are observed in the APG case. Also, the maximum in the production occurs at $y^+ = 11$, exactly where the production and direct dissipation are equal in magnitude.

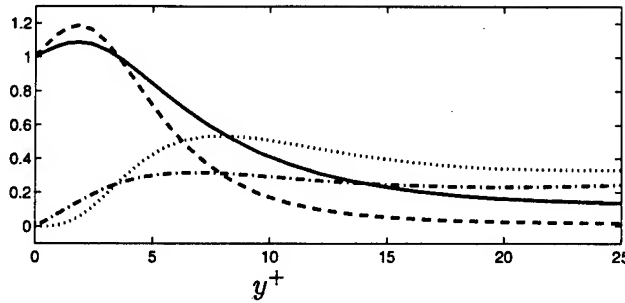


Figure 6. Energy budget for APG: -- Dissipation; ... Production; — Transport; - . - Pressure gradient term.

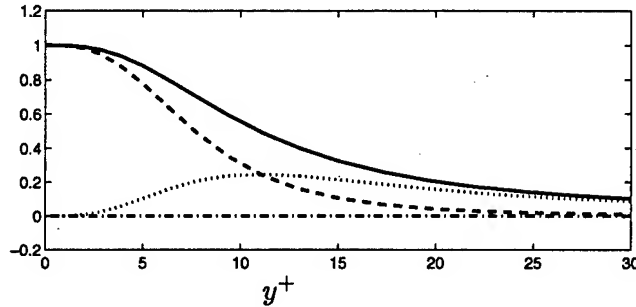


Figure 7. Energy budget for ZPG: -- Dissipation; ... Production; — Transport; - . - Pressure gradient term.

3.4. THE SEPARATED CASE

The equations (5) and (2) constitute a problem with inner and outer solutions. This problem has been treated with the method of matched asymptotic expansions by, among others, Mellor [6] and Afzal [1]. The aim is to obtain higher order terms in the matching of the inner and outer solutions. The small parameter that is used in the expansions is u_τ/U , which is related to the Reynolds number through the logarithmic friction law.

The presentation here will be very brief and only the inner part is discussed. Equation (6) can be formulated as

$$\tau^* = \frac{1}{u_*^2} \left(\nu \frac{\partial u}{\partial y} - \langle u'v' \rangle \right) \quad (10)$$

where u_* is a velocity scale that depends on y and can be expressed in either + or p units,

$$u_*^2 = u_\tau^2 + \frac{u_p^3}{u_\tau} y^+ = u_\tau^2 + u_p^2 y^p, \quad (11)$$

where u_p is defined from (8) and $y^p = yu_p/\nu$.

If u_* is used as the velocity scale, the velocity derivative can be formulated as,

$$\nu \frac{\partial u}{\partial y} \frac{1}{u_*^2} = \left(\frac{\partial u}{\partial y} \right)^* . \quad (12)$$

The matching between the inner and outer equations as described by Afzal [1] results in

$$y^* \left(\frac{\partial u}{\partial y} \right)^* = \frac{1}{\kappa} . \quad (13)$$

If the equation above is integrated the following expression in + units is obtained,

$$u^+ = \frac{1}{\kappa} \left(\ln y^+ - 2 \ln \frac{\sqrt{1 + K^+ y^+} + 1}{2} + 2(\sqrt{1 + K^+ y^+} - 1) \right) + B \quad (14)$$

with

$$K^+ = \frac{\beta}{\frac{u_p}{U} Re_{\delta^*}} = \left(\frac{u_p}{u_\tau} \right)^3 \quad (15)$$

Equation (14) is the same expression as Afzal [1] arrived at. The velocity profiles from the DNS of Na and Moin close to the point of separation are shown together with the standard log law and the extended log law (14) in figure 8. The separation occurs at $x = 158$ and the four velocity profiles are shown at $x = 150, 155, 157, 158$.

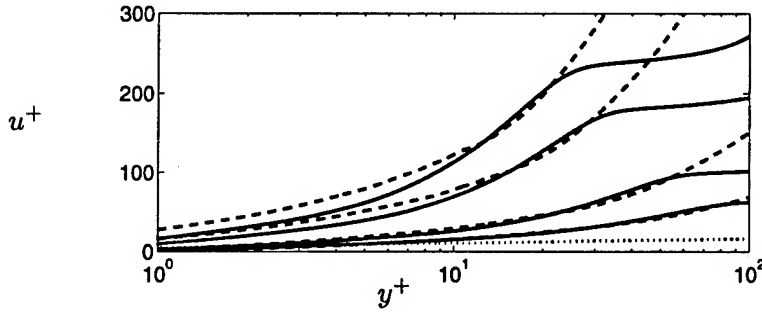


Figure 8. — DNS; - - (14) with $\kappa = 0.41$ and $B = -2$; $\cdots u^+ = \frac{1}{0.41} \ln y^+ + 5.1$

When $u_p \rightarrow 0$ equation 13 reduces to

$$y^+ \frac{\partial u^+}{\partial y^+} = \frac{1}{\kappa} , \quad (16)$$

and the usual log law is recovered. If $u_\tau \rightarrow 0$ equation 13 reduces to,

$$\sqrt{y^p} \frac{\partial u^p}{\partial y^p} = \frac{1}{\kappa}, \quad (17)$$

and the half power law is obtained,

$$u^p \equiv \frac{u}{u_p} = \frac{1}{\kappa} 2\sqrt{y^p} + C \quad (18)$$

The same velocity profiles as in figure 8 are plotted together with the half power law (18) in figure 9.

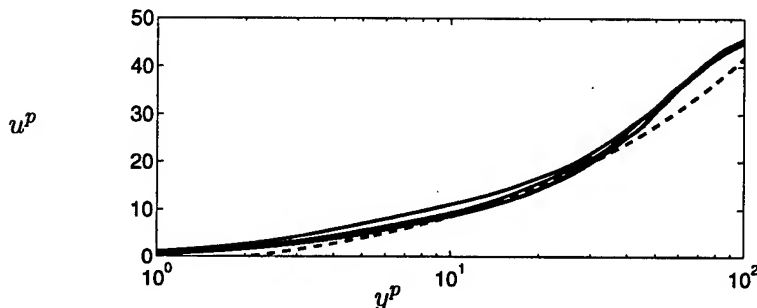


Figure 9. — DNS; - - (18) with $\kappa = 0.41$ and $C = -7$

An interesting observation is that equation (18) leads to a shape factor of two with a small correction due to the constant C . The correction vanishes for large Reynolds numbers when $u_p/U \rightarrow 0$. In both DNS at low Reynolds numbers (Spalart [12]) and experiments at large Reynolds numbers (Skåre and Krogstad [9]) of flows near separation a shape factor close to two was observed.

4. Conclusions

The parallelization of the code on distributed memory machines is an important step towards larger simulations. Even though the code performs well on shared memory systems, the limited memory on these kind of machines is an obstacle when performing larger simulations.

The simulation presented here is done with a considerable stronger adverse pressure gradient than earlier work by the authors [10]. The results were compared with a zero pressure gradient simulation and some effects of the pressure gradient could be explained by an analysis of the boundary layer equations. Also, with data from these simulations with a well defined pressure gradient and a constant pressure gradient parameter β , it is

possible to compare and validate some recent theoretical work considering relations between mean flow parameters such as those presented in [10]. The data from a separated flow from the simulation of Na and Moin [8] was compared with some recent theoretical work considering higher order terms in the logarithmic region in APG flows, such as those presented in [1]

Acknowledgments

Computer time was provided by the Center for Parallel Computers (PDC) at the Royal Institute of Technology (KTH), the The National Supercomputer Center in Sweden (NSC) at Linköping University, and The San Diego Supercomputer Center (SDSC) at the University of California. In addition we thank Prof. Parviz Moin and Na Yang at Stanford University for letting us use the data from their simulation.

References

1. N. Afzal. Wake layer in a turbulent boundary layer with pressure gradient: a new approach. In Gersten K., editor, *IUTAM Symposium on Asymptotic Methods for Turbulent Shear flows at High Reynolds Numbers*, pages 95–118. Kluwer Academic Publishers, 1996.
2. F. H. Clauser. Turbulent boundary layers in adverse pressure gradients. *J. Aero. Sci.*, 21:91–108, 1954.
3. R. A. W. M. Henkes. Scaling of equilibrium boundary layers under adverse pressure gradient using turbulence models. *AIAA J.*, 36:320–326, 1998.
4. A. Lundbladh, D. S. Henningson, and A. V. Johansson. An efficient spectral integration method for the solution of the Navier-Stokes equations. FFA-TN 1992-28, Aeronautical Research Institute of Sweden, Bromma, 1992.
5. A. Lundbladh, P. J. Schmid, S. Berlin, and D. S. Henningson. Simulation of bypass transition in spatially evolving flows. Proceedings of the AGARD Symposium on Application of Direct and Large Eddy Simulation to Transition and Turbulence, AGARD-CP-551, 1994.
6. G. L. Mellor. The large Reynolds number, asymptotic theory of turbulent boundary layers. *Intl J. Engng Sci.*, 10:851–873, 1972.
7. G. L. Mellor and D. M. Gibson. Equilibrium turbulent boundary layers. *J. Fluid Mech.*, 24:225–253, 1966.
8. Y. Na and P. Moin. Direct numerical simulation of a separated turbulent boundary layer. *J. Fluid Mech.*, 374:379–405, 1998.
9. P. E. Skåre and P.-Å. Krogstad. A turbulent equilibrium boundary layer near separation. *J. Fluid Mech.*, 272:319–348, 1994.
10. M. Skote, R. A. W. M. Henkes, and D. S. Henningson. Direct numerical simulation of self-similar turbulent boundary layers in adverse pressure gradients. *Flow, Turbulence and Combustion*, 60:47–85, 1998.
11. P. R. Spalart and G. N. Coleman. Numerical study of a separation bubble with heat transfer. *European J. Mechanics B/Fluids*, 16:169, 1997.
12. P. R. Spalart and A. Leonard. Direct numerical simulation of equilibrium turbulent boundary layers. In *Turbulent Shear Flows 5*, pages 234–252. Springer, 1987.
13. P. R. Spalart and J. H. Watmuff. Experimental and numerical study of a turbulent boundary layer with pressure gradients. *J. Fluid Mech.*, 249:337–371, 1993.

A HIGH-ORDER ACCURATE COMPACT FINITE DIFFERENCE ALGORITHM FOR THE INCOMPRESSIBLE NAVIER-STOKES EQUATIONS

R. STEIJL AND H.W.M. HOEIJMAKERS
University of Twente
Department of Mechanical Engineering
P.O. Box 217
7500 AE Enschede
The Netherlands

1. Introduction

The present paper describes a newly developed Navier-Stokes solver of fourth-order global spatial accuracy and second-order accuracy in time. The algorithm uses an explicit discretisation for the convection terms and an implicit formulation for the viscous terms. Compact-differences are used in the spatial discretisation. They offer a combination of flexibility of boundary conditions and spectral-like resolution (Lele(1992)).

A domain decomposition technique is used to enable efficient parallelisation with the Message Passing Interface (MPI). The current method is developed for Direct Numerical Simulation of three-dimensional vortical flows, for example those in aircraft wake vortex research, and may be the basis of an extension to a Large Eddy Simulation method in future work. A high-order accurate low-pass filter is used to stabilise the solution procedure. This filter is likely extendible to be used in an LES method.

The present paper describes details of spatial discretisation, parallelisation and presents some results of unsteady incompressible vortical flow simulations.

2. Numerical method

2.1. GOVERNING EQUATIONS

The fractional time-step method due to Kim and Moin(1986) is used. This method consists of two stages. The first stage consists of computing an

intermediate velocity field with components v_i , using the second order (in time) Adams-Bashfort method for the nonlinear convection terms (H_i) and the Crank-Nicholson scheme for the viscous terms. Thus:

$$v_i - u_i^n = -\Delta t \left(\frac{3}{2} H_i^n - \frac{1}{2} H_i^{n-1} \right) + \frac{\Delta t}{2Re} (\nabla^2 v_i + \nabla^2 u_i^n) \quad (1)$$

Where Re is the Reynolds number based on characteristic length scale and velocity and n denotes the time level. In three-dimensional simulations $i = 1, \dots, 3$. The nonlinear convection terms H_i are used in skew-symmetric form

$$H_i = \frac{1}{2} \left[\frac{\partial u_i u_j}{\partial x_j} + u_j \frac{\partial u_i}{\partial x_j} \right] \quad (2)$$

since it is shown in Kravchenko and Moin(1997) that this results in minimal aliasing errors.

Equation (1) can be rewritten as a Helmholtz equation for v_i :

$$\left(1 - \frac{\Delta t}{2Re} \nabla^2 \right) v_i = -\Delta t \left(\frac{3}{2} H_i^n - \frac{1}{2} H_i^{n-1} \right) + \left(1 + \frac{\Delta t}{2Re} \nabla^2 \right) u_i \quad (3)$$

A modified pressure ϕ can now be introduced, related to the actual pressure by $p = \phi - (\Delta t/2Re)\nabla^2 \phi$, which can be shown to obey the relation:

$$\nabla^2 \phi = \frac{1}{\Delta t} \frac{\partial v_i}{\partial x_i} \quad (4)$$

Finally the velocity at time level $n + 1$ is computed from:

$$u_i^{n+1} = v_i - \Delta t \frac{\partial \phi}{\partial x_i} \quad (5)$$

This time-advancement scheme is second-order accurate in time.

2.2. SPATIAL DISCRETISATION

The computational domain is divided in a number of sub-domains to enable parallelisation. In each sub-domain a uniform mesh spacing h is used in all directions. On this mesh, first derivatives in equations (3),(4) and (5) are computed using compact finite differences of sixth-order accuracy. The global conservation expressions derived in Lele(1992) are used in this work since the discretised equations are conservation equations.

The Helmholtz equations for the intermediate velocity field v_i (3) and the Poisson equation (4) for the modified pressure ϕ can be written in general form as

$$\Delta f - \lambda f = r \quad (6)$$

with $f = v_i$, $\lambda = \frac{2Re}{\Delta t}$ and $r = 2Re(\frac{3}{2}H_i^n - \frac{1}{2}H_i^{n-1}) - (\frac{2Re}{\Delta t} + \nabla^2)u_i$ for the momentum equations. For the pressure equation $f = \phi$, $\lambda = 0$ and $r = \frac{1}{\Delta t} \frac{\partial v_i}{\partial x_i}$. These equations are solved using a fourth-order compact difference iterative Helmholtz solver.

In two dimensions the method is based on a similar direct method described in Sun and Zhuang(1997), that is based on:

$$h^{-2} \begin{pmatrix} -\frac{1}{4} & -1 & -\frac{1}{4} \\ -1 & 5 + \frac{\lambda h^2 + 12}{8} \lambda h^2 & -1 \\ -\frac{1}{4} & -1 & -\frac{1}{4} \end{pmatrix} f(i, j) = -\frac{3}{2} r(i, j) - \frac{h^2}{8} (\lambda r + \Delta r)_{i,j} + O(h^4) \quad (7)$$

For the three-dimensional simulations, an equivalent expression is derived in Appendix A:

$$\begin{aligned} h^{-2} \left[\left(C_1 + \frac{\lambda h^2 + 12}{6} \right) f(i, j, k) + C_2 \{ p(i \pm 1, j, k) + p(i, j \pm 1, k) + p(i, j, k \pm 1) \} \right. \\ \left. + C_3 \{ p(i \pm 1, j \pm 1, k) + p(i \pm 1, j, k \pm 1) + p(i, j \pm 1, k \pm 1) \} + C_4 p(i \pm 1, j \pm 1, k \pm 1) \right] = \\ -2r(i, j, k) - \frac{h^2}{6} (\lambda^2 f + \lambda r + \Delta r)_{i,j,k} + O(h^4) \end{aligned} \quad (8)$$

with C_1, C_2, C_3 and C_4 given in Appendix A. Points near boundaries need a special treatment, expressions are given for (8) in Appendix B for both Dirichlet and Neumann boundary conditions.

2.3. SOLUTION PROCEDURE

The conjugate gradient method is used to solve the sparse-matrix systems that result from the discretisation of both Helmholtz equations for intermediate velocity and Poisson equation for the pressure. The regularity of the discretisation matrices is used to compute the required matrix-vector multiplications with minimum memory usage and maximum computational efficiency. In case Neumann boundary conditions are prescribed for either the Helmholtz equations or the Poisson equation a non-symmetric matrix results. Then, for this equation the bi-conjugate gradient method is used that involves two matrix-vector multiplications per iteration.

3. Filter operations

3.1. PRINCIPLES AND 1-DIMENSIONAL RELATIONS

Consider a uniform mesh of spacing h . A quantity f on this mesh can be filtered using an expression of the form (Lele(1992)):

$$\alpha \hat{f}_{i-1} + \hat{f}_i + \alpha \hat{f}_{i+1} = \sum_{k=0}^N a_k \frac{[f_{i+k} + f_{i-k}]}{2} + O(h^{2N}) \quad (9)$$

where \hat{f}_i is the filtered value of quantity f at node x_i . The coefficients a_k are determined by matching the Taylor series coefficients of various orders. Matching Taylor series coefficients up to order $2N$ results in N equations for $N + 1$ unknown a_k . An additional equation is required to determine

TABLE 1. Values of a_k for various orders of formal accuracy.

Order	N	a_0	a_1	a_2	a_3	a_4	a_5
4	2	$\frac{5+6\alpha}{8}$	$\frac{1+2\alpha}{2}$	$\frac{-1+2\alpha}{8}$			
6	3	$\frac{11+10\alpha}{16}$	$\frac{15+34\alpha}{32}$	$\frac{-3+6\alpha}{16}$	$\frac{1-2\alpha}{32}$		
8	4	$\frac{93+70\alpha}{128}$	$\frac{7+18\alpha}{16}$	$\frac{-7+14\alpha}{32}$	$\frac{1-2\alpha}{16}$	$\frac{-1+2\alpha}{128}$	
10	5	$\frac{193+126\alpha}{256}$	$\frac{105+302\alpha}{256}$	$\frac{-15+30\alpha}{64}$	$\frac{45-90\alpha}{512}$	$\frac{-5+10\alpha}{256}$	$\frac{1-2\alpha}{512}$

a_k . This equation can be obtained by imposing that the *transfer function* $T(w)$, i.e. the ratio of amplitudes of waves with wavenumber w before and after filtering, of operation (9) is 0 for wavenumber equal to π . This ensures that the *odd-even decoupling* mode is filtered out completely. For 4th, 6th, 8th and 10th order accuracy the coefficients a_k are given in table 1. The $T(w)$ is plotted in figure 1 for filters of equation (9) for $\alpha = 0.25$, it can be seen that increasing the order of accuracy of the filter makes the operation less dissipative. For filters of equation (9), with a symmetric stencil, the transfer function is real.

Near the boundaries of the domain a special treatment is necessary: one can either lower the order and thus decrease the stencil width or use filters with a non-symmetric stencil. For 10th order accuracy, the first and last 5 nodes of a domain require a special form of the discretisation. The transfer function for these expressions has both a real and imaginary part, plotted in figures 2 and 3, respectively. The imaginary part denotes the dispersive behaviour of the filter operation, the real part the dissipative part.

3.2. EXTENSION TO MULTI-DIMENSIONAL FILTERING

In the two-dimensional situation, a quantity f can be filtered using an expression of the form:

$$\begin{pmatrix} \beta & \alpha & \beta \\ \alpha & 1 & \alpha \\ \beta & \alpha & \beta \end{pmatrix} \hat{f}_{i,j} = \begin{pmatrix} \frac{a_4}{4} & \frac{a_5}{8} & \frac{a_2}{4} & \frac{a_5}{8} & \frac{a_4}{4} \\ \frac{a_5}{8} & \frac{a_3}{4} & \frac{a_1}{4} & \frac{a_3}{4} & \frac{a_5}{8} \\ \frac{a_2}{4} & \frac{a_1}{4} & a_0 & \frac{a_1}{4} & \frac{a_2}{4} \\ \frac{a_5}{8} & \frac{a_3}{4} & \frac{a_1}{4} & \frac{a_3}{4} & \frac{a_5}{8} \\ \frac{a_4}{4} & \frac{a_5}{8} & \frac{a_2}{4} & \frac{a_5}{8} & \frac{a_4}{4} \end{pmatrix} f_{i,j} \quad (10)$$

for 4th order accuracy, where $\hat{f}_{i,j}$ is the filtered value of quantity f at node (x_i, y_j) , and the coefficients a_i are functions of both α and β .

Again, Taylor series development and matching of coefficients determine a_k in the presence of the additional requirement that odd-even decoupling is filtered out in both directions.

However, a_k can be determined more easily by a generalised tensor product of 1-dimensional relations.

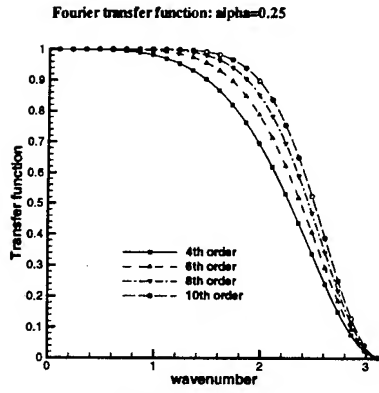


Figure 1. Transfer function for symmetric filters.

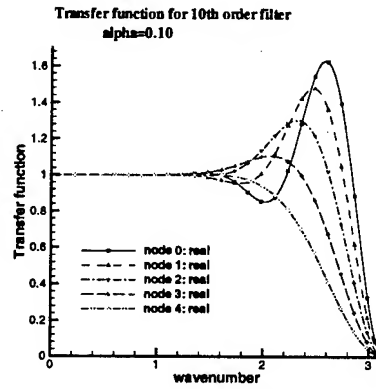


Figure 2. Real part of transfer function for non-symmetric filters.

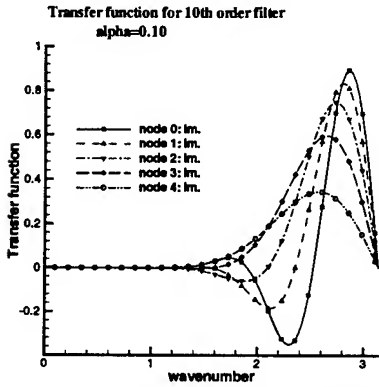


Figure 3. Imaginary part of transfer function for non-symmetric filters.

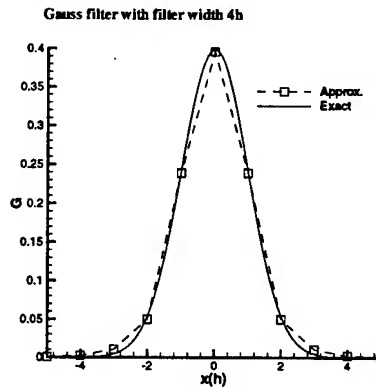


Figure 4. Approximation of Gauss filter.

4. Extension to LES formalism

In LES a filter operation

$$\bar{f}(x) = \int_{-\infty}^{\infty} G(x-x')f(x')dx' \quad (11)$$

is applied to the Navier-Stokes equations, where G denotes the filter kernel, which for a Gauss filter with filter width $4h$ is given by

$$G(x-x') = \frac{\sqrt{2}}{\sqrt{\pi}\Delta} \exp^{-2(x-x')^2/\Delta^2} \quad (12)$$

In discrete space, filter operation (11) is obtained by application of filter operation (9). For second order accuracy of (9), the Gauss filter (12) is well approximated for $\alpha = -0.2$ in both real space, see figure 4, and Fourier space (Adams and Leonard(1999)). The filter operation implemented in the present work can therefore be used in a future extension to LES.

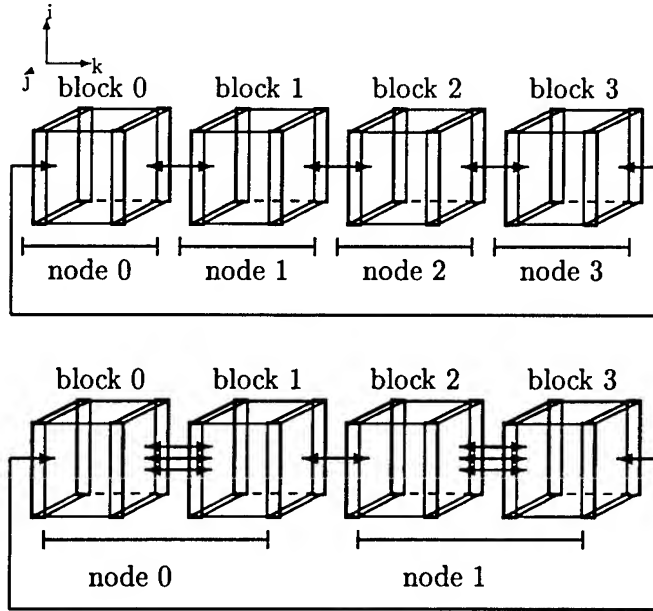


Figure 5. Example topology: 4 grid blocks on 4 and 2 processors.

5. Parallel procedure

The present multi-block Navier-Stokes solver is parallelised using the Message Passing Interface (MPI). The so-called SPMD (Single Program Multiple Data) paradigm is used, i.e. a number of processors run the same program. However, the effect of different programs on different processors is obtained by taking branches within this single program on the basis of process rank. Figure 5 schematically shows the situation when 4 grid blocks are connected in k direction. Periodic boundary conditions are assumed so that the left boundary of block 0 matches the right boundary of block 3. Initial solution, mesh and boundary conditions for each grid block are stored in separate files. Upon initialising, the program on each processor reads these files for the grid blocks that are assigned to that node.

The first processor (node 0) then determines the topology of the complete mesh and checks whether the coordinates of mesh points that overlap match. Node 0 broadcasts the topological information to all other nodes. Now, each node starts the computational procedure on the assigned grid blocks. At the end of each intermediate stage and end of a time step the in-

formation in the overlap regions is exchanged with the adjacent grid blocks. Since the number of grid blocks can be greater than the number of processors, this does not necessarily involve MPI Send/Receive operations. This is shown in figure 5, where 4 grid blocks are distributed over 4 processors and 2 processors, respectively. Single arrows denote MPI Send/Receive operations, triple arrows data exchange within a node. In both types of data communication the overlap data is stored in dynamically allocated temporary arrays. Apart from the routines in which these arrays are filled, the part of the program in which the actual calculations takes place is unaffected by the parallelisation.

6. Results

In this section results of numerical simulations of a pair of counter-rotating parallel trailing vortices are shown for two different meshes and different filter parameters, see table 2. Figure 6 gives the initial pressure field. Periodic boundary conditions are prescribed on the z -min and z -max faces. The initial velocity field of the vortices is given by:

$$\begin{aligned} u(x, y) &= \frac{(y-y_c)\Gamma}{2\pi} \frac{[1-\exp(-1.256r^2/r_c^2)]}{r^2} \\ v(x, y) &= -\frac{(x-x_c)\Gamma}{2\pi} \frac{[1-\exp(-1.256r^2/r_c^2)]}{r^2} \end{aligned} \quad (13)$$

with $r^2 = (x-x_c)^2 + (y-y_c)^2$, where the vortex center is located in (x_c, y_c) . r_c is the viscous core radius. The constant in the exponent is chosen to position the maximum of azimuthal velocity ($u_{\theta, max}$) at r_c . Exact theory gives: $r_c(t) \sim \sqrt{t}$ and $u_{\theta, max} \sim 1/\sqrt{t}$. The exact translational speed of the equivalent point-vortex system is given by $\frac{\Gamma}{2\pi a}$ with a the spacing in horizontal direction. The Reynolds number $\frac{\Gamma}{\nu} = \pm 1.3 \times 10^5$.

In figure 7 this exact result is compared with the computational results. The exact result is matched very well for both mesh resolutions. The two coarse-mesh simulations with highest dissipation ($\alpha = 0.05$ and $\alpha = 0.10$) depart from the exact result in the final stages of the simulation.

Figure 8 shows the decay of azimuthal velocity in the vortex core as a function of time. Figure 9 similarly shows the decay of the vorticity. For both figures results are plotted for the fine mesh, giving a resolution of about 12 points per vortex in the direction normal to the vortex axis. Even with this resolution the correct behaviour is observed for the viscous decay.

The simulations on both the coarse and fine mesh were performed on 4 SGI 250 MHz R10000 nodes of a Cray Origin 2000. For the 1.7×10^7 node mesh a total memory of ± 600 MByte was used. The simulations were performed for 1000 time steps that took a total of ± 250 hours to complete.

TABLE 2. Simulations done for trailing vortices

Mesh/block	Number of blocks	Number of mesh points	Filter type	Filter order	α
$81 \times 81 \times 16$	4	$\pm 4.2 \times 10^5$	non-symm.	10	0.05
$81 \times 81 \times 16$	4	$\pm 4.2 \times 10^5$	non-symm.	10	0.10
$81 \times 81 \times 16$	4	$\pm 4.2 \times 10^5$	non-symm.	10	0.25
$161 \times 161 \times 16$	4	$\pm 1.7 \times 10^6$	non-symm.	10	0.05
$161 \times 161 \times 16$	4	$\pm 1.7 \times 10^6$	non-symm.	10	0.25

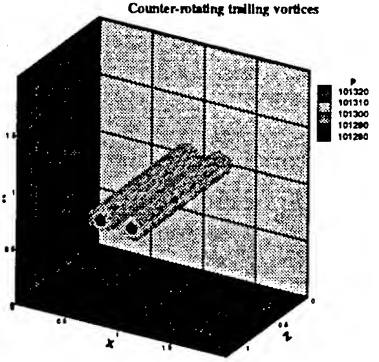


Figure 6. Initial pressure field

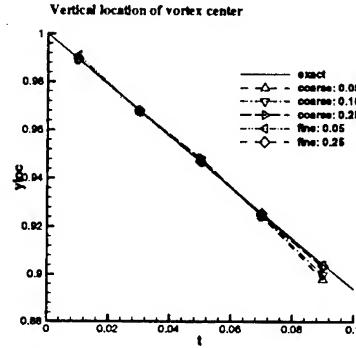


Figure 7. Vertical displacement of vortex

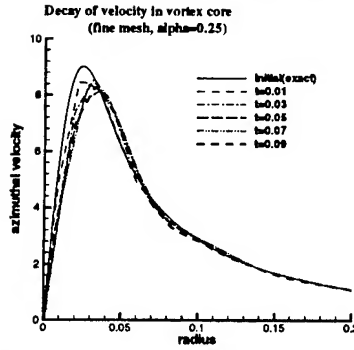


Figure 8. Decay of azimuthal velocity in vortex core

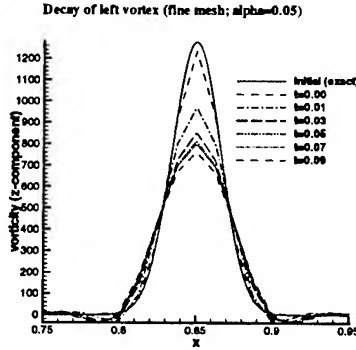


Figure 9. Decay of vorticity in vortex core

7. Conclusions

The present paper describes a higher-order accurate Navier-Stokes solver for incompressible flow. A compact-difference Laplace operator was derived for the three-dimensional simulations and applied to the implicit updates of the velocity field and in the equation for the pressure. The computations

show that a stable and accurate solution procedure is obtained when this compact-difference formulation is combined with a multi-dimensional low-pass filter that is introduced in the present work. Furthermore, it was shown how the method was efficiently parallelised using a domain decomposition technique in combination with message passing.

8. Acknowledgement

The authors are grateful for financial support from FOM (foundation for Fundamental Research of Matter) through project 97-PR-1598.

References

- Adams, N.A., Leonard, A. (1999) Deconvolution of subgrid-scales for the simulation of shock-turbulence interaction, *INI/ERCOTAC Third Workshop on DNS/LES, Cambridge, May 12-14, 1999*
- Kim, J., Moin, P. (1986) The structure of the vorticity field in turbulent channel flow, *Journal of Fluid Mechanics* **162**, pp. 339-363
- Kravchenko, A.G., Moin, P. (1997) On the effect of numerical errors in Large Eddy Simulations of turbulent flows, *J. Comp. Phys.* **131**, pp. 310-322
- Lele, S.K. (1992) Compact finite difference schemes with spectral-like resolution, *J. Comp. Phys.* **103**, pp. 16-42
- Sun, Xian-He, Zhuang, Yu (1997) A high-Order Direct Solver for Helmholtz Equations with Neumann Boundary Conditions, *ICASE Report No. 97-11*

A. Three-dimensional compact-difference Laplace operator

Consider the 27-point stencil around the mesh point (i, j, k) . On this stencil a discrete three dimensional Laplacian operator can be obtained:

$$\begin{aligned} -[\Delta f(i, j, k) + \alpha \{ \Delta f(i \pm 1, j, k) + \Delta f(i, j \pm 1, k) + \Delta f(i, j, k \pm 1) \}] = \\ h^{-2} [C_1 f(i, j, k) + C_2 \{ f(i \pm 1, j, k) + f(i, j \pm 1, k) + f(i, j, k \pm 1) \} \\ + C_3 \{ f(i \pm 1, j \pm 1, k) + f(i \pm 1, j, k \pm 1) + f(i, j \pm 1, k \pm 1) \} \\ + C_4 f(i \pm 1, j \pm 1, k \pm 1)] + O(h^4) \end{aligned} \quad (14)$$

The coefficients $\alpha, C_1, C_2, C_3, C_4$ remain to be determined by matching Taylor coefficients. The left-hand side of equation (14) can be written as:

$$\begin{aligned} (1 + 6\alpha) \Delta(i, j, k) + \alpha h^2 \left[\frac{\partial^4 f}{\partial x^4} + \frac{\partial^4 f}{\partial y^4} + \frac{\partial^4 f}{\partial z^4} + 2 \left\{ \frac{\partial^4 f}{\partial x^2 \partial y^2} + \frac{\partial^4 f}{\partial x^2 \partial z^2} + \frac{\partial^4 f}{\partial y^2 \partial z^2} \right\} \right] + \\ + \frac{\alpha h^4}{12} \left[\frac{\partial^6 f}{\partial x^6} + \frac{\partial^6 f}{\partial y^6} + \frac{\partial^6 f}{\partial z^6} + \frac{\partial^6 f}{\partial x^4 \partial y^2} + \frac{\partial^6 f}{\partial x^4 \partial z^2} + \frac{\partial^6 f}{\partial x^2 \partial y^4} + \frac{\partial^6 f}{\partial x^2 \partial z^4} + \frac{\partial^6 f}{\partial y^4 \partial z^2} + \frac{\partial^6 f}{\partial y^2 \partial z^4} \right] + O(h^8) \end{aligned} \quad (15)$$

Using Taylor expansions it can be shown that

$$\begin{aligned} f(i \pm 1, j, k) + f(i, j \pm 1, k) + f(i, j, k \pm 1) = 6f(i, j, k) + h^2 \Delta(i, j, k) \\ + \frac{h^4}{12} \left[\frac{\partial^4 f}{\partial x^4} + \frac{\partial^4 f}{\partial y^4} + \frac{\partial^4 f}{\partial z^4} \right] + \frac{h^6}{360} \left[\frac{\partial^6 f}{\partial x^6} + \frac{\partial^6 f}{\partial y^6} + \frac{\partial^6 f}{\partial z^6} \right] + O(h^8) \end{aligned} \quad (16)$$

Similarly,

$$\begin{aligned} f(i \pm 1, j \pm 1, k) + f(i \pm 1, j, k \pm 1) + f(i, j \pm 1, k \pm 1) = 12f(i, j, k) + 4h^2 \Delta(i, j, k) + \\ \frac{h^4}{3} \left[\frac{\partial^4 f}{\partial x^4} + \frac{\partial^4 f}{\partial y^4} + \frac{\partial^4 f}{\partial z^4} + 3 \left\{ \frac{\partial^4 f}{\partial x^2 \partial y^2} + \frac{\partial^4 f}{\partial x^2 \partial z^2} + \frac{\partial^4 f}{\partial y^2 \partial z^2} \right\} \right] + h^6 \left[\frac{1}{90} \left\{ \frac{\partial^6 f}{\partial x^6} + \frac{\partial^6 f}{\partial y^6} + \frac{\partial^6 f}{\partial z^6} \right\} + \right. \\ \left. \frac{1}{12} \left\{ \frac{\partial^6 f}{\partial x^4 \partial y^2} + \frac{\partial^6 f}{\partial x^4 \partial z^2} + \frac{\partial^6 f}{\partial x^2 \partial y^4} + \frac{\partial^6 f}{\partial x^2 \partial z^4} + \frac{\partial^6 f}{\partial y^4 \partial z^2} + \frac{\partial^6 f}{\partial y^2 \partial z^4} \right\} \right] + O(h^8) \end{aligned} \quad (17)$$

and

$$\begin{aligned} f(i \pm 1, j \pm 1, k \pm 1) = \\ 8f(i, j, k) + 4h^2 \Delta(i, j, k) + h^4 \left[\frac{1}{3} \left\{ \frac{\partial^4 f}{\partial x^4} + \frac{\partial^4 f}{\partial y^4} + \frac{\partial^4 f}{\partial z^4} \right\} + 2 \left\{ \frac{\partial^4 f}{\partial x^2 \partial y^2} + \frac{\partial^4 f}{\partial x^2 \partial z^2} + \frac{\partial^4 f}{\partial y^2 \partial z^2} \right\} \right] + \\ h^6 \left[\frac{1}{90} \left\{ \frac{\partial^6 f}{\partial x^6} + \frac{\partial^6 f}{\partial y^6} + \frac{\partial^6 f}{\partial z^6} \right\} + \frac{1}{6} \left\{ \frac{\partial^6 f}{\partial x^4 \partial y^2} + \frac{\partial^6 f}{\partial x^4 \partial z^2} + \frac{\partial^6 f}{\partial x^2 \partial y^4} + \frac{\partial^6 f}{\partial x^2 \partial z^4} + \frac{\partial^6 f}{\partial y^4 \partial z^2} + \frac{\partial^6 f}{\partial y^2 \partial z^4} \right\} \right] + O(h^8) \end{aligned} \quad (18)$$

Substitution of relations (15), (16), (17) and (18) in equation (14) gives for 4th-order accuracy with C_4 as parameter:

$$\begin{cases} C_1 + 6C_2 + 12C_3 + 8C_4 = 0 \\ C_2 + 4C_3 + 4C_4 = -(1 + 6\alpha) \\ C_2 + 4C_3 + 4C_4 = -12\alpha \\ C_3 + 2C_4 = -2\alpha \end{cases} \Rightarrow \begin{cases} \alpha = \frac{1}{6} \\ C_1 = 8 - 8C_4 \\ C_2 = -(\frac{2}{3} - 4C_4) \\ C_3 = -(\frac{1}{3} + 2C_4) \end{cases} \quad (19)$$

To check whether result (19) is correct, equation (14) can be written for f independent of k as:

$$\begin{aligned} & -\left[(1+2\alpha)\Delta f(i,j,k) + \alpha\{\Delta f(i\pm 1,j,k) + \Delta f(i,j\pm 1,k)\}\right] = \\ & h^{-2}\left[(C_1+2C_2)f(i,j,k) + (C_2+2C_3)\{f(i\pm 1,j,k) + f(i,j\pm 1,k)\}\right. \\ & \quad \left.+ (C_3+2C_4)\{f(i\pm 1,j\pm 1,k) + f(i\pm 1,j,k\pm 1)\}\right. \\ & \quad \left.+ 2C_4f(i\pm 1,j\pm 1,k)\right] + O(h^4) \end{aligned} \quad (20)$$

With (19) this can be written as the two-dimensional expression from Sun and Zhuang(1997):

$$\begin{aligned} & -\left[\Delta f(i,j,k) + \frac{1}{8}\{\Delta f(i\pm 1,j,k) + \Delta f(i,j\pm 1,k)\}\right] = \\ & h^{-2}\left[5f(i,j,k) - \{f(i\pm 1,j,k) + f(i,j\pm 1,k)\} - \frac{1}{4}f(i\pm 1,j\pm 1,k)\right] + O(h^4) \end{aligned} \quad (21)$$

B. Boundary conditions for compact-difference Laplace operator

This section presents the boundary contributions $-2hU$ in the right-hand side of discretised Helmholtz or Poisson equation for a face, an edge and a vertex of the cubic computational domain. The treatment for other faces, edges and vertices is equivalent. For Neumann boundary conditions only the expression for a face is shown for brevity.

B.1. BOUNDARY TREATMENT OF POINTS ON FACES OF DOMAIN

For Dirichlet boundary conditions, the contribution to U for the $i = 1$ face is given by

$$U(0,j,k) = -\frac{1}{2h}\left[C_2f(0,j,k) + C_3\{f(0,j\pm 1,k) + f(0,j,k\pm 1)\} + C_4f(0,j\pm 1,k\pm 1)\right] \quad (22)$$

and similarly for the other faces of the domain.

B.2. BOUNDARY TREATMENT OF POINTS ON EDGES OF DOMAIN

For Dirichlet boundary conditions, the contribution to U for the for the $j = 1, k = 1$ edge can easily seen to be given by

$$\begin{aligned} U(i) = & -\frac{1}{2h}\left[C_2\{f(i,0,1) + f(i,1,0)\} + \right. \\ & C_3\{f(i,0,0) + f(i,0,2) + f(i,2,0) + f(i\pm 1,0,1) + f(i\pm 1,1,0)\} + \\ & \left. C_4\{f(i\pm 1,0,0) + f(i\pm 1,0,2) + f(i\pm 1,2,0)\}\right] \end{aligned} \quad (23)$$

B.3. BOUNDARY TREATMENT OF POINTS ON VERTICES OF DOMAIN

For the vertex $(1, 1, 1)$ similarly follows

$$\begin{aligned}
 U(1, 1, 1) = & -\frac{1}{2h} \left[C_2 \{ f(1, 1, 0) + f(1, 0, 1) + f(0, 1, 1) \} + \right. \\
 & C_3 \{ f(1 \pm 1, 1 \pm 1, 0) + f(1 \pm 1, 0, 1) + f(0, 2, 1) + p(1, 0, 2) + f(0, 1, 2) \} + \\
 & \left. C_4 \{ f(1 \pm 1, 0, 1 \pm 1) + f(0, 2, 1 \pm 1) + f(2, 2, 0) \} \right] \quad (24)
 \end{aligned}$$

B.4. NEUMANN BOUNDARY ON FACE OF DOMAIN

For Neumann boundary conditions on a face, the contribution to U for the $i = 0$ is given by

$$\begin{aligned}
 U(0, j, k) = & -2f_x(0, j, k) + \quad (25) \\
 & \frac{\lambda h^2}{6} \left[C_2 f_x(0, j, k) + C_3 \{ f_x(0, j, k \pm 1) + f_x(0, j \pm 1, k) \} + C_4 f_x(0, j \pm 1, k \pm 1) \right] + \\
 & \frac{h^2}{6} \left[C_2 r_x(0, j, k) + C_3 \{ r_x(0, j, k \pm 1) + r_x(0, j \pm 1, k) \} + C_4 r_x(0, j \pm 1, k \pm 1) \right] + O(h^4)
 \end{aligned}$$

Large Eddy Simulation of the Turbulent Flow around a Circular Cylinder with Non-eddy Viscosity SGS model

Mingde Su , .Qinjun Kang
Department of Engineering Mechanics
Tsinghua University

1. Introduction

The rapid development of the modern computer in speed and memory provides a powerful tool to investigate the turbulence. Recent direct numerical simulation (DNS) of the Navier-Stokes equation has demonstrated its capability to describe the details of the turbulent flow. However, the ratio of the largest scale to the smallest scale of vortexes in turbulent flow increases with the Reynolds number of the flow rapidly, hence the scale of the computational domain must be larger than the largest scale and the mesh scale should be less than or at least equal to the scale of the smallest vortex,. Then the mesh number is very large and the required memory of computer will be so enormous to exceed the limit of the recent supercomputer even if the Reynolds number is moderate. As a compromise method, the large eddy simulation(LES) emerges as the times, in which the vortexes with mesh-like scale can be described and the influence of the movement with the smaller scale to the simulated movement with large scale is achieved through the subgrid scale modeling. When the mesh scale is small sufficiently, the major performance and details of the turbulence can be displayed.

In the present paper, the LES tool is used in the numerical simulation of the turbulent flow around a circular cylinder with the subcritical Reynolds number of 3900. As we know, at Reynolds numbers between 300 and 2×10^5 , i.e. sub-critical range, the flow is especially a challenging problem in computational fluid dynamics, for it is accompanied by a laminar boundary layer including unsteady separations and reattachments, flow reversals at the cylinder surface and in the near wake, adverse pressure gradients, transition of free shear layers and a turbulent wake with random and periodic Reynolds stress of comparable magnitudes. Therefore to simulate this turbulent flow is the most suitable object of LES..

In early stage, many 2D numerical simulations of the turbulent flow past a circle were made. However, Mittal, Balachandar and our results show that the 3D effect in the numerical simulation of the turbulent flow around a circle with Reynolds number of the moderate Reynolds number is specially evident. (Beaudan & Moin; Jordan & Ragab; ,Lu, Dalton & Zhang; Sun & Dalton). In the present paper, the turbulent flow around a circle with Reynolds number of 3900 is simulated by 2D and 3D LES and their results are compared each other. The comparison discovers the three dimensional effect of the turbulence. The details of the turbulent flow are described through the LES of the 3D flow. The present paper consists of the following four parts: the non-eddy viscosity stimulate small scale SGS modeling is introduced in the 2. Section. After the belief introduction of the numerical method and boundary conditions, the results of 2D LES of the turbulent flow is presented and compared with the experimental data in 3. Section. The 4. Section presents the results of 3D LES of the turbulent flow in details. Not only the statistical average values such as drag coefficient, Strouhal number etc. are compared with experimental data and other numerical results, but also the 3D structures of the near wake of the flow around circle cylinder are displayed. The present results discover the region of backscatt in the near wake. The reason to cause 3D effect is

explained with the results of 3D LES. In the 5. section, some useful conclusions is obtained.

2. Non-eddy viscosity SGS model and numerical method

In the large eddy simulation, to consider the influence of the small scale movement to the large scale movement, Subgrid Scale (SGS) model must be used. When the SGS quasi-Reynolds stresses occupy the small parts of the turbulence stresses, the results of LES is not so sensitizing to the SGS modeling. It is an important performance of LES. When the mesh scale is sufficiently small, the effect of the SGS modeling to the results of LES is no essential. However, in the LES of the complex turbulent flow, the SGS model has large effect to the results of LES. Recently, the development and design of new SGS model become a focus of the investigation of many theoretical scientists. In the present paper, the non-eddy viscosity stimulated small scale SGS model is selected to use, which is developed by Shah & Ferziger in 1997. The basic idea of the scale similarity of Bardina provides a goal representation of the instantaneous energy transfer between the large and small scale movements. But Bardina's model gives smaller mean dissipation because forward and backward energy transfer are nearly balanced. Shah & Ferziger find it is plausible that if higher order terms are included in the Bardina's approximation for u_i^* (instead filtered velocity U_i), Bardina's model can provide sufficient mean dissipation, yet retain other favorable characteristics of this model. Thus Shah's model is proposed in the following form for the SGS stress:

$$\tau_{ij} = \overline{u_i^* u_j^*} - \overline{u_i^*} \overline{u_j^*} \quad (1)$$

where u_i^* is declined as the solution of a partial differential operator using the filtered velocity U_i as a source term:

$$L(u_i^*) = U_i \quad L = L_x L_y L_z \quad (2)$$

where L_x is a differential operator:

$$L_x = \left(1 + C_1 \frac{\partial}{\partial x} + C_2 \frac{\partial^2}{\partial x^2} \right) \quad (3)$$

L_y, L_z have similar form. The filter operation is defined in a similar manner:

$$\overline{u_i^*} = \mathfrak{S}(u_i^*) \quad \mathfrak{S} = \mathfrak{S}_x \mathfrak{S}_y \mathfrak{S}_z \quad (4)$$

where

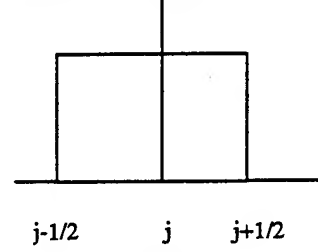
$$\mathfrak{S}_x = \left(1 + D_1 \frac{\partial}{\partial x} + D_2 \frac{\partial^2}{\partial x^2} \right) \quad (5)$$

The operators were chosen to have factored form rather than a simple three dimensional form for computational convenience. Substituting u_i^* and $\overline{u_i^*}$ into (1) gives the modeled SGS stress. Both L, \mathfrak{S} are smoothing operator (for $C_2, D_2 > 0$) The coefficients C_1, C_2, D_1, D_2 are the parameters in the present model and determine the extent to which the small scales of the resolved field are used in the SGS model. u_i^* is obtained by sequential inversion of L_x, L_y, L_z in (3). The filtering operation $\overline{\quad}$ in (4) requires an explicit application of $\mathfrak{S}_x, \mathfrak{S}_y, \mathfrak{S}_z$ to u_i^* . When the coefficients in L, \mathfrak{S} are identical then $\mathfrak{S}L^{-1} = I$ and $u_i^* = U_i$. The essence of the model is the stimulation of small scales of filtered field to create the SGS stresses.

To determine the coefficients in the filtering operation, consider the following expression for u_i^* in one dimension:

$$U = u^* + C_1 \frac{du^*}{dx} + C_2 \frac{d^2 u^*}{dx^2} \quad (6)$$

It is a local Taylor series approximation for the filtered quantity in term of the unfiltered quantity. For the non-symmetric box filter shown in Fig. 1., where j refers to computational nodal:



$$G(x - x_j) = \begin{cases} 1/\Delta & \text{for } \frac{\Delta}{2} < |x - x_j| \\ 0 & \text{for } |x - x_j| > \frac{\Delta}{2} \end{cases} \quad (7)$$

$$\Delta = (\Delta_j + \Delta_{j-1}) / 2$$

Fig. 1 shows a nonsymmetric box filter. Filtering u by using this box filter gives

$$U^{(j)} = \int_{-\infty}^{\infty} G(x - x_j) u(x) dx = u(x_j) + \frac{\Delta_j - \Delta_{j-1}}{4} \frac{du}{dx} \Big|_j + \frac{\Delta_j^2 - \Delta_j \Delta_{j-1} + \Delta_{j-1}^2}{24} \frac{d^2 u}{dx^2} \Big|_j + O(\Delta^3) \quad (8)$$

where the Taylor series expansion of u(x) around x_j is used, The superscript denote that U is filtered values in space $(x_j - \Delta_{j-1}/2, x_j + \Delta_j/2)$. Thus, u^* will be a second-order approximation to u if the coefficients in (6) and (8) are matched. A finite difference approximation to the operator L_x of (2.6) can be written as

$$U_j = au_{j-1}^* + bu_j^* + cu_{j+1}^* \quad (9)$$

Substituting the Taylor series expansion for u_{j-1}^*, u_{j+1}^* about j-th nodal into (9), we obtain

$$U_j = (a + b + c)u_j^* + (ch_j - ah_{j-1}) \frac{du^*}{dx} \Big|_j + \left(c \frac{h_j^2}{2} + a \frac{h_{j-1}^2}{2} \right) \frac{d^2 u^*}{dx^2} \Big|_j + O(ch_j^2 - ah_{j-1}^2) \quad (10)$$

where $h_j = x_{j+1} - x_j$. Matching the coefficients in (8) and (10) gives values of a,b,c as below:

$$a = \frac{h_j^2(m^2 - 3m) + h_j h_{j-1}(3m - m^2) + h_{j-1}^2 m^2}{12h_{j-1}(h_j + h_{j-1})}$$

$$b = 1 - a - c$$

$$c = \frac{h_j^2 m^2 + h_j h_{j-1}(3m - m^2) + h_{j-1}^2(m^2 - 3m)}{12h_{j-1}(h_j + h_{j-1})}$$

$$m = \frac{\Delta_j + \Delta_{j-1}}{h_j + h_{j-1}} \quad (11)$$

Here u is replaced by u^* in (8) and the third order small error is ignored and

$$C_1 = ch_j - ah_{j-1} \quad C_2 = c \frac{h_j^2}{2} + a \frac{h_{j-1}^2}{2}$$

which are coefficients in (6). To determine u_j^* by using (9), boundary condition for u^* is required, which can be chosen to be same as those for U on the boundary. Extending (9) into all direction, the

operators L_x, L_y, L_z are determined. The operators S_x, S_y, S_z are determined too under different spatial filtering size. It is necessary to note that u^* will no longer be a second order approximation of u when the operation L_x in x-direction is extent to three dimensions by its sequential application.

In the numerical simulation of the complex flow, the nonorthogonal coordinate system is used. In this case, the coordinate transformation from (x, y, z) to (ξ, η, ζ) , the later is an arbitrary curviline coordinate system, in which the grids have uniform scale. Then the filter is completed in the coordinate system (ξ, η, ζ) and the quasi-Reynolds stresses are calculated as below:

$$\tau_{i,j}^T = \beta_i^j \beta_j^i (\overline{u_i^* u_j^*} - \overline{u_i^*} \overline{u_j^*}) \quad (12)$$

where β_i^j ; β_j^i co - factor of $\partial x_j / \partial \xi_i$ in J

where x_i are the coordinates of a Cartesian coordinate system; ξ_i are the coordinates of the general curvilinear system, J is the Jacobian determinant of the translation between the two coordinate systems. u_i are the resolved velocity components which are along the x_i direction of the Cartesian coordinate system in stead of along the coordinate line.

In the present paper, the second-order QUICK difference scheme in space is used. This scheme has conservation and is an upwind scheme. The discretization of the governing equations is completed with finite volume method. In the incompressible flows, the momentum equations link the velocities to the respective pressure gradients whereas the continuity equation does not link the pressure gradients explicitly. In the present work, the nonstaggered grid system is accepted. Storing the variables at the geometric center of the control volume coupled with the use of the linear interpolation for the internodal variation usually leads to nonphysical oscillation or the so-called red-black checkerboard splitting of the pressure field and the associated difficulties in obtaining a converged solution. A solution to overcome this difficulty is to use the momentum interpolation technique to evaluate cell face variables from the cell centered quantities. The conception of momentum interpolation was proposed first by Rhie & Chow . This technique together with the SIMPLEC algorithm are implemented in the present numerical simulation.

3. Numerical results and discussion

While the final object of our series work is to simulate the flow with complex geometry, so that, the arbitrary nonorthogonal curvilinear coordinate system is used. In the present paper, the scales of computational domain in three directions for different cases are listed in Table 1. Here x is the direction main flow, y is normal direction to the ax of the cylinder and x -direction. z is spanwise direction, i.e. the axial direction of the cylinder. The forward edge of the computational domain, i.e. the upstream boundary of the computational domain is L_f far from the circle, the top and bottom boundaries are L_b , far from the cylinder. The downstream locates L_d far from it. D is diameter of the cylinder. the computational domain and partial grid system near circular cylinder is displayed in Fig.2. The grid number can be found in Table 1. The finest grid is on the surface of cylinder, its scale in radial direction is $0.015R$. . So the logarithmic law on wall and no-slip boundary condition are automatically selected according to the value of $y^+ \equiv \frac{u_\tau y}{\nu} > 5$ or < 5 , where y is normal distance of grid center point from the circular cylinder surface and u_τ is viscous shear velocity.

Table 1

RE	3900	
Case	2D	3D

Simulation Method	LES	LES
Grid number	422x181	192x142x32
grid number on circle surface	240	120
Domain scale	60Dx40D	60Dx40Dx4D
L_r	20D	20D
$L_{x,r}$	20D	20D
L_z	40D	40D
L_y	4D	4D

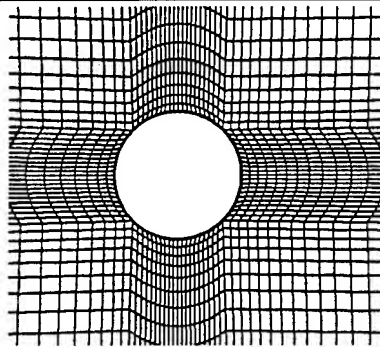


Fig.2. Geometry of computational domain and grids near cylinder

From Table 2. It can be found that the difference between experimental data and the numerical result of statistical average values of 2D LES in this case is evident(See Table 2). The experimental and other numerical simulation show such fact: in the flow with sub-critical Reynolds number of some thousands the 3D effect is the most evident. The present LES confirms this fact again. In Table 2., the statistical average values of different cases are listed and compared. In Fig.3, the averaged streamlines for 2D and 3D are compared and the 3D effect is displayed clearly.

In Figs.4 - 7, some results of the present simulation are compared with other numerical results, the comparison shows the present results of 3D LES are near experimental and DNS results. Fig.8 and 9 display the spanwise variations of the pressure and vorticity. In addition, in the present computation, the backscatt in wake is discover. As we know, normally, the kinematical energy of turbulence is transferred from large vortex to small vortex, it is called as cascade phenomena. In fact, in some location and time, there is also an inverse progress, i.e. transpiration of the kinematical energy of turbulence from small vortex to large vortex, i.e. backscatt. In those case, the dissipation of the kinematical energy of turbulence should be negative. In the LES with eddy viscosity coefficient, e.g. Smagorinsky SGS Modeling, the negative dissipation cannot appear, because the eddy viscosity coefficient is always positive. In the LES with dynamic SGS model, the negative eddy viscosity coefficient can appear, however it will remain a long time to cause the divergence of the computation. Hence, in the calculation, some forced limiter must be used and the obtained backscatt is no real. In the present computation, the non-eddy viscosity stimulate SGS modeling is adopted and the computation of the eddy viscosity coefficient of turbulence is not necessary, therefore the backscatt will not induce the divergence of computation. That means that in the region of near wake the probability of eventuating the negative dissipation of the kinematical energy of turbulence is larger than far wake. It is clear that the kinematical energy of turbulence is dissipated

and the rolling of the small vortex is nominal.

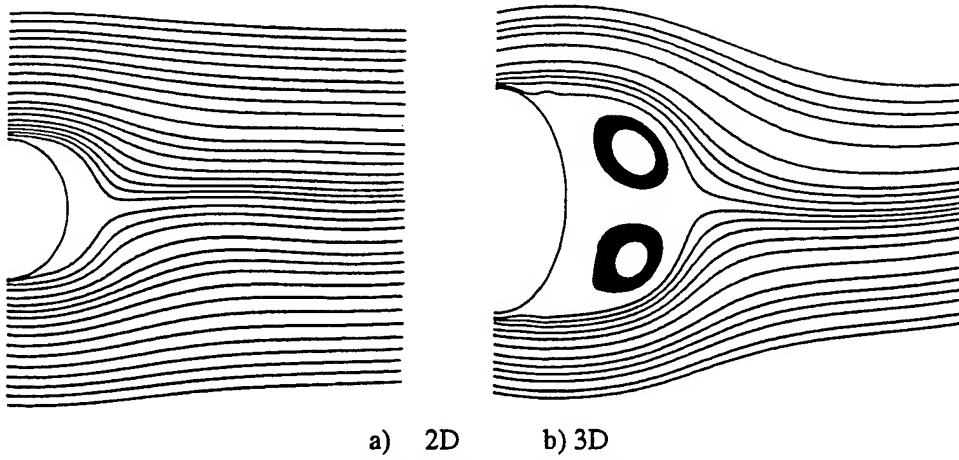


Fig. 3. Time average streamline

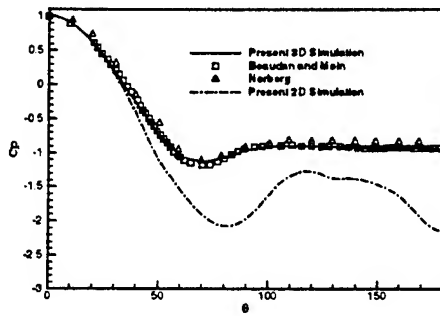


Fig.4 Coefficient of pressure on surface

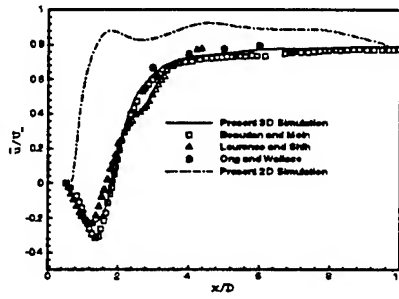


Fig.5. Distribution of average velocity in x-direction (over time and spanwise direction) along the central line in wake

Table 2.

RE	100		20000				3900				
	Present	Braza [4]	Present	exp.	Sun et.al. (2D)[21]	Lu et.al. [12]	Present		exp.	Beaudan	
							(2D)	(3D)		(2D)	(3D)
\bar{C}_D	1.38	1.37	1.25	1.20	1.30	1.15	1.54	0.96	0.98	1.74	1.00
C_f	± 0.4	± 0.4	± 0.8 (rms0.57)		± 0.8	± 0.6	± 1.5			± 2.15	
S_t	0.172	0.170	0.233	0.21	0.286	0.205	0.301	0.223	0.215	0.263	0.203

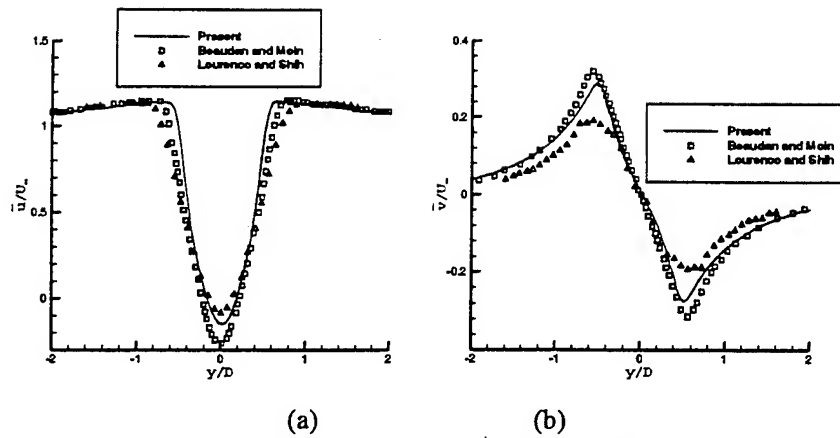


Fig. 6 Average velocity at $x/D = 154$

(a): in x-direction; (b): in y-direction

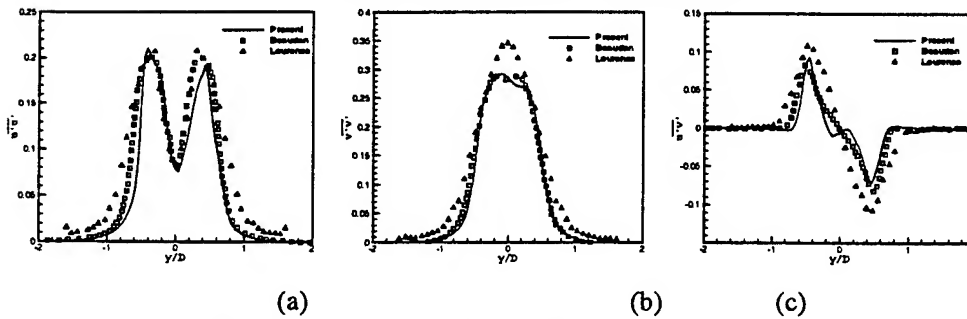


Fig. 7 Reynolds stress at $x/D = 154$

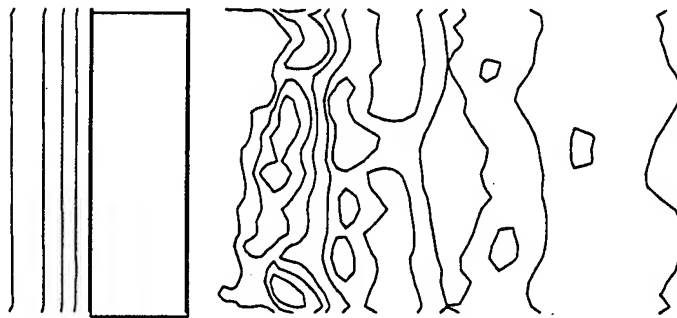


Fig. 8. Contours of pressure at $x-z$ plane ($y=0.0$)

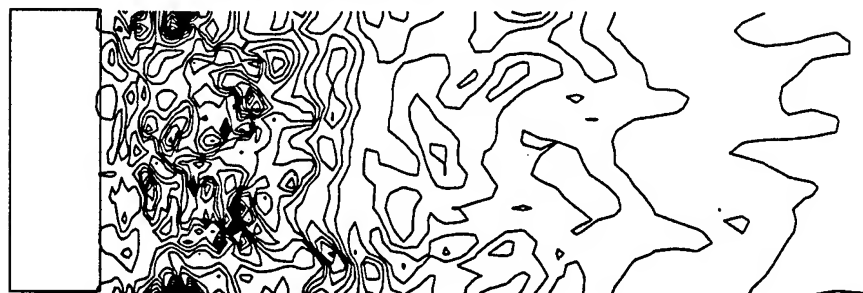


Fig. 9 Instantaneous spanwise vorticity; $y=0$

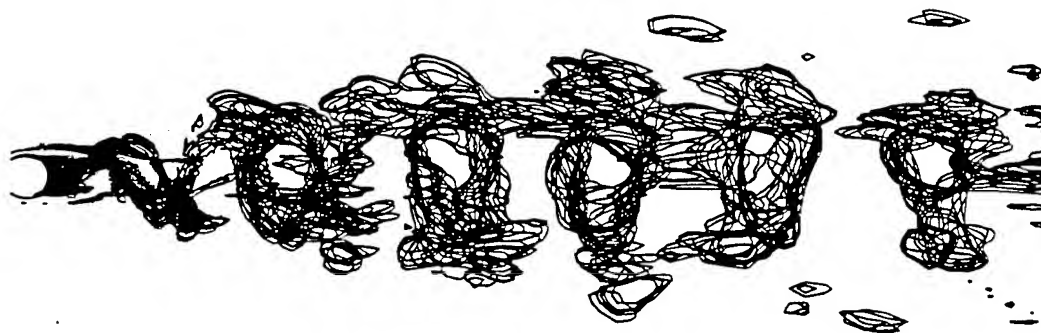


Fig. 10 Contours of $\omega_z = 0.2$

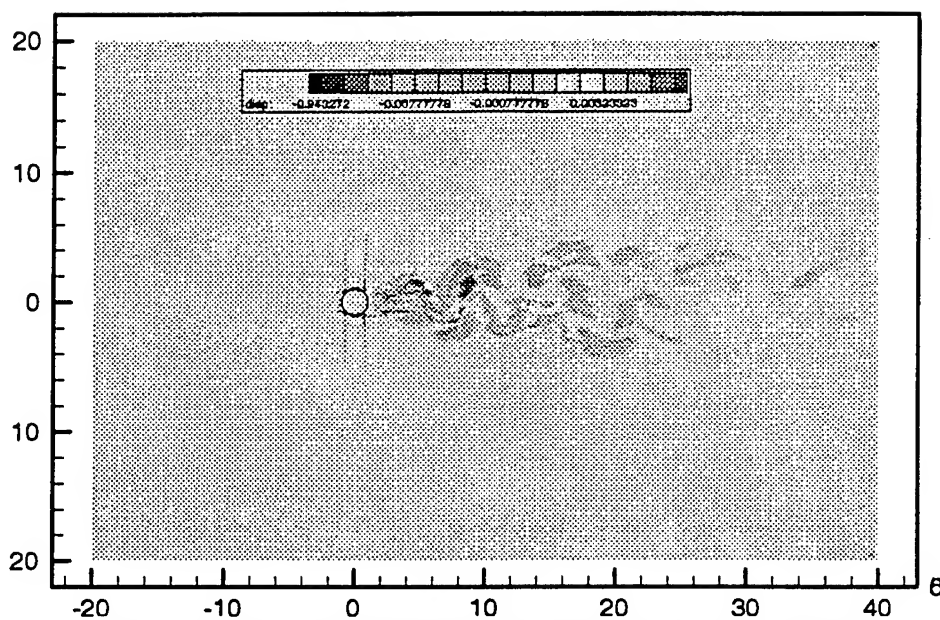


Fig. 11. Distribution of dissipation of turbulence energy at a moment

4. Conclusions

The main conclusions can be summarized as below:

- a) In the present work, the numerical method, boundary condition are available for the LES. This conclusion is proved by the detail comparison of the present results with the results of Baudan et.al. work and experimental data.
- b) Noneddy viscosity stimulate SGS model is accepted to avoid the given single parameter in Smagorinsky. Computation shows that the SSS modeling of LES is better than the Smagorinsky modeling for both 2D and 3D simulation. SSS model has been extent into the LES of the complex turbulent flow. It is necessary specially for:solving the industrial problems.
- c) The 3D effect is specially evident for the case with the moderate sub-critical Reynolds number of 3900. According to the analysis of the flow structure, specially the spanwise movement in the flow, the reason of the 3D effect is explained.
- d) The databank established by LES can be applied in the further analysis of

the turbulent flow, e.g. vortex structure, coherent flow, backscatt phenomena etc.

Of course, It is still necessary to simulate the turbulent flow with high sub-critical Reynolds number of 20000 by using 3D LES. It is useful to understand the 3D effect further.

Acknowledgments

This work is supported by the National Climb Plan, National Fund of Science and Fund of Doctor-point of the National Education Committee.

References

1. Bardina, J., Ph. D. dissertation, Dept. Mech. Engr., Standford University, Stanford, California, USA.
Beaudan P. and Moin P. Report No. TF-62, Thermosciences Division, Department of mechanical engineering, Stanford University, 1994
- 3 Berger, E. and Wille, R., Periodic flow phenomena. *Ann. Rev. Fluid Mech.* 1972, 4, 313-340
- 4 Braza M., Chassaing P. and Ha Mind, H.. *J. Fluid Mech.* 1986, Vol. 165, 79-130
- 5 Deardorff, J.W. *J. Fluid Mech.* Vol.41 pp453-480 (1970)
- 6 Germano, M., Piomelli, U., Moin, P., & Cabot, W *Phys. Fluids A* 3, p1760-1765 (1991)
- 7 Jordan, S.A. and Ragab, S.A. *J. Fluids Engr.* Vol.120, pp243-252
- 8 Leonard, A., *Adv. In Geophys.*, 18A, 237, 1974.
- 9 Leonard, B.P. *Comput. Meths. Appl. Mech. Eng.*, 1979, Vol.19 59-98
- 10 Leslie, D. C., *Theories of turbulence*, Oxford U. Press, 1973.
- 11 Lesieur, M., *Trubulence in fluids*, Second ed., Kluwer, Dordrecht, 1991.
- 12 Lu X.Y., Dalton C. and Zhang J.F. 1996 SME/OMAE, Florence, June.
- 13 Mittal, R. and Balachandar, S., *Phys. Fluids*, 7 (8), August 1995
- 14 Morkovin, M.V., . *ASME Symp. on fully separated flows*, Philadelphia, Pa., 1964, 102-119
- 15 Norberg, C., 1987, Pub. No.87/2, Dept. of Appl. Thermodynamics and Fluid Mech. Chalmer Uni. of Tech., Gothenburg, Sweden.
- 16 Rhie, C.M. & Chow, W.L. 1983. *AIAA J.*, Vol.21, pp1525-1532
- 17 Patankar, S. V., *J. Heat transfer*, vol. 101, 29
- 18 Shah, k. B. and Ferziger, J. H., *Center for Turbulence Research Annual Research Brefs* 1995.
- 19 Smagorinsky, J., , *Mon. Wea. Rev.*, 91, 99, 1963.
- 20 Su, M.D. Tang, G.F. Fu, S. J. *of Wind Eng. And Aero Dyn.* Vol. 79/3 pp289-306 (1999)
- 21 Sun X. and Dalton C.. 1994 ASME/WAM.
- 22 Yokuda, S. and Ramaprian B.R.,. *Phys. Fluids* 1990 A, 2, 784-791.

DIRECT NUMERICAL SIMULATION OF THE MICRO-FLUID DYNAMICS OF ACOUSTIC LINERS

Christopher K.W. Tam and Konstantin A. Kurbatskii

Florida State University
Department of Mathematics
Tallahassee, FL 32306-4510
tam@math.fsu.edu

1. Introduction

Nowadays, acoustic liners are essential for jet engine noise suppression. In the case of resonant liners, the openings of the resonators are usually very small. Because of the small dimensions, the flow field around the mouth of the resonators has not been directly observed or measured experimentally. This is so in spite of the fact that most acoustic energy dissipation takes place in this region. Present day understanding of the flow field and dissipation mechanisms of resonant liners are largely theoretical or is based on experiments using much larger scale models. The Reynolds numbers of these large models are, however, not the same as those of the actual resonators of the liner.

At the present time, it is a standard practice to use semi-empirical methods to calculate the impedance of a liner; e.g., Kraft, Yu and Kwan¹, Hersh and Walker², Jones³. The origin and basic concepts of most of these methods can be traced back to the work of Melling⁴. Melling recognized that, depending on the sound-pressure-level (SPL), a liner can behave linearly or nonlinearly. In the linear regime, the flow at the opening of a resonator is assumed to be laminar and parallel. These assumptions are true for flows in long tubes at low Reynolds number. On starting from these assumptions, Melling presented analysis to show that the dissipative or resistive losses may be of the Poiseuille type or the Helmholtz type (the latter being frequency dependent). Essentially, the losses come about because of viscous dissipation in the shear layer as shown in Figure 1a. Since the flow passage in the opening of the resonator has a finite length, an end-correction^{5,6} was added to account for the extra losses. In the nonlinear regime, it is generally assumed that a turbulent jet forms at the mouth of the resonator as illustrated in Figure 1b. Early experimental observations by Ingard & Labate⁷ and Ingard & Ising⁸ on flow from relatively large orifices appeared to provide the basis for the turbulent jet model. The turbulent jet model was adopted in the theoretical work of Sirignano⁹ and Zinn¹⁰. Recently, the observation of jetting was reported by Hersh and Walker² (but we are unable to find the size of the orifice in their experiment). When a turbulent jet is formed, the primary mechanism of dissipation is turbulence. In the semi-empirical approach, most investigators employed a discharge coefficient to lump all the turbulence dissipation into a single unknown. There

is, however, no generally accepted method to find the value of the discharge coefficient.

The primary objective of this investigation is to obtain a better understanding of the flow field and physics around the opening of a liner resonator when excited by incident acoustic waves. Specifically, we are interested in the mechanisms by which the acoustic energy is dissipated. We will investigate both the linear as well as the nonlinear regime. It is also our plan to perform a parametric study of the effects of frequency, intensity and angle of incidence of the incident sound waves on the flow field.

To accomplish our objectives, we will perform direct numerical simulation of the flow field around and inside a liner resonator under the excitation of plane acoustic waves. Unlike physical experiments, the smallness of the opening of the resonator is not a hindrance to our numerical simulation. There are two distinct advantages in using direct numerical simulation. The first advantage is that by using a well-designed computation mesh, it is possible to resolve and observe even very small-scale features of the flow. This will allow us to make a precise estimate of the viscous dissipation rate. Secondly, we can impose the correct Reynolds number in the numerical experiments. This avoids the basic mismatch of Reynolds number problem when using a much larger model in a physical experiment. To ensure that the numerical simulation is of high quality, the 7-point stencil Dispersion-Relation-Preserving (DRP) scheme¹¹ is used. The DRP scheme is a computational aeroacoustics method designed to minimize numerical dispersion and dissipation¹². The scheme has been applied successfully even to the screech tone problem¹³ in which very small amplitude sound waves were captured in the presence of supersonic flows and shockwaves. Good agreements were found between the computed screech tone frequencies and intensities with experimental measurements.

At low incident acoustic intensity, our numerical simulations indicate that the flow in the channel of the resonator opening is not in the form of a slug flow as suggested by Melling⁴ and others. The unsteady boundary layer flow has jet-like velocity profiles which are responsible for most of the viscous dissipation. At high acoustic intensity, a new dissipation mechanism due to the shedding of micro-vortices is observed. The mechanism is extremely efficient. In all our simulations, even at sound level as high as 160 dB, a turbulent jet flow at the mouth of the resonator has never been observed. This differs from the experimental observations of Ingard and coworkers^{7,8}. We believe that the difference is a matter of Reynolds number.

2. Mathematical Model, Grid Design and Computational Algorithm

2.1. MATHEMATICAL MODEL

We will consider the case of a single resonator in a static environment. Essentially, we are interested to find the micro-fluid flow field of a two-dimensional resonator induced by incident plane acoustic waves as shown in Figure 2.

Typical dimension of the resonator opening, D , is quite small. For this reason, the viscous effect is anticipated to be important near the mouth of the resonator. The governing equations are the compressible Navier-Stokes and energy equations. In dimensionless form with length scale = D (the width of the resonator opening), velocity scale = a_∞ (the sound speed), time scale = $\frac{D}{a_\infty}$, density scale = ρ_∞ (ambient gas density) and pressure and stress scale = $\rho_\infty a_\infty^2$, these equations may be written as,

$$\frac{\partial \rho}{\partial t} + \rho \frac{\partial u_j}{\partial x_j} + u_j \frac{\partial \rho}{\partial x_j} = 0 \quad (1)$$

$$\frac{\partial u_i}{\partial t} + u_j \frac{\partial u_i}{\partial x_j} = -\frac{1}{\rho} \frac{\partial p}{\partial x_i} + \frac{1}{\rho} \frac{\partial \tau_{ij}}{\partial x_j} \quad (2)$$

$$\frac{\partial p}{\partial t} + u_j \frac{\partial p}{\partial x_j} + \gamma p \frac{\partial u_j}{\partial x_j} = 0 \quad (3)$$

$$\tau_{ij} = \frac{1}{R_D} \left(\frac{\partial u_i}{\partial x_j} + \frac{\partial u_j}{\partial x_i} \right), \quad (4)$$

$$R_D = \frac{Da_\infty}{\nu} \text{ (Reynolds number).}$$

On the walls, the no-slip boundary conditions are to be enforced.

2.2. GRID DESIGN

The present problem is one with large disparate length scales. Away from the opening of the resonator, viscosity is unimportant. In these inviscid regions, both outside and inside the resonator, the length scale is the acoustic wavelength λ . Adjacent to the walls at the opening of the resonator, thin unsteady viscous wall layers would develop. The thickness of these layers, δ , is much smaller than the width of the opening; i.e., $D \gg \delta$. For jet engine liners, the acoustic wave length λ is much larger than D . Thus there is a length scale difference of an order of magnitude or more given by

$$\lambda \gg D \gg \delta. \quad (5)$$

To provide adequate local spatial resolution needed in different regions of the physical domain, a special grid design becomes necessary.

Figure 3 shows the computation domain used in the simulations. Figure 4 gives the mesh size distribution inside and at the opening of the resonator. A square mesh is used everywhere. There are six blocks shown in this figure. The block located right at the opening of the resonator has the finest mesh with size $\Delta_1 = 0.0125D$. The mesh size of each adjacent block increases by a factor of 2 in the direction going away from the opening. Thus the block with mesh size Δ_n has an actual size equal to $2^{n-1}\Delta_1$. We will use the 7-point DRP scheme in the computation. This scheme has a spatial resolution of seven mesh points per wavelength. Therefore, based on the largest mesh size used inside the resonator, we are confident that the mesh design of Figure 4 can adequately resolve up to the 5th transverse and the 12th longitudinal standing acoustic modes of the resonator.

Figure 5 provides the grid distribution outside the resonator. There are 8 blocks surrounding the block with the finest mesh at the mouth of the resonator. Again the mesh size of the adjacent block increases by a factor of 2 as indicated. The largest mesh size is $2^8 = 256$ times that of the smallest mesh or 3.2 times the size of the resonator opening. As has been noted before, viscous effect is unimportant away from the mouth of the resonator. Accordingly, in our computer code, the viscous terms of equations (1) to (3) are dropped except in the blocks with the five smallest mesh sizes. In other words, the Euler equations instead of the Navier-Stokes equations are solved in the blocks with coarse meshes.

2.3. COMPUTATIONAL ALGORITHM

Equations (1) to (4) are discretized according to the 7-point stencil DRP scheme^{11,12}. To eliminate spurious numerical waves, artificial selective damping terms are added as

suggested in Ref. [14], [12]. For instance, the x -momentum equation of (2) after discretization in two steps has the form,

$$\begin{aligned}
K_{\ell,m}^{(n)} = & -\frac{u_{\ell,m}^{(n)}}{\Delta x} \sum_{j=-3}^3 a_j u_{\ell+j,m}^{(n)} - \frac{v_{\ell,m}^{(n)}}{\Delta y} \sum_{j=-3}^3 a_j u_{\ell,m+j}^{(n)} \\
& + \frac{1}{\rho_{\ell,m}^{(n)}} \left[\frac{1}{\Delta x} \sum_{j=-3}^3 a_j \left(-p_{\ell+j,m}^{(n)} + (\tau_{xx})_{\ell+j,m}^{(n)} + \frac{\Delta x}{\Delta y} (\tau_{xy})_{\ell,m+j}^{(n)} \right) \right] \\
& - \frac{1}{R_{\Delta} \Delta x} \sum_{j=-3}^3 d_j \left(u_{\ell+j,m}^{(n)} + u_{\ell,m+j}^{(n)} \right)
\end{aligned} \tag{6}$$

$$u_{\ell,m}^{(n+1)} = u_{\ell,m}^{(n)} + \Delta t \sum_{j=0}^3 b_j K_{\ell,m}^{(n-j)} \tag{7}$$

where ℓ, m are the spatial indices in the x - and y -directions. Superscript n is the time level. $R_{\Delta} = \frac{\Delta a_{\infty}}{\nu_a}$ is the artificial mesh Reynolds number; Δ is the local mesh size in physical units. The last term of (6) is the artificial selective damping term^{14,12}.

The change in mesh size between two computation blocks requires the use of special stencils for mesh points in the buffer region. To avoid unnecessary computation, the local time step, Δt , also changes by a factor of 2 between adjacent blocks in exactly the same way as the mesh size. A more detailed description of this multi-size-mesh, multi-time-step algorithm is provided in Ref. [15].

On the wall surfaces, inside and outside the resonator, the ghost point method¹⁶ is used to enforce the wall boundary conditions. We use the no-slip boundary conditions along the walls adjacent to the computation blocks with the two smallest mesh. For the remaining walls, the zero normal velocity boundary condition is enforced.

Along the artificial outside boundaries of the computation domain (see Figures 3 and 5), a special set of boundary conditions is required. These boundary conditions perform two very different functions. First, it must generate the incident and the reflected waves (the wave system above the flat wall outside the resonator) as if the domain is semi-infinite. Second, the boundary conditions must allow the acoustic disturbances generated by the resonator to leave the computation domain without reflection. In this work, we use the split variable method¹⁷. A perfectly matched layer (PML)¹⁸ is used at the outermost mesh block of the computation domain.

It is known that spurious numerical waves are usually generated at the boundaries of the computation domain. If ignored, these waves could lead to numerical instability. To suppress the generation of these spurious waves, additional artificial selective damping terms, beyond that needed for general background damping discussed before, are added around the boundaries of the computation domain shown in Figure 3. In this work, we follow the scheme used in Ref. [13]. Special treatment of corner points employed in Ref. [13] is also adopted here for the four corner points at the opening of the resonator.

3. The Flow Field Excited by Low Intensity Sound

In this section, the results of our direct numerical simulation of the flow and acoustic fields of the resonator under the excitation of low intensity sound waves are reported.

Throughout this work, the dimensions of the resonator (see Figure 2) are taken to be,

$$D = T = 0.8 \text{ mm}, \quad L = 36D, \quad W = 14D. \quad (8)$$

The temperature is 15° C. The speed of sound and the kinematic viscosity of air are 340 m/sec and 0.145 cm²/sec, respectively. Based on the depth of the resonator, the quarter wave resonance frequency is approximately 3 KHz.

In all the simulations, the incident and reflected sound field in the absence of the resonator is used as the initial condition outside the resonator. Inside the resonator, the initial condition used is

$$p = \frac{1}{\gamma}, \quad \rho = 1, \quad u = v = 0. \quad (9)$$

The numerical solution is marched in time until the transient disturbances have left the computation domain. All the observations and measurements reported here are made after a time periodic state is established in the computation domain.

Figure 6a shows the instantaneous streamline pattern around the opening of the resonator at 120 dB incident sound-pressure-level and 3 KHz frequency. The angle of incidence is 30°. The flow is laminar and unsteady. Figure 6b shows the v -velocity profile at three levels. The top figure is at $y = 0.2$, which is slightly above the opening. The middle and bottom figures are at the top and bottom of the opening. Of interest is the jet-like velocity profile adjacent to the walls of the opening. This velocity profile is quite different from that given in Melling⁴. It is certainly not slug flow as assumed by some past investigators.

The purpose of an acoustic liner is to dissipate the energy of the incident acoustic waves. With the velocity field determined, it is straightforward to calculate the rate of energy dissipation due to viscosity. The time averaged dissipation rate at (x, y) , $\bar{D}(x, y)$, is given by (in dimensional units)

$$\bar{D}(x, y) = \frac{1}{T} \int_0^T \sigma_{ij} \frac{\partial u_i}{\partial x} dt \quad (10)$$

where $\sigma_{ij} = \mu \left(\frac{\partial u_i}{\partial x_j} + \frac{\partial u_j}{\partial x_i} \right)$ and T is the period of oscillation. Figure 7 shows a contour map of $\bar{D}(x, y)$ in the region at the mouth of the resonator. As expected, most of the energy dissipation takes place adjacent to the walls of the opening of the resonator. The shear gradient of the jet-like boundary layer flows is responsible for most of the dissipation. The total energy dissipation rate, E_{viscous} , may be found by integrating (10) over the mouth region of the resonator

$$E_{\text{viscous}} = \iint_{\text{resonator}} \bar{D}(x, y) dx dy. \quad (11)$$

The energy flux of the incident acoustic waves through an area equal to the opening of the oscillator is equal to,

$$E_{\text{incident}} = \frac{\bar{p}^2 D}{\rho_{\infty} a_{\infty}} \quad (12)$$

where an overbar indicates the time average. Measured value from the numerical simulation yield $E_{\text{viscous}}/E_{\text{incident}} = 0.57$. In other words, about 60% of the acoustic energy flux is dissipated. This is a typical value at low incident sound intensity. Thus in the linear regime, the dissipation rate is low.

4. The Flow Field Excited by High Intensity Sound

It turns out when the incident sound-pressure-level (SPL) is increased to 150 dB, the flow around the opening of the resonator changes drastically. The flow pattern is quite unexpected. The phenomenon is neither laminar nor turbulent. It is slightly chaotic and aperiodic; a state somewhere between laminar and turbulent.

4.1. THE PHENOMENON OF VORTEX SHEDDING

Under high intensity incident sound waves, the shedding of micro-vortices occurs at the opening of the resonator. Figure 8 shows the instantaneous streamline pattern of the flow field at 150 dB SPL and 3 KHz frequency. The closed streamlines represent vortices. These vortices are shedded from the corners of the opening.

With vortex shedding under forcing at the resonance frequency, the flow velocity at the resonator opening is extremely high. Figure 9 shows the v -velocity distribution along the centerline of the opening. In the presence of strong vortices the v -velocity component may reach an instantaneous value as high as 0.1 to 0.2 Mach number. This is very high flow velocity.

4.2. SHEDDING OF MICRO-VORTICES AS A DISSIPATION MECHANISM

Each shedded micro-vortex carries with it a certain amount of kinetic energy. This energy comes originally from the incident acoustic waves. The kinetic energy associated with the rotational motion of the vortex cannot be converted back into acoustic wave energy. It is dissipated into heat through viscosity. In this way, the shedding of micro-vortices becomes a significant dissipation mechanism.

To determine the efficiency of this dissipation mechanism, we measured the rotational velocity, v_θ , of a number of free vortices from our numerical simulations. The averaged kinematic energy of the vortex per unit span, K , is given by

$$K = \pi \int_0^R \rho(r) v_\theta^2(r) r dr \quad (13)$$

where R is the size of the vortex. By counting the number of shedded free vortices over a long period of time, the averaged number of vortices shedded per oscillation period, N , is easily determined. The shedding frequency is equal to $\frac{N}{T}$ where T is the period. The rate of energy dissipation is given by

$$E_{\text{shedding}} = \frac{KN}{T}.$$

For the case of incident sound at 150 dB, 3 KHz and θ (the angle of incidence) = 30° , it is found that $N = 6.4$. The ratio of the energy dissipation rate by vortex shedding to the energy flux rate of the incident acoustic wave on an area equal to the opening of the

resonator, $E_{\text{shedding}}/E_{\text{incident}}$, is found to be equal to 7.5. On comparing this with the dissipation rate due to viscosity, the vortex shedding mechanism is about 12.5 times more efficient. Thus an acoustic liner is most effective when there is vortex shedding.

4.3. A PARAMETRIC STUDY OF THE VORTEX SHEDDING PHENOMENON

A parametric study of the vortex shedding phenomenon was carried out. The resonator has dimensions given by (8). Our first objective was to determine the frequency and sound-pressure-level (SPL) at which vortex shedding would occur and also its sensitivity to the angle of incidence. Figure 10 gives the boundary between vortex shedding and no vortex shedding in the frequency-SPL (in dB) plane. As can be seen, vortex shedding occurs when the frequency of the incident sound waves is near but not necessarily at the resonance frequency. However, the SPL must be sufficiently high indicating that the phenomenon is highly nonlinear.

The vortex shedding phenomenon appear to be not sensitive to the angle of incidence. This is, perhaps, not surprising. Since the size of the resonator opening is much smaller than an acoustic wavelength, the resonator sees essentially a time fluctuating field outside irrespective of its original direction of propagation. Moreover, the effectiveness of vortex shedding as a dissipation mechanism of acoustic energy is also only weakly dependent on the angle of incidence. Let E be the total energy dissipation rate. That is, it is the sum of the rate of energy dissipation by vortex shedding and that by viscosity around the mouth region of the resonator. Suppose E_i is the energy flux rate of the incoming sound on an area equal to that of the opening of the resonator. The ratio $\frac{E}{E_i}$ is a measure of the effectiveness of the resonator in dissipating acoustic energy. Figure 11 shows the variation of $\frac{E}{E_i}$ with the angle of incidence at incident sound SPL of 150 dB SPL and 3 KHz frequency. There is only a small difference between normal and grazing incidence. There is vortex shedding irrespective of the angle of incidence.

5. Concluding Remarks

The physical size of the holes of a typical jet engine liner is so small that, as far as is known, the flow field around them has never been observed experimentally. In the past, semi-empirical models of the flow field had been developed. They were used to predict the impedance properties of the liners. These models were either formulated theoretically or based on experiments in which much larger size models were used. Because of the size difference, the correct Reynolds number was not reproduced in these experiments.

In this work, the micro-fluid dynamics of a typical liner resonator under acoustic excitation is investigated by direct numerical simulation. It is to be emphasized that the small physical size of the liner holes presents no hindrance to numerical simulation. The correct Reynolds number is imposed in all the simulations. Results of the present simulations appear to be quite different from what was conjectured theoretically or observed experimentally using larger scale models. At low sound intensity, we observe strong oscillatory boundary layer with jet-like velocity profile around the resonator opening. Most of the dissipation is contributed by the shear gradients of the unsteady boundary layer flows. We have not found slug flow nor Poiseuille-type flow, which are the building blocks of many semi-empirical theories.

At high sound intensity, we observe the shedding of micro-vortices from the mouth of the resonator. These micro-vortices carry with them a significant quantity of kinetic

energy which is eventually dissipated into heat. Our measurements have shown that the shedding of micro-vortices is a very efficient energy dissipation mechanism. It is definitely a desirable feature of an acoustic liner. We found that the angle of incidence of incoming sound waves is not a sensitive parameter of the vortex shedding phenomenon. On the other hand, vortex shedding occurs only when the incident sound-pressure-level exceeds a certain critical value and only at frequencies close to the resonance frequency of the resonator.

References

1. Kraft, R.E., Yu, J. and Kwan, H.W. (1997) "Acoustic Treatment Impedance Models for High Frequencies," AIAA Paper 97-1653.
2. Hersh, A.S. and Walker, B.E. (1995) "Acoustic Behavior of Helmholtz Resonators: Part 1, Nonlinear Model," AIAA Paper 95-0078.
3. Jones, M. (1997) "An Improved Model for Parallel-Element Liner Impedance Prediction," AIAA Paper 97-1649.
4. Melling, T.H. (1973) "The Acoustic Impedance of Perforates at Medium and High Sound Pressure Levels," *Journal of Sound and Vibration*, Vol. 29, No. 1, pp. 1-65.
5. Sivian, L.J. (1935) "Acoustic Impedance of Small Orifices," *Journal Acoustical Society of America*, Vol. 7, pp. 94-101.
6. Ingard, U. (1953) "On the Theory and Design of Acoustic Resonators," *Journal Acoustical Society of America*, Vol. 25, pp. 1037-1062.
7. Ingard, U. and Labate, S. (1950) "Acoustic Circulation Effects and the Nonlinear Impedance of Orifices," *Journal Acoustical Society of America*, Vol. 22, pp. 211-219.
8. Ingard, U., and Ising, H. (1967) "Acoustic Nonlinearity of an Orifice," *Journal Acoustical Society of America*, Vol. 42, pp. 6-17.
9. Sirignano, W.A. (1966) "Nonlinear Dissipation in Acoustic Liners," Princeton University A.M.S. Report 553-F31-40.
10. Zinn, B.T. (1970) "A Theoretical Study of Non-Linear Damping by Helmholtz Resonators," *Journal of Sound and Vibration*, Vol. 13, pp. 347-356.
11. Tam, C.K.W. and Webb, J.C. (1993) "Dispersion-Relation-Preserving Finite Difference Schemes for Computational Acoustics," *Journal of Computational Physics*, Vol. 107, pp. 262-281.
12. Tam, C.K.W. (1995) "Computational Aeroacoustics: Issues and Methods," *AIAA Journal*, Vol. 33, pp. 1788-1796.
13. Shen, H. and Tam, C.K.W. (1998) "Numerical Simulation of the Generation of Axisymmetric Mode Jet Screech Tones," *AIAA Journal*, Vol. 36, pp. 1801-1807.
14. Tam, C.K.W., Webb, J.C. and Dong, Z. (1993) "A Study of the Short Wave Components in Computation Acoustics," *Journal of Computational Acoustics*, Vol. 1, pp. 1-30.
15. Tam, C.K.W. and Kurbatskii, K.A. (1999) "Micro-Fluid Dynamics and Acoustics of Resonant Liners," AIAA Paper 99-1850.
16. Tam, C.K.W. and Dong, Z. (1994) "Wall Boundary Conditions for High-Order Finite Difference Schemes in Computational Aeroacoustics," *Theoretical and Computational Fluid Dynamics*, Vol. 8, pp. 303-322.
17. Tam, C.K.W. (1998) "Advances in Numerical Boundary Conditions for Computational Aeroacoustics," *Journal of Computational Acoustics*, Vol. 6, pp. 377-402.
18. Tam, C.K.W. (1998) Auriault, L. and Cambuli, F., "Perfectly Matched Layer as an Absorbing Boundary Condition for the Linearized Euler Equations in Open and Ducted Domains," *Journal of Computational Physics*, Vol. 144, pp. 213-234.

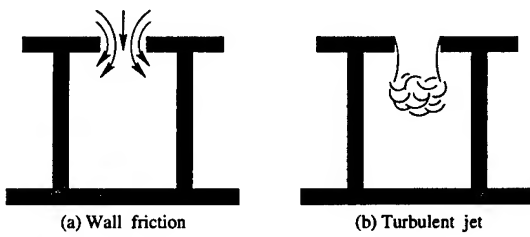


Figure 1. Dissipation Mechanisms. (a) Low sound intensity, (b) High sound intensity.

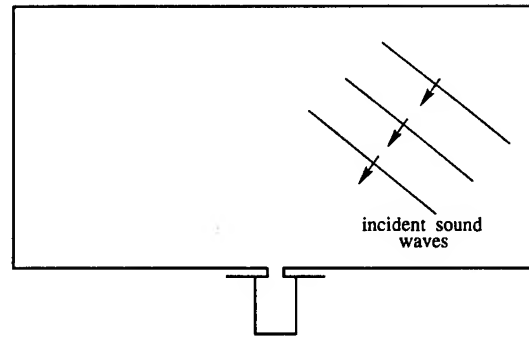


Figure 3. The computational domain.

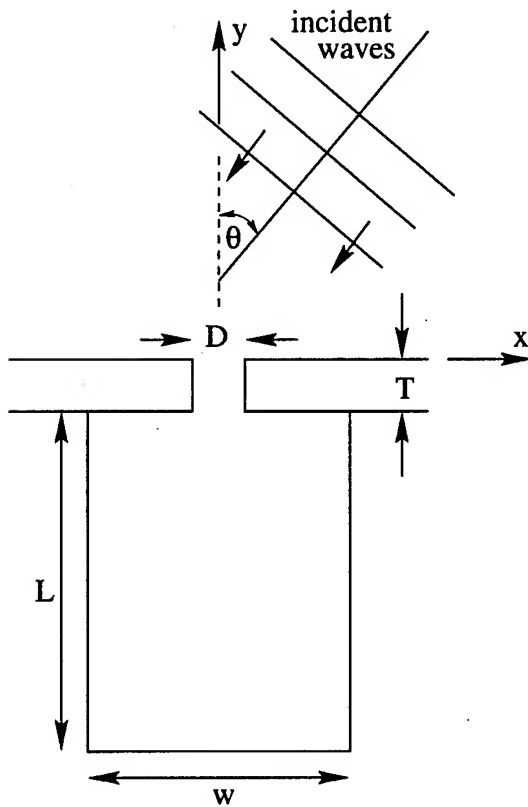


Figure 2. Mathematical model used in numerical simulation.

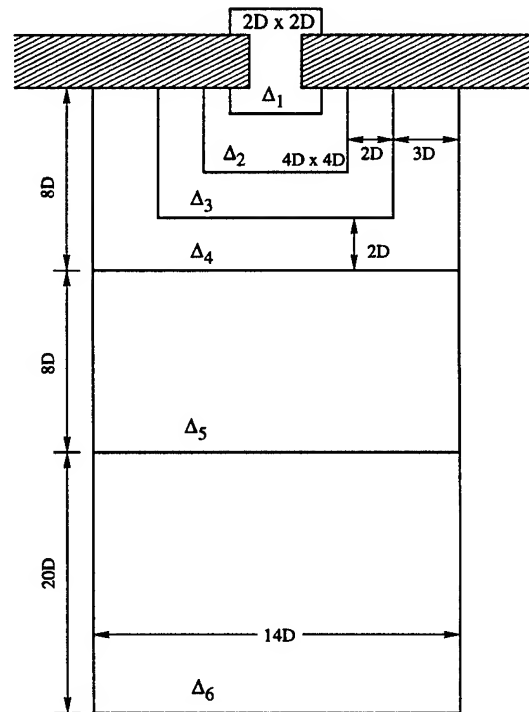


Figure 4. Grid distribution inside and at the mouth of the resonator. Mesh size: $\Delta_1 = 0.0125D$, $\Delta_n = 2^{n-1}\Delta_1$, $n = 2, \dots, 6$.

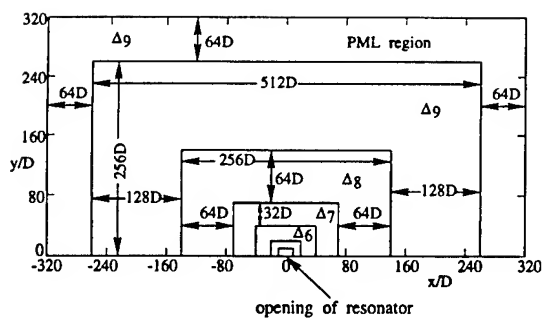


Figure 5. Grid distribution outside the resonator. Mesh size: $\Delta_1 = 0.0125D$, $\Delta_n = 2^{n-1}\Delta_1$, $n = 2, \dots, 9$.

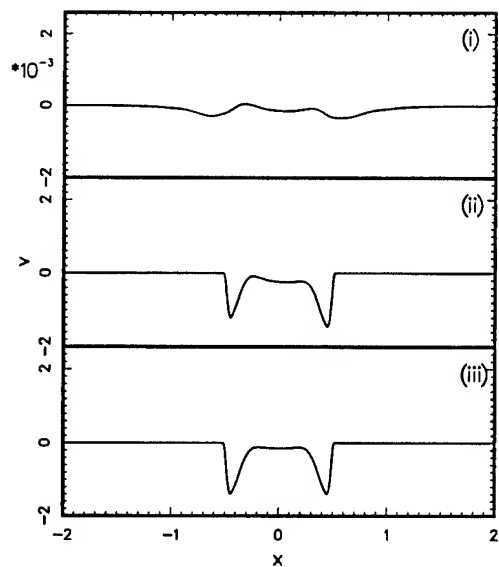


Figure 6b. Instantaneous velocity distribution (v-component) near the mouth of the resonator. (i) along $y=0.2$, (ii) along $y=0.0$, (iii) along $y=-1.0$

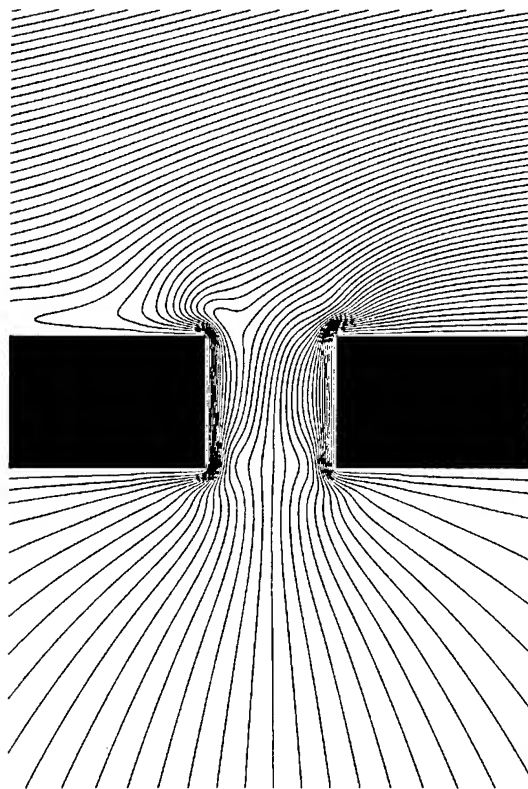


Figure 6a. Instantaneous streamline pattern at the mouth of the resonator. $SPL = 120dB$, $f = 3KHz$, $\theta = 30^\circ$.

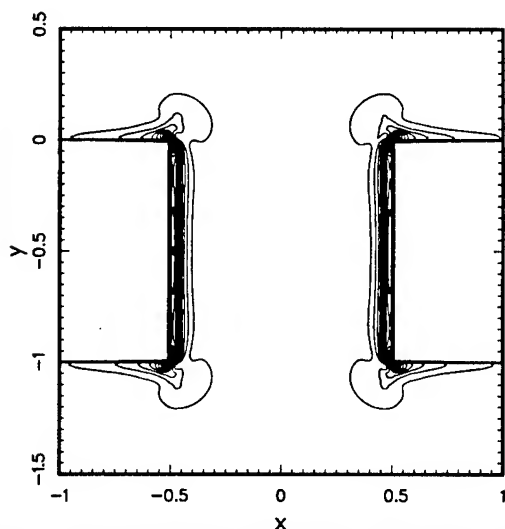


Figure 7. Contours of time-averaged dissipation rate.

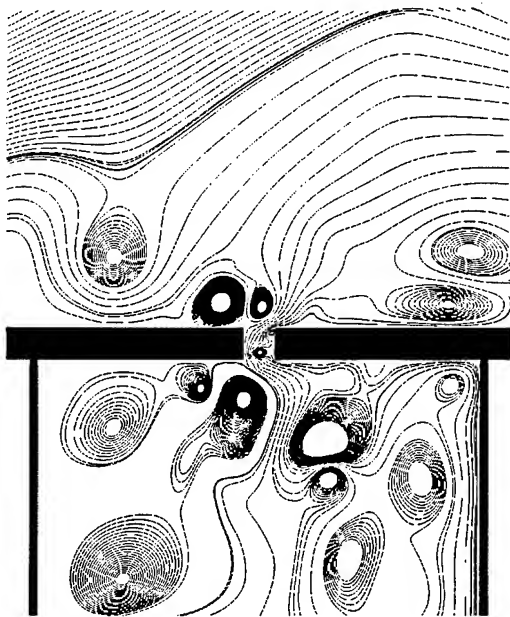


Figure 8. Instantaneous streamline pattern showing the shedding of micro-vortices at the mouth of the resonator. $SPL = 150dB$, frequency = $3KHz$, $\theta = 30^\circ$. Size of the opening = $0.8 \times 0.8 mm$, size of resonator = $1.12 \times 2.88 cm$.

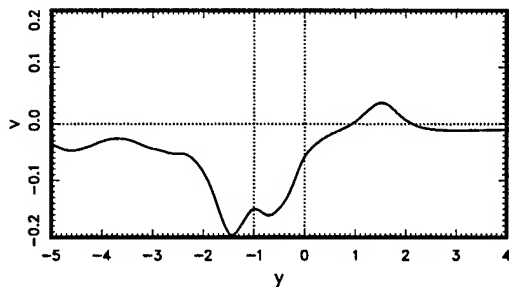


Figure 9. Instantaneous velocity distribution (v-component) along the centerline of the opening of the resonator. Incident sound wave $SPL = 150dB$, $f = 3KHz$, $\theta = 60^\circ$.

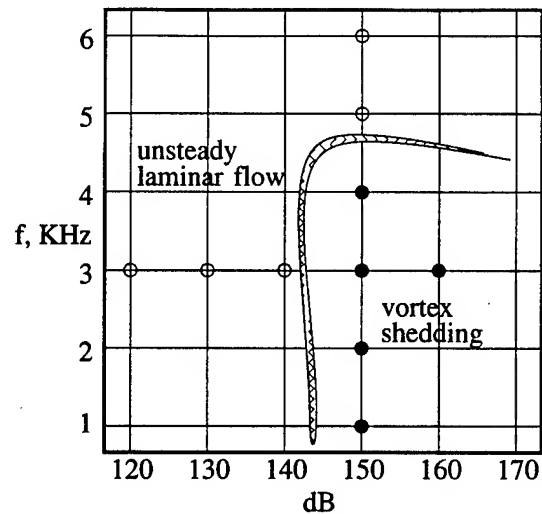


Figure 10. The boundary between vortex shedding and no vortex shedding in the frequency-sound intensity plane. • vortex shedding, ○ no vortex shedding. Resonance frequency of resonator = $3KHz$.

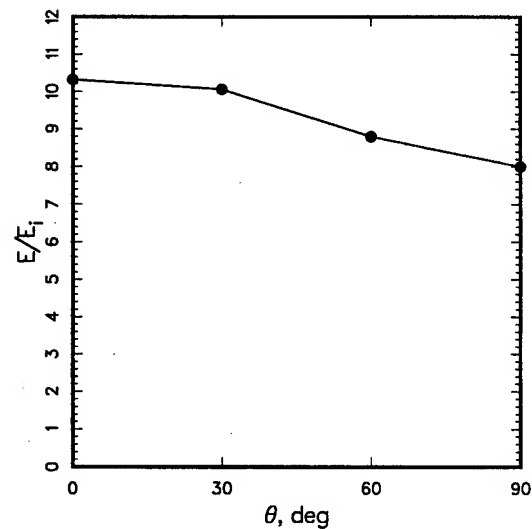


Figure 11. Variation of energy dissipation rate with angle of incidence at $150dB SPL$ and $f = 3KHz$.

DIRECT NUMERICAL SIMULATION OF EXPANDING COMPRESSIBLE FLOWS

TH.C. TREURNIET AND F.T.M. NIEUWSTADT

J.M. Burgers Centre

Laboratory for Aero- & Hydrodynamics

Delft University of Technology

Rotterdamseweg 145, 2628 AL Delft, The Netherlands

1. Introduction

Gas explosions can have severe implications, both in terms of structural damages and loss of human life. Therefore a lot of effort is put in the prediction and computation of gas explosions, for instance to be used in the design phase of industrial plants with the objective to decrease the damages in case an explosion occurs. For this numerical tools need to be developed that can compute an explosion and its effects realistically.

The heat release by the explosion generates as a result of its expansion a flow. This flow is in general turbulent. The turbulence increases mixing by which the combustion of the explosive material in the flame front is accelerated. As a result of this acceleration the heat release increases and the turbulence increases further. In other words there exists a positive feedback loop between turbulence and the explosive combustion process. The consequence is that the strength of the explosion is increased substantially over the level when no effect of turbulence would be present. It is felt that the modelling of this feedback is a weak point in the present models which compute explosions.

Our aim is to gain more insight into this problem by performing a Direct Numerical Simulation (DNS) of a gas explosion. The DNS consists of a numerical solution of the compressible Navier Stokes equations in the zero-Mach number formulation, combined with a flame front propagation model. In this formulation we assume that the density of the flow depends on the temperature only, $\rho = \rho(T)$. Therefore, all acoustic effects are eliminated and the problem can be solved, using a standard pressure correction method as applied in incompressible flow computations. The method assumes that

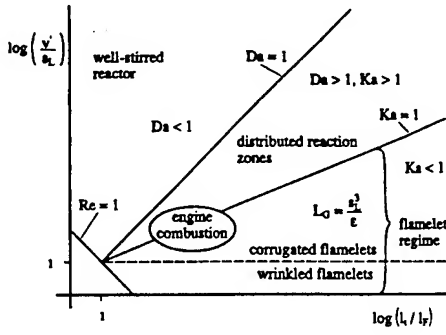


Figure 1. Different regimes in premixed turbulent combustion. Da is the Damköhler number, defined as the ratio of the turbulent time scale to the combustion time scale. Ka is the Karlovitz, the ratio between the combustion time scale and the Kolmogorov time scale. v' and s_L are the turbulent and the flame velocity; l_t and l_f the turbulent and combustion length scale.

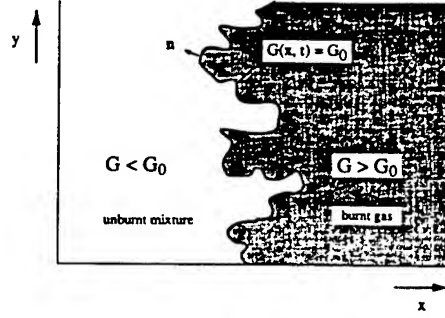


Figure 2. Burnt and unburnt gas regions separated by a thin flame surface at $G(x, t) = G_0$. (From Bray *et al.*, 1993.)

we have an open flow with a constant pressure. In relation to a real explosion this is certainly a limitation. Nevertheless, it is still very useful to gain more insight in the turbulence-combustion interaction and should lead to a better understanding and modelling of the influence of turbulence on premixed turbulent combustion. The flame front propagation model that we use to model the combustion, assumes that the actual combustion takes place in a thin layer. This assumption only holds, when the length scales related to the combustion process are smaller than the turbulent length scales. This is only true in the flamelet regime.

In present article, we present the first results of our DNS for the simulation of an explosion. An description of the method is given along with some results to test this model. These first tests look promising and indicate that it is very well possible to use DNS techniques in premixed combustion.

2. Premixed Combustion

As we have argued in the introduction, the explosive combustion will be accelerated due to turbulent mixing. In premixed turbulent combustion we can distinguish different regimes as shown in figure 1.

Let us concentrate on the flamelet regime where the chemical length scales are smaller than the turbulent length scales and which can be considered as representative for an explosive combustion process. In this case the combustion takes place in a very thin layer, which propagates through

the medium. This is called the flame front.

2.1. THE G-EQUATION

The position \mathbf{x} of this flame front, which propagates through the medium with a velocity s_{fl} , normal \mathbf{n} to the flame front, is given by:

$$\frac{d\mathbf{x}}{dt} = \mathbf{u} + \mathbf{n}s_{fl} \quad (1)$$

where \mathbf{u} is the fluid velocity. Let us introduce a scalar field G . We can write the normal on an isosurface $G = \text{const.}$ by:

$$\mathbf{n} = -\frac{\nabla G}{|\nabla G|}. \quad (2)$$

We now assume that the flame front is given by a particular value of $G(\mathbf{x}, t)$, say $G(\mathbf{x}, t) = G_0$. If we differentiate this result with respect to t , we get:

$$\frac{\partial G}{\partial t} + \nabla G \cdot \frac{\partial \mathbf{x}}{\partial t} \Big|_{G=G_0} = 0 \quad (3)$$

Combining this equation with (1), we find

$$\frac{\partial G}{\partial t} + \mathbf{u} \cdot \nabla G = s_{fl} |\nabla G| \quad (4)$$

which is called the kinematic G-equation. It provides an equation for a scalar field in which an isosurface G_0 denotes the flame front, see figure 2. The numerical treatment of this equation is discussed in section 4.

The scalar G has no clear physical property but in some cases, G is interpreted as a distance function. In that case, the value $G(\mathbf{x}) - G_0$ indicates the shortest distance between \mathbf{x} and the flame front

In (4), the G-equation is presented for incompressible flows. Piana *et al.* shows that for a compressible flow the laminar flame front propagation speed s_{fl} should be scaled with the density in order to correct for the velocity gradient over the flame front so use an effective velocity w :

$$w = s_{fl} \frac{\rho_u}{\rho} \quad (5)$$

where ρ_u is the density of the unburnt mixture.

In practice, this scaling does not work perfectly. The gradient of G tends to become larger at the position of the level G_0 . This increase in gradient causes problems when we want to relate the release of energy to G , section 3.2. This is probably due to the large velocity gradient over the flame front.

The reinitialisation of G , (see also section 4.5), addresses this problem and avoids large gradients in G . The reinitialisation is carried out after each time step in a way that $|\nabla G|$ is set equal to unity over the whole domain. (Sussman *et al.*, 1994) achieved this by solving

$$\frac{\partial G}{\partial t} = S(G^0 - G_0) (1 - |\nabla G|) \quad (6)$$

until a steady state is reached starting with the initial condition $G(t = 0) = G^0$. $S(\dots)$ is the sign function. Equation (6) has the property that G remains unchanged at the interface G_0 . Away from the interface G will converge to $|\nabla G| = 1$. In that case G can be interpreted as a distance function.

3. Basic Flow equations

To solve the explosion problem, we must combine the flame front given by the G -equation with the equations that describe the dynamics of the flow. The process that causes the flow, is the expansion due to the heat release of the explosion. The resulting velocities are quite modest, i.e. much smaller than the speed of sound. Therefore, we must consider an expanding compressible flow in which the Mach number remains small. To eliminate all acoustic effects from the problem, we assume that the density depends only on the temperature. The equation of state thus becomes $\rho = \rho(T)$. This assumption is only valid in open flows, where the pressure remains constant. Furthermore we assume the fluid to be a calorically perfect gas and the pressure p to remain constant. Therefore the equation of state becomes

$$\rho(T) = \frac{1}{T}. \quad (7)$$

3.1. COMPRESSIBLE FLOW EQUATIONS

The equations governing the flow field are the compressible Navier Stokes equations which in non dimensional form read:

$$\frac{\partial \rho}{\partial t} + \nabla \cdot \mathbf{m} = 0 \quad (8)$$

$$\frac{\partial \mathbf{m}}{\partial t} + \nabla \cdot (\mathbf{m} \mathbf{u}) = -\nabla p + \frac{1}{Re} \nabla^2 \mathbf{u} \quad (9)$$

where \mathbf{u} is the velocity and \mathbf{m} the massflux $\rho \mathbf{u}$. p is the pressure and Re the Reynolds number. For a constant pressure the energy equation in

non-dimensional form is given by

$$\frac{\partial T}{\partial t} + \mathbf{u} \cdot \nabla T = \frac{1}{Re Pr} \frac{\nabla \cdot (\lambda \nabla T)}{\rho c_p} + \frac{q}{\rho c_p}. \quad (10)$$

where T is the temperature and Pr the Prandtl number. λ and c_p are respectively the thermal conductivity and specific heat, both in non dimensional form. We assume the thermal conductivity and specific heat to be constant. The non-dimensionalisation of the equation is chosen such that these values reduce to unity. The last term in the energy equation denotes the source term which in our case is due to the chemical reaction.

For a Direct Numerical Simulation (DNS) of an explosion the equations (8, 9 and 10) must be solved numerically together with the equation of state (7) and the G-equation (4).

3.2. FLOW-COMBUSTION COUPLING

The flow and the combustion process are coupled by the source term in the energy equation (10). In the flamelet regime, the chemical length scales will be smaller than the turbulent scales. This means that the numerical grid is usually too coarse to resolve all the chemical length scales. As a result, the numerical flame thickness will be larger than the real flame thickness. Our aim is now to find a relation between G and the amount of energy released q , which keeps the flame as thin as possible and which is independent of the shape of G and the grid spacing.

To derive such a relation, we look at the case of a one dimensional flame, propagating through a premixed medium. We can derive a theoretical solution for this case and in figure 3 we illustrate the variation of various variables through this one-dimensional flame front.

The maximum flame speed is:

$$s_{max} = s_{fl} C_{exp} \quad (11)$$

The maximum speed of the unburnt fluid which is pushed forward by the flame is:

$$u_{max} = s_{fl} (C_{exp} - 1) \quad (12)$$

The amount of energy released per unit of time by such a flame is constant so that

$$\int_{-\infty}^{\infty} q dx = const. \quad (13)$$

The amount of energy released per unit length and time can now be written as

$$q = s_{fl} (C_{exp} - 1) f(x) \quad (14)$$

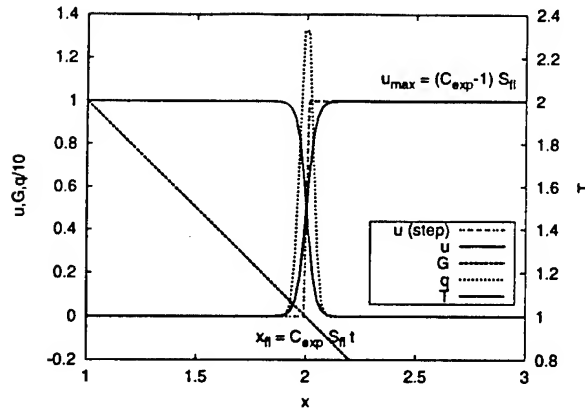


Figure 3. Theoretical profiles of the velocity, the temperature, G and q as a function of the position x in a one dimensional flame. $S_{fl} = 1$ and $C_{exp} = 2$.

where s_{fl} is the flame speed and C_{exp} is the expansion coefficient which denotes the expansion of the medium over the flame or

$$C_{exp} = \frac{\rho_u}{\rho_b}. \quad (15)$$

The $f(x)$ denotes the distribution of the energy release around the level $G(x_0) = G_0$ which should satisfy

$$\int_{-\infty}^{\infty} f(x) dx = 1. \quad (16)$$

Let us chose a Gaussian distribution for $f(x)$ so that

$$f(x) = \frac{e^{-\left(\frac{x-x_0}{\delta}\right)^2}}{\delta\sqrt{\pi}}. \quad (17)$$

where the length scale δ denotes the thickness of the flame .

When we linearise $G(x)$ around the level G_0 , we get

$$G(x) \approx G_0 + \left. \frac{\partial G}{\partial x} \right|_{x=x_0} (x - x_0) \quad (18)$$

When we substitute the linearised expression (18) into (17), we get

$$f(G) = \frac{e^{-\left(\frac{G-G_0}{\delta \left| \nabla G \right|_{x=x_0}}\right)^2}}{\delta \sqrt{\pi}}, \quad (19)$$

which still depends on knowledge about the position x_0 . In section 2.1, we have described a method to reinitialise G . This method adjusts G in a way that $|\nabla G|$ remains unity and becomes independent of the position x . Therefore, the relation between the energy release and G can then be written as:

$$q = s_{fl}(C_{exp} - 1) \frac{e^{-\left(\frac{G - G_0}{\delta |\nabla G|}\right)^2}}{\delta \sqrt{\pi}}. \quad (20)$$

This expresses q as a function of G only. The thickness of the flame is only determined by δ and does not depend on the shape of G or the grid spacing.

4. Numerical Treatment

4.1. PREDICTOR

To solve our problem, we use a second-order predictor-corrector projection scheme (Najm *et al.*, 1998) on a staggered grid. In this scheme, the evolution of the velocity and the energy field are coupled in order to stabilise the computation which in our case concerns flows with large density variations.

First we integrate the G -equation and the energy equation (10), using a second order Adams Bashfort scheme to get a prediction of G^* and the temperature T^* .

$$\frac{G^* - G^n}{\Delta t} = \frac{3}{2} \frac{\partial G}{\partial t} \Big|_n - \frac{1}{2} \frac{\partial G}{\partial t} \Big|^{n-1} \quad (21)$$

$$\frac{T^* - T^n}{\Delta t} = \frac{3}{2} \frac{\partial T}{\partial t} \Big|_n - \frac{1}{2} \frac{\partial T}{\partial t} \Big|^{n-1} \quad (22)$$

where $\partial G/\partial t|_n$ and $\partial T/\partial t|_n$ are discretised using a flux-limiting scheme for the advection terms and a central scheme for the diffusive terms. The discretisation of the spatial derivatives is discussed in more detail in the sections 4.3 and 4.4. The density ρ^* can now be calculated from the equation of state (7). The flow can be solved using a pressure correction method.

Next we integrate the momentum equations (9), again with a second-order Adams Bashfort scheme, given by

$$\frac{\mathbf{m}' - \mathbf{m}^n}{\Delta t} = \frac{3}{2} \frac{\partial \mathbf{m}}{\partial t} \Big|_n - \frac{1}{2} \frac{\partial \mathbf{m}}{\partial t} \Big|^{n-1} \quad (23)$$

where

$$\frac{\partial \mathbf{m}}{\partial t} \Big|_n = -\nabla(\mathbf{m}^n \mathbf{u}^n) + \frac{1}{Re} \nabla^2 \mathbf{u}^n. \quad (24)$$

\mathbf{m}' is called the intermediate velocity. The spatial derivatives are discretised, using a second-order central scheme.

Conservation of mass is enforced by the pressure.

$$\frac{\mathbf{m}^* - \mathbf{m}^n}{\Delta t} + \nabla \cdot (\mathbf{m}^n \mathbf{u}^n) = -\nabla p^* + \frac{1}{Re} \nabla^2 \mathbf{u}^n \quad (25)$$

Subtracting both expressions (23) and (25), gives

$$\frac{\mathbf{m}^* - \mathbf{m}'}{\Delta t} = -\nabla p^*. \quad (26)$$

Conservation of mass (8) gives

$$\frac{\nabla \mathbf{m}'}{\Delta t} = \nabla^2 p^* \Delta t + \left. \frac{\partial \rho}{\partial t} \right|^* \quad (27)$$

which has the form of a discrete Poisson equation for the pressure. $\partial \rho / \partial t|^*$ cannot be evaluated directly and is given by the following second order discretisation:

$$\left. \frac{\partial \rho}{\partial t} \right|^* = \frac{1}{2\Delta t} (3\rho^* - 4\rho^n + \rho^{n-1}) \quad (28)$$

We solve the system for the pressure and correct the intermediate velocity by using (26) which gives us a prediction of the mass flux on the new time. We can compute the velocity from the mass flux and the density.

This is the usual pressure correction method, as is applied in the case of incompressible flows. This predictor step is known to be stable for temperature and density ratios up to 2. For higher density ratios, a corrector step is needed to stabilise the scheme.

4.2. CORRECTOR

The corrected values for G and the energy are obtained, using a second-order quasi Crank-Nicolson integration. The temporal derivatives of G and the temperature on the new time level $n+1$ are estimated with the predicted values indicated with $*$.

$$\frac{G^{n+1} - G^n}{\Delta t} = \frac{1}{2} \left(\left. \frac{\partial G}{\partial t} \right|^n + \left. \frac{\partial G}{\partial t} \right|^* \right) \quad (29)$$

$$\frac{T^{n+1} - T^n}{\Delta t} = \frac{1}{2} \left(\left. \frac{\partial T}{\partial t} \right|^n + \left. \frac{\partial T}{\partial t} \right|^* \right) \quad (30)$$

The new density ρ^{n+1} is found, using the equation of state.

The new intermediate mass flux \mathbf{m}'' is given by

$$\frac{\mathbf{m}'' - \mathbf{m}^n}{\Delta t} = \frac{1}{2} \left(\left. \frac{\partial \mathbf{m}}{\partial t} \right|^n + \left. \frac{\partial \mathbf{m}}{\partial t} \right|^* \right) \quad (31)$$

where the estimate of the temporal derivative on the new time step is based on the discretisation of the predicted mass flux and velocity field according to

$$\left. \frac{\partial m}{\partial t} \right|^* = -\nabla(m^* u^*) + \frac{1}{Re} \nabla^2 u^*. \quad (32)$$

The pressure is then solved, using density on the new time step,

$$\frac{\nabla m''}{\Delta t} = \nabla^2 p^{n+1} \Delta t + \left. \frac{\partial \rho}{\partial t} \right|^{n+1} \quad (33)$$

and corrected with

$$\frac{m^{n+1} - m''}{\Delta t} = -\nabla p^{n+1}, \quad (34)$$

where

$$\left. \frac{\partial \rho}{\partial t} \right|^{n+1} = \frac{1}{2\Delta t} (3\rho^{n+1} - 4\rho^n + \rho^{n-1}). \quad (35)$$

4.3. SPATIAL DISCRETISATION OF THE G-EQUATION

The G-equation, equation (4) has the form of a hyperbolic differential equation with a source term in the right hand side. This source term has the form of an advection term and can also be included in the advection term on the left hand side. Since we use a finite volume method. It is convenient to write equation (4) in its conserved form which reads

$$\frac{\partial G}{\partial t} + \nabla \cdot (u + nw)G = -(w\kappa + \nabla \cdot u)G \quad (36)$$

where the curvature κ is defined by:

$$\kappa = \nabla \cdot n = \nabla \cdot \left(-\frac{\nabla G}{|\nabla G|} \right). \quad (37)$$

When we look for a numerical solution of this equation, we have to use the effective velocity $u_{eff} = u + nw$ instead of u in our advection scheme.

In one dimension we can write (36) in discretised form as

$$\frac{\partial G}{\partial t} = \frac{u_{eff,i-1} G_{i-\frac{1}{2}} - u_{eff,i} G_{i+\frac{1}{2}}}{\Delta x_i} + G_i \left(\frac{u_i - u_{i-1}}{\Delta x_i} + \kappa_i \right) \quad (38)$$

where κ_i reads

$$\kappa_i = \frac{n_{i+1} - n_i}{\Delta x_i} \quad \text{with} \quad n_i = \frac{G_{i+1} - G_i}{\Delta x h_i} \sqrt{\left(\frac{\Delta x h_i}{G_{i+1} - G_i} \right)^2}. \quad (39)$$

It should be noted that κ is defined at the pressure and G positions while the different components of the normal \mathbf{n} are defined at the velocity points. This complicates the discretisation of the $|\nabla G|$ term in more than one dimension.

To discretise the advection term in the lhs of (36), we use a flux-limiting scheme with a Van Leer limiter. In one dimension and assuming that $u_{eff} > 0$, this scheme reads

$$G_{i+\frac{1}{2}} = G_i + \frac{1}{2}\phi(r_{i+\frac{1}{2}})(G_i - G_{i-1}) \quad \text{with} \quad r_{i+\frac{1}{2}} = \frac{G_{i+1} - G_i}{G_i - G_{i-1}}. \quad (40)$$

$G_{i+\frac{1}{2}}$ denotes the approximation of G at the position of the velocity u_i . The first term on the right hand side of (40) denotes the upwind term, which is known to be diffusive. The second term on the right hand side, containing the flux limiter ϕ , is an anti diffusive term. From the literature, several expressions of ϕ are known. In our code we used the Van Leer flux limiter, given by:

$$\phi(r) = \frac{r + |r|}{r + 1}. \quad (41)$$

The expressions given above for one dimension can be easily extended to more dimensions.

4.4. NUMERICAL TREATMENT OF THE ENERGY EQUATION

The advection term in the energy equation (10) is discretised with help of a second order flux-limiting scheme with the Van Leer flux limiter, equation (41). The diffusive term is discretised, using a second order central scheme. The computation of the source term q is described in section 3.2.

4.5. NUMERICAL TREATMENT OF THE REINITIALISATION PROCEDURE

The equation (6) used for reinitialisation can be rewritten as

$$\frac{\partial G}{\partial t} + \mathbf{v} \cdot \nabla G = S(G^0 - G_0) \quad (42)$$

with

$$\mathbf{v} = S(G^0 - G_0) \frac{\nabla G}{|\nabla G|} = S(G^0 - G_0) \mathbf{n} \quad (43)$$

where \mathbf{v} is a unit normal vector pointing outwards from the level G_0 . In this form the equation can be interpreted as a nonlinear hyperbolic equation. G is updated using

$$G^{n+1} = G^n - \Delta t S(G^0 - G_0) (|\nabla G^n| - 1). \quad (44)$$

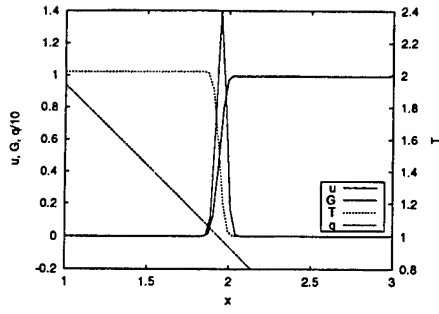


Figure 4. Profiles of the velocity, temperature, G and q for a one dimensional flame as a function of the position x at $t = 1$. $\delta = 0.04$. The number of grid points is 100. $S_{fl} = 1$ and $C_{exp} = 2$

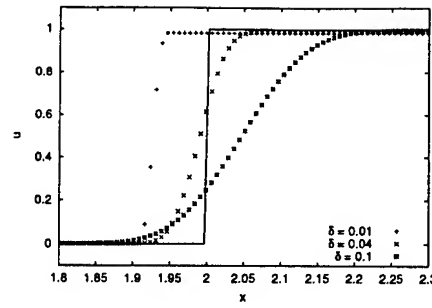


Figure 5. Velocity profile for different values of the flame thickness at $t = 1$. The number of grid points is 400. $S_{fl} = 1$ and $C_{exp} = 2$

Note that the time step Δt in equation (44) is not related to the time step used for stepping through the G , energy and momentum equations. We used the discretisation, described in (Sussman *et al.*, 1994) to solve the equations.

5. Results

In this section, we present some preliminary results obtained with the method described in this article. The results described below are solutions of a one dimensional open channel for which we have discussed the theoretical solution in section 3.2. The channel is bounded by a wall at $x = 0$. At $x = 3$, outflow boundary conditions are applied. The gas is ignited at $x = 0$. Figure 4 shows the solution of this problem at $t = 1$.

The results compare very well with the theoretical values shown in figure 3. The position of the flame, x_{fl} , is located at the right position. The jump in the velocity and temperature are also as expected. In figure 5, we can observe the influence of different values of the flame thickness δ on the velocity profile.

When we decrease the flame thickness, the results get less accurate. One of the reasons is that the continuous distribution of the heat release, equation (20), is represented in a discrete way. The smaller this distribution gets, the more inaccurate this representation becomes. The profile of $\delta = 0.01$ shows a flame velocity which is about 5% lower than expected. u_{max} is about 2% lower. In this case, when the numerical flame thickness is about 4 grid cells, the model still gives reasonable results.

The profile of G in figure 4 is a straight line with $|\nabla G| = 1$. This is achieved by ten iterations in the reinitialisation procedure. In figure 6, we

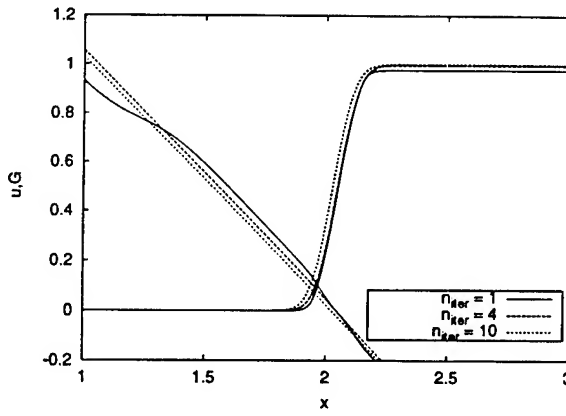


Figure 6. The velocity u and G as a function of x at $t = 1$ for a different number of iterations in the reinitialisation procedure. $\delta = 0.04$, $S_{fl} = 1$, $C_{exp} = 2$, 400 grid points.

show the results of the same problem, solved with a different number of iterations in the reinitialisation procedure which shows that $|\nabla G|$ remains close to unity, even for a low number of iterations. The solution gets better for a higher number of iterations, but the velocity profile is not very sensitive to deviations of the ideal solution.

6. Conclusion

It can be concluded that the method described in this article can be used in the simulation of a premixed combustion. The method is able to handle flow as a result of expansion due to the release of heat in a combustion process properly.

The G -equation model is applicable as a way to model the combustion process. The method to couple the combustion process and the flow field is able to represent thin flame fronts and releases the right amount of energy at the position of the flame front without knowledge of the position of the flame front.

References

- Habib N. Najm, Peter S. Wyckoff and Omar M. Knio, A Semi-implicit Numerical Scheme for Reacting Flow, I. Stiff Chemistry, *J. Comp. Phys.*, **143**, 381-402, (1998)
- K.N.C Bray and N. Peters, Laminar Flamelets in Turbulent Flames, in *Turbulent Reacting Flows*, edited by Paul A. Libby and Forman A. Williams, London (1993), p. 63.
- Mark Sussman, Peter Smereka and Stanley Osher, A Level Set Approach for Computing Solutions to Incompressible Two-Phase Flow, *J. Comp. Phys.*, **114**, 146-159, (1994)
- J. Piana, D. Veynante and S. Candel, Direct Numerical Simulation Analysis of the G -equation in Premixed Combustion, in *Direct and Large Eddy Simulation II*, edited by Jean-Pierre Chollet et al., Dordrecht (1996), p. 321.

LARGE EDDY SIMULATIONS OF RECTANGULAR JETS IN CROSSFLOW: EFFECT OF HOLE ASPECT RATIO

Mayank Tyagi and Sumanta Acharya
Mechanical Engineering Department
Louisiana State University
Baton Rouge, LA 70803

ABSTRACT

Large eddy simulations of rectangular jets in crossflow are performed to study the effect of hole geometry on the penetration and spread of the coolant jet. Three different holes of aspect ratio 0.5, 1.0 and 2.0 are studied. In the present study, the jet to crossflow blowing ratio is 0.5 and the jet Reynolds number is approximately 4,700.

It is observed that the dynamics of jets in crossflow are influenced significantly by the hole geometry for low jet to mainstream velocity ratios near the hole exit. The vertical penetration is greatest for the aspect ratio 2.0 and least for the aspect ratio 0.5. Dynamics of various steady as well as unsteady flow structures for different holes is markedly distinct at this Reynolds number. The separation between the leading and trailing edges of holes controls the evolution of the counter rotating vortex pair (CVP) near the jet exit. The relative strength of horseshoe vortex as compared to CVP changes with the hole geometry.

NOMENCLATURE

X	Streamwise direction
Y	Normal (to wall) direction
Z	Spanwise direction
V_{jet}	Jet velocity
D	Spanwise dimension of rectangular hole
L	Streamwise dimension of rectangular hole
R	Blowing ratio of jet to crossflow
U	X-component of averaged velocity
V	Y-component of averaged velocity
W	Z-component of averaged velocity
$u'v', v'w', u'w'$	components of Reynolds stress tensor.

INTRODUCTION

Film cooling of turbine blades, where rows of coolant jets are injected into the hot crossflow, is a commonly used technique to maintain the blade temperatures below a threshold value. The coolant jets are deflected and strained by the crossflow and provide coverage of the blade surface from the hot gases. The interaction of the coolant jets with the crossflow involves complex and unsteady structures like the horseshoe vortex, the counter rotating vortex pair (CVP) and wake vortices. These structures control the jet penetration and its spreading rate.

The hole geometry is an important parameter that controls the development of the flow structures and the penetration and spreading of the jet (Haven (1996), Haven and Kurosaka (1997)). The vertical and lateral spreading of the jet, in turn, govern the film cooling effectiveness. This was studied by Haven (1996) using PIV technique that has limited information about the spatial and temporal characteristics of the flow. The objective of this paper

is to numerically investigate the effect of hole aspect ratio on the dispersion of film cooling jet. The numerical study will be done through time and space accurate simulations of the filtered Navier Stokes equations (Large Eddy Simulations). Although the focus of the paper is on the flow field, a qualitative idea of the heat transfer can be obtained by examining the dispersion of the jet in the crossflow and by the shear stress distribution at the wall.

The majority of the reported computational studies on the jet-in-crossflow configuration have primarily solved the Reynolds-Averaged-Navier-Stokes (RANS) equations, and due to the intrinsic time-averaging that is associated with these equations, the dynamical nature of the vortical structures can not be predicted. Further, turbulence models have to be introduced, and the accuracy of the time-averaged calculations is itself compromised by the validity of the model. Examples of RANS calculations are those of Patankar et al., (1977), Sykes et al. (1986), Kim and Benson (1992), and Garg and Gaugler, (1994, 1995). Since the dynamics of the large scale features are important, the large scales have to be predicted correctly and the interactions of small scales must be modeled accurately. This requirement calls for large eddy simulations (LES), where all structures beyond a certain filter size are resolved, and the unresolved scales are modeled. More recently, Muldoon and Acharya (1999) have presented time-and space-accurate Direct Numerical Simulations (DNS) for a normally injected jet. Jones and Wille (1996) and Yuan and Street (1996) have presented Large Eddy Simulations (LES) that resolve the dynamics of the large scales and model the small scales, for a normally injected jet, and observed some of the reported phenomena in the experiments. As noted earlier, the main aim of this paper is to perform LES to understand the effect of the hole geometry on the penetration and mixing of the jet with the crossflow.

COMPUTATIONAL METHOD

The unsteady three-dimensional Navier Stokes equations are solved using the projection method (Chorin, 1967). This is a fractional step approach in which an intermediate velocity field is calculated by neglecting the pressure gradients, and the pressure field is obtained as a solution to a Poisson equation derived using the continuity equation. This pressure field is used to update the velocity in the projection step. The temporal discretization is done using a second-order accurate Adams-Bashforth scheme. The calculation of the convective terms is done by a conservative formulation. A third order accurate upwind biased finite difference scheme is used for these terms. The viscous dissipation terms are discretized using a fourth order accurate central difference scheme.

In LES, the governing equations are obtained by applying a filtering operation on the Navier-Stokes equations and the continuity equation. The filter function is represented as the convolution operator (Ghosal and Moin, 1995). The unfiltered fields give rise to subgrid scale stresses that require modeling. Following the dynamic mixed method of Zang et al (1993), these stresses are decomposed into a resolved part and an unresolved part. The resolved part is the Galilean invariant form of Bardina's (1983) scale similarity model (Speziale, 1985). The dynamic Smagorinsky model is used for the unresolved part of the stress and the dynamic coefficient is test filtered to avoid numerical instabilities. The issue of filtering is very important for such numerically accurate simulations. On a non-uniform grid the filtering operator becomes a function of spatial location and hence gives rise to commutation error leading to low order of accuracy even with very high order accurate schemes (Ghosal and Moin, 1995). The issue of dependence of dynamic coefficient on aspect ratio of the grid cells when using grid based filters

needs to be addressed on such non-uniform grids (Scotti et al, 1997). These issues are evaded here by using uniform grids with isotropic aspect ratio. In particular, the flow contains structures in almost all parts of the computational domain and hence, all parts of the domain need to be resolved with equal importance. The top hat filter is used for following reasons (Zhou et al, 1989 and Ghosal, 1999). It is easy to implement in a finite difference code. It has compact support, unlike Gaussian or exponential filters which violate this requirement for grid-based filtering. It is a positive or realizable filter i.e. if it filters a non-negative field, the filtered field is always non-negative.

PROBLEM DESCRIPTION

A schematic of the physical problem studied is shown in Figure 1. Three hole aspect ratios $L/D = 0.5$, 1.0 and 2.0 are investigated and are designated as hole A, B and C respectively. A uniform Cartesian grid of $122 \times 52 \times 32$ points is used for a domain of $12D \times 5D \times 3D$ (Figure 1). At the inflow, a fully developed turbulent boundary layer profile is prescribed. The velocity field is specified at the jet inlet from the experiments of Ajersch et al (1995). The hole B case is the numerical simulation for the experiments of Ajersch et al (1995). The Reynolds number based on the jet velocity and the hole spanwise dimension is 4700. A periodic boundary condition is applied in the spanwise direction. The domain size is chosen such that free-stream conditions at the inlet can be used as the boundary conditions along the top plane. At the outflow, a convective boundary condition is used where the wave speed is determined from a flux balance. Inlet planes are placed at $X/D = -3.25$ for hole A, $X/D = -3.5$ for hole B and $X/D = -3.0$ for hole C.

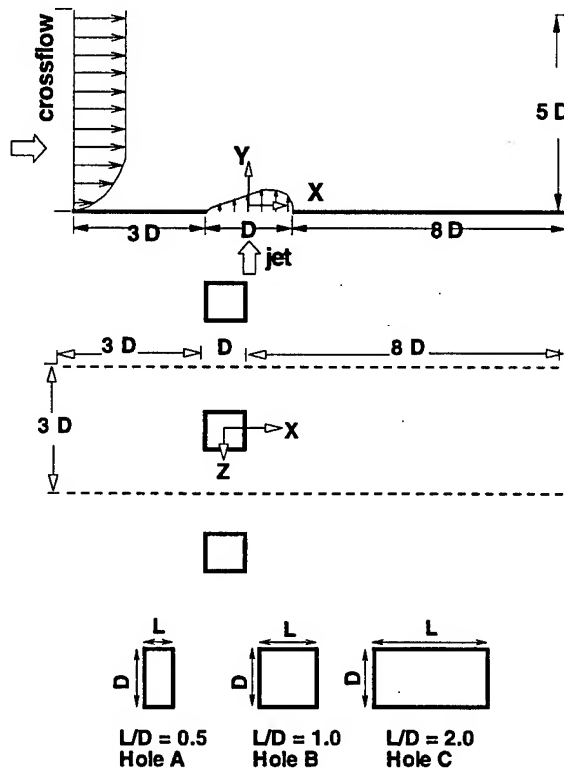


Figure 1: Schematic of the computational domain.

RESULTS

Results are presented for three hole aspect ratio cases at various planes of the computational domain. The X-component of the mean velocity field and the root mean square fluctuations are presented in figure 2. The velocity profiles show a double peaked profile for all the holes; however, the location and magnitude of the peaks are different indicating that size and strength of flow structures obtained for three cases are different. For holes B and C, negative values of the meanflow profile at downstream locations represent large recirculation regions. The u_{rms} profile at $X/D = 1.0$ shows that hole A has a maximum close to the wall which clearly indicates that for this case the vertical jet penetration is the smallest, and that the jet trajectory is closest to the wall. At downstream planes, the location of u_{rms} maximum shifts towards the leeward edge of the bent jet. For the case of hole B and C, there is a local maximum in u_{rms} profile at downstream planes between the wall and the leeward edge of the jet indicating enhanced mixing.

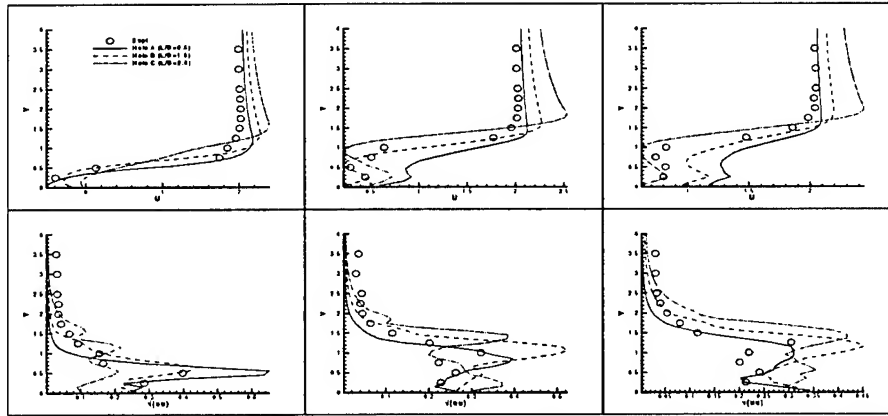


Figure 2: Mean X component and u_{rms} profiles at $X/D = 1.0, 3.0$ and 5.0 and $Z/D = 0.0$.

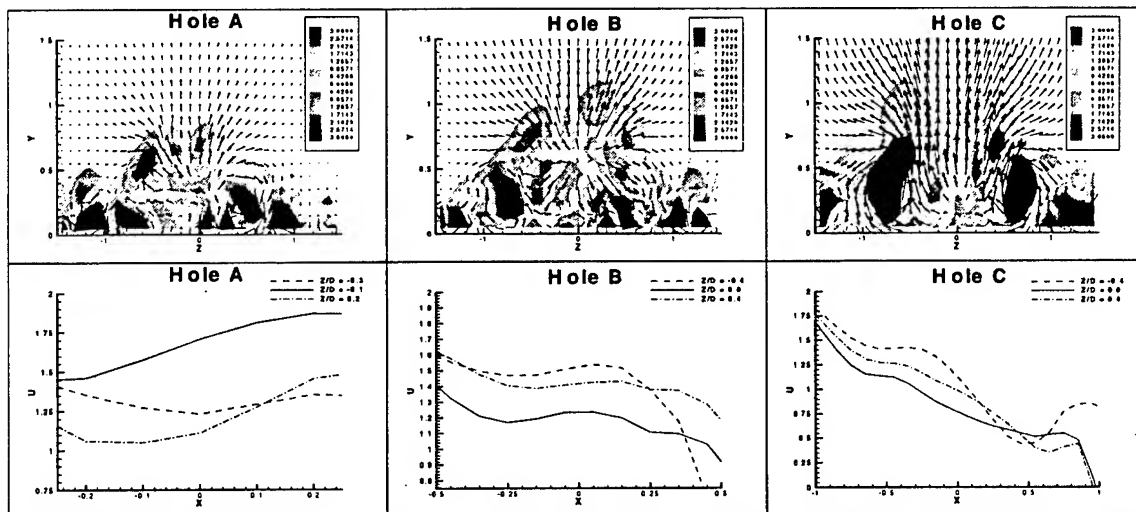


Figure 3 Instantaneous velocity vectors and contours of ω_x at $X/D = 1.0$, Profiles of X-component of velocity at various Z-planes across the holes at $Y/D = 0.4$ to show the warping of mainflow.

The presence of local maxima or minima in the spanwise direction for the streamwise component of velocity would tilt the ω_z into ω_x . The local maximum in spanwise direction for the u-velocity component is designated as 'concave warping' and the local minimum is designated as 'convex warping' by Haven and Kurosaka (1997). In the instantaneous contours of ω_x at $X/D = 1.0$ (Figure 3), we observe anti-kidney vorticity over the CVP for hole A. It is also noted that the u-profiles at the leading and trailing edges of the holes warp in similar fashion as observed by Haven (1996). The local maximum around jet center plane in main flow profile along the spanwise direction will tilt the leading edge spanwise vorticity into anti-kidney pair. However, the warping of profile for hole A is not to the extent as observed by Haven (1996). This might be due to prescription of time averaged jet exit profile and higher jet Reynolds number as compared to Haven (1996). The local minimum around the jet center plane would yield a kidney pair above the CVP that is formed by sidewall vorticity of holes.

One interesting observation is made about the relative strengths of horseshoe vortex and CVP for various cases. For hole A, the horseshoe vortex has higher levels of ω_x as compared to CVP. The velocity field induced by these vortices at the location over the CVP may result in the vorticity in the opposite sense of CVP. For hole C, the CVP is stronger than horseshoe vortex. The resultant induced velocity field would still have the same sense of vorticity as CVP except it peels off at a location somewhere above the CVP due to opposing nature of horseshoe vortex. At the trailing edge of hole the warping of reverse mainflow in the wake region gives rise to anti-kidney vorticity between the CVP (figure 11).

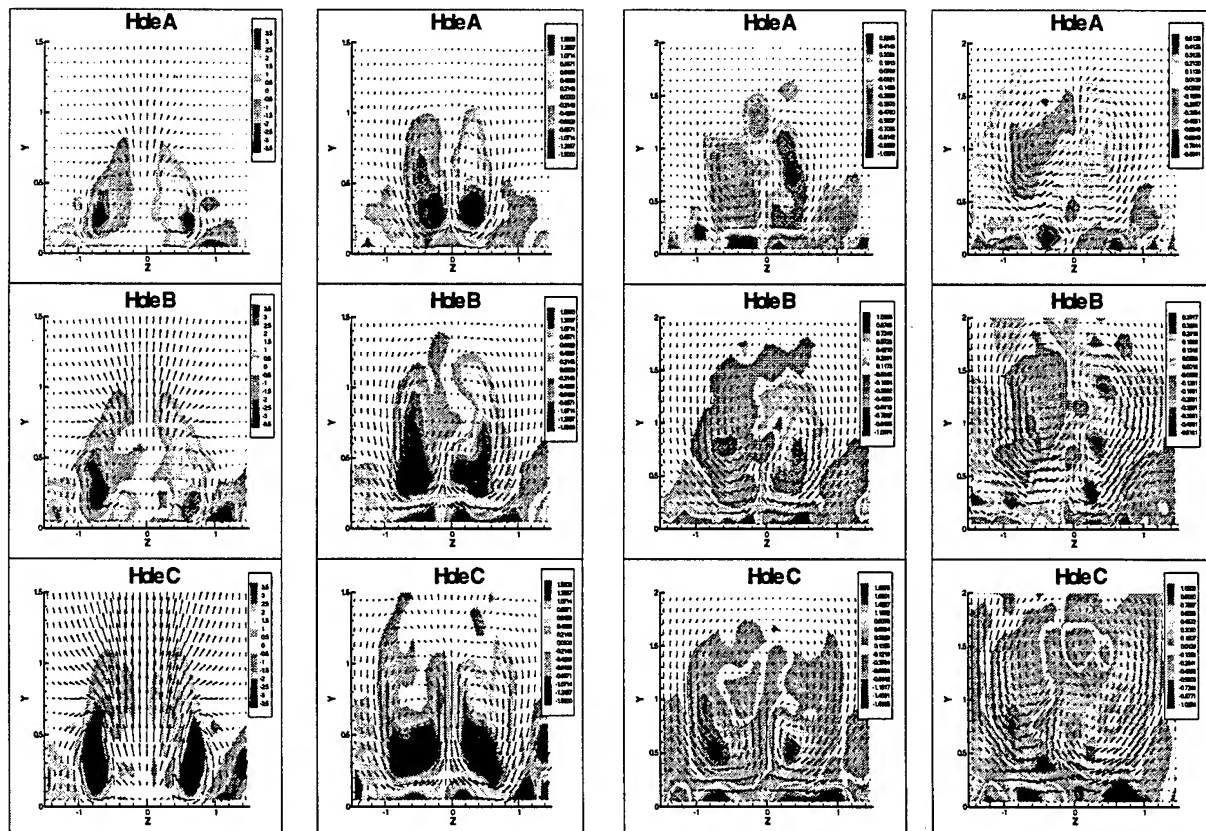


Figure 4 Time averaged velocity vectors and contours of ω_x at planes $X/D = 1.0, 3.0, 5.0$ and 7.0 .

The contours of time averaged velocity vectors and ω_x for various cases are shown at $X/D = 1.0, 3.0, 5.0$ and 7.0 in figure 4. The asymmetry in the time-averaged results is attributed to the asymmetric boundary condition at the jet exit prescribed from the experimental data of Ajersch et al (1995). The jet penetration is least for hole A. The CVP weakens for this case more rapidly as compared to other cases. The time-averaged contours show the breakup of CVP into multi-decked CVP at down stream planes for hole B. The jet penetration is highest for hole C at all planes and the CVP degenerates into smaller structures with same sense of vorticity. These smaller structures interact amongst themselves in a highly unsteady manner at further downstream planes. As noted earlier, the unsteady anti-kidney vortex pair over the CVP (hole A) will inhibit the jet lift off near the hole region while the kidney vortex pair over the CVP (hole C) will assist the jet lift off. The lateral spread of the CVP also increases with the hole aspect ratio. The contours of Reynolds stress $v'w'$ at various X-planes are presented in figure 5. The values of Reynolds stress $v'w'$ are high near the edges of CVP at $X/D = 1.0$ and 3.0 . The nature of this stress component is to damp these vortical structures. The distribution of this stress component becomes patchy at the locations where the CVP degenerates into smaller vortices. The large values of $v'w'$ in the mainstream over the CVP at $X/D = 1.0$ for hole C corresponds to the stresses acting on the leeward edge of the jet

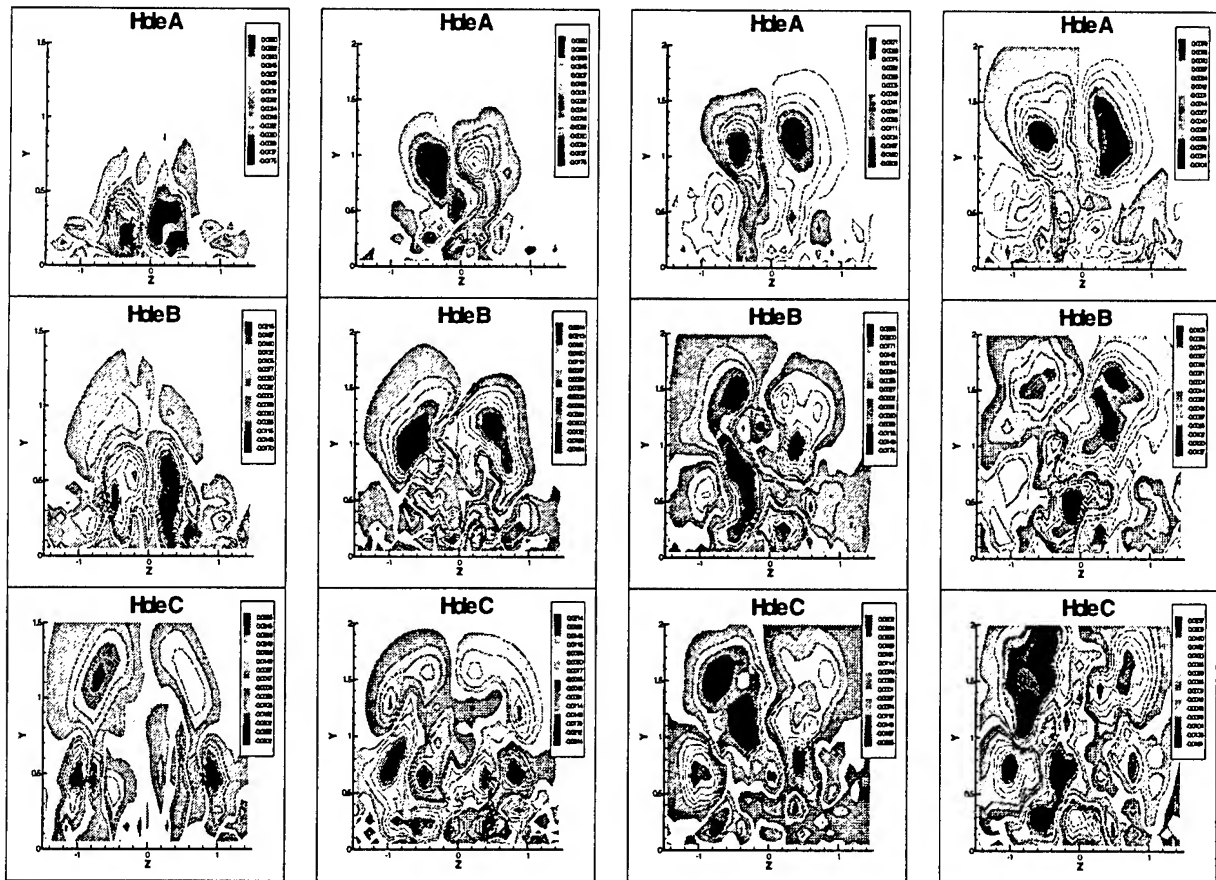


Figure 5 Contours of Reynolds stress $v'w'$ at planes $X/D = 1.0, 3.0, 5.0$ and 7.0 .

Instantaneous velocity vectors and contours of ω_y are presented at $Y/D = 0.1$ in figure 6. Reynolds stress $u'w'$ is presented for various cases at the same plane in figure 7. The reverse flow in the wake region of the holes is has the maximum around jet center plane. This leads to the formation of anti-kidney vortices at the trailing edges of the holes (figure 11). The footprints of wake vortices are confined below the CVP for hole A. There is evidence of reorientation of horseshoe vortex close to jet corner around the trailing edge of hole B. For hole C, around $X/D = 3.0$, we observe strong signatures of ω_y near the periodic boundaries. Since, vorticity can not be generated within the flow or at the wall in the normal direction, one can deduce that these upright vortices are generated as a result of reorientation of horseshoe vortices (Kelso et al (1994), Fric and Roshko (1990)). The magnitude of $u'w'$ is largest for hole C as compared to other cases. This is because of enhanced crossflow entrainment into the wake of large aspect ratio hole. Large values of $u'w'$ in bigger spanwise extent for hole C also indicate the larger lateral spreading of the jet.

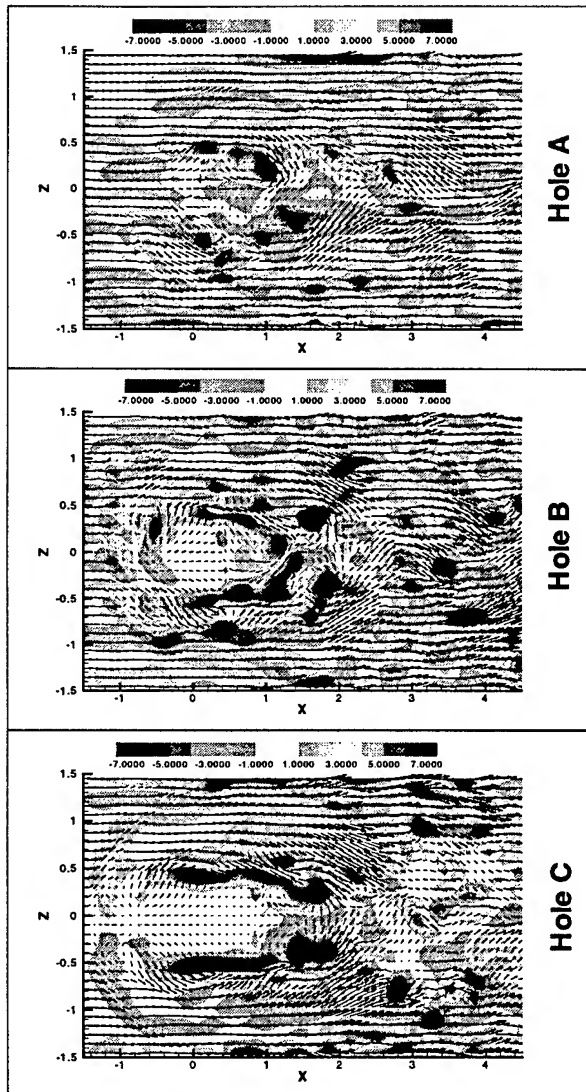


Figure 6 Contours of ω_y and instantaneous velocity vectors at $Y/D = 0.1$

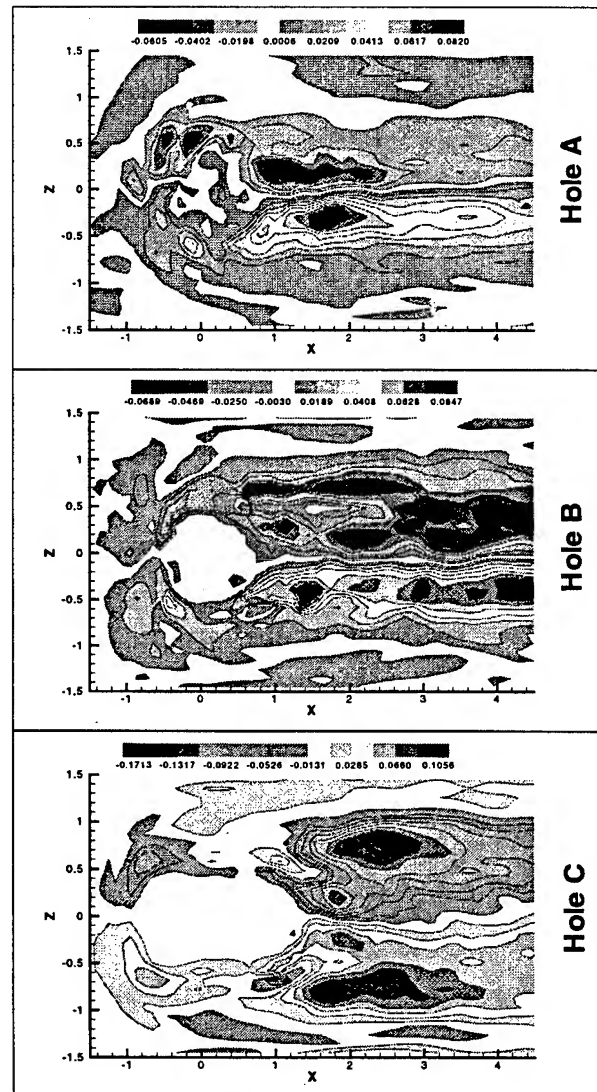


Figure 7 Contours of Reynolds stress $u'w'$ at $Y/D = 0.1$

The Z-component of vorticity as well as instantaneous velocity field is presented at $Z/D = 0.0$ in figure 8. The Reynolds stress $u'v'$ for the various cases is presented on the same plane in figure 9. We observe a strong horseshoe vortex system in front of the jet for holes B and C and spanwise rollups of vortices at the leeward edge of the jet. The vertical penetration of the jet increases with the aspect ratio of the hole. There are events of reattachment and ejection along the wall below the roller vortices. Clearly, the coverage of the wall by jet changes dynamically and thereby changes the film cooling effectiveness. Reynolds stress $u'v'$ corresponding to the horseshoe vortex is largest for hole C while the patches of $u'v'$ at the leeward edge of the jet corresponding to rollup vortices are largest for hole A and tendency of this stress is to damp these vortices. The positive values of $u'v'$ near the wall are observed at further downstream locations from jet center for hole A as compared to hole C. The negative values of $u'v'$ at the windward edge of the jet represents the mixing at the jet-crossflow interface.

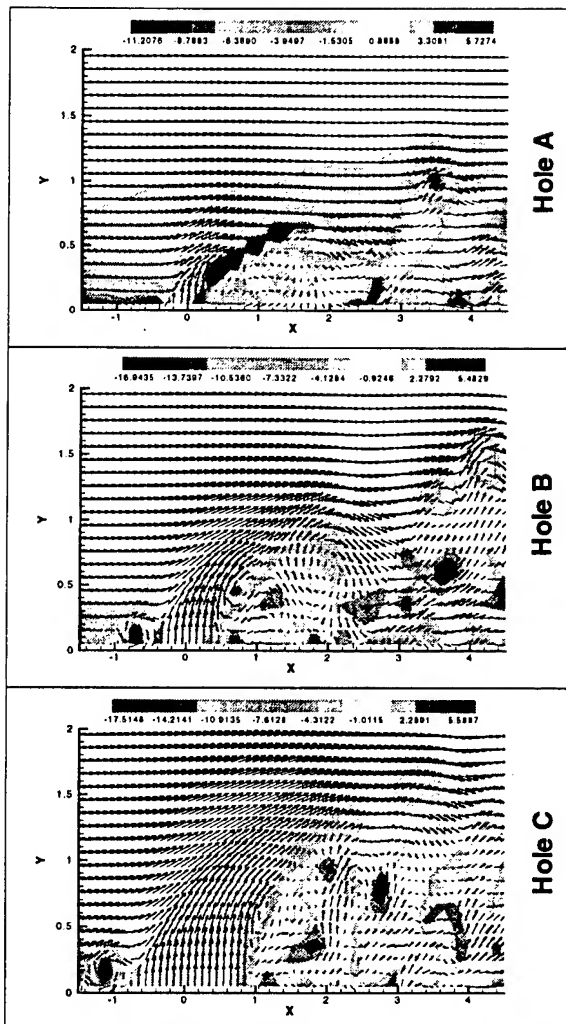


Figure 8 Contours of ω_z and instantaneous velocity vectors at $Z/D = 0.0$.

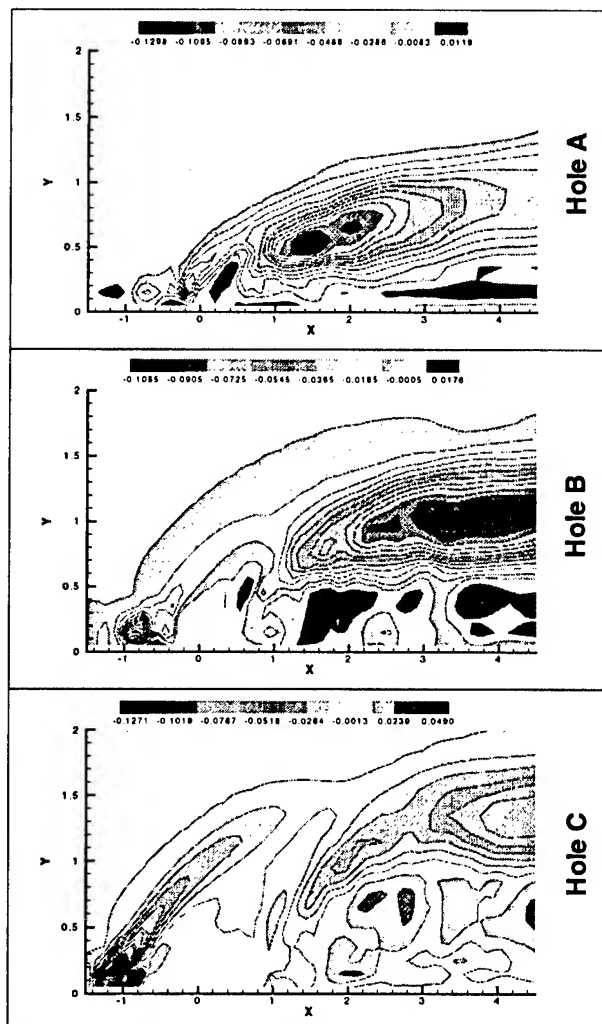


Figure 9 Contours of Reynolds stress $u'v'$ at $Z/D = 0.0$

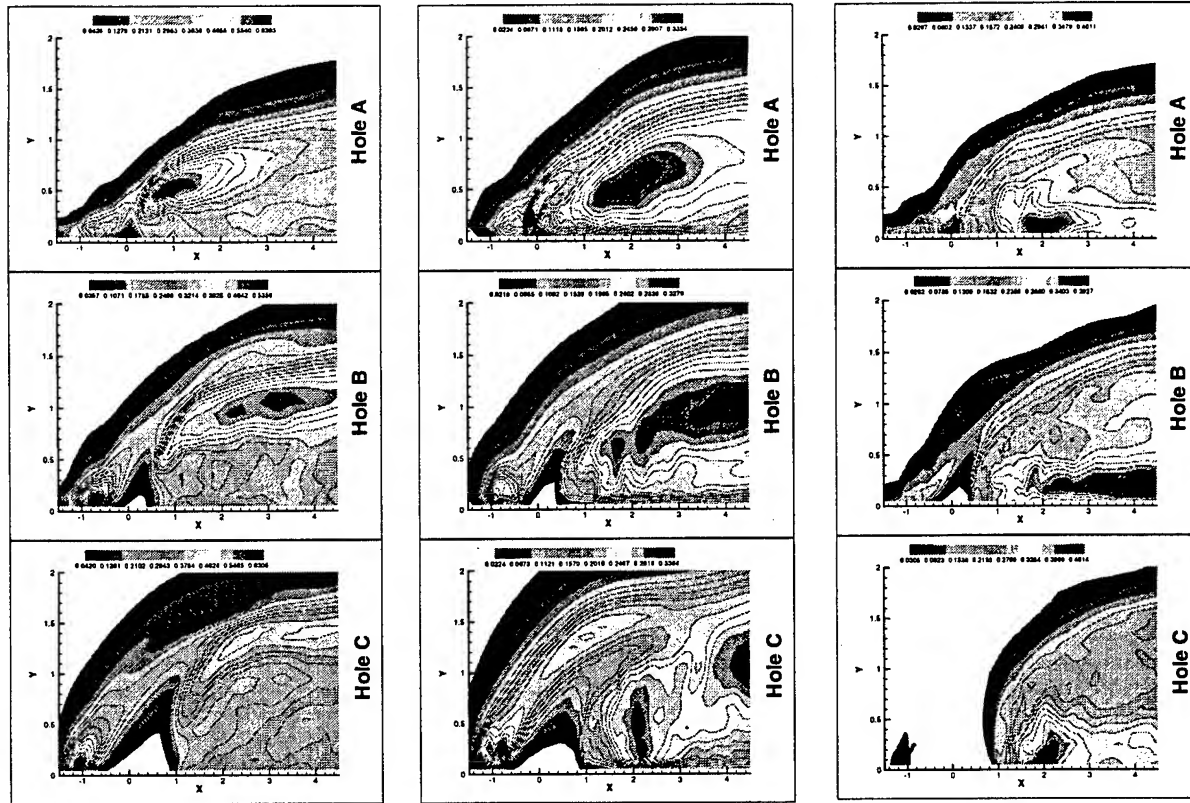


Figure 10 Contours of u_{rms} , v_{rms} and w_{rms} at $Z/D = 0.0$.

In Figure 10, we present the rms values of u , v and w fluctuation field. The contours of u_{rms} and v_{rms} show local large values in front of the jet corresponding to the location of horseshoe vortex in the cases of hole B and C. The u_{rms} values are largest at the leeward edge of the jet in the wake region for hole A and least for hole C. The values of v_{rms} in the wake region along the leeward edge of the jet indicate that normal stresses result in enhanced mixing of coolant jet with the entrained wake. These normal stresses are largest for hole A and lowest for hole C in the near jet field. However, on further downstream planes the trend is reversed. The value of w_{rms} is highest for hole C and lowest for hole A in the wake region. The value of w_{rms} on the windward edge of the jet for hole C is negligible as compared to other cases. The leeward edge of the jet is much farther into the mainflow for hole C as compared to the other cases where it is closer to the wall and entrained crossflow. Clearly, greater mixing is achieved for hole A and B as compared to hole C in the wake region of jet.

Contours of ω_x , ω_z and wall shear stress is presented in figure 11. The values of shear stress correlates with ω_z in front of the jet and with ω_x in the wake region. There is clear indication of the presence of ω_x at the trailing edge of the hole A and B in the opposite sense of CVP. Moreover, most of the vorticity in CVP comes from the sidewalls of the holes and warped mainflow (reverse flow) at the trailing edge will distort and reorient the trailing edge ω_z into X-direction. The contours of ω_z in front of the jet for holes B and C indicate the presence of horseshoe vortex. Signature of horseshoe vortex for hole A is seen after it bends around the jet in the contours of ω_x . The value of shear stress increases locally in front of the jet due to horseshoe vortex. Using Reynolds analogy of heat transfer and skin friction coefficient, one may expect a

higher heat transfer at this location. Large values are obtained along the sidewalls of holes. The low values indicate the separation events in the flow field.

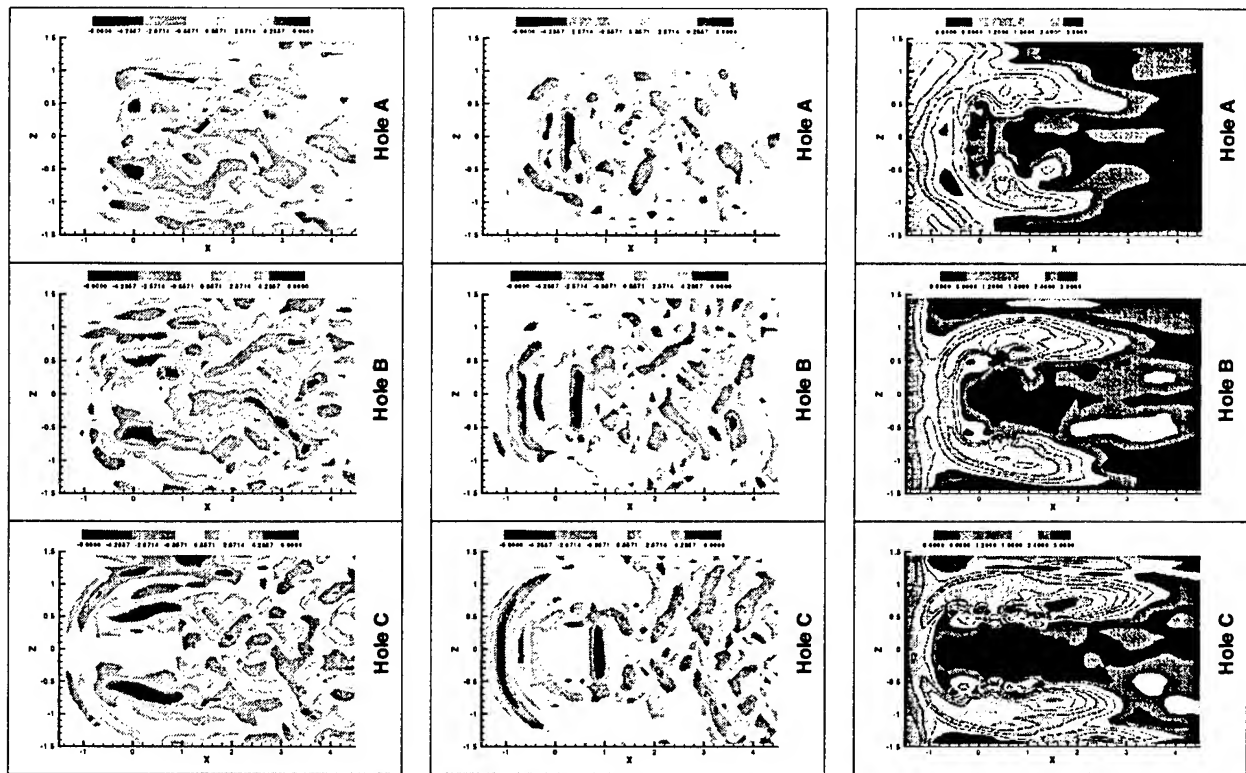


Figure 11 Contours of ω_x, ω_z and wall shear stress at $Y/D = 0.1$

CONCLUSION

Large eddy simulations of the jet-in-crossflow for three rectangular holes were performed. The results obtained are consistent with the experimental observations of various researchers (Haven, 1996, Andreopolous and Rodi, 1984, Fric and Roshko, 1994, Ajersch et al, 1995, Kelso et al, 1996). The following represent some of the major observations made in this study.

- The dispersion of jet in the mainstream is distinctly different for the three different hole geometries (Haven (1996) and Haven and Kurosaka (1997)). Dynamics and evolution of various flow structures is influenced by the hole geometry in the near jet region for the three hole aspect ratios investigated in this paper at this Reynolds number.
- For hole A, the streamwise velocity profile warps in same sense as observed by Haven (1996) (though not to the same extent). This leads to the evolution of leading edge as well as trailing edge vorticity that has the opposite sense between the CVP. The jet penetration is also smaller due to the counteracting induced velocity of this pair on the CVP.
- For hole B, the mixing in the wake region is enhanced and the jet penetrates farther into the mainflow as compared to hole A. The reverse flow in the wake region warps the crossflow profiles such that it leads to the evolution of trailing edge vorticity into anti-CVP vorticity. CVP breaks up into a multiple decked structure at downstream locations
- For hole C, the horseshoe structure is dominant in front of the jet. The jet penetration is highest in this case. The CVP breaks down into multiple decked structure and these smaller

vortices interact dynamically at further downstream locations. Large entrainment of the crossflow fluid is observed in the wake region for this case.

- The wake vortices are observed in all cases. However, the lateral migration of these vortices is largest for hole C and smallest for hole A.
- From the instantaneous snapshot at $X/D = 1.0$, it is clear that the horseshoe is relatively stronger than the CVP for hole A while the CVP is stronger than the horseshoe for hole C. It may be conjectured that the induced motion over the CVP itself leads to the formation of anti-kidney pair above the CVP for hole A. Similar arguments can explain the kidney pair above the CVP for hole C.
- The shear stress $u'w'$ magnitude correlates well with the lateral spreading of the jet. The shear stress $v'w'$ acts to damp the secondary vortex motions while $u'v'$ controls the jet penetration and the mixing at the jet-mainstream interface. Distinct distributions for various cases indicate differences in the dynamics and evolution of flow structures in corresponding cases.
- Contours of vorticity on a plane parallel to wall correlates well with the wall shear stress. The ω_x correlates in the wake region with shear stress, while ω_z correlates in front of the jet.

ACKNOWLEDGMENTS

This work was supported by a grant (NAG3-1641) from NASA-Lewis. Contract monitors were Dr. Chi Wang and Dr. Ray Gaugler. Their support is gratefully acknowledged.

REFERENCES

- Ajersch, P., Zhou, J.M., Ketler, S., Salcudean, M. and Gartshore, I. A. (1995), *Multiple jets in a crossflow: detailed measurements and numerical simulations*, ASME 95-GT-9.
- Andreopoulos, J. and Rodi, W. (1984), *Experimental investigation of jets in a crossflow*. J. Fluid Mech., Vol. 138, pp. 93-127.
- Andreopoulos, J. (1985), *On the structure of jets in a crossflow*. J. Fluid Mech., Vol. 157, pp. 163-197.
- Bardina, J, Ferziger, J.H. and Reynolds, W.C. (1983), *Improved turbulence models based on large eddy simulations of homogeneous, incompressible turbulent flows*, Report TF-19, Thermosciences Div., Eng., Dept. Mech. Stanford Univ.
- Batchelor, G.K. (1953), *Theory of homogeneous turbulence*, Cambridge University Press.
- Chong, M.S., Soria, J., Perry, A.E., Chacin, J., Cantwell, B.J. and Na, Y. (1998), *Turbulence structures of wall-bounded shear flows found using DNS data*, J. Fluid Mech., Vol. 357, pp. 225-247.
- Chorin, A.J. (1967), *A numerical method for solving incompressible viscous flow problems*, J. Comp. Phy., Vol. 2 pp. 12-26.
- Coelho, S.L.V. and Hunt, J.C.R. (1989), *The dynamics of the near field of strong jets in crossflows*, J. Fluid Mech., Vol. 200 pp. 95-120.
- Dubois, T., Jauberteau, F. and Temam, R. (1999), *Dynamic multilevel methods and the numerical simulation of turbulence*, Cambridge University Press.
- Fric, T.F. and Roshko, A. (1994), *Vortical structure in the wake of a transverse jet*. J. Fluid Mech., Vol. 279, pp.1-47.
- Garg, V. K., and Gaugler R. E., (1995), *Effect of velocity and temperature distribution at the hole exit on film cooling of turbine blades*, ASME paper 95-GT-2

- Garg, V. K., and Gaugler R. E. (1994), *Prediction of film cooling on gas turbine airfoils*, ASME paper 94-GT-2
- Ghosal, S. (1999), *Mathematical and physical constraints on large eddy simulation of turbulence*, AIAA Journal, Vol. 37, no. 4, pp.425-433.
- Ghosal, S. and Moin, P. (1995), *The basic equations for the large eddy simulations of the turbulent flows in complex geometry*, J. Comp. Phy., Vol. 118, pp.24-37.
- Haven, B.A. (1996), *The effect of hole geometry on the near field character of crossflow jets*, PhD. thesis, University of Washington.
- Haven, B.A. and Kurosaka, M. (1997), *Kidney and anti-kidney vortices in crossflow jets*, J. Fluid Mech., Vol 352, pp.27-64.
- Jones, W. P. and Wille, M. (1996), *Large eddy simulation of a round jet in crossflow*, Engineering Turbulence Modeling and Experiments 3. Ed. Rodi, W. and Bergeles, G. pp.199-209
- Jordan, S.A. (1994), *Use of the large eddy simulation dynamic model for turbulent shear driven cavity flows*, ASME FED-Vol. 184 pp. 141-150.
- Kelso, R.M., Delo, C. and Smits, A.J. (1993), *Unsteady wake structures in transverse jets*, Fluid Dynamics Panel Symposium, UK, AGARD-CP-534.
- Kelso, R.M., Lim, T.T. and Perry, A.E. (1996), *An experimental study of round jets in cross-flow*, J. Fluid Mech., Vol. 306, pp.111-144.
- Kim, S.W., and Benson, T.J. (1992), *Calculation of a circular jet in crossflow with a multiple-time-scale turbulence model*, Int. J. Comp. Phys. Vol 59. pp. 308-315
- Muldoon, F. and Acharya, S. (1999), *Numerical investigation of the dynamical behavior of a row of square jets in crossflow over a surface*, (To be presented at ASME-IGTI 99)
- Patankar, S. V. Basu, D. K. and Alpay, S. A. (1977), *Prediction of the three-dimensional velocity field of a deflected turbulent jet*, Trans. SME I: J. Fluids Engng 99, pp. 758-762
- Scotti, A., Meneveau, C. and Fatica, M. (1997), *Dynamic Smagorinsky model for anisotropic grids*. Phys. Fluids. Vol. 9 pp. 1856-1858.
- Speziale, C.G. (1985), *Galilean Invariance of subgrid scale stress models in large eddy simulation of turbulence*, J. Fluid Mech. Vol. 156, pp. 55-62.
- Sykes, R. I., Lewellen, W. S. and Parker, S. F. (1986), *On the vorticity dynamics of a turbulent jet in a crossflow*, J. Fluid Mech. vol. 80, pp. 49-80
- Yuan L.L., and Street, R. L. (1996), *Large Eddy Simulation of a Jet in Crossflow*, ASME Fluids Engineering Division Vol. 242, pp.253-260
- Zang, Y., Street, R.L. and Koseff, J.R. (1993), *A dynamic mixed subgrid scale model and its application to turbulent recirculating flows*, Phys. Fluids A Vol. 5 no. 12 pp. 3186-3196.
- Zhou, Y., Vahala, G. and Hossain, M. (1989), *A critical look at the use of filters in large eddy simulations*, Phys. lett. A Vol. 139 no. 7 pp. 330-332.

COMPRESSIBLE LARGE EDDY SIMULATION USING UNSTRUCTURED GRID: SUPERSONIC BOUNDARY LAYER

GERALD URBIN AND DOYLE KNIGHT

Rutgers University

Mechanical and Aerospace Engineering

Piscataway, N.J. 08854-8058, USA

Abstract. A Mach 3 adiabatic turbulent boundary layer is studied using Large Eddy Simulation (LES). The filtered compressible Navier-Stokes equations are solved on a three-dimensional unstructured grid of tetrahedral cells. A compressible extension of the method of Lund is developed to generate the inflow conditions. Different tests on subgrid scale model and grid refinements are studied. The friction velocity predicted is accurate within a few percent; profiles of Reynolds shear and normal stresses are in good agreement with experimental data as well. The objective of this preliminary study is to assess the capability of the unstructured compressible LES method.

1. Introduction

Most of the Large Eddy Simulation (LES) subgrid scale models developed to date have been applied to incompressible or subsonic flows. Also, most LES research has employed structured meshes in the context of finite-difference or spectral methods. A more thorough development of LES methods, in the context of compressible flow and unstructured grids (which can more readily handle complex geometries) is presented in this paper.

A three-dimensional LES algorithm for unstructured meshes has been developed in our laboratory. The algorithm is second- or third-order accurate in space and second- or fourth-order in time. It has previously been validated in the case of the decay of isotropic turbulence (Knight *et al.*, 1998) and low Mach number channel flow (Okongo *et al.*, 1998).

Preliminary results on a Mach 3 adiabatic turbulent boundary layer developing on a flat plate were presented at the 37th AIAA Aerospace

Sciences Meeting and Exhibit (Urbain *et al.*, 1999). The aim of this paper is to complete and to improve this study. In the first part, our rescaling-reintroducing process is detailed and discussed. Secondly, the influence of the subgrid-scale model and the convergence of the predictions with grid refinements are evaluated.

2. LES Methodology

In this section we summarize the LES methodology, including the governing equations, SGS model, numerical implementation and parallelization. Details are presented in (Knight *et al.*, 1998) and (Okongo *et al.*, 1998).

2.1. GOVERNING EQUATIONS

The governing equations are the three-dimensional filtered Navier-Stokes equations. For a function f , its filtered form \bar{f} and its Favre-averaged form \tilde{f} are

$$\bar{f} \equiv \frac{1}{V} \int_V G f dV \quad \tilde{f} \equiv \frac{\rho f}{\bar{\rho}}$$

where G is the filtering function and ρ is the density. From the Navier-Stokes equations for the instantaneous flow variables density (ρ), velocity in the i th coordinate direction (u_i), pressure (p) and temperature (T), Favre-averaging and spatial filtering yield the filtered Navier-Stokes equations (here written using the Einstein summation notation where repeated indices denote summation)

$$\begin{aligned} \frac{\partial \bar{\rho}}{\partial t} + \frac{\partial \bar{\rho} \tilde{u}_k}{\partial x_k} &= 0 \\ \frac{\partial \bar{\rho} \tilde{u}_i}{\partial t} + \frac{\partial \bar{\rho} \tilde{u}_i \tilde{u}_k}{\partial x_k} &= -\frac{\partial \bar{p}}{\partial x_i} + \frac{\partial \bar{T}_{ik}}{\partial x_k} \\ \frac{\partial \bar{\rho} \tilde{e}}{\partial t} + \frac{\partial}{\partial x_k} (\bar{\rho} \tilde{e} + \bar{p}) \tilde{u}_k &= \frac{\partial}{\partial x_k} (Q_k + T_{ik} \tilde{u}_i) \\ \bar{p} &= \bar{\rho} R \tilde{T} \end{aligned}$$

where

$$\begin{aligned} T_{ik} &= \tau_{ik} + \bar{\sigma}_{ik} & Q_k &= Q_k + \bar{q}_k \\ \tau_{ik} &= -\bar{\rho}(\tilde{u}_i \tilde{u}_k - \tilde{u}_i \tilde{u}_k) & Q_k &= -\bar{\rho} c_p (\tilde{T} \tilde{u}_k - \tilde{T} \tilde{u}_k) \\ \bar{\sigma}_{ik} &= \mu(\tilde{T}) \left(-\frac{2}{3} \frac{\partial \tilde{u}_j}{\partial \tilde{x}_j} \delta_{ik} + \frac{\partial \tilde{u}_i}{\partial x_k} + \frac{\partial \tilde{u}_k}{\partial x_i} \right) & \bar{q}_k &= k(\tilde{T}) \frac{\partial \tilde{T}}{\partial x_k} \\ \bar{\rho} \tilde{k} &= \frac{1}{2} (\overline{\rho u_i u_i} - \bar{\rho} \tilde{u}_i \tilde{u}_i) = -\frac{1}{2} \tau_{ii} & \bar{\rho} \tilde{e} &= \bar{\rho} c_v \tilde{T} + \frac{1}{2} \bar{\rho} \tilde{u}_i \tilde{u}_i + \bar{\rho} \tilde{k} \end{aligned}$$

It is to be noticed that the specific form of the energy equation was found (Martin *et al.*, 1999) to provide an accurate model of the SGS turbulent diffusion in decaying compressible isotropic turbulence. Two different SGS models are implemented in the LES code. The first is the classical constant-coefficient Smagorinsky model

$$\begin{aligned}\tilde{S}_{ij} &\equiv \frac{1}{2} \left(\frac{\partial \tilde{u}_i}{\partial \tilde{x}_j} + \frac{\partial \tilde{u}_j}{\partial \tilde{x}_i} \right) \\ \tau_{ij} &= 2C_R \bar{\rho} \Delta^2 \sqrt{\tilde{S}_{mn} \tilde{S}_{mn}} \left(\tilde{S}_{ij} - \frac{1}{3} \tilde{S}_{kk} \delta_{ij} \right) \\ Q_j &= \bar{\rho} c_p \frac{C_R}{Pr_t} \Delta^2 \sqrt{\tilde{S}_{mn} \tilde{S}_{mn}} \frac{\partial \tilde{T}}{\partial x_j}\end{aligned}$$

where $C_R = 0.00423$ is the model coefficient, and Δ is the length scale which is related to the local grid size (Knight *et al.*, 1998). For boundary layer flows, Δ is modified by the Van Driest damping factor $D = 1 - e^{-n^+/A}$ where $A = 26$, $n^+ = nu_\tau/\nu_w$ is the normal distance to the (nearest) solid boundary normalized by the viscous length scale ν_w/U_τ where ν_w is the kinematic viscosity evaluated at the wall and U_τ is the local friction velocity. The second model is MILES (Boris *et al.*, 1992) wherein the inherent dissipation in the numerical algorithm is taken as the SGS model (*i.e.*, $C_R = 0$).

2.2. NUMERICAL METHOD

We simplify the notation by hereafter dropping the tilde and overbar. Furthermore, the flow variables are nondimensionalized using the reference density ρ_∞ , velocity U_∞ , static temperature T_∞ and length scale L , with Mach number $M_\infty = U_\infty/\sqrt{\gamma RT_\infty}$. The governing equations may be written in finite volume form for a control volume V with surface ∂V :

$$\frac{d}{dt} \int_V Q dV + \int_{\partial V} (F\hat{i} + G\hat{j} + H\hat{k}) \cdot \hat{n} dA = 0 \quad (1)$$

where

$$\begin{aligned}Q &= \begin{Bmatrix} \rho \\ \rho u \\ \rho v \\ \rho w \\ \rho e \end{Bmatrix} & F &= \begin{Bmatrix} \rho u \\ \rho u^2 + p - T_{xx} \\ \rho uv - T_{xy} \\ \rho uw - T_{xz} \\ (\rho e + p)u - Q_x - \beta_x \end{Bmatrix} \\ G &= \begin{Bmatrix} \rho v \\ \rho uv - T_{xy} \\ \rho v^2 + p - T_{yy} \\ \rho vw - T_{yz} \\ (\rho e + p)v - Q_y - \beta_y \end{Bmatrix} & H &= \begin{Bmatrix} \rho w \\ \rho uw - T_{xz} \\ \rho vw - T_{yz} \\ \rho w^2 + p - T_{zz} \\ (\rho e + p)w - Q_z - \beta_z \end{Bmatrix}\end{aligned}$$

$$\beta_x = \mathcal{T}_{xx}u + \mathcal{T}_{xy}v + \mathcal{T}_{xz}w$$

$$\beta_y = \mathcal{T}_{xy}u + \mathcal{T}_{yy}v + \mathcal{T}_{yz}w$$

$$\beta_z = \mathcal{T}_{xz}u + \mathcal{T}_{yz}v + \mathcal{T}_{zz}w$$

An unstructured grid of tetrahedra is employed, with a cell-centered storage architecture. The cell-averaged values, stored at the centroid of each tetrahedron of volume V_i are $Q_i = \frac{1}{V_i} \int_{V_i} Q dV$. The inviscid fluxes are computed using an exact one-dimensional Riemann solver (Godunov's method (Gottlieb *et al.*, 1988)) applied normal to each face. The inviscid flux computations require the values of each variable on either side of the cell faces. These values are obtained from the cell-averaged values by second-order or third-order function reconstruction using the Least Squares method of (Ollivier *et al.*, 1997). More details on the reconstruction schemes are given in (Okongo *et al.*, 1998).

The viscous fluxes and heat transfer are computed by application of Gauss' theorem to the control volume whose vertices are the centroids of the cells which share each node. The second-order accurate scheme (in 2-D) is given by (Knight *et al.*, 1994).

3. Rescaling-reintroducing Method

3.1. STATE OF ART

There have been only a few DNS studies of compressible turbulent boundary layers. DNS of a spatially developing boundary layer (*i.e.*, the "natural" configuration) requires such high resolution that one usually chooses to simulate just the earliest stage of transition to turbulence (Fasel *et al.*, 1990; Joslin *et al.*, 1993; Kleiser *et al.*, 1991). An exception is (Rai *et al.*, 1993) who performed a DNS of complete spatial transition; however, the cost was high (*i.e.*, 800 hours on a CRAY YMP). Although DNS proves to be a very efficient tool in temporal boundary layers (streamwise-periodic cases, which allow reduction in the physical domain and computational effort (Guo *et al.*, 1995; Le *et al.*, 1997; Lund *et al.*, 1998; Spalart *et al.*, 1987; Spalart *et al.*, 1988)), it is nonetheless limited to low Reynolds numbers.

LES computations enable to consider higher Reynolds number flows (Ducros *et al.*, 1996; Elhady *et al.*, 1994). Nevertheless simulating a spatially-developing turbulent boundary layer from the transition process to a fully developed turbulent state needs a lengthy development domain. It is still prohibitively expensive.

Different methods enable to consider a smaller domain (which is desirable in order to reduce the cost associated with such a simulation). One approach consist in using quasi-periodic boundary conditions in the streamwise direction. Accounting for the spatial growth in the inflow conditions

can be done by adding source terms to the Navier-Stokes equations (Spalart *et al.*, 1988). Notice that the resulting transformed equations require a special-purpose flow solver and need to introduce a coordinate transformation that can not well be extended to a compressible unstructured grid code. (Lund *et al.*, 1998) propose an alternative method that is more promising.

3.2. RESCALING-REINTRODUCING METHOD

A compressible extension of the method of (Lund *et al.*, 1998) is next developed. The simulation generates its own inflow conditions through a sequence of operations where the flowfield at a downstream station is rescaled and reintroduced at the inflow boundary (Fig. 1). The idea is to decompose each flowfield components into a mean and fluctuating part, and then to apply the appropriate scaling law to each one separately. It is to be noticed that such a method can be used to generate the inflow database for a second computation, like a compression corner flow (Urbin *et al.*, 1999).

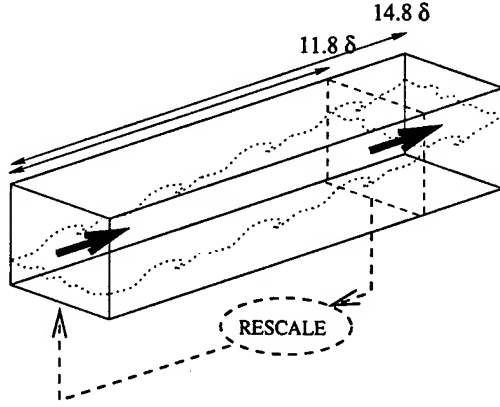


Figure 1. Computational domain: Flow at the downstream station is rescaled and reintroduced.

Decompose each of the quantities u in a mean part U and an instantaneous time fluctuating part u''

$$U \equiv \frac{1}{t_f - t_i} \int_{t_i}^{t_f} u dt \quad u'' \equiv u - U$$

As a compressible flow is considered, we note the Van Driest - Fernholz & Finley transformation of a quantity U as U_{vd} . In case of an adiabatic plate flow, it writes:

$$U_{vd} = \frac{1}{b} \sin^{-1}(bU) \quad \text{with} \quad b = \sqrt{\frac{\frac{\gamma-1}{2} M_\infty^2 P_r}{1 + \frac{\gamma-1}{2} M_\infty^2 P_r}}$$

where $Pr = 0.89$ is the mean turbulent Prandtl number.

The multi-layer scaling holds in compressible turbulent boundary layers as in incompressible one (Fernholz *et al.*, 1980). Let us consider the inner region and the outer region of the boundary layer separately. On the inner side, a straightforward extension of the classical Law of the Wall reads in Van Driest coordinates:

$$U_{vd}^{inn} = U_\tau(x) \times f_1(y^+) \quad \text{with} \quad f_1(y^+) = \frac{1}{\kappa} \ln(y^+) + C$$

where $y^+ = (U_\tau/\nu) \times y$ is the wall coordinate, U_τ is the mean friction velocity, κ is Von Karman's constant, and C is a constant.

On the outer side, the defect law reads, also in Van Driest coordinates:

$$U_{vd}^\infty - U_{vd}^{out} = U_\tau(x) \times f_2(\eta)$$

where $\eta = y/\delta$ is the outer coordinate, δ is the boundary layer thickness, U^∞ is the free-stream velocity and f_2 is a second universal function (at this stage, there is no need to define it more precisely).

As f_1 and f_2 are supposed to be independent of the streamwise position x considered, the velocity U_{rec} at the downstream station to be recycled and the velocity U_{inl} at the inlet can be linked as:

$$U_{vd,inl}^{inn} = \beta \times U_{vd,rec}(y_{inl}^+)$$

and in the outer region:

$$U_{vd,inl}^{out} = \beta \times U_{vd,rec}(\eta_{inl}) + (1 - \beta) \times U^\infty$$

where $\beta = U_{\tau,inl}/U_{\tau,rec}$ is the ratio of friction velocity between the inlet station and the recycled station. It is to be noticed that y_{inl}^+ and η_{inl} are the inner and outer coordinates at the inlet station, but $U_{vd,rec}$ is evaluated at the recycle station.

The fluctuating part of the velocity is decomposed in a similar way. The velocity fluctuation reads in the inner domain and in the outer domain:

$$u_{inl}''^{inn} = \beta \times u_{rec}''(y_{inl}^+, z, t) \quad u_{inl}''^{out} = \beta \times u_{rec}''(\eta_{inl}, z, t)$$

The scaling for the wall-normal velocity compound, between the recycle and the inlet stations is assumed as:

$$V_{inl}^{inn} = V_{rec}(y_{inl}^+) \quad V_{inl}^{out} = V_{rec}(\eta_{inl})$$

It is to be noticed that such a simple scaling is used as a convenient approximation that avoid to compute the derivatives $\partial U_\tau/\partial x$ and $\partial \delta/\partial x$ needed

to be consistent with the streamwise velocity scaling. Such approximation appears to be sufficient for a zero pressure gradient boundary layer (Arad *et al.*, 1999).

For the spanwise velocity compound no scaling is needed as the mean should stay zero. The v'' and w'' velocity fluctuations scaling are the same as for u'' .

The temperature is scaled to take into account the compressibility effects as well. As the streamwise pressure gradient is negligible compared to the wall normal temperature gradient, the next scaling is used:

$$T_{inl}^{inn} = T_{rec}(y_{inl}^+) \quad T_{inl}^{out} = T_{rec}(\eta_{inl})$$

In a supersonic boundary layer the pressure fluctuations are negligible compared to the temperature fluctuations as well, let us write:

$$T_{inl}^{''inn} = T_{rec}''(y_{inl}^+, z, t) \quad T_{inl}^{''out} = T_{rec}''(\eta_{inl}, z, t)$$

At this stage, the entire profiles, valid over the entire layer, are obtained by forming a weighted average of the inner and outer profile, as proposed by (Lund *et al.*, 1998):

$$u_{inl} = (U_{inl}^{inn} + u_{inl}^{''inn}) \times (1 - W(\eta_{inl})) + (U_{inl}^{out} + u_{inl}^{''out}) \times W(\eta_{inl})$$

The weighting function W is defined as:

$$W(\eta) = \frac{1}{2} \left(1 + \frac{\tanh \left[\frac{4(\eta-B)}{(1-2B)\times\eta+B} \right]}{\tanh(4)} \right)$$

using $B = 0.2$ to provide a smooth transition at $y/\delta = 0.2$ (Lund *et al.*, 1998).

The last stage of the rescaling process consists in determining U_τ and δ at the inlet. Best results have been obtained by imposing the ratio $U_{\tau,inl}/U_{\tau,rec}$ and $\delta_{inl}/\delta_{rec}$ according to the combined Law of the Wall and Wake (Smits *et al.*, 1996) and the next classical empirical correlation:

$$\frac{\delta_{rec}}{\delta_{inl}} = \left(1 + \frac{x_{rec} - x_{inl}}{\delta_{inl}} \times 0.37^{\frac{1}{1-1/5}} \times Re_{\delta_{inl}}^{-\frac{1/5}{1-1/5}} \right)^{1-1/5}$$

where $Re_{\delta_{inl}}$ is the Reynolds number based on the incoming boundary layer thickness. Here $Re_{\delta_{inl}} = 2 \times 10^4$, $U_{\tau,inl}/U_{\tau,rec} = 1.030$ and $\delta_{inl}/\delta_{rec} = 0.787$.

4. Configuration

A Mach 3 adiabatic flat plate turbulent boundary layer at Reynolds number $Re_\delta = 2 \times 10^4$ is simulated (to simplify the notation, we use $\delta \equiv \delta_{inl}$).

Allowing x, y and z to denote the streamwise, transverse and spanwise directions, respectively, the computational domain is $L_x = 14.8\delta$, $L_y = 3.4\delta$ and $L_z = 4.4\delta$. The spanwise width L_z is approximately six times the experimental spanwise streak spacing (assuming the compressible turbulent boundary layer streaks scale in accordance with incompressible experimental results). The streamwise length L_x is approximately three times the mean experimental streamwise streak size. The height L_y is based on the requirement that acoustic disturbances originating at the upper boundary do not interact with the boundary layer on the lower wall. The baseline grid resolution is 1,600,000 tetrahedral cells. The grid at the wall uses 101×65 nodes. The nodal grid is stretched uniformly in the y using a geometric factor of 1.088. The height Δn of the first cell adjacent to the boundary is less than one wall unit ($\Delta n U_\tau / \nu_w < 1$ where ν_w is the kinematic viscosity at the wall, $U_\tau = \sqrt{\tau_w / \rho_w}$ is the friction velocity, τ_w is the wall shear stress and ρ_w is the density at the wall).

In order to provide converged data, the primitive variables are averaged in spanwise direction and the statistical evaluations are performed on a period longer than $t_f - t_i = 40\delta / U_\infty$. The notation for the combined temporal and spanwise average is

$$\langle\langle f \rangle\rangle \equiv \frac{1}{L_z} \frac{1}{t_f - t_i} \int_0^{L_z} \int_{t_i}^{t_f} f dt dz$$

5. Baseline Smagorinsky

The preliminary computation uses the Smagorinsky subgrid-scale model. Such a LES has run for 135 inertial time-scales δ / U_∞ (Fig. 2). The different results have been presented in the paper (Urbain *et al.*, 1999). Good predictions of the adiabatic wall temperature, temperature-velocity relationship (Walz *et al.*, 1969) (Fig. 3), mean streamwise velocity profile (Fig. 4), Reynolds normal stress (Fig. 9) and Reynolds shear stress profiles (Fig. 10) have been achieved.

The present aim is to evaluate the influence of the subgrid-scale model and the convergence of the predictions with grid refinements.

6. Influence of SGS Model: Baseline MILES

With the objective of examining the influence of the Subgrid Scale Model on the flow prediction, we perform a simulation using no explicit turbulence model at all. The energy dissipation is then only due to fluid viscosity and numerical dissipation. In this sense, we perform a Monotone Integrated Large Eddy Simulation (MILES). In practice, the previous simulation was

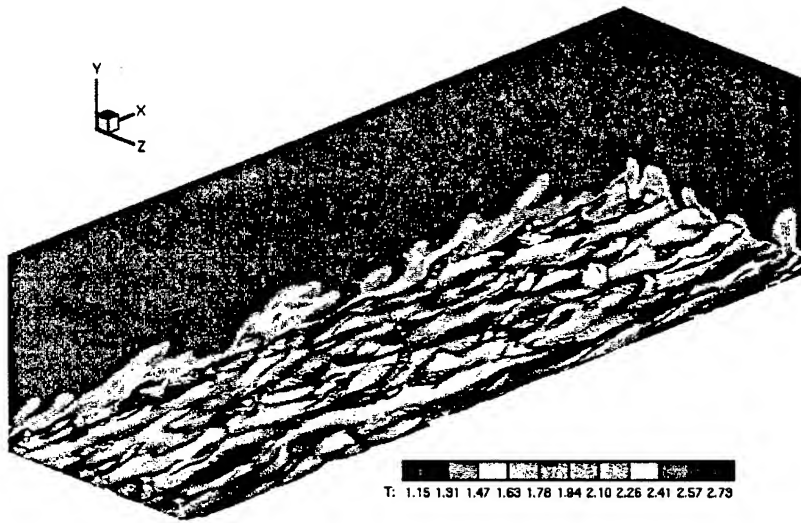


Figure 2. Instantaneous contour plot of temperature. Streaks shown with an high temperature isosurface

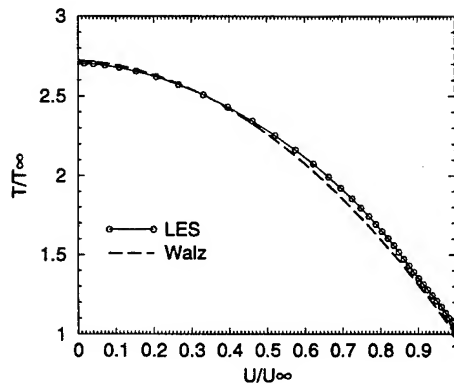


Figure 3. Temperature velocity relationship: comparison with the quadratic profile.

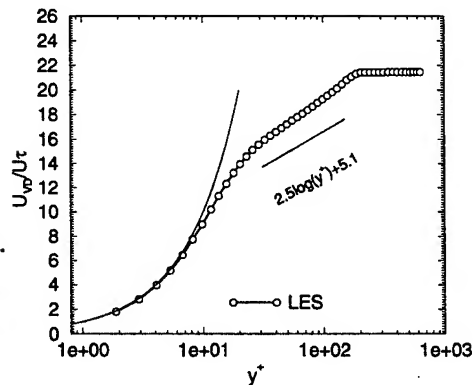


Figure 4. Mean streamwise velocity profile (Preliminary result).

stopped at the time $t = 135\delta/U_\infty$. Now we run it again from this time, without the SGS. Such a technique assures that the configuration is unmodified, and it provides an excellent flow initiation that minimize transient period.

For a total elapsed time of $t = 230\delta/U_\infty$, the streamwise mean profile (Fig. 5) is virtually identical to the previous LES result. The same trend is observed by comparing the streamwise and wall-normal velocity fluctuations (Fig. 6 and 7). The beneficial effect of the Smagorinsky model appears

TABLE 1. Simulation Parameter and Grid Size at the Wall and at the Boundary Layer Edge (Respectively in Wall Unit and δ Unit)

Name	SGS	$\Delta X^+ \cdot \Delta Y_{wall}^+ \cdot \Delta Z^+$	$\Delta X^\delta \cdot \Delta Y_{y=\delta}^\delta \cdot \Delta Z^\delta$
Baseline Smagorinsky	yes	$28 \times 0.9 \times 13$	$0.15 \times 0.086 \times 0.069$
Baseline MILES	no	$28 \times 0.9 \times 13$	$0.15 \times 0.086 \times 0.069$
DX2 MILES Coarse	no	$56 \times 0.9 \times 13$	$0.30 \times 0.086 \times 0.069$
DY2 MILES Coarse	no	$28 \times 1.7 \times 13$	$0.15 \times 0.165 \times 0.069$
DZ2 MILES Coarse	no	$28 \times 0.9 \times 26$	$0.15 \times 0.086 \times 0.137$
Refined MILES	no	$18 \times 1.5 \times 6.5$	$0.10 \times 0.140 \times 0.034$

to be very limited. In fact the local turbulent viscosity predicted by the model never exceeds 27% of the molecular viscosity. It is not our aim here to discuss the reason for such a behavior, that is surely specific to the use of the Godunov scheme with the 2nd order LS reconstruction. The practical conclusion is that there is no more need for the Smagorinsky model, so all of the remaining computations are performed without the SGS model.

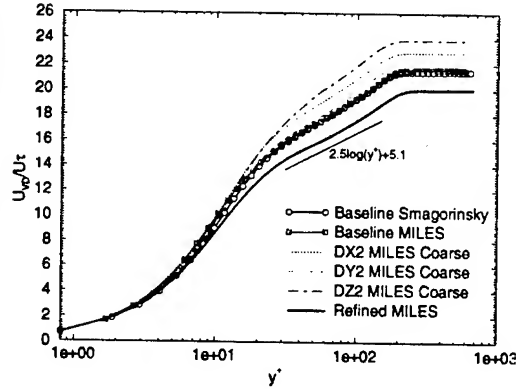


Figure 5. Mean streamwise velocity profile.

7. Grid coarsening: DX2, DY2, DZ2

The LES and MILES grid size follows the classical recommendations for turbulent subsonic boundary layer, but it has never been proven that they apply for supersonic boundary layer as well. Different grids refinements tests are needed. We separately consider streamwise, wall-normal and spanwise directions (respectively x , y and z). The previous LES needed 3500 CPU hours on SGI-R10000 for a total elapsed time of $135\delta/U_\infty$. Computing multiple finer grids simulations would require substantially more computer resources. An alternative approach is to perform the multiple tests on coarser grids. The question is to know which direction is the more sensitive with mesh coarsening (*a fortiori* mesh refinement). The answer will enable the design of a better grid.

Three tests are performed (DX2, DY2 and DZ2) using respectively grids

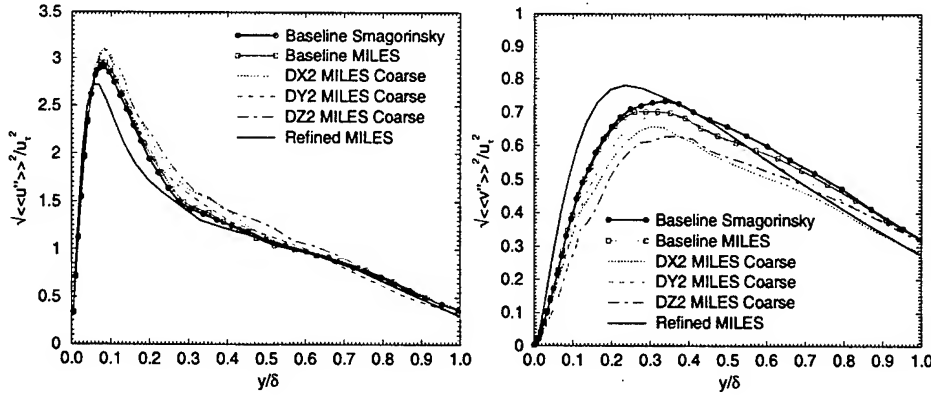


Figure 6. Longitudinal Reynolds stress. Figure 7. Wall-normal Reynolds stress.

enlarged by a factor 2 in x, y and z directions (Table 1). Everything else stays the same. No SGS model is employed and thus cases DX2, DY2 and DZ2 are MILES. The initial flow field characteristics are interpolated from the LES computation at its final time $t = 135\delta/U_\infty$. An additional elapsed time of $86\delta/U_\infty$ is employed for each case to enable transient period to disappear and to obtain suitable statistical average.

TABLE 2. Friction velocity

Name	U_τ/U_∞
Baseline Smagorinsky	0.0532
Baseline MILES	0.0528
DX2 MILES Coarse	0.0490
DY2 MILES Coarse	0.0513
DZ2 MILES Coarse	0.0482
Refined MILES	0.0563
Empirical Friction Law	0.0544-0.0598

The streamwise mean profile is drastically overestimated for DX2 and DZ2 in the logarithmic region as observed in Fig. 5. The deviation from the empirical and classical approximation $U_{vd}/U_\tau = 2.5 \log(y^+) + 5.1$ is greater. Such a behavior is mainly due to the friction velocity underprediction (Table 2). DX2 and DZ2 respectively predict a friction velocity 7.7% and 9.5% smaller than the MILES prediction (initial grid). On the contrary, DY2 underestimates it by less than 3%. Furthermore, the maximum streamwise Reynolds stresses is a little bit increased (Fig. 6) and the maximum wall-normal Reynolds stresses is decreased (Fig. 7). These observations are effectively typical of an under-resolved LES.

Based on the observations that the baseline simulation appears to be very sensitive to the resolution in x and z direction, and nearly insensitive with the resolution in y direction, a refined grid has been designed (Table 1: Refined MILES). As expected, the friction velocity increases : $U_\tau/U_\infty = 0.0563$ (Table 2). The deviation from the empirical and classical approximation $U_{vd}/U_\tau = 2.5 \log(y^+) + 5.1$ is now reduced (Fig. 5).

Further improvement can reasonably be achieved but at this stage the MILES prediction accuracy is comparable to the reference DNS (Lund *et al.*, 1998).

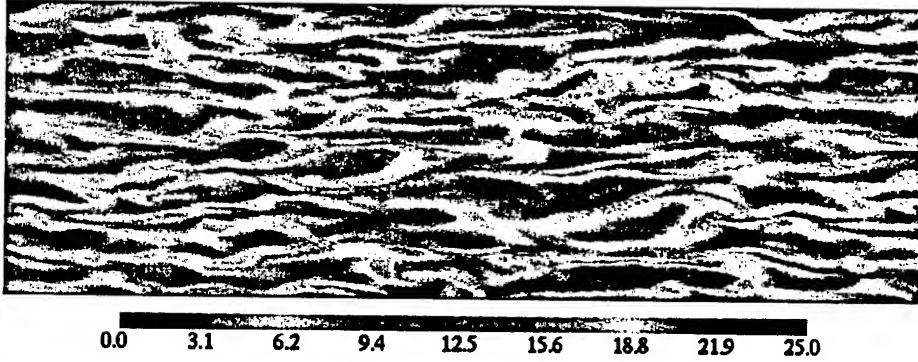


Figure 8. Streaks shown with contour plot of high vorticity modulus. Cut $Y^+ = 25$.

The refined MILES does not use a grid as fine as required by DNS. In classical LES the grid at the wall has to be fine enough to resolve the first hairpin-vortices (Fig. 8) whose size is roughly one hundred wall units. The phenomena is so complex that it can not be modeled by classical SGS. At the wall, the refined MILES grid is only 50% coarser in wall-normal Y direction than the DNS one from (Adams *et al.*, 1997), for a same Mach number and comparable Reynolds number. In the other directions: $\Delta X_{MILES}^+ > 300\% \Delta X_{DNS}^+$ and $\Delta Z_{MILES}^+ > 300\% \Delta Z_{DNS}^+$. At the edge of the boundary layer, the mesh size ratio is now larger: $\Delta Y_{MILES}^\delta = 700\% \Delta Y_{DNS}^\delta$. The unstructured grid method should be able to increase ΔX_{MILES}^δ and ΔZ_{MILES}^δ in order to reduce required computer resources but the present MILES computation does not use this advantage.

8. Validation Against Experimental Data

No friction velocity U_τ experimental data is available at Reynolds number $Re_\delta = 2 \times 10^4$ and Mach number $M = 3$. The theoretical value based on the friction law obtained from the combined Law of the Wall and Wake (using the classical coefficients $\kappa = 0.41$; $C = 5.0$; $\Pi = 0.55$) is 0.0544. Nevertheless at such low Reynolds number the validity of this value for Π

is doubtful (Fernholz *et al.*, 1980). A large discrepancy appears between the experimental data. $\Pi = 0.12$ seems to be a reasonable average value, which give $U_\tau/U_\infty = 0.0598$. The refined MILES prediction is so less than 6% accurate.

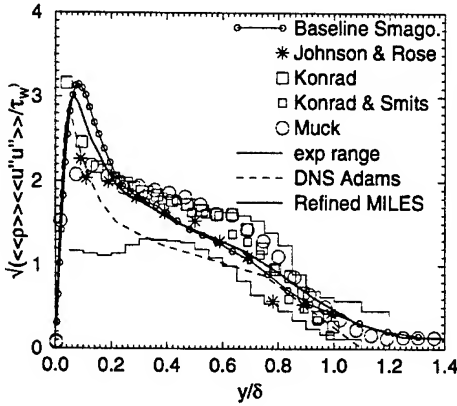


Figure 9. Streamwise Reynolds stress.

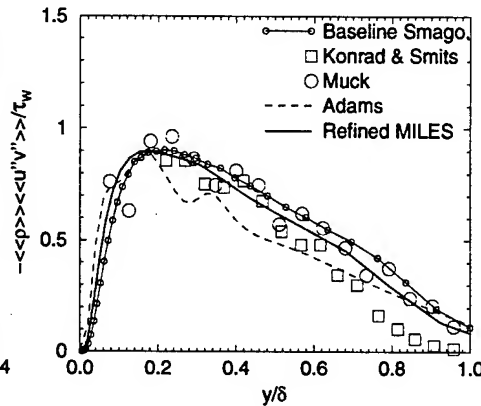


Figure 10. Reynolds shear stress.

TABLE 3. Flow Parameters

Name	Mach n°	Re_δ
Refined MILES & Baseline Smagorinsky	3.0	20×10^3
DNS (Adams <i>et al.</i> , 1997)	3.0	25×10^3
Exp1 (Johnson <i>et al.</i> , 1975)	2.9	1000×10^3
Exp2 (Konrad <i>et al.</i> , 1993)	2.9	1590×10^3
Exp3 (Konrad <i>et al.</i> , 1998)	2.87	1900×10^3
Exp4 (Muck <i>et al.</i> , 1984)	2.87	1638×10^3
Exp5 (Zheltovodov <i>et al.</i> , 1986)	1.7-9.4	up to 2000×10^3

ALL CASES WITH ADIABATIC WALL

For further validations, the mean streamwise resolved turbulent kinematic normal stress $\langle u''u'' \rangle$, normalized using the local mean density $\langle \rho \rangle$ and wall shear stress τ_w , is shown in Fig. 9. As discussed in (Zheltovodov *et al.*, 1986; Smits *et al.*, 1996), the scaling $\langle \rho \rangle \langle u''u'' \rangle / \tau_w$ provides an approximate self-similar correlation of experimental data for supersonic flat plate zero pressure gradient adiabatic boundary layers, although the measurements close to the wall are subject to considerable uncertainty. Here are displayed data from (Konrad *et al.*, 1998; Johnson *et al.*, 1975; Muck *et al.*, 1984; Konrad *et al.*, 1993), as well as upper and lower bounds of an extensive set of experimental data for the

Mach number range $M = 1.72 - 9.4$ in accordance with generalizations of (Zhel'tovodov *et al.*, 1986). The characteristics of the different experiments are displayed in Table 3. The computed results show good agreement with experiment for the main part of the boundary layer ($y/\delta > 0.2$), despite a significantly higher experimental Reynolds number. The decreasing slope corresponds precisely to (Johnson *et al.*, 1975) data. For $y/\delta < 0.2$ the presence of the typical high level peak in the near wall region is supported by experimental data of (Konrad *et al.*, 1993) and the DNS data from (Adams *et al.*, 1997), which is nearly at the same Reynolds number as the LES. But no conclusion can be drawn about the precise y position and the width of this peak without further experimental data or DNS.

In Fig. 10 the Reynolds shear stress distributions are shown for the same experiments and the DNS. Again, the data fit well in the outer part of the boundary layer. The maximum value and the decreasing slope are again well predicted.

9. Conclusion

In addition to the preliminary study (Urbain *et al.*, 1999) multiple Large Eddy Simulations of a Mach 3 adiabatic turbulent boundary layer developing on a flat plate are presented. With the objective of examining the influence of the Subgrid Scale Model on the flow prediction, we perform a simulation using no explicit turbulence model at all. In this sense, we perform a Monotone Integrated Large Eddy Simulation (MILES). The statistical predictions (mean velocity, normal Reynolds stress and Reynolds shear stress) appear to be as accurate as the LES one. All things considered, the refined MILES predicts a better friction velocity within a few percent error and a correct mean streamwise velocity profile. The adiabatic wall temperature, temperature-velocity relationship, Reynolds normal stress, Reynolds shear stress profiles are accurately predicted as well. It establishes more firmly the unstructured grid method and the rescaling-reintroducing process.

10. Acknowledgments

This research is supported by AFOSR under Grant Number F49620-99-1-0008 monitored by Dr. L. Sakell. The computations were performed at Rutgers University and the National Center for Supercomputing Applications and the Scientific Computing Facility Boston University under Grant CTS980016N.

References

Adams N.A. Direct Numerical Simulation of Turbulent Supersonic Boundary Layer Flow.

- Advances in DNS/LES*, Proceedings of the First AFOSR International Conference on DNS/LES, Greyden Press Columbus, pp 29-40, 1997.
- E. Arad and M. Wolfshtein. Analysis of Equilibrium Adverse Pressure Gradient Boundary Layer Using Large Eddy Simulation. AIAA Paper 99-0420, 1999.
- J. Boris, F. Grinstein, E. Oran, and R. Kolbe. New Insights into Large Eddy Simulation. *Fluid Dynamics Research*, 10:199-228, 1992.
- F. Ducros, P. Comte, and M. Lesieur. Large Eddy Simulation of Transition to Turbulence in a Boundary Layer Developing Spatially over a Flat Plate. *Journal of Fluid Mechanics*, 326:1-36, 1996.
- N. El-Hady, T. Zang, and U. Piomelli. Applications of the Dynamic Subgrid-Scale Model to Axisymmetric Transitional Boundary Layer at High Speed. *Physics of Fluids*, 6:1299-1309, 1994.
- H. Fasel and U. Konzelmann. Non-Parallel Stability of a Flat-Plate Boundary Layer Using the Complete Navier-Stokes Equations. *Journal of Fluid Mechanics*, 221:311-347, 1990.
- H. Fernholz and P. Finley. A Critical Commentary on Mean Flow Data for Two-dimensional Compressible Turbulent Boundary Layers. *AGARD Report*, 253:59-63, 1980.
- J. Gottlieb and C. Groth. Assessment of Riemann Solvers for Unsteady One-Dimensional Inviscid Flows of Perfect Gases. *Journal of Computational Physics*, 78:437-458, 1988.
- Y. Guo, N. Adams, and L. Kleiser. Modeling of Non-Parallel Effects in Temporal Direct Numerical Simulation of Compressible Boundary Layer. *Theoretical and Computational Fluid Dynamics*, 7:141-157, 1995.
- D. Johnson and W. Rose. Laser Velocimeter and Hot Wire Anemometer Comparison in a Supersonic Boundary Layer. *AIAA Journal*, 13:512-515, 1975.
- R. Joslin, C. Street, and C. Chang. Spatial Direct Numerical Simulation of Boundary Layer Transition Mechanism: Validation of PSE Theory. *Theoretical and Computational Fluid Dynamics*, 4:271-288, 1993.
- L. Kleiser and T. Zang. Numerical Simulation of Transition in Wall-Bounded Shear Flows. *Annual Review of Fluid Mechanics*, 23:495-537, 1991.
- D. Knight. A Fully Implicit Navier-Stokes Algorithm Using an Unstructured Grid and Flux Difference Splitting. *Applied Numerical Mathematics*, 16:101-128, 1994.
- D. Knight and G. Degrez. Shock Wave Boundary Layer Interactions in High Mach Number Flows - A Critical Survey of Current CFD Prediction Capabilities. *AGARD AR-319*, Volume 2, 1998.
- D. Knight, G. Zhou, N. Okong'o, and V. Shukla. Compressible Large Eddy Simulation Using Unstructured Grids. AIAA Paper 98-0535, 1998.
- W. Konrad. A Three Dimensional Supersonic Turbulent Boundary Layer Generated by an Isentropic Compression. *Ph.D Thesis*, Princeton University NJ, 1993.
- W. Konrad and A. Smits. Turbulence Measurements in a Three-Dimensional Boundary Layer in Supersonic Flow. *Journal of Fluid Mechanics*, 372:1-23, 1998.
- H. Le, P. Moin, and J. Kim. Direct Numerical Simulation of Turbulent Flow over a Backward Facing Step. *Journal of Fluid Mechanics*, 330:349-349, 1997.
- S. Lee, S. Lele, and P. Moin. Interaction of Isotropic Turbulence with Shock Waves: Effect of Shock Strength. *Journal of Fluid Mechanics*, 300:383-407, 1997.
- T. Lund, X. Wu, and K. Squires. Generation of Turbulent Inflow Data for Spatially- Developing Boundary Layer Simulations. *Journal of Computational Physics*, 140(2):233-258, 1998.
- M. Martin, U. Piomelli and G. Candler. A Priori Tests of SGS Models in Compressible Turbulence. 3rd ASME/JSME Joint Fluids Engineering Conference, July 18-23, 1999, San Francisco USA.
- K. Muck, E. Spina, and A. Smits. Compilation of Turbulence Data for an 8 degree Compression Corner at Mach 2.9. Report MAE-1642, April 1984.
- N. Okong'o and D. Knight. Compressible Large Eddy Simulation Using Unstructured Grids: Channel and Boundary Layer Flows. AIAA Paper 98-3315, 1998.

- C. F. Ollivier-Gooch. High Order ENO Schemes for Unstructured Meshes Based on Least Squares Reconstruction. AIAA Paper No. 97-0540, 1997.
- M. Rai and P. Moin. Direct Numerical Simulation of Transition and Turbulence in Spatially Evolving Boundary Layer. *Journal of Computational Physics*, 109:162-192, 1993.
- A. Smits and J.-P. Dussauge. *Turbulent Shear Layers in Supersonic Flow*. American Institute of Physics, New York, 1996.
- P. Spalart. Direct Simulation of a Turbulent Boundary Layer up to $Re_\theta = 1410$. *Journal of Fluid Mechanics*, 187:61-98, 1988.
- P. Spalart and K. Yang. Numerical Study of Ribbon-Induced Transition in Blasius Flow. *Journal of Fluid Mechanics*, 178:345-365, 1987.
- G. Urbin, C. Brun, and O. Metais. Large Eddy Simulation of Three-Dimensional Spatially Evolving Round Jets. In *11th Turbulent Shear Flows Conference*, Grenoble, France, September 1997.
- G. Urbin, D. Knight, A. Zheltovodov. Compressible Large Eddy Simulation using Unstructured Grid: Supersonic Turbulent Boundary Layer and Compression Corner. AIAA Paper 99-0427, 1999.
- A. Walz. *Boundary Layers of Flow and Temperature*. MIT Press, 1969.
- A.A. Zheltovodov, V.N. Yakovlev. Stages of Development, Gas Dynamic Structure and Turbulence Characteristics of Turbulent Compressible Separated Flows in the Vicinity of 2-D Obstacles. Preprint No 27-86, Inst. of Theoretical and Applied Mechanics, USSR Acad. of Sciences, Novosibirsk, 1986, 55 p. (in Russian)

THE STRETCHED-VORTEX SGS MODEL IN PHYSICAL SPACE

T. VOELKL, D.I. PULLIN AND R.D. HENDERSON
*Graduate Aeronautical Laboratories 105-50,
California Institute of Technology,
Pasadena, California 91125*

1. Introduction

The stretched-vortex subgrid stress model for the large-eddy simulation of turbulent flows has been developed to the stage where it can be applied to realistic flow at large Reynolds numbers [1] [2]. The basic assumption of this model [3] is that the subgrid vortex structure consists of straight, stretched vortices containing a nearly axisymmetric subgrid vorticity field. Vortices of this type, such as the Burgers vortex and the stretched-spiral vortex have provided fair quantitative estimates of turbulence fine-scale properties [4]. These structures are probably an oversimplified model of fine-scale turbulence, but may nevertheless contain sufficient of the vortex-stretching and energy cascade physics characteristic of the small scales to provide a reasonable basis for subgrid-stress modelling for LES. The resulting subgrid stresses are

$$\tau_{ij} = K \left(\delta_{ij} - e_i^v e_j^v \right), \quad (1)$$

where K is the subgrid energy and e_i^v , $i = 1, 2, 3$ are the direction cosines of the subgrid vortex axis. The local subgrid dissipation ϵ_{sgs} is equal to the product of K with the component of \tilde{S}_{ij} aligned with the vortex axis. A class of simple models is obtained when it is assumed that the subgrid vortices are aligned with the eigenvectors of the rate-of-strain tensor \tilde{S}_{ij} [1]. Utilizing an assumed Kolmogorov form for the local subgrid energy spectrum, the model estimates the turbulent energy production at the resolved-scale cutoff in terms of the model parameters ϵ and the Kolmogorov prefactor \mathcal{K}_0 and adjusts these parameters locally so as to continue the cascade through the cutoff to the subgrid vortex structures where the dissipation takes place.

In an earlier version of the stretched-vortex model which operates within a Fourier-Galerkin pseudo-spectral computation of the resolved flow, the

principal model parameters \mathcal{K}_0 , ϵ and K were estimated by patching the calculated resolved-scale energy spectrum to an averaged subgrid spectrum at the resolved-scale cutoff. This was done using either volume averages and shell-summed 3D spectra (isotropic turbulence [1]) or plane-averages and 2D spectra (eg channel flow [2]). No double filtering is needed in order to estimate model parameters and direct estimates of the subgrid contribution to turbulent transport are provided.

2. Physical-space version of the stretched-vortex SGS model

This ‘spectral version’ of the stretched-vortex model has the disadvantage that it is not easily applied to flows with complex boundary conditions, for which pure spectral methods are inappropriate. To remedy this, a version of a stretched-vortex SGS model is proposed and tested, in which model parameters are calculated locally using resolved-flow estimates of the second-order velocity structure functions $\tilde{F}_2 = \delta\tilde{U}_1^2(\mathbf{r}) + \delta\tilde{U}_2^2(\mathbf{r}) + \delta\tilde{U}_3^2(\mathbf{r})$ where \tilde{U}_i is the resolved field and δ refers to a difference operation. This idea was first developed for eddy-viscosity SGS modelling by Lesieur and Métais [5] [6]. We presently adapt the structure function approach to the kinematics of the stretched-vortex SGS model, resulting in a model that operates in physical space, and that in principal can be incorporated into any numerical method for which resolved-flow velocity differences and velocity gradients are available at the cutoff scale.

Given our assumptions concerning the subgrid structure of the vorticity field, it is possible to derive a set of kinematic relations for the local form of the energy spectrum in terms of the assumed subgrid anisotropy as represented by the orientation geometry of the subgrid vortex [3]. The following equation can then be derived for homogeneous anisotropic turbulence,

$$F_2 = \tilde{F}_2 + \frac{2}{\pi} \int_{\phi=0}^{2\pi} \int_{k=k_c}^{\infty} E(k) \left[1 - J_0 \left(kr \sqrt{1 - \sin^2 \alpha \cos^2 \phi} \right) \right] dk d\phi, \quad (2)$$

where J_0 is the zeroth-order Bessel function, $F_2(r)$ is the full second order structure function, \tilde{F}_2 is the contribution from scales larger than the grid cutoff $k_c = \pi/\Delta$ and the integral term is the contribution from the subgrid scales. In (2), α denotes the angle between the normal to the plane of a circle of radius $r = |\mathbf{r}|$ over which the average is taken, and the subgrid vortex axis. F_2 can be estimated from an integral similar to that in (2), but with the lower limit of the k -integral replaced by $k = 0$. Using $\tilde{F}_2 = \delta\tilde{U}_1^2(\mathbf{r}) + \delta\tilde{U}_2^2(\mathbf{r}) + \delta\tilde{U}_3^2(\mathbf{r})$ and a Kolmogorov spectrum in the inte-

grals leads to the result

$$\mathcal{K}_0 \epsilon^{2/3} = \frac{\overline{\delta \tilde{U}_1^2(\mathbf{r})} + \overline{\delta \tilde{U}_2^2(\mathbf{r})} + \overline{\delta \tilde{U}_3^2(\mathbf{r})}}{\frac{2}{\pi} \Delta^{2/3} \int_{\phi=0}^{2\pi} \int_{u=0}^{\pi} u^{-5/3} \left[1 - J_0 \left(u \frac{r}{\Delta} \sqrt{1 - \sin^2 \alpha \cos^2 \phi} \right) \right] du d\phi} \quad (3)$$

All quantities on the right-hand side of (3) are known. The numerator can be estimated from a four-point approximation applied to local resolved-field velocity differences [5]. The denominator can be found by either a fast table lookup of the prior-evaluated double integral or from an asymptotic approximation (or a combination of these). Once $\mathcal{K}_0 \epsilon^{2/3}$ is known, the subgrid energy can be calculated and the model SGS stresses evaluated. The subgrid energy spectrum is assumed to have a sharp viscous cutoff at $k = J/\eta$, $\eta = (\nu^3/\epsilon)^{1/4}$, so that J remains as a model parameter. An alternative is to use the Lundgren [7] spectrum for the stretched-spiral vortex (with the stretching strain in the Lundgren result replaced by the absolute value of the component of the resolved rate-of-strain tensor along the subgrid-vortex axis). This model would be free of parameters but is more complicated than the present simple cutoff model. A reasonable choice is $J = 1$, based on cutoff at the local Kolmogorov scale, but the choice $J = \infty$ can be shown to give a more efficient model computationally. For a given numerical treatment of the resolved flow, the overall model performance seems to be insensitive to J over the broad range $O(1) \leq J \leq \infty$, for moderate to large Reynolds numbers.

This physical-space version of the model has been tested for decaying isotropic turbulence. Three different numerical methods have been utilized; a Fourier-Galerkin pseudo-spectral method, dealiased by the "3/2 rule", a code based on a fourth-order Padé scheme [8] and the spectral element code Prism [9]. The decaying isotropic turbulence tests were set up to match experiment [10]. Results for the decaying turbulence tests for the three methods are shown in Figure 1. All codes produce reasonable if somewhat low estimates of the subgrid energy (Figure 2), a quantity not computed by some SGS models without additional modelling.

3. Subgrid model for flux of a passive scalar

We outline here a model for the subgrid flux of a passive scalar based on the stretched-vortex model. It is assumed that a passive scalar ϕ is convected and diffused in a given turbulent flow. For incompressible constant density flow, the appropriate filtered equation for ϕ is

$$\frac{\partial \tilde{\phi}}{\partial t} + \frac{\partial}{\partial x_j} (\tilde{\phi} \tilde{U}_j) = -\frac{\partial F_i}{\partial x_i} + D \frac{\partial^2 \tilde{\phi}}{\partial x_j \partial x_j}, \quad (4)$$

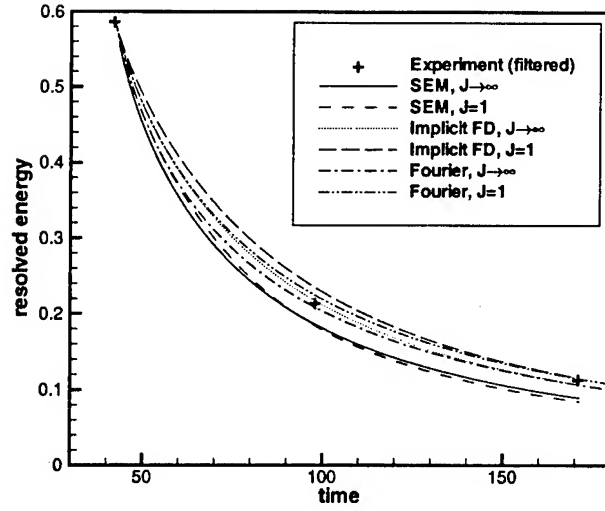


Figure 1. Decay of isotropic turbulence, physical-space version of stretched-vortex SGS model. Resolved scale energy. Symbols, [10].

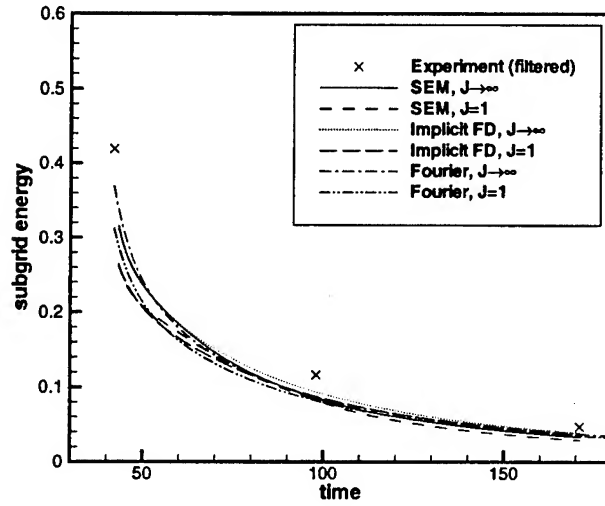


Figure 2. Decay of isotropic turbulence, physical-space version of stretched-vortex SGS model. Subgrid-scale energy. Symbols, [10].

where, $F_i = \widetilde{\phi U_i} - \bar{\phi} \bar{U}_i$ is the flux of ϕ produced by the subgrid velocity field.

The flux F_i is modelled by the convection of ϕ by an axisymmetric subgrid vortex. In "subgrid vortex" polar co-ordinates r, θ the subgrid velocity field is assumed to be $u_\theta = r\Omega(r)$ where $\Omega(r) = \Gamma R^{-2} \hat{\Omega}(\xi)$ is the local angular velocity, $\xi = r/R$, Γ is the vortex circulation and R its characteristic radius. In vortex co-ordinates, the solution of the convection ($D = 0$) equation is

$$\phi(r, \theta, t) = \sum_{n=-\infty}^{\infty} \phi_n(r) e^{in(\theta - \Omega(r)t)}, \quad (5)$$

where the $\phi_n(r)$, $\phi_{-n}(r) = \phi_n^*(r)$, are the Fourier coefficients at time $t = 0$. From (5) and the specified velocity field, an integral modelling F_i can be written, giving the flux of ϕ averaged over a cylindrical volume of radius R_1 where R_1 is of order of a cell dimension, and a mixing time T . When this result is averaged over the phase angles of the ϕ_n using a random phase approximation, and over the expectation of Γ assumed equally likely to be positive/negative, it can be shown that, provided the dimensionless parameter $\Gamma T/R^2$ is not large, the integral for F_i can be reduced to an approximate form

$$F_i = -\frac{1}{2} K T \left(\frac{\partial \tilde{\phi}}{\partial x'_i} \right), \quad i = 1, 2, \quad K = \frac{\Gamma^2}{R_1^2} \int_0^{R_1/R} \xi^3 \hat{\Omega}^2(\xi) d\xi, \quad (6)$$

where $x'_1 = r \cos \theta$, $x'_2 = r \sin \theta$ and K is the subgrid energy contained in the volume. The dependence on the vortex variables R , Γ , the volume dimension R_1 and the vortex velocity $r\Omega$ are now contained entirely within K .

In laboratory co-ordinates x_i , the flux expression is

$$F_i = -\mu_{im} \frac{\partial \tilde{\phi}}{\partial x_m}, \quad \mu_{im} = \frac{1}{2} \Delta x K^{1/2} (\delta_{im} - e_i^v e_m^v), \quad (7)$$

Δx is the local cell size. Equation (7) takes the form of a tensor-eddy diffusivity model of the subgrid scalar flux. Both the subgrid energy K and the e_i^v are available from the subgrid stress model. Hence we have a realizable model which requires only the additional calculation of the resolved temperature gradients.

4. Conclusion

We have proposed and tested a physical-space version of the stretched-vortex subgrid stress model for the large-eddy simulation of turbulent flows.

The basic model operation is similar to the first version of the model, but uses local second-order structure functions of the resolved field to estimate model parameters. The circular average used in (2) should be suitable for the calculation of wall-bounded flows, when the circle axis is aligned with the local wall normal. A model for the inclusion of the flux of a passive scalar based on convection of the scalar by the assumed velocity field of the subgrid vortex structure has been suggested. Work is in progress to apply these models to wall bounded flows and to the mixing of a passive scalar by a turbulent field.

Acknowledgement

This work was supported partially by the National Science Foundation under Grant CTS-9634222 and partially by the Academic Strategic Alliances Program of the Accelerated Strategic Computing Initiative (ASCI/ASAP) under subcontract no. B341492 of DOE contract W-7405-ENG-48.

References

1. A. Misra and D. I. Pullin. A vortex-based subgrid model for large-eddy simulation. *Phys. Fluids*, **9**, 2243-2454 1997.
2. A. Misra, D. I. Pullin and D. C. Chan. Large-eddy simulation using the stretched-vortex SGS model. *Advances in DNS/LES. Proceedings of the First AFOSR International Conference on DNS /LES*, (Ed. Chaoqun Liu, Zhining Liu), Greyden Press (Columbus), 385-392. 1997.
3. D.I Pullin and P.G. Saffman. Reynolds stresses and one-dimensional spectra for vortex models of homogeneous anisotropic turbulence. *Phys Fluids*, **6** :1787-1796, 1994.
4. D. I. Pullin and P. G. Saffman Vortex dynamics in turbulence. *Ann. Rev. Fluid Mech.*, **30**, 31-51, 1998.
5. O. Métais & M. Lesieur. Spectral large-eddy simulations of isotropic and stably stratified turbulence. *J. Fluid Mech.*, **239**:157-194, 1992.
6. M. Lesieur and O. Métais. New trends in large-eddy simulation. *Ann Rev. Fluid Mech.* **28**, 45, 1996.
7. T.S. Lundgren. Strained spiral vortex model for turbulent fine structure. *Phys Fluids*, **25**:2193-2203, 1982.
8. S.K. Lele. Compact finite-difference schemes with spectral-like resolution. *J. Comp. Phys.*, **103**:16-42, 1992.
9. R. D. Henderson and G. E. Karniadakis. Unstructured spectral element methods for simulation of turbulent flows. *J. Comput. Phys.*, **122**:191-217, 1995.
10. G. Comte-Bellot and S. Corrsin. Simple Eulerian time correlation of full and narrow-band velocity signals in grid-generated isotropic turbulence. *J. Fluid Mech.* **48**, 273-337, 1971.

APPLICATION AND COMPARISON OF TWO SGS MODELS IN LARGE EDDY SIMULATION OF FREE TURBULENT JET FLOW

HONG YAN, MINGDE SU

Department of Engineering Mechanics, Tsinghua University, Beijing 100084, P.R.China

ABSTRACT- Large eddy simulations of spatially evolved turbulent round jets were presented. The two SGS models called the standard Smagorinsky's eddy viscosity model and the non-eddy viscosity stimulated small scale (SSS) model developed by Shah & Ferziger[1] were applied. The Reynolds number of the flow was taken to 10000 based on the orifice diameter and the axial velocity in the orifice. The comparison between these two models showed that the standard Smagorinsky's viscosity model with Smagorinsky's constant of 0.1 underestimated the turbulent intensity, while the SSS model showed a better agreement with the experiment. Also the SSS model was used to investigate the development of vortex. The convective boundary condition at the outflow boundary was adopted to ensure less effect of noise on the upstream.

KEYWORDS Stimulated small scale model, Smagorinsky's eddy viscosity model, Round jet, Large eddy simulation

INTRODUCTION

Jets are important in many practical applications. Mixing, aeroacoustics, combustion, propulsion and flame stability are intimately related to the instability mechanisms and large-scale structures of this flow. Jets are also considered as one of the prototypes of free shear flows and the studies on this flow geometry help to the further understanding of free shear flows. For both theoretical and practical reasons, the considerable research efforts[2-6], involving either experiments, theoretical analyses or numerical simulations, are devoted to investigating the characteristics of jet flows.

Numerical simulation is increasingly recognized as an attractive method to study turbulent flows. Compared to laboratory experiments, the structure of the instantaneous flow fields obtained through spatially evolving computer simulations is free from experimental problems such as the effects of probe interference. The numerical computations also have the advantage of being free from problems with hot wire measurements such as high turbulence levels and flow reversal and also allowing a more precise control of the effect of boundary conditions on the flow investigated. On the other hand, numerical simulations bring some problems. First, the influence of finite computational domain on real jet flow can not be neglected and unsuitable outflow boundary conditions will introduce unphysical reflections to the upstream. The second difficulty is the formulation of the lateral boundaries, which must ensure the entrainment of this flow to be correctly described.

Among three kinds of numerical methods to turbulence simulation, turbulence models are seldom used to compute jet flow. Direct numerical simulation (DNS)[7] is the most exact approach, but it is also extremely time-consuming and memory-demanding. Therefore, large eddy simulation (LES) is chosen in the present paper.

Smagorinsky's eddy viscosity model is the most commonly used subgrid scale (SGS) model and has been applied successfully to a variety of turbulent flows since this model captures the dissipative nature of turbulence. However, it is unable to account for reverse transfer of energy from subgrid to resolved scales (backscatter).

Recently, a non-eddy viscosity subgrid scale model called stimulated small scale (SSS) model has been proposed by Shah & Ferziger. This procedure does not require the assumption

of homogeneity and permits backscatter of energy from small to large scales. Shah & Ferziger applied this model to a second order finite volume simulation of plane channel flow at high Reynolds numbers. The results compared to ones provided by the Smagorinsky and dynamic eddy-viscosity models and the spectral LES showed that this model not only captured the dissipative nature of turbulence but also provided more reasonable energy transfer between the resolved and unresolved scales. To my knowledge, few publications appeared on this model, therefore lots of practice on this new non-eddy viscosity subgrid scale model will be needed to verify its merits.

In the view of the above discussion, the objective of this paper is to present a LES of a spatially developing turbulent round jet flow. The effects of the above two LES models on the numerical simulation of jet flows will be investigated and the energy dissipation obtained by the SSS model will be shown.

MATHEMATICAL FORMULATION

The space filtered Navier-Stokes equations for incompressible flows can be written in the following nondimensional form

$$\frac{\partial \bar{u}_i}{\partial x_i} = 0 \quad (1)$$

$$\frac{\partial \bar{u}_i}{\partial t} + \frac{\partial(\bar{u}_i \bar{u}_j)}{\partial x_j} = -\frac{\partial \bar{p}}{\partial x_i} - \frac{\partial \tau_{ij}}{\partial x_j} + \frac{1}{Re} \frac{\partial^2 \bar{u}_i}{\partial x_j \partial x_j} \quad (2)$$

Eqs. (1) and (2) govern the large scale motion. The large scales are influenced by the small scales via the SGS stress.

$$\tau_{ij} = \overline{u_i u_j} - \bar{u}_i \bar{u}_j \quad (3)$$

To close the system of equations the SGS stress should be modeled. The Smagorinsky model can be thought of as an adaptation of the Boussinesq concept to the subgrid scale. It is

$$\tau_{ij} - \delta_{ij} \tau_{kk} / 3 = -2\nu_T \bar{S}_{ij} = -\nu_T \left(\frac{\partial \bar{u}_i}{\partial x_j} + \frac{\partial \bar{u}_j}{\partial x_i} \right) \quad (4)$$

where ν_T is the eddy viscosity $\nu_T = (C_S \Delta)^2 |\bar{S}|$. \bar{S}_{ij} is the strain-rate tensor of the filtered velocity field. Δ is the filter width and C_S is Smagorinsky constant, taken as 0.1 in the present simulation.

The SGS model of another type is the non-eddy viscosity model and the stimulated small scale (SSS) model is of this case. The model of this type not only permits backscatter and gives a good representation of instantaneous energy transfer between the large and small scales, but also provides more reasonable energy dissipation. In this model, the SGS stress can be written as

$$\tau_{ij} = \widehat{u_i^* u_j^*} - \bar{u}_i \bar{u}_j \quad (5)$$

where u_i^* is defined implicitly in terms of the filtered velocity \bar{u}_i by a differential operator \tilde{L} .

$$\tilde{L}(u_i^*) = \bar{u}_i \quad (6)$$

where $\tilde{L} = \tilde{L}_x \tilde{L}_y \tilde{L}_z$. \tilde{L}_x, \tilde{L}_y and \tilde{L}_z are of similar form. The filtering operating \wedge is defined in a similar manner.

$$\widehat{u_i^*} = \tilde{V}(u_i^*) \quad (7)$$

where $\tilde{V} = \tilde{V}_x \tilde{V}_y \tilde{V}_z$ is the explicit operator and is similar to the operator \tilde{L} . The operators \tilde{L} and \tilde{V} are of second order operators. So the SGS stress τ_{ij} can be approximated in terms of the filtered velocity by the implicit and explicit operators.

To understand this procedure, consider the expression u_i^* in one dimension. \tilde{L}_x and \tilde{V}_x are defined as

$$\tilde{L}_x = (1 + C_1 \frac{\partial}{\partial x} + C_2 \frac{\partial^2}{\partial x^2}) \quad (8)$$

$$\tilde{V}_x = (1 + D_1 \frac{\partial}{\partial x} + D_2 \frac{\partial^2}{\partial x^2}) \quad (9)$$

The coefficients in \tilde{L}_x and \tilde{V}_x operators can be identical. With the operator \tilde{L}_x Eq.(6) is rewritten as

$$\bar{u} = u^* + C_1 \frac{du^*}{dx} + C_2 \frac{d^2 u^*}{dx^2} = \tilde{L}_x(u^*) \quad (10)$$

This is a local Taylor series approximation for the filtered quantity in terms of the unfiltered quantity. The nonsymmetric box filter gives

$$G_j = G(x - x_j) = \begin{cases} 1/\Delta & \text{if } -\Delta_{j-1}/2 < x - x_j < \Delta_j/2 \\ 1/(2\Delta) & \text{if } x - x_j = -\Delta_{j-1}/2 \text{ or } x - x_j = \Delta_j/2 \\ 0 & \text{if } x - x_j < -\Delta_{j-1}/2 \text{ or } x - x_j > \Delta_j/2 \end{cases} \quad (11)$$

where Δ is the filter width, the filtering operation defined by

$$\bar{u}(x) = \int_{-\infty}^{\infty} G(x - x') u(x') dx' \quad (12)$$

gives

$$\bar{u}(x_j) = \frac{2}{\Delta_j + \Delta_{j-1}} \int_{x_j - \frac{\Delta_{j-1}}{2}}^{x_j + \frac{\Delta_j}{2}} u(x') dx' \quad (13)$$

Taylor series expansion of $u(x')$ around x_j leads to

$$\bar{u}(x_j) = u(x_j) + \frac{\Delta_j - \Delta_{j-1}}{4} \frac{du}{dx} \Big|_j + \frac{\Delta_j^2 - \Delta_j \Delta_{j-1} + \Delta_{j-1}^2}{24} \frac{d^2 u}{dx^2} \Big|_j + O(\Delta^3) \quad (14)$$

Thus, u^* will be a second order approximation to u if the coefficients in Eqs.(10) and (14) are matched. Extension to three dimensions consists of sequential application of \tilde{L} operators in each direction. A finite difference approximation to the operator L_x of Eq.(10) can be written as

$$\bar{u}_j = a u_{j-1}^* + b u_j^* + c u_{j+1}^* \quad (15)$$

Substituting the Taylor series expansion for u_{j-1}^* and u_{j+1}^* about the node j into Eq.(15) and matching the coefficients in Eq.(14), one obtains

$$\begin{aligned}
a &= \frac{h_j^2(m^2 - 3m) + h_j h_{j-1}(3m - m^2) + h_{j-1}^2 m^2}{12h_{j-1}(h_j + h_{j-1})} \\
c &= \frac{h_j^2 m^2 + h_j h_{j-1}(3m - m^2) + h_{j-1}^2(m^2 - 3m)}{12h_j(h_j + h_{j-1})} \\
b &= 1 - (a + c)
\end{aligned} \tag{16}$$

where $h_j = x_{j+1} - x_j$, m is the filter-grid ratio $m = (\Delta_j + \Delta_{j-1})/(h_j + h_{j-1})$.

Table 1 shows the coefficients (a, b, c) for the finite difference stencil for various m .

Table 1 Coefficients (a, b, c) corresponding to various filter-grid ratio m

(a, b, c)	filter-grid ratio $m = \sqrt{12(1 - b)}$
$(1, 22, 1)/24$	1
$(1, 6, 1)/8$	$\sqrt{3}$
$(1, 4, 1)/6$	2

The operator \tilde{L}_x is solved with certain combination of a, b, c and the operator \tilde{V}_x is identical to \tilde{L}_x . The procedure for computing the SGS stress consists of the following three steps:

1. Choose a filter-grid ratio (m) for each direction. This determines the coefficients a, b, c .
2. Compute u^* by inverting a set of tridiagonal systems in each direction.
3. Substitute u^* into Eq.(5) and apply the filtering operator \tilde{V} to obtain the SGS stress τ_{ij} .

COMPUTATIONAL METHOD

To be convenient, the N-S equations are written as

$$\nabla \cdot \vec{V} = 0 \tag{17}$$

$$\frac{\partial \vec{V}}{\partial t} = -\nabla P - \nabla(\vec{V}\vec{V}) + \nabla(2(\nu_l + \nu_T)\vec{S}) \tag{18}$$

where \vec{V} is the velocity vector, P the pressure and ν_l the kinematic viscosity of the fluid.

The time integration of Eq. (18) has been with a second-order Adams-Bashforth scheme[8].

$$\frac{\vec{V}^* - \vec{V}^n}{\Delta t} = \frac{3}{2}(-A^n - P^n + D^n) - \frac{1}{2}(-A^{n-1} - P^{n-1} + D^{n-1}) \tag{19}$$

in which A stands for discrete advection operator, P for the discrete pressure operator, D for the discrete diffusion operator and Δt for the time step. The newly computed velocity will not be divergence free, so we perform a pressure correction step.

$$\frac{\vec{V}^{n+1} - \vec{V}^*}{\Delta t} = -\nabla P^{n+1} \tag{20}$$

Taking the divergence of this equation and setting the divergence of the velocity at time level $n + 1$ equal to zero, leads to the following Poisson equation for the pressure correction.

$$\nabla^2 P^{n+1} = \frac{1}{\Delta t} \nabla \cdot \vec{V}^* \tag{21}$$

The Poisson equation for the pressure correction is solved using a Gauss-Chebyshev transforms in the streamwise direction and then solving the tridiagonal matrixes in the radial direction. After the solution of the Poisson equation, the velocity is corrected with help of Eq.(20).

Third-order and fourth-order compact finite difference scheme is used to calculate the first and second derivatives of the variables in the convective terms and the viscous terms respectively.

A staggered grid arrangement is adopted, where the pressure and other scale variables are defined in the center of the cell while velocity components are defined on the surfaces. Uniform meshes are used in the streamwise. The grid spacing in the radial direction is nonuniform with the grid points clustered near the jet orifice. Due to the limit of computational conditions, the computational domain is taken equal to 25 orifice diameters and 15 orifice diameters in the streamwise and radial direction respectively. The grid consists of 514×150 points in the streamwise and radial direction respectively.

BOUNDARY CONDITIONS

Four types of boundaries can be distinguished: the inflow, outflow, lateral and centerline boundary, each of which requires a different boundary condition.

At the inflow boundary of the jet, all velocity components are specified.

$$u_x(0, r, t) = U_0 = \begin{cases} 1 & r \leq R \\ 0 & r > R \end{cases} \quad u_r(0, r, t) = 0 \quad (22)$$

in which u_x and u_r denote the velocity components in the streamwise and radial directions. R is the orifice radius and U_0 is the axial velocity in the orifice.

At the outflow boundary the convective boundary condition[9] is used to reduce its effect on the upstream.

$$\frac{\partial \vec{V}}{\partial t} + \bar{U} \frac{\partial \vec{V}}{\partial x} = 0 \quad (23)$$

where \bar{U} is the mean velocity over the outflow boundary.

The centerline boundary condition is written as

$$\frac{\partial u_x}{\partial r} \Big|_{r=0} = 0 \quad u_r(x, 0, t) = 0 \quad (24)$$

At the lateral boundary, all the first derivative in the radial direction is set to be zero.

$$\frac{\partial u_x}{\partial r} \Big|_{r=R_{max}} = 0 \quad \frac{\partial u_r}{\partial r} \Big|_{r=R_{max}} = 0 \quad (25)$$

where R_{max} is the largest radius of the computational domain.

The pressure boundary condition is defined as $\frac{\partial p}{\partial \vec{n}} = 0$ and \vec{n} is the unit normal on the boundary.

The initial condition for the computation is set to

$$u_x(x, r, 0) = u_x(0, r, t) \quad u_r(x, r, 0) = u_r(0, r, t) \quad p = 0 \quad (26)$$

The numerical method outlined above is implemented on PC's. For a gridsize of 514×150 and $\Delta t = 0.005$, the code takes 90 hours.

RESULTS AND DISCUSSIONS

The results obtained by the Smagorinsky's eddy viscosity model and the stimulated small scale (SSS) model are plotted in Fig.1 ~ Fig.5, in which all the variables are averaged from $t = 200 \sim t = 400$. Fig.1 depicts the mean streamwise velocity at $Re = 1 \cdot 10^4$. U_c is the mean streamwise velocity on the centerline. The normalized mean velocities are not very consistent with the experimental results of Sami[10] at $Re = 22 \cdot 10^4$. Near the jet exit, very strong momentum transfer occurs. The axisymmetric hypothesis in the present computation does not allow the convection and diffusion of momentum across the centerline. Furthermore, the Smagorinsky model with only a constant does not represent the whole jet flow. So the Smagorinsky model gives worse mean velocity distribution than the SSS model does.

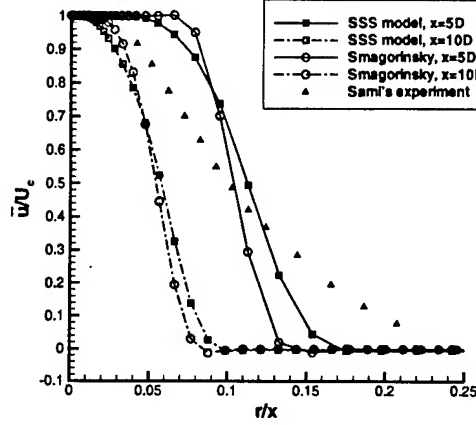


Fig.1 The normalized mean streamwise velocity versus the radius

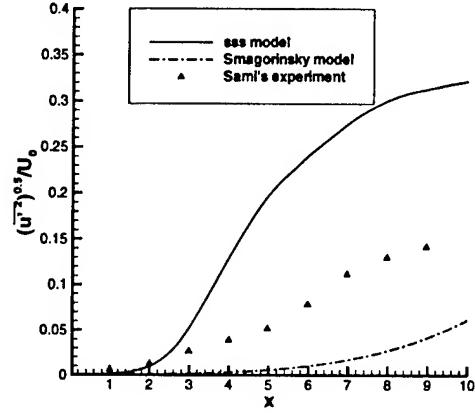


Fig.2 The turbulent intensity versus the streamwise

Fig.2 and Fig.3 show the turbulent intensity distribution. In Fig.2 the end of the potential core coincides with a substantial increase in the streamwise turbulent intensity along the centerline. It can be seen that in the SSS model the turbulent transition is increasing from a very low level $O(0.01)$ to a high level of $O(0.3)$ in a qualitatively correct manner, while the Smagorinsky model underestimates the turbulent intensity. The level of the turbulent intensity reaches a maximum value and decreases to an asymptotic self-similarity behavior normalized by the centerline velocity. Both the LES and Sami's experimental results show similar behavior in the radial direction, shown in Fig.3. The SSS model gives a better agreement with experimental results. It is also of the case in Reynolds shear stress component, shown in Fig.4. The LES compares relatively well with the Sami's experiment data and have the same qualitatively and asymptotic behavior. In both the LES and the experimental data, Reynolds shear stress component increases with x and shows the same transitional behavior as the turbulence intensity, i.e. an initial increase followed by a decrease towards an asymptotic self-similarity behavior.

Fig.5 describes the variation of the turbulent kinetic energy versus the normalized radius. The turbulent kinetic energy increases to a maximum at the edge of the jet and decays further out.

In the view of the above discussion, the results provided by the SSS model show a better agreement with Sami's experimental data than the Smagorinsky model.

An important character of the SSS model is that it can provide reasonable energy transfer between the large and small scales, especially it can represent reverse transfer of energy from subgrid to resolved scales (backscatter).

Fig.6 shows the energy dissipation at $t = 400$. Near the jet exit, intense turbulence makes the flow heterogeneous and the backscatter (the energy dissipation is positive) obvi-

ously exists, while in the downstream flow is fully developed turbulent and the most energy is transferred from large scales to small scales, which complies to the principle of energy transfer in turbulent flows.

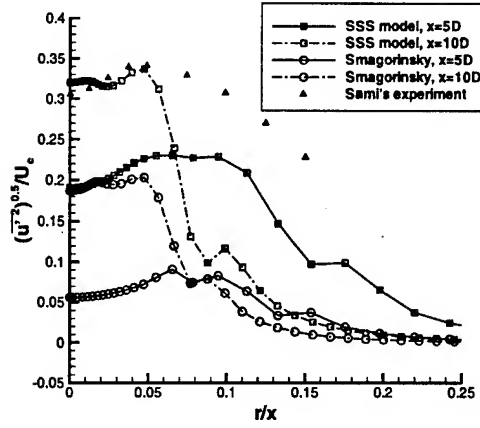


Fig.3 The turbulent intensity versus the radius

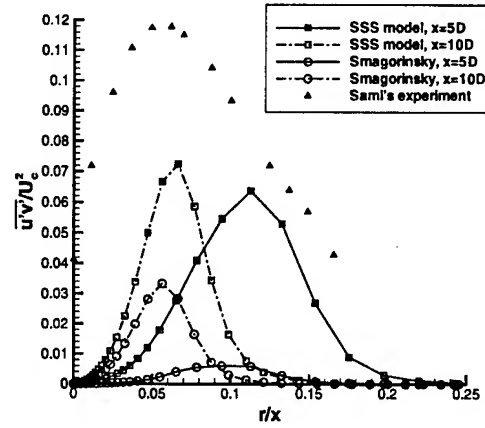


Fig.4 The Reynolds shear stress component versus the radius

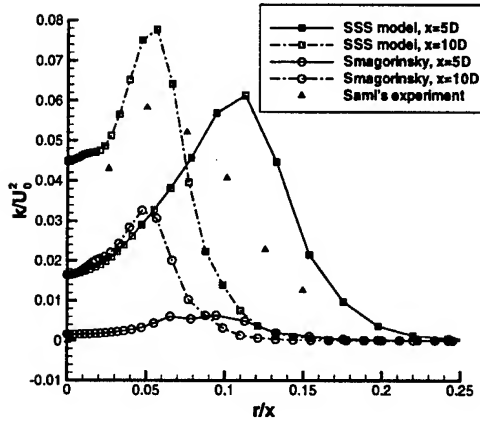


Fig.5 The turbulent kinetic energy

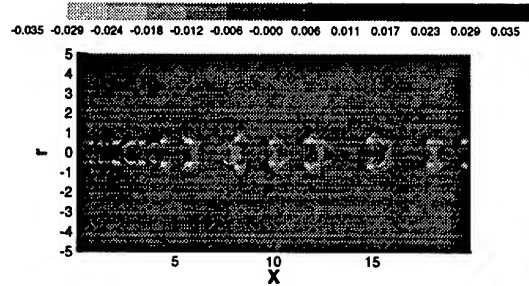


Fig.6 The energy dissipation

CONCLUSIONS

The large eddy simulation of axisymmetric round jet has been presented with two SGS models used for comparison. A new non-eddy viscosity SGS mode called the Stimulated Small Scale (SSS) model proposed by Shah & Ferziger was applied to the present simulation. According to the principle of the SSS model, this model can not only accounts for the energy dissipation, but also represents a good instantaneous energy transfer between the large and small scales.

Mean velocities, turbulent intensities, Reynold shear stress and turbulent kinetic energy were determined by the SSS model and the Smagorinsky eddy viscosity model at $Re = 1 \cdot 10^4$. The LES results compared with the experimental data of Sami et al at $Re = 22 \cdot 10^4$ showed

that the stimulated small scale (SSS) model provided a better agreement with the experiment data than the Smagorinsky model.

The SSS model was utilized to describe the energy dissipation and the backscatter in the round jet was captured. The convective boundary condition at the outflow boundary ensured the less reflect on the upstream.

ACKNOWLEDGEMENTS

This project is supported by National Climbing Plan, National Foundation of Science , Doctoral Foundation of the National Education Committee and Hydrodynamic opening laboratory in Wuxi in P.R.China.

REFERENCES

- 1 Shah K.B. and Ferziger J.H. A new non-eddy viscosity subgrid-scale model and its application to channel flow. 1995, Center for Turbulence Research Annual Research Briefs.
- 2 Reynolds A.J. Observation of a liquid-into-liquid jet. *J. Fluid Mech.* 1962,14:552
- 3 Batchelor G.K and Gill A.E. Analysis of the stability of axisymmetric jets. *J. Fluid Mech.* 1962,14:529
- 4 Martin J.E. and Meiburg E. Numerical investigation of the three dimensionally evolving jets subje to axisymmetric and azimuthal perturbations. *J. Fluid Mech.* 1991,230:271
- 5 Grinstein F.F and DeVore C.R. Dynamics of coherent structures and transition to turbulence in free square jets. *Phys. Fluids* 1997,8(5):1237
- 6 Akselvoll K. and Moin P. Large eddy simulation of turbulent confined coannular jets. *J. Fluid Mech.* 1996,315:387
- 7 Stanley S. and Sarkar S. Simulations of spatially developing two-dimensional shear layers and jets. *Theoretical and computational fluid dynamics.* 1997,9:121
- 8 Boersma B.J Brethouwer G. And Nieuwstadt F.T.M. A numerical investigate on the effect of the inflow conditions on the self-similar region of a round jet. *Phy. Fluid* 1998 10(4):899
- 9 Lowery P.S, Reynolds W.C. and Mansour N.N. Passive scalar entrainment and mixing in a forced, spatially developing mixing layer. 1987,AIAA-87-0132
- 10 Sami S., Carmody T. and Rouse H. Jet diffusion in the region of flow establishment. *J.Fluid Mech.* 1967,27:231

DIRECT NUMERICAL SIMULATION OF GÖRTLER INSTABILITY IN HYPERSONIC BOUNDARY LAYERS

C. W. WHANG AND X. ZHONG

*Mechanical and Aerospace Engineering Department
University of California, Los Angeles, CA, 90095*

1. Introduction

The transition of hypersonic boundary layer flow is one of the fundamental problems in fluid mechanics. In general, boundary layer flows become turbulent in three steps: 1) receptivity, 2) linear growth of disturbance, and 3) nonlinear effects in which the flow breaks down to turbulence. Görtler instability is one of many B-L instability mechanisms. Görtler vortices appear in boundary layer flow along concave surfaces due to the imbalance between pressure and centrifugal force. Many practical engineering designs involve concave surfaces such as engine inlet. Therefore, Görtler instability become an important subject in fluid mechanics.

For Görtler instability, it has been shown that the region of linear development of disturbances are relatively shorter than nonlinear developing region; therefore, nonlinear effects are mainly considered in Görtler instability. For nonlinear studies, Direct Numerical Simulation (DNS) which solve full Navier Stokes equations is an efficient method.

Previously there have been many DNS studies to solve nonlinear Görtler problems. Hall(1988) demonstrated that nonlinear evolution of stream-wise Görtler vortices produces inflectional profiles which will presumably break down. Lee and Liu(1992) and Liu(1991) numerically showed mushroom like vortex due to nonlinear growth of Görtler vortices. Liu and Domaradzki(1993), Yu and Liu(1994), and Li and Malik(1995) studied secondary instability effects on Görtler vortices. Secondary instability is produced by interaction between TS waves and Görtler vortices.

Li and Domaradzki(1993) dealt with Görtler problem using Direct Numerical Simulation (DNS). Initial disturbances were obtained from Linear Stability Theory (LST) since initial stage of growing Görtler vortices is linear. They showed that Görtler vortices become turbulent due to the

spanwise velocity gradient as well as the normal velocity gradient. They mentioned that varicose mode of secondary instability is related to the normal velocity gradient and the sinuous mode is to the spanwise gradient and concluded that sinuous mode is dominant. Li and Malik(1995) used PSE (parabolic stability equation) method, and studied nonlinear effects of Görtler vortices. In their approach, they showed there are two kinds of secondary instability modes; even and odd. The even mode is related to the varicos mode, and the odd mode is to the sinous mode.

Most DNS works have considered simple geometry without shock and flat plate boundary layer mean flow. In this project, blunt body with bow shock which contains concave surface is considered, and 2-D mean flow is obtained from solving the full Navier Stokes equations. Görtler instability is investigated using two approaches: LST and DNS. Normal mode linear stability analysis is used for the initial disturbances for linear and nonlinear simulation and to verify the simulation code. DNS is used to simulate linear and nonlinear development of Görtler vortices in hypersonic boundary layers. Characteristics of nonlinear Görtler instability will be investigated.

2. Linear Stability Analysis

Although region for linear development of Görtler mode is much shorter than the nonlinear region, we can obtain lots of useful information from linear stability analysis. Along the concave surface, T-S wave (or shear mode) as well as Görtler mode exists. Parametric studies on the relative stability of Görtler and shear mode can be studied by LST. Linear stability analysis also help us to verify the numerical simulation code.

In the derivation of disturbance equations, we closely followed Malik's(Malik, 1990) formulation for cartesian coordinates. Coordinate transformation is applied to transform cartesian coordinates into curve linear system in order to include curvature effects.

The linear stability code for Görtler instability has been verified by comparing with available published papers(Whang *et al.*, 1999). Both shear and Görtler modes have been considered in the analysis. Unstable shear mode as well as Görtler mode exist along the concave surface; therefore, it is important to invetigate which mode is dominant. At hypersonic speed limit, second shear mode dominates the first mode; therefore Görtler modes and second shear modes are compared in the analysis.

Figure 1 shows the maximum temporal growth rates of Görtler and shear modes at constant Reynold's number (Re_δ) which is $\frac{U_\infty^* \rho_\infty^* \delta^*}{\mu_\infty^*}$ where δ^* is boundary layer thinkness. Each lines of Görtler modes indicates constant Görtler number (G) defined as $Re_\delta \sqrt{\frac{\delta}{R}}$. Reynold's number (Re_δ) is fixed as 1500, and radius of curvature changes in order to study Görtler

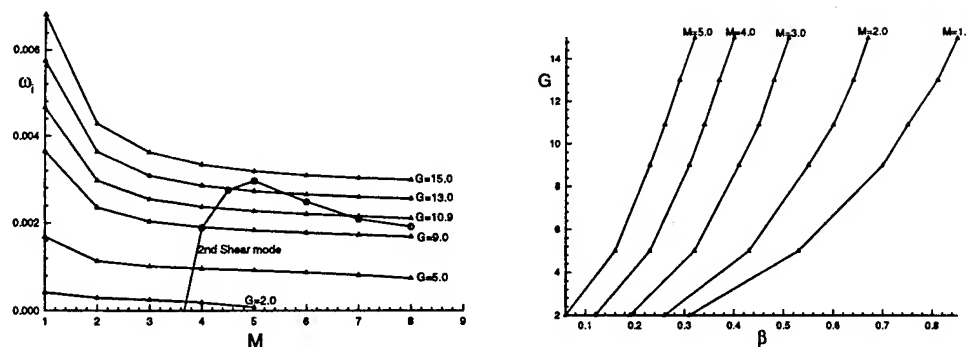


Figure 1. Comparison of the maximum growth rates of Görtler modes and second shear modes at $Re_\delta = 1500$. There is a critical Görtler number over which Görtler modes are dominant. Wavenumber, β , decreases as Mach number increases at fixed Görtler number.

number effects. As Görtler number increases, the maximum growth rates increase. Increasing Görtler number at fixed Reynolds number represents increase of curvature effects. As curvature increases, flow become more unstable (Whang *et al.*, 1999). It is also true for shear mode, but it does not affect the stability condition as much as for Görtler mode. Therefore in Fig. 1, second shear mode at $G = 15.0$ is only shown. The figure shows that there is a critical Görtler number over which Görtler mode dominates second shear mode at hypersonic speed limit.

At low mach number, Görtler modes dominate second shear mode. However, this is the region dominated by first shear modes which are not computed in this analysis. According to Mack's (Mack, 1984) results for flat plate at $Re_\delta = 1500$, we can roughly compare growth rates of Görtler modes and first shear modes. If Görtler number is greater than 15.0, Görtler modes dominate first shear modes.

Compressibility effects of Görtler modes are shown in Fig. 1. As Mach number increases, growth rate decreases. However, at hypersonic limit, stability effects of compressibility become less important. When Mach number is greater than 5, growth rates become constant. It is the same results as Spall and Malik (Spall *et al.*, 1983).

Figure 1 also shows relationship between spanwise wave number, β , which gives the maximum growth rates, and Mach number, M . As Mach number increases, the wave number decreases. El-Hady *et al.* (El-Hady *et al.*, 1983) also mentioned this trend in their linear stability analysis.

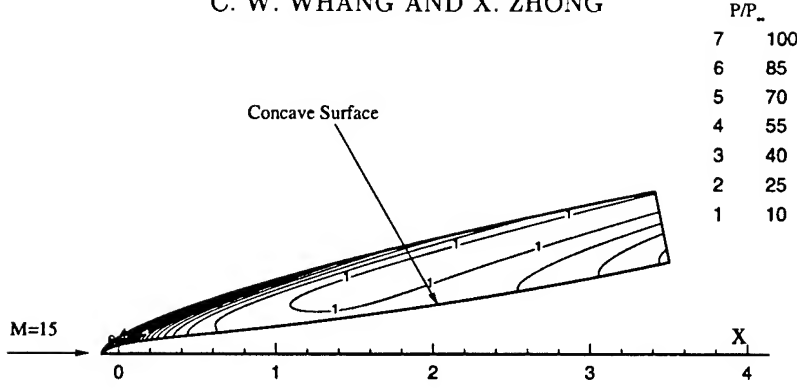


Figure 2. Pressure contours for the steady mean flow at $M_\infty = 15$, $T_\infty^* = 101.059$ K, $P_\infty^* = 10.3$ Pa, $T_w^* = 1000$ K, $Re_\infty = 150753.17$.

3. Görtler Vortices along Blunt Body with Concave Surface

3.1. 2-D MEAN FLOW

The steady flow solutions of the Navier-Stokes equations for the viscous hypersonic flow over blunt body is simulated using a fifth order explicit upwind scheme and shock fitting method (Zhong, 1997). Eight computational zones are used to carry out the simulation with a total of 1288×121 grids. Stretched grids are used in streamwise direction as well as in wall normal direction in order to resolve rapid changes of flow properties near the stagnation point in zone 1 and viscous layers. For other zones, streamwise stretching is not necessary; however, it is used in current analysis.

First three zones are parabolic blunt body, and concave surface is extended in the other zones. Using polynomial equations, we make continuous and smooth curves. At transition points between two polynomial equations, zeroth, first, and second order derivatives are matched; therefore, curves are continuous till second order derivatives. More smooth curves can be generated by matching the third order and more, but in our analysis, we matched till second order in order to get continuous radius curvature which is a function of first and second order derivatives. For the concave surface, we used large radius of curvature to avoid shock formation due to compressive waves inside the computational domains.

Freestream Mach number (M_∞) is 15. Temperature (T_∞^*) and pressure (P_∞^*) in freestream are 101.059 K and 10.3 Pa respectively. Unit Reynolds number, Re_∞ , is 150753.175. The body surface is assumed to be a non-slip wall with an isothermal wall temperature $T_w^* = 1000$ K.

Solutions of the steady mean pressure contours are shown in Fig. 2. Pressure is nondimensionalized by the flow variables in the freestream in

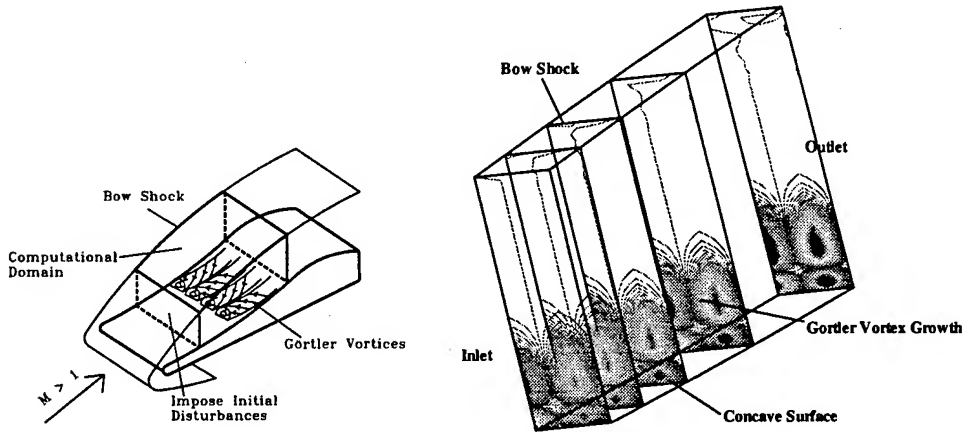


Figure 3. Temperature distribution of the primary Görtler modes along the streamwise direction at $G = 6.71$, $M = 7.89$, $Re = 4.23 \times 10^5$, and $\beta = 0.1$.

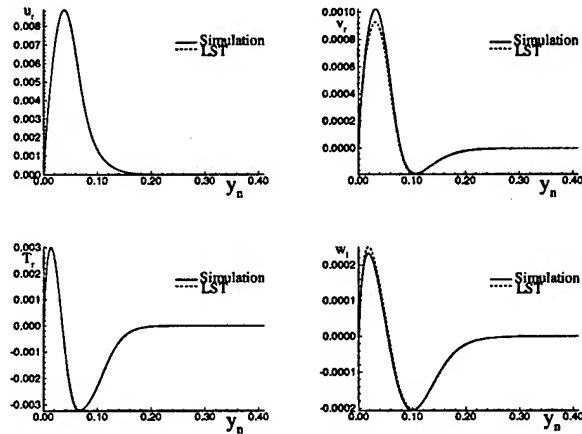


Figure 4. Distributions of imposed disturbances at $I=100$ of zone 7 at $G = 6.71$, $M = 7.89$, $Re = 4.23 \times 10^5$, and $\beta = 0.1$. Results are compared with LST results.

front of shock. The figure shows the effect of concavity on the pressure field. Concave wall starts when x is approximately 0.5m, and flow properties change after that point.

3.2. CASE I: LINEAR GROWTH OF GÖRTLER VORTICES

Simulation code can be verified by comparing simulated results with those obtained from linear stability analysis. 3-D disturbed flow is computed using 2-D mean flow. Concave surfaces are included in zone 4-8. Calculated

Görtler number is between 2.5 to 10.9, and Mach number behind shock is in the range of 6 to 8.9. Since Görtler number is relatively low at such high Mach number, zone 4 and 5 do not have unstable modes according to LST calculation. Görtler mode becomes unstable in zone 6. Disturbances are imposed in inlet of zone 7. Inlet Görtler number (G) and Reynolds number (Re_x) are 6.71 and 4.23×10^5 . Inlet disturbances of the primary Görtler modes are obtained from linear stability analysis using the simulated mean flow.

Inlet boundary conditions are

$$\begin{aligned} u &= \bar{U}(x, y, z) + \epsilon \hat{u}_r(x, y, z, t) \cos(\beta z) \\ v &= \bar{V}(x, y, z) + \epsilon \hat{v}_r(x, y, z, t) \cos(\beta z) \\ w &= \bar{W}(x, y, z) - \epsilon \hat{w}_i(x, y, z, t) \sin(\beta z) \\ p &= \bar{P}(x, y, z) + \epsilon \hat{p}_r(x, y, z, t) \cos(\beta z) \\ T &= \bar{T}(x, y, z) + \epsilon \hat{T}_r(x, y, z, t) \cos(\beta z) \end{aligned} \quad (1)$$

where \hat{u}_r , \hat{v}_r , \hat{w}_i , \hat{p}_r , and \hat{T}_r are eigenfunctions obtained from LST. Other eigenfunctions (\hat{u}_i , \hat{v}_i , \hat{w}_r , \hat{p}_i , and \hat{T}_i) are zero. Since steady Görtler vortices are observed in experiments, we study spatial Görtler instability. In spatial linear stability analysis, ω is zero; therefore, eigenfunctions do not depend on time, and initial disturbances at inlet of zone 7 are fixed as time changes. Inlet disturbances propagates spatially and converged to steady state condition.

We used four points in z -direction to cover one wavelength of spanwise disturbances. Spectral method is applied to spanwise direction to get accurate results. Wavelength is calculated from wavenumber β . In the current computation, β , which is nondimensionalized by boundary layer thickness, δ , is 0.1. It gives maximum growth rate of Görtler mode.

To verify Navier Stokes solver, simulated results are compared with those obtained from LST. We set ϵ is 0.001 which makes disturbances grow linearly. Figure 3 shows the temperature perturbation contours of primary Görtler modes along the streamwise direction. The perturbation contains two peaks along wall normal direction. The growth of the Görtler vortices in the streamwise direction is shown by the intensity of the disturbances. Figure 4 show distributions of simulated disturbances in normal direction at later station. y_n indicates the wall normal distance. LST results are also plotted in the same figures. The results show a good agreement between LST and Navier Stokes results.

3.3. CASE II : NON-LINEAR GROWTH OF GÖRTLER VORTICES

It is an important topic how Görtler vortices break down to turbulence. Experiments showed that it is mainly due to the interaction of nonlinear

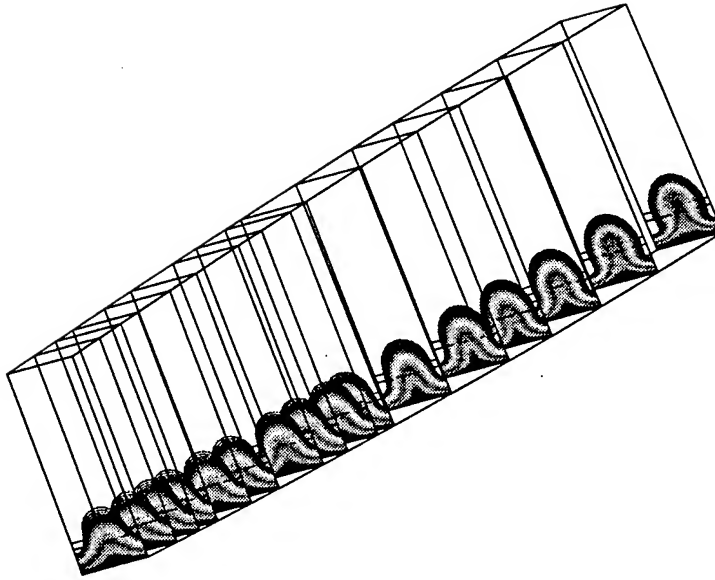


Figure 5. Distributions of iso-contours of streamwise mean velocity along the streamwise direction. The size of grids is $321 \times 121 \times 16$. Mushroom shaped vortices develop.

growth of Görtler vortices and other forms of disturbances. In nonlinear growing process, mushroom shaped vortices are produced since the counter-rotating vortices pump fluid with a low streamwise velocity away from the wall. There are two regions in Görtler vortices which are peak (low velocity region) and valley (high velocity region). These two regions produce the mushroom shaped vortices. Interaction between these vortices and traveling wave is the main factor of breaking down to turbulences.

To study nonlinear effects of Görtler instability, large amplitude disturbances are introduced at inlet of zone 7. The amplitude of the initial Görtler vortices is about $0.3U_\infty$. Two zones (zone 7 and zone 8) are used in nonlinear simulation. Mach number behind shock is between 7.89 to 8.92. Reynold's number (Re_x) is in the range of 4.23×10^5 to 8.49×10^5 . Each zones are resolved by $161 \times 121 \times 16$ grids. In the simulation, parallel computing is applied to reduce the computational time. Six nodes are applied to each zones.

Figure 5 shows distributions of streamwise velocities as flow moves downstream. The development of mushroom shaped vortices is well represented in the figure. Bow shock does not have much effects on flow field. The iso-contours of streamwise mean velocity at four different streamwise locations are shown in figure 6. Peak and valley regions are clearly shown. While the middle region (peak) tends to go up, others becomes narrower.

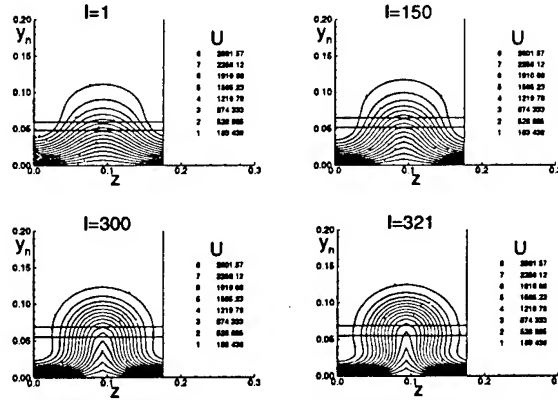


Figure 6. Iso-contours of the mean streamwise velocity in the cross-stream plane for several streamwise locations.

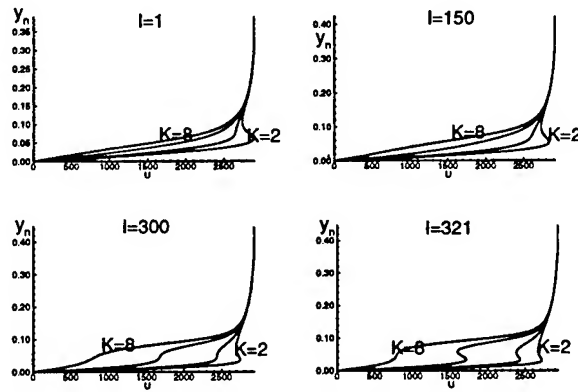


Figure 7. Profiles of the streamwise velocity in the vertical direction at four different streamwise locations. Velocity of the peak region ($K=6$) near the wall increases as flow moves downstream.

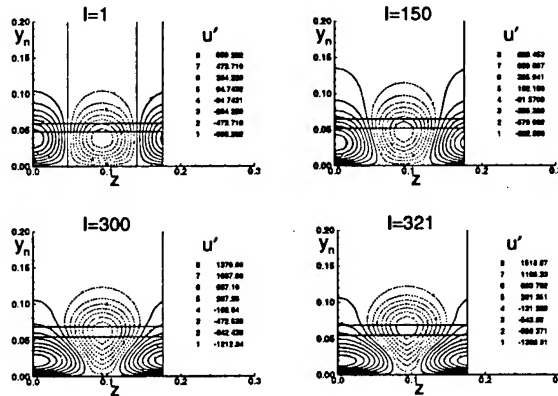


Figure 8. Streamwise velocity disturbance contours at four different streamwise locations. Disturbances in valley region moves to the peak region of Görtler vortices.

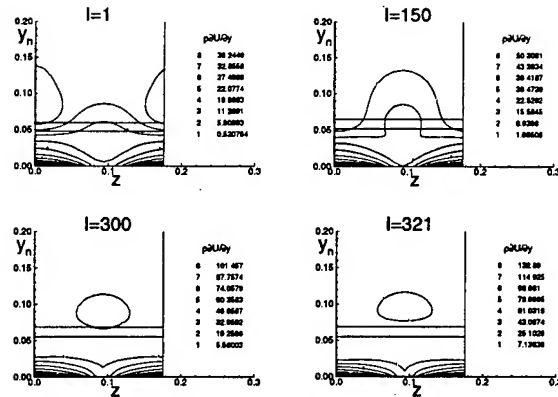


Figure 9. Iso-contours of normal gradient of the mean streamwise velocity in the cross-stream plane for several streamwise locations.

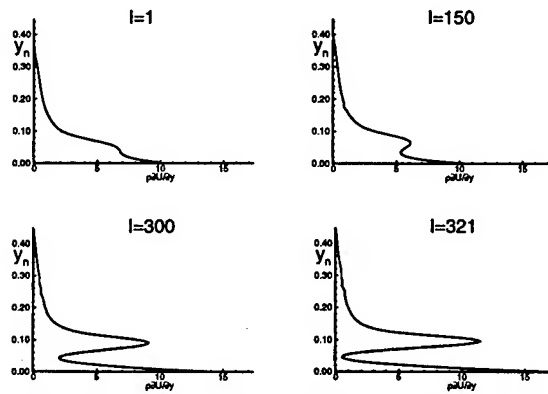


Figure 10. Profiles of normal gradient of the mean streamwise velocity in the vertical direction at peak region. Inflection points develop along the streamwise direction.

Profiles of the streamwise velocity in the vertical direction at four different spanwise locations are shown in Fig. 7. Velocity in peak region increases near the wall, and inflection points develop. Liu and Domaradzki(1993) mentioned that the Görtler vortices pump vertically the low-speed fluid away from the wall in the peak region and push the high speed fluid toward the wall in the valley region. However, there is the limitation of growing thickness of the peak, and high speed fluid starts to transfer to the peak region, and mushroom shaped vortices are produced. Streamwise velocity perturbation contours shown in Fig. 8 represent fluid near the wall in peak region is transferred to the valley.

In Görtler instability, inflection points develop in wall normal and spanwise directions, and inviscid instability problem become important. Derivatives of the streamwise velocity show clear development of inflection points.

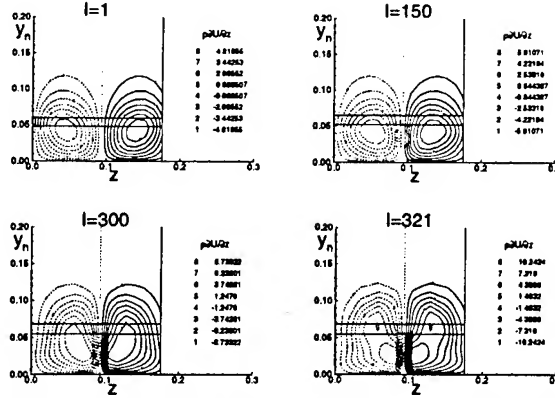


Figure 11. Iso-contours of spanwise gradient of the mean streamwise velocity in the cross-stream plane for several streamwise locations

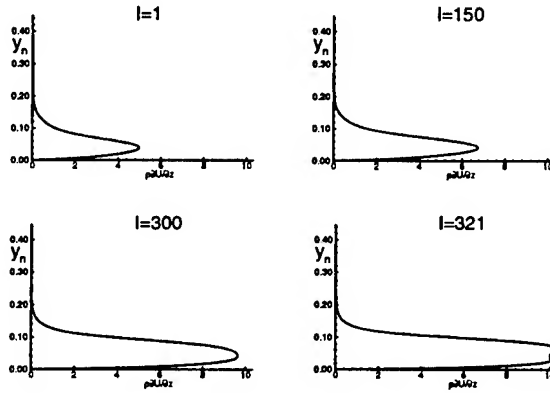


Figure 12. Profiles of spanwise gradient of the mean streamwise velocity in the vertical direction at peak region. Inflection points develop along the streamwise direction.

Figure 9 shows iso-contour of $\rho \frac{\partial U}{\partial y}$ in four different streamwise locations. Structure in peak region (low velocity region) changes as the flow moves. The vertical shear has its maximum in the low velocity region. Distributions of the normal streamwise velocity gradients at the spanwise location, in which the magnitude of $\rho \frac{\partial U}{\partial y}$ is the maximum, are shown in Fig. 10. Inflection points develop in the peak region. The magnitude increases as the flow moves which means that effects of inflection points increase.

Figure 11 and 12 show profiles of spanwise velocity gradients, $\rho \frac{\partial U}{\partial z}$, at four different streamwise locations. Both figures also represent the development of inflection points. Inflectional profiles appear in spanwise direction as well as normal direction, and they are related to secondary instability which is inviscid instability. Using energy conversion mechanism, Yu *et al.*(1994) showed that sinuous mode of secondary instability is related

to normal velocity gradient, and various mode is related to the spanwise gradient.

4. Summary

In this paper, linear and nonlinear development of Görtler vortices were investigated. Parametric studies on relation between Görtler and shear modes were considered by linear stability analysis. At hypersonic speed limit, the maximum growth rates of Görtler and shear modes were computed. Mach number varied 1 to 8, and Re_δ is fixed as 1500. There is a critical Görtler number over which Görtler modes are dominant. Increase of Görtler number indicates increase of concave surface effects. Concavity destabilizes the flow, but it affects more Görtler modes than shear mode. Changing curvature causes dramatic changes in growth rate of Görtler mode but little changes for the second shear mode.

Mean flow along the blunt body which includes concave wall was simulated by a fifth-order explicit unsteady computer code. It showed the effect of concavity on the pressure field. Disturbances computed by the stability code were added in inlet of zone 7. Simulation results were compared with results predicted by LST. There were good agreements between two results.

Finally we studied nonlinear effects of Görtler vortices. Simulation showed the development of high and low velocity regions in Görtler vortices. The transfer of high speed fluid in valley region into the peak produced mushroom shaped vortices. Inflection points developed in nonlinear growth of Görtler vortices. The profiles of normal and spanwise velocity gradient showed the inflectional points which induce the inviscid instability problem.

5. Future Works

Work is in progress to include bow shock effects, nose bluntness and more detailed studies on nonlinear Görtler instability. To study bow shock effects on Görtler instability, boundary layer flow without shock will be investigated. Nonlinear study of Görtler instability includes interactions with other forms of disturbances(eg. TS waves, cross flow effects etc.) and mixing effects when fuel injection is applied in front of engine inlet.

6. Acknowledgments

This research was supported by the Air Force Office of Scientific Research under grant number F49620-97-1-0030 monitored by Dr. Len Sakell.

References

- El-Hady, N.M. and Verma, A.K. (1983) Growth of Görtler Vortices in Compressible Boundary Layers along Curved Surfaces, *J. Engineering and Appl. Sciences* Vol. 2, pp. 213-238
- Hall P. (1988), The nonlinear development of Görtler vortices in growing boundary layers, *J. Fluid Mech.* Vol. 193, pp. 243-266
- Lee K. and Liu J. T. C. (1992), On the growth of mushroomlike structure in nonlinear spatially developing Görtler vortex flow, *Phys. Fluids* Vol. 4(1), pp. 95-103
- Li F. and Malik M. R. (1995), Fundamental and subharmonic secondary instabilities of Görtler vortices, *J. Fluid Mech.* Vol. 297, pp. 77-100
- Liu J. T. C. (1991), On scalar transport in nonlinearly developing Görtler vortex flow *Geophys. Astrophys. Fluid Dynamics* Vol. 58, pp. 133-145
- Liu W. and Domaradzki J. A. (1993), Direct numerical simulation of transition to turbulence in Görtler flow, *J. Fluid Mech* Vol. 246, pp. 267-299
- Mack, L.M. (1984) Boundary layer linear stability theory, *AGARD Rep. No. 709*
- Malik, M.R. (1990) Numerical methods for hypersonic boundary layer stability, *J. Comput. Phys.* Vol. 86, pp. 376-413
- Spall, R.E. and Malik, M.R. (1989) Görtler Vortices in Supersonic and Hypersonic Boundary Layers, *Phys. Fluids* Vol. 1(11), pp. 1822-1835
- Whang, C.W. and Zhong, X. (1999) Direct Numerical Simulation of Görtler Instability in Hypersonic Boundary Layers, *AIAA paper 99-0291*
- Yu X. and Liu J. T. C. (1994), On the mechanism of sinuous and varicose modes in three-dimensional viscous secondary instability of nonlinear Görtler rolls, *Phys. Fluids* Vol. 6(2), pp. 736-750
- Zhong, X. (1997) Direct numerical simulation of hypersonic boundary-layer transition over blunt leading edges, part I: a new numerical method and validation, *AIAA paper 97-0755*.

STUDY ON TRANSPORTATION OF PASSIVE SCALAR IN SHEARLESS MIXING LAYER BY LARGE EDDY SIMULATION*

ZHANG Zhaoshun and CHEN Yu Guang and CUI Guixiang and XU Chunxiao

Department of Engineering Mechanics, Tsinghua University, Beijing CHINA

L. SHAO and J.P. BERTOGLIO

Laboratory of Fluid Mechanics and Acoustics, Ecole Centrale de Lyon, FRANCE

1. INTRODUCTION

The turbulent transportation of mass and energy is of great importance in engineering and natural environment. Classic theories of turbulent transportation of passive scalar in isotropic turbulence have been proposed by Oboukhov^[1] and Batchelor^[2], etc. However, recent experimental and numerical studies show that intermittence appears in passive scalar fluctuations while the fluid turbulence is isotropic and its PDF is Gaussian^{[3], [4]}. Therefore it is worth to have detailed study of the transportation of passive scalar in turbulence from either theoretical or practical view. In this paper we focus on the problem of transportation of passive scalar in the inhomogeneous turbulence and take the homogeneous turbulence case as an example for verification. The shearless mixing layer is an ideal case for studying the turbulent transportation process without the influence of the instability mechanism introduced by mean shear. Experimental results of transportation of passive scalar in shearless mixing layer have been provided by Veeravalli and Warhaft (1989)^[5] and they are good resources for verification of numerical study. Both direct numerical simulation (DNS) and large eddy simulation (LES) are good choices for better understanding of the mechanism and prediction of quantitative properties in the turbulent transportation. For instance, the entrainment in a decaying shearless mixing layer was studied by Brigg et al.^[6] at Reynolds number of 40 based on the Taylor microscale λ and $q = \sqrt{u_i u_i}$ by use of DNS. For the investigation of turbulent transportation of inhomogeneous passive scalar field, e.g. the concentration and temperature, a line source or sheet source of passive scalar is a good testing case in both homogeneous and inhomogeneous turbulence. Experimental results for the turbulent transportation of a line source in shearless turbulent mixing layer are also available (Veeravalli and Warhaft, 1990)^[7]. We applied LES to the investigation of the turbulent transportation of passive scalar in the inhomogeneous turbulence. We found great intermittence of velocity fluctuation in the shearless mixing layer previously^[8] and we will disclose that much greater intermittence of passive scalar fluctuations also occurs in the shearless mixing layer. The great intermittence of passive scalar results in the increment of the mean flux of passive scalar, which is important in prediction of the heat and mass transfer in engineering and environment.

2. PHYSICAL MODEL AND NUMERICAL METHOD

The shearless mixing layer is composed of two blocks of homogeneous turbulence with different length scales and kinetic energy, the initial velocity fluctuations in the two blocks, as shown in Figure 1, are homogeneous and nearly isotropic. The initial temperature distributions can be imposed in different profiles, such as pure random with zero mean, constant gradient with or without fluctuations and a plane source which is simulated by a Gaussian function with small variance. The mixing process takes place between two blocks of the shearless mixing layer while the mixing region is expanding. In this paper we put a plane sheet

* A project co-sponsored by CNNSF(19732005), Chinese Ministry of Science and Technology LIAMA and Dassault Aviation

of temperature between two homogeneous turbulence, it is a physical model to simulate a line source of heated wire in the shearless mixing layer in a wind tunnel as Veeravalli and Warhaft^[7] did in their experiment. While the turbulence is decaying and temperature fluctuations are developing in streamwise direction, the turbulence is decaying and temperature fluctuations are evolving in time in the numerical simulation.

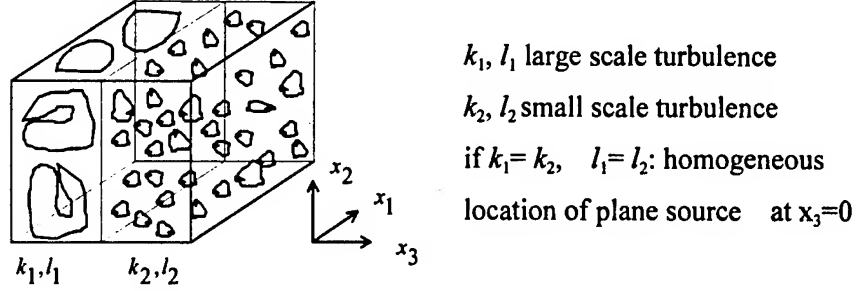


Figure 1 Illustration of the shearless mixing layer

The governing equations of the flow field are the Navier-Stokes equation and energy transport equation, which can be written in physical space as

$$\frac{\partial u_i}{\partial x_i} = 0 \quad (1)$$

$$\frac{\partial u_i}{\partial t} + u_j \frac{\partial u_i}{\partial x_j} = -\frac{1}{\rho} \frac{\partial p}{\partial x_i} + \nu \frac{\partial^2 u_i}{\partial x_j \partial x_j} \quad (2)$$

$$\frac{\partial \theta}{\partial t} + u_j \frac{\partial \theta}{\partial x_j} = \kappa \frac{\partial^2 \theta}{\partial x_j \partial x_j} \quad (3)$$

For the shearless mixing layer without mean velocity (or with constant mean velocity) we can use the periodical condition in all three direction and all flow variables are transformed by Fourier expansion as follows

$$\begin{aligned} u_i(\vec{x}, t) &= \sum_{\vec{k}} \hat{u}_i(\vec{k}, t) \exp\{i\vec{k} \cdot \vec{x}\} \\ \theta(\vec{x}, t) &= \sum_{\vec{k}} \hat{\theta}(\vec{k}, t) \exp\{i\vec{k} \cdot \vec{x}\} \\ p(\vec{x}, t) &= \sum_{\vec{k}} \hat{p}(\vec{k}, t) \exp\{i\vec{k} \cdot \vec{x}\} \end{aligned} \quad (4)$$

Then the governing equation can also be transferred into spectrum space as

$$k_i \cdot \hat{u}_i = 0 \quad (5)$$

$$\frac{\partial \hat{u}_i}{\partial t} + i k_j \hat{u}_i \hat{u}_j = -\frac{1}{\rho} i k_i \hat{p} - (\nu + \nu_t) k^2 \hat{u}_i \quad (6)$$

$$\frac{\partial \hat{\theta}}{\partial t} + i k_j \hat{\theta} \hat{u}_j = -(\kappa + \kappa_t) k^2 \hat{\theta} \quad (7)$$

in which ν and κ are the molecular viscosity and diffusivity respectively and ν_t and κ_t are the turbulent viscosity and diffusivity when the LES is carried out. The ratio of ν to κ is known as Prantdl number and we accept a value of 0.7 for air and consider it as same for turbulent transportation process, that is $\nu_t / \kappa_t = 0.7$ which has been verified by others.^[9]

By use of periodical condition in the shearless mixing layer two mixing layers will develop in the box, one from the middle and another from the box boundary. Two mixing layers are approaching and the

computation must be stopped when two mixing layers are nearly merging together. Usually it takes about 3 turnover time for two mixing layers to merge together, therefore the computing time is long enough to study the development of the transportation of passive scalar.

The spatial resolution is $64 \times 64 \times 64$ for LES, the second order Runge-Kutta scheme is used for the time integration and the time step is determined by CFL criterion. When the Large eddy simulation is carried out in spectral space, the eddy viscosity of the subgrid stress is evaluated by the Chollet-Lesieur model^[10] in spectral space as

$$\nu_t(k, t) = C_{cl} \sqrt{\frac{E(k_c)}{k_c}} \quad (8)$$

with $C_{cl}=0.267$. This is a simple subgrid model, however it is quite good for the shearless mixing layer. We have also tested Smagorinsky model and a spectrum eddy viscosity model with the variation of wave number k and results of the velocity field are of same accuracy in comparison with the experimental data.^[10]

Following Rogallo^[11] the generation of the initial random velocity field can be described briefly as below

$$\bar{u}(\bar{k}, 0) = \alpha(\bar{k}) \bar{e}'_1 + \beta(\bar{k}) \bar{e}'_2 \quad (9)$$

in which \bar{e}'_1, \bar{e}'_2 are unit vectors perpendicular to wave number \bar{k} , thus the velocity field satisfies the continuity equation $\bar{k}_i \cdot \bar{u}_i = 0$. The random variable $\alpha(\bar{k}), \beta(\bar{k})$ are then determined by the energy constraints $\iint_{A(k)} \bar{u} \cdot \bar{u}^* dA(k) = E(k)$ in which $E(k)$ is the von Karman spectrum:

$$E(k) = E(k_p) 2^{17/6} \frac{(k/k_p)^4}{[1 + (k/k_p)^2]^{7/6}} \quad (10)$$

where $E(k_p)$ is the peak of spectrum determined by the total energy and k_p the wave number of peak spectrum. The initial temperature fluctuations was generated in the same way

$$\hat{\theta}(\bar{k}) = \sqrt{\frac{f_\theta(k)}{4\pi k^2}} \exp(i2\pi\alpha(\bar{k})) \quad (11)$$

in which $\hat{\theta}(\bar{k})$ is the initial spectrum for temperature fluctuations and $f_\theta(k)$ the energy spectrum of $\hat{\theta}(\bar{k})$, which is also taken as the von Karman spectrum. $\alpha(\bar{k})$ is the random variable of white noise.

A number of testing cases have been completed. For majority of the testing cases the initial kinetic energy and dissipation rates of the shearless mixing layer are: $k_1=730\text{cm}^2/\text{s}^2$, $\epsilon_1=10957\text{cm}^2/\text{s}^3$, $k_2=230\text{cm}^2/\text{s}^2$, $\epsilon_2=4056\text{cm}^2/\text{s}^3$. The Taylor microscale λ in the two blocks of initially homogeneous turbulence are $\lambda_1=0.33\text{cm}$ and $\lambda_2=0.30\text{cm}$ and the Reynolds numbers are $\text{Re}_1=q_1\lambda_1/\nu=78$, $\text{Re}_2=40$ respectively.

3 THE RESULTS

To verify the code we check the turbulence spectrum with the well-known Comte-Bellot spectrum^[13] with satisfaction and put the passive scalar into the turbulence when the decay rate of turbulence energy is approaching to -1.3 .

3.1 Prediction of mean temperature profile and variance of temperature fluctuations

The computational results of this case have been compared with the experimental results of Veeravalli and Warhaft^{[5], [7]} in good agreement. For the examination of the feasibility of the numerical code, the evolution of the half width of the mean temperature profile and the variance of the temperature fluctuation are compared with the experimental results which are shown in Figure 2(a) and 2(b). At the early stage of the evolution, say less than 0.1 eddy turnover time, the prediction by the LES is apparently different from the

measurements. After short period, however, the LES prediction is in fairly good agreement with experimental results.

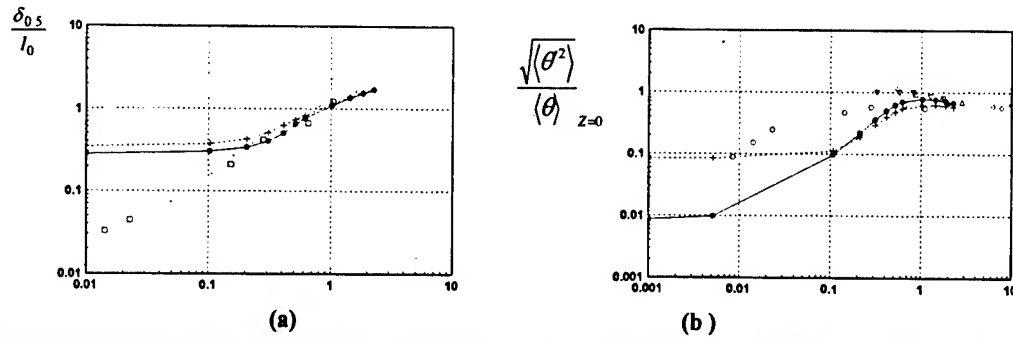


Figure 2 The evolution of (a) the half width of mean temperature profile, (b) the variance of the temperature fluctuations
 Computed results: solid line—thinner thickness of the initial line source; dashed line—larger thickness
 Experimental results: ○ and □—by Stapouhntzis et al (1986)^[14], ▲—by Veeravalli et al. 1990^[7]

Figure 3 presents the profiles of mean temperature and the variance of temperature fluctuations in homogeneous turbulence, the later profile is characterized by the double peaks at earlier development. It is in good agreement with experiments of Veeravalli et al^[5]. The appearance of double peak in the profiles of variance can be easily interpreted by the transportation equations of temperature since there is high great gradients of mean temperature.

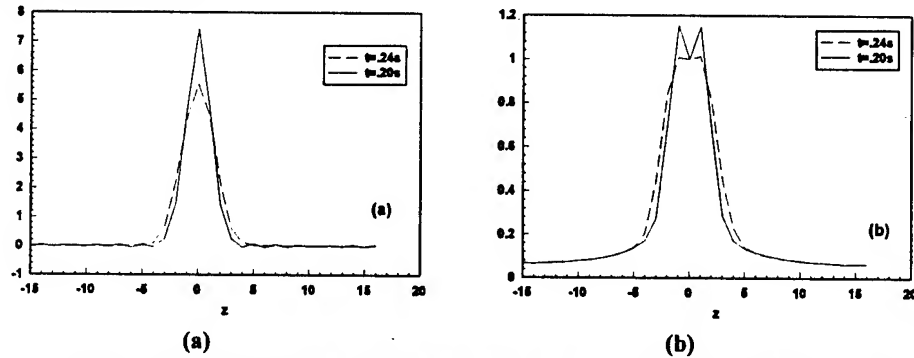


Figure 3 Profiles of (a) mean temperature (b) variance of temperature fluctuations in the homogeneous turbulence, the variance normalized by the value at $z=0$

Figure 4 shows the profiles of mean temperature and the variance of temperature fluctuations in the inhomogeneous turbulence. The obvious asymmetrical profiles result from the inhomogeneity of turbulence, however it is more asymmetrical in the variance profile. Note that the peaks of the profiles are located in the region with larger scale of turbulence.

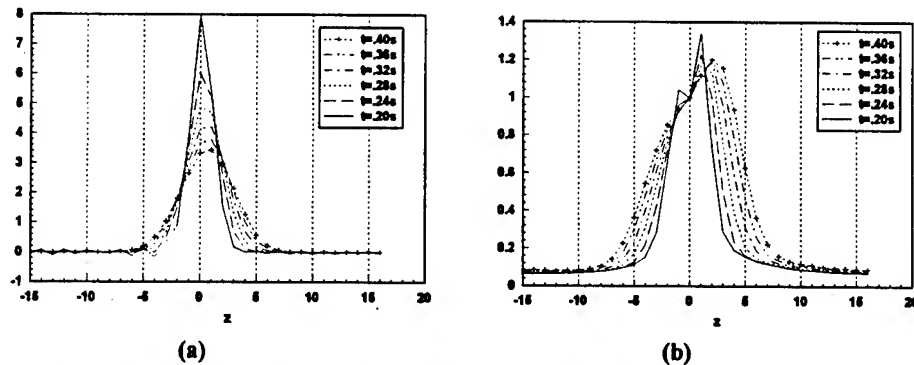


Figure 4 Profiles of (a) mean temperature (b) variance of temperature fluctuations in the inhomogeneous turbulence, the variance normalized by the value at $z=0$

Figure 5 and 6 presents the budget of the intensity of temperature fluctuations in the inhomogeneous turbulence from both the experiment^[7] and our computation, the labels P, T, D, A stand for the production, transportation, diffusion and advection of the intensity of temperature fluctuations. In the mixing region the production term becomes negative, it is typical of inhomogeneous turbulence and the computational results well simulate the phenomenon.

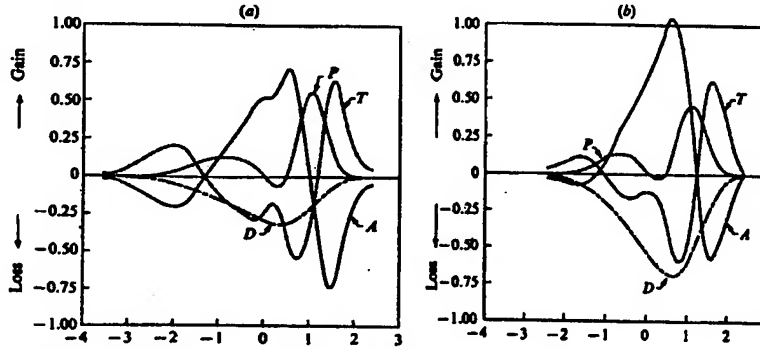


Figure 5 The budget of intensity of temperature fluctuations^[7], (a) at earlier stage; (b) at later stage

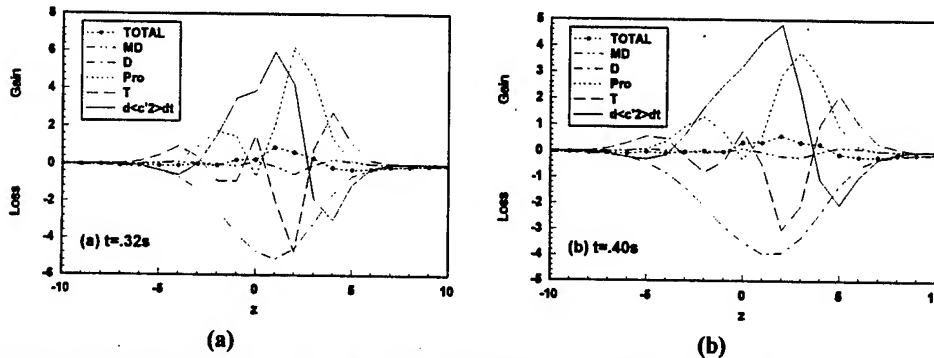


Figure 6 The budget of intensity of temperature fluctuations by computation, (a) at earlier stage; (b) at later stage

Figure 7 demonstrates the budget of turbulent thermal flux $\langle \theta'w' \rangle$, it also shows good agreement between computational and experimental results

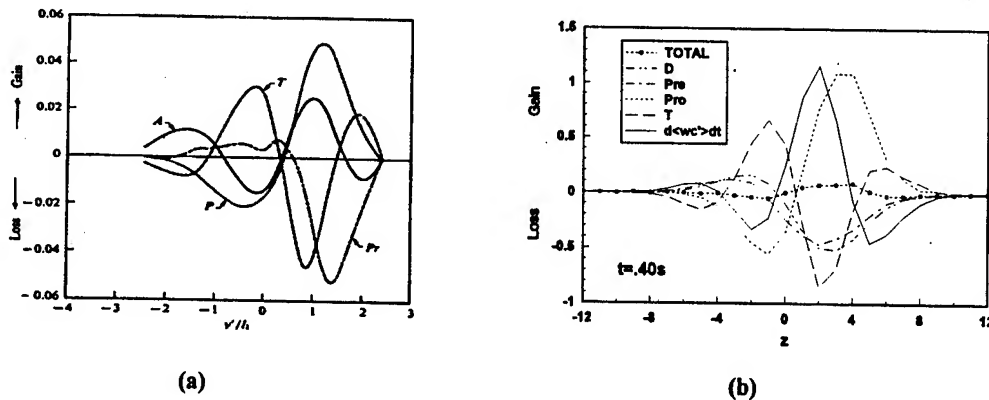


Figure 7 The budget of thermal flux in the inhomogeneous turbulence, (a) experiment^[7]; (b) computation

All mean properties of the temperature field, shown above, are in good agreement with the experimental results^{[5],[7]} and it indicates that the LES with simple subgrid model is a good choice for investigation of the passive scalar in the inhomogeneous turbulence.

3.2 Prediction of turbulent thermal energy flux

Briggs et al have found that the turbulent thermal energy flux, predicted by DNS in the case of step function of mean temperature profile, is much greater than that calculated by phenomenological modelling^[6]. We have found the same results in the case of a plane sheet source of passive scalar. Figure 8 shows the result.

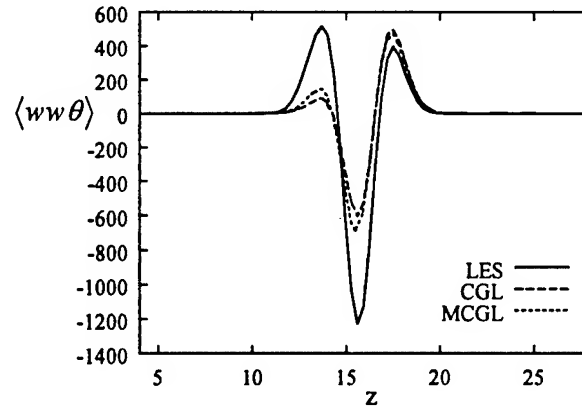


Figure 8 The turbulent transportation thermal energy in shearless mixing layer CGL—Craft Graham & Launder^[15]

The underestimation of the turbulent thermal flux results from equilibrium hypothesis in the phenomenological modelling in which the intermittent effects are ignored as we have mentioned in a previous paper^[8] and others.^[14] In fact the flatness of temperature fluctuations is considerably high as demonstrated in Figure 9 and 10.

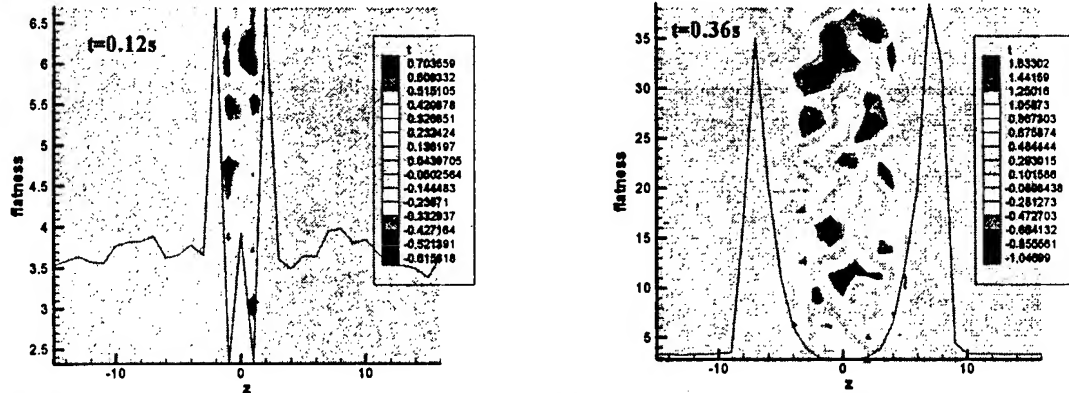


Figure 9 Flatness profile F verse z and iso-contour of temperature fluctuations on x - z plane in homogeneous turbulence

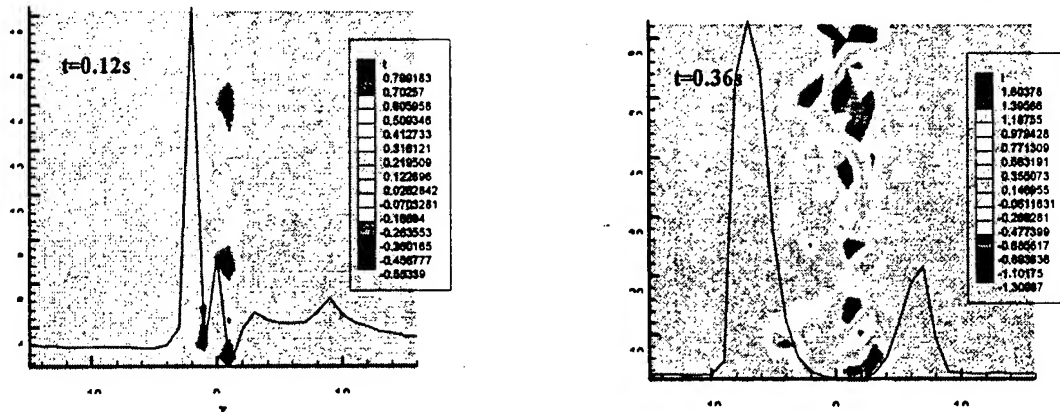


Figure 10 Flatness profile F verse z and iso-contour of temperature fluctuations on x - z plane in inhomogeneous turbulence

High flatness indicates the great intermittence of the random function. The typical iso-contours of

temperature fluctuation are also shown in Figure 9 and 10 where it clearly reveals that the passive scalar fluctuations are highly non-uniform and the high flatness occurs at the border between large and small scales of temperature fluctuation. It should be also mentioned that the higher flatness located in the region where both turbulence scale and energy are smaller in the inhomogeneous turbulence. This is also typical of inhomogeneous turbulence.

4 CONCLUDING REMARKS

The LES of the turbulent transportation of passive scalar in shearless mixing layer is acceptable with simple subgrid model. The results of LES are in good agreement with available experimental data, including the budgets of the variance of temperature fluctuations and turbulent thermal flux, etc. The phenomenological model underestimates the turbulent thermal flux and the reason is the high intermittence in temperature fluctuations when they are transported in inhomogeneous turbulence. To well understand the turbulent mixing of passive scalar, including the refined subgrid model of LES and simulation by DNS, the investigation of intermittence is needed.

REFERENCES

- [1] Monin A.S. and Yaglom A.M. 1975 Statistical fluid mechanics vol.1 and vol.2 MIT Press
- [2] Batchelor G.K. 1953 The theory of homogeneous turbulence Cambridge University Press
- [3] Jayesh and Z. Warhaft 1992 Probability distribution, conditional dissipation, and transportation of passive temperature fluctuations in grid-generated turbulence *Physics of Fluids A* 4:2292
- [4] Pumir A. 1994 A numerical study of the mixing of a passive scalar in three dimensions in the presence of mean gradients *Physics of Fluids A* 6:2118
- [5] Veeravalli S. and Warhaft Z. 1989 The shearless turbulence mixing layer *JFM* 207:191
- [6] Briggs D.A. and J.H. Ferziger and Koseff J.R. and Monismith S.G. 1996 Entrainment in a shear-free turbulent mixing layer *JFM* 310:215
- [7] Veeravalli S. and Warhaft Z. 1990 Thermal dispersion from a line source in the shearless turbulence mixing layer *JFM* 216:35
- [8] Zhang Z. et al. 1999 Effect of plane strain on inhomogeneous *SCIENCE IN CHINA A* 42:154
- [9] Cabot W. And Moin P. 1993 Large eddy simulation of scalar transport with the dynamic subgrid-scale model. In 'Large eddy simulation of complex engineering and geophysical flows' Cambridge University Press p141
- [10] Chollet J.P. and Lesieur M. 1981 Parameterization of small scales of three dimensional isotropic turbulence utilizing spectrum closure *J. of Atm. Sci.*, 38:2747
- [11] Shao, L. et al 1990 Large eddy simulation of the interaction between two distinct turbulent velocity scales in *Advances in Turbulence 3*, Springer-Verlag page 101-121
- [12] Rogallo R.S. 1981 Numerical experiments in homogeneous turbulence TM81315 NASA
- [13] Comte-Bellot G. and Corrin S. 1971 Simple Eulerian time correlation of full- and narrow-band velocity signals in grid-generated, 'isotropic' turbulence *JFM* 48:273
- [14] Stapountzis, H. and Sawford, B.L. and Hunt, J.C.R. and Britter, R.E. 1986 Structure of the temperature field downwind of a line source in grid turbulence *JFM* 165:401-424
- [15] Craft T.J. and Graham L.J. and Launder B.E. 1993 Impinging jet studies for turbulent model assessment II. An examination of the performance of four turbulent models *Intl. J. Heat Mass Transfer* 36: 2685

DNS OF BOUNDARY-LAYER RECEPTIVITY TO FREESTREAM SOUND FOR HYPERSONIC FLOWS OVER BLUNT ELLIPTICAL CONES

XIAOLIN ZHONG

*Mechanical and Aerospace Engineering Department
University of California, Los Angeles, California 90095*

1. Introduction

This paper is concerned with the problem of leading-edge receptivity of 3-D hypersonic boundary layers over a blunt elliptical cone. The receptivity of boundary layers to disturbances is the process of converting environmental disturbances into instability waves in the boundary layers. It provides important initial conditions in terms of amplitude, frequency, and phase for the study of development of instability waves in the boundary layers (Goldstein, 1989; Saric, 1994). Most theoretical results on boundary-layer receptivity have been obtained from the asymptotic analysis of incompressible flows. The asymptotic analysis explains how the long wavelength freestream acoustic disturbances enter a boundary layer and generate short-wavelength Tollmien-Schlichting (T-S) waves downstream of the leading edge. Recently, direct numerical simulation (DNS) of the Navier-Stokes equations has been used as a research tool in the studies of stability and transition. Examples of the DNS studies on the receptivity of boundary layers can be found in (Murdock, 1981; Lin, 1992; Buter, 1994; Casalis, 1994; Corke, 1996). Most of these studies have been for incompressible or low-speed compressible boundary layers.

Not much work has been done on the receptivity of hypersonic boundary layers. The receptivity of 3-D hypersonic flow over elliptical cones is affected by many interacting flow mechanisms. The uneven strength of the bow shock over the elliptical cone creates a circumferential pressure gradient. Such a pressure gradient generates inflectional cross flow velocity. It is expected that inviscid inflectional instability will have an important effect on such flows. In addition, the receptivity of hypersonic boundary layers over blunt bodies is altered considerably by the presence of the bow shocks

which are located very close to body surfaces at hypersonic Mach numbers. Stability and transition of hypersonic boundary layers are affected by nose bluntness and by the boundary-layer swallowing of entropy layers created by bow shocks. For such complex unsteady flows, the numerical simulation of the full Navier-Stokes equations are able to generate detailed flow field information for the studies of the receptivity process.

We have been working on the numerical simulation of hypersonic boundary-layer receptivity and stability (Zhong, 1997a; Zhong, 1998). We developed and validated a set of fifth and seventh-order shock-fitting schemes for the DNS of practical hypersonic flows over blunt bodies with bow shocks. The use of the shock-fitting method makes it possible to accurately compute the physical transient bow-shock interactions, and the development of instability waves in the boundary layers. Subsequently, we (Zhong, 1997b) used the new schemes to conduct DNS studies of the receptivity of a hypersonic boundary layer to freestream acoustic disturbances for a Mach 15 flow over a parabolic leading edge. Local parallel linear stability analysis (LST) of the hypersonic boundary layer over the blunt wedge was also conducted to compare with DNS results and to identify instability modes obtained by the DNS studies.

The objective of this paper is to present the study of the receptivity of 3-D hypersonic boundary layers over 2:1 elliptical blunt bodies at Mach 15. Some of the preliminary results were presented in an AIAA meeting (Zhong, 1999). The disturbances are freestream weak monochromatic planar acoustic waves. Both steady and unsteady flow fields between the bow shock and the boundary layer are numerically simulated by using a 5th-order shock-fitting scheme. The wave modes in the boundary layer generated by the freestream disturbances are studied based on the simulation results. Local parallel linear stability analysis is conducted to compare with numerical results in order to gain more insight on perturbation fields obtained by the solutions of the 3-D Navier-Stokes equations.

2. Equations, Numerical Methods, Code Validation

The governing equations and numerical methods are briefly summarized here. Details can be found in (Zhong, 1997a; Zhong, 1997b). The governing equations are the unsteady 3-D Navier-Stokes equations written for the computation in the conservation-law form:

$$\frac{\partial U^*}{\partial t^*} + \frac{\partial F_j^*}{\partial x_j^*} + \frac{\partial F_{vj}^*}{\partial x_j^*} = 0 \quad (1)$$

where superscript “*” represents dimensional variables, and

$$U^* = \{\rho^*, \rho^* u_1^*, \rho^* u_2^*, \rho^* u_3^*, e^*\} \quad (2)$$

The gas is assumed to be thermally and calorically perfect. The viscosity and heat conductivity coefficients are calculated using Sutherland's law and the assumption of constant Prandtl number. To compute flow over a blunt body with a curved surface, the Navier-Stokes equations are transformed into body-fitted curvilinear computational coordinates in a computational domain bounded by the bow shock and the body surface. The location and the movement of the bow shock is not known in advance and they are solved together with other flow variables.

The results presented in this paper are nondimensional unless stated otherwise. We nondimensionalize the velocities with respect to the freestream velocity U_∞ , length scales with respect to a reference length d^* given by the body surface equation, density with respect to ρ_∞^* , pressure with respect to p_∞^* , temperature with respect to T_∞^* , time with respect to d^*/U_∞^* , vorticity with respect to U_∞^*/d^* , entropy with respect to C_p^* , wave number with respect to $1/d^*$, etc. The dimensionless flow variables are denoted by the same dimensional notation but without the superscript "*".

The numerical methods for spatial discretization of the 3-D Navier-Stokes equations are a fifth-order shock-fitting scheme in streamwise and wall-normal directions, and a Fourier collocation method in the periodic spanwise flow direction, i.e., the azimuthal direction of a cone geometry. The spatially discretized equations are advanced in time using Low-Storage Runge-Kutta schemes of up to third order. The 3-D fifth-order shock fitting computer codes for Navier-Stokes equations have been extensively tested and validated for many steady and unsteady flow simulations. Some of the validation results are presented in (Zhong, 1998; Zhong, 1999). In addition, numerical accuracies of the results are evaluated by grid refinement studies.

3. Receptivity Simulations

The numerical simulation for the receptivity of 3-D hypersonic flows over a blunt elliptical cone is carried out using our 3-D fifth-order shock fitting scheme where the outer grid line is the bow shock. The unsteady bow shock shape and shock oscillations are solved as part of the computational solution. In the simulations, steady flow solutions are first obtained by advancing the unsteady flow computations for the case of no freestream wave. Subsequently, unsteady viscous flows are computed by imposing a planar acoustic single-frequency disturbance wave on the steady flow variables at the freestream side of the bow shock. The shock/disturbance interactions and generation of boundary waves are solved using the nonlinear Rankine-Hugoniot relations at the shock and the Navier-Stokes equations in the flow fields. The unsteady calculations are carried out for about 15 to 30 periods in time until the unsteady solutions reach a time periodic state. Finally,

the unsteady computations are carried out for additional periods in time to perform FFT on the perturbation field to obtain the Fourier amplitudes and phase angles for the perturbations of the unsteady flow variables in the flow field.

The freestream disturbances are assumed to be weak monochromatic planar acoustic waves with wave front normal to the center line of the body. The perturbations of flow variables in the freestream introduced by the freestream acoustic wave before reaching the bow shock can be written in the following form:

$$q'_{\infty} = |q'|_{\infty} e^{i(kx - \omega t)} \quad (3)$$

where $|q'|$ represents one of the flow variables, $|u'|$, $|v'|$, $|w'|$, $|p'|$, and $|\rho'|$. The freestream perturbation amplitudes satisfy the following relations: $|u'|_{\infty} M_{\infty} = |p'|_{\infty} / \gamma = |\rho'|_{\infty} = \epsilon$, where ϵ represents the freestream wave magnitude. The parameter k is the dimensionless freestream wave number which is related to the dimensionless circular frequency ω by: $\omega = k(1 + M_{\infty}^{-1})$. The dimensionless frequency F is defined as: $F = \frac{\omega^* \nu^*}{U_{\infty}^*}$.

4. Receptivity of Blunt Elliptical Cone at $M = 15$

This paper considers a 2:1 blunt elliptical cone with a Mach 15 freestream. The specific test case is the receptivity to weak freestream acoustic disturbance waves by a Mach 15 hypersonic flow past an elliptical blunt cone at zero angle of attack. The body surface is specified by:

$$x^* = \frac{y^{*2}}{2r_y^*} + \frac{z^{*2}}{2r_z^*} - d^* \quad (4)$$

where r_y^* and r_z^* are the major and minor nose radius of curvatures. In the present simulations, the flow conditions are

$$\begin{array}{lll} M_{\infty} = 15 & \epsilon = 5 \times 10^{-3} & T_{0\infty}^* = 5980 \text{ K} \\ T_w^* = 1000 \text{ K} & \gamma = 1.4 & Pr = 0.72 \\ \text{Reference length } d^* = 0.01m & & Re_{\infty} = 0.60266 \times 10^5/m \\ \text{Nose Radius } r_y^* = .0125m \text{ and } r_y^* : r_z^* = 4 : 1 & & \end{array}$$

The body surface is assumed to be a non-slip wall with an isothermal wall temperature T_w^* . So far, one unsteady case with freestream dimensionless frequency of the disturbance wave $F \times 10^6 = 4274$ has been computed and presented in this paper. The results presented in this paper are obtained using two sets of grids: $92 \times 31 \times 64$ and $92 \times 61 \times 64$ grids. Theoretical results on the stagnation point heating rates and on inviscid vorticity jump across curved bow shock are used to compare with numerical solutions.

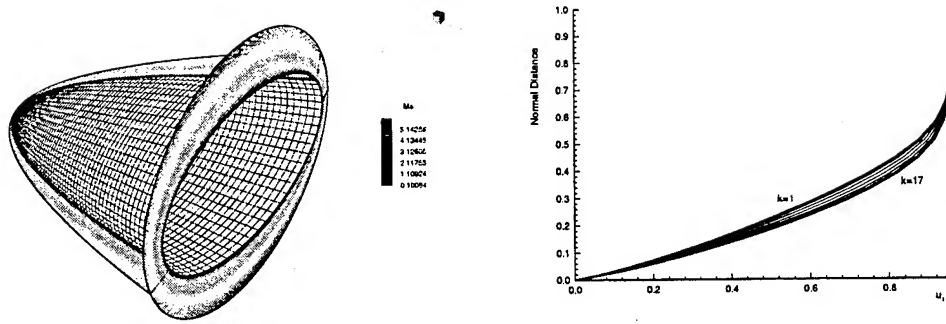


Figure 1. 3-D Mach number contours and streamwise velocity distributions along wall normal directions for several k grid lines located at the $x = 0.61289$ grid station.

5. Steady Flow Solutions

Figure 1 shows 3-D steady solutions for Mach number contours and the distribution of streamwise velocity along wall normal directions. The wall-normal distance is normalized by local shock standoff distance. The uneven strength of the bow shock in the major ($k = 1$) and minor ($k = 17$) axes creates the circumferential pressure gradient and cross flow velocity. The cross mass flow thickens the boundary layer and enlarges the standoff distance in the minor $k = 17$ axis. On the other hand, the streamwise velocity is not affected much by the circumferential pressure gradient.

Table 1. Comparison of Stagnation-Point Heating Coefficients

Grid	N-S Calculations	Fay & Riddell
92×31×32	.016804	.016324
92×61×64	.016802	.016324

The numerical results on the heating rate at the stagnation point are compared with those of boundary layer theory obtained by Fay and Riddell (Fay, 1958). Fay and Riddell showed that the stagnation point heating coefficient h for hypersonic flow over an axisymmetric blunt cone is:

$$h = q_w / (T_e - T_w) = 0.763 Pr^{-0.6} c_p \sqrt{\rho_e \mu_e K} \left(\frac{\rho_w \mu_w}{\rho_e \mu_e} \right)^{0.1} \quad (5)$$

where K is the streamwise velocity gradient obtained approximately by the Newtonian theory for hypersonic flow at the stagnation point. In this paper, Fay and Riddle's result is used based on the nose radius of the minor axis.

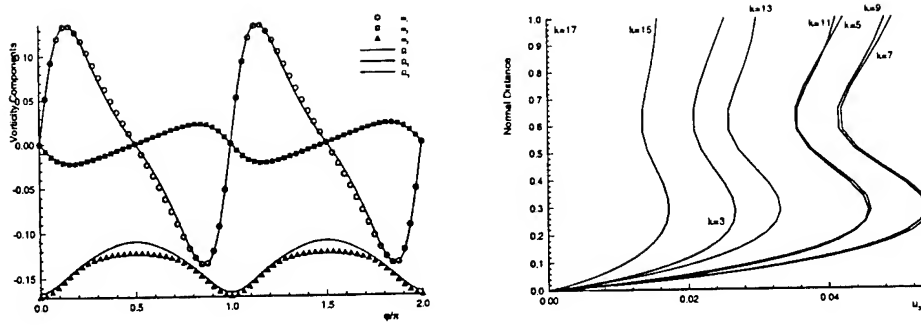


Figure 2. The distribution of vorticity components immediately behind the bow shock (inviscid theoretical results: ω_i ; numerical solutions: Ω_i), and the cross-flow (circumferential) velocity distributions along wall normal directions for several k grid lines located at the $x = 0.61289$ grid station.

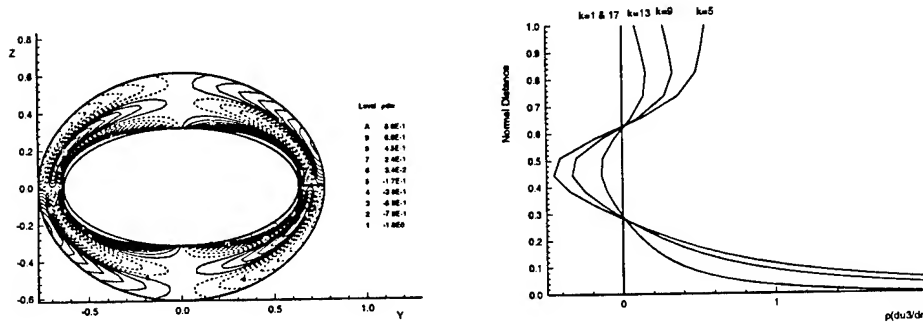


Figure 3. Contours of $\rho du_\phi/dn$ and distributions of $\rho du_\phi/dn$ along wall normal directions for several k grid lines located at the $x = 0.61289$ grid station.

The computational and theoretical results are summarized in Table 1. The agreement between the two sets of results is reasonably good.

The steady cross flow is examined in more detail by studying the vorticity and velocity distribution in the circumferential direction. Local body fitted coordinates (s, n, ϕ) with unit vectors $(\mathbf{e}_1, \mathbf{e}_2, \mathbf{e}_3)$ are defined to compute velocity and vorticity components, where \mathbf{e}_2 is the wall normal direction, \mathbf{e}_3 is the circumferential direction which is normal to a $k = \text{constant}$ grid surface, and $\mathbf{e}_1 = \mathbf{e}_2 \times \mathbf{e}_3$ defines the streamwise direction. The cross flow generates a streamwise vorticity component in the shock layer. According to Crocco's theorem, the curved bow shock generates an entropy gradient and inviscid vorticity behind the shock. The inviscid vorticity jump across

the bow shock can be derived (Hayes, 1957) using the Rankine-Hugoniot relation and Crocco's theorem or momentum equation in the direction normal to the shock. For a bow shock in a uniform freestream flow, the vorticity vector behind the shock depends only on the density ratio across the shock and the shock curvature tensor, i.e.,

$$\vec{\omega}_{\text{shk}} = \frac{(1 - \rho_{\infty}/\rho_s)^2}{\rho_{\infty}/\rho_s} (\vec{n} \times \vec{u}_s \cdot \mathbf{K}) \quad (6)$$

where $\mathbf{K} = \nabla \vec{n}$, \vec{u}_s is tangential velocity at the shock, and \vec{n} is the shock unit normal vector. The equation above can be used to compare the vorticity vector behind the shock using numerically obtained shock curvature. Figure 2 shows the vorticity components immediately behind the bow shock and the cross-flow velocity distributions along wall normal directions for several k grid lines at the $x = 0.61289$ grid station. The figure shows the generation of streamwise vorticity by the cross flow. The inviscid theoretical results computed by Eq. (6) agree well with viscous numerical solutions for the streamwise and wall-normal vorticity component. The small differences in circumferential vorticity component are due to viscous effects of the Navier-Stokes solutions which are not accounted for in the theoretical formula Eq. (6). It is found that the two results agree better when the shock layer is separated with the boundary layer as the shock is moving away from the boundary layer farther downstream.

The cross-flow velocity distributions along wall normal directions for several k grid lines in Fig. 2 shows that there are cross flow inflection points which are located outside of the boundary layer and are in the middle of the flow channel bounded by the bow shock and the wall. For compressible boundary layers over flat plates, Lin and Lees (Lees, 1946) showed that inviscid instability appears when there is a generalized inflection point defined by the zeros of $d(\rho du_{\phi}/dn)/dy$. Figure 3 shows the contours of $\rho du_{\phi}/dn$ and distribution of $\rho du_{\phi}/dn$ along wall normal directions for several k grid lines located at the $x = 0.61289$ grid station. The figure shows that there are generalized inflection points in the middle of the shock layers, outside of the boundary. It is expected there is inviscid inflectional instability in the inviscid shock layer due to the cross flow effect.

6. Unsteady Flow Solutions

Having obtained the steady flow solution, the generation of boundary-layer waves by freestream acoustic disturbances is simulated for 3-D hypersonic flow over a blunt elliptical cone with a freestream disturbance wave of dimensionless frequency $F \times 10^6 = 4247.9$. The forcing acoustic wave in the freestream has a dimensional wave number of $\alpha = 240m^{-1}$ in the x direc-

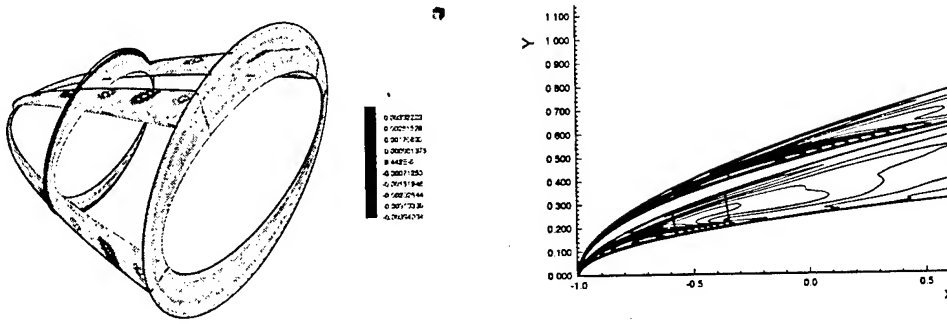


Figure 4. Instantaneous 3-D entropy perturbations and contours of streamwise velocity perturbation amplitudes induced by freestream planar acoustic disturbances in two cross sections along the major ($k = 1$) and minor ($k = 17$) axes.

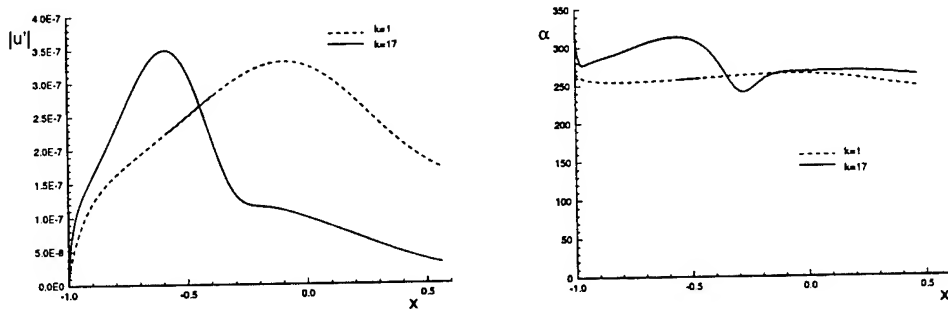


Figure 5. The distribution of streamwise velocity perturbation amplitudes and wave numbers α along the major ($k = 1$) and minor ($k = 17$) axes

tion. Figure 4 shows 3-D contours for the instantaneous entropy perturbation s' after the unsteady computations are carried out for enough periods in time that periodic solutions have been reached in the entire flow field. The instantaneous contours show the development of wave modes in the boundary layer along the surface. Figure 4 also shows contours of streamwise velocity perturbation amplitudes in two cross sections along the major ($k = 1$) and minor ($k = 17$) axes. The upper and lower contours are those along the major and minor axis respectively. The amplitudes (and phase angles) of the perturbations are obtained by performing temporal FFT on perturbation variables. The local wave number can be obtained from the phase angle by $\alpha_r = |\frac{d\phi}{ds}|$, where ϕ is the phase angle, α_r is wave number, and s is the local surface length. The local wave speed can be calculated

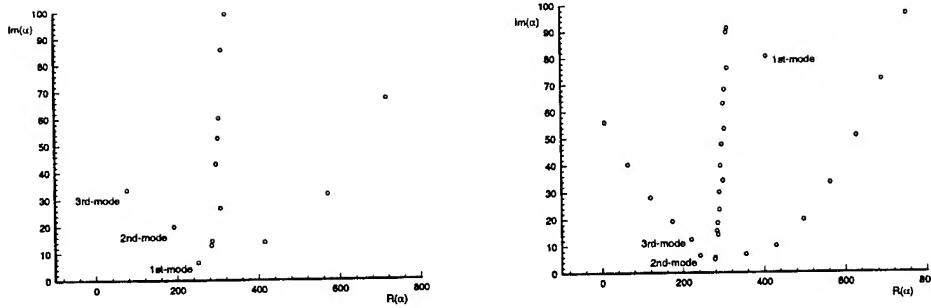


Figure 6. Dimensional eigenvalue spectra (in m^{-1}) of the complex wave number α in two mean flow sections at the major (left figure) and minor (right figure) axis at the $x = -0.36$ grid station.

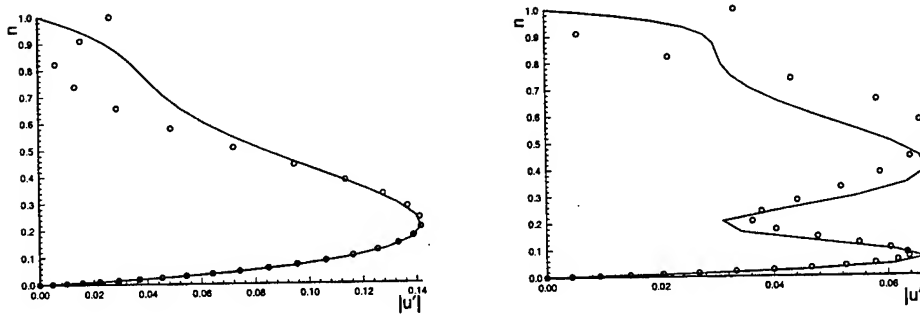


Figure 7. Distribution of streamwise velocity perturbation amplitudes along wall normal direction for $k = 1$ (left figure, line: LST first mode, circles: N-S results) and $k = 17$ (right figure, line: LST second mode, circles: N-S results) grid lines located at the $x = -0.36$ grid station.

by $c = \frac{\omega}{\alpha}$. Figure 5 shows the distribution of $|u'|$ amplitudes and local wave number α along the major and minor axes at a wall-parallel grid line near the wall surface ($j = 10$ grid line). Both Figs. 4 and 5 show that the velocity perturbation in the boundary layer develops a peak in amplitudes near the leading edge region. The peaks are the maximum induced strength of the first mode in the boundary layer. The freestream forcing waves enter the boundary layer and always generate first modes near the leading edge, which decay rapidly afterward to convert to second modes. The figures also show that the peaks of the first mode is reached earlier in the minor axis ($k = 17$) than the major axis ($k = 1$). This is due to the fact that the minor axis has a thicker boundary layer which develops a peak in $|u'|$ perturba-

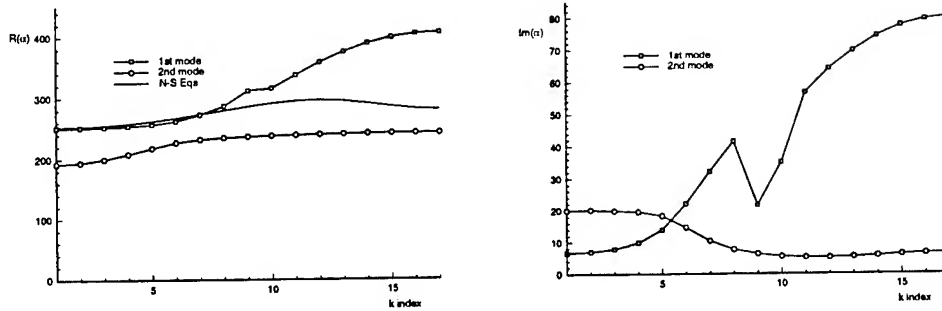


Figure 8. Distribution of real and imaginary part of the dimensional wave number α (in m^{-1}) along the circumferential k direction at the $x = -0.36$ grid station.

tions faster with a larger wave number. The larger wave number means slower wave speed in the minor axis.

The preceding picture of hypersonic receptivity near the leading edge can be further analyzed by comparisons with the first mode and second mode structure obtained by linear stability analysis for a perturbation in the form of $q' = |q'|e^{i(\alpha s - \omega t)}$, where ω is the frequency and α is the wave number. The mode structure induced by the freestream acoustic wave can be identified using a local normal-mode parallel stability analysis. The stability analysis is carried out at each local mean flow section using local parallel assumption. Spatial stability analysis is used by specifying the same frequency as those of the forcing ω using a global LST code. The stream-wise wave number $\alpha = \alpha_r + i\alpha_i$ are obtained as the eigenvalues in the analysis. The disturbances in the wall-normal direction are obtained as an eigenfunction.

Figure 6 shows dimensional eigenvalue spectra in two mean flow sections at the major and minor axis at the $x = -0.36$ grid station. The first and second modes are marked in the figure. The figure shows that in the major axis, the first modes are dominant modes with real part of wave number close to the freestream forcing wave number of $k = 240m^{-1}$. On the other hand, as the station moves to the the minor axis, the first modes develop a very large decay rate and much higher wave numbers than the forcing wave number k , while the second modes become less stable and has a wave number in resonance with the forcing frequency. Therefore, in the minor axis, the flow induced perturbations are dominated by the second mode structure while the first modes have a large decay rate. Figure 7 compares the perturbation amplitudes obtained by DNS with the eigenfunctions of the first modes in the major axis and the second modes in the minor axis.

The numerical solutions agree well with LST results in the boundary layer. The comparisons show indeed that the induced waves in the boundary layer are dominated by the first modes in the major axis, while the solutions have already developed a second mode structure in the minor axis. The comparison also shows that the numerical solutions capture the mode structure accurately in the boundary layer region.

Figure 8 shows the distribution of real and imaginary parts of the wave number α along the circumferential k direction at the $x = -0.36$ grid station. The local wave numbers of the numerical solutions compare well with linear stability results at the major axis and gradually convert to that of the second modes. The figure shows that the wave modes of the Navier-Stokes solutions develop from the first modes to the second modes along the wall while maintaining a relatively constant wave number and wave speed. The wave number of the Navier-Stokes solutions are roughly equal to that of the forcing wave number. Therefore, in the receptivity process, the least stable boundary layer instability modes having the closest wave number to the forcing wave number will interact with the forcing waves and be excited. The receptivity coefficient can be defined as the ratio of freestream perturbation magnitude versus the peak first mode amplitude. In this case it is found that the receptivity parameter is $\delta = 1.9\%$, which is very small.

7. Summary and Discussions

The leading-edge receptivity of 3-D hypersonic boundary layers to freestream acoustic disturbances has been studied by the numerical simulation of Mach 15 mean flows over a blunt 2:1 elliptical cone. Steady flow solution for Mach 15 flow over the 2:1 elliptical cone shows the secondary flow with inflection points created by the uneven strength of the bow shock.

Unsteady receptivity solutions are generated and analyzed for one test case of freestream planar acoustic waves. The results show that the receptivity of hypersonic boundary layers always generate first modes on the wall in the leading edge region. As the waves propagate downstream, the first modes reach a peak and decay rapidly. The perturbations then develop into second modes. The dominant modes, both first and second modes, excited in the boundary layer by the freestream forcing waves maintain relatively the same wave number α_r , corresponding to that of the freestream forcing waves. The first or second modes are selected when their wave numbers are very close that wave number corresponding to the forcing frequency due to a resonance interaction between the forcing wave and those of the instability waves. For the present flow conditions, the receptivity is weak with a receptivity parameter corresponding to the maximum first mode in

the range of 0.19 % for velocity perturbations.

Future work includes: parametric studies on the effects of Mach numbers, Reynolds numbers, wall cooling, nose bluntness, surface curvature, and the entropy layers on the receptivity; and comparisons of receptivity results with 3-D PSE calculations.

8. Acknowledgments

This research was supported by the Air Force Office of Scientific Research under grant number F49620-97-1-0030 monitored by Dr. Len Sakell.

References

- Buter, T. A. and Reed, H. L., Boundary Layer Receptivity to Free-Stream Vorticity, *Physics of Fluids*, Vol. 6, No. 10, 1994, pp. 3368-3379.
- Casalis, G. and Cantaloube, B., Receptivity by Direct Numerical Simulation, *Direct and Large-Eddy Simulation I*, Vol. P. R. Voke et al., editors, pp. 237-248, Kluwer Academic Publishers, 1994.
- Corke, T. C. and Haddad, O., Receptivity to sound on a parabolic leading edge, *In Transitional Boundary Layers in Aeronautics*, Vol. Edited by R.A.W.M. Henkes and J. L. van Ingen, pp. 403-412, North-Holland, Amsterdam, 1996.
- Fay, J. A. and Riddell, F. R., Theory of Stagnation Point Heat Transfer in Dissociated Air, *Journal of the Aeronautical Sciences*, Vol. 25, 1958, pp. 73-85.
- Goldstein, M. E. and Hultgren, L. S., Boundary-Layer Receptivity to Long-Wave Free-Stream Disturbances, *Annual Review of Fluid Mechanics*, Vol. 21, pp. 137-166 1989.
- Hayes, W. D., The vorticity jump across a gasdynamic discontinuity, *Journal of Fluid Mechanics*, Vol. 26, 1957, pp. 433-436.
- Lees, L. and Lin, C. C., Investigation of the Stability of the Laminar Boundary Layer in Compressible Fluid, *NACA TN No. 1115*, 1946.
- Lin, N., Reed, H. L., and Saric, W. S., Effect of Leading-Edge Geometry on Boundary-Layer Receptivity to Freestream Sound, *Instability, Transition, and Turbulence*, Vol. M. Y. Hussaini et al., editors, pp. 421-440, Springer-Verlag, 1992.
- Murdock, J. W., Tollmien-Schlichting Waves Generated by Unsteady Flow over Parabolic Cylinders, *AIAA paper 81-0199*, 1981.
- Saric, W. S., Reed, H. L., and Kerschen, E. J., Leading Edge Receptivity to Sound: Experiments, DNS, and Theory, *AIAA Paper 94-2222*, 1994.
- Zhong, X., Direct Numerical Simulation of Hypersonic Boundary-Layer Transition Over Blunt Leading Edges, Part I: New Numerical Methods and Validation (Invited), *AIAA paper 97-0755*, 1997.
- Zhong, X., Direct Numerical Simulation of Hypersonic Boundary-Layer Transition Over Blunt Leading Edges, Part II: Receptivity to Sound (Invited), *AIAA paper 97-0756*, January 1997.
- Zhong, X., High-Order Finite-Difference Schemes for Numerical Simulation of Hypersonic Boundary-Layer Transition, *Journal of Computational Physics*, Vol. 144, August 1998, pp. 662-709.
- Zhong, X. and Dong, H., Hypersonic Boundary-Layer Receptivity to Freestream Disturbances Over an Elliptic Cross-Section Cone, *AIAA paper 99-0409*, 1999.

SCIENTIFIC ORGANIZING COMMITTEE

Knut Bech	SINTEF (Norway)
Carlo Benocci	Von Karman Institute (Belgium)
Sedat Biringen	University of Colorado
Ken Bray	Cambridge University (United Kingdom)
Joel Ferziger	Stanford University
Rainer Friedrich	Technische Universitaet Muenchen (Germany)
Tom Gatski	NASA Langley Research Center
Fernando Grinstein	US Naval Research Laboratory
Ken Jansen	Rensselaer Polytechnic Institute
Arne Johansson	KTH (Sweden)
George Karniadakis	Brown University
Doyle Knight	Rutgers - The State University of New Jersey
Marcel Lesieur	L.E.G.I. (France)
Chaoqun Liu	Louisiana Tech
Suresh Menon	Georgia Tech
Yutaka Miyake	Osaka University (Japan)
Ugo Piomelli	University of Maryland
Wolfgang Rodi	Universitaet Karlsruhe (Germany)
Len Sakell	AFOSR
Kyle Squires	Arizona State University
Zhaoshun Zhang	Tsinghua University (People's Republic of China)

LOCAL ORGANIZING COMMITTEE

Omar Besbes
Boris Chernyavsky
Gerald Carrier
Yuri Gulak
Doyle Knight
Sophia Lefantzi
Min Li
Helene Press
Frederic Thivet
Gerald Urbin
Weili Zhang

CONFERENCE PARTICIPANTS

Krister Alvelius
Department of Mechanics
KTH, SE-100 44 Stockholm
Sweden
Tel: 46-8-7907195
Fax: 46-8-7969850
Email: kristera@mech.kth.se

Juan H. Agui
The City College of New York
Department of Mechanical Engineering
140 St and Convent Ave
New York, NY 10031, USA
Tel: 212-650-6706
Fax: 212-650-8013
Email: agu4841@me-mail.engr.ccny.cuny.edu

Yiannis Andreopoulos
Department of Mechanical Engineering
City College of New York
New York, NY 10031, USA
Tel: 212-650-5206
Fax: 212-650-8013
Email: andre@me-mail.engr.ccny.cuny.edu

Omar Besbes
Residence Omar El Khayam, rue 7311
El Menzah IX B, 1004 Tunis, Tunisia

Thomas J. Beutner
AFOSR/NA, 801 N. Randolph Street
Arlington, VA 22203-1977, USA
Tel: 703-696-6961
Fax: 703-696-8451
Email: tom.beutner@afosr.af.mil

Gregory A. Blaisdell
School of Aeronautics and Astronautics
Purdue University, 1282 Grissom Hall
West Lafayette, IN 47907-1282, USA
Tel: 765-494-1490
Fax: 765-494-0307
Email: blaisdel@ecn.purdue.edu

Laurent Blin
LMFN/CORIA, UMR 6614, INSA
Avenue de l' Universite -BP 8-76801
St Etienne du Rouvray Cedex, France
Tel: 33-2-32-95-98-15
Fax: 33-2-32-95-97-80
Email: blin@coria.fr

Rene van Buuren
Meteorenstraat 34
7521 XR Enschede, The Netherlands
Tel: 31-53-4894030
Fax: 31-53-4894888
Email: r.vanbuuren@math.utwente.nl

Xiaodan Cai
Aerospace Research Corp.
Long Island, USA
Tel: 516-632-5777
Fax: 516-632-5765
Email: cai@thaerocomp.com

Graham Candler
University of Minnesota
110 Union Street SE
Minneapolis, MN 55455, USA
Tel: 612-625-2364
Fax: 612-626-1558
Email: candler@aem.umn.edu

Gerald Carrier
Dept of Mech and Aero Engineering
Rutgers University
98 Brett Road
Piscataway, NJ 08854-8058, USA
Tel: 732-445-4351
Fax: 732-445-3124
Email: carrierg@jove.rutgers.edu

Scott Collis
6100 Main St., MS 321
Houston, TX 77005, USA
Tel: 713-527-8101
Fax: 713-285-5423
Email: collis@rice.edu

Julian Andrzej Domaradzki
Aero and Mech Engineering
University of Southern California
Los Angeles, CA 90089-1191, USA
Tel: 213-740-5357
Fax: 213-740-7774
Email: jad@spock.usc.edu

Gregory S. Elliott
Dept of Mech and Aero Engineering
Rutgers University
98 Brett Road
Piscataway, NJ 08854-8058, USA
Tel: 732-445-3282
Fax: 732-445-3124
Email: gelliott@jove.rutgers.edu

James Flanagan
Center for Computer Aids
Rutgers University, CAIP
96 Frelinghuysen Road
706 CoRE Building
Piscataway, NJ 08854, USA
Tel: 732-445-3443
Fax: 732-445-0547
Email: jlf@caip.rutgers.edu

Boris Chernyavsky
Dept of Mech and Aero Engineering
Rutgers University
98 Brett Road
Piscataway, NJ 08854-8058, USA
Tel: 732-445-4351
Fax: 732-445-3124
Email: bchern@jove.rutgers.edu

Pierre Comte
LEGI, BP 53 F38041
Grenoble Cedex 9, France
Tel: 33-(0)-476825121
Fax: 33-(0)-476825271
Email: Pierre.Comte@hmg.inpg.fr

Cornelus H. Driesen
Nicolaas van Catsweg 20, 3411 EH
Lopic-Cabaun
The Netherlands
Tel: 31-53-4894030
Fax: 31-53-4894030
Email: c.h.driesen@math.utwente.nl

Brijesh Eshpuniyani
School of Aeronautics and Astronautics
Purdue University
1282 Grissom Hall
West Lafayette, IN 47907-1282, USA
Tel: 765-494-7864
Fax: 765-494-0307
Email: Eshpuniy@ecn.purdue.edu

John F. Foss
National Science Foundation
CTS Div., Room 525
4201 Wilson Blvd.
Arlington, VA 22230, USA
Tel: 703-306-1371
Fax: 703-306-0319
Email: jfoss@nsf.gov

Rainer Friedrich
Lehrstuhl für Fluidmechanik
Technische Universität München
Arcisstr. 21, D-8000
München, Germany
Fax: 49-89-28916145
Email: r.friedrich@lrz.tu-muenchen.de

Sean C. Garrick
Department of Mechanical Engineering
University of Minnesota
11 Church Street S.E.
Minneapolis, MN 55455-0111, USA
Tel: 612-624-5741
Fax: 612-624-5230
Email: garrick@me.umn.edu

Karman N. Ghia
Department of Aerospace Eng.
and Engineering Mechanics
University of Cincinnati
PO Box 210070
Cincinnati, OH 45221-0070, USA
Tel: 513-556-3243
Fax: 513-556-5038
Email: kghia@cfdrl.uc.edu

Minwei Grong
502 West 141 St., Apt. 3B
New York, NY 10031, USA
Tel: 212-650-8464
Fax: 212-650-8134
Email: gon3795@me-mail.engr.ccny.cuny.edu

Yuriy Gulak
Dept of Mech and Aero Engineering
Rutgers University
98 Brett Road
Piscataway, NJ 08854-8058, USA
Tel: 732-445-5850
Fax: 732-445-3124
Email: ygulak@rci.rutgers.edu

Kiyosi Horiuti
Department of Mechano-Aerospace Eng
Tokyo Institute of Technology
2-12-1 O-okayama Meguro-ku
Tokyo 152 Japan
Tel: 81-3-5734-2638
Fax: 81-3-5734-3982
Email: khoriuti@mes.titech.ac.jp

Osamu Inoue
Institute of Fluid Science
Tohoku University
2-1-1 Katahira Aoba-ku
Sendai 980, Japan
Fax: 81-2-2217-5311
Email: inoue@ifs.tohoku.ac.jp

Kenneth Jansen
Rensselaer Polytechnic Institute
110 8th St
Troy NY 12180, USA
Tel: 518-276-6755
Fax: 518-276-6025
Email: jansen@rpi.edu

Karl W. Jenkins
CFD Laboratory, Engineering Dept
Cambridge University
Trumpington Street
Cambridge, CB2 1PZ, UK
Tel: 44-(0)-1223-332748
Fax: 44-(0)-1223-332662
Email: kwj20@eng.cam.ac.uk

Li Jiang
College of Engineering and Science
Campus Box 10, PO Box 10348, CTH 128
Louisiana Tech. University
Ruston, LA 71272-0001, USA
Email: ljiang@engr.latech.edu

Takeo Kajishima	George-Sosei Karamanos
Department of Mechanical Engineering	Brown University
Osaka University, 2-1 Yamadaoka, Suita	Center of Fluid Mechanics
Osaka, 565-0871, Japan	Providence, RI 02912, USA
Tel: 81-6-6879-7249	Tel: 401-863-3694
Fax: 81-6-6879-7250	Email: gkaram@cfm.brown.edu
Email: kajisima@mech.eng.osaka-u.ac.jp	

George Karniadakis	Doyle D. Knight
Division of Applied Mathematics	Dept of Mech and Aero Eng
Brown University	Rutgers University
Providence, RI 02912, USA	98 Brett Road
Tel: 401-863-1217	Piscataway, NJ 08854-8058, USA
Fax: 401-863-3369	Tel: 732-445-4464
Email: gk@cfm.brown.edu	Fax: 732-445-3124
	Email: knight@jove.rutgers.edu

Hans Kuerten	Foluso Ladeinde
Dept of Mechanical Engineering	Aerospace Research Corp
Eindhoven University of Technology	Long Island, USA
PO Box 513, 5600 MB Eindhoven	Tel: 516-632-8816
The Netherlands	Fax: 516-632-5765
Tel: 31-(0)-40-2472362	Email: ladeinde@mech.eng.sunysb.edu
Fax: 31-(0)-40-2475399	
Email: j.g.m.kuerten@wtb.tue.nl	

Sophia N. Lefantzi	Min Li
Dept of Mech and Aero Engineering	Dept of Mech and Aero Engineering
Rutgers University	Rutgers University
98 Brett Road	98 Brett Road
Piscataway, NJ 08854-8058, USA	Piscataway, NJ 08854-8058, USA
Tel: 732-445-4351	Tel: 732-445-4351
Fax: 732-445-3124	Fax: 732-445-3124
Email: lefantzi@jove.rutgers.edu	Email: limin@jove.rutgers.edu

Chaoqun Liu	Pino Martin
College of Engineering and Science	1400 South Second Street, No. 3305
Campus Box 10	Minneapolis, MN 55454, USA
PO Box 10348, CTH 128	Tel: 612-626-8082
Louisiana Tech. University	Email: pino@aem.umn.edu
Ruston, LA 71272-0001, USA	
Tel: 318-257-2257	
Fax: 318-257-3823	
Email: cliu@engr.latech.edu	

Andres Tejada Martinez
Dept of Mech, Aero Eng
and Mechanics
Rensselaer Polytechnic Institute
110 8th Street
Troy, NY, USA
Tel: 518-276-6904
Email: tejada@rpi.edu

Charles Meneveau
Department of Mechanical Engineering
The Johns Hopkins University
3400 N. Charles Street
Baltimore, MD 21218, USA
Tel: 410-516-7802
Fax: 410-516-7254
Email: meneveau@jhu.edu

Suresh Menon
School of Aerospace Eng.
Georgia Inst of Tech
Atlanta, GA 30332, USA
Tel: 404-894-9126
Fax: 404-894-2760
Email:
suresh.menon@aerospace.gatech.edu

Su Mingde
Department of Engineering Mechanics
Tsinghua University
Beijing 100084, PR China
Tel: 86-10-62785103
Fax: 86-10-62785103
Email: sumd@tsinghua.edu.cn

Brian E. Mitchell
GE Corporate R&D, Bldg K1
Room ES203, PO Box 8
Schenectady, NY 12301, USA
Tel: 518-387-7845
Fax: 518-387-7104
Email: mitchellb@crd.ge.com

Yutaka Miyake
2-1 Yamada-oka
Suita, 565-0871, Japan
Tel: 81-6-6879-7248
Fax: 81-6-6879-7250
Email: miyake@mech.eng.osaka-univ.ac.jp

Robert Moser
Dept of Theo and Applied Mechanics
University of Illinois
104 South Wright Street
Urbana, IL 61801, USA
Fax: 217-244-5707
Email: r-moser@uiuc.edu

Farouk Owis
241 Kaufmann Daukworth Hall
Aerospace Engineering Dept
Old Dominion University
Norfolk, VA 23529, USA
Tel: 757-489-2250
Fax: 757-683-3200
Email: owis@aero.odu.edu

Jean Marc Pace
Commissariat a l' Energie Atomique
BP 12, 91680 Bruyeres-le-Chatel
France
Tel: 33-(1)-69-264888
jeanmarc.pace@cea.bruyeres.fr

Garry Pantelis
ANSTO, PMB 1 Menai, NSW
2234, Australia
Tel: 61-2-97173056
Fax: 61-2-97179273
Email: gpa@ansto.gov.au

Andrea Pascarelli
Department of Mechanical Engineering
University of Maryland
College Park, MD 20742, USA
Tel: 301-405-4311
Fax: 301-314-9477
Email: pandrea@eng.umd.edu

Richard Pelz
Dept of Mech and Aero Engineering
Rutgers University
98 Brett Road
Piscataway, N.J, 08854-8058, USA
Tel: 732-445-3653
Fax: 732-445-3124
Email: pelz@jove.rutgers.edu

Dave Pruett
James Madison University
Department of Mathematics
Harrisonburg, VA 22807, USA
Tel: 540-568-6227
Fax: 540-568-6857
Email: dpruett@math.jmu.edu

James J. Riley
Department of Mechanical Engineering
University of Washington
Box 352600
Seattle, WA 98195, USA
Fax: 206-685-8047
Email: rileyj@u.washington.edu

Hua Shan
Louisiana Tech. University
CTH-132, CNSM
PO Box 10348
Ruston, LA 71272, USA
Tel: 318-257-2311
Fax: 318-257-3823
Email: hshan@engr.latech.edu

Vijay Shukla
Dept of Mech and Aero Engineering
Rutgers University
98 Brett Road
Piscataway, NJ 08854-8058, USA
Tel: 732-445-4351
Fax: 732-445-3124
Email: vishukla@jove.rutgers.edu

Erwin Simons
Von Karman Inst. for Fluid Dynamics
Waterloose steenweg 72, B-1640
Sint-Genese, Belgium
Tel: 32-2-3599611
Fax: 32-2-3599600
Email: simons@vki.ac.be

Martin Skote
Department of Mechanics, KTH
S-100 44 Stockholm
Sweden
Tel: 46-8-7907161
Fax: 46-8-7907577
Email: mskote@mech.kth.se

Rene Steijl
Dept of Mechanical Engineering
University of Twente
PO Box 217
7500 AE Enschede
The Netherlands
Tel: 31-(0)-53-489-3550
Fax: 31-(0)-53-489-3695
Email: rsteijl@wb.utwente.nl

Christopher Tam
Department of Mathematics
Florida State University
Tallahassee, FL 32306-4510, USA
Tel: 850-644-2455
Fax: 850-644-4053
Email: tam@math.fsu.edu

Frederic Thivet
Dept of Mech and Aero Engineering
Rutgers University
98 Brett Road
Piscataway, NJ 08854-8058, USA
Tel: 732-445-6668
Fax: 732-445-3124
Email: thivet@cert.fr

Makoto Tsubokura
Tokyo Institute of Technology
Tokyo 152 Japan
Tel: 81-45-924-5558
Fax: 81-45-924-5516
Email: tsubo@depe.titech.ac.jp

Gerald Urbin
Dept of Mech and Aero Engineering
Rutgers University
98 Brett Road
Piscataway, N.J, 08854-8058, USA
Tel: 732-445-4351
Fax: 732-445-3124
Email: urbin@jove.rutgers.edu

Tobias Voelkl
M/C 301-46
California Institute of Technology
Pasadena, CA 91125, USA
Tel: 626-395-4455
Fax: 626-449-2677
Email: tobias@galcit.caltech.edu

Chong W. Whang
Mech and Aero Engineering Dept
University of California at Los Angeles
Engineering IV Building
420 Westwood Plaza
Los Angeles, CA 90095-1597, USA
Tel: 310-825-5614k
Fax: 310-206-4830
Email: chong@seas.ucla.edu

Theo Treurniet
Laboratory for Aero and Hydrodynamics
Rotterdamseweg 145
2826 AL Delft
The Netherlands
Tel: 31-15-278-2861
Fax: 31-15-278-2947
Email: T.C.Treurniet@wbmt.tudelft.nl

Mayank Tyagi
2508 CEBA Bldg.
Mechanical Engineering Department
Louisiana State University
Baton Rouge, LA 70803, USA
Tel: 225-388-5217
Fax: 225-334-6989
Email: mtyagi@surya.me.lsu.edu

Luc Vervisch
CORIA-CNRS-INSA de Rouen
France
Tel: 33-2-32-95-97-85 (82)
Fax: 33-2-32-95-97-80
Email: vervisch@coria.fr

Stefan Volker
Dept of Theo and Applied Mechanics
University of Illinois
104 S Wright St
Urgana, IL 61801
Tel: 217-333-3578
Fax: 217-244-5707
Email: volker@uiuc.edu

Zhexuan Wang
285 Fort Washington Ave., No. 37,
New York, NY 10032, USA
Tel: 712-781-9515
Email: wangzx@ns.ustcer.com

Abdelfattah Zebib
Dept of Mech and Aero Engineering
Rutgers University
98 Brett Road
Piscataway, NJ 08854-8058, USA
Tel: 732-445-2248
Fax: 732-445-3124
Email: zebib@jove.rutgers.edu

Wei-Li Zhang
Dept of Mech and Aero Engineering
Rutgers University
98 Brett Road
Piscataway, NJ 08854-8058, USA
Tel: 732-445-4351
Fax: 732-445-3124
Email: zhangw@jove.rutgers.edu

Zhaoshun Zhang
Dept of Engineering Mechanics
Tsinghua University
Beijing 100084, PR China
Tel: 86-10-62785551
Fax: 86-10-62788789
Email: demzss@mail.tsinghua.edu.cn

Xiaolin Zhong
Mech and Aero Engineering Dept
University of California at Los Angeles
46-147C Engineering IV Building
420 Westwood Plaza
Los Angeles, CA 90095-1597, USA
Tel: 310-825-2905
Fax: 310-206-4830
Email: xiaolin@seas.ucla.edu